Dissecting the Dynamics of DNA Methyltransferase 1 and Related Nuclear Proteins in Living Cells

Katrin Schneider

München 2014

Dissecting the Dynamics of DNA Methyltransferase 1 and Related Nuclear Proteins in Living Cells

Dissertation
an der Fakultät für Biologie
der Ludwig-Maximilians-Universität München

vorgelegt von
Katrin Monika Schneider
aus München

München, den 30. April 2014

Erstgutachter:	Prof. Dr. Heinrich Leonhardt
Zweitgutachter:	PD Dr. Steffen Dietzel
Tag der Abgabe:	30. April 2014
Tag der mündlichen Prüfung:	24. Juni 2014

Content

Summary

DNA methylation is an indispensable process during development and maintaining the DNA methylation pattern after DNA replication is crucial for proper cellular function in mammals. Misregulation of this process is involved in cancer formation. The key protein is the maintenance DNA methyltransferase 1 (Dnmt1), an essential epigenetic factor that reestablishes methylation of hemimethylated CpG sites generated during DNA replication in S phase. Two domains of Dnmt1, the proliferating cell nuclear antigen (PCNA) binding domain (PBD) and the targeting sequence (TS) domain are responsible for targeting the enzyme to replication sites and to constitutive heterochromatin. However, their cell cycle-dependent coordinated action and regulation are still unclear. In order to understand the regulation of Dnmt1 as well as other nuclear factors, they have to be studied not only *in vitro*, but also under dynamic *in vivo* conditions. Advanced fluorescence microscopy offers a variety of methods, to gain insights into epigenetic regulation *in vivo*.

Therefore, we set out to dissect the cell cycle-dependent dynamics of Dnmt1. In our approach, we combined fluorescence recovery after photobleaching (FRAP) with kinetic modeling, complemented by 3D-structured illumination microscopy, which allowed us to obtain detailed information about the spatio-temporal dynamics of Dnmt1 and its regulation. By analyzing GFP-Dnmt1 mutants, we showed that both the PBD- and the TS domain-mediated interactions are necessary and sufficient for the localization and the dynamics of Dnmt1 in S phase. Based on our customized kinetic model, we estimated an average target binding time for the PBD to PCNA and the TS domain to constitutive heterochromatin of about 10 s and 22 s, respectively. Altogether, we propose a two-loading-platform model, in which PCNA and heterochromatin function as relatively immobile platforms during S phase. In early S phase, binding of the PBD to PCNA predominates. In late S phase, the heterochromatic marks, the TS domain binds to, are in close proximity to replication sites, leading to a strong TS domain-mediated interaction that dominates the Dnmt1 dynamics in late S phase.

Furthermore, fluorescent microscopy and biochemical methods enabled us to further investigate the proteins Uhrf (ubiquitin-like, containing PHD and RING finger domains) 1, an essential factor for maintenance methylation *in vivo*, its homologue Uhrf2 and the histone variant H2A.Z, exemplifying another level of epigenetic regulation. We demonstrated, for example, that an alternative splice variant of H2A.Z, H2A.Z.2.2, severely destabilizes nucleosomes and that Uhrf2 dynamics depend on the methylation of H3K9. Emphasizing the methodological aspect of this work, it should be mentioned that we could also develop new strategies to label DNA sequences in living cells, characterize nanoparticles as vectors for nucleic acids and reveal hidden interactions of the cell cycle regulator nuclear interaction partner of anaplastic lymphoma kinase (NIPA). The continuous integration of microscopy developments in biological research will help in the future to dissect nuclear regulatory networks *in vivo*.

Zusammenfassung

DNA-Methylierung ist ein essentieller Vorgang während der Entwicklung und die Erhaltung der DNA-Methylierungsprofile ist äußerst wichtig für die korrekte Funktion der Zellen in Säugern. Die fehlerhafte Regulation dieses Vorgangs kann zur Entstehung von Krebs führen. Das entscheidende Protein ist die DNA-Methyltransferase 1 (Dnmt1), ein essentielles Protein, das die Methylierung an hemimethylierten CpG-Stellen nach der Replikation in der S Phase wiederherstellt. Zwei Dnmt1 Domänen, die „proliferating cell nuclear antigen (PCNA) binding domain“ (PBD) und die „targeting sequence“ (TS) Domäne, sind verantwortlich dafür, dass Dnmt1 gezielt an Replikationsstellen und an konstitutives Heterochromatin gebunden wird. Allerdings ist die zellzyklusabhängige Funktionsweise und Regulation der Interaktionen immer noch unbekannt. Um die Regulation von Dnmt1 und anderen Faktoren im Kern zu verstehen, müssen deren Interaktionen nicht nur *in vitro*, sondern auch unter dynamischen *in vivo* Bedingungen untersucht werden. Moderne Fluoreszenzmikroskopie bietet eine Auswahl von Methoden, die uns erlauben *in vivo* Einblicke in die epigenetische Regulation zu erhalten.

Aus diesem Grund haben wir begonnen die zellzyklusabhängige Dynamik von Dnmt1 zu analysieren. In unserem Ansatz haben wir die Methode „fluorescence recovery after photobleaching” (FRAP) mit kinetischen Modellen kombiniert und „3D-structured illumination microscopy“ ergänzend angewandt. Dieser Ansatz ermöglicht es detaillierte räumliche und zeitliche Informationen über die Dynamik von Dnmt1 und deren Regulation zu erhalten. Durch die Analyse von GFP-Dnmt1 Mutanten konnten wir zeigen, dass die Interaktionen, die durch die PBD und die TS Domäne vermittelt werden, sowohl notwendig, als auch ausreichend sind für die Lokalisation und die Dynamik von Dnmt1 in der S Phase. Mit Hilfe unseres maßgeschneiderten kinetischen Models konnten wir eine mittlere Interaktionszeit für die PBD mit PCNA von etwa 10 s und von der TS Domäne mit konstitutivem Heterochromatin von etwa 22 s ermitteln. Aufgrund dieser Ergebnisse stellen wir ein „two-loading-platform“ Modell auf, in dem PCNA und Heterochromatin als relativ stabile Plattformen während der S Phase betrachtet werden. In der frühen S Phase überwiegt die Bindung der PBD an PCNA. In der späten S Phase hingegen sind spezifischen Heterochromatin Bindestellen, an die die TS Domäne bindet, nahe der replizierenden Regionen. Dies führt zu einer starken Bindung, vermittelt durch die TS Domäne, die die Dnmt1 Dynamik in der späten S Phase dominiert.

Darüber hinaus haben wir durch Fluoreszenzmikroskopie und biochemische Methoden ein tieferes Verständnis über die Funktion der Proteine Uhrf (“ubiquitin-like, containing PHD and RING finger domains“) 1, ein essentieller Faktor für die Aufrechterhaltung der DNA Methylierung, das homologe Protein Uhrf2 und der Histonvariante H2A.Z, beispielhaft für ein weiteres Level der epigenetischen Regulation, erhalten. Wir konnten zum Beispiel zeigen, dass eine alternative Splicevariante von H2A.Z, H2A.Z.2.2, Nukleosomen stark destabilisiert und dass die Uhrf2 Dynamik von der Methylierung von H3K9 abhängt. Der methodischen Aspekt dieser Arbeit wird außerdem durch die Entwicklung neuer

Strategien für die Markierung von DNA-Sequenzen in lebenden Zellen, die Charakterisierung von Nanopartikel als Vektoren für Nukleinsäuren und die Aufdeckung versteckter Interaktionen des Zellzyklusregulators „nuclear interaction partner of anaplastic lymphoma kinase“ (NIPA) betont. Der kontiniuierliche Transfer neuer Entwicklungen aus der Mikroskopie in die biologische Forschung wird uns in Zukunft behilflich sein *in vivo* die regulatorischen Netzwerke im Zellkern aufzuklären.

1. Introduction

1.1 Epigenetics

Every human being develops from a single totipotent cell. The DNA sequence within this cell is replicated during each cell division leading to almost identical genetic information in all somatic cells of the body. However, our adult body consists of over 400 different cell types with diverse functions and morphology (Vickaryous and Hall, 2006). This large diversity is generated by cell type specific regulation of gene expression. Heritable information that directs these regulatory processes, but is not encoded in the DNA sequence, is summarized under the term epigenetics (epi, Greek: *επί*- over, above, outer). Epigenetic processes do not only play a major role in differentiation and development, but are also involved in cellular aging and the development of cancer (Hannum et al., 2013, Dawson and Kouzarides, 2012). Moreover, multiple diseases, apart from cancer, are linked to epigenetic factors and processes. Examples are single gene disorders, caused by mutations in genes coding for epigenetic factors, including the Rett syndrome or the ATRX syndrome (Feinberg, 2007). In addition, imprinted gene disorders are linked to epigenetics. Genomic imprinting describes the selective repression of either the paternally or maternally inherited allele by epigenetic mechanisms (Morison et al., 2005). Epigenetic alterations in genes or their control regions can lead to diseases, e.g. the Beckwith-Wiedemann Syndrome (Choufani et al., 2013). Recently, even common complex diseases like rheumatoid arthritis or epilepsy have been discussed in connection with epigenetics (Liu et al., 2013b, Qureshi and Mehler, 2010).

The classical definition of epigenetics reads: “The study of mitotically and/or meiotically heritable changes in gene function that cannot be explained by changes in DNA sequence” (Russo et al., 1996). This includes many diverse processes like the DNA methylation system, histone modifications, histone variants, nucleosome positioning and non-coding RNA (Figure 1). Accordingly, prions are included in this definition, as they are proteins that pass on their changes that are not based on DNA sequence (Halfmann and Lindquist, 2010). In addition to the modified DNA base 5-methylcytosin (5mC) the new DNA modifications 5-hydroxymethylcytosin (5hmC), 5-formylcytosin (5fC) and 5-carboxcytosin (5caC) have recently been discovered, forming a complex DNA modification system (Figure 1). Some of the epigenetic marks occur only for short time frames during the cell cycle and are therefore not classically heritable. Hence, a recent definition has shifted the focus more to chromatin structure: “… the structural adaptation of chromosomal regions so as to register, signal or perpetuate altered activity states.” (Bird, 2007). This chromatin structure-based definition paints a much more dynamic picture of the epigenetic landscape that will be the major focus in this thesis.

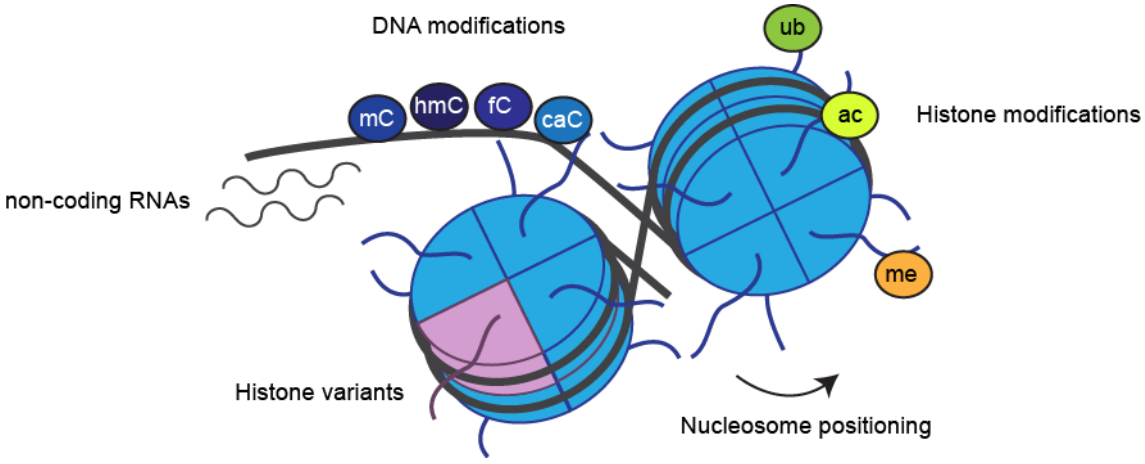

Figure 1: Epigenetic mechanisms. DNA can be methylated (mC), further oxidized to hmC, fC and caC or transcribed to non-coding RNA. Further epigenetic mechanisms are nucleosome positioning, incorporation of histone variants or posttranslational modification of histones, e.g. methylation (me), acetylation (ac) or ubiquitination (ub).

Chromatin structure and organization

The structural basis of chromatin is a chain of basic single building units, called nucleosomes. In each nucleosome, 145-147 base pairs of DNA are wrapped around a histone octamer, consisting of two histone 2A and histone 2B dimers (H2A-H2B) and a tetramer built up of two histone 3 and histone 4 dimers $(H3\text{-}H4)_2$ (Luger et al., 1997). The resulting 11 nm fiber is further compacted to the 30 nm fiber involving the linker histone H1 (Li and Reinberg, 2011), however, the presence of the 30 nm fiber *in vivo* is highly debated and details about the higher order chromatin structure still need to be investigated (Maeshima et al., 2010). In general, interphase chromatin is subdivided into open, transcriptionally active euchromatin and condensed, transcriptionally inactive heterochromatin (Politz et al., 2013). It has been proposed that euchromatic fibers harbor six nucleosomes per 11 nm, whereas the compaction increases in heterochromatin to a packing density of 11-12 nucleosomes per 11 nm (Bassett et al., 2009). Furthermore, heterochromatin can be subdivided into constitutive and facultative heterochromatin. Both describe silent and compacted chromatin, but only facultative heterochromatin has the potential to switch to a more euchromatic state (Trojer and Reinberg, 2007). Constitutive heterochromatin is found at the telomeres, the centromere and at pericentromeric regions, all composed of DNA tandem repeats (Politz et al., 2013). In mouse cells, the centromeric region and the pericentromeric region mainly consist of minor satellite DNA and major satellite DNA, respectively (Probst and Almouzni, 2011). Not only the degree of packaging, but also the localization of chromatin domains in the nucleus affects gene expression. As a general rule, the chromatin at the nuclear periphery and around the nucleoli is rather gene poor and composed of silent heterochromatin, whereas the area in between is gene rich and composed of active euchromatin (Joffe et al., 2010). Prominent heterochromatic structures in mouse cells are the so-called chromocenters. In chromocenters, the pericentromeric regions of multiple chromosomes form tightly packed foci in the nucleus. The number and localization of chromocenters differs among cell types and

species and the clustering of heterochromatic domains could facilitate repression of repetitive sequence recombination and transposon silencing (Padeken and Heun, 2013, Cerda et al., 1999).

Nucleosomal modifications and positioning

Epigenetic mechanisms can change the higher order chromatin structure and thereby directly influence, for example, the accessibility of the DNA to transcription factors. Direct structural changes are created by altered charges, which form internucleosomal or intranucleosomal links. Modifications of the N-terminal tails of histones, or of the histone core are able to induce structural changes. Histones can be methylated, acetylated, phosphorylated, ubiquitinated, sumoylated, ADP-ribosylated or deiminated, amongst others (Kouzarides, 2007). For instance, acetylation of lysines neutralizes the positive charges of the histones and loosens the DNA-histone interaction in the nucleosome (Zentner and Henikoff, 2013, Shogren-Knaak et al., 2006). Combinations of histone modifications, often referred to as a histone code, can change chromatin structure to a larger extend by facilitating nucleosome sliding or repositioning (Cosgrove et al., 2004). Insertion, movement or removal of nucleosomes is carried out by so-called nucleosome remodelers. This process has been documented at the transcriptional start site resulting in nucleosome free regions (Zhang et al., 2011). Another mechanism to functionally alter chromatin structure is the incorporation of histone variants, which is further explained in chapter 1.3. Furthermore, some histone variants are differently modified at their N-terminal ends in contrast to the canonical histones, thus creating specific modifications with a potential impact on chromatin structure (Luger, 2006). Finally, there are indications that DNA methylation exerts a direct effect on nucleosome stability (Collings et al., 2013, Lee and Lee, 2012).

Epigenetic readers, writers and erasers

Histone modifications or DNA methylation can also indirectly influence chromatin structure and gene expression by activating or inactivating other proteins or pathways. In this case, the modifications act as signals for specific epigenetic reader proteins. These readers then recruit writers or erasers, establishing or removing new regulatory marks that directly change chromatin structure or trigger signaling cascades (Figure 2). Often, multiple epigenetic mechanisms act together within the regulatory networks. The establishment of heterochromatic sequences at pericentromeric heterochromatin in early development, for example, has been reported to require the interplay of non-coding RNA, histone modifications (H3K9me3) and DNA methylation (Cedar and Bergman, 2009).

The role of epigenetic marks in signaling is especially interesting in the field of DNA methylation, as a whole new set of modifications and their writers, readers and erasers have been recently identified, which are further discussed in the next chapter. This discovery has raised many exiting questions and strengthens the importance of this research field.

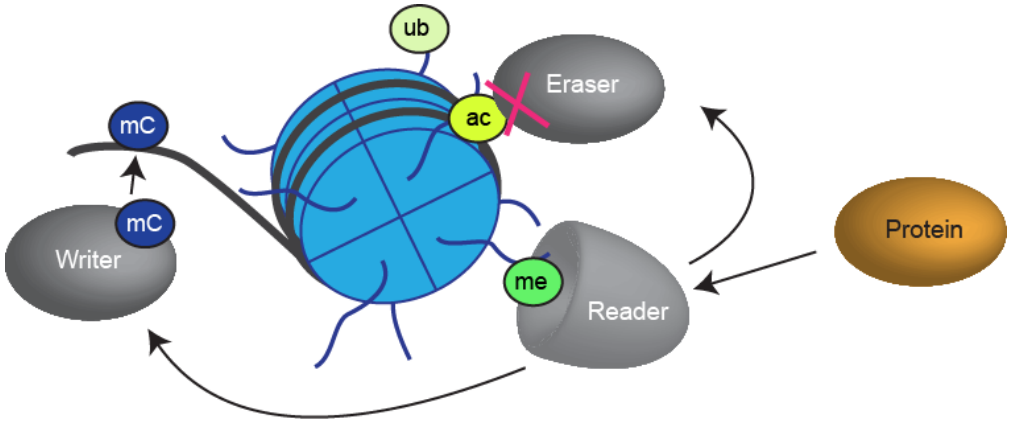

Figure 2: Readers, writers and erasers of epigenetic modifications. DNA or histone modifications have to be established and maintained by writers and can be removed by erasers. In order to lead to a functional output, the marks have to be identified by specific readers that process these signals and activate or inactivate other proteins or pathways.

1.2 DNA methylation

DNA methylation is present in most species, including fungi, plants and animals. Interestingly, many model organisms like *Drosophila melanogaster*, *Saccharomyces cerevisiae*, *Saccharomyces pombe* and *Caenorhabditis elegans* have no or only low DNA methylation levels (Feng et al., 2010, Zemach et al., 2010). In mammals, methylation of position 5 of cytosine (5mC) in a cytosine-phosphatidyl-guanine (CpG) context is the predominant DNA modification. Nevertheless, in embryonic stem cells (ESC) significant methylation levels in a CpA context have been detected (Ziller et al., 2011, Ramsahoye et al., 2000, Lister et al., 2009). In plants, methylation is found in many contexts, such as CG, CNG (N = A,C,T,G) and CHH (H= A, C, T) (Henderson and Jacobsen, 2007).

In the mammalian genome, CpG sites are underrepresented possibly due to mutagenic pressure as 5mC can be deaminated to thymidine, but a majority of 60-80% of these rare CpG sites are methylated (Smith and Meissner, 2013). Interestingly, DNA regions with a high density of CpG sites, called CpG islands are predominantly unmethylated (Bird et al., 1985). CpG islands are often located in promoters of housekeeping genes or genes that are regulated during development (Meissner et al., 2008). The high CG content due to the CpG density might facilitate their transcription (Moore et al., 2013). In contrast, methylation of CpG islands leads to stable silencing of the associated genes. However, the majority of CpG islands stays hypomethylated during development, whereas hypermethylation can be detected in cancer or aging (Richardson, 2003). Especially, CpG islands in promoter regions do not seem to play a role in tissue specific methylation. Tissue specific methylation rather correlates with the methylation status of CpG islands outside of promoter regions, so-called orphan CpG islands, which often include transcriptional start sites for long non-coding RNAs (Illingworth et al., 2010). Besides methylation at promoters and the first exon that usually results in transcriptional silencing, the role of methylation in gene bodies is still controversial (Brenet et al., 2011). Correlation with high gene expression has been reported, but cannot be found in slowly dividing cells (Aran et al., 2011).

Recently, a role of gene body DNA methylation in regulation of alternative promoters has been proposed (Maunakea et al., 2010). Besides this gene specific context, many non-coding repetitive sequences are methylated, including pericentromeric repeats and transposable elements (Smith and Meissner, 2013). DNA methylation is one of the mechanisms to keep these non-coding sequences compacted and silent in order to ensure genome integrity.

In contrast to other epigenetic processes, DNA methylation is especially important in the persistence of silent epigenetic states. While other epigenetic processes, like histone modifications can be metaphorized as a door that is opened or closed, representing active or inactive chromatin regions, DNA methylation rather represents the key to the door locking the silent epigenetic state (Cedar and Bergman, 2009). The establishment of persistent silent epigenetic states by DNA methylation is not only important during embryonic development, but also during adult stem cell differentiation of the neural or hematopoietic lineage (Smith and Meissner, 2013). The most striking changes in DNA methylation levels occur during embryonic development. Global waves of demethylation occur during early embryogenesis and during the formation of the gametocytes in the embryo. Interestingly, the paternal genome is demethylated much faster compared to the maternal genome in the zygote and remethylation of the parental genome in the primordial germ cells also occurs on a shorter time frame (Seisenberger et al., 2013). The DNA methylation level changes are supposed to increase the epigenomic plasticity and to reset imprinted regions.

Methylation of cytosine in mammals is catalyzed by the family of DNA methyltransferases (Dnmt). This family consists of 5 methyltransferases Dnmt1, Dnmt3a, Dnmt3b, Dnmt3L and Dnmt2 (Figure 3). Dnmt3a and Dnmt3b set the methylation marks *de novo* during embryogenesis assisted by the cofactor Dnmt3L (Moore et al., 2013). Knockout studies in mice reveal that Dnmt3b is required earlier in development compared to Dnmt3a, as knockout mice lacking Dnmt3b are not viable, whereas *Dnmt3a* knockout mice survive about 4 weeks after birth (Okano et al., 1999). Once the methylation marks are established, they are maintained by Dnmt1 during DNA replication and repair (Mortusewicz et al., 2005, Bird, 2002, Bestor, 2000). Dnmt2 lacks the N-terminal regulatory region and is structurally very similar to the bacterial DNA methyltransferase M.*HhaI* (Dong et al., 2001). It is still under discussion, whether the highly conserved Dnmt2 is capable of DNA methylation, but it has been reported that Dnmt2 is able to methylate tRNA promoting tRNA stability and protein synthesis (Schaefer and Lyko, 2010, Goll et al., 2006, Hermann et al., 2003, Tuorto et al., 2012).

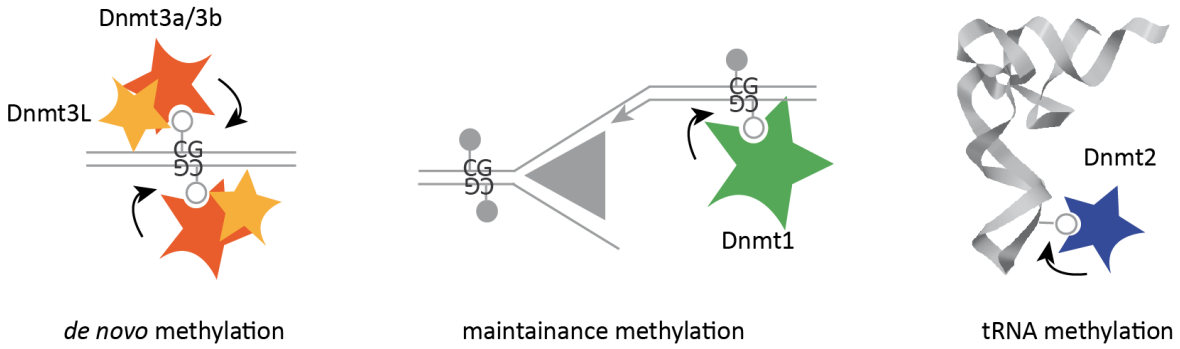

Figure 3: Roles of DNA methyltransferases. Dnmt3a and Dnmt3b methylate CpG sites *de novo* during early embryogenesis assisted by the cofactor Dnmt3L. Dnmt1 fully methylates hemimethylated CpG sites during DNA replication and repair. Dnmt2 methylates tRNAs. Closed circles represent methylated, open circles unmethylated sites.

How the target sites of *de novo* methylation are identified still remains unclear, but different mechanisms have been suggested (Moore et al., 2013, Smith and Meissner, 2013). Targeting could either occur by direct recruitment of Dnmts or by blocking of DNA sites that are supposed to be protected from methylation. In both cases, binding of transcription factors, RNAs, histone modifications, histone variants or a combination of multiple processes are likely to be involved. Furthermore, methylation marks can be removed actively or passively by a lack of maintenance. There has been a long search for demethylases, however, no enzyme that cuts the methyl group from cytosine has been discovered so far in mammals. Recently, there has been increasing evidence that the removal of methyl groups occurs via another pathway. It has been discovered that the ten-eleven-translocation (Tet) proteins oxidize 5-methylcytosin (5mC) to 5-hydroxymethylcytosin (5hmC) and further to 5-formylcytosin (5fC) and finally to 5-carboxcytosin (5caC) (Ito et al., 2011, Tahiliani et al., 2009). The new DNA bases, especially 5hmC might not be recognized by Dnmt1 and therefore lead to passive demethylation (Hashimoto et al., 2012). Active demethylation probably includes DNA repair mechanisms. 5fC and 5caC are, for example, recognized by the thymine-DNA glycosylase (TDG) followed by base excision repair (BER) (Shen et al., 2013). Alternatively, the AID (activation induced cytidine deaminase) and APOBEC (apolipoprotein B mRNA editing enzyme, catalytic polypeptide-like) family enzymes can deaminate 5hmC to 5-hydroxyuracil (5hmU) which is recognized by the BER pathway (Guo et al., 2011). Moreover, the new bases might not only be intermediates during removal of methylation, but also act as signals detected by specific readers influencing gene expression. Recently, a study has identified readers of 5hmC, 5fC and 5caC in comparison to 5mC readers (Spruijt et al., 2013). Specific readers for each modification were identified and the interactions with 5mC and 5hmC were shown to change during differentiation, giving first hints towards the functional significance of the newly discovered DNA bases.

The readers of the classical 5mC marks are termed methyl-CpG-binding proteins (MBP) and can be categorized in three groups, namely proteins containing either (1) a methyl-CpG-binding domain

(MBD), or (2) a zinc finger (ZnF; Cys_2His_2) domain or (3) proteins that are ubiquitin-like, containing PHD and RING finger domains (Uhrf) (Buck-Koehntop and Defossez, 2013). In general, the MBPs influence chromatin organization or transcriptional activity directly or indirectly by recruiting other factors (Fournier et al., 2012). The majority of the MBPs mediate crosstalk between DNA methylation and other epigenetic processes like histone modifications. For instance, MeCP2, an MBD protein, binds methylated DNA and recruits histone deacetylases (HDAC) leading to transcriptional repression (Nan et al., 1998). Further MBD proteins are MBD1, MBD2, MBD3, MBD4, MBD5 and MBD6 of which MBD1, 2 and 4 bind methylated DNA, whereas MBD 3, 5 and 6 are excluded from methylated DNA (Buck-Koehntop and Defossez, 2013). Similar to MBD proteins, many ZnF proteins bind methylated DNA in a sequence-specific context (Buck-Koehntop and Defossez, 2013). Uhrf1 has a strong affinity for hemimethylated sites and is able to bind Dnmt1 and target it to them. The Uhrf family will be discussed in detail in chapter 1.2.3.

Misregulation of DNA methylation is a hallmark of cancer development. Tumor cells are characterized by global hypomethylation and local hypermethylation at CpG islands (Berman et al., 2012). Hypomethylation of repetitive sequences causes genomic instability, whereas hypermethylation at promoters of tumor suppressor genes enhances cell proliferation and reduces levels of apoptosis (Portela and Esteller, 2010, Esteller, 2011). One successful strategy of cancer treatment has been the chemotherapeutic agent 5-aza-desoxycytidine that covalently links Dnmts to DNA thereby inhibiting their function. Since 2004, 5-aza-dC has been approved as a drug against myelodysplastic syndrome (Kaminskas et al., 2005).

1.2.1 Dnmt1

The regulation and the molecular mechanism of Dnmt1 has been a popular field of research for many years. The knockout of *Dnmt1* in mice is recessive embryonic lethal before embryonic day 11 (Li et al., 1992). Surprisingly, the corresponding ESCs are still viable containing DNA methylation levels reduced by about two thirds. In MEF cells, the knockout leads to p53-induced apoptosis that can be overcome by depletion of p53 (Lande-Diner et al., 2007).

Dnmt1 is composed of a C-terminal catalytic domain and a large N-terminal regulatory region connected by a linker consisting of several alternating lysine-glycine (KG) repeats (Figure 4). In contrast to bacterial methyltransferases, the catalytic domain alone is not active (Cheng, 1995, Margot et al., 2000), demonstrating that the regulation by the N-terminal domain is essential for the activity of mammalian Dnmt1. However, a truncation of half of the N-terminal domain is still catalytically active (Jeltsch, 2006). In line with this, the first 118 amino acids of the N-terminus missing in an oocyte specific isoform of Dnmt1 are dispensable for proper enzyme function. This region contains a domain binding to the Dnmt1-associated protein 1 (DMAP1) and is supposed to function in transcriptional

repression (Rountree et al., 2000). Nuclear import of Dnmt1 is achieved by at least one nuclear localization signal (NLS) located in the N-terminal region (Cardoso and Leonhardt, 1999).

Figure 4: Dnmt1 domain architecture. The protein consists of a C-terminal catalytic domain and an N-terminal regulatory region interconnected by a linker. The domains in the regulatory region include the DMAP, the PBD, a NLS, the TS domain, a CXXC domain and two BAH domains.

This work focuses on two domains of Dnmt1, namely the protein proliferating cell nuclear antigen (PCNA)-binding domain (PBD) and the targeting sequence (TS) domain. The PBD mediates the transient interaction with PCNA and is not essential for the catalytic reaction, but enhances the methylation efficiency about 2-fold (Schermelleh et al., 2007, Chuang et al., 1997). PCNA forms a trimeric ring around the DNA and interacts with a large number of proteins, serving as a loading platform during replication and repair (Moldovan et al., 2007). The second domain mediating cell cycle-dependent targeting of Dnmt1, the TS domain, targets Dnmt1 to constitutive heterochromatin (Easwaran et al., 2004, Leonhardt et al., 1992). Furthermore, the TS domain has been implicated in several other interactions or mechanisms. A bipartite interface within the TS domain was found to be responsible for dimerization of Dnmt1 (Fellinger et al., 2009) and the TS domain was also reported to mediate the interaction with Uhrf1 (Frauer and Leonhardt, 2011, Achour et al., 2008, Felle et al., 2011b, Bashtrykov et al., 2013). The crystal structure of Dnmt1 hints at an autoinhibitory role of the TS domain, where the TS domain has to be unfolded from the catalytic domain in order to allow binding of 5mC (Takeshita et al., 2011).

A similar autoinhibitory role was proposed for the CXXC domain, localized downstream of the TS domain (Song et al., 2011). The CXXC domain can bind to unmethylated CpG sites, however, its function is still under discussion as it has been reported that it is dispensable for maintenance methylation (Frauer et al., 2011, Bestor, 1992). The polybromo homology domain (PBHD) (Liu et al., 1998) containing two bromo adjacent homology (BAH) domains, thought to mediate protein-protein interactions involved in gene silencing (Jurkowska et al., 2011). It has been reported that the PBHD interacts with the ubiquitin carrier protein (Ubc) 9, which sumoylates Dnmt1, leading to an enhanced catalytic activity of Dnmt1 (Lee and Muller, 2009), but the detailed function of the PBHD remains unclear. As a further regulatory mechanism, an interaction between the C- and the N-terminus seems to be required for the catalytic activity of Dnmt1 (Margot et al., 2003). The enzymatic reaction of Dnmts involves the formation of a covalent complex between the C6 position of the cytosine ring and the sulfhydryl group of the cystein in the conserved PC motif of the catalytic domain (motif IV).

Thereafter, the methyl group is transferred from the donor S-adenosyl-L-methionine (SAM) to the C5 of the cytosine, followed by the release of the Dnmt by β elimination (Goll and Bestor, 2005).

Dnmt1 is ubiquitously expressed in various tissues, but increased levels of Dnmt1 have been detected in many cancers (Peng et al., 2005, Saito et al., 2003, Robertson et al., 1999). Given that alterations of Dnmt1 expression levels can lead to malignancies, it is important that protein expression, stability and activity are tightly controlled. One mechanism controlling Dnmt1 abundance is the ubiquitination of Dnmt1 by Uhrf1 leading to proteasomal degradation of Dnmt1 (Du et al., 2010, Qin, 2011). The ubiquitination of Dnmt1 is triggered by acetylation of Dnmt1 by Tat-interactive protein 60 (Tip60). In contrast, Usp7 and HDAC1 protect Dnmt1 from degradation by deubiquitination and deacetylation of Dnmt1, respectively. Dnmt1 expression is, for instance, regulated by the Ras-AP-1 and the pRb-E2F signaling pathways (Rouleau et al., 1995, McCabe et al., 2005).

1.2.2 Coupling of maintenance methylation to the cell cycle

The abundance of Dnmt1 is not only regulated during differentiation, but also during cell cycle progression. The protein amounts are highest in S phase and start to decrease in late S phase or G2 with lowest levels in G1 (Du et al., 2010, Vogel et al., 1988). Besides cell phase specific expression levels of Dnmt1, the interaction with important binding partners also ensures faithful maintenance methylation of replicated DNA. For instance, the interaction of Dnmt1 with PCNA via the PBD, couples the localization of Dnmt1 tightly to DNA replication.

In somatic mouse cells, at least three stages of replication are clearly distinguishable by replication markers like PCNA or nucleotide analogues like bromodeoxyuridine (BrdU) or ethynyldeoxyuridine (EdU). The cells pass from early to mid and then to late S phase (Figure 5) (Somanathan et al., 2001, Dimitrova and Berezney, 2002, Leonhardt et al., 2000, Goldman et al., 1984). In early S phase, euchromatic regions are replicated leading to a pattern of multiple small foci distributed in the nucleus, but excluded from the nucleoli and the nuclear periphery. In mid S phase, an enrichment of replication foci at the nuclear periphery and around nucleoli is observable. In mid S Phase replication foci, facultative heterochromatin is replicated, followed by replication of constitutive heterochromatin in late S phase. In mouse cells, constitutive heterochromatin clusters in chromocenters, resulting in large horseshoe-shaped replication foci upon heterochromatin replication. The molecular mechanism of the chromatin-dependent replication timing is not yet fully investigated, but there are indications that it is created by a stochastic process. The prerequisites for this so-called relative efficiency model are an increasing efficiency of origin of replication activation over time and more efficient firing of some origins of replication, thus creating an asynchronous process (Rhind, 2006). The latter could be created by different compaction states of chromatin that regulate the accessibility of origins and thereby influence the firing efficiency. The domino effect model states that replication affects the

surrounding chromatin structure, leading to an increased firing efficiency of origins in close proximity to already replicating regions (Sporbert et al., 2002). The influence of chromatin compaction on replication timing is supported by the finding that histone acetylation can lead to a shift towards earlier replication timing (Kemp et al., 2005, Casas-Delucchi et al., 2012). Furthermore, the replication timing of 20% of the genome changes during ESC differentiation, in line with the fact that loci specific chromatin compaction is drastically altered during differentiation (Hiratani et al., 2008).

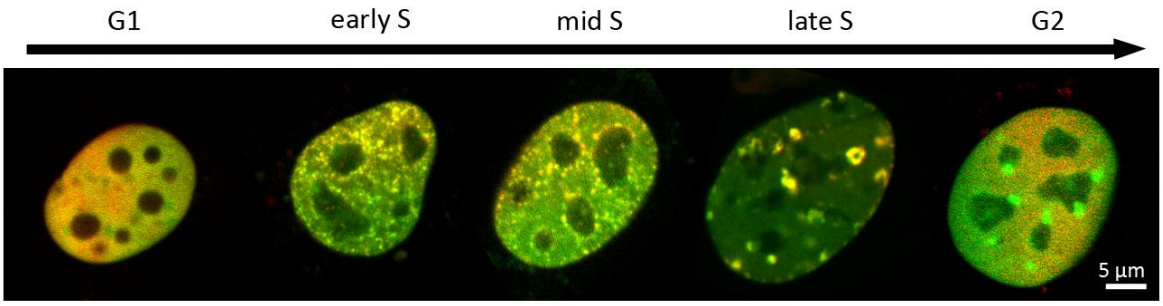

Figure 5: Cell cycle-dependent localization of GFP-Dnmt1wt and RFP-PCNA in mouse fibroblast cells. Replication sites are marked by RFP-PCNA (red). GFP-Dnmt1 (green) displays a diffuse nuclear distribution in G1 and association with replication sites in early to mid S phase. In late S phase, GFP-Dnmt1 associates strongly with constitutive heterochromatin at chromocenters of mouse cells which persists into G2 phase.

Dnmt1 largely colocalizes with the replication pattern observed for PCNA during early and mid S phase. However, at the end of late S phase, a part of the Dnmt1 population remains associated with the chromocenters although replication progresses further. At the onset of G2 Dnmt1 is still enriched at constitutive heterochromatin. There are two possible explanations for this phenomenon. Dnmt1 either completes the DNA methylation at the densely methylated heterochromatic regions or Dnmt1 acts as an anchor for further processes (Easwaran et al., 2004).

1.2.3 Uhrf1 and Uhrf2

Interaction with PCNA causes enrichment of Dnmt1 at hemimethylated sites, but a second mechanism targets Dnmt1 directly to hemimethylated sites via interaction with the protein Uhrf1 (also known as Np95 or ICBP90). This became apparent in 2007, when it has been discovered that the knockout of *Uhrf1* leads to reduced DNA methylation levels, mimicking the phenotype of the *Dnmt1* knockout in mice (Bostick et al., 2007, Sharif et al., 2007). One year later, structural studies reported that Uhrf1 binds to hemimethylated CpG sites by flipping out the methylated cytosine base (Arita et al., 2008, Avvakumov et al., 2008, Hashimoto et al., 2008). Based on these results, the model proposed, that Uhrf1 targets Dnmt1 to hemimethylated sites in the DNA sequence, although Dnmt1 seems to have an intrinsic preference for hemimethylated DNA (Bashtrykov et al., 2012, Frauer and Leonhardt, 2009). Furthermore, the ability of Uhrf1 to bind histone modifications provides a link between histone modifications and DNA methylation (Rottach et al., 2010, Liu et al., 2013a, Rothbart et al., 2012).

Uhrf1 is a multidomain protein, composed of an ubiquitin-like (Ubl) domain, a tandem tudor domain (TTD), a plant homeodomain (PHD), a SET (Suv39, Enhancer-of-zeste, Trithorax) and RING associated (SRA) domain and a really interesting new gene (RING) domain (Figure 6). The SRA domain mediates the interaction with hemimethylated DNA, whereas the TTD and the PHD mediate the interaction with histone modifications. The TTD, together with the PHD, selectively bind to H3K9me3. H3K9me3 is a repressive mark, characteristic for constitutive heterochromatin, set by the methyltransferases Suppressor of Variegation (Suv)39h1 and Suv39h2 (Peters et al., 2001). Uhrf1 is a member of the RING-finger type E3 ligase family. Typically, the RING-finger type E3 ligases are involved in the ubiquitination pathway and indeed the RING domain enables Uhrf1 to ubiquitinate Dnmt1 leading to the proteasomal degradation of Dnmt1 (see 1.2.1). In addition, Uhrf1 harbors an Ubl domain at the N-terminus. This domain might be involved in the proteasomal degradation pathway, but its function has not been fully elucidated yet (Bronner et al., 2013).

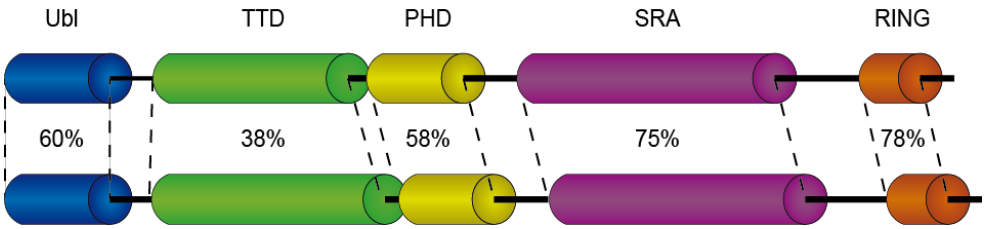

Figure 6: Uhrf1 and Uhrf2 domain architecture and homology. Uhrf1 and Uhrf2 contain a Ubl domain, a TTD, a PHD, a SRA domain and a RING domain. The homology based on the primary protein sequence between the domains in both proteins is depicted in percent.

Similar to Dnmt1, Uhrf1 is upregulated in many cancers and, hence, considered to be a marker or a potential target for cancer therapies (Mousli et al., 2003, Unoki et al., 2009). Furthermore, Uhrf1 is constitutively expressed during the cell cycle in cancerous cell lines, in contrast to a peak in expression in late G1 and at the G2/M transition in non-cancerous cell lines (Mousli et al., 2003).

The second member of the Uhrf family is Uhrf2 (also known as Np97 or NIRF). Uhrf2 shows a remarkable structure and even sequence conservation to Uhrf1 (Bronner et al., 2007, Pichler et al., 2011). However, there are some differences between the two proteins, especially in the TTD (Figure 6). Uhrf2 has been reported to be involved in the degradation of nuclear protein aggregates (Iwata et al., 2009), but it is not clear whether Uhrf2 has a functional role in DNA methylation. Therefore, a highly interesting question is thus whether the two proteins are functionally redundant or whether Uhrf2 possesses a distinct role.

1.3 Epigenetic regulation by histone variants

Besides DNA methylation and histone modifications, the importance of histone variants in the context of chromatin structure and gene expression has become more and more evident. Histone variants are

important for many processes, such as DNA repair, transcriptional regulation and epigenetic reprogramming (Bernstein and Hake, 2006). The incorporation of histone variants changes epigenetic states either directly or indirectly by recruiting different reader proteins through a variety of mechanisms. For instance, some histone variants harbor specific sites that can be differently modified compared to canonical histones or introduce structural changes facilitating nucleosome sliding or eviction by changing the histone-DNA or histone-histone interfaces (Luger, 2006).

Canonical histones are only expressed in S phase, they are encoded in gene clusters that do not contain introns and the mRNA is characterized by a 3'-stem loop, which is not polyadenylated. These characteristics are, however, not found for histone variants, which are differently regulated, expressed throughout the cell cycle, contain introns and have a polyadenylated mRNA (Marzluff et al., 2008). The incorporation and eviction of histone variants is promoted by specific chaperones (Park and Luger, 2008). For example, the exchange of H2A-H2B with H2A.Z can be catalyzed by the complex p400/NuA4/Tip60 (E1A-binding protein p400/nucleosomal acetyltransferase of H4/Tat-interactive protein 60) or by SRCAP (Snf2-Related CREBBP activator protein) (Billon and Cote, 2012). In nucleosomes always two copies of every histone are present. Therefore, either one or both histones of one type can be exchanged with variants. Furthermore, different histone variants can be combined in one nucleosome, leading to a great number of possible nucleosome compositions.

So far, variations of the core histones H2A, H2B and H3 have been identified in mammals. The largest family of variants has been described for H2A (Figure 7). A well known variant is H2A.X, which is phosphorylated at serine 139, if DNA double strand breaks occur (γH2A.X) and facilitates the DNA repair process (van Attikum and Gasser, 2005). Another example is macroH2A that is incorporated to a great extend into the inactive X chromosome and is involved in the transcriptional repression on this chromosome and also on autosomes (Gamble and Kraus, 2010). The histone variants H2A.BBD (bar body deficient) and H2A.Z are related to chromatin stability. H2A.BBD is only detected in mammals and has been reported to be involved in spermatogenesis. Furthermore, the incorporation of H2A.BBD in somatic cells has been shown to destabilize the nucleosome (Gautier et al., 2004).

H2A.Z is conserved between different species and is essential in mouse, *drosophila* and *xenopus* (Bonisch and Hake, 2012). It is, hence, not surprising that this variant functions in a variety of processes including transcriptional regulation, DNA repair, heterochromatin formation, chromosome segregation and mitosis (Bonisch and Hake, 2012). Based on the various functions regarding chromatin stability, the dynamics of the H2A histone variants and their splice forms are of special interest for this work.

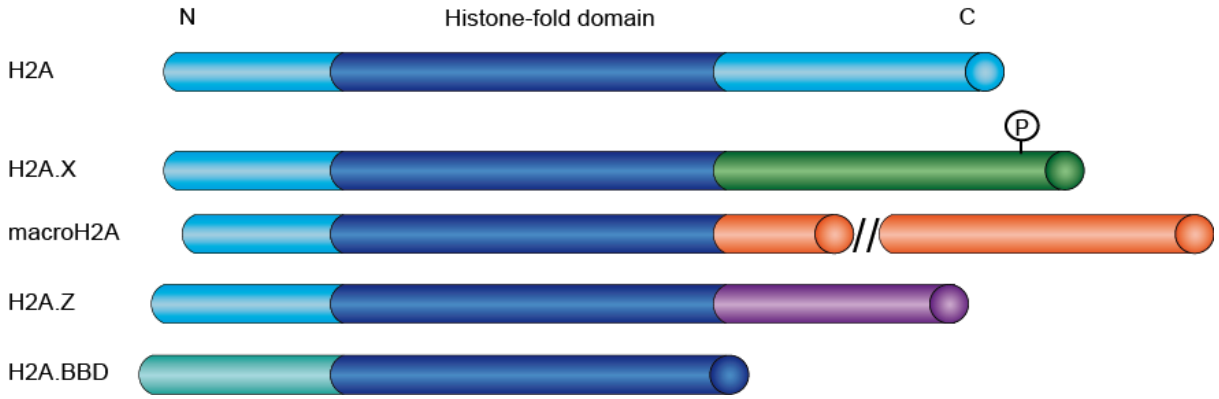

Figure 7: Schematic representation of human H2A variants. In contrast to the canonical H2A, H2A.X harbors a special C-terminal region prone for phosphorylation and macroH2A contains a large macro domain at the C-terminus. The C-terminal region is also specific in H2A.Z, whereas H2A.BBD lacks the C-terminal domain and has an N-terminal domain that is distinct from the other H2A variants.

1.4 Spatial and temporal dynamics of nuclear processes

1.4.1 Nuclear protein dynamics

Most of the processes and interactions, which have been introduced in the previous chapters, are highly dynamic. With the start of this century it became clear that many of the interactions thought to be highly stable are indeed very transient (Phair and Misteli, 2000). For instance, a lot of chromatin-binding proteins like HP1 or even the histone H1 constantly bind and unbind their target (Stasevich et al., 2010, Schmiedeberg et al., 2004, Cheutin et al., 2003). Apparently, chromatin, including the canonical core histones, provides a relatively stable framework, where other proteins transiently bind to. Further stable proteins are located in the nuclear lamina such as lamin A and lamin B or nucleoporins like NUP153 (Xu and Powers, 2013, Moir et al., 2000). Furthermore, several nuclear compartments not enclosed by a membrane, appear as relatively stable regions in the nucleus. These nuclear compartments include nucleoli, nuclear speckles, replication foci, PML bodies and Cajal bodies (Spector, 2001) and they are to some extend dynamic. For example, the spatial distribution of replication foci changes in a complex pattern during S phase (see 1.2.2). The proteins in the replication complexes are continuously exchanged. Furthermore, nuclear compartments could be self-assembling or self-organizing complexes that are created by accumulation of specific factors binding to each other with high affinity (Hemmerich et al., 2011).

Regarding the question of how proteins find their target, a theory states that many nuclear factors passively diffuse through the crowded nucleus in order to find their target in a kind of a random-scanning mechanism (Gorski et al., 2006). As diffusion of small molecules is very fast in the range of 30-80 $\mu m^2/s$ (Braga et al., 2004), this random-scanning mechanism, in combination with transient binding events, could be a fast and energy efficient way to target proteins. Furthermore, this combination allows a very fast reaction to external factors without the need of guided unbinding of

chromatin factors. Fine-tuning the strength of association and dissociation rates in combination with the abundance of proteins, contribute to the creation of nuclear organization (Hemmerich et al., 2011). In essential cellular processes, chaperones aid the assembly of nuclear components (Ellis, 2006). PCNA, for instance, forms a trimeric ring around DNA and is loaded onto DNA by the chaperone replication factor C (RFC) (Indiani and O'Donnell, 2006). After loading to DNA, the complex slides along DNA in one dimension. The dynamic landscape in the nucleus seems to be necessary to provide stability as well as plasticity in the cell (Misteli, 2001). A goal of this work is the analysis of the temporal and spatial kinetics of this nuclear dynamic landscape. Therefore, there is an increasing need for methods that do not only provide a snapshot of the current state, but allow insights into the dynamic interplay of proteins. A very effective technique is advanced fluorescence microscopy.

1.4.2 Fluorescence microscopy techniques to study epigenetic processes *in vivo*

The field of fluorescence microscopy has been rapidly growing in the last two decades. The availability of high speed microscopes in combination with fluorescent proteins like the green fluorescent protein (GFP) has created a variety of methods. The so-called F-techniques include fluorescence recovery after photobleaching (FRAP), fluorescence loss in photobleaching (FLIP), Förster resonance energy transfer (FRET), fluorescence lifetime imaging microscopy (FLIM) and fluorescence correlation spectroscopy (FCS) (Ishikawa-Ankerhold et al., 2012). The F-techniques are complemented by single particle tracking (SPT) (Siebrasse et al., 2007). Furthermore, a variety of correlation spectroscopy methods related to FCS like raster scan image correlation spectroscopy (RICS) have been developed (Digman and Gratton, 2012).

Initially, FRAP was developed to investigate the lateral movement of membrane proteins (Axelrod et al., 1976), but it was later also used for kinetic analysis of intracellular as well as nuclear proteins. The techniques FRAP and FLIP exploit the fact that a fluorescent molecule, fused to the protein of interest, can be irreversibly bleached by a strong laser pulse. Fluorescent proteins in a cell appear in a dynamic equilibrium. After bleaching a distinct region or spot in a FRAP experiment this equilibrium is disturbed and diffusion of the bleached and unbleached proteins within the compartment can be visualized (Figure 8). Dependent on their mobility, the molecules restore the steady state equilibrium of the fluorescence distribution. The mobility of the proteins is dependent on their size and their specific or unspecific interactions with other molecules (van Royen et al., 2009). The fluorescence intensity in the bleached region is recorded over time by live cell microscopy.

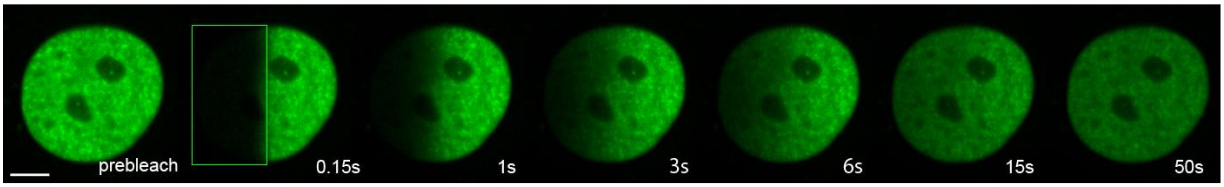

Figure 8: Recovery of the fluorescence after bleaching half of the nucleus. C2C12 cells expressing GFP-Dnmt1 in early S phase. The bleached region is indicated as a rectangle around the left half of the nucleus. Recovery is reached after about 50 s. Scale bar: 5 µm.

In contrast to FRAP, in a FLIP experiment a region in a specific compartment is repeatedly bleached over time and the fluorescent intensity in an unbleached compartment or region is measured (Figure 9). The advantage of the latter approach is that no damage by bleaching is induced in the observed area. Furthermore, the exchange of molecules between different compartments can be easily analyzed. In this way, for example, the rate of nucleocytoplasmic shuttling is measured (Koster et al., 2005). FLIP is complementary to FRAP experiments as it adds the possibility of visualizing the immobile protein fraction in the cell. Specialized techniques like microirradiation are used to analyze the dynamic involvement of proteins in DNA repair (Figure 9). In microirradiation experiments, DNA damage sites are created with a strong UV laser in living cells to visualize the accumulation of tagged proteins to the DNA damage sites (Mortusewicz et al., 2007). A specialized variation of FRAP for the analysis of DNA methylation is the trapping assay (Schermelleh et al., 2005). This method uses the covalent attachment of the methyltransferases to its target sites in the DNA by incorporation of the nucleotide analog 5-aza-dC in S phase. The degree of immobilization of Dnmts can be measured by FRAP experiments (Figure 9). If Dnmt1 is highly active, many Dnmt1 molecules will be trapped by 5-aza-dC, leading to a large immobile fraction after a short time frame.

Kinetic modeling of FRAP data allows the estimation of diffusion coefficients and even binding rates of the analyzed proteins. FRAP has major advantages in contrast to *in vitro* techniques like binding assays with fluorescently labeled proteins or surface plasmon resonance (SPR). First, as it is an *in vivo* method it allows for the observation of the protein in near native conditions. In addition, a compartment and cell cycle-dependent approach is possible to temporally and spatially characterize the mobility of a protein. However, interactions are only indirectly characterized by comparing kinetics of the wild type protein with its mutants or with knockout cell lines.

In order to get deeper insights into protein binding properties and functions, not only the temporal dynamics, but also the spatial changes have to be analyzed. Maximizing resolution is a major goal and major breakthroughs have been achieved in the last decades. The main techniques to overcome the resolution limit of about 200 nm in conventional light microscopy are 3D structured illumination microscopy (3D-SIM), stimulated emission depletion (STED) and a variety of localization microscopy methods like direct stochastic optical reconstruction microscopy (STORM) or photoactivated

localization microscopy (PALM) (Schermelleh et al., 2010). Among these techniques, 3D-SIM is especially suitable for super-resolution images in the nucleus, because the high axial resolution is not limited to total internal reflection fluorescence (TIRF) setups. Furthermore, it is possible to acquire images in three colors, allowing a comparison of the detailed localization of up to three different molecules.

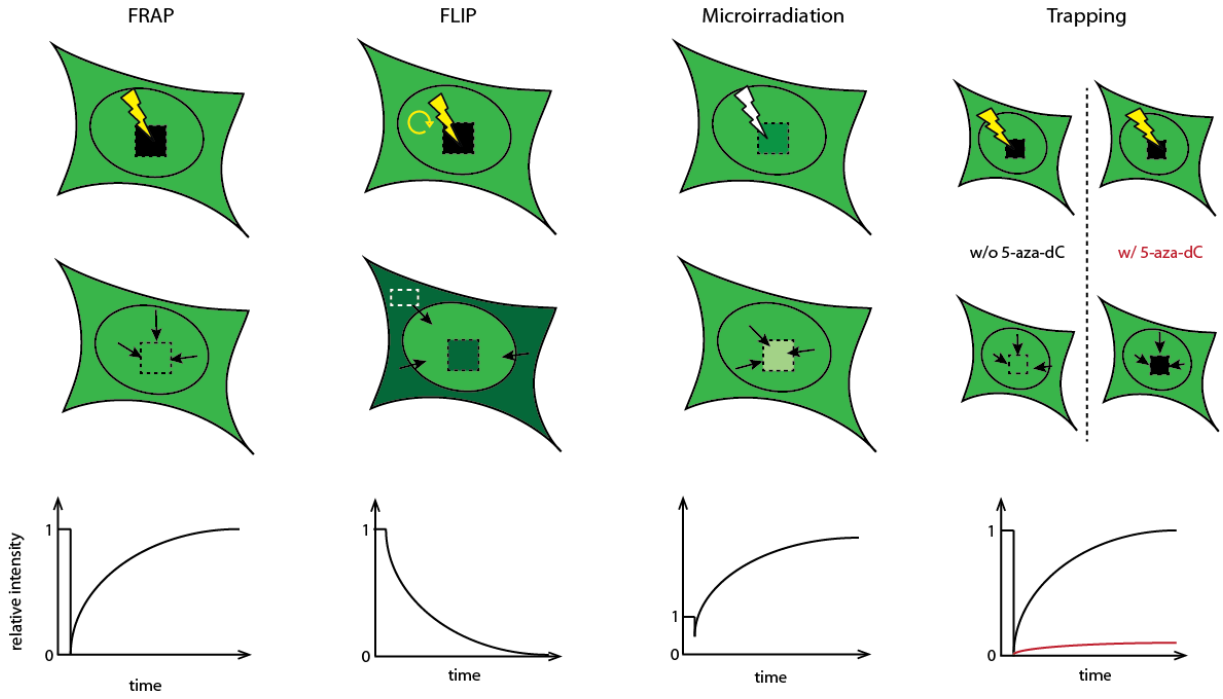

Figure 9: Bleaching techniques to determine the mobility of molecules in living cells. In FRAP experiments, a region in the cell is bleached and the recovery is measured over time. In FLIP experiments, a region is repeatedly bleached and the loss of fluorescence in another region or compartment is analyzed. During microirradiation, DNA damage is induced by a UV-laser and the recruitment of proteins to this area is analyzed. Therefore, if the protein is enriched, the relative intensity rises to values larger than one. In the specialized trapping assay, Dnmts are covalently bound to 5-aza-dC in the DNA. After addition of 5-aza-dC, it is incorporated into DNA in S phase and active Dnmt1 is trapped, leading to a decreased mobile fraction of Dnmts in FRAP experiments (black: without 5-aza-dC, red: with 5-aza-dC).

1.4.3 Labeling and transfection strategies

The investigation of nuclear processes is further challenged by the labeling of the structure or protein of interest and the delivery of the labeled molecules into the cell.

Labeling of the designated proteins, protein modifications, DNA or RNA sequences or single bases provides the basis for the imaging methods that have been described before. Apart from standard techniques like immunofluorescent labeling with antibodies in fixed cells or fluorescent tagging of proteins with GFP or other fluorescent proteins, a wide range of specialized techniques has been developed. For instance, nanobodies, small functionalized camelid antibodies, are currently used to label proteins or modifications in living cells (Romer et al., 2011). Alternatively, short labeled Fab antibody fragments can be injected into living cells or small GFP-tagged domains like the MBD can be

used to detect DNA modifications like 5mC (Kimura et al., 2010). Another challenge is the specific labeling of DNA sequences. Besides existing methods like polydactyl zinc finger proteins (PZF) (Lindhout et al., 2007), a new approach exploits the designer transcription activator-like effectors (dTALE). TAL effectors are injected from pathogenic *Xanthomonas* bacteria into plant cells in order to activate gene expression in their host, facilitating bacterial survival and proliferation (Mak et al., 2013). Binding to specific DNA sequences is achieved by the central DNA-binding domain, containing tandem amino acid repeats that differ by repeat-variable-diresidues (RVD). The code, which RVDs detect each of the four nucleotides in DNA, has been unraveled and has since then allowed for the construction of dTALEs binding to user-defined sequences (Boch et al., 2009, Moscou and Bogdanove, 2009). By expression of fluorescently tagged dTALEs, DNA sequences can be labeled specifically and their temporal and spatial distribution can be monitored in living cells. The application of dTALEs for sequence specific DNA labeling has, thus, been demonstrated and characterized in this work.

Besides labeling nuclear structures, a second challenge is the delivery of nucleic acids (DNA, RNA) and proteins to the cells. Typically, specific gene expression vectors are transferred into cells with the help of cationic lipid reagents resulting in the synthesis of the encoded proteins in the cells. However, large complex proteins like antibodies are often inefficiently folded or assembled and transfer of purified proteins into cells often leads to endosomal entrapment of the proteins or high cell toxicity (Mellert et al., 2012). Therefore, new strategies need to be developed. Highly tunable transfer vectors are mesoporous silica nanoparticles (Cauda et al., 2009, Rathousky et al., 2004). They are taken up by mammalian cells via endocytosis or pinocytosis (Slowing et al., 2008). Introduction of various internal or external chemical functional groups can optimize their properties like biocompatibility, cellular uptake or the capability of loading and releasing molecules (Giri et al., 2007). For example, the functionalization of the nanoparticle surface with protoporphyrin IX increases the cellular uptake of nanoparticles and their release from the endosome upon illumination with UV light (Schlossbauer et al., 2012). Mesoporous silica particles are not only an effective research tool, but they also have a potential in medical applications. At the moment, the development of strategies to deliver drugs to specific tissues in the human body is an emerging field of research. Functionalized nanoparticles could be a way to bring the drug to a specific region, allowing release only in the target area (Mai and Meng, 2013).

1.5 Aims of this work

Although many nuclear processes have been studied extensively, the majority of the results only represent snapshots in the dynamic and complex interplay of large regulatory networks. Therefore, the aim of this work was to get deeper insights into the spatio-temporal dynamics of nuclear proteins with a major focus on Dnmt1.

At first, I set out to dissect the cell cycle-dependent dynamics of Dnmt1. To address this question, I performed FRAP experiments with GFP-Dnmt1^{wt} and a set of mutants to analyze the role of the PBD and the TS domain during different stages of the cell cycle with high temporal resolution. By applying a tailored kinetic modeling approach, I tried to decipher the specific mean residence times for the different interactions and the corresponding fractions of interacting molecules. Furthermore, using 3D-SIM super-resolution microscopy, I wanted to gain further information about the localization of Dnmt1 in late S phase with high spatial resolution and correlate it with the findings about Dnmt1 dynamics. As Uhrf1 is the potential binding partner of the TS domain-mediated interaction and has an essential role in DNA methylation, I also aimed at obtaining more information about Uhrf1 and at studying the differences between Uhrf1 and its homologue Uhrf2.

Furthermore, I wanted to further develop our FRAP approach and apply it to other nuclear proteins like the histone variant H2A.Z or the cell cycle regulator nuclear interaction partner of anaplastic lymphoma kinase (NIPA). In addition, I tried to find tools that facilitate the analysis of nuclear dynamics and processes. Therefore, I have set out to exploit dTALEs for the labeling of DNA sequences in living cells and to characterize mesoporous silica nanoparticles, which can be used to transfer molecules into cells.

2. Results

2.1 Dissection of cell cycle-dependent dynamics of Dnmt1 by FRAP and diffusion-coupled modeling

Nucleic Acids Research Advance Access published March 27, 2013

Nucleic Acids Research, 2013, 1–17
doi:10.1093/nar/gkt191

Dissection of cell cycle–dependent dynamics of Dnmt1 by FRAP and diffusion-coupled modeling

Katrin Schneider[1], Christiane Fuchs[2], Akos Dobay[1], Andrea Rottach[1], Weihua Qin[1], Patricia Wolf[1], José M. Álvarez-Castro[1], Marcus M. Nalaskowski[3], Elisabeth Kremmer[4], Volker Schmid[5], Heinrich Leonhardt[1] and Lothar Schermelleh[1,*]

[1]Department of Biology and Center for Integrated Protein Science, Ludwig Maximilians University Munich (LMU), 82152 Planegg-Martinsried, Germany, [2]Institute for Bioinformatics and Systems Biology, Helmholtz Zentrum München, German Research Center for Environmental Health, 85764 Neuherberg, Germany, [3]Department of Biochemistry and Signal Transduction, University Medical Center Hamburg-Eppendorf, 20246 Hamburg, Germany, [4]Institute of Molecular Immunology, Helmholtz Zentrum München, German Research Center for Environmental Health, 81377 Munich, Germany and [5]Department of Statistics, Ludwig Maximilians University Munich (LMU), 80539 Munich, Germany

Received November 15, 2012; Revised February 26, 2013; Accepted February 27, 2013

ABSTRACT

DNA methyltransferase 1 (Dnmt1) reestablishes methylation of hemimethylated CpG sites generated during DNA replication in mammalian cells. Two subdomains, the proliferating cell nuclear antigen (PCNA)-binding domain (PBD) and the targeting sequence (TS) domain, target Dnmt1 to the replication sites in S phase. We aimed to dissect the details of the cell cycle–dependent coordinated activity of both domains. To that end, we combined super-resolution 3D-structured illumination microscopy and fluorescence recovery after photobleaching (FRAP) experiments of GFP-Dnmt1 wild type and mutant constructs in somatic mouse cells. To interpret the differences in FRAP kinetics, we refined existing data analysis and modeling approaches to (i) account for the heterogeneous and variable distribution of Dnmt1-binding sites in different cell cycle stages; (ii) allow diffusion-coupled dynamics; (iii) accommodate multiple binding classes. We find that transient PBD-dependent interaction directly at replication sites is the predominant specific interaction in early S phase (residence time $T_{res} \leq 10$ s). In late S phase, this binding class is taken over by a substantially stronger ($T_{res} \sim 22$ s) TS domain-dependent interaction at PCNA-enriched replication sites and at nearby pericentromeric heterochromatin subregions. We propose a two-loading-platform-model of additional PCNA-independent loading at post-replicative, heterochromatic Dnmt1 target sites to ensure faithful maintenance of densely methylated genomic regions.

INTRODUCTION

DNA methylation is an essential epigenetic mechanism in mammals involved in gene regulation, genomic imprinting, X inactivation and carcinogenesis (1–3). Once established *de novo* during cell differentiation, the genomic methylation pattern is maintained by the DNA methyltransferase 1 (Dnmt1), a 183 kDa–sized enzyme that transfers methyl groups to hemimethylated substrate CpG sites generated during DNA synthesis in S phase (2,4,5). Hence, it seems obvious that the regulation of Dnmt1 is tightly coupled to DNA replication. In fact, using fluorescence recovery after photobleaching (FRAP), we have previously reported that Dnmt1 associates with replication foci (RF) by a highly transient interaction with the replication clamp proliferating cell nuclear antigen (PCNA) in early S phase via the PCNA-binding domain (PBD) of Dnmt1, enhancing the efficiency of covalent complex formation at its substrate sites (6,7). PCNA forms a homotrimeric ring around the DNA at replication forks and operates as a quasi-immobile

*To whom correspondence should be addressed. Tel: +44 1865 613264; Fax: +44 1865 613340; Email: lothar.schermelleh@bioch.ox.ac.uk
Present addresses:
Akos Dobay, Institute of Evolutionary Biology and Environmental Studies, University of Zurich, 8057 Zurich, Switzerland.
José M. Álvarez-Castro, Department of Genetics, University of Santiago de Compostela, 27002 Lugo, Spain.
Lothar Schermelleh, Department of Biochemistry, University of Oxford, Oxford OX1 QU3, United Kingdom.

The authors wish it to be known that, in their opinion, the first two authors should be regarded as joint First Authors.

loading platform for various replication-associated factors (8,9). Furthermore, the targeting sequence (TS) domain has been found to mediate association of Dnmt1 to constitutive heterochromatin from late S phase into G2 (10,11), the latter finding challenging the strict coupling to the replication process. In addition, the TS domain was implicated in the interaction with Uhrf1 (12). Uhrf1 is an essential cofactor in the DNA methylation process and it has been proposed that Uhrf1 targets Dnmt1 to hemimethylated sites (13–17). Although the role and regulation of Dnmt1 has been a popular field of research for many years, the details and functional implications of the cell cycle–dependent coordinated binding activity of the PBD and the TS domain still remain elusive.

FRAP techniques offer an effective tool to study *in vivo* the mobility of cellular proteins and to gain a better understanding of molecular interactions that drive or limit the mobility of fluorescent fusions expressed in cells (18–21). By bleaching a subpopulation of fluorescent proteins and by analyzing the redistribution of fluorescence over time, one can obtain measures of the half-time of recovery and the size of mobile fractions. To furthermore extract kinetic parameters from fluorescence recovery curves, one can describe the underlying dynamics of the proteins by a set of differential equations and apply a fitting procedure. Such kinetic modeling approaches can be useful to detect and quantify distinct dynamic populations [mobility classes (MCs)] and have been successfully used to quantitatively characterize diffusion and to some extent interactions inside living cells (22–24). Within the nucleus, the mobility of protein factors can be limited by binding to rather immobile structures, most prominently to chromatin, or to stationary enzyme complexes, such as the replication machinery, transcription domains or splicing speckles (25–27). The majority of these interactions are surprisingly transient to accommodate dynamic exchange, which is pivotal to provide cellular plasticity and efficient responses to external signals (28–30).

We aimed to extract quantitative measures of the binding properties of Dnmt1 *in vivo*. Unlike for many other nuclear factors, Dnmt1-binding sites are non-homogeneously distributed with association sites constantly changing their location throughout the cell cycle. To characterize the contribution of the PBD and TS domain on these changing interactions, we analyzed the mobility of wild type and mutants of GFP-tagged Dnmt1. In particular, we interpreted the differences between the mutants by modeling FRAP experiments where half of the nucleus is bleached. As the spatial distribution of the different binding sites is unknown a priori, we modified classical reaction-diffusion models in a way that diffusion is simplified into a two-compartment exchange model and binding events are averaged over the entire half-nucleus. This model also takes into account potential multiple binding partners of proteins with different binding affinities.

Our results provide evidence that the collective integrity of the PBD and TS domain is necessary and sufficient for the entire S phase–dependent targeting of Dnmt1 to its localization sites. Transient PBD-mediated interaction at RF is the predominant specific interaction in early S phase, while in late S phase, this binding class is relegated by an ~2-fold stronger TS domain-dependent binding. Supported by super-resolution imaging with 3D-structured illumination microscopy (3D-SIM) (31,32) we show that TS binding is not restricted to replication sites but also occurs PCNA/PBD-independently at postreplicative constitutive heterochromatin. We propose a two-loading-platform-model in which the increasing density of hemimethylated CpG sites in conjunction with increased level of heterochromatin marks at postreplicative heterochromatin in late S phase provides high-affinity binding sites for TS-mediated binding of Dnmt1. PCNA-independent loading downstream of replication thus provides a mechanism to ensure maintenance of densely methylated heterochromatic DNA sequences.

MATERIALS AND METHODS

Expression constructs and cell culture

The expression constructs, 1xGFP, 2xGFP, 4xGFP, GFP-Dnmt1^{wt}, GFP-Dnmt1^{Q162E} and GFP-Dnmt1$^{\Delta TS}$ have been described previously (6,33,34). GFP-Dnmt1$^{Q162E/\Delta TS}$ was derived from GFP-Dnmt1$^{\Delta TS}$ by overlap extension PCR. Mouse C2C12 myoblast cells were cultured in DMEM supplemented with 20% fetal bovine serum and 50 µg/ml gentamycine. For live cell experiments, cells were seeded in Lab-Tek chamber slides (Nunc) or µ-slides (Ibidi), using either pools of stably expressing cells or transiently transfected cells.

Creation of stably expressing cells has been described before (6). For transient transfections, cells were grown up to 30-40% confluence and transfected with TransFectin transfection reagent (Bio-Rad) or FuGENE HD (Roche) according to the manufacturer's instructions. Cells were then incubated overnight (TransFectin) or ~40 h (FuGENE HD) before performing FRAP experiments (6).

Only moderately expressing cells with unsuspicious morphology were chosen for further analysis. The overall Dnmt1 level of endogenous and ectopically expressed protein was determined for all analyzed constructs and cell lines by immunofluorescence labeling using a novel Dnmt1-specific rat monoclonal antibody 5A10. Quantitative analysis of labeling intensities revealed on average 2-fold increased protein levels compared with non-transfected control cells confirming no major overexpression of the GFP-Dnmt1 fusion constructs (see Supplementary Methods and Supplementary Figure S1 for details on the antibody characterization and the immunofluorescence assay).

EdU pulse labeling, immunofluorescence staining and structured illumination microscopy

Cells, stably expressing GFP-Dnmt1 fusions were seeded on No. 1.5H precision coverslips (Marienfeld Superior), formaldehyde fixed and permeabilized with ice-cold methanol. For labeling of postreplicative DNA, 5 µM 5-ethnyl-2'-deoxyuridine (EdU) was added to the growth medium 60 min before fixation. Endogenous PCNA was fluorescently labeled either with a rat monoclonal

antibody 16D10 (35) or a mouse monoclonal antibody PC10 (Abcam) and secondary antibodies conjugated to Alexa Fluor 594 (Invitrogen) or CF405S (Biotium). GFP was postlabeled with ATTO488 conjugated GFP-Booster (ChromoTek). EdU was detected by Cu (I) catalyzed cycloaddition ('click-chemistry') of 20 µM Alexa Fluor 594 Azide (Invitrogen) diluted in 0.1 M Tris/HCl (pH 8.6) containing 4 mM $CuSO_4$ and 50 mM Na-ascorbate. Cells were counterstained with 1 µg/ml 4',6-diamidino-2-phenylindole and embedded in Vectashield (Vector Laboratories).

3D-SIM was performed on a DeltaVision OMX V3 (Applied Precision) system equipped with a 100×/1.40 NA PlanApo oil immersion objective (Olympus), Cascade II:512 EMCCD cameras (Photometrics) and 405, 488 and 593 nm diode lasers. Structured illumination (SI) image stacks were acquired with a z-distance of 125 nm and with 15 raw SI images per plane (5 phases, 3 angles). The SI raw data were then computationally reconstructed with channel specifically measured optical transfer functions using the softWoRX 4.0 software package (Applied Precision) to obtain a super-resolution image stack with a lateral (x,y) resolution of ~120 nm and an axial (z) resolution of ~300 nm (31). Images from the different color channels were registered with alignment parameter obtained from calibration measurements with 0.2 µm diameter TetraSpeck beads (Invitrogen).

Live cell microscopy and quantitative FRAP analysis

Live cell imaging and FRAP experiments were typically performed on an Ultra*VIEW* VoX spinning disc microscope with integrated FRAP PhotoKinesis accessory (PerkinElmer) assembled to an Axio Observer D1 inverted stand (Zeiss) and using a 63×/1.4 NA Plan-Apochromat oil immersion objective. The microscope was equipped with a heated environmental chamber set to 37°C. Fluorophores were excited with 488 nm or 561 nm solid-state diode laser lines. Confocal image series were typically recorded with 14-bit image depth, a frame size of 256 × 256 pixels, a pixel size of 110 nm and with time intervals of 154 ms. For photobleaching experiments, the bleach regions, typically with a length of 8–10 µm, were chosen to cover the anterior half of the oval-shaped nucleus. Photobleaching was performed using two iterations with the acousto-optical tunable filter (AOTF) of the 488 nm and the 514 nm laser line set to 100% transmission. Typically, 20 prebleach and 780 postbleach frames were recorded for each series. In some cases, FRAP experiments were performed on a TCS SP5 AOBS confocal laser scanning microscope (Leica) using comparable settings as previously described (6).

Data correction, normalization and quantitative evaluations were performed by automated processing with ImageJ (http://rsb.info.nih.gov/ij/) using a set of self-developed macros followed by calculations in Excel. Details are provided in the Supplementary Methods and in Supplementary Figure S4.

Mathematical model

The mathematical models used to statistically infer the kinetic parameters from corrected and normalized FRAP datasets are based on a compartmental approach and biochemical kinetic principles. The model for diffusion-uncoupled FRAP, i.e. for molecules that diffuse much more rapidly than they bind or unbind, has previously been described (22,36). A model for diffusion-coupled FRAP is developed in this work and illustrated in Figure 4A; a similar approach has been taken in (37). The model considers transitions between the bound and the free state of a protein with *association rate constant* k_{on} and *dissociation rate constant* k_{off} . As substantiated in the Supplementary Methods, the association and dissociation dynamics can be expressed in terms of linear ordinary differential equations (ODEs) when replacing k_{on} by an *effective association rate constant* k^*_{on}. The ODEs are given below. While bound proteins remain fixed at the respective binding sites, free proteins diffuse through the nucleus, thus changing their locations. Movements between the bleached and the unbleached section are modeled with a *diffusion rate constant* k_{diff}. Its value depends on the geometry of the cell and is not immediately eligible for interpretation purposes. See the Supplementary Methods for details on the modeling of the movement of proteins.

Bleached and unbleached molecules are assumed to behave identically, and therefore it suffices to focus on one type only. Hence, let P^{free}_{bl}, P^{free}_{unbl}, P^{bound}_{bl} and P^{bound}_{unbl} denote the fractions of unbleached free and bound proteins in the bleached and unbleached sections, measured with respect to all unbleached proteins in the nucleus. These four parameters sum up to one such that one of them can be left out. Define $P^{free} = P^{free}_{bl} + P^{free}_{unbl}$ and $P^{bound} = P^{bound}_{bl} + P^{bound}_{unbl}$. The overall dynamics of unbleached proteins is described by

$$\frac{dP^{free}_{bl}}{dt} = -k^*_{on}P^{free}_{bl} + k_{off}P^{bound}_{bl} + k_{diff}\left(f_{bl}P^{free}_{unbl} - (1-f_{bl})P^{free}_{bl}\right), \quad (1)$$

$$\frac{dP^{free}_{unbl}}{dt} = -k^*_{on}P^{free}_{unbl} + k_{off}\left(1 - P^{free}_{bl} - P^{free}_{unbl} - P^{bound}_{bl}\right) - k_{diff}\left(f_{bl}P^{free}_{unbl} - (1-f_{bl})P^{free}_{bl}\right), \quad (2)$$

$$\frac{dP^{bound}_{bl}}{dt} = k^*_{on}P^{free}_{bl} - k_{off}P^{bound}_{bl}. \quad (3)$$

The recovery curve equals $F = \left(P^{free}_{bl} + P^{bound}_{bl}\right)/f_{bl}$. This term was adjusted to the data normalization procedure described in the Supplementary Methods and approaches the value one as time progresses.

There is possibly more than one type of binding partner for Dnmt1, i.e. the protein may sometimes associate to a partner of one type and sometimes to a partner of another type. These partners may differ with respect to the affinity of Dnmt1 to enter the bound state and the mean residence times in this state. All binding partners with identical or similar kinetic properties are gathered in one MC.

This term seems more appropriate than *classes of binding sites* (22) because different sites with identical kinetic properties cannot be distinguished using FRAP data. The number of MCs could hence be smaller than the number of different binding partners. Furthermore binding-unrelated processes like anomalous diffusion can fall into an MC.

Suppose there are M classes of kinetically different binding partners for the protein of interest, labeled with numbers $i \in \{1,...,M\}$. For all i, define $P_{bl}^{bound,i}$ and $P_{unbl}^{bound,i}$ as the fractions of type-i bound proteins in the bleached and unbleached sections, respectively, with $P^{bound,i} = P_{bl}^{bound,i} + P_{unbl}^{bound,i}$. Let $f_i = P^{bound,i}/P^{bound}$ be the fraction of type-i bound proteins with respect to all bound proteins. Furthermore, denote by $k_{on,i}^*$ and $k_{off,i}$ the association and dissociation rate constants corresponding to the ith MC. Then, the recovery is described by

$$\frac{dP_{bl}^{free}}{dt} = -P_{bl}^{free}\sum_{i=1}^{M} k_{on,i}^* + \sum_{i=1}^{M} k_{off,i}P_{bl}^{bound,i} + k_{diff}\left(f_{bl}P_{unbl}^{free} - (1-f_{bl})P_{bl}^{free}\right), \tag{4}$$

$$\frac{dP_{unbl}^{free}}{dt} = -P_{unbl}^{free}\sum_{i=1}^{M} k_{on,i}^* + \sum_{i=1}^{M} k_{off,i}P_{unbl}^{bound,i} - k_{diff}\left(f_{bl}P_{unbl}^{free} - (1-f_{bl})P_{bl}^{free}\right), \tag{5}$$

$$\frac{dP_{bl}^{bound,i}}{dt} = k_{on,i}^* P_{bl}^{free} - k_{off,i}P_{bl}^{bound,i}, \tag{6}$$

$$\frac{dP_{unbl}^{bound,i}}{dt} = k_{on,i}^* P_{unbl}^{free} - k_{off,i}P_{unbl}^{bound,i}, \tag{7}$$

where $i = 1,...,M$. The fluorescence intensity is $F = \left(P_{bl}^{free} + \sum_{i=1}^{M} P_{bl}^{bound,i}\right)/f_{bl}$.

Parameter estimation

The mathematical model contains several unknowns: The model parameters $k_{on,i}^*$, $k_{off,i}$ and k_{diff}, the initial values F_0, $P_{bl,0}^{free}$, $P_{bl,0}^{bound}$ for the components F, P_{bl}^{free}, P_{bl}^{bound}, etc. and the fractions f_{bl}, f_i of bleached proteins, bound proteins of type i, etc. Due to computational effort, parameter redundancies and strong correlation between some parameters, it is not meaningful to statistically infer all these unknowns simultaneously. Instead, some values were fixed as follows: k_{diff} and f_{bl} were experimentally determined (see Supplementary Table S3, Figure 4B and the data normalization description above). The smallest k_{off} value was set to 0.005 (see the Results section). F_0 was chosen equal to the first value of the FRAP curve. $P_{bl,0}^{free}$ was set equal to $f_{bl}F_0$. The association rates result from the other estimates as $k_{on,i}^* = k_{off,i}f_i(1-P^{free})/P^{free}$. Statistical inference of all remaining variables was carried out by least squares estimation. The ODEs (1)–(3) and (4)–(7) were numerically solved with the Euler scheme with step length 0.03, which corresponded to one-fifth of the observation interval. All software was written in R (R Development Core Team, 2011, R Foundation for Statistical Computing, Vienna, Austria).

We estimated the model parameters for each FRAP curve separately and compared the estimates for curves from the same cell cycle phase and Dnmt1 construct afterwards. For more details about the numerics, see the Supplementary Methods.

Model choice

In our analysis, we estimate models with different numbers of MCs. Because the models are nested, the inclusion of more MCs always leads to a better or at least equally good fit. However, one may ask whether the additional computational effort for multiple MCs is worth the improved matching of the data. At first glance, model choice criteria like the Akaike information criterion (AIC) (38) seem appropriate. In our application, however, the difference in the mean squared residuals for different models is typically small owing to parameter redundancies. Because of the large number of model parameters, the AIC will often favor less MCs although the curvature of the recovery curves is better described by more complex models. For that reason, we developed a model selection criterion that penalizes complexity less rigorously and is specific to our application. Due to the relatively small noise in the FRAP curves (Figure 3B and Supplementary Figure S6), we do not expect to overfit the data. The criterion reads as follows.

As explained in the Results section, the up to three MCs are further distinguished into one or two distinctive mobility classes (DMCs) and up to one catalytic mobility class (CMC). These have to fulfill three rules:

(1) If a DMC or CMC is present, the fraction P^{bound} of bound proteins should be above a certain threshold:

$$P^{bound} \geq \varepsilon_{bound}.$$

Otherwise the DMCs and CMC are discarded, and we assume no MCs for this FRAP curve.

(2) Two distinct MCs should differ substantially in their dissociation rates. In the model with two DMCs that means that one should have

$$\frac{k_{off,DMC1} - k_{off,DMC2}}{k_{off,DMC2}} \geq \delta_{DMC} \quad \text{or} \quad \frac{k_{off,DMC2} - k_{off,CMC}}{k_{off,CMC}} \geq \delta_{CMC}.$$

Otherwise we assume the effective number of DMCs to be one.

(3) An MC only truly contributes to the model if it reaches a certain size:

$$f_{DMC1}P^{bound} \geq \varepsilon_{DMC} \text{ and } f_{DMC2}P^{bound} \geq \varepsilon_{DMC} \text{ and } f_{CMC}P^{bound} \geq \varepsilon_{CMC}.$$

Otherwise we assume the effective number of DMCs to be one.

We derive appropriate values for the above thresholds by cluster analysis; see the Supplementary Methods for details and results. For each measured curve, we now

select the model that yields the best fit. This is typically the model with two DMCs and one CMC, but in many cases, the fit of the model with one DMC and one CMC is equally good and hence preferred. For the chosen model, the original number of DMCs is replaced by the effective number of DMCs as determined by the above rules (Supplementary Figure S9). Then, for each cell cycle phase and protein construct, the primarily chosen effective number of DMCs is determined. The model with the according number of DMCs is chosen for this phase and construct. Supplementary Table S3 displays the mean estimates for the selected model for all FRAP curves. These results always assume the original number of DMCs and do not further reduce it to an effective number.

RESULTS

Necessity and sufficiency of the PBD and TS domain for S phase–specific targeting of Dnmt1

Our aim was to analyze the S phase–dependent regulation of the Dnmt1-binding behavior. To that end, we investigated four GFP fusions: wild type Dnmt1 (GFP-Dnmt1^{wt}), the full-length Dnmt1 carrying a point mutation (GFP-Dnmt1^{Q162E}) within the PBD (6), a Dnmt1 mutant carrying a deletion of a highly conserved part of the TS domain comprising the amino acids 459–501 (GFP-Dnmt1$^{\Delta TS}$) and a Dnmt1 double mutant containing both mutations (GFP-Dnmt1$^{Q162E/\Delta TS}$) (Figure 1A). To identify different cell cycle stages, we first co-expressed GFP-Dnmt1 constructs with PCNA fused to monomeric red fluorescent protein (RFP-PCNA) in mouse C2C12 myoblast cells and acquired confocal mid sections of the living cells (Figure 1B). As previously described (6), GFP-Dnmt1^{wt} co-localized with RFP-PCNA at RF in early S phase. Co-localization with RF was also apparent in late S phase, when DNA of pericentromeric heterochromatin (pHC) is replicated. In contrast, the double mutant GFP-Dnmt1$^{Q162E/\Delta TS}$ was diffusely distributed within nuclei throughout interphase, suggesting a deficiency to target RF during S phase. GFP-Dnmt1$^{\Delta TS}$ still accumulated at RF in early and late S phase, but showed a slightly weaker association compared with GFP-Dnmt1^{wt}, indicating the activity of PBD-mediated targeting in all S phase stages, independent of the presence of the TS domain (Figure 1B and Supplementary Figure S2). As previously reported, GFP-Dnmt1^{Q162E} showed a diffuse nuclear distribution in early S phase but notable association to pHC replicating in late S phase (6). Together, this suggests that the PBD-mediated interaction with PCNA is necessary for the Dnmt1 localization in early S phase, but evidently not for the association at pHC in late S phase.

For a more detailed view on the spatial relationships of wild-type and mutant Dnmt1 and PCNA at RF, we used super-resolution 3D-SIM (31,32). Owing to the ~8-fold improved volumetric resolution of 3D-SIM (39), we could clearly notice subtle variations in the Dnmt1 localization that escaped detection with conventional imaging (Figure 2 and Supplementary Figure S3). In late S phase, GFP-Dnmt1^{wt} coincides to a large extent with immunofluorescently labeled endogenous PCNA foci in locally decondensed parts of otherwise homogenously compacted chromocenters with some Dnmt1 signal extending slightly (by a few 100 nm) beyond the PCNA signal. Interestingly, RF outside of chromocenters showed almost no enrichment of Dnmt1 (Figure 2A). In contrast, early S phase cells showed a more balanced co-localization at RF (Supplementary Figure S3A). Co-immunostaining of non-transfected cells with the Dnmt1-specific monoclonal antibody 5A10 confirmed the same localization characteristics for the endogenous Dnmt1, hence excluding potential artifacts by the GFP-tagging or overexpression (Supplementary Figure S3B). As opposed to this, GFP-Dnmt1$^{\Delta TS}$ precisely co-localized with all PCNA marked RF inside and outside of chromocenters (Figure 2B). GFP-Dnmt1^{Q162E}, similar to the wild type, displayed an enrichment at chromocenter-associated RF but also in the nearby regions of the chromocenters that were more compacted. We further noted these regions to become larger toward the end of late S phase, indicating that TS-mediated binding primarily occurs at postreplicative pHC (Supplementary Figure S3C). Pulse replication labeling with 5-ethenyl-2'-deoxyuridine and co-staining with PCNA confirmed the association of both, wild type and the PBD mutant Dnmt1 to postreplicative pHC (Figure 2D). Hence, we conclude a strict co-localization of the ΔTS mutant with PCNA at replication sites in late S phase, whereas both TS domain-containing constructs (GFP-Dnmt1^{Q162E} stronger than GFP-Dnmt1^{wt}) show a non-strict co-localization and a tendency to bind adjacent postreplicative pHC.

To gain further knowledge about the cell cycle–dependent dynamics of Dnmt1, we compared FRAP kinetics of mutant proteins with those of GFP-Dnmt1^{wt} in early S phase, late S phase and non-S phase cells with diffuse localization. The latter comprises mostly G1 cells but may also contain a smaller subset of late G2 phase cells, according to the different lengths of both stages. The comparison was done by half-nucleus FRAP analyses to quantify the strength and contribution of the PBD- and TS domain–mediated interactions in the distinct stages (Figure 3A). For a thorough quantitative evaluation of half-nucleus FRAP data, which preceded the application of the mathematical model, we developed an improved protocol for image registration, nuclear segmentation and data normalization (details described in Supplementary Methods and Supplementary Figure S4).

Initial controls revealed that the additional expression of RFP-PCNA influenced the kinetics of GFP-Dnmt1^{wt} (Supplementary Figure S5). Hence, to avoid any biasing effects, we decided not to co-express RFP-PCNA, but instead to collectively analyze all nuclei with diffuse nuclear distribution of the respective GFP fusion protein. Control measurements of diffusely localized GFP-Dnmt1^{Q162E} in RFP-PCNA co-expressing cells revealed no difference between the 'early S phase' and 'G1/late G2' group (data not shown). We quantitatively analyzed half-nucleus FRAP experiments of 10–20

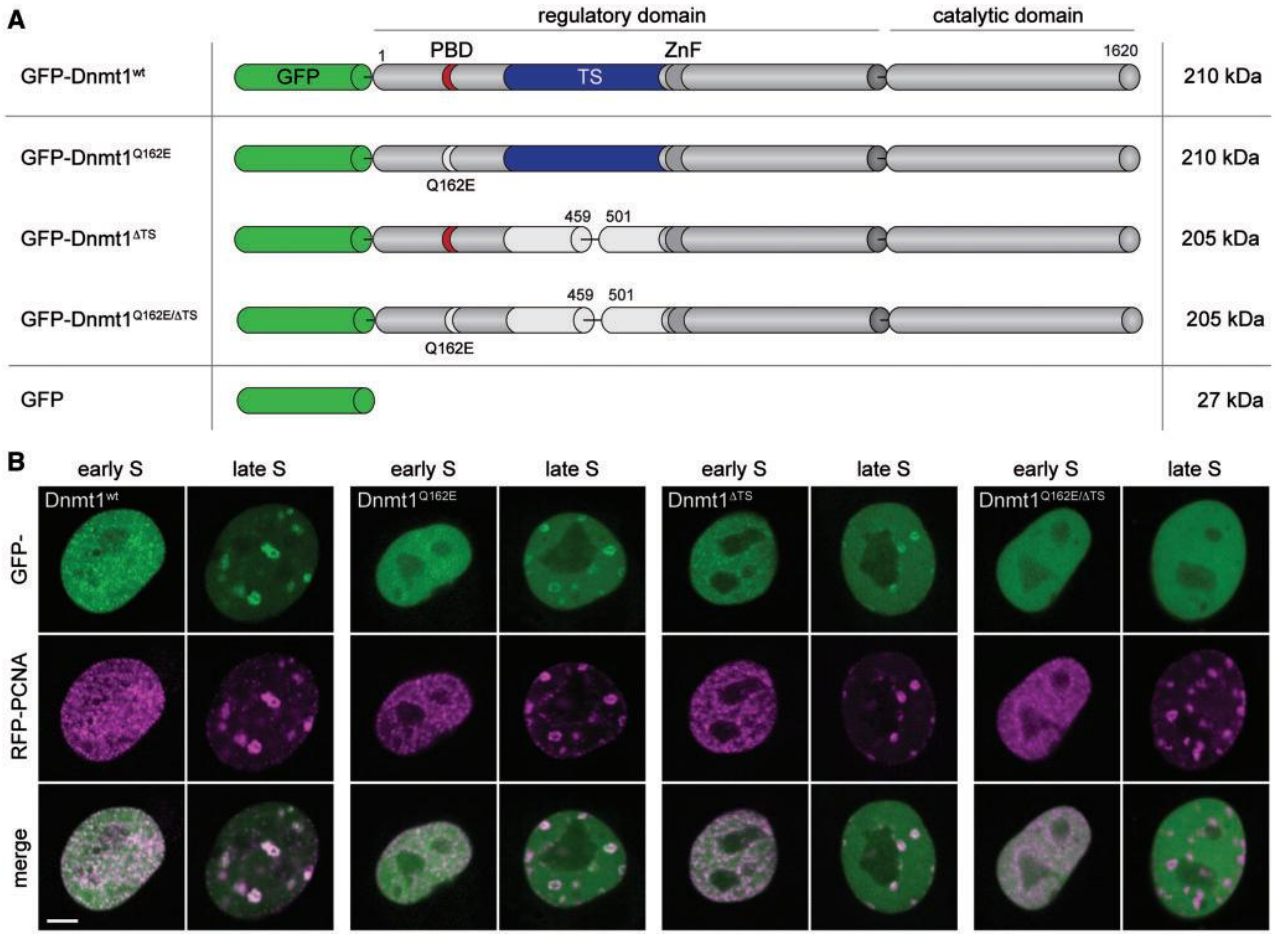

Figure 1. Domain structure and subnuclear localization of GFP-Dnmt1 constructs. (**A**) Dnmt1 consists of a large N-terminal regulatory domain containing PBD, TS domain and a CXXC zinc finger (ZnF) domain, and a conserved C-terminal catalytic domain. The point mutation of a highly conserved glutamine to glutamic acid introduced within the PBD eliminates interaction with the replication machinery (GFP-Dnmt1^{Q162E}). A deletion in the central part of the TS domain (GFP-Dnmt1$^{\Delta TS}$) was introduced to abolish interaction with constitutive heterochromatin. Furthermore a construct containing both mutations was generated (GFP-Dnmt1$^{Q162E/\Delta TS}$). GFP alone is used as a control for a non-binding protein. (**B**) Spinning disk confocal mid sections of GFP-Dnmt1 wild type (wt) and mutant constructs in live mouse C2C12 cells co-expressing RFP-PCNA to mark RF. In early S phase, GFP-Dnmt1^{wt} accumulates at RF, whereas PCNA-binding deficient GFP-Dnmt1^{Q162E} is diffusely distributed throughout the nucleus. GFP-Dnmt1$^{\Delta TS}$ is still associated with RF, but not as prominently as GFP-Dnmt1^{wt}. In late S phase GFP-Dnmt1^{wt}, GFP-Dnmt1^{Q162E} and GFP-Dnmt1$^{\Delta TS}$ accumulate at larger RF of late replicating pHC, although with slightly less strong enrichment observed for both mutants. GFP-Dnmt1$^{Q162E/\Delta TS}$ is distributed diffusely in the nucleus throughout interphase. Scale bar: 5 µm.

datasets for each construct and categorized cell cycle stage(s) (Figure 3B and Supplementary Figure S6) and determined half-times of the recovery ($t_{1/2}$) and mobile fractions (*MF*) (Supplementary Table S1)

In accordance with our previous observations (6), GFP-Dnmt1^{wt} showed a moderately reduced mobility in early S phase ($t_{1/2}$ 6.3 ± 0.3 s) compared with G1/late G2 phase ($t_{1/2}$ 3.3 ± 0.1 s) (Figure 3B and C). In late S phase, the recovery was even more reduced ($t_{1/2}$ 8.3 ± 0.6 s). Recovery kinetics of the GFP-Dnmt1$^{Q162E/\Delta TS}$ double mutant comprising all interphase stages revealed the same fast recovery kinetics ($t_{1/2}$ 3.6 ± 0.3 s) as observed for GFP-Dnmt1^{wt} in G1/late G2 phase, suggesting the complete loss of any S phase–specific interaction. The result implies that the collective integrity of PBD and the TS domain is necessary and sufficient for the entire S phase–dependent targeting of Dnmt1 to its localization sites.

Next, we analyzed both single mutants, GFP-Dnmt1^{Q162E} and GFP-Dnmt1$^{\Delta TS}$, to dissect the specific role of both domains in early S phase and late S phase. In agreement with our previous analyses of GFP-Dnmt1^{Q162E}, the kinetics measured for the pooled G1/late G2 and early S phase cells showing a diffuse distribution, was almost identical to that of GFP-Dnmt1^{wt} diffusely distributed only in G1/late G2 phase ($t_{1/2}$ 3.1 ± 0.2 s versus 3.3 ± 0.1 s) consistent with the loss of PCNA interaction in early S phase. In late S phase, despite localizing similar to GFP-Dnmt1^{wt}, the kinetics was slightly faster ($t_{1/2}$ 5.4 ± 0.4 s), indicating a contribution of the PBD to the binding behavior of Dnmt1^{wt} also in late S phase. However, the recovery was still slower as compared with the cells with diffuse localization, pointing toward an additional TS domain interaction. Comparing the wild-type construct with GFP-Dnmt1$^{\Delta TS}$, the mutant

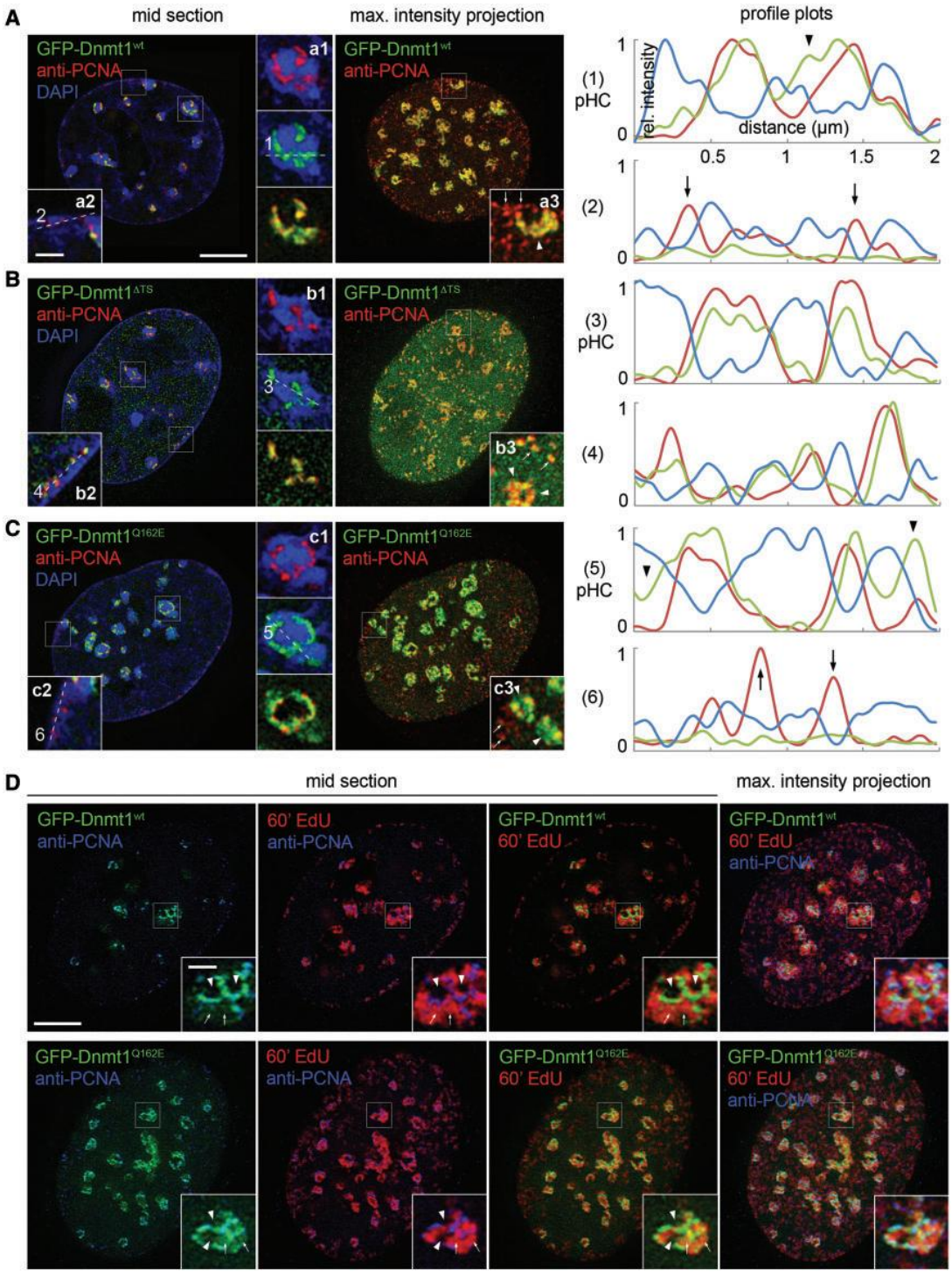

Figure 2. Super-resolution imaging of heterochromatin association of GFP-Dnmt1 constructs in late S phase. (**A–C**) 3D-SIM optical mid sections and z-projections from of C2C12 cells expressing GFP-Dnmt1 wild type and mutant constructs immunostained with antibodies against endogenous PCNA. Profile plots were scaled between minimum and maximum intensity values for each nucleus. (A) GFP-Dnmt1^{wt} co-localizes largely but not strictly with PCNA inside ~200 nm wide lacunas within otherwise densely packed DAPI-intense chromocenters of clustered pHC (inset a1, arrowheads in profile plot 1 and inset a3). Anti-PCNA-labeled RF outside of chromocenters show only minor or no association of Dnmt1 (inset a2, arrows in profile plot 2 and inset a3). (B) GFP-Dnmt1$^{\Delta TS}$ strictly co-localizes with PCNA at RF inside and outside chromocenters (insets b1 + b2 and profile plots 3 + 4). An increased diffuse fraction is visible as small grainy evenly distributed nucleoplasmic background. (C) GFP-Dnmt1^{Q162E} does not strictly co-localize with PCNA, but also associates with adjacent regions of pHC (arrowheads, inset c3 and profile plot 5). No association is detected in RF outside chromocenters (arrows, inset c3 and profile plot 6). (**D**) Additional replication labeling with a 60-min EdU pulse prior fixation. Association of GFP-Dnmt1^{wt} and GFP-Dnmt1^{Q162E} to chromocenter regions outside of PCNA foci is restricted to the bulk of EdU-labeled postreplicative chromatin (insets, arrows), while unlabeled, presumably not yet replicated chromocenter regions are still void of GFP-Dnmt1 (insets, arrowheads). Scale bars: 5 µm and 1 µm (insets).

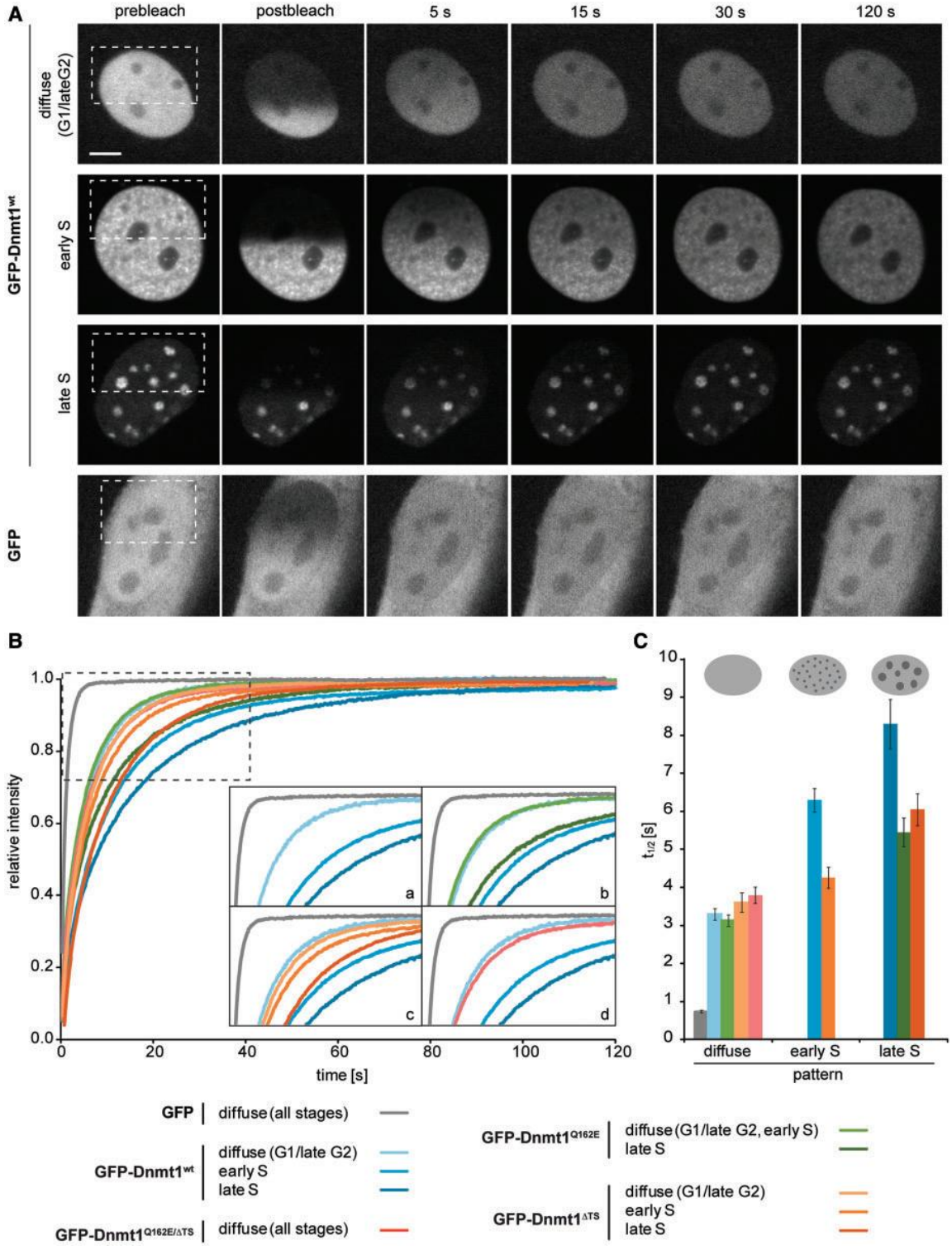

Figure 3. Quantitative FRAP evaluation of GFP and GFP-Dnmt1 constructs. (**A**) Representative time frames of exemplary half-nucleus FRAP series recorded with spinning disk confocal microscopy. Scale bar: 5 µm. (**B**) Mean recovery curves displayed for all measured constructs and cell cycle stages. The inset illustrates cycle-dependent kinetics of GFP and GFP-Dnmt1^{wt} alone (a), and in comparison with GFP-Dnmt1^{Q162E} (b), GFP-Dnmt1$^{\Delta TS}$ (c) and GFP-Dnmt1$^{Q162E/\Delta TS}$ (d). GFP-Dnmt1^{wt} in cells with diffuse localization shows a decreased mobility compared with GFP. The GFP-Dnmt1^{wt} mobility decreases stepwise in early S phase and in late S phase. The mobility of GFP-Dnmt1^{Q162E} in G1 (late G2) and early S cells (diffuse nuclear localization, pooled) is almost identical to GFP-Dnmt1^{wt} G1 (late G2) cells. In late S phase, a moderately increased mobility is observed for both, GFP-Dnmt1^{Q162E} and GFP-Dnmt1$^{\Delta TS}$ mutants compared with GFP-Dnmt1^{wt}. Of note, despite comparable overall kinetics, both curves (dark green, dark orange) are clearly different in their shape. In early S phase, the $t_{1/2}$ of GFP-Dnmt1$^{\Delta TS}$ is reduced compared to GFP-Dnmt1^{wt}. GFP-Dnmt1$^{Q162E/\Delta TS}$ (all interphase stages, pooled) displays kinetics almost identical to GFP-Dnmt1^{wt} in cells with diffuse localization. For clarity, error bars are omitted here, but shown in Supplementary Figure S6. (**C**) Half-times of recovery ($t_{1/2}$) determined for each construct and distribution pattern. Error bars represent SEM.

showed also faster kinetics in late S phase ($t_{1/2}$ 6.0 ± 0.4 s), suggesting that the TS domain together with the PBD are necessary for the wild-type kinetics in late S phase. Besides the role of the TS domain in late S phase, this mutation also enhanced the mobility in early S phase ($t_{1/2}$ 4.2 ± 0.3 s) in accordance with the fact that the early S phase pattern of RF association was less prominent (Figure 1B). This result indicates that the binding by the PBD domain to RF is necessary, but not sufficient for the early S phase–specific localization of Dnmt1.

We also noted that the mobile fractions (*MF*) of the wild-type construct within the observation time of 2 min dropped from around 100% in non-S phase to ~98% in early and late S phase. This directs to a small immobile fraction of covalently bound Dnmt1 involved in the covalent complex formation during the enzymatic reaction (Supplementary Table S1). This observation is consistent with a rather slow speed of the enzyme reaction measured *in vitro* with hemimethylated substrate (40–43). A small immobile fraction (~1%) was also noted for the Dnmt1 mutant construct.

To test the general ability as well as differences in the efficiency of the investigated regulatory Dnmt1 mutants to undergo covalent complex formation *in vivo*, we measured the time-dependent immobilization by FRAP on incubation with the mechanism-based inhibitor 5-aza-2'-deoxycytidine (44) (see Supplementary Methods for details on the trapping assay). In agreement with the observed small immobile fractions, all mutants became immobilized albeit with variable efficiencies, with GFP-Dnmt1^{wt} being already fully immobilized within 30–45 min (corresponding to a trapping rate of ~3% min^{-1}), followed by GFP-Dnmt1^{Q162E}, GFP-Dnmt1$^{\Delta TS}$ and GFP-Dnmt1$^{Q162E/\Delta TS}$ (only ~10% h^{-1}) (Supplementary Figure S7).

We conclude that the PBD and the TS domain are the only domains directly involved in S phase–specific targeting of Dnmt1 with respect to localization and kinetics and that both domains contribute to enhance the efficiency to initiate the catalytic reaction *in vivo*. To decipher the exact relationship of PBD- and TS domain–mediated binding in early and late S phase, however, a more sophisticated analysis is needed.

Kinetic modeling of half-nucleus FRAP with multiple binding classes and diffusion-coupled dynamics

We next sought to characterize the contribution of the PBD- and TS domain–mediated interactions in different stages of the cell cycle in a more precise quantitative manner. Hence, we utilized mathematical modeling to estimate the fraction of protein bound by these domains and the binding strength in the different cell cycle stages.

The choice of the model was based on several considerations. First, to take account for the heterogeneous spatial distribution of binding sites that strongly varies in different cell cycle stages. Second, to correct for diffusion-related effects. Third, to deal with multiple potentially superimposing interactions, or binding classes, respectively, including a small fraction of protein covalently bound during the catalytic reaction (Figure 4A). Such a level of complexity goes beyond the assumptions of FRAP analysis based on present reaction-diffusion models (45–48). Therefore, we decided to use a compartmental approach with size-calibrated diffusion correction, suitable for experiments with half-nucleus bleaching, which ensure representative distribution of binding sites in all cell cycle stages. Each of the two halves was then considered as a well-mixed homogeneous interaction system where proteins can bind to different binding partners (22,36).

Taking diffusion into account is especially important for assessing nuclear proteins as most of them undergo transient interactions in a diffusion-coupled behavior (18,46). This is also true for Dnmt1 (Supplementary Figure S8). To approximate the diffusion of the protein, we introduced a size-dependent correction factor (k_{diff}) as a measure for the exchange of free molecules between the bleached and unbleached half to approximate the diffusion of the protein as similarly performed in (37) (Figure 4A; see Materials and Methods). To estimate this exchange parameter, we performed FRAP calibration measurements of GFP monomers, dimers and tetramers, as they have known sizes and are presumably inert in cells (Figure 4B). The k_{diff} value corresponding to the size of GFP-Dnmt1 was extrapolated from the k_{diff} values experimentally determined for the other three constructs in the same cell line using an exponential regression curve (Figure 4B and Supplementary Table S2).

We noted that the normalized FRAP curves of GFP-Dnmt1 constructs, in particular those from S phase cells, typically did not reach a straight plateau after 2-min observation time. Instead, they still followed a slight incline. As outlined above, this might be attributed to a small fraction of molecules actively involved in covalent complex formation during methyl group transfer. *In vitro* measurements have previously demonstrated a rather slow catalytic reaction of human DNMT1 on hemimethylated DNA in the range of 1–22 min per CpG (40–43). To account for this possibility, we added a class with variable fraction size but a small fixed dissociation rate (k_{off}). This class is referred to as CMC. As opposed to that, classes with free k_{off} values will be referred to as DMC. The k_{off} value for the CMC was chosen to be 0.005 s^{-1}, which is equivalent to a mean residence time of 200 s (40). By fixing it, we avoided an additional free parameter in our fitting procedure. To further decrease the number of free parameters in our model, we also fixed the bleached fraction f_{bl} to an experimentally determined value for each FRAP experiment (see Materials and Methods). Altogether we estimated the k_{off} values of up to two DMCs, the fraction sizes of bound proteins (one CMC and two DMCs), and the remaining pool of free molecules (f_{free}).

Although this modeling approach does not cover the whole details of our experimental system, it concentrates on the characterization of the interactions while still integrating some essential information on the diffusion process and therefore provides a way to interpret the differences between the different forms of Dnmt1 during the different phases of the cell cycle. In conclusion, our compartmental model uses an experimentally

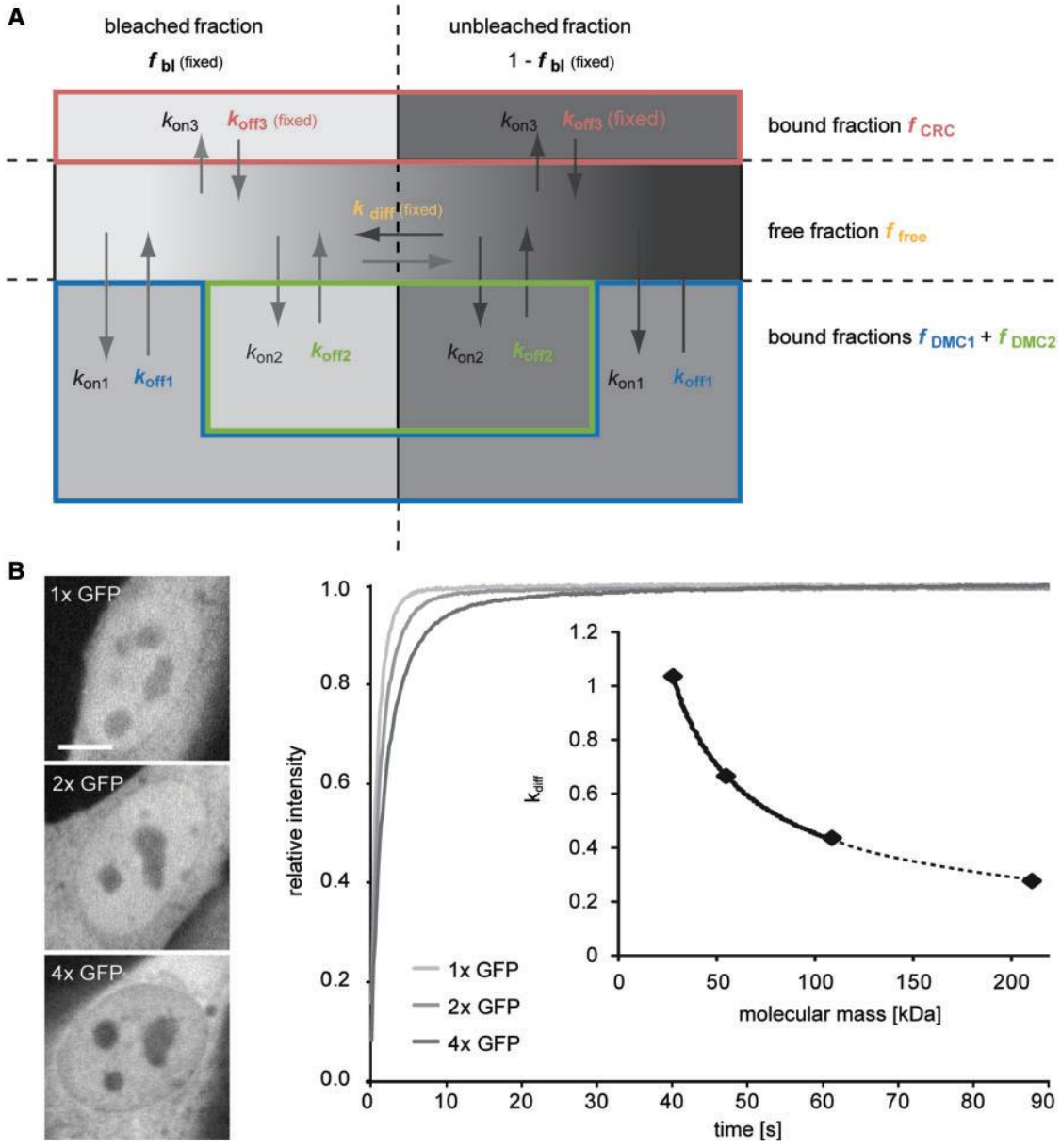

Figure 4. Refined diffusion-coupled compartmental model for three MCs and determination of k_{diff} from GFP multimer measurements. (**A**) The nuclear compartment is divided into four main compartments: bleached and unbleached molecules in the bound or free state, respectively. The bound state can be subdivided into three compartments with specific properties. For Dnmt1, we choose two DMCs (DMC1 and DMC2, blue and green frame, respectively) and one CMC (red frame) with a fixed k_{off}. Molecules bind and unbind with association and dissociation rates given by $k_{on,i}$ and $k_{off,i}$, respectively. In our refined modeling approach, the parameter f_{bl} is experimentally determined for each individual FRAP series. Migration of molecules is implemented in the model by introducing a new diffusion rate constant k_{diff}. This parameter corrects for the size-dependent exchange of the free molecules between the bleached and unbleached compartment. Parameter and variables entering the sets of differential equations are written in bold; predetermined/fixed values are indicated. (**B**) Quantitative FRAP evaluation of GFP multimers. The GFP mobility of the dimer and the tetramer decreases stepwise as compared with the monomer. The k_{diff} factor for the GFP constructs is estimated from the model with no DMC/CMC. From these values, the corresponding k_{diff} factor for the size of GFP-Dnmt1 is estimated using an exponential regression curve (inset diagram).

determined cell type–specific correction for size-dependent diffusion effects and can extract up to three dissociation rates and the sizes of all bound pools and the remaining free pool. This way we took into account several interaction partners, diffusion-coupled dynamics and the irregular distribution of binding sites of the protein.

Quantifying the properties of the PBD- and TS domain–mediated binding by FRAP modeling

We applied the enhanced kinetic model to our FRAP data of GFP-Dnmt1^{wt} and mutants. For each FRAP curve, the parameters of three differential equation models were determined using least squares estimation. These models

accounted for (i) no DMC/CMC, i.e. free proteins only, (ii) one DMC plus CMC or (iii) two DMCs plus CMC. The k_{diff} values were chosen according to the respective protein sizes (Supplementary Table S2). For each individual FRAP curve, the most appropriate model was determined based on the mean squared residuals and certain restrictions on the fraction sizes and magnitudes of the dissociation rates (see Materials and Methods). Then, for each construct and cell cycle phase, we identified the model that was preferentially chosen for the majority of datasets (Supplementary Figure S9). This model was then used to determine the final mean k_{off} values, the reciprocal mean residence times $T_{res} = 1/ k_{off}$ as well as the corresponding fraction sizes for all measured constructs and cell cycle stages (Figure 5 and Supplementary Table S3).

Model estimation for our reference FRAP measurements with GFP monomers and dimers provided a clear tendency of having no DMC (100% free fraction), whereas most FRAP curves of GFP-tetramers were best explained by a large free fraction (>91%) plus a smaller fraction of reduced mobility (<8%). Notably, the T_{res} determined for this fraction was rather high and showed a large variation indicating a GFP-multimer–specific effect. Analyzing the GFP-Dnmt1 constructs, we observed that a small fraction (f_{CMC} 1–4%) was always assigned to the class of molecules potentially involved in the catalytic process (CMC). Estimation of the size of the CMC is numerically difficult owing to the small fraction size. We hence do not interpret those estimates here.

For GFP-Dnmt1^{wt} expressing cells in G1/late G2, our model likewise estimated a large free fraction of ~80% and a population of ~19% with a relatively low mean residence time (T_{res} ~8 s). In early S phase, the bound fraction doubled to ~40% owing to binding to immobilized PCNA trimeric rings at replication forks (6, 49). The mean residence time measured for this class was with T_{res} ~10 s slightly higher. The largest fraction of 56% was still assigned to the free pool. In late S phase cells, the bound fraction remained in a similar range with 48%. Importantly, concomitant with binding to pHC at chromocenters, the model identified two distinct DMCs: 18% of the proteins were still bound with an intermediate strength (DMC1: T_{res} ~10 s), and an additional 28% with a substantially higher strength (DMC2: T_{res} ~22 s).

An 18–22% fraction with consistent kinetics was constitutively present in all cell cycle stages of the investigated GFP-Dnmt1 constructs. The nature of this constitutive MC remains unclear. In addition to the mutants described here, we performed FRAP analyses of a series of mutant constructs with deletions of potential interacting regions within the regulatory domain of Dnmt1, which included N-terminal truncations of various length (data not shown) and deletion within the ZnF domain (50). None of these mutants showed faster kinetics than GFP-Dnmt1^{wt} in diffuse cells. We therefore attribute this constitutive class to an anomalous diffusive behavior (see discussion) and not to particular DNA/chromatin binding mediated by a specific domain.

The modeling of FRAP data of the GFP-Dnmt1^{Q162E} mutant revealed a modest reduction of the DMC1 fraction size as compared with the level of GFP-Dnmt1^{wt} in all measured phases (diffuse, late S) (DMC1: 10–14%; T_{res} ~9 s). In late S phase cells, a second slower DMC with similar strength was still retained (DMC2: 23%; T_{res} ~19 s). From these results, we conclude that Dnmt1 binds PCNA at replication sites of early S phase cells with a mean residence time of ~10 s and with no more than 20–25% of the nuclear Dnmt1 pool being involved in this reaction. The binding of the Dnmt1 constructs with intact PBD to PCNA, as well as complete loss of the interaction by introduction of the Q162E point mutation was confirmed biochemically by co-immunoprecipitation (Supplementary Figure S10). In late S phase, only a minor decrease in the mean residence times of the first and second DMC was observable for GFP-Dnmt1^{Q162E} as compared with the wild type, indicating that the PBD does contribute, if only to a small extent, to the binding strength in late S phase. However, the overall bound fraction of molecules decreased compared with GFP-Dnmt1^{wt} in late S phase (66% versus 52%) causing an overall faster FRAP kinetics. The double mutant GFP-Dnmt1$^{Q162E/\Delta TS}$ did not establish any association pattern throughout interphase. In accordance, the extracted kinetic properties were almost identical to those of GFP-Dnmt1^{wt} in G1/late G2 (19%; T_{res} ~8 s).

Modeling of GFP-Dnmt1$^{\Delta TS}$ in early S phase revealed a modest reduction of the fraction size and binding strength (DMC1: 30%; T_{res} ~8.5 s compared with 39%; T_{res} ~10 s in the wild type). This could argue for either a stabilization of the PCNA complex at the replication sites by the TS domain or may hint to the presence of a minor fraction of strong binding sites, which is too small to be identified as a distinct class. In late S phase, still only one DMC was identified for GFP-Dnmt1$^{\Delta TS}$ (DMC1: 40%, T_{res} ~9 s), similar to GFP-Dnmt1^{wt} in early S phase. This suggests a prevalence of TS domain–mediated binding over PBD mediated, provided that the conditions for TS binding are complied (i.e. high density of hemimethylated CpG sites in conjunction with heterochromatic marks; see discussion below). In this case, binding to PCNA does only seem to play a supportive role. This view is also in accordance with the finding that in late S phase, the Q162E mutation alone does not change the DMC1 or DMC2 substantially, but only leads to a moderate increase in free protein.

DISCUSSION

We addressed the complex problem of dissecting the cell cycle–dependent regulation of Dnmt1 by super-resolution 3D imaging, FRAP and kinetic modeling. Two main factors add to the complexity of the analysis. First, Dnmt1 is a large enzyme with multiple regulatory subdomains, interaction partners and cell cycle–dependent regulation. Second, the distribution pattern of Dnmt1 is highly variable throughout the cell cycle. Hence, we chose a global approach using half-nucleus FRAP to capture in all cases representative fractions of bound molecules and binding sites. Previous studies often used spot bleaching with a defined geometry that allowed the extraction of diffusion coefficients (24,51,52). However, such models

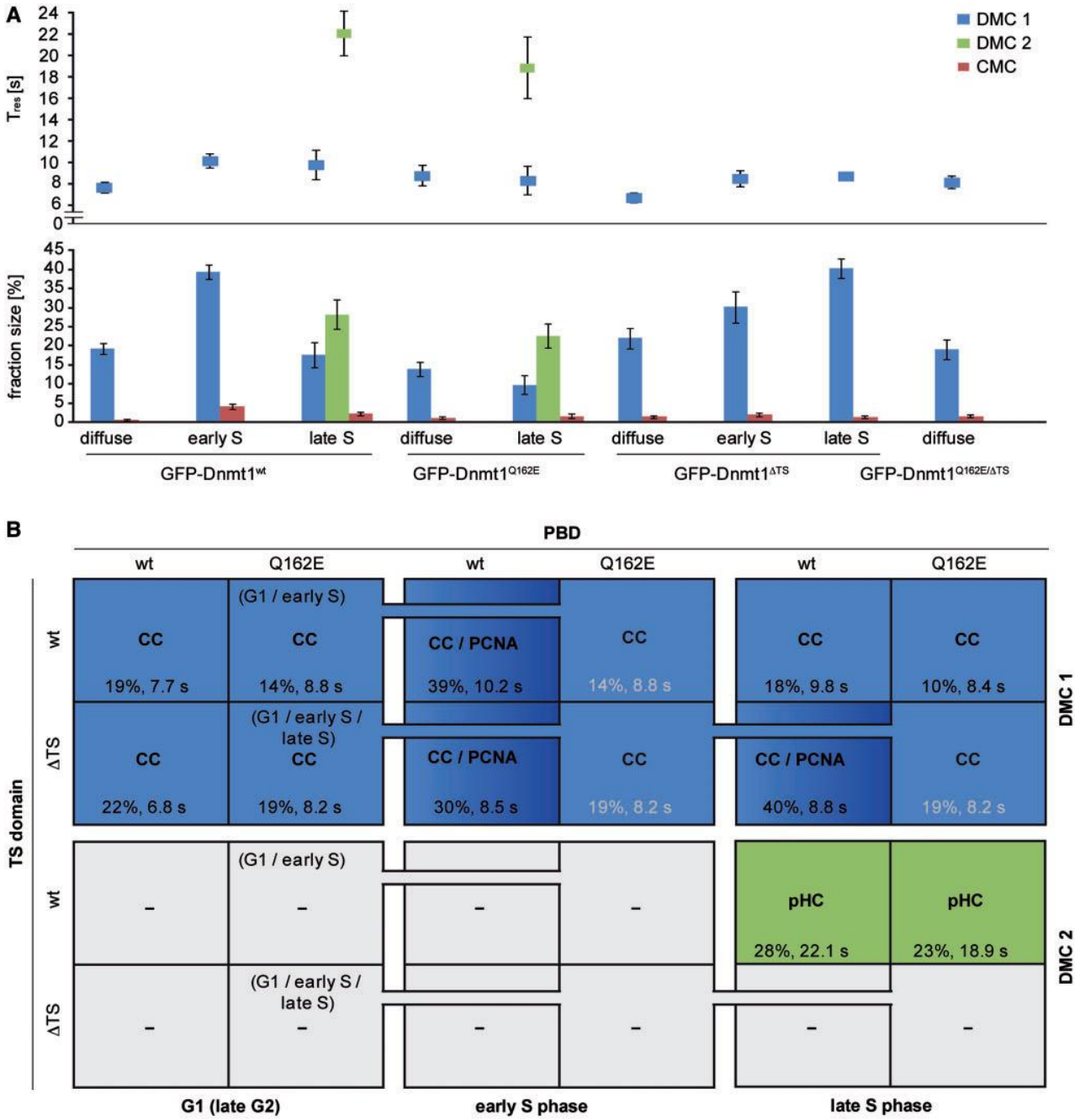

Figure 5. Parameters extracted from the kinetic modeling of GFP-Dnmt1 constructs. (**A**) Mean residence times (T_{res}, upper panel) and fractions of bound molecules (f_{bound}, lower panel) in three different classes (DMC1, DMC2, CMC) are displayed (not displayed free fractions add to 100% total amount). In all analyzed GFP-Dnmt1 constructs, a fast population of molecules was identified with mean residence times between 6 s and 10 s (DMC1). The fraction of this fast population (DMC1) typically varies between 10% and 22%, but rises for GFP-Dnmt1^{wt} in early S phase (40%) and for GFP-Dnmt1$^{\Delta TS}$ in early and late S phase (30 and 40%, respectively) due to the interaction with PCNA. A second, slower class (DMC2) was determined for both constructs with intact TS domain in late S phase with residence times varying from 19 to 22 s (DMC2) and an average size between 23 and 28%, respectively. The size of the CMC with a fixed T_{res} of 200 s varies between 0 and 4.1%. Bars indicate SEM. (**B**) Parameters are sorted according to their targets PCNA and pHC and the constitutively present unspecified MC (constitutive class, CC).

typically only included no more than one additional binding class, while we expected multiple interactions. Therefore, none of the previous models was immediately applicable to our case, which prompted us to devise a customized model.

To eliminate a weak point of diffusion-uncoupled approaches, we further corrected for size-dependent diffusion using a calibration factor that was experimentally determined from measurements of GFP multimer proteins. Anomalous diffusion behavior has previously

been shown for GFP and dextran in the nucleus (53–55). This indicates that calculation of size-dependent diffusion differences according to the Stokes-Einstein relation might lead to wrong parameter estimates for proteins in the nucleus (56), especially when large size differences like between GFP and Dnmt1 are taken into account.

FRAP measurements are sensitive to experimental conditions and set-ups (57). We tried to correct for most conceivable external influences during image evaluation by using a tailored workflow of postprocessing steps (see Supplementary Materials and Methods). This involved image registration, constrained automated nuclear segmentation and three-step normalization/correction. Altogether, this allows us to compensate for lateral cell movement, nuclear import and export, bleaching due to image acquisition and variations in bleaching depth, which otherwise potentially affect the raw data and subsequent modeling results. Moreover, we modeled a slow CMC using a low fixed k_{off} value, taking into account that a small fraction of molecules is likely to be involved in catalysis and thereby transiently immobilized by a covalent complex formation (40,43). Finally, we also reduced the number of free parameters by fixing the size of the bleached fraction to a value experimentally determined for each FRAP series. The number of DMCs was determined by model choice rules, which are oriented toward the numerical properties of the model.

Although our model allows for three distinct MC, we possibly cannot estimate their number and properties beyond all doubt, mostly because two or more distinct interactions may fall into one MC (see Materials and Methods). If interaction strengths of multiple interactions are relatively close to each other, they may not be detected as separate classes but be captured as one with an intermediate mixed k_{off}. The appearance of such parameter redundancies depends on the model and the values of the underlying parameters (e.g. 58). However, different dynamics can still be distinguished indirectly by a changed fraction size. An example for mixed interactions in one class is the similar kinetics of the non-specified *constitutive class* and of GFP-Dnmt1^{wt} binding to PCNA. This rather small constitutive fraction may be attributed to one or more residual transient interactions. So far, we could not detect any specific subdomain of Dnmt1 that would be responsible for a transient interaction throughout the cell cycle (data not shown). Thus, we tend to attribute this to an anomalous diffusive behavior within the nucleus that is identified as a pseudo-binding class. This may be caused by restrained accessibility of dense chromatin domains and transient trapping inside of small chromatin lacunas ('corralling') generating a 'pseudo' binding effect and/or by unspecific transient binding with a broad distribution of binding affinities (53,54,59). Dnmt1 could also be constitutively present in a free diffusing complex including interacting proteins like PCNA or Uhrf1. In fact, Dnmt1 interactions have been described for a variety of proteins including other DNA methyltransferases, chromatin modifiers and transcriptional regulators (60). Interactions with high molecular weight complexes could potentially slow down diffusion of GFP-Dnmt1 and thus contribute to the observed dynamics.

Another limitation of our method is the precision limit imposed by a still large cell-to-cell variability due to (i) technical reasons like residual uncorrected cell motion or z-drift, irradiation/transfection-induced DNA damage or cell cycle arrest or (ii) biological reasons such as variations in endogenous expression and methylation levels or local environment. Therefore, for example, the quantification of the apparently small CMC gives no robust results. However, by estimating the kinetic parameters for each FRAP curve separately, we take into account this extrinsic noise and quantify it through standard errors. Finally, using experimental FRAP data, it can never be ruled out that the kinetics are influenced by variations in k_{on} rates. However, the method does not allow assessing changes in the accessibility of the binding sites. These technical limitations could only be solved using large-scale simulations and even more complex models.

Despite these potential shortcomings, by application of our method, one can still obtain a detailed picture of the distinct cell cycle–dependent dynamics of proteins. We have shown that the PBD and the TS domain are the only domains involved in direct S phase-dependent targeting of Dnmt1 and responsible for delaying its mobility. Furthermore, we discriminated two different MCs that could be matched to these two different domains of Dnmt1. In this study, we quantified the time they bind on average and found the binding via the TS domain to be >2-fold stronger than via the PBD, whereas the corresponding fractions of bound protein were in a similar size range between 20 and 30%.

In accordance with previous studies, we show that the more transient interaction with PCNA increases the concentration of Dnmt1 at replication sites to enhance the efficiency of maintenance DNA methylation (7). In addition, we have characterized the stronger binding properties of the TS domain. The related MC was only present in late S phase, when pericentric heterochromatin (pHC) clustered in DAPI dense chromocenters is replicated, suggesting a switch between PBD-mediated binding in early S phase to the TS domain–mediated binding in late S phase. The analysis of the single mutants, however, hinted at a somewhat more complex situation, as the deletion within the TS domain also influenced GFP-Dnmt1 kinetics in early S phase and the mutation in the PBD influenced the GFP-Dnmt1 localization in late S phase. This rather argues for a more subtle continuous change in binding balance instead of a simple on/off switching. Hence, association via the TS domain might occur also in early S phase, but at much lower abundance. Indeed a substantial minority (8/21) of early S phase cells could be better fitted with two respective distinct MCs, indicating some cell-to-cell variability, possibly in transition to mid S phase. On the other hand, PBD-mediated co-localization with PCNA is also observed in late S phase. However, as the fraction size with the respective faster off-rate is reduced to non-S phase level, this Dnmt1 fraction may be handed over to form a late S phase–specific, more stable complex, such that the TS domain–specific off-rate becomes

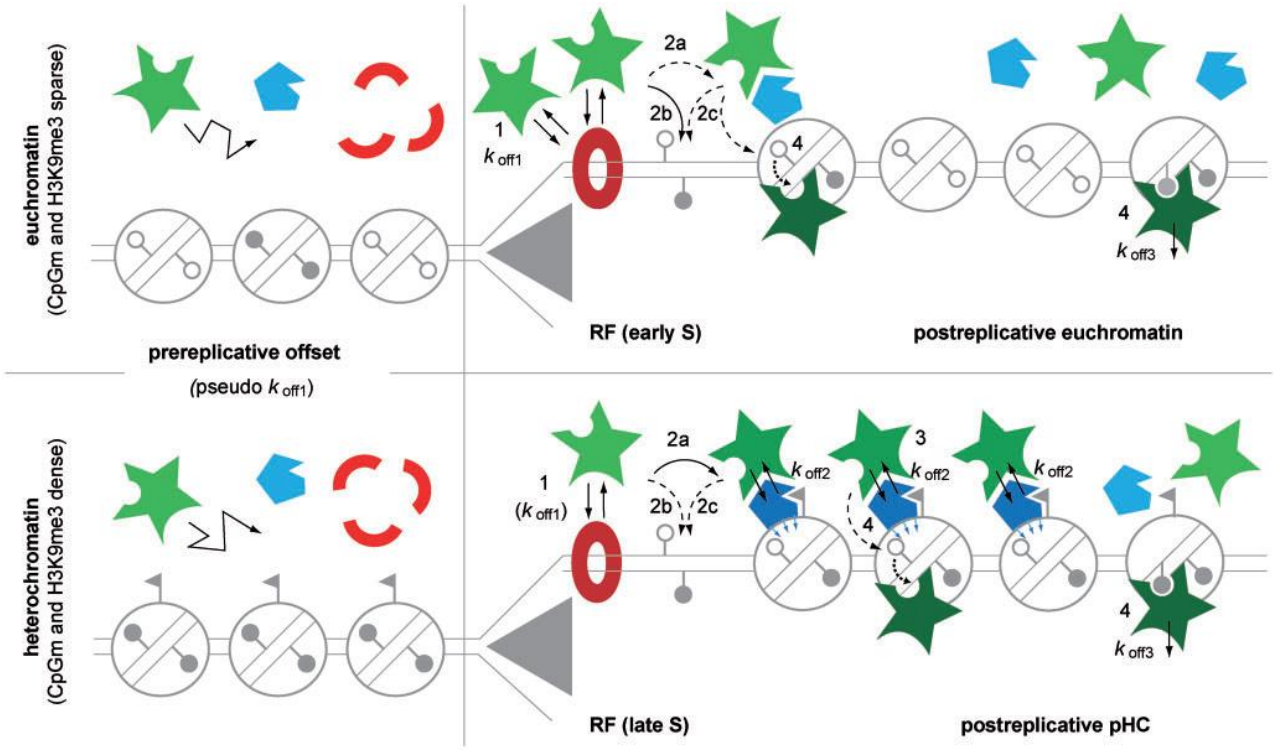

Figure 6. Two-loading-platform-model for the cell cycle–dependent targeting of Dnmt1 to RF and pHC. Schematic representation not drawn to scale. Closed and open lollipops indicate methylated and non-methylated CpG sites, respectively; flags indicate heterochromatin specific marker (e.g. H3K9me3). Dnmt1 is depicted in green. The model postulates two auxiliary factors that act as immobilizing platforms under certain conditions: PCNA (red) that assembles as trimeric ring at the replication fork throughout S phase, and a second unspecified factor (e.g. Uhrf1, blue) that binds strongly to hemimethylated postreplicative heterochromatin. Independent of replication, most Dnmt1 molecules (~80% in G1, >50% in S phase) are freely roaming the nucleoplasm (left column). In addition, a non-specified MC with a pseudo $k_{off,1}$ is constitutively present throughout interphase, which may be attributed to either non-specific binding to chromatin or transient trapping ('corralling') of the large enzyme in the nucleoplasmic environment. When replicating euchromatic sequences in early S phase (upper row) an additional ~20% fraction of the Dnmt1 pool transiently binds via the PBD to immobilized PCNA rings (red donut) with a mean residence time ($1/k_{off,1}$) of ~10 s (1). Targeting to PCNA at RF enhances the efficiency of a small fraction of Dnmt1 to form metastable covalent complexes ($k_{off,1}$) with hemimethylated CpG substrate sites in close vicinity. This may occur on already assembled nucleosomes, likely involving complex formation with one or several auxiliary factors (2 a), or directly on the naked DNA substrate adjacent to PCNA (2 b) or to nucleosomes (2 c). In late S phase, replication through chromatin with now abundant heterochromatic marks in conjunction with dense CpG methylation triggers the generation of high-affinity binding sites for an auxiliary protein. These may then act as second loading platform (dark blue pentagons) for TS-mediated binding with mean residence time ($1 / k_{off,2}$) of ~22 s involving ~25% of the Dnmt1 pool. Formation of this transient complex with subsequent substrate binding of a small subset of molecules occurs either directly at the replication fork promoted by PBD-mediated targeting, or PCNA independently at already displaced postreplicative heterochromatin chromatin that may have escaped loading in the first instance (3). This second PCNA-independent loading complex may be assembled well into G2 phase, until all hemimethylated Dnmt1 target sites are fully methylated, which finally triggers disassembly of the loading complex and dissociation of Dnmt1 (4). Of note, this conceptual model is based on the differential availability of binding sites and the free interplay of forces. While higher affinity binding sites are occasionally generated also in early S phase, they may be too sparse to constitute a separate MC.

predominant. In this stage, PCNA binding would thus be an auxiliary factor for TS-mediated binding of a Dnmt1 subfraction. Besides, supported by super-resolution microscopy, we provide evidence for additional PCNA/PBD-independent binding to pHC. The latter seems to be dependent not only on the heterochromatic context alone, but also on the presence of hemimethylated postreplicative DNA as precondition. Accordingly we did not observe any pHC association in early S phase. It is tempting to speculate that the observed kinetics reflect the binding of the TS domain to Uhrf1, an essential epigenetic factor that has previously been shown to target Dnmt1 to hemimethylated CpG sites and to bind trimethylated H3K9 (13–17). However, we cannot rule out other/additional modes of binding of the TS domain to pHC. In support of a role of Uhrf1 as a docking platform for Dnmt1, a previous FRAP study demonstrated a much slower recovery of GFP-Uhrf1 compared to GFP-Dnmt1^{wt} in mouse embryonic stem cells (61).

In light of our data we propose a conceptual two-loading-platform model (outlined in Figure 6). According to this, the kinetic balance would shift from predominant PCNA/PBD binding in early S phase, toward TS-mediated binding in later S phase stages when replicating densely methylated heterochromatic sequences. This shift would be triggered by the strongly increased appearance of hemimethylated CpG sites in conjunction with heterochromatic marks (e.g., H3K9me3). These would then offer the target for the formation of a

stable complex (involving e.g. Uhrf1) that acts as a second Dnmt1 loading platform on postreplicative chromatin sites. PCNA-independent loading complexes may persist also beyond S phase, until all hemimethylated Dnmt1 target sites are fully methylated, which in turn triggers complex disassembly and gradual loss of TS-mediated binding in G2 phase. Such a mechanism would thus safeguard faithful maintenance of dense methylation at constitutive heterochromatin important for genome stability (3), against the backdrop of a rather slow and inefficient catalytic reaction (40).

While we favor a model of free interplay of forces in conjunction with a cell cycle dependent varying abundance of high affinity binding sites, we cannot rule out an effect by an induced conformational change of the Dnmt1 protein to expose the TS domain at the onset of late S phase. In this context, several modifications have been reported like acetylation, ubiquitination, phosphorylation, methylation and sumoylation, resulting in a change in activity and/or abundance of Dnmt1 (60,62–64). For example, it has been shown that Uhrf1 ubiquitinates Dnmt1 at the C-terminal part of the TS domain (33). Further studies will have to address the exact interplay of Uhrf1 and Dnmt1 as a function of variable (hemi)methylation density and the role of posttranslational modifications of Dnmt1.

In the present study, we have reached substantial improvements on the experimental conditions and workflow for the quantitative and qualitative evaluation of half-nucleus FRAP experiments. Still, extracting definite answers from modeling of such FRAP data remains difficult and to some extent limited. Of note, our analysis involved multiple decisions on the data normalization, fixation of parameters, model choice, etc. Although all steps have been carried out with greatest care, this deterministic approach will still fall to some extent short. New stochastic modeling approaches may be able to realistically take into account random events and may hence better explain intrinsic variability of the FRAP curves. Nonetheless, this article provides a framework for the global assessment and quantitative measurement of diffusion-coupled nuclear protein dynamics with heterogeneous and variable distribution of binding sites, e.g. during cell cycle and development.

Our approach provided new insights into the complex cell cycle dependent regulation of the multi-domain protein Dnmt1 in the epigenetic network. We arrived at a probabilistic two-loading-platform model that provides a possible explanation how PBD and TS domain act cooperatively to faithfully maintain genomic methylation patterns through cell cycle and cell divisions. Further studies will address the mechanistic nature of the complex formation involving the TS domain and the targeting of Dnmt1 to hemimethylated sites.

SUPPLEMENTARY DATA

Supplementary Data are available at NAR Online: Supplementary Tables 1–3, Supplementary Figures 1–10, Supplementary Methods and Supplementary References [65–68].

ACKNOWLEDGMENTS

We thank Joachim Hermisson and Julia Sommer for helpful discussions. We are grateful to Florian Rieß, Susanne Giehler, Andreas Maiser, Anna Ullraum, Carina Frauer and Thomas Pyttel for technical help. We further thank Nikola Müller and Garwin Pichler for critical comments on the manuscript.

FUNDING

Deutsche Forschungsgemeinschaft [DFG SFB TR5 and SFB 684 to H.L and L.S.]; Nanosystems Initiative Munich [NIM to H.L.]; Bundesministerium für Bildung und Forschung (BMBF) Episys program [to H.L.]. K.S. was supported by the International Doctorate Program NanoBioTechnology (IDK-NBT) and the International Max Planck Research School for Molecular and Cellular Life Sciences (IMPRS-LS). P.W. is a fellow of the Graduate School Life Science Munich (LSM). CF was supported by the European Union within the European Research Council (ERC) grant LatentCauses. Funding for open access charge: Deutsche Forschungsgemeinschaft [SFB TR5 to L.S.].

Conflict of interest statement. None declared.

REFERENCES

1. Reik,W. (2007) Stability and flexibility of epigenetic gene regulation in mammalian development. *Nature*, **447**, 425–432.
2. Bird,A. (2002) DNA methylation patterns and epigenetic memory. *Genes Dev.*, **16**, 6–21.
3. Gaudet,F., Hodgson,J.G., Eden,A., Jackson-Grusby,L., Dausman,J., Gray,J.W., Leonhardt,H. and Jaenisch,R. (2003) Induction of tumors in mice by genomic hypomethylation. *Science*, **300**, 489–492.
4. Bestor,T.H. (2000) The DNA methyltransferases of mammals. *Hum. Mol. Genet.*, **9**, 2395–2402.
5. Prokhortchouk,E. and Defossez,P.A. (2008) The cell biology of DNA methylation in mammals. *Biochim. Biophys. Acta.*, **1783**, 2167–2173.
6. Schermelleh,L., Haemmer,A., Spada,F., Rosing,N., Meilinger,D., Rothbauer,U., Cardoso,M.C. and Leonhardt,H. (2007) Dynamics of Dnmt1 interaction with the replication machinery and its role in postreplicative maintenance of DNA methylation. *Nucleic Acids Res.*, **35**, 4301–4312.
7. Spada,F., Haemmer,A., Kuch,D., Rothbauer,U., Schermelleh,L., Kremmer,E., Carell,T., Langst,G. and Leonhardt,H. (2007) DNMT1 but not its interaction with the replication machinery is required for maintenance of DNA methylation in human cells. *J. Cell Biol.*, **176**, 565–571.
8. Chuang,L.S., Ian,H.I., Koh,T.W., Ng,H.H., Xu,G. and Li,B.F. (1997) Human DNA-(Cytosine-5) Methyltransferase-PCNA Complex as a Target for p21WAF1. *Science*, **277**, 1996–2000.
9. Moldovan,G.L., Pfander,B. and Jentsch,S. (2007) PCNA, the maestro of the replication fork. *Cell*, **129**, 665–679.
10. Leonhardt,H., Page,A.W., Weier,H.U. and Bestor,T.H. (1992) A targeting sequence directs DNA methyltransferase to sites of DNA replication in mammalian nuclei. *Cell*, **71**, 865–873.
11. Easwaran,H.P., Schermelleh,L., Leonhardt,H. and Cardoso,M.C. (2004) Replication-independent chromatin loading of Dnmt1 during G2 and M phases. *EMBO Rep.*, **5**, 1181–1186.

12. Frauer,C. and Leonhardt,H. (2011) Twists and turns of DNA methylation. *Proc. Natl Acad. Sci. USA*, **108**, 8919–8920.
13. Sharif,J., Muto,M., Takebayashi,S., Suetake,I., Iwamatsu,A., Endo,T.A., Shinga,J., Mizutani-Koseki,Y., Toyoda,T., Okamura,K. *et al.* (2007) The SRA protein Np95 mediates epigenetic inheritance by recruiting Dnmt1 to methylated DNA. *Nature*, **450**, 908–912.
14. Arita,K., Ariyoshi,M., Tochio,H., Nakamura,Y. and Shirakawa,M. (2008) Recognition of hemi-methylated DNA by the SRA protein UHRF1 by a base-flipping mechanism. *Nature*, **455**, 818–821.
15. Avvakumov,G.V., Walker,J.R., Xue,S., Li,Y., Duan,S., Bronner,C., Arrowsmith,C.H. and Dhe-Paganon,S. (2008) Structural basis for recognition of hemi-methylated DNA by the SRA domain of human UHRF1. *Nature*, **455**, 822–825.
16. Hashimoto,H., Horton,J.R., Zhang,X., Bostick,M., Jacobsen,S.E. and Cheng,X. (2008) The SRA domain of UHRF1 flips 5-methylcytosine out of the DNA helix. *Nature*, **455**, 826–829.
17. Bostick,M., Kim,J.K., Esteve,P.O., Clark,A., Pradhan,S. and Jacobsen,S.E. (2007) UHRF1 plays a role in maintaining DNA methylation in mammalian cells. *Science*, **317**, 1760–1764.
18. Sprague,B.L. and McNally,J.G. (2005) FRAP analysis of binding: proper and fitting. *Trends Cell Biol.*, **15**, 84–91.
19. Reits,E.A. and Neefjes,J.J. (2001) From fixed to FRAP: measuring protein mobility and activity in living cells. *Nat. Cell Biol.*, **3**, E145–E147.
20. Phair,R.D. and Misteli,T. (2001) Kinetic modelling approaches to *in vivo* imaging. *Nat. Rev. Mol. Cell Biol.*, **2**, 898–907.
21. Lippincott-Schwartz,J. and Patterson,G.H. (2003) Development and use of fluorescent protein markers in living cells. *Science*, **300**, 87–91.
22. Phair,R.D., Scaffidi,P., Elbi,C., Vecerova,J., Dey,A., Ozato,K., Brown,D.T., Hager,G., Bustin,M. and Misteli,T. (2004) Global nature of dynamic protein-chromatin interactions *in vivo*: three-dimensional genome scanning and dynamic interaction networks of chromatin proteins. *Mol. Cell Biol.*, **24**, 6393–6402.
23. Axelrod,D., Koppel,D.E., Schlessinger,J., Elson,E. and Webb,W.W. (1976) Mobility measurement by analysis of fluorescence photobleaching recovery kinetics. *Biophys. J.*, **16**, 1055–1069.
24. Stasevich,T.J., Mueller,F., Brown,D.T. and McNally,J.G. (2010) Dissecting the binding mechanism of the linker histone in live cells: an integrated FRAP analysis. *EMBO J.*, **29**, 1225–1234.
25. Houtsmuller,A.B. and Vermeulen,W. (2001) Macromolecular dynamics in living cell nuclei revealed by fluorescence redistribution after photobleaching. *Histochem. Cell Biol.*, **115**, 13–21.
26. Dundr,M. and Misteli,T. (2001) Functional architecture in the cell nucleus. *Biochem. J.*, **356**, 297–310.
27. Cardoso,M.C., Schneider,K., Martin,R.M. and Leonhardt,H. (2012) Structure, function and dynamics of nuclear subcompartments. *Curr. Opin. Cell Biol.*, **24**, 79–85.
28. Gorski,S.A., Dundr,M. and Misteli,T. (2006) The road much traveled: trafficking in the cell nucleus. *Curr. Opin. Cell Biol.*, **18**, 284–290.
29. Misteli,T. (2001) Protein dynamics: implications for nuclear architecture and gene expression. *Science*, **291**, 843–847.
30. Meshorer,E. and Misteli,T. (2006) Chromatin in pluripotent embryonic stem cells and differentiation. *Nat. Rev. Mol. Cell Biol.*, **7**, 540–546.
31. Schermelleh,L., Carlton,P.M., Haase,S., Shao,L., Winoto,L., Kner,P., Burke,B., Cardoso,M.C., Agard,D.A., Gustafsson,M.G. *et al.* (2008) Subdiffraction multicolor imaging of the nuclear periphery with 3D structured illumination microscopy. *Science*, **320**, 1332–1336.
32. Gustafsson,M.G., Shao,L., Carlton,P.M., Wang,C.J., Golubovskaya,I.N., Cande,W.Z., Agard,D.A. and Sedat,J.W. (2008) Three-dimensional resolution doubling in wide-field fluorescence microscopy by structured illumination. *Biophys. J.*, **94**, 4957–4970.
33. Qin,W., Leonhardt,H. and Spada,F. (2011) Usp7 and Uhrf1 control ubiquitination and stability of the maintenance DNA methyltransferase Dnmt1. *J. Cell Biochem.*, **112**, 439–444.
34. Seibel,N.M., Eljouni,J., Nalaskowski,M.M. and Hampe,W. (2007) Nuclear localization of enhanced green fluorescent protein homomultimers. *Anal. Biochem.*, **368**, 95–99.
35. Rottach,A., Kremmer,E., Nowak,D., Boisguerin,P., Volkmer,R., Cardoso,M.C., Leonhardt,H. and Rothbauer,U. (2008) Generation and characterization of a rat monoclonal antibody specific for PCNA. *Hybridoma*, **27**, 91–98.
36. Phair,R.D., Gorski,S.A. and Misteli,T. (2004) Measurement of dynamic protein binding to chromatin *in vivo*, using photobleaching microscopy. *Methods Enzymol.*, **375**, 393–414.
37. Carrero,G., Crawford,E., Hendzel,M.J. and de Vries,G. (2004) Characterizing fluorescence recovery curves for nuclear proteins undergoing binding events. *Bull. Math. Biol.*, **66**, 1515–1545.
38. Akaike,H. (1973) Information theory and an extension of the maximum likelihood principle. In: Petrov,B.N. and Csaki,F. (eds), *2nd International Symposium on Information Theory*. Akademiai Kiado, Budapest, pp. 267–281.
39. Schermelleh,L., Heintzmann,R. and Leonhardt,H. (2010) A guide to super-resolution fluorescence microscopy. *J. Cell Biol.*, **190**, 165–175.
40. Song,J., Rechkoblit,O., Bestor,T.H. and Patel,D.J. (2011) Structure of DNMT1-DNA complex reveals a role for autoinhibition in maintenance DNA methylation. *Science*, **331**, 1036–1040.
41. Bacolla,A., Pradhan,S., Roberts,R.J. and Wells,R.D. (1999) Recombinant human DNA (cytosine-5) methyltransferase. II. Steady-state kinetics reveal allosteric activation by methylated dna. *J. Biol. Chem.*, **274**, 33011–33019.
42. Wood,R.J., McKelvie,J.C., Maynard-Smith,M.D. and Roach,P.L. (2010) A real-time assay for CpG-specific cytosine-C5 methyltransferase activity. *Nucleic Acids Res.*, **38**, e107.
43. Pradhan,S., Bacolla,A., Wells,R.D. and Roberts,R.J. (1999) Recombinant human DNA (cytosine-5) methyltransferase. I. Expression, purification, and comparison of de novo and maintenance methylation. *J. Biol. Chem.*, **274**, 33002–33010.
44. Schermelleh,L., Spada,F., Easwaran,H.P., Zolghadr,K., Margot,J.B., Cardoso,M.C. and Leonhardt,H. (2005) Trapped in action: direct visualization of DNA methyltransferase activity in living cells. *Nat. Methods*, **2**, 751–756.
45. Braga,J., McNally,J.G. and Carmo-Fonseca,M. (2007) A reaction-diffusion model to study RNA motion by quantitative fluorescence recovery after photobleaching. *Biophys. J.*, **92**, 2694–2703.
46. Beaudouin,J., Mora-Bermudez,F., Klee,T., Daigle,N. and Ellenberg,J. (2006) Dissecting the contribution of diffusion and interactions to the mobility of nuclear proteins. *Biophys. J.*, **90**, 1878–1894.
47. Sprague,B.L., Pego,R.L., Stavreva,D.A. and McNally,J.G. (2004) Analysis of binding reactions by fluorescence recovery after photobleaching. *Biophys. J.*, **86**, 3473–3495.
48. Mai,J., Trump,S., Ali,R., Schiltz,R.L., Hager,G., Hanke,T., Lehmann,I. and Attinger,S. (2011) Are assumptions about the model type necessary in reaction-diffusion modeling? A FRAP application. *Biophys. J.*, **100**, 1178–1188.
49. Sporbert,A., Domaing,P., Leonhardt,H. and Cardoso,M.C. (2005) PCNA acts as a stationary loading platform for transiently interacting Okazaki fragment maturation proteins. *Nucleic Acids Res.*, **33**, 3521–3528.
50. Frauer,C., Rottach,A., Meilinger,D., Bultmann,S., Fellinger,K., Hasenoder,S., Wang,M., Qin,W., Soding,J., Spada,F. *et al.* (2011) Different binding properties and function of CXXC zinc finger domains in Dnmt1 and Tet1. *PLoS One*, **6**, e16627.
51. Erdel,F., Schubert,T., Marth,C., Langst,G. and Rippe,K. (2010) Human ISWI chromatin-remodeling complexes sample nucleosomes via transient binding reactions and become immobilized at active sites. *Proc. Natl Acad. Sci. USA*, **107**, 19873–19878.
52. Xouri,G., Squire,A., Dimaki,M., Geverts,B., Verveer,P.J., Taraviras,S., Nishitani,H., Houtsmuller,A.B., Bastiaens,P.I. and Lygerou,Z. (2007) Cdt1 associates dynamically with chromatin throughout G1 and recruits Geminin onto chromatin. *EMBO J.*, **26**, 1303–1314.
53. Wachsmuth,M., Waldeck,W. and Langowski,J. (2000) Anomalous diffusion of fluorescent probes inside living cell nuclei investigated

by spatially-resolved fluorescence correlation spectroscopy. *J. Mol. Biol.*, **298**, 677–689.
54. Bancaud,A., Huet,S., Daigle,N., Mozziconacci,J., Beaudouin,J. and Ellenberg,J. (2009) Molecular crowding affects diffusion and binding of nuclear proteins in heterochromatin and reveals the fractal organization of chromatin. *EMBO J.*, **28**, 3785–3798.
55. Banks,D.S. and Fradin,C. (2005) Anomalous diffusion of proteins due to molecular crowding. *Biophys. J.*, **89**, 2960–2971.
56. Dross,N., Spriet,C., Zwerger,M., Muller,G., Waldeck,W. and Langowski,J. (2009) Mapping eGFP oligomer mobility in living cell nuclei. *PLoS One*, **4**, e5041.
57. Trembecka,D.O., Kuzak,M. and Dobrucki,J.W. (2010) Conditions for using FRAP as a quantitative technique—influence of the bleaching protocol. *Cytometry A*, **77**, 366–370.
58. Seber,G.A.F. and Wild,C.J. (1989) *Nonlinear Regression*. John Wiley, New York.
59. Weiss,M., Elsner,M., Kartberg,F. and Nilsson,T. (2004) Anomalous subdiffusion is a measure for cytoplasmic crowding in living cells. *Biophys. J.*, **87**, 3518–3524.
60. Qin,W., Leonhardt,H. and Pichler,G. (2011) Regulation of DNA methyltransferase 1 by interactions and modifications. *Nucleus*, **2**, 392–402.
61. Rottach,A., Frauer,C., Pichler,G., Bonapace,I.M., Spada,F. and Leonhardt,H. (2010) The multi-domain protein Np95 connects DNA methylation and histone modification. *Nucleic Acids Res.*, **38**, 1796–1804.
62. Lee,B. and Muller,M.T. (2009) SUMOylation enhances DNA methyltransferase 1 activity. *Biochem. J.*, **421**, 449–461.
63. Esteve,P.O., Chang,Y., Samaranayake,M., Upadhyay,A.K., Horton,J.R., Feehery,G.R., Cheng,X. and Pradhan,S. (2011) A methylation and phosphorylation switch between an adjacent lysine and serine determines human DNMT1 stability. *Nat. Struct. Mol. Biol.*, **18**, 42–48.
64. Du,Z., Song,J., Wang,Y., Zhao,Y., Guda,K., Yang,S., Kao,H.Y., Xu,Y., Willis,J., Markowitz,S.D. *et al.* (2010) DNMT1 stability is regulated by proteins coordinating deubiquitination and acetylation-driven ubiquitination. *Sci. Signal.*, **3**, ra80.
65. Nelder,J.A. and Mead,R. (1965) A simplex method for function minimization. *Comput. J.*, **7**, 308–313.
66. Fuchs,C. (2013) *Inference for Diffusion Processes*. Springer, Heidelberg.
67. Lei,H., Oh,S.P., Okano,M., Juttermann,R., Goss,K.A., Jaenisch,R. and Li,E. (1996) De novo DNA cytosine methyltransferase activities in mouse embryonic stem cells. *Development*, **122**, 3195–3205.
68. Meilinger,D., Fellinger,K., Bultmann,S., Rothbauer,U., Bonapace,I.M., Klinkert,W.E., Spada,F. and Leonhardt,H. (2009) Np95 interacts with de novo DNA methyltransferases, Dnmt3a and Dnmt3b, and mediates epigenetic silencing of the viral CMV promoter in embryonic stem cells. *EMBO Rep.*, **10**, 1259–1264.

SUPPLEMENTARY METHODS

Expression constructs and cell culture

The expression construct GFP-Dnmt1^{C1229W} has been previously described (1). *Dnmt1*$^{-/-}$ and wild type J1 mouse embryonic stem cells (C/C) (2), either non-transfected or stably transfected with GFP-Dnmt1^{wt}, GFP-Dnmt1^{Q162E} and GFP-Dnmt1$^{\Delta TS}$ were cultured without feeder cells in gelatinized flasks. Culture conditions and creation of stably expressing cells has been described before (3).

In vivo Dnmt1 trapping assay

The trapping assay to measure postreplicative methylation efficiency in living cells was previously described (1). 5-Aza-2'-deoxycytidine (Sigma) was added at a final concentration of 30 µM and cells were incubated for the indicated periods before performing FRAP experiments. Microscope settings and quantitative FRAP analysis are described in Material and Methods (live cell microscopy and quantitative FRAP analysis).

Dnmt1 immunostaining and evaluation of relative expression levels

Non-transfected and transiently or stably transfected cells expressing GFP-Dnmt1 fusions were seeded on No. 1.5H precision coverslips (Marienfeld Superior), formaldehyde fixed and permeabilized with 0.5% Triton-X-100 or ice-cold methanol, if PCNA was detected. Endogenous PCNA was fluorescently labeled with the mouse monoclonal antibody PC10 (Abcam) and a secondary anti-mouse antibody conjugated to Alexa Fluor 594 (Invitrogen). The rat IgG1 monoclonal antibody 5A10 was raised against murine Dnmt1 with an N-terminal His_6-tag. The protein was purified from Sf9 insect cells via recombinant baculoviruses. Immunization, generation of hybridomas and ELISA screening was performed as previously described (4). Secondary antibodies were conjugated to Alexa Fluor 488 or Alexa Fluor 594 (Invitrogen). Cells were counterstained with 1 µg/ml 4',6-diamidino-2-phenylindole and embedded in Vectashield (Vector Laboratories).
Mean intensity levels of Dnmt1 (endogenous and exogenous) in the nucleus were measured on 2 µm image stacks (0.5 µm z-distance) in Volocity 6.1 (PerkinElmer) using the SD based automatic threshold function on the DAPI staining. Objects below 200 µm³ were excluded and objects separated with an object size guide of 1200 µm³. For evaluation of the transfected cells, only low to moderate expressing cells with a mean nuclear GFP intensity between 500 and 2000 grey values were considered (analogous to FRAP experiments). For the calculation of the anti-Dnmt1 fluorescence intensities, background subtracted mean intensities of at least 20 cells (transiently transfected) or 70 cells (non-transfected and stably transfected cells), respectively, were averaged. Finally relative ratios of transfected over non-transfected cells were calculated and the standard deviations were determined.

Co-immunoprecipitation and western blot analysis

Co-immunoprecipitation and western blot analysis was performed as previously described (5) with the following changes. For extract preparation 150 mM NaCl, 1 mg/ml DNaseI (AppliChem), 2 mM $MgCl_2$

and 1x protease inhibitor mix (Serva) were included in the lysis buffer. For dilution of lysates and for washing steps an immunoprecipitation buffer was used (20 mM Tris-HCl pH 7.5, 150 mM NaCl, 0.5 mM EDTA).
The following primary monoclonal antibodies were used for immunoblotting: rat anti-Dnmt1 5A10 (see Dnmt1 immunostaining and evaluation of relative expression levels), rat anti-PCNA 16D10 (4), mouse anti-GFP (Roche) and mouse anti-β-Actin (Sigma-Aldrich). Secondary anti-rat and anti-mouse antibodies were either conjugated to HRP (Dianova) or Alexa Fluor 594/647 (Invitrogen).

Data correction and normalization

Imported image series were intensity normalized, converted to 8-bit and Gauss-filtered (2 pixel radius). Datasets showing lateral movement of cells were corrected by image registration using the *StackReg* plug-in of ImageJ starting with a frame where approximately half recovery was reached. Mean intensities over time were extracted from four regions of interest (ROIs): The total nuclear area (T) was defined manually or by applying the *Autothreshold* function of ImageJ on the prebleach frame and on the last frame. The overlapping region of both threshold-defined areas was used to create the minimal ROI. This ROI was then divided into a bleached *(*B) and an unbleached area, where the coordinates of the bleached ROI were used to determine the bleaching border (the last line perpendicular to the major axis of the nucleus, Supplementary Figure 4 A). Finally, a background ROI (BG) outside of the cell was defined manually or with the *Autothreshold* function. The mean gray values over time were measured and pasted to an MS Excel worksheet.

Raw data (Supplementary Figure 4 B) from T and B regions were background subtracted resulting in T' and B' with T_t' representing the data according to the respective time point *t*. A reference value $T'_{\text{postbleach}}$ was defined as the average of the resulting postbleach values from time points 10-20 after bleaching, and $T'_{\text{prebleach}}$ as the average of the last five prebleach values. Additional gain or loss of total fluorescence during postbleach acquisition may potentially be caused by nuclear import, bleaching-by-acquisition and flux of unbleached molecules from above and below the recorded optical plane. In order to correct for such effects, the postbleach values were corrected by multiplication with $T'_{\text{postbleach}}/T_t'$. Accordingly, prebleach values were multiplied with $T'_{\text{prebleach}}/T_t'$ leading to T_t'' and B_t''. To correct for cell-to-cell differences in bleaching depth, we subtracted a value Φ from all mean fluorescence values T_t'' and B_t''. The value Φ was determined from the mean fluorescence in the distal part (50%) of the bleached region at the first postbleach time point as follows: To measure the bleaching depth, we determined fluorescence intensity profiles of the total nuclear region along the major axis of the nucleus and determined the number of pixels in the nucleus (T region) for each line along the axis at the first postbleach time point (Supplementary Figure 4 C). The bleaching depth Φ was then determined with the following Equation (S 1), where P stands for the number of pixels of each line in the T region $i \in \{1, \dots, 256\}$ along the axis as $P_{\text{postbleach},i}$ and the mean fluorescence intensity of the lines as $I_{\text{postbleach},i}$, respectively, until 50% of the bleached lines indicated by h:

$$\Phi = \frac{\sum_{i=1}^{h}\left(P_{\text{postbleach},i} \times (I_{\text{postbleach},i} - BG_{\text{postbleach}})\right)}{\sum_{i=1}^{h} P_{\text{postbleach},i}}. \qquad (S1)$$

The corrected values for T_t''' and B_t''' were divided by the respective means of the last five prebleach values $T'''_{\text{prebleach}}$ to account for intensity differences in the bleached and unbleached regions before bleaching. The corrected relative intensity values in the bleached region were finally corrected for the loss of fluorescence due to half nucleus bleaching. This was achieved by dividing each value B_t'''' through the corresponding total nuclear value T_t'''' resulting in B_t'''''. After complete recovery, the resulting fluorescence intensities will level off around the value 1, subject to stochastic fluctuations (Supplementary Figure 4 D). The bleached fraction was given by $f_{\text{bl}} = 1 - T'''_{\text{postbleach}}/T'''_{\text{prebleach}}$ using the Φ corrected values. Calculation of the mobile fraction (*MF*) was performed by $MF = \left(B''''_{plateau} - B''''_{postbleach}\right)/\left(1 - B''''_{postbleach}\right)$. $B_{plateau}$ was defined as the average intensity of the last 20 frames. For the half time recovery ($t_{1/2}$) the according time to $F_{1/2}$ was chosen from the results with $F_{1/2} = \left(B'''''_{plateau} - B'''''_{postbleach}\right)/2 + B'''''_{postbleach}$.

Mathematical model

The mathematical models used for the statistical analysis of the recovery curves are based on a compartmental approach and biochemical kinetic principles. The model for diffusion-uncoupled FRAP, i.e. for molecules that diffuse much more rapidly than they bind or unbind, has previously been described (6-7). A model for diffusion-coupled FRAP is developed in this work; a similar approach has been taken in (8). The compartmental description of the diffusion-coupled model is illustrated in Figure 4 A; the diffusion-uncoupled model is a simplification thereof. Both models consider transitions between the bound and the free state of a protein with *association rate constant* k_{on} and *dissociation rate constant* k_{off}. Dissociation follows a linear process, while association is originally of second order. However, the product of k_{on} and the concentration [BS] of available binding sites can be assumed constant (9), resulting in an *effective association rate constant* $k^*_{\text{on}} = k_{\text{on}}[\text{BS}]$. This simplification allows the conversion of the second order association process to a pseudo-first order process. Hence, the association and dissociation dynamics can be expressed in terms of linear ordinary differential equations (ODEs), which are given below. While bound proteins remain fixed at the respective binding sites, free proteins diffuse through the nucleus, thus changing their locations among the bleached and the unbleached sections. In diffusion-uncoupled FRAP, diffusion of free molecules happens so rapidly that their concentration is identical in the bleached and in the unbleached section. Hence, it is not necessary to model the location of a free molecule. In a diffusion-coupled situation, on the other hand, movements between the bleached and the unbleached section are modeled with a *diffusion rate constant* k_{diff}. Every two molecules that are located at the same distance from the bleaching border are supposed to cross this border within a certain time interval with the same probability, no matter whether the direction of diffusion is from the bleached to the unbleached area or the other way round. If, however, the bleached fraction f_{bl} is not equal to one half, the sizes of the bleached and unbleached sections differ. Then, due to the geometry of the bleached area, several of the proteins in the larger

section are located further away from the bleaching border than the proteins in the smaller area. In order to account for this imbalance, the probabilities for diffusion events in the two possible directions are weighted with factors f_{bl} and $1-f_{\mathrm{bl}}$, respectively. The value of k_{diff} depends on the geometry of the cell and is not immediately eligible for interpretation purposes.

Bleached and unbleached molecules are assumed to behave identically, and therefore it suffices to focus on one type only. The following considerations model the dynamics of the unbleached molecules as these are visible through their fluorescence. Let $P_{\mathrm{bl}}^{\mathrm{free}}$, $P_{\mathrm{unbl}}^{\mathrm{free}}$, $P_{\mathrm{bl}}^{\mathrm{bound}}$ and $P_{\mathrm{unbl}}^{\mathrm{bound}}$ denote the fractions of unbleached free and bound proteins in the bleached and unbleached sections, measured with respect to all unbleached proteins in the nucleus. These four parameters sum up to one such that one of them can be left out. Define $P^{\mathrm{free}} = P_{\mathrm{bl}}^{\mathrm{free}} + P_{\mathrm{unbl}}^{\mathrm{free}}$ and $P^{\mathrm{bound}} = P_{\mathrm{bl}}^{\mathrm{bound}} + P_{\mathrm{unbl}}^{\mathrm{bound}}$. In diffusion-uncoupled FRAP, one has $P_{\mathrm{bl}}^{\mathrm{free}} = f_{\mathrm{bl}}P^{\mathrm{free}}$ and $P_{\mathrm{unbl}}^{\mathrm{free}} = (1-f_{\mathrm{bl}})P^{\mathrm{free}}$. The overall dynamics of unbleached proteins in diffusion-uncoupled FRAP is described by

$$\frac{dP^{\mathrm{free}}}{dt} = -(k_{\mathrm{on}}^{*} + k_{\mathrm{off}})P^{\mathrm{free}} + k_{\mathrm{off}}, \qquad (\mathrm{S}\,2)$$

$$\frac{\mathrm{dP_{bl}^{bound}}}{\mathrm{dt}} = \mathrm{k_{on}^{*}f_{bl}P^{free}} - \mathrm{k_{off}P_{bl}^{bound}}. \qquad (\mathrm{S}\,3)$$

In case of diffusion-coupled FRAP, one has

$$\frac{\mathrm{dP_{bl}^{free}}}{\mathrm{dt}} = -\mathrm{k_{on}^{*}P_{bl}^{free}} + \mathrm{k_{off}P_{bl}^{bound}} + \mathrm{k_{diff}(f_{bl}P_{unbl}^{free} - (1-f_{bl})P_{bl}^{free})}, \qquad (\mathrm{S}\,4)$$

$$\frac{\mathrm{dP_{unbl}^{free}}}{\mathrm{dt}} = -\mathrm{k_{on}^{*}P_{unbl}^{free}} + \mathrm{k_{off}}\left(1 - \mathrm{P_{bl}^{free}} - \mathrm{P_{unbl}^{free}} - \mathrm{P_{bl}^{bound}}\right) - \mathrm{k_{diff}}\left(\mathrm{f_{bl}P_{unbl}^{free}} - (1-\mathrm{f_{bl}})\mathrm{P_{bl}^{free}}\right), \qquad (\mathrm{S}\,5)$$

$$\frac{\mathrm{dP_{bl}^{bound}}}{\mathrm{dt}} = \mathrm{k_{on}^{*}P_{bl}^{free}} - \mathrm{k_{off}P_{bl}^{bound}}. \qquad (\mathrm{S}\,6)$$

In case of $\mathrm{k_{diff}} \gg \mathrm{k_{on}^{*}}, \mathrm{k_{off}}$, i.e. for diffusion-uncoupled FRAP, Equations (S 4)-(S 6) are dominated by the diffusion rather than binding dynamics until $P_{\mathrm{bl}}^{\mathrm{free}} \approx f_{\mathrm{bl}}P^{\mathrm{free}}$, which is the basic assumption of diffusion-uncoupled recovery. Hence, the two models are consistent. In both setups, the recovery curve equals

$$F = \frac{P_{\mathrm{bl}}^{\mathrm{free}} + P_{\mathrm{bl}}^{\mathrm{bound}}}{f_{\mathrm{bl}}}.$$

This term was adjusted to the data normalization procedure described above and approaches the value one as time progresses. From (S 2)-(S 3) and (S 4)-(S 6)above, one arrives at differential equations for the fluorescence F. Interestingly, in case of diffusion-uncoupled recovery, the ODE for F is independent of P^{free} and $P_{\mathrm{bl}}^{\mathrm{bound}}$. Its explicit solution reads

$$F(t) = 1 + (F_0 - 1)\exp(-k_{\mathrm{off}}(t - t_0)),$$

where F_0 is the initial value at time t_0. This equation does not contain k_{on}^{*}, and hence this parameter cannot be estimated directly from the recovery curve. However, we assume the nucleus to be in chemical equilibrium. Therefore the fraction P^{free} is presumed to be constant, i.e. $dP^{\mathrm{free}}/dt = 0$. From this, one obtains

$$P^{\mathrm{free}} = \frac{k_{\mathrm{off}}}{k_{\mathrm{on}}^{*} + k_{\mathrm{off}}}.$$

Hence, approximation of k_{on}^{*} is possible if estimates are available for k_{off} and P^{free}.

There is possibly more than one type of binding partner for Dnmt1, i.e. the protein may sometimes associate to a partner of one type and sometimes to a partner of another type. These partners may

differ with respect to the affinity of Dnmt1 to enter the bound state and the mean residence times in this state. All binding partners with identical or similar kinetic properties are gathered in one *mobility class* (MC). This term seems more appropriate than *classes of binding sites* (6), because different sites with identical kinetic properties cannot be distinguished using FRAP data. The number of MCs could hence be smaller than the number of different binding partners. Furthermore binding-unrelated processes like anomalous diffusion can fall into an MC.

Suppose there are M classes of kinetically different binding partners for the protein of interest, labeled with numbers $i \in \{1, \dots, M\}$. For all i, define $P_{\mathrm{bl}}^{\mathrm{bound},i}$ and $P_{\mathrm{unbl}}^{\mathrm{bound},i}$ as the fractions of type-i bound proteins in the bleached and unbleached sections, respectively, with $P^{\mathrm{bound},i} = P_{\mathrm{bl}}^{\mathrm{bound},i} + P_{\mathrm{unbl}}^{\mathrm{bound},i}$. Let $f_i = P^{\mathrm{bound},i}/P^{\mathrm{bound}}$ be the fraction of type-i bound proteins with respect to all bound proteins. Furthermore, denote by $k_{\mathrm{on},i}^*$ and $k_{\mathrm{off},i}$ the association and dissociation rate constants corresponding to the ith MC. Then, the diffusion-uncoupled recovery is described by

$$\frac{dP^{\mathrm{free}}}{dt} = -\left(k_{\mathrm{off},M} + \sum_{i=1}^{M} k_{\mathrm{on},i}^*\right)P^{\mathrm{free}} + k_{\mathrm{off},M} + \sum_{i=1}^{M-1}(k_{\mathrm{off},i} - k_{\mathrm{off},M})P^{\mathrm{bound},i},$$

$$\frac{dP_{\mathrm{bl}}^{\mathrm{bound},i}}{dt} = k_{\mathrm{on},i}^* f_{\mathrm{bl}} P^{\mathrm{free}} - k_{\mathrm{off},i} P_{\mathrm{bl}}^{\mathrm{bound},i},$$

$$\frac{dP_{\mathrm{unbl}}^{\mathrm{bound},i}}{dt} = k_{\mathrm{on},i}^*(1 - f_{\mathrm{bl}})P^{\mathrm{free}} - k_{\mathrm{off},i} P_{\mathrm{unbl}}^{\mathrm{bound},i},$$

where $i = 1, \dots, M$. For diffusion-coupled FRAP, one has

$$\frac{\mathrm{dP_{bl}^{free}}}{\mathrm{dt}} = -\mathrm{P_{bl}^{free}}\sum_{\mathrm{i=1}}^{\mathrm{M}} \mathrm{k_{on,i}^*} + \sum_{\mathrm{i=1}}^{\mathrm{M}} \mathrm{k_{off,i}} \mathrm{P_{bl}^{bound,i}} + \mathrm{k_{diff}}(\mathrm{f_{bl}} \mathrm{P_{unbl}^{free}} - (1 - \mathrm{f_{bl}})\mathrm{P_{bl}^{free}}), \qquad (\mathrm{S}\ 7)$$

$$\frac{\mathrm{dP_{unbl}^{free}}}{\mathrm{dt}} = -\mathrm{P_{unbl}^{free}}\sum_{\mathrm{i=1}}^{\mathrm{M}} \mathrm{k_{on,i}^*} + \sum_{\mathrm{i=1}}^{\mathrm{M}} \mathrm{k_{off,i}} \mathrm{P_{unbl}^{bound,i}} - \mathrm{k_{diff}}(\mathrm{f_{bl}} \mathrm{P_{unbl}^{free}} - (1 - \mathrm{f_{bl}})\mathrm{P_{bl}^{free}}), \qquad (\mathrm{S}\ 8)$$

$$\frac{\mathrm{dP_{bl}^{bound,i}}}{\mathrm{dt}} = \mathrm{k_{on,i}^*} \mathrm{P_{bl}^{free}} - \mathrm{k_{off,i}} \mathrm{P_{bl}^{bound,i}}, \qquad (\mathrm{S}\ 9)$$

$$\frac{\mathrm{dP_{unbl}^{bound,i}}}{\mathrm{dt}} = \mathrm{k_{on,i}^*} \mathrm{P_{unbl}^{free}} - \mathrm{k_{off,i}} \mathrm{P_{unbl}^{bound,i}}. \qquad (\mathrm{S}\ 10)$$

In both cases, the observed fluorescence intensity is

$$F = \frac{P_{\mathrm{bl}}^{\mathrm{free}} + \sum_{i=1}^{M} P_{\mathrm{bl}}^{\mathrm{bound},i}}{f_{\mathrm{bl}}}.$$

Parameter estimation

The mathematical model contains several unknowns: The model parameters $k_{\mathrm{on},i}^*$, $k_{\mathrm{off},i}$ and k_{diff}, the initial values $F_0, P_{\mathrm{bl},0}^{\mathrm{free}}, P_{\mathrm{bl},0}^{\mathrm{bound}}$ for the components $F, P_{\mathrm{bl}}^{\mathrm{free}}, P_{\mathrm{bl}}^{\mathrm{bound}}$ etc., and the fractions f_{bl}, f_i of bleached proteins, bound proteins of type i etc. Due to computational effort, parameter redundancies and strong correlation between some parameters, it is not meaningful to statistically infer all these unknowns simultaneously. Instead, some values were fixed as follows: k_{diff} and f_{bl} were experimentally determined (see Supplementary Table 1, Figure 4 B and the data normalization description above). The smallest k_{off} value was set to 0.005 (see the Results section). F_0 was chosen equal to the first value of the FRAP curve. $P_{\mathrm{bl},0}^{\mathrm{free}}$ was set equal to $f_{\mathrm{bl}}F_0$. The association rates result from the other estimates as $k_{\mathrm{on,i}}^* = k_{\mathrm{off},i} f_i\,(1 - P^{\mathrm{free}})/P^{\mathrm{free}}$ as explained below. Statistical inference of all remaining variables was carried out by least squares estimation. To that end, the Nelder-Mead algorithm (10)

was applied to find combinations of parameter values which minimize the sum of squared residuals between the observed FRAP curve and its simulated counterpart. In most cases, the output of the optimization procedure depended on the initial guesses of all unknown variables. Hence, several initial guesses were randomly drawn and passed to the Nelder-Mead algorithm. The overall best fit was then chosen from the set of return values. This procedure was continued until the global optimum did not change anymore. In case of diffusion-uncoupled FRAP, the modeled recovery curves can be calculated by means of explicit functions as described in detail below. For diffusion-coupled FRAP, the ODEs (S 4)-(S 6) and (S 7)-(S 10) were numerically solved with the Euler scheme with step length 0.03, which corresponded to one fifth of the observation interval. All software was written in R (R Development Core Team, 2011, R Foundation for Statistical Computing, Vienna, Austria).

We estimated the model parameters for each FRAP curve separately and compared the estimates for curves from the same cell cycle phase and Dnmt1 construct afterwards. An alternative would have been to simply consider the average curve for each phase and construct and to derive parameters for this mean course. In our opinion, however, the second procedure would cause a loss of information. Averaging did not seem appropriate to us as there is undoubtedly extrinsic noise. Our analysis additionally yields insight about uncertainties caused by cell-to-cell variability.

Numerics

In our analyses, we always assume the system to be in chemical equilibrium. For both diffusion-coupled and diffusion-uncoupled FRAP, the system of ODEs is linear, and hence there is an explicit solution of the above ODEs available. For diffusion-coupled FRAP, however, this involves the (typically approximate) computation of a matrix exponential. For that reason, we prefer to numerically solve the ODEs of the diffusion-coupled model. For diffusion-uncoupled FRAP, an exact computation of the solution of the ODEs is easily possible, see (11).

For diffusion-coupled FRAP, we proceed as follows: Assume

$$F_0, P_{\mathrm{bl},0}^{\mathrm{free}}, P^{\mathrm{free}}, f_1, \dots, f_{M-1}, k_{\mathrm{off},1,\dots,}k_{\mathrm{off},M}, k_{\mathrm{diff}}$$

to be given. In practice, we determine $F_0, P_{\mathrm{bl},0}^{\mathrm{free}}$ and k_{diff} experimentally as described above. The remaining $2M$ variables are estimated statistically, i.e. they are optimized using the Nelder-Mead algorithm. In order to avoid non-identifiabilities, we require $k_{\mathrm{off},1} \geq k_{\mathrm{off},2} \geq \cdots \geq k_{\mathrm{off},M}$. From the above parameters, we compute

- $f_M = 1 - f_1 - \cdots - f_{M-1}$
- $P_{\mathrm{unbl},0}^{\mathrm{free}} = P^{\mathrm{free}} - P_{\mathrm{bl},0}^{\mathrm{free}}$
- $P_{\mathrm{bl},0}^{\mathrm{bound}} = f_{bl}F_0 - P_{\mathrm{bl},0}^{\mathrm{free}}$
- $P^{\mathrm{bound}} = 1 - P^{\mathrm{free}}$
- $P_{\mathrm{unbl},0}^{\mathrm{bound}} = P^{\mathrm{bound}} - P_{\mathrm{bl},0}^{\mathrm{bound}}$
- $P_{\mathrm{bl},0}^{\mathrm{bound},i} = f_i P_{\mathrm{bl},0}^{\mathrm{bound}}$ for $i = 1, \dots, M$
- $P_{\mathrm{unbl},0}^{\mathrm{bound},i} = f_i P_{\mathrm{unbl},0}^{\mathrm{bound}}$ for $i = 1, \dots, M$
- $k_{\mathrm{on},i}^{*} = k_{\mathrm{off},i} f_i \frac{1-P^{\mathrm{free}}}{P^{\mathrm{free}}}$ for $i = 1, \dots, M$

These values are now used to numerically solve the diffusion-coupled ODE model.

Model choice

In our analysis, we estimate models with different numbers of MCs. Since the models are nested, the inclusion of more MCs always leads to a better or at least equally good fit. However, one may ask whether the additional computational effort for multiple MCs is worth the improved matching of the data. At first glance, model choice criteria like the Akaike information criterion (AIC) (12) seem appropriate. In our application, however, the difference in the mean squared residuals for different models is typically small due to the already mentioned parameter redundancies. Because of the large number of model parameters, the AIC will often favor less MCs although the curvature of the recovery curves is better described by more complex models. For that reason, we developed a model selection criterion which penalizes complexity less rigorously and is specific to our application. Due to the relatively small noise in the FRAP curves (Figure 3 B and Supplementary Figure 6), we do not expect to overfit the data. The criterion reads as follows: As explained in the Results section, the up to three MCs are further distinguished into one or two distinctive mobility classes (DMCs) and up to one catalytic mobility class (CMC). These have to fulfill three rules:

(1) If a DMC or CMC is present, the fraction P^{bound} of bound proteins should be above a certain threshold:

$$P^{\text{bound}} \geq \varepsilon_{\text{bound}}.$$

Otherwise the DMCs and CMC are discarded, and we assume no MCs for this FRAP curve.

(2) Two distinct MCs should differ substantially in their dissociation rates. In the model with two DMCs that means that one should have

$$\frac{k_{\text{off,DMC1}} - k_{\text{off,DMC2}}}{k_{\text{off,DMC2}}} \geq \delta_{\text{DMC}} \quad \text{or} \quad \frac{k_{\text{off,DMC2}} - k_{\text{off,CMC}}}{k_{\text{off,CMC}}} \geq \delta_{\text{CMC}}.$$

Otherwise we assume the effective number of DMCs to be one.

(3) An MC only truly contributes to the model if it reaches a certain size:

$$f_{\text{DMC1}} P^{\text{bound}} \geq \varepsilon_{\text{DMC}} \quad \text{and} \quad f_{\text{DMC2}} P^{\text{bound}} \geq \varepsilon_{\text{DMC}} \quad \text{and} \quad f_{\text{CMC}} P^{\text{bound}} \geq \varepsilon_{\text{CMC}}.$$

Otherwise we assume the effective number of DMCs to be one.

We derive appropriate values for the above thresholds by cluster analysis. To that end, we consider the best fits for all FRAP curves and all models. From these, we select the corresponding marginal estimates which are in a critical region. For example, we consider the set of all P^{bound} estimates that are between 0% and 10%. These sets are separately divided into two clusters such that the sum of variances within the clusters is minimized. The resulting thresholds are $\varepsilon_{\text{bound}} = 3.5\%$, $\varepsilon_{\text{DMC}} = 5\%$, $\varepsilon_{\text{CMC}} = 2 \cdot 10^{-7}\%$, $\delta_{\text{DMC}} = 10^{-4}$ and $\delta_{\text{CMC}} = 3.77$.

For each measured curve, we now select the model which yielded the best fit. This is typically the model with two DMCs and one CMC, but in many cases the fit of the model with one DMC and one CMC is equally good and hence preferred. For the chosen model, the original number of DMCs is replaced by the effective number of DMCs as determined by the above rules. This effective number enters Supplementary Figure 9. Then, for each cell cycle phase and protein construct, the primarily chosen effective number of DMCs is determined. The model with the according number of DMCs is

chosen for this phase and construct. Supplementary Table 2 displays the mean estimates for the so chosen model for all FRAP curves. These results always assume the original number of DMCs and do not further reduce it to an effective number.

SUPPLEMENTARY REFERENCES

1. Schermelleh, L., Spada, F., Easwaran, H.P., Zolghadr, K., Margot, J.B., Cardoso, M.C. and Leonhardt, H. (2005) Trapped in action: direct visualization of DNA methyltransferase activity in living cells. *Nat Methods*, **2**, 751-756.
2. Lei, H., Oh, S.P., Okano, M., Juttermann, R., Goss, K.A., Jaenisch, R. and Li, E. (1996) De novo DNA cytosine methyltransferase activities in mouse embryonic stem cells. *Development*, **122**, 3195-3205.
3. Schermelleh, L., Haemmer, A., Spada, F., Rosing, N., Meilinger, D., Rothbauer, U., Cardoso, M.C. and Leonhardt, H. (2007) Dynamics of Dnmt1 interaction with the replication machinery and its role in postreplicative maintenance of DNA methylation. *Nucleic Acids Res*, **35**, 4301-4312.
4. Rottach, A., Kremmer, E., Nowak, D., Boisguerin, P., Volkmer, R., Cardoso, M.C., Leonhardt, H. and Rothbauer, U. (2008) Generation and characterization of a rat monoclonal antibody specific for PCNA. *Hybridoma (Larchmt)*, **27**, 91-98.
5. Meilinger, D., Fellinger, K., Bultmann, S., Rothbauer, U., Bonapace, I.M., Klinkert, W.E., Spada, F. and Leonhardt, H. (2009) Np95 interacts with de novo DNA methyltransferases, Dnmt3a and Dnmt3b, and mediates epigenetic silencing of the viral CMV promoter in embryonic stem cells. *EMBO Rep*, **10**, 1259-1264.
6. Phair, R.D., Scaffidi, P., Elbi, C., Vecerova, J., Dey, A., Ozato, K., Brown, D.T., Hager, G., Bustin, M. and Misteli, T. (2004) Global nature of dynamic protein-chromatin interactions in vivo: three-dimensional genome scanning and dynamic interaction networks of chromatin proteins. *Mol Cell Biol*, **24**, 6393-6402.
7. Phair, R.D., Gorski, S.A. and Misteli, T. (2004) Measurement of dynamic protein binding to chromatin in vivo, using photobleaching microscopy. *Methods Enzymol*, **375**, 393-414.
8. Carrero, G., Crawford, E., Hendzel, M.J. and de Vries, G. (2004) Characterizing fluorescence recovery curves for nuclear proteins undergoing binding events. *Bull Math Biol*, **66**, 1515-1545.
9. Sprague, B.L. and McNally, J.G. (2005) FRAP analysis of binding: proper and fitting. *Trends Cell Biol*, **15**, 84-91.
10. Nelder, J.A. and Mead, R. (1965) A Simplex Method for Function Minimization. *Comput J*, **7**, 308-313.
11. Fuchs, C. (2013) *Inference for Diffusion Processes*. Springer, Heidelberg.
12. Akaike, H. (1973) In Petrov, B. N. and Csaki, F. (eds.), *2nd International Symposium on Information Theory*, Budapest: Akademiai Kiado, pp. 267-281.

SUPPLEMENTARY FIGURES

S1

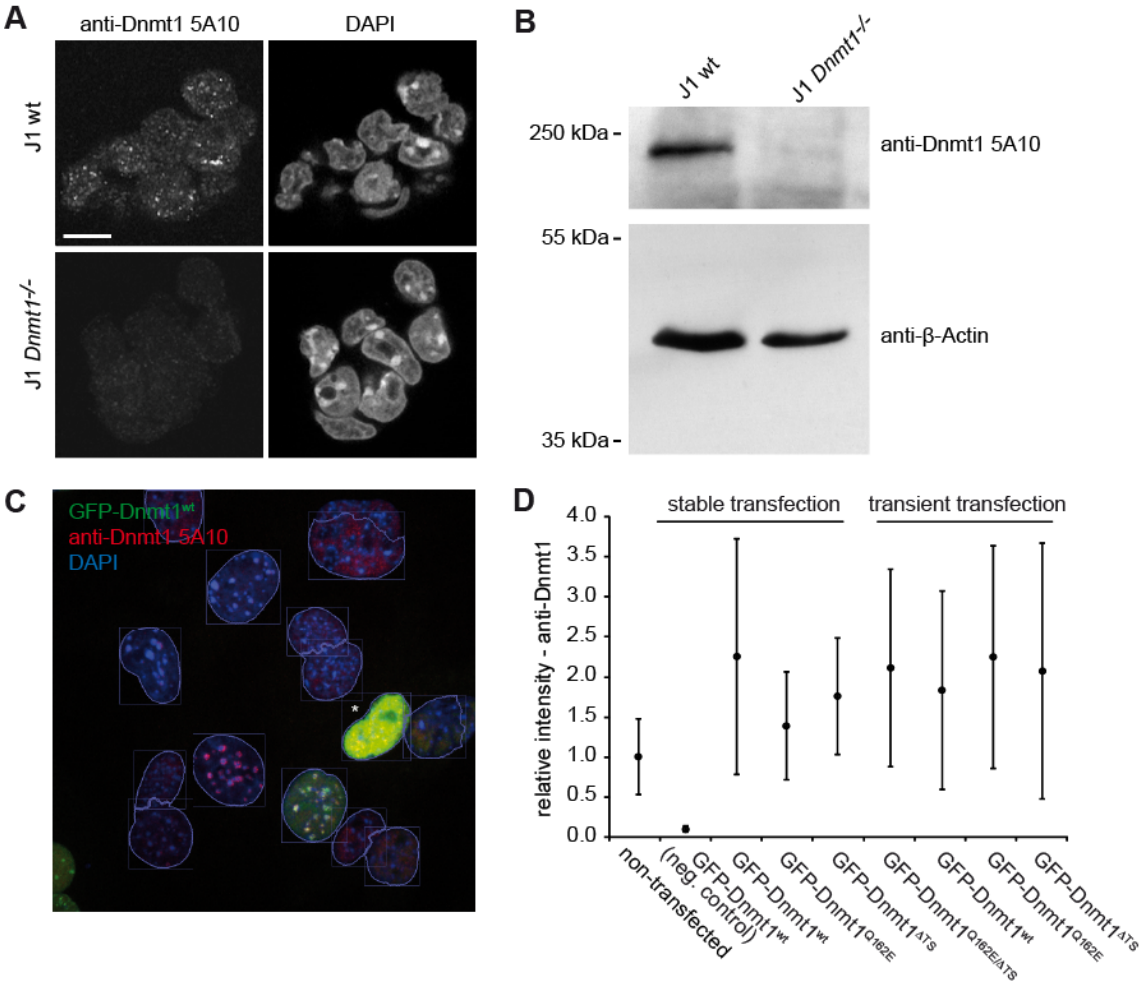

Supplementary Figure 1. Specificity test of the anti-Dnmt1 antibody 5A10 and levels of ectopic and endogenous Dnmt1 expression. (**A**) Immunostaining of J1 wt and *Dnmt1*$^{-/-}$ embryonic stem cells (C/C) shows a typical Dnmt1 staining pattern in the wt cells, but no nuclear enrichment in the *Dnmt1*$^{-/-}$ cells. Scale bar: 10 µm. (**B**) Western blot analysis gives no signal of the anti-Dnmt1 5A10 antibody in J1 *Dnmt1*$^{-/-}$ cells (C/C), but a clear band of 183 kDa in the J1 wt cells. β-Actin (42 kDa) was used as a loading control. (**C**) Automated quantification of Dnmt1 expression levels using Volocity software (PerkinElmer). The screenshot shows a representative extended focus image used for the evaluation. Nuclei were segmented according to their DAPI signal and the mean nuclear intensities of the Dnmt1 antibody signal and of the GFP signal determined. Highly overexpressing cells (example marked by asterisk) were excluded form the analysis (analogue to the FRAP experiments below). (**D**) Quantitative evaluation of anti-Dnmt1 5A10 antibody signal intensity in GFP-Dnmt1 expressing cells (representing the endogenous and ectopically expressed Dnmt1) relative to non-transfected C2C12 cells (endogenous only). For the negative control no primary antibody was used. Error bars indicate standard deviations.

S2

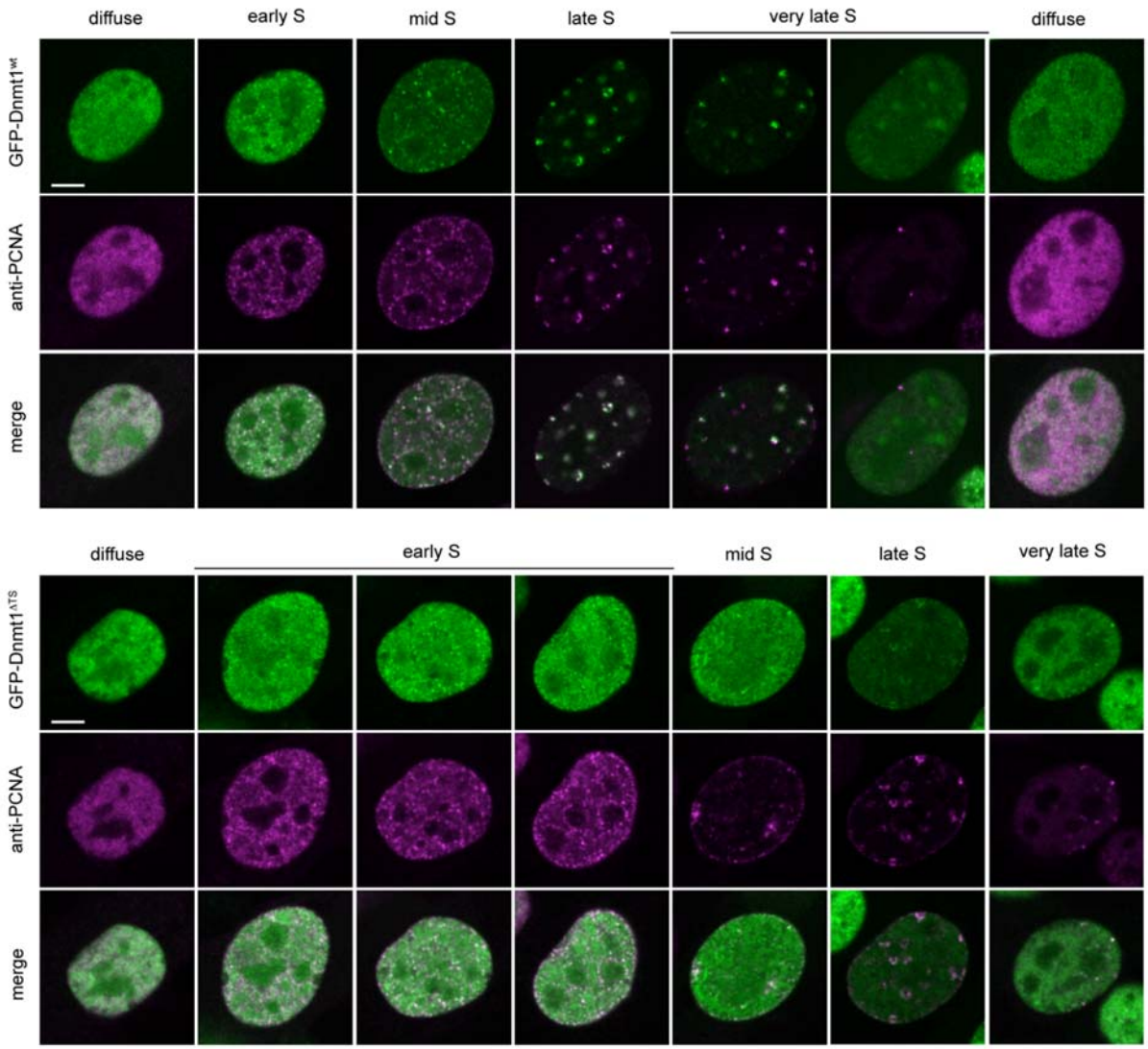

Supplementary Figure 2. Localization of GFP-Dnmt1^{wt} and GFP-Dnmt1$^{\Delta TS}$ in relation to endogenous PCNA. GFP-Dnmt1^{wt} and GFP-Dnmt1$^{\Delta TS}$ are depicted in green and PCNA is depicted in magenta. From early S phase until the beginning of late S phase GFP-Dnmt1^{wt} is associated with replication foci, highlighted by spots of immobilized PCNA. GFP-Dnmt1^{wt} remains to some extent enriched at heterochromatic regions in very late S phase and in transition to G2. GFP-Dnmt1$^{\Delta TS}$ shows less prominent association with replication foci throughout all S phase stages. In contrast to the wild type, no enrichment at heterochromatic regions is apparent in very late S phase. Scale bars: 5 µm.

S3

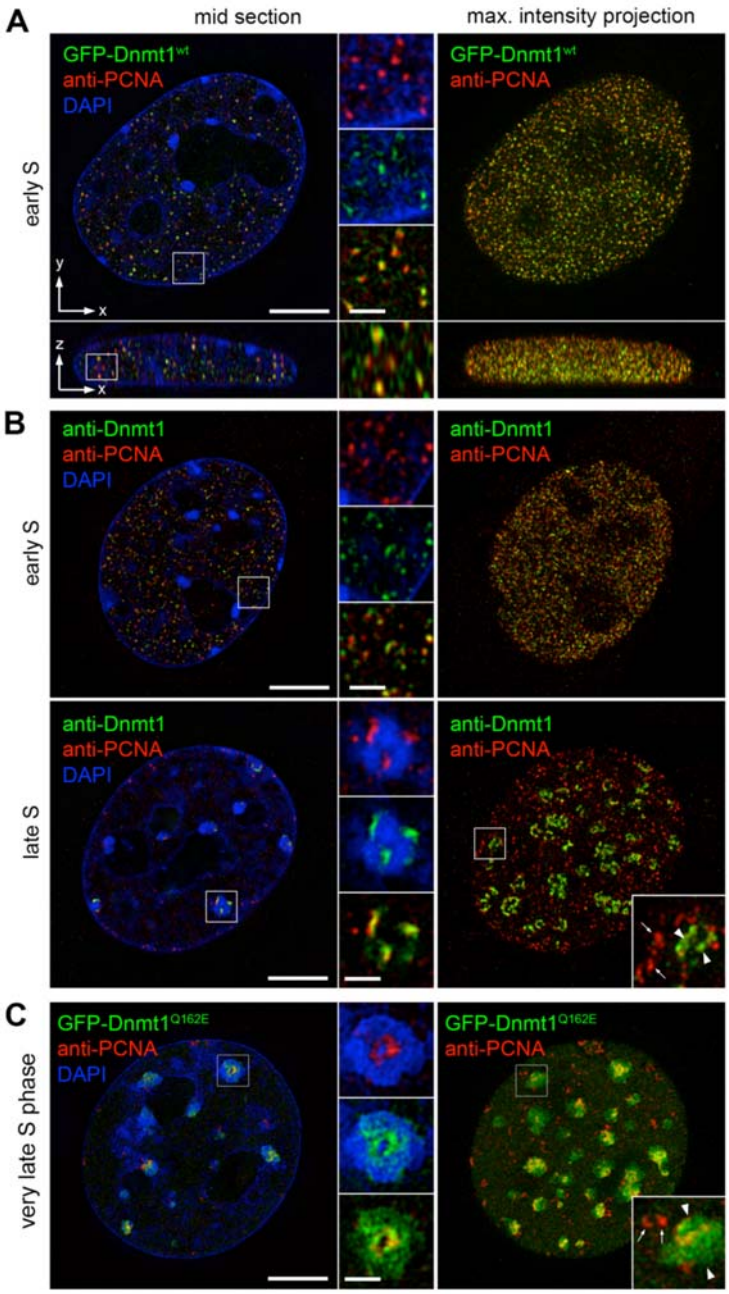

Supplementary Figure 3. Super-resolution imaging of GFP-Dnmt1 constructs and endogenous Dnmt1. (**A**) C2C12 cell in early S-phase expressing GFP-Dnmt1^{wt} and immunostained with antibodies against endogenous PCNA (complementary to Fig 2 A) demonstrates a high degree of co-localization but variable amount of GFP-Dnmt1 associated with early S-phase replication foci (RF). Lateral and orthogonal cross section and z-projection of a 3D-SIM image stack is shown. (**B**) Co-staining of endogenous Dnmt1 using the 5A10 antibody together with PCNA reveal the same characteristic distribution pattern in early and late S phase as observed for GFP-Dnmt1^{wt} in C2C12 cells (compare panel A and Fig 2 A). (**C**) C2C12 cell expressing GFP-Dnmt1^{Q162E} in a very late S-phase stage as identified by only a few remaining PCNA labeled replication sites (complementary to Fig 2 C). In this

stage the region of pHC association extends over almost the entire chromocenter volume indicating binding to postreplicative pHC only. Scale bars: 5 µm and 1 µm (insets).

S4

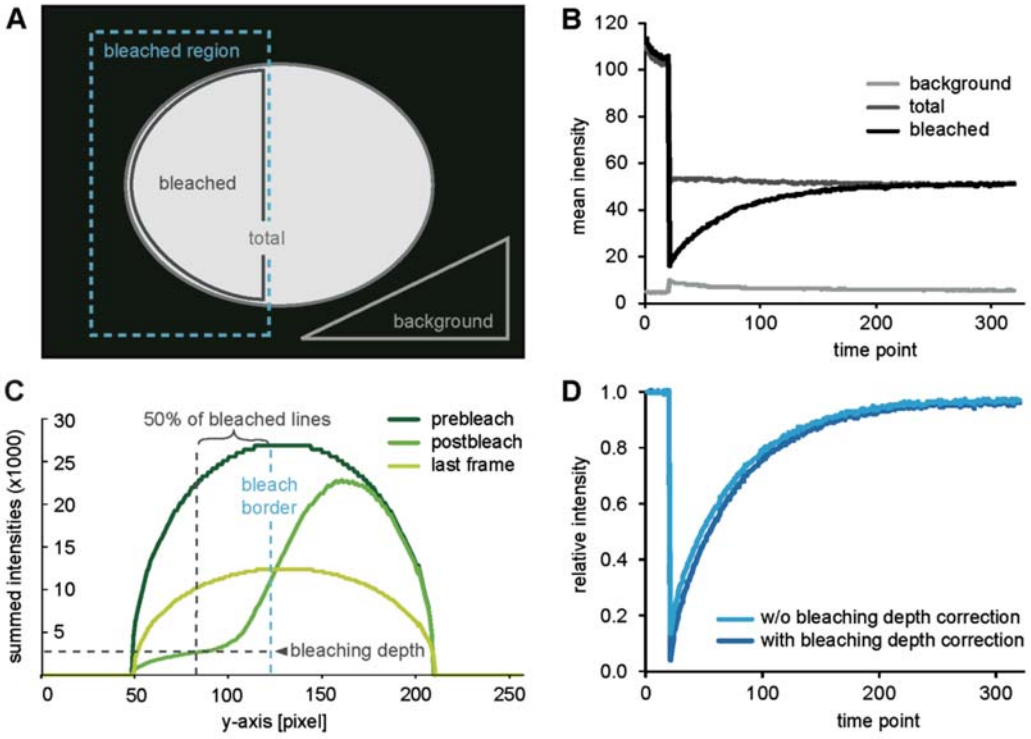

Supplementary Figure 4. Quantitative evaluation of FRAP experiments. (**A**) The three evaluation ROIs (bleached, total, background) are represented schematically. (**B**) Mean intensity over time in the ROIs depicted in A for an example FRAP experiment (GFP-Dnmt1^{wt} with diffuse localization). (**C**) Determination of the bleaching depth in the distal part of the schematic nucleus. The mean fluorescence intensity of each line along the nucleus from the bleached to unbleached region is illustrated for the prebleach, the postbleach and the last frame. The bleaching depth is determined by the average intensity in the region containing 50% of the bleached lines distal to the bleach boarder. (**D**) Comparison of the corrected and normalized data depicted in B without and with bleaching depth correction.

S5

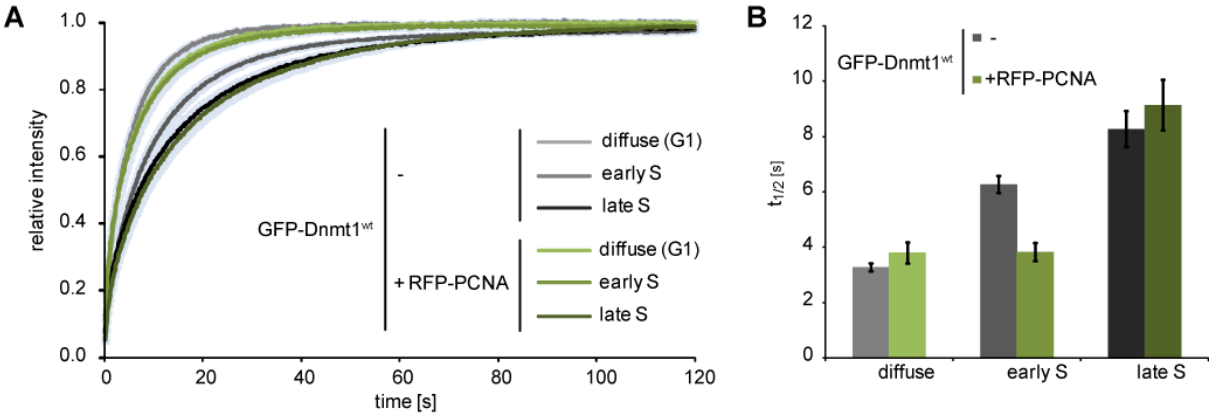

Supplementary Figure 5. Quantitative FRAP evaluation of GFP-Dnmt1^{wt} with and without RFP-PCNA coexpression. (**A**) Mean recovery curves and (**B**) half times of recovery ($t_{1/2}$) are displayed. Coexpression of RFP-PCNA causes an enhanced mobility of GFP-Dnmt1^{wt} in early S.

S6

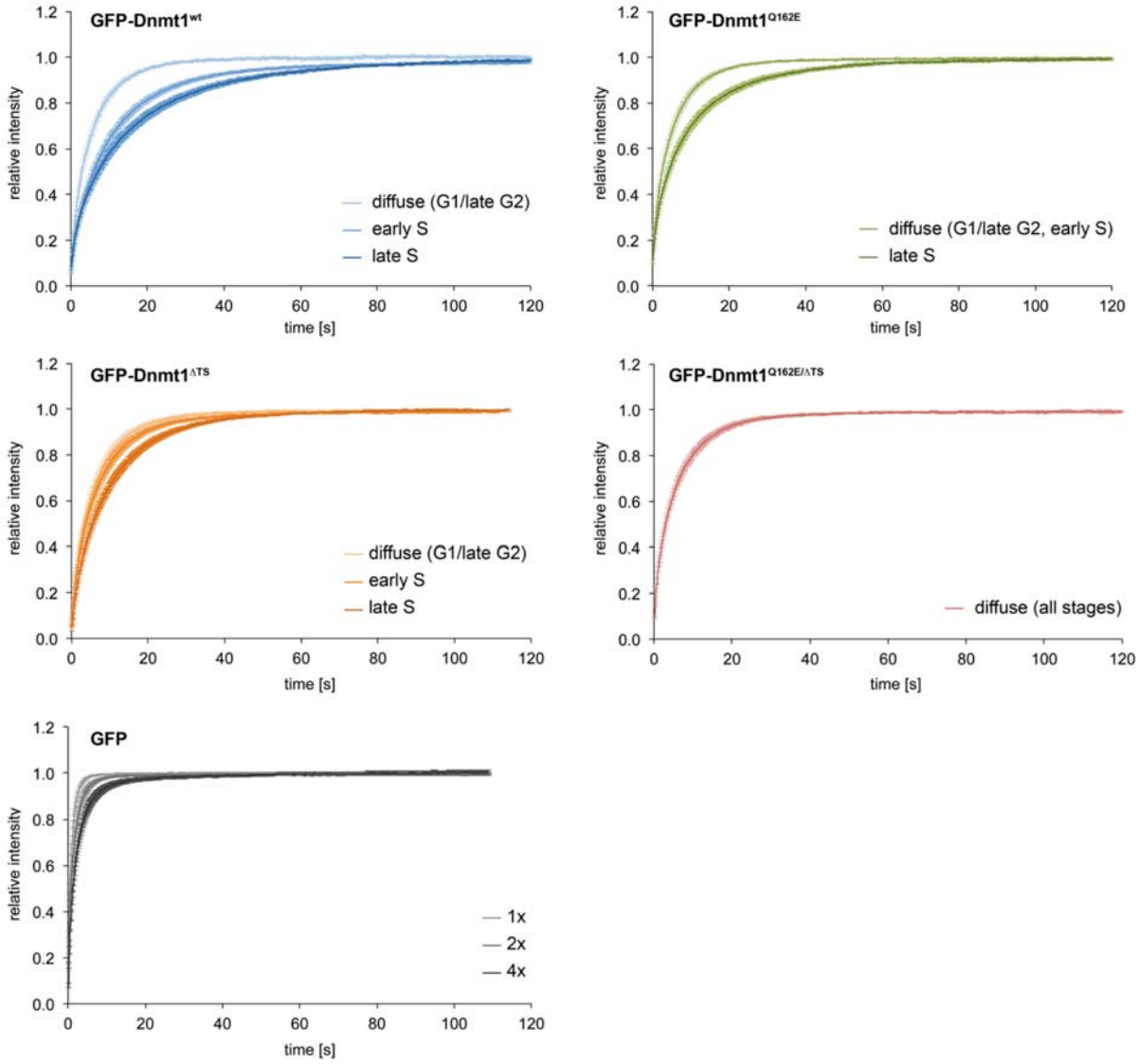

Supplementary Figure 6. Quantitative FRAP evaluation of GFP and GFP-Dnmt1 constructs. Averaged recovery curves displayed for all measured constructs and cell cycle stage including error bars representing the standard error of the mean for every time point (complementary to Fig 3 B).

S7

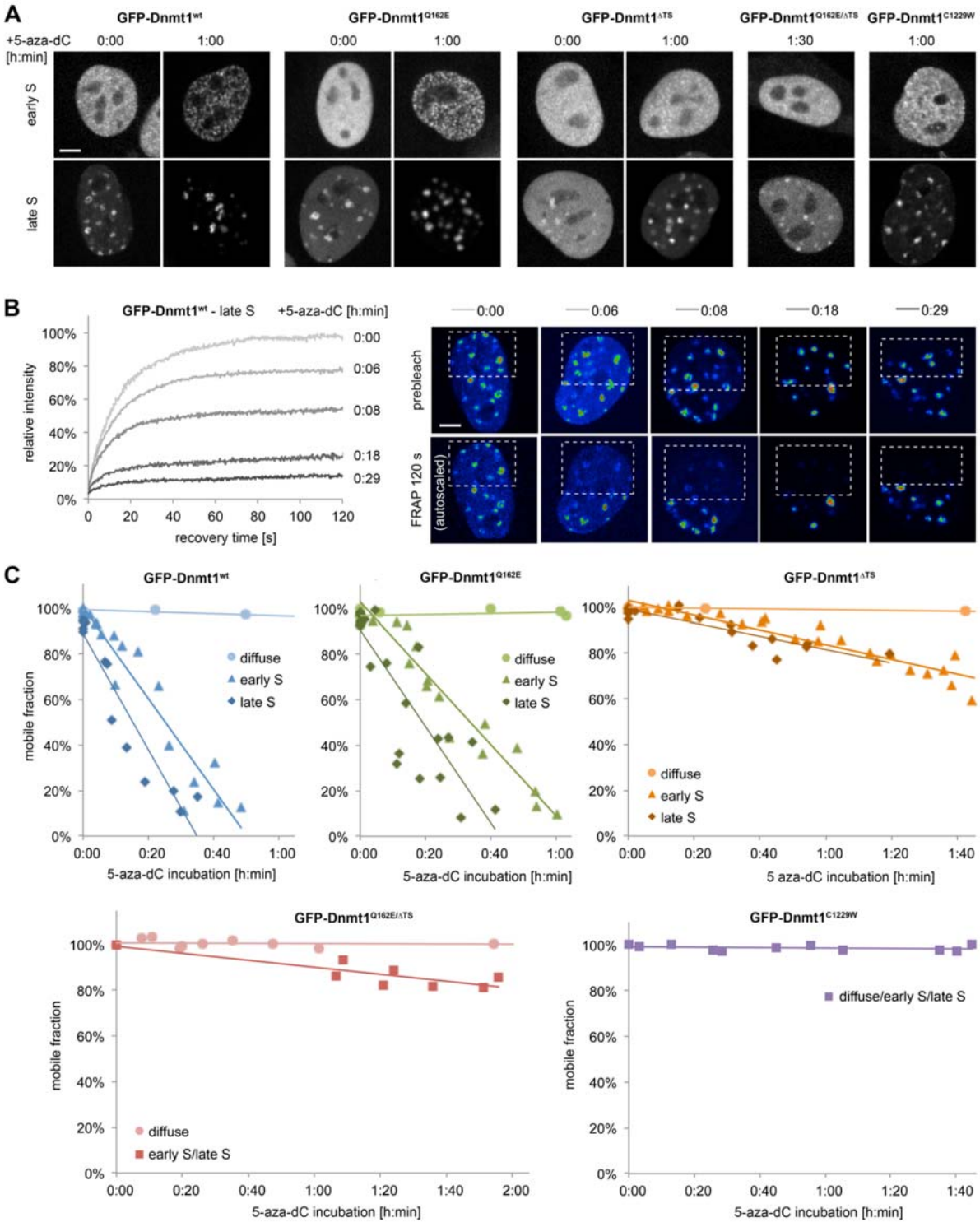

Supplementary Figure 7. Covalent complex formation of GFP constructs analyzed by *in vivo* trapping assay (**A**) Confocal mid sections of representative cells are displayed before (time point 0:00) and after treatment with the mechanism-based inhibitor 5-aza-dC for 60 min (1:00) or 90 min (1:30), respectively. Upon treatment GFP-Dnmt1^{wt} shows a much stronger focal aggregation at RF

and complete depletion of the diffuse fraction. This indicates the immobilization of the mobile enzyme pool due to irreversible covalent complex formation at 5-aza-dC substituted hemi-methylated substrate sites continuously generated during replication progression. GFP-Dnmt1^{Q162E} shows a similar strong enrichment at RF and depletion of the diffuse fraction after 60 min of treatment. The degree of 5-aza-dC-induced RF-association is less prominent for GFP- Dnmt1$^{\Delta TS}$ and the least prominent for the GFP-Dnmt1$^{Q162E/\Delta TS}$. In contrast, a catalytic mutant construct GFP-Dnmt1^{C1229W}, that is unable to form the transient covalent enzyme-substrate complex required for the methyl group transfer, shows no apparent enriched aggregation at RF upon 5-aza-dC treatment. (**B**) Quantitative measurement of the 5-aza-dC-induced immobilization by time-dependent FRAP analysis. Example FRAP measurements of late S phase cells at different 5-aza-dC incubation times (left panel) and the corresponding confocal mid sections of the prebleach time point and 120 s after bleaching (right panel) are shown. The mobile fraction as determined from the recovery plateau reached after 120 s decreases with incubation time. (**C**) Time-dependent decrease of the mobile fractions of GFP-Dnmt1^{wt}, the regulatory mutants GFP-Dnmt1^{Q162E}, GFP- Dnmt1$^{\Delta TS}$, GFP- Dnmt1$^{Q162E/\Delta TS}$ and catalytically inactive mutant GFP-Dnmt1^{C1229W} in early and late S phase upon 5-aza-dC treatment. The results highlight the general ability of all analyzed regulatory mutants, but not the catalytic mutant, to undergo covalent complex formation that initiates the enzymatic reaction. Moreover, clear differences in the efficiency of immobilization become apparent between the analyzed constructs, with the fastest trapping rate observed for GFP-Dnmt1^{wt} followed by GFP-Dnmt1^{Q162E}, GFP- Dnmt1$^{\Delta TS}$ and GFP- Dnmt1$^{Q162E/\Delta TS}$. Linear trend lines are depicted for every construct and cell cycle stage.

S8

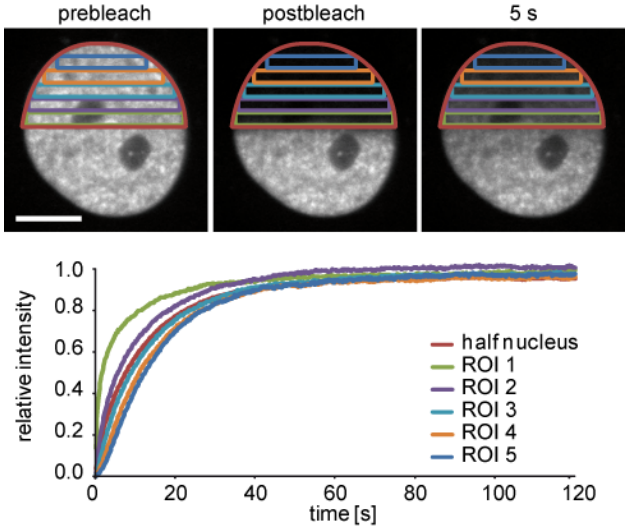

Supplementary Figure 8. Kinetic dependence of GFP-Dnmt1^{wt} on the distance to the bleach border – diffusion-coupled kinetics. Representative images from a FRAP time series and the corresponding recovery curves after half nucleus FRAP (red line) from different evaluation regions of interest (ROIs) as indicated. A stepwise decreased initial mobility is detectable for ROIs that are distant to the bleach border indicating diffusion-coupled kinetics.

S9

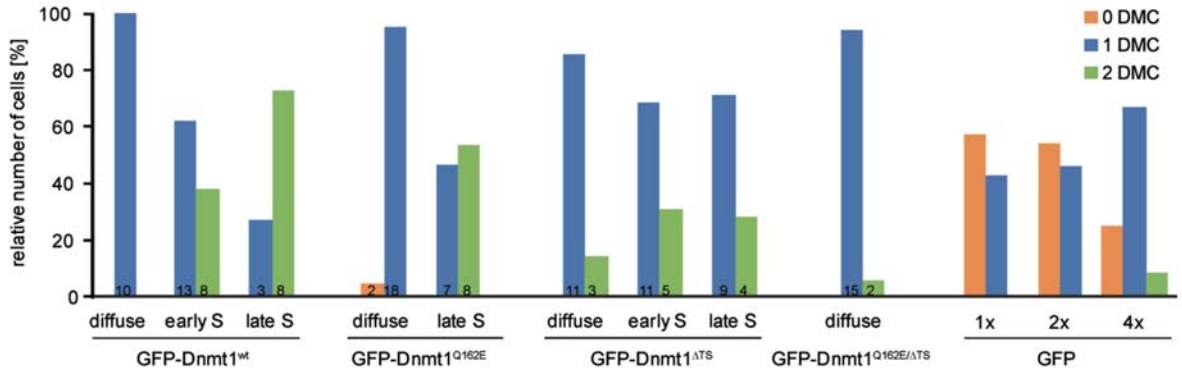

Supplementary Figure 9. Relative number of FRAP experiments with zero, one or two distinctive mobility classes. The dominating number of FRAP experiments with the GFP multimers are fitted with 100% free fraction (0 DMC), except for the GFP tetramer (1 DMC). Using our model a preference for one DMC is found for all GFP-Dnmt1 constructs with diffuse localization and in early S phase cells. A preference for two DMCs is found in late S phase independently of the construct. The dominant DMC classification was chosen for further quantifications.

S10

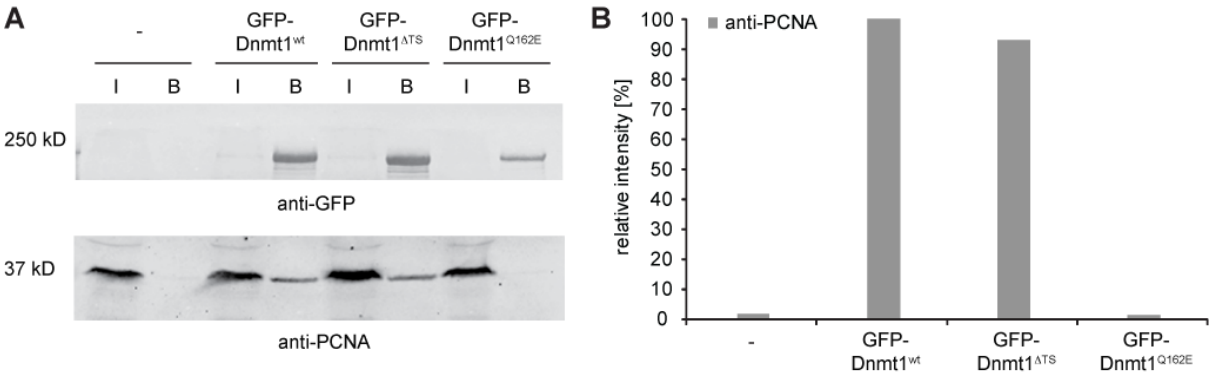

Supplementary Figure 10. Interaction between Dnmt1 and PCNA is abolished by Q162E mutation, but not TS deletion. (**A**) PCNA is co-precipitated with GFP-Dnmt1 from *Dnmt1*$^{-/-}$ mouse embryonic stem (C/C) cells. Protein extracts of C/C cells without or with stably expressing GFP-Dnmt1^{wt}, GFP-Dnmt1^{Q162E} or GFP-Dnmt1$^{\Delta TS}$ were immunoprecipitated with the GFP-Trap (ChromoTek). The immunoprecipitated proteins were separated by SDS-PAGE and detected by GFP or PCNA specific antibodies. (**B**) Quantification of co-precipitated PCNA relative to the amount co-precipitated with GFP-Dnmt1^{wt}.

SUPPLEMENTARY TABLES

S1

Constructs	stage	*N*	*MF* [%]	$t_{1/2}$ [s]
GFP-Dnmt1^{wt}	diffuse	10	99.7±0.3	3.3±0.1
	early S	21	97.5±0.5	6.3±0.3
	late S	11	98.3±0.5	8.3±0.6
GFP-Dnmt1^{Q162E}	diffuse	20	99.4±0.4	3.1±0.2
	late S	15	99.1±0.5	5.4±0.4
GFP-Dmnt1$^{\Delta TS}$	diffuse	14	99.2±0.5	3.8±0.2
	early S	16	98.9±0.5	4.2±0.3
	late S	14	99.4±0.3	6.0±0.4
GFP-Dmnt1$^{Q162E/\Delta TS}$	diffuse	17	98.9±0.6	3.6±0.3
GFP multimers	1x	14	100.2±0.4	0.7±0.03
	2x	13	99.2±0.4	1.0±0.1
	4x	12	100.2±1.4	1.5±0.2

Supplementary Table 1. Cell cycle dependent kinetic properties of GFP and GFP-Dnmt1 constructs analyzed by FRAP. N indicates the number of analyzed cells, MF the mobile fraction and $t_{1/2}$ the half time of recovery. Values larger than 100% are due to technical deviations. Mean values ± SEM are listed.

S2

Constructs	size [kDa]	k_{diff}
1x GFP	27	1.04
2x GFP	54	0.67
4x GFP	108	0.44
GFP-Dnmt1^{wt}	210	*0.28*

Supplementary Table 1. Size-dependent k_{diff} values of GFP-Dnmt1^{wt} and GFP multimers. k_{diff} values are extracted by kinetic modeling of the GFP multimer FRAP data except for GFP-Dnmt1^{wt}, which was extrapolated from the other k_{diff} values.

S3

Constructs	stage	*N*	f_{free} [%]	DMC	f_{DMC1} [%]	$T_{res, DMC1}$ [s]	$k_{off, DMC1}$ [1/s]	f_{DMC2} [%]	$T_{res, DMC2}$ [s]	$k_{off, DMC2}$ [1/s]	f_{CMC} [%]
GFP-Dnmt1^{wt}	diffuse	10	80.2±1.4	1	19.2±1.4	7.7±0.5	0.14+0.01	-	-	-	0.6±0.3
	early S	21	56.5±2.1	1	39.3±1.8	10.2±0.7	0.11±0.01	-	-	-	4.1±0.6
	late S	11	51.9±2.6	2	17.6±3.2	9.8±1.4	0.25±0.11	28.2±3.8	22.1±2.1	0.05±0.00	2.3±0.6
GFP-Dnmt1^{Q162E}	diffuse	20	84.8±1.9	1	13.9±1.9	8.8±1.0	0.18±0.06	-	-	-	1.2±0.3
	late S	15	65.9±2.5	2	9.8±2.5	8.5±1.3	0.59±0.27	22.6±2.3	18.9±2.9	0.07±0.01	1.6±0.6
GFP-Dmnt1$^{\Delta TS}$	diffuse	14	76.5±2.8	1	22.0±2.6	6.8±0.5	0.16±0.01	-	-	-	1.5±0.4
	early S	16	67.9±4.2	1	30.1±4.1	8.5±0.8	0.13±0.01	-	-	-	2.0±0.5
	late S	14	58.3±2.5	1	40.3±2.6	8.8±0.2	0.12±0.00	-	-	-	1.4±0.3
GFP-Dmnt1$^{Q162E/\Delta TS}$	diffuse	17	79.2±2.6	1	19.1±2.6	8.2±0.6	0.13±0.01	-	-	-	1.7±0.4
GFP multimers	1x	14	100.0	0	-	-	-	-	-	-	-
	2x	13	100.0	0	-	-	-	-	-	-	-
	4x	12	91.1±2.8	1	8.0±2.7	14.9±5.6	0.39±0.014	-	-	-	0.9±0.5

Supplementary Table 3. Cell cycle dependent properties of GFP and GFP-Dnmt1 constructs extracted by kinetic modeling. N indicates the number of analyzed cells and DMC the number of distinctive mobility classes determined by the kinetic modeling. The fraction of bound proteins is subdivided into f_{DMC1}, f_{DMC2} and f_{CMC} representing the fractions of proteins bound with the kinetics of DMC1, DMC2 or CMC, respectively. The fraction of unbound proteins is denoted as f_{free}. k_{off} indicates the dissociation rate, T_{res} the mean residence time given by $1/k_{off}$ for DMC1 and DMC2, if present. All listed values are mean values ± SEM. Note that mean(T_{res}) is computed as mean($1/k_{off}$) and deviates from 1/mean(k_{off}).

2.2 Cooperative DNA and histone binding by Uhrf2 links two major repressive epigenetic pathways

ARTICLE
Journal of Cellular Biochemistry 112:2585–2593 (2011)

Journal of Cellular Biochemistry

Cooperative DNA and Histone Binding by Uhrf2 Links the Two Major Repressive Epigenetic Pathways

Garwin Pichler, Patricia Wolf, Christine S. Schmidt, Daniela Meilinger, Katrin Schneider, Carina Frauer, Karin Fellinger, Andrea Rottach, and Heinrich Leonhardt*

Ludwig Maximilians University Munich, Department of Biology II and Center for Integrated Protein Science Munich (CIPS^{M}), Großhaderner Str. 2, 82152 Planegg-Martinsried, Germany

ABSTRACT

Gene expression is regulated by DNA as well as histone modifications but the crosstalk and mechanistic link between these epigenetic signals are still poorly understood. Here we investigate the multi-domain protein Uhrf2 that is similar to Uhrf1, an essential cofactor of maintenance DNA methylation. Binding assays demonstrate a cooperative interplay of Uhrf2 domains that induces preference for hemimethylated DNA, the substrate of maintenance methylation, and enhances binding to H3K9me3 heterochromatin marks. FRAP analyses revealed that localization and binding dynamics of Uhrf2 in vivo require an intact tandem Tudor domain and depend on H3K9 trimethylation but not on DNA methylation. Besides the cooperative DNA and histone binding that is characteristic for Uhrf2, we also found an opposite expression pattern of *uhrf1* and *uhrf2* during differentiation. While *uhrf1* is mainly expressed in pluripotent stem cells, *uhrf2* is upregulated during differentiation and highly expressed in differentiated mouse tissues. Ectopic expression of Uhrf2 in *uhrf1*$^{-/-}$ embryonic stem cells did not restore DNA methylation at major satellites indicating functional differences. We propose that the cooperative interplay of Uhrf2 domains may contribute to a tighter epigenetic control of gene expression in differentiated cells. J. Cell. Biochem. 112: 2585–2593, 2011.

KEY WORDS: UHRF1; UHRF2; DNA METHYLATION; HISTONE MODIFICATIONS; EPIGENETICS

DNA methylation and histone modifications are major epigenetic marks involved in the regulation of gene expression, inheritance of chromatin states, genome stability, and cellular differentiation [Bird, 2002; Kouzarides, 2007; Reik, 2007]. Misregulation of epigenetic pathways, like erroneous DNA methylation, may lead to cancer and other diseases [Jones and Baylin, 2007]. Open questions concern the crosstalk and mechanistic link between different epigenetic signals.

Genome-scale DNA methylation studies revealed a connection between DNA methylation and histone modifications. Specifically, DNA methylation correlates with the absence of H3K4 methylation and presence of H3K9 methylation [Meissner et al., 2008]. This correlation may in part be caused by DNA methyltransferases specifically recognizing histone modifications. For instance, the de novo DNA methyltransferase Dnmt3a and its cofactor Dnmt3L specifically recognize unmethylated H3K4 mediated by the ATRX-Dnmt3-Dnmt3L (ADD) domain [Ooi et al., 2007; Otani et al., 2009]. Dnmt1, which is involved in maintenance methylation during DNA replication and DNA repair [Leonhardt et al., 1992; Mortusewicz et al., 2005], specifically methylates hemimethylated DNA [Bestor and Ingram, 1983; Pradhan et al., 1997] and associates with constitutive heterochromatin via its targeting sequence (TS) domain [Easwaran et al., 2004].

Recently, Uhrf1 (also known as Np95 or ICBP90) has been shown to link DNA and histone modifications and has emerged as an essential cofactor for the maintenance of genomic DNA methylation. Genetic ablation of *uhrf1* leads to remarkable genomic hypomethylation, a phenotype similar to *dnmt1*$^{-/-}$ embryonic stem cells (ESCs) [Bostick et al., 2007; Sharif et al., 2007]. Uhrf1 binds hemimethylated DNA via a SET and RING associated domain (SRA) domain and targets Dnmt1 to its substrate of maintenance DNA methylation [Bostick et al., 2007; Sharif et al., 2007; Arita et al., 2008; Avvakumov et al., 2008; Hashimoto et al., 2008; Qian et al., 2008; Rottach et al., 2010]. This targeting activity of Uhrf1 is based on specific binding to the heterochromatin mark H3K9me3 via a tandem Tudor domain (TTD) [Karagianni et al., 2008; Rottach et al.,

Additional supporting information may be found in the online version of this article.

Grant sponsor: Deutsche Forschungsgemeinschaft (DFG).

Karin Fellinger's present address is Intervet International GmbH, Unterschleissheim, Germany.

*Correspondence to: Dr. Heinrich Leonhardt, Department of Biology II, Ludwig Maximilians University Munich, 82152 Planegg-Martinsried, Germany. E-mail: h.leonhardt@lmu.de

Received 1 April 2011; Accepted 11 May 2011 • DOI 10.1002/jcb.23185 • © 2011 Wiley-Liss, Inc.
Published online 19 May 2011 in Wiley Online Library (wileyonlinelibrary.com).

2010]. In addition, Uhrf1 interacts with Dnmt3a and Dnmt3b and with histone modifying enzymes like HDAC1, G9a, and Tip60 [Unoki et al., 2004; Achour et al., 2009; Kim et al., 2009; Meilinger et al., 2009]. Finally, Uhrf1 displays E3 ubiquitin ligase activity for histone H3 [Citterio et al., 2004] and is involved in large scale reorganization of chromocenters [Papait et al., 2008].

Interestingly, a second member of the Uhrf family, Uhrf2, harbors similar domains [Bronner et al., 2007]. Until now, the only known function of Uhrf2 is a role in intranuclear degradation of polyglutamine aggregates [Iwata et al., 2009]. In this study, we systematically investigated the function and interplay of distinct Uhrf2 domains in DNA and histone tail substrate recognition and report first hints on cell-type specific functions of Uhrf1 and Uhrf2.

MATERIALS AND METHODS

EXPRESSION CONSTRUCTS

Expression constructs for GFP, RFP-PCNA, Uhrf1-GFP, and GFP constructs of Dnmt1 were described previously [Sporbert et al., 2005; Fellinger et al., 2009; Meilinger et al., 2009]. All Uhrf2 expression constructs were derived by PCR from mouse *uhrf2*-myc cDNA (MR210744, ORIGENE). To obtain GFP fusion constructs, the *uhrf1* cDNA [Rottach et al., 2010] was replaced by *uhrf2* encoding PCR fragments in the pCAG-*uhrf1*-GFP vector. The deletion and point mutant expression constructs were derived from the corresponding wild-type constructs by overlap extension PCR [Ho et al., 1989] and PCR-based mutagenesis. The following start and end amino acids were chosen: Uhrf2 tandem Tudor domain, amino acids 118–312; Uhrf2 PHD domain, amino acids 325–395; Uhrf2 tandem Tudor–PHD domain, amino acids 118–395; Uhrf1 tandem Tudor–PHD domain, amino acids 121–370. The linker exchange constructs were derived by PCR using overlapping primers that contained the partial linker sequence. Amino acid sequences of the linkers: Uhrf1: KERRPLIASPSQPPA; Uhrf2: GAHPISFADGKF. All constructs were verified by DNA sequencing. Throughout this study enhanced GFP constructs were used and for simplicity referred to as GFP fusions.

CELL CULTURE, TRANSFECTION, CELL SORTING, AND DIFFERENTIATION

HEK293T cells, MEFs, and ESCs were cultured and transfected as described [Schermelleh et al., 2007; Rottach et al., 2010] with the exception that Lipofectamin (Invitrogen) was used for transfection of MEFs. E14 *uhrf1*$^{-/-}$ ESCs were transfected with Uhrf1-GFP and Uhrf2-GFP expression constructs using FuGENE HD (Roche) according to the manufacturer's instructions. ESCs were sorted for GFP positive cells 48 h after transfection with a FACS Aria II instrument (Becton Dikinson). ESC strains wt E14, wt J1, and E14 *uhrf1*$^{-/-}$ were cultured and differentiated to embryoid bodies as described [Szwagierczak et al., 2010]. The ESC strain wt JM8A3.N1 (EUCOMM, Germany) was cultured in Knockout D-MEM (Gibco-BRL, Grand-Island, NY) medium containing 10% fetal bovine serum (PAA Laboratories GmbH, Austria), 0.1 mM β-mercaptoethanol (Gibco-BRL), 2 mM L-glutamine, 100 U/ml penicillin, 100 μg/ml streptomycin (PAA Laboratories GmbH). The medium was supplemented with 1,000 U/ml recombinant mouse LIF (Millipore, Temecula, CA).

RNA ISOLATION, CDNA SYNTHESIS, AND QUANTITATIVE REAL-TIME PCR

RNA isolation and cDNA synthesis were performed as described [Szwagierczak et al., 2010]. Equal amounts of cDNA were used for Real-time PCR with TaqMan Gene Expression Master Mix (Applied Biosystems) on the 7500 Fast Real-time PCR System (Applied Biosystems) according to the manufacturer's instructions. The following TaqMan Gene expression assays were used: Gapdh (Assay ID: Mm99999915_g1), uhrf1 (Assay ID: Mm00477865_m1) and uhrf2 (Assay ID: Mm00520043_m1). Gene expression levels were normalized to Gapdh and calculated using the comparative C_T Method ($\Delta\Delta C_T$ Method).

IN VITRO DNA BINDING AND HISTONE-TAIL PEPTIDE BINDING ASSAY

The in vitro binding assays were performed as described previously [Frauer and Leonhardt, 2009; Rottach et al., 2010]. NoCpG DNA substrates were produced in a primer extension reaction [Frauer and Leonhardt, 2009] others by hybridization of two DNA oligos (Supplementary Fig. S7B–D). Histone-tail peptides were purchased as TAMRA conjugates (PSL, Germany; Supplementary Fig. S7A). Peptides were added in a molar ratio 1.5:1 (peptide/GFP fusion) and the binding reaction was performed at RT for 15 min with constant mixing. For combined assays, samples were additionally incubated with either H3K9me3 or H3K9ac histone-tail peptides in a molar ratio 1.5:1 (peptide/GFP fusion) or increasing amount of DNA substrate as indicated. The binding reaction was performed at RT for 60 min with constant mixing.

IMMUNOFLOURESCENCE STAINING AND ANTIBODIES

For immunostaining, MEF cells and ESCs were grown on cover slips and transiently transfected with Uhrf2-GFP (MEF cells), or co-transfected with Uhrf2-GFP and RFP-PCNA (ESCs). Cells were fixed with 2.0% or 3.7% formaldehyde in PBS and permeabilized in PBS containing 0.2% Triton X-100. The post-translational histone modification H3K9me3 was detected via a rabbit primary antibody (Active Motif) and a secondary anti-rabbit antibody conjugated to Alexa Fluor 594 (Molecular Probes, Eugene, OR). The antibodies were diluted 1:1,000 or 1:500, respectively, in PBS containing 0.02% Tween-20 and 2% BSA. GFP-Binder (ChromoTek, Germany) was used to boost GFP signals and was labeled with Alexa Fluor 488. Cells were counterstained with DAPI and mounted in Vectashield (Vector Laboratories, Burlingame, CA). Images of the cells were obtained using a TCS SP5 AOBS confocal laser scanning microscope (Leica, Wetzlar, Germany) with a 63x/1.4 NA Plan-Apochromat oil immersion objective. GFP, Alexa Fluor 488, RFP, and Alexa Fluor 594 were excited with a 488-nm argon laser and a 561-nm diode laser, respectively. Image series were recorded with a frame size of 512 × 512 pixels, a pixel size of 100 nm and with a detection pinhole size of 1 Airy Unit.

LIVE CELL MICROSCOPY AND FLUORESCENCE RECOVERY AFTER PHOTOBLEACHING (FRAP) ANALYSIS

Live cell imaging and FRAP analyses were performed as described [Schermelleh et al., 2007] with the exception that imported images were intensity normalized, converted to 8-bit and Gauss-filtered (2 pixel radius). Data sets showing lateral movement were corrected by image registration using the StackReg plug-in of ImageJ [Abramoff et al., 2004] starting with a frame when approximately half recovery was reached. Within the first 30 s after bleaching, images were taken every 150 ms and then in intervals of 1 s.

DNA METHYLATION ANALYSIS

Genomic DNA was isolated with the QIAmp DNA Mini Kit (Qiagen) and 1.5 μg were bisulfite converted using the EZ DNA Methylation-Gold Kit (Zymo research) according to the manufacturer's instructions. Primer sequences for major satellites were AAAAT-GAGAAACATCCACTTG (forward primer) and CCATGATTTT-CAGTTTTCTT (reverse primer). For amplification we used Qiagen Hot Start Polymerase in 1× Qiagen Hot Start Polymerase buffer supplemented with 0.2 mM dNTPs, 0.2 μM forward primer, 0.2 μM reverse primer, 1.3 mM betaine (Sigma) and 60 mM tetramethylammonium-chloride (TMAC, Sigma). Major satellites were amplified in a single amplification and pyrosequencing reactions were carried out by Varionostic GmbH (Ulm, Germany).

STATISTICAL ANALYSIS

Results were expressed as means ± SD or means ± SEM. The difference between two mean values was analyzed by Student's *t*-test and was considered as statistically significant in case of $P < 0.05$ (*) and highly significant for $P < 0.001$ (**).

RESULTS

OPPOSITE EXPRESSION PATTERN OF *UHRF1* AND *UHRF2* DURING DIFFERENTIATION

Recently, Uhrf1 has emerged as an essential factor for the maintenance of DNA methylation. Sequence analyses revealed that Uhrf2 harbors five recognizable domains similar to Uhrf1 (Fig. 1A), but its role in the regulation of DNA methylation is still unclear. We compared the expression pattern of *uhrf1* and *uhrf2* in ESCs and somatic cells, during differentiation and in differentiated mouse tissues (Fig. 1B–D and Supplementary Fig. S1). Interestingly, both genes show opposite expression patterns; while *uhrf1* is expressed in ESCs and down regulated during differentiation, which is consistent with previous reports [Muto et al., 1995; Fujimori et al., 1998; Hopfner et al., 2000], *uhrf2* is upregulated and highly expressed in differentiated mouse tissues. The switch in the expression pattern argues against a functional redundancy of both genes and is consistent with the drastic loss of DNA methylation in *uhrf1*$^{-/-}$ ESCs despite the presence of intact *uhrf2* alleles. Therefore, the opposite expression pattern of both genes suggests different functional roles of *uhrf1* and *uhrf2* in development.

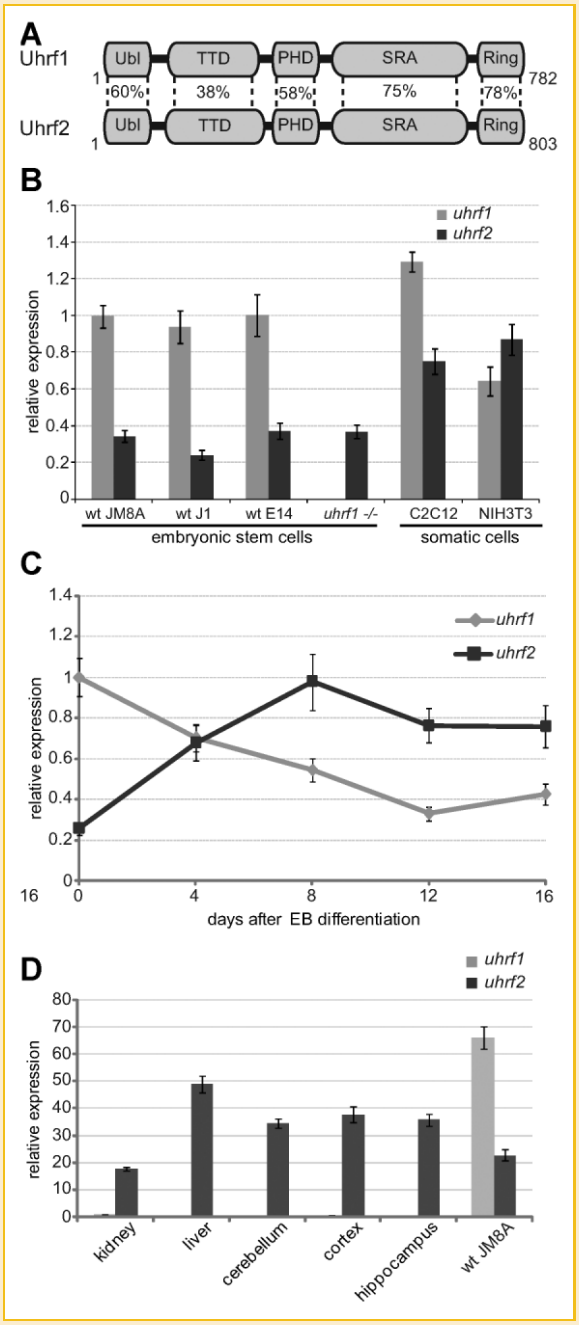

Fig. 1. Opposite expression pattern of *uhrf1* and *uhrf2* during differentiation. A: Schematic outline of the multi-domain architecture of Uhrf1 in comparison to Uhrf2. An N-terminal ubiquitin-like domain (Ubl) is followed by a tandem Tudor domain (TTD), a plant homeodomain (PHD), a SET and RING associated (SRA) domain and a C-terminal really interesting new gene (RING) domain. Numbers indicate primary sequence similarities of single domains determined by BlastP search [Altschul, 1991]. Expression analysis of *uhrf1* and *uhrf2* by Real-time PCR in ESCs and somatic cells (B), during differentiation of wt J1 ESCs (C) and in various adult mouse tissues in comparison to the expression data in ESCs (D). Expression levels are relative to *uhrf1* in wtJM8A (B), day 0 of differentiation (C) and to kidney (D) (*uhrf1* set to 1). Shown are means ± SD of at least two independent experiments.

COOPERATIVE BINDING OF REPRESSIVE EPIGENETIC MARKS BY UHRF2

To investigate DNA and histone-tail binding preferences of Uhrf2 in vitro, we used a versatile binding assay developed for GFP fusion proteins [Rothbauer et al., 2008; Frauer and Leonhardt, 2009; Rottach et al., 2010]. Similar to Uhrf1, histone-tail peptide binding assays revealed that Uhrf2 preferentially binds to H3(1–20) and H3K9me3 peptides (Fig. 2A). This binding activity of Uhrf2 is mediated by the TTD but not the PHD domain (Fig. 2B). Consistently, acetylation of H3K9, underrepresented in heterochromatin,

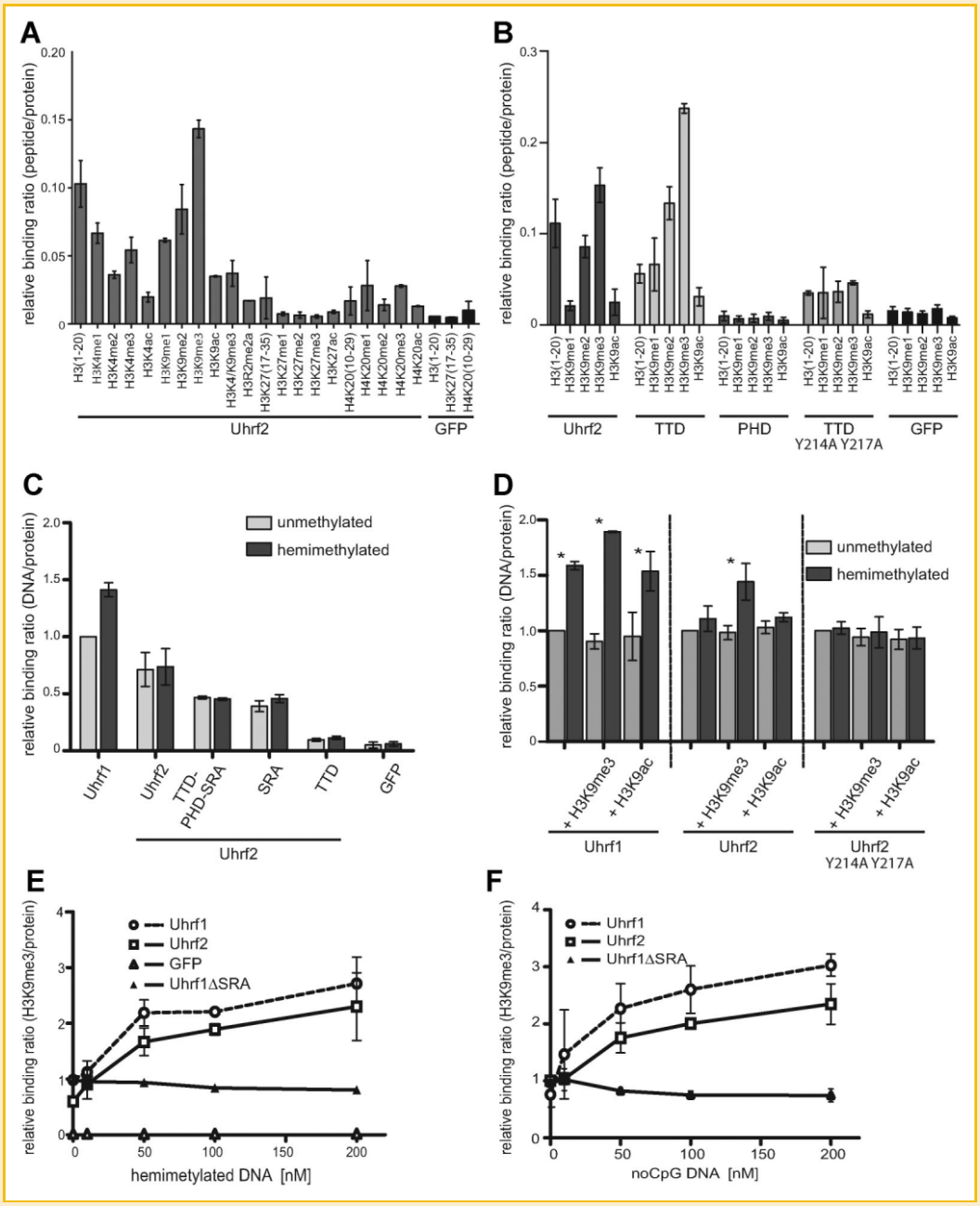

Fig. 2. Cooperative binding of repressive epigenetic marks by Uhrf2. In vitro binding ratios of fluorescently labeled substrate over bound GFP fusion proteins were determined. A: Histone H3- and H4-tail binding specificities of Uhrf2. Shown are means ± SD of biological duplicates. B: Histone H3 tail binding specificity of Uhrf2, its tandem Tudor domain (TTD), its PHD domain and its TTD mutant (Y214A Y217A). Shown are means ± SEM of at least three independent experiments. C: DNA binding properties of Uhrf1, Uhrf2 and of single (SRA, TTD) and combined Uhrf2 domains (TTD–PHD–SRA). Shown are means ± SEM of three independent experiments. D: DNA binding properties of Uhrf1, Uhrf2 and Uhrf2 Y214A Y217A in combination with histone-tail peptide binding. Shown are means ± SD of three independent experiments (Uhrf1, Uhrf2) and of two independent experiments (Uhrf2 Y214A Y217A). Values were normalized to the binding ratio of each GFP fusion for unmethylated DNA without histone-tail peptide. Statistical significance of differences between the binding ratios with un- and hemimethylated DNA is indicated; $^{*}P < 0.05$. E + F: H3K9me3 peptide binding by Uhrf1, Uhrf2, and Uhrf1ΔSRA with increasing concentrations of DNA substrate containing either one central hemimethylated (E) or noCpG site (F). Shown are means ± SD of biological duplicates. Values were normalized to the binding ratio of Uhrf1ΔSRA without DNA.

prevented the binding of Uhrf2 and its TTD. The binding of Uhrf1 to H3K9me3 is mediated by an aromatic cage in the TTD [Rottach et al., 2010]. Site-directed mutagenesis of Uhrf2 changing the two conserved tyrosine residues to alanine (Y214A Y217A) (Supplementary Fig. S2) abolished specific peptide binding (Fig. 2B) and supports a function of the aromatic cage in H3K9me3 recognition.

Whereas Uhrf1 preferentially binds to hemimethylated DNA, Uhrf2 failed to show a preference for hemi-over unmethylated DNA (Fig. 2C). These differences in DNA binding preferences between Uhrf1 and Uhrf2 were confirmed by electrophoretic mobility shifts (Supplementary Fig. S3). To further investigate the functional interplay between DNA and histone binding we performed combined binding assays (Fig. 2D). Interestingly, binding to heterochromatin-specific H3K9me3 peptides induced a significant preference of Uhrf2 for hemi-over unmethylated DNA. Uhrf1 already on its own showed preference for hemimethylated DNA that was further enhanced by binding to H3K9me3 peptides. To test the specificity of this cooperativity we mutated the aromatic cage in Uhrf2 that is necessary for H3K9me3 histone-tail peptide binding. The mutated Uhrf2 (Y214A Y217A) showed comparable DNA binding activity as the wild-type Uhrf2 but addition of heterochromatin-specific H3K9me3 peptides did not induce preference for hemi-over unmethylated DNA (Fig. 2D).

In the reverse experiment, addition of DNA enhanced binding of Uhrf1 and Uhrf2 to the H3K9me3 peptide (Fig. 2E,F). This was not observed for the DNA binding mutant of Uhrf1 (Uhrf1ΔSRA) which showed constant peptide binding with increasing DNA concentrations. These findings suggest that single binding events of distinct Uhrf2 domains lead to multivalent engagement of different repressive epigenetic marks. In fact, multivalent engagement of DNA and histone tail peptides via the SRA domain and the TTD, respectively, results in affinity enhancement and additional specificity for hemimethylated DNA, the substrate of maintenance methylation.

CELLULAR LOCALIZATION AND DYNAMICS OF UHRF2 DEPEND ON HISTONE H3K9 METHYLATION

To monitor the subcellular localization of Uhrf2, we expressed Uhrf2-GFP constructs in cells with different genetic backgrounds. In wild type (wt) ESCs, Uhrf2 is localized in the nucleus and is enriched at pericentric heterochromatin (PH) (Fig. 3A,B and Supplementary Fig. S4A–C). To investigate which epigenetic marks at PH are recognized by Uhrf2 we determined the localization of Uhrf2 in genetically modified ESCs either lacking all three major DNA methyltransferases Dnmt1, Dnmt3a, and Dnmt3b (TKO) [Tsumura et al., 2006] or ESCs lacking the two major H3K9 methyltransferases Suv39H1/H2 (*Suv39h dn*) [Lehnertz et al., 2003]. TKO cells are practically devoid of genomic DNA methylation and *Suv39h dn* ESCs show substantially reduced H3K9me3 levels. We found Uhrf2 localized at PH in TKO but not in *Suv39h dn* ESCs, indicating that localization of Uhrf2 is dependent on H3K9 but not on DNA methylation (Fig. 3A). Consistently, immunostaining of wt mouse embryonic fibroblasts (MEFs) showed co-localization of Uhrf2 and H3K9me3 marks at PH, which was not observed in *Suv39h dn* MEFs [Peters et al., 2001] (Fig. 3B). Also, mutations in the TTD (Uhrf2 Y214A Y217A) that abolished binding to H3K9me3 peptides in vitro

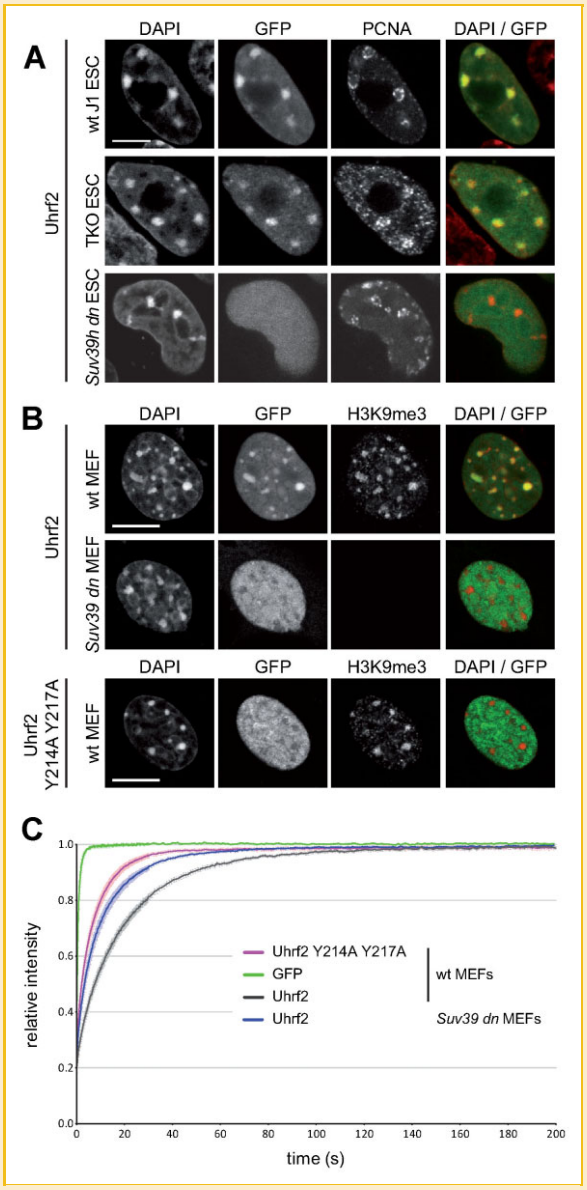

Fig. 3. Cellular localization and dynamics of Uhrf2 depend on histone H3K9 methylation. A: Confocal mid sections of fixed wt J1, TKO and *Suv39h dn* ESCs transiently expressing Uhrf2-GFP and RFP-PCNA and counterstained with DAPI, which preferentially highlights PH. Merged images are displayed on the right side (GFP: green; DAPI: red). Scale bar 5 μm. B: Confocal mid sections of fixed wt MEFs and *Suv39h dn* MEFs transiently expressing Uhrf2-GFP or Uhrf2 Y214A Y217A-GFP were immunostained for H3K9me3 and counterstained with DAPI. Merged images are displayed on the right side (GFP: green; DAPI: red). Scale bar 5 μm. C: Dynamics of Uhrf2-GFP and Uhrf2 Y214A Y217A-GFP in living MEFs determined by half nucleus FRAP analysis. GFP is shown as reference. Curves represent means ± SEM from at least 8 nuclei.

disrupted enrichment at PH in wt MEFs (Fig. 3B). The dependence of Uhrf2 localization on H3K9me3 was also confirmed by quantitative correlation analysis (Supplementary Fig. S4D,E).

To investigate the effect of H3K9me3 on the dynamics of Uhrf2 in living cells we performed quantitative fluorescence recovery after photobleaching (FRAP) analyses in wt and *Suv39h dn* MEFs. We chose to bleach half nuclei to include a representative number of

interactions from different nuclear domains and structures in the bleached area [Rottach et al., 2010]. Recovery of Uhrf2-GFP fluorescence in *Suv39h dn* MEFs (half-time $t_{1/2} = 5.9 \pm 0.6$ s) and of the TTD mutant in wt MEFs ($t_{1/2} = 3.2 \pm 0.4$ s) was considerably faster than the recovery of Uhrf2-GFP in wt MEFs ($t_{1/2} = 11.8 \pm 0.6$ s) pointing to a crucial role of H3K9me3 in Uhrf2 dynamics in living cells (Fig. 3C). Taken together, these results clearly demonstrate that the interaction of Uhrf2 with the heterochromatin mark H3K9me3 is required for the localization at PH and affects binding dynamics in living cells.

COOPERATIVE BINDING OF THE COMBINED UHRF2 TTD–PHD DOMAIN

Recently, several studies showed multivalent binding to histone-tail peptides [Ruthenburg et al., 2007]. In case of Uhrf1 and Uhrf2, the TTD is followed by a second histone-tail binding domain, a PHD domain (Fig. 1A). As the isolated PHD domains of Uhrf1 and Uhrf2 did not show binding to H3 histone-tail peptides (Fig. 2B) [Rottach et al., 2010], we tested whether the combination of the PHD and the TTD results in cooperative histone-tail binding. Surprisingly, the combined TTD–PHD domain of Uhrf2 displayed a fourfold increased binding to H3K9me2/me3 in comparison to the single TTD, which was not observed for the corresponding construct of Uhrf1 (Figs. 2B and 4A).

Sequence alignments of the combined domains revealed two striking differences between Uhrf1 and Uhrf2. Firstly, Uhrf2 harbors an additional stretch of 33 highly conserved amino acids present in the TTD (Supplementary Fig. S5A). Secondly, the linker region between the TTD and PHD domain of Uhrf2 is highly conserved, whereas this region is highly diverse in Uhrf1 (Supplementary Fig. S5A). To test which sequence is responsible for the observed cooperative interplay between PHD and TTD, we generated and tested different hybrid and deletion constructs (Supplementary Fig. S5B). Notably, replacement of the native linker in the Uhrf2 TTD–PHD construct by the Uhrf1 linker caused decreased relative binding ratios to H3K9me2/3 comparable to the single Uhrf2 TTD (Fig. 4B). Transferring the Uhrf2 linker to the Uhrf1 TTD–PHD construct as well as deletion of the Uhrf2 stretch region did not affect the binding to H3K9me3 peptides (Fig. 4B).

These results suggest that the cooperative interplay of different Uhrf2 domains, which is responsible for the increased binding to heterochromatin marks, is dependent on the highly conserved linker region connecting the TTD and PHD domains. A similar functional importance of linker sequences has been described for BPTF and histone lysine demethylases [Li et al., 2006; Horton et al., 2010].

UHRF1 AND UHRF2 ARE NOT FUNCTIONALLY REDUNDANT IN ESCS

To investigate whether Uhrf1 and Uhrf2 are functionally redundant we performed interaction and rescue assays. Like Uhrf1, also Uhrf2 interacts with Dnmts (Supplementary Fig. S6) suggesting a similar function in DNA methylation. To test for such a functional role, we ectopically expressed Uhrf2-GFP or Uhrf1-GFP in *uhrf1*$^{-/-}$ ESCs and determined DNA methylation levels at major satellites by pyrosequencing. While ectopic expression of Uhrf1-GFP led to significant increase of DNA methylation levels at CpG sites of major satellite DNA in *uhrf1*$^{-/-}$ ESCs, Uhrf2-GFP did not restore DNA methylation at these sites (Fig. 5). These results point to functional differences between Uhrf1 and Uhrf2 in vivo.

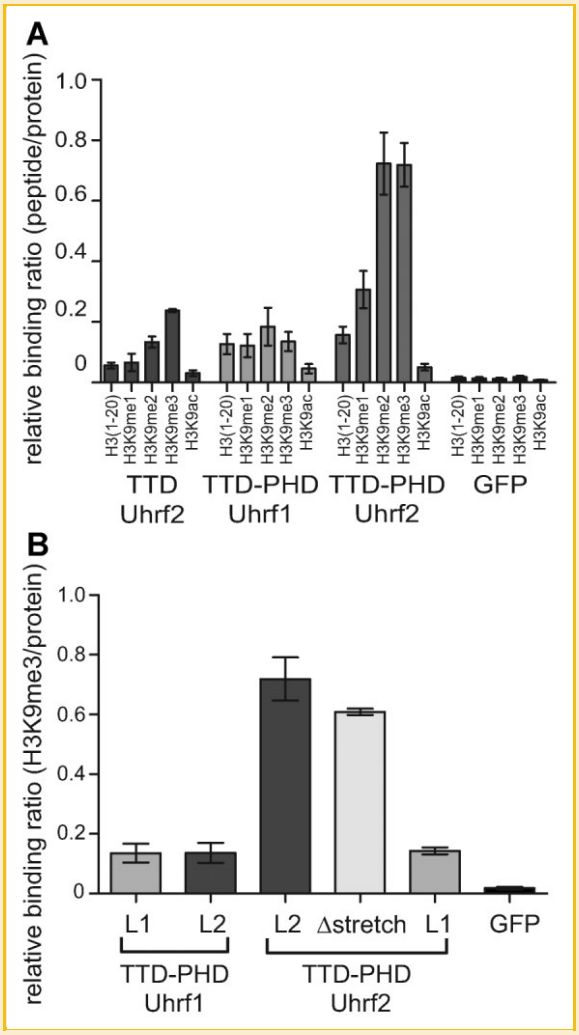

Fig. 4. Cooperative binding of the combined tandem Tudor–PHD domain of Uhrf2. A: Histone H3 N-terminal tail binding specificity of the TTD of Uhrf2 and of the combined TTD and PHD domain (TTD–PHD) of Uhrf1 and Uhrf2. Shown are means ± SEM from at least six independent experiments. B: Histone H3K9me3 binding of the combined TTD–PHD domains of Uhrf1 and Uhrf2, hybrid proteins (L1 and L2 specify inserted linker sequences derived from Uhrf1 and Uhrf2, respectively) and a stretch deletion Uhrf2 construct. Shown are means ± SEM from at least three independent experiments.

DISCUSSION

Over the past decades many different histone modifications were discovered that are involved in epigenetic gene regulation. A key question is how these histone marks are linked to DNA methylation pattern and how this complex epigenetic information is integrated and translated into defined chromatin structures and gene expression levels. Epigenetic regulators that bind DNA and histone marks are ideally suited to link these pathways and intramolecular interactions between different binding domains may contribute to

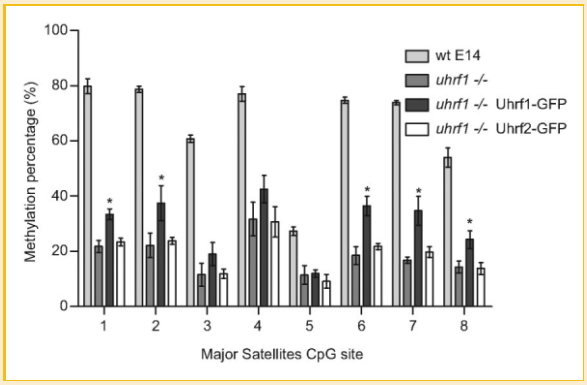

Fig. 5. Uhrf1 and Uhrf2 are not functionally redundant in ESCs. DNA methylation analysis of wt E14 ESCs, *uhrf1*$^{-/-}$ ESCs and of *uhrf1*$^{-/-}$ ESCs ectopically expressing Uhrf1-GFP or Uhrf2-GFP. ESCs transiently expressing Uhrf1-GFP and Uhrf2-GFP were isolated by FACS sorting 48 h after transfection and CpG methylation levels of major satellites repeats were analysed by bisulfite treatment, PCR amplification and direct pyrosequencing. Statistical significance of differences in DNA methylation levels between *uhrf1*$^{-/-}$ ESCs and *uhrf1*$^{-/-}$ ESCs with ectopically expressed Uhrf1-GFP or Uhrf2-GFP are indicated; $^{*}P < 0.05$. Shown are means ± SD from three independent experiments.

substrate specificity and epigenetic regulation [Hashimoto et al., 2009].

Recently, Uhrf1, an essential factor for the maintenance of DNA methylation, has been shown to bind to repressive DNA and histone modifications via an SRA and a tandem Tudor domain, respectively. Here we provide the first systematic characterization of the second member of the Uhrf family, Uhrf2, and demonstrate that Uhrf2 binds to the H3K9me3 heterochromatin mark via an aromatic cage of a tandem Tudor domain (TTD). Mutations in the aromatic cage abolished binding to H3K9me3 histone-tail peptides in vitro and prevented enrichment of Uhrf2 at pericentric heterochromatin in vivo. Interestingly, similar mutations in the aromatic cage of Uhrf1 prevented repression of $p16^{INK4A}$ [Nady et al., 2011] suggesting a link between H3K9me3 binding and a function of Uhrf proteins in gene repression.

Our results point to a complex regulation of substrate recognition by Uhrf2 involving cooperative binding domains and critical linker sequences. In contrast to Uhrf1, preferential binding of Uhrf2 to hemimethylated DNA, the substrate of DNA maintenance methylation, was only induced upon simultaneous binding to H3K9me3 histone-tail peptides. Binding of Uhrf1 and Uhrf2 to DNA in turn enhanced binding to H3K9me3 histone-tail peptides. Consistently, SILAC-based proteomic analysis identified enrichment of UHRF1 at nucleosomes containing repressive DNA and H3K9 methylation marks [Bartke et al., 2010]. Together, these data demonstrate a cooperative interplay between DNA and histone tail binding domains of Uhrf1 and Uhrf2. A similar effect was reported for MSL3 that specifically binds to H4K20me1 via a chromodomain only in the presence of DNA [Kim et al., 2010].

An additional level of complexity was added by recent studies showing multivalent binding of histone-tail peptides by mixed two-effector modules [Ruthenburg et al., 2007]. Notably, the combined TTD–PHD domain of Uhrf2, but not of Uhrf1, showed enhanced binding to H3K9me3 histone-tail peptides. This cooperativity was dependent on the highly conserved linker region connecting the TTD and PHD domains. Similarly, an important role was attributed to the linker sequence between the histone binding domain (PHD) and the histone modifying domain of jumanji histone lysine demethylases [Horton et al., 2010].

The dramatic loss of DNA methylation in *uhrf1*$^{-/-}$ ESCs [Bostick et al., 2007; Sharif et al., 2007] is remarkable, especially considering the presence of the *uhrf2* gene, which encodes a highly similar protein as demonstrated in this study. As one possible explanation for this lack of functional redundancy we found, in contrast to *uhrf1*, relatively low *uhrf2* mRNA levels in ESCs, which were not affected by genetic *uhrf1* ablation. Moreover, both genes also show opposite expression patterns during differentiation. The failure of ectopically expressed Uhrf2 to restore DNA methylation in *uhrf1* deficient cells clearly points to functional differences between both proteins in vivo. However, more definitive insights into the specific function(s) of Uhrf2 will require targeted mutations and subsequent analyses of pluripotent as well as differentiated cells. Based on the cooperative binding of Uhrf2 domains to repressive DNA and histone marks we propose that Uhrf2 might contribute to a tighter control of gene repression in differentiated cells as compared to a less stringent control by Uhrf1 in pluripotent ESCs.

ACKNOWLEDGMENTS

The authors are grateful to En Li (Novartis Institutes for Biomedical Research, Boston, MA) for J1 ESCs, to Masaki Okano (RIKEN Center for Developmental Biology, Kobe, Japan) for TKO ESCs, to Thomas Jenuwein (Max-Planck Institute of Immunobiology and Epigenetics, Freiburg, Germany) for the *Suv39h dn* MEFs and to Gunnar Schotta (Adolf-Butenandt-Institute, Faculty of Medicine, Ludwig Maximilians University Munich, Germany) for the *Suv39h dn* ESCs. This work was supported by the Nanosystems Initiative Munich (NIM) and by grants from the Deutsche Forschungsgemeinschaft (DFG) SFB646 and SFB684 to H.L. G.P., C.S.S., K.S., and C.F. were supported by the International Doctorate Program NanoBioTechnology (IDK-NBT) and the International Max Planck Research School for Molecular and Cellular Life Sciences (IMPRS-LS). PW is a fellow of the Graduate School Life Science Munich (LSM).

REFERENCES

Abramoff MD, Magelhaes PJ, Ram SJ. 2004. Image processing with ImageJ. Biophotonics Int 11:36–42.

Achour M, Fuhrmann G, Alhosin M, Ronde P, Chataigneau T, Mousli M, Schini-Kerth VB, Bronner C. 2009. UHRF1 recruits the histone acetyltransferase Tip60 and controls its expression and activity. Biochem Biophys Res Commun 390:523–528.

Altschul SF. 1991. Amino acid substitution matrices from an information theoretic perspective. J Mol Biol 219:555–565.

Arita K, Ariyoshi M, Tochio H, Nakamura Y, Shirakawa M. 2008. Recognition of hemi-methylated DNA by the SRA protein UHRF1 by a base-flipping mechanism. Nature 455:818–821.

Avvakumov GV, Walker JR, Xue S, Li Y, Duan S, Bronner C, Arrowsmith CH, Dhe-Paganon S. 2008. Structural basis for recognition of hemi-methylated DNA by the SRA domain of human UHRF1. Nature 455:822–825.

Bartke T, Vermeulen M, Xhemalce B, Robson SC, Mann M, Kouzarides T. 2010. Nucleosome-interacting proteins regulated by DNA and histone methylation. Cell 143:470–484.

Bestor TH, Ingram VM. 1983. Two DNA methyltransferases from murine erythroleukemia cells: Purification, sequence specificity, and mode of interaction with DNA. Proc Natl Acad Sci USA 80:5559–5563.

Bird A. 2002. DNA methylation patterns and epigenetic memory. Genes Dev 16:6–21.

Bostick M, Kim JK, Esteve PO, Clark A, Pradhan S, Jacobsen SE. 2007. UHRF1 plays a role in maintaining DNA methylation in mammalian cells. Science 317:1760–1764.

Bronner C, Achour M, Arima Y, Chataigneau T, Saya H, Schini-Kerth VB. 2007. The UHRF family: Oncogenes that are drugable targets for cancer therapy in the near future? Pharmacol Ther 115:419–434.

Citterio E, Papait R, Nicassio F, Vecchi M, Gomiero P, Mantovani R, Di Fiore PP, Bonapace IM. 2004. Np95 is a histone-binding protein endowed with ubiquitin ligase activity. Mol Cell Biol 24:2526–2535.

Easwaran HP, Schermelleh L, Leonhardt H, Cardoso MC. 2004. Replication-independent chromatin loading of Dnmt1 during G2 and M phases. EMBO Rep 5:1181–1186.

Fellinger K, Rothbauer U, Felle M, Langst G, Leonhardt H. 2009. Dimerization of DNA methyltransferase 1 is mediated by its regulatory domain. J Cell Biochem 106:521–528.

Frauer C, Leonhardt H. 2009. A versatile non-radioactive assay for DNA methyltransferase activity and DNA binding. Nucleic Acids Res 37:e22.

Fujimori A, Matsuda Y, Takemoto Y, Hashimoto Y, Kubo E, Araki R, Fukumura R, Mita K, Tatsumi K, Muto M. 1998. Cloning and mapping of Np95 gene which encodes a novel nuclear protein associated with cell proliferation. Mamm Genome 9:1032–1035.

Hashimoto H, Horton JR, Zhang X, Bostick M, Jacobsen SE, Cheng X. 2008. The SRA domain of UHRF1 flips 5-methylcytosine out of the DNA helix. Nature 455:826–829.

Hashimoto H, Horton JR, Zhang X, Cheng X. 2009. UHRF1, a modular multi-domain protein, regulates replication-coupled crosstalk between DNA methylation and histone modifications. Epigenetics 4:8–14.

Ho SN, Hunt HD, Horton RM, Pullen JK, Pease LR. 1989. Site-directed mutagenesis by overlap extension using the polymerase chain reaction. Gene 77:51–59.

Hopfner R, Mousli M, Jeltsch JM, Voulgaris A, Lutz Y, Marin C, Bellocq JP, Oudet P, Bronner C. 2000. ICBP90, a novel human CCAAT binding protein, involved in the regulation of topoisomerase IIalpha expression. Cancer Res 60:121–128.

Horton JR, Upadhyay AK, Qi HH, Zhang X, Shi Y, Cheng X. 2010. Enzymatic and structural insights for substrate specificity of a family of jumonji histone lysine demethylases. Nat Struct Mol Biol 17:38–43.

Iwata A, Nagashima Y, Matsumoto L, Suzuki T, Yamanaka T, Date H, Deoka K, Nukina N, Tsuji S. 2009. Intranuclear degradation of polyglutamine aggregates by the ubiquitin-proteasome system. J Biol Chem 284:9796–9803.

Jones PA, Baylin SB. 2007. The epigenomics of cancer. Cell 128:683–692.

Karagianni P, Amazit L, Qin J, Wong J. 2008. ICBP90, a novel methyl K9 H3 binding protein linking protein ubiquitination with heterochromatin formation. Mol Cell Biol 28:705–717.

Kim JK, Esteve PO, Jacobsen SE, Pradhan S. 2009. UHRF1 binds G9a and participates in p21 transcriptional regulation in mammalian cells. Nucleic Acids Res 37:493–505.

Kim D, Blus BJ, Chandra V, Huang P, Rastinejad F, Khorasanizadeh S. 2010. Corecognition of DNA and a methylated histone tail by the MSL3 chromodomain. Nat Struct Mol Biol 17:1027–1029.

Kouzarides T. 2007. Chromatin modifications and their function. Cell 128:693–705.

Lehnertz B, Ueda Y, Derijck AA, Braunschweig U, Perez-Burgos L, Kubicek S, Chen T, Li E, Jenuwein T, Peters AH. 2003. Suv39h-mediated histone H3 lysine 9 methylation directs DNA methylation to major satellite repeats at pericentric heterochromatin. Curr Biol 13:1192–1200.

Leonhardt H, Page AW, Weier HU, Bestor TH. 1992. A targeting sequence directs DNA methyltransferase to sites of DNA replication in mammalian nuclei. Cell 71:865–873.

Li H, Ilin S, Wang W, Duncan EM, Wysocka J, Allis CD, Patel DJ. 2006. Molecular basis for site-specific read-out of histone H3K4me3 by the BPTF PHD finger of NURF. Nature 442:91–95.

Meilinger D, Fellinger K, Bultmann S, Rothbauer U, Bonapace IM, Klinkert WE, Spada F, Leonhardt H. 2009. Np95 interacts with de novo DNA methyltransferases, Dnmt3a and Dnmt3b, and mediates epigenetic silencing of the viral CMV promoter in embryonic stem cells. EMBO Rep 10:1259–1264.

Meissner A, Mikkelsen TS, Gu H, Wernig M, Hanna J, Sivachenko A, Zhang X, Bernstein BE, Nusbaum C, Jaffe DB, Gnirke A, Jaenisch R, Lander ES. 2008. Genome-scale DNA methylation maps of pluripotent and differentiated cells. Nature 454:766–770.

Mortusewicz O, Schermelleh L, Walter J, Cardoso MC, Leonhardt H. 2005. Recruitment of DNA methyltransferase I to DNA repair sites. Proc Natl Acad Sci USA 102:8905–8909.

Muto M, Utsuyama M, Horiguchi T, Kubo E, Sado T, Hirokawa K. 1995. The characterization of the monoclonal antibody Th-10a, specific for a nuclear protein appearing in the S phase of the cell cycle in normal thymocytes and its unregulated expression in lymphoma cell lines. Cell Prolif 28:645–657.

Nady N, Lemak A, Walker JR, Avvakumov GV, Kareta MS, Achour M, Xue S, Duan S, Allali-Hassani A, Zuo X, Wang YX, Bronner C, Chedin F, Arrowsmith CH, Dhe-Paganon S. 2011. Recognition of multivalent histone states associated with heterochromatin by UHRF1. J Biol Chem. [Epub ahead of print].

Ooi SK, Qiu C, Bernstein E, Li K, Jia D, Yang Z, Erdjument-Bromage H, Tempst P, Lin SP, Allis CD, Cheng X, Bestor TH. 2007. DNMT3L connects unmethylated lysine 4 of histone H3 to de novo methylation of DNA. Nature 448:714–717.

Otani J, Nankumo T, Arita K, Inamoto S, Ariyoshi M, Shirakawa M. 2009. Structural basis for recognition of H3K4 methylation status by the DNA methyltransferase 3A ATRX-DNMT3-DNMT3L domain. EMBO Rep 10:1235–1241.

Papait R, Pistore C, Grazini U, Babbio F, Cogliati S, Pecoraro D, Brino L, Morand AL, Dechampesme AM, Spada F, Leonhardt H, McBlane F, Oudet P, Bonapace IM. 2008. The PHD domain of Np95 (mUHRF1) is involved in large-scale reorganization of pericentromeric heterochromatin. Mol Biol Cell 19:3554–3563.

Peters AH, O'Carroll D, Scherthan H, Mechtler K, Sauer S, Schofer C, Weipoltshammer K, Pagani M, Lachner M, Kohlmaier A, Opravil S, Doyle M, Sibilia M, Jenuwein T. 2001. Loss of the Suv39h histone methyltransferases impairs mammalian heterochromatin and genome stability. Cell 107:323–337.

Pradhan S, Talbot D, Sha M, Benner J, Hornstra L, Li E, Jaenisch R, Roberts RJ. 1997. Baculovirus-mediated expression and characterization of the full-length murine DNA methyltransferase. Nucleic Acids Res 25:4666–4673.

Qian C, Li S, Jakoncic J, Zeng L, Walsh MJ, Zhou MM. 2008. Structure and hemimethylated CpG binding of the SRA domain from human UHRF1. J Biol Chem 283(50):34490–34494.

Reik W. 2007. Stability and flexibility of epigenetic gene regulation in mammalian development. Nature 447:425–432.

Rothbauer U, Zolghadr K, Muyldermans S, Schepers A, Cardoso MC, Leonhardt H. 2008. A versatile nanotrap for biochemical and functional studies with fluorescent fusion proteins. Mol Cell Proteomics 7:282–289.

Rottach A, Frauer C, Pichler G, Bonapace IM, Spada F, Leonhardt H. 2010. The multi-domain protein Np95 connects DNA methylation and histone modification. Nucleic Acids Res 38:1796–1804.

Ruthenburg AJ, Li H, Patel DJ, Allis CD. 2007. Multivalent engagement of chromatin modifications by linked binding modules. Nat Rev Mol Cell Biol 8:983–994.

Schermelleh L, Haemmer A, Spada F, Rosing N, Meilinger D, Rothbauer U, Cardoso MC, Leonhardt H. 2007. Dynamics of Dnmt1 interaction with the replication machinery and its role in postreplicative maintenance of DNA methylation. Nucleic Acids Res 35:4301–4312.

Sharif J, Muto M, Takebayashi S, Suetake I, Iwamatsu A, Endo TA, Shinga J, Mizutani-Koseki Y, Toyoda T, Okamura K, Tajima S, Mitsuya K, Okano M, Koseki H. 2007. The SRA protein Np95 mediates epigenetic inheritance by recruiting Dnmt1 to methylated DNA. Nature 450:908–912.

Sporbert A, Domaing P, Leonhardt H, Cardoso MC. 2005. PCNA acts as a stationary loading platform for transiently interacting Okazaki fragment maturation proteins. Nucleic Acids Res 33:3521–3528.

Szwagierczak A, Bultmann S, Schmidt CS, Spada F, Leonhardt H. 2010. Sensitive enzymatic quantification of 5-hydroxymethylcytosine in genomic DNA. Nucleic Acids Res 38:e181.

Tsumura A, Hayakawa T, Kumaki Y, Takebayashi S, Sakaue M, Matsuoka C, Shimotohno K, Ishikawa F, Li E, Ueda HR, Nakayama J, Okano M. 2006. Maintenance of self-renewal ability of mouse embryonic stem cells in the absence of DNA methyltransferases Dnmt1, Dnmt3a and Dnmt3b. Genes Cells 11:805–814.

Unoki M, Nishidate T, Nakamura Y. 2004. ICBP90, an E2F-1 target, recruits HDAC1 and binds to methyl-CpG through its SRA domain. Oncogene 23: 7601–7610.

Supplementary Information

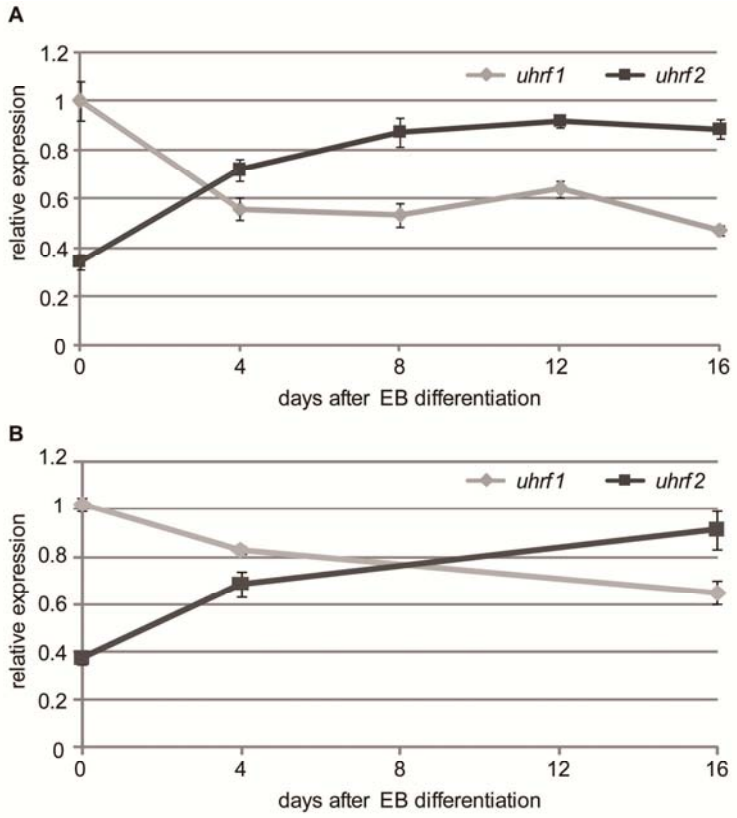

Supplementary Figure S1. Opposite expression pattern of *uhrf1* and *uhrf2*. Expression analyses of *uhrf1* and *uhrf2* by Real-time PCR during differentiation of ESCs with two different genetic backgrounds (wt E14 (**A**) and wt JM8A (**B**)). Transcript levels of *uhrf1* at day 0 of EB formation are used as reference point (set to 1). Shown are means ± SD from three technical replicates of one biological experiment.

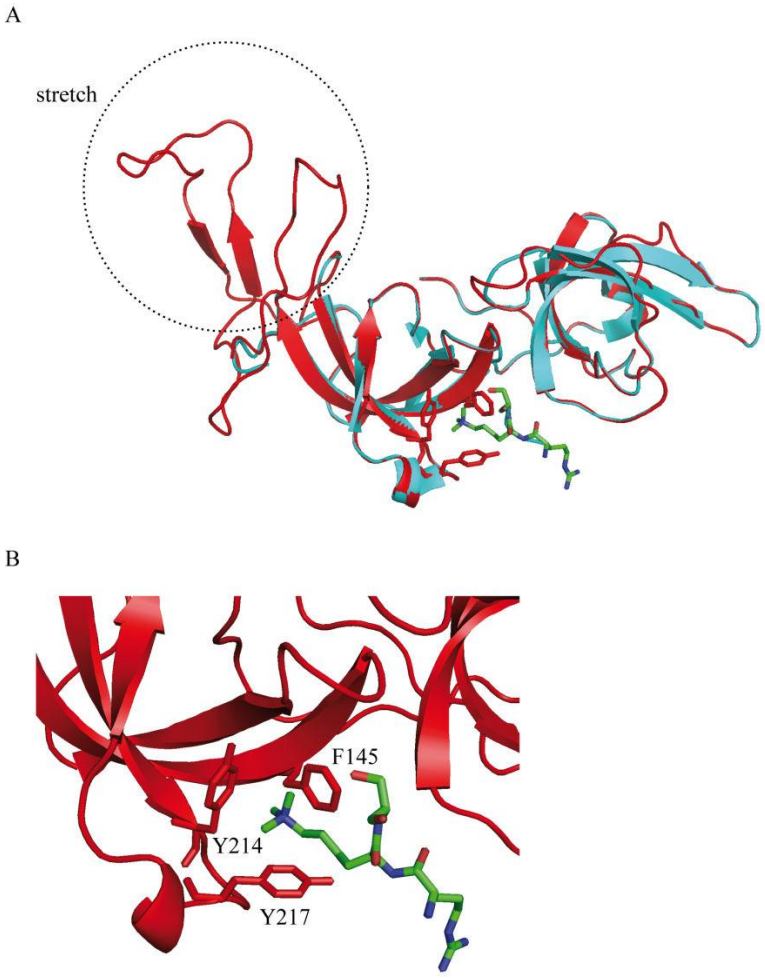

Supplementary Figure S2. Model of the tandem Tudor domain (TTD) of Uhrf2. (**A**) A model of the TTD of Uhrf2 was generated using SWISS Model [Arnold et al., 2006; Guex and Peitsch, 1997] with the solved structure of the TTD of Uhrf1 (PDB: 3DB3) as template. Both structures, the Uhrf2 model in red and the Uhrf1 template in cyan, are superimposed in PyMOL [Schrodinger, 2010]. (**B**) H3K9me3 is embedded in an aromatic cage formed by three aromatic residues of Uhrf2.

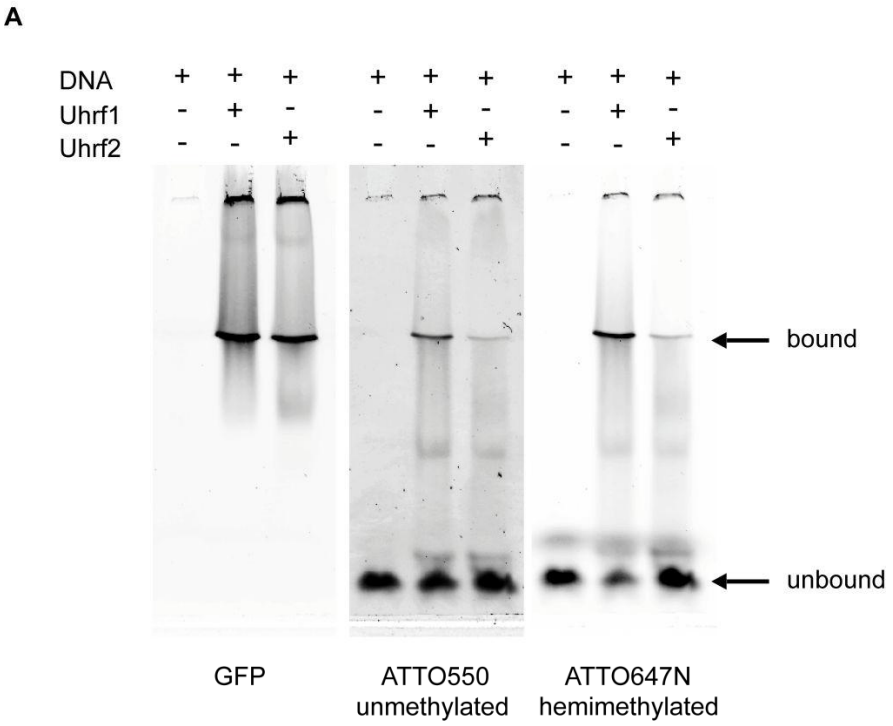

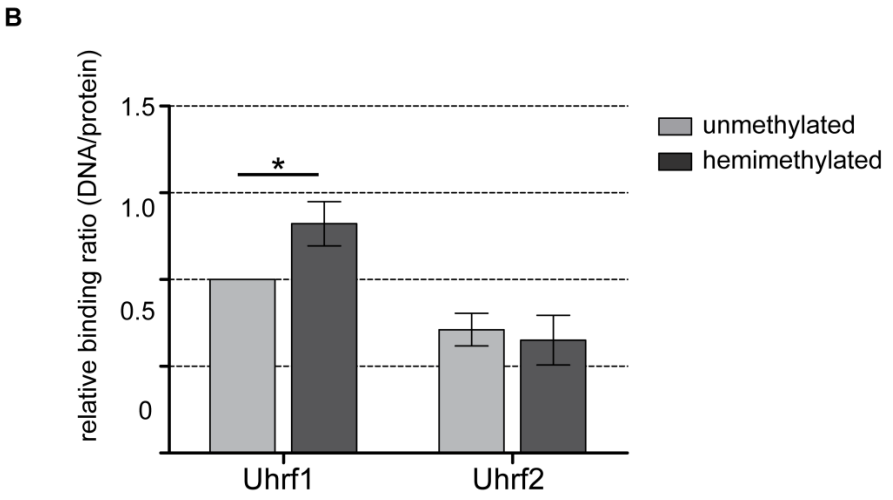

Supplementary Figure S3. Electrophoretic mobility shift of Uhrf1 and Uhrf2. (**A**) Un- and hemimethylated DNA substrates (1 pmol each in direct competition) were incubated with 0.63 pmol purified Uhrf1-GFP or Uhrf2-GFP. Samples were subjected to 3.5% non-denaturing PAGE and analyzed with a fluorescence scanner (Typhoon TRIO scanner, GE Healthcare) to detect ATTO550 (unmethylated substrate), ATTO647N (hemimethylated substrate) and GFP. (**B**) Band intensities were quantified with ImageJ [Abramoff, 2004]. To quantify bound DNA/protein ratios, grey values of unbound DNA bands were subtracted from the corresponding DNA input bands and subsequently normalized by the grey values of the GFP bands. All values were normalized to the relative binding ratio of Uhrf1 to unmethylated substrate. Shown are means ± SD from three independent experiments. Statistical significance between the binding ratios of un- and hemimethylated DNA is indicated; *$P < 0.05$.

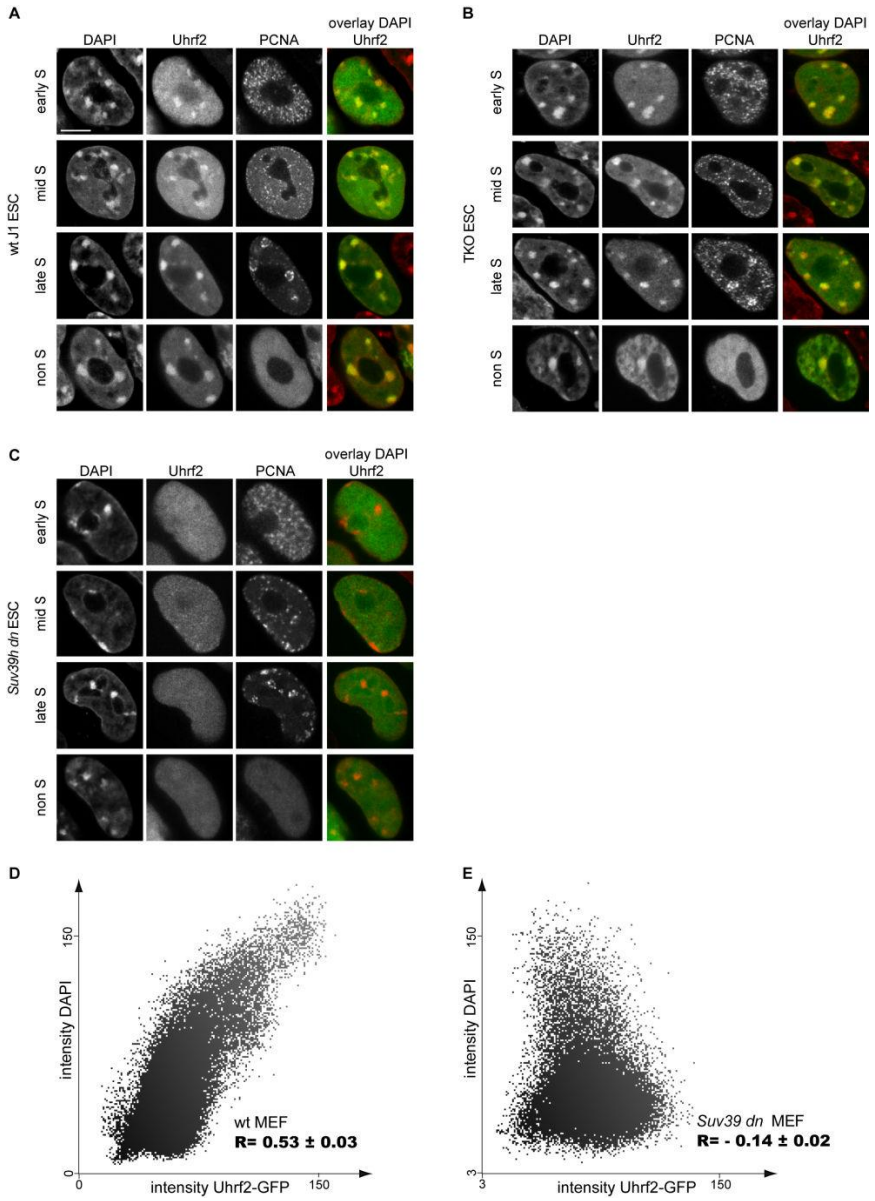

Supplementary Figure S4. Cell-cycle dependent localization of Uhrf2 in cells with different genetic backgrounds. Confocal mid sections of fixed wt J1 (**A**), TKO (**B**) and *Suv39h dn* ESCs (**C**), transiently expressing Uhrf2-GFP. Cells were co-transfected with a RFP-PCNA expression vector to distinguish S phase stages [Sporbert et al., 2005] and counterstained with DAPI. Merged images are displayed on the right. Scale bar 5 µm. In wt J1 and TKO ESCs the Uhrf2 fusion protein accumulates at pericentric heterochromatin independent of the cell-cycle stage and methylation levels (**A**) (**B**). In contrast, Uhrf2-GFP shows a fully dispersed nuclear distribution in *Suv39h dn* cells indicating the dependency on H3K9me3 methylation for localization at PH *in vivo* (**C**). (**D**) and (**E**) Scatter blot of GFP-Uhrf2 and DAPI signals in wt MEFs and *Suv39h dn* MEFs. The corresponding Pearson correlation coefficients R ± SEM are calculated from ten analysed cells. The software Volocity (Perkin Elmer) was used for analysis, selecting the cell nucleus as region of interest. Note that Pearson correlation coefficients range from +1 to -1 for perfect to no co-localization.

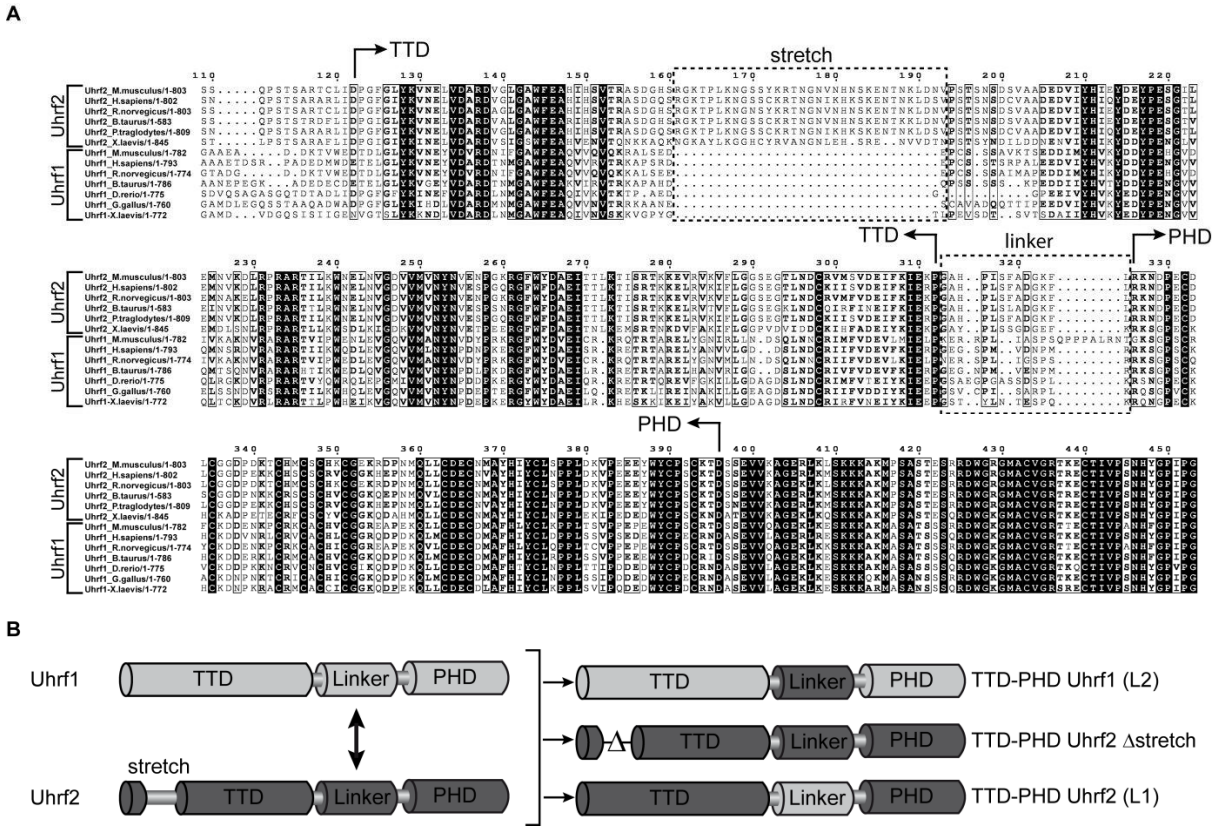

Supplementary Figure S5. Alignment and recombination of Uhrf1 and Uhrf2 domains. (**A**) Alignment of the tandem Tudor domain (TTD) and PHD domains from vertebrate Uhrf2 and Uhrf1 orthologs. Accession numbers for Uhrf2: *Homo sapiens* CAH74119.1; *Bos taurus* AAI48950.1; *Mus musculus* Q7TMI3; *Rattus norvegicus* NP_001101055.1; *Pan troglodytes* XP_528534.2; *Xenopus laevis* AAI28674.1. Accession numbers for Uhrf1: *Homo sapiens* Q96T88.1; *Bos taurus* AAI51672.1; *Mus musculus* Q8VDF2.2; *Rattus norvegicus* Q7TPK1.2; *Dario rerio* NP_998242.1; *Xenopus laevis* AAI28674.1, *Gallus gallus* XP_418269.2. Arrows show the start and end positions of the TTD and PHD domains. Absolutely conserved residues are black shaded, while positions showing conservative substitutions are boxed with residues in bold face. The additional stretch region found in the TTD of Uhrf2 and the linker region between TTD and PHD finger are boxed with dotted black lines. (**B**) Schematic outline of engineered constructs including the deletion of the stretch region and the swapping of linker sequences.

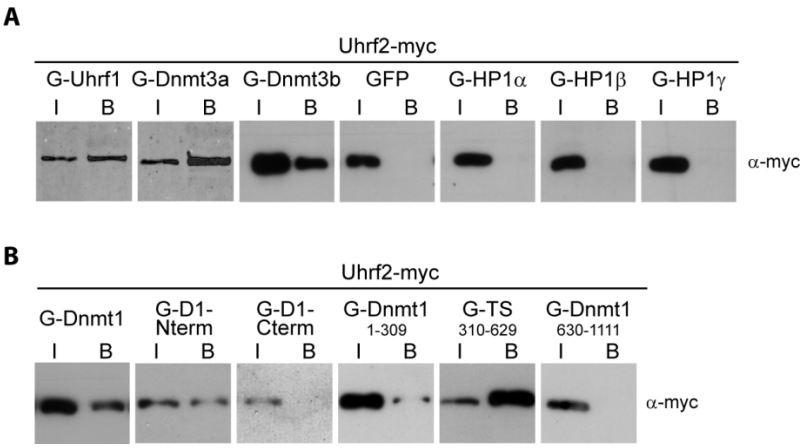

Supplementary Figure S6. Uhrf2 interacts with Uhrf1, Dnmt1 and Dnmt3a/b. (**A**) Co-immunoprecipation of Uhrf2-myc and GFP-Uhrf1, GFP-Dnmt3a, GFP-Dnmt3b, GFP-HP1α, GFP-HP1β, GFP-HP1γ or GFP transiently co-expressed in HEK293T cells. Note that Uhrf2 interacts with Uhrf1, Dnmt3a and Dnmt3b. (**B**) Co-immunoprecipation of Uhrf2-myc and GFP-Dnmt1 constructs transiently co-expressed in HEK293T cells: GFP-Dnmt1 (G-Dnmt1), GFP-fusions of the N-terminal and C-terminal part of Dnmt1 (G-D1-Nterm, G-D1-Cterm) and truncated Dnmt1 constructs (G-Dnmt1 1-309, G-TS 310-629, G-Dnmt1 630-1111). Note that Uhrf2 interacts with full-length Dnmt1, the N-terminal part and the targeting sequence (G-TS 310-629). One percent of input (I) relative to bound fractions (B) was loaded. Co-immunoprecipitation was performed using the GFP trap [Rothbauer et al., 2008]. Co-precipitated myc-tagged proteins were detected using a mouse monoclonal primary anti-myc antibody (Invitrogen, Germany) and an HRP- or Cy5-conjugated secondary anti-mouse antibody (Sigma, Germany, or Jackson ImmunoResearch Laboratories, USA, respectively).

A

Peptide name	Peptide sequence	Peptide labelling
H3K4me1	ART X1 QTARKSTGGKAPRKQLK	TAMRA at C-terminus
H3K4me2	ART X2 QTARKSTGGKAPRKQLK	
H3K4me3	ART X3 QTARKSTGGKAPRKQLK	
H3K4ac	ART Z QTARKSTGGKAPRKQLK	
H3K4/9un	ARTKQTARKSTGGKAPRKQLK	
H3K9me1	ARTKQTAR X1 STGGKAPRKQLK	
H3K9me2	ARTKQTAR X2 STGGKAPRKQLK	
H3K9me3	ARTKQTAR X3 STGGKAPRKQLK	
H3K9ac	ARTKQTAR Z STGGKAPRKQLK	
H3R2me2a	A X4 TKQTARSTGGKAPRKQLK	
H3K4me3K9me3	ART X3 QTAR X3 STGGKAPRKQLK	
H3K27un	RKQLATKAARKSAPATGGVK	TAMRA at N-terminus
H3K27me1	RKQLATKAAR X1 SAPATGGVK	
H3K27me2	RKQLATKAAR X2 SAPATGGVK	
H3K27me3	RKQLATKAAR X3 SAPATGGVK	
H3K27ac	RKQLATKAAR Z SAPATGGVK	
H4K20un	LGKGGAKRHRKVLRDNIQGI	
H4K20me1	LGKGGAKRHR X1 VLRDNIQGI	
H4K20me2	LGKGGAKRHR X2 VLRDNIQGI	
H4K20me3	LGKGGAKRHR X3 VLRDNIQGI	
H4K20ac	LGKGGAKRHR Z VLRDNIQGI	

X1: Lysine(me1); X2: Lysine(me2); X3: Lysine(me3); X4: Arginine(me2 asymmetric) Z: Lysine(ac)

B

DNA substrate	DNA sequence	DNA labelling
CGup	CTCAACAACTAACTACCATCCGGACCAGAAGAGTCATCATGG	no
MGup	CTCAACAACTAACTACCATCMGGACCAGAAGAGTCATCATGG	no
noCpG	CTCAACAACTAACTACCATCCTGACCAGAAGAGTCATCATGG	no
um647N	CCATGATGACTCTTCTGGTCCGGATGGTAGTTAGTTGTTGAG	ATTO647N at 5´end
um700	CCATGATGACTCTTCTGGTCCGGATGGTAGTTAGTTGTTGAG	ATTO700 at 5´end
Fill-In-550	CCATGATGACTCTTCTGGTC	ATTO550 at 5´end
Fill-In-590	CCATGATGACTCTTCTGGTC	ATTO590 at 5´end
Fill-In-647N	CCATGATGACTCTTCTGGTC	ATTO647N at 5´end
Fill-In-700	CCATGATGACTCTTCTGGTC	ATTO700 at 5´end

C

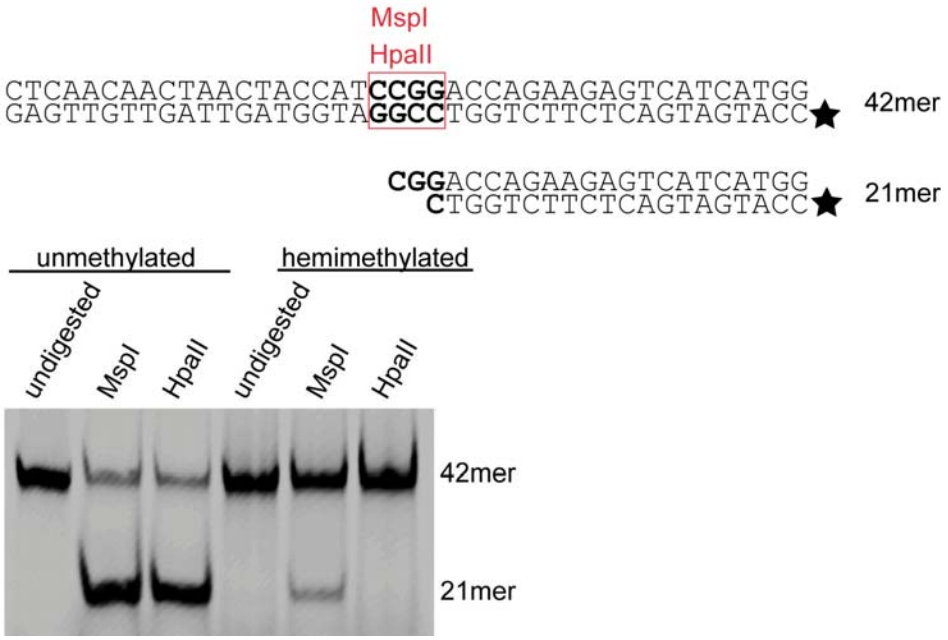

Supplementary Figure S7. Histone-tail peptide and DNA sequences and quality control of DNA substrates. (**A**) Amino acid sequence of TAMRA-labelled peptides for *in vitro* histone-tail peptide binding assays. Histone-tail peptides were purchased as TAMRA conjugates (PSL, Germany). (**B**) DNA oligos used for preparation of double-stranded probes for *in vitro*

DNA binding assays. M: 5-methyl-cytosine. For hybridization, DNA oligos were mixed in equimolar amounts, heated to 92°C and cooled down to room temperature. DNA substrates for Figure 2F were completed in a primer extension reaction. By using a control set of DNA probes with identical sequence but different fluorescent labels we observed effects due to probe preparation and/or unspecific binding of ATTO dyes (data not shown). The values obtained from the control set were used to normalize every probe/protein pair. (**C**) Quality control of DNA substrates. Un- and hemimethylated DNA substrates (2 pmol; Atto647N labelled) were digested with 1 unit MspI or HpaII and analyzed by 15% non-denaturing PAGE for CpG methylation. Note that unmethylated DNA substrate is digested by both enzymes, whereas hemimethylated substrate is only cut by MspI. Enzyme recognition motifs are boxed and asterisks represent ATTO labels.

Supplementary References

Abramoff MD, Magelhaes, P.J., Ram, S.J. 2004. Image Processing with ImageJ. Biophotonics International 11:36-42.

Arnold K, Bordoli L, Kopp J, Schwede T. 2006. The SWISS-MODEL workspace: a web-based environment for protein structure homology modelling. Bioinformatics 22:195-201.

Guex N, Peitsch MC. 1997. SWISS-MODEL and the Swiss-PdbViewer: an environment for comparative protein modeling. Electrophoresis 18:2714-23.

Rothbauer U, Zolghadr K, Muyldermans S, Schepers A, Cardoso MC, Leonhardt H. 2008. A versatile nanotrap for biochemical and functional studies with fluorescent fusion proteins. Mol Cell Proteomics 7:282-9.

Schrodinger, LLC. 2010. The PyMOL Molecular Graphics System, Version 1.3editor^editors.

Sporbert A, Domaing P, Leonhardt H, Cardoso MC. 2005. PCNA acts as a stationary loading platform for transiently interacting Okazaki fragment maturation proteins. Nucleic Acids Res 33:3521-8.

2.3 H2A.Z.2.2 is an alternatively spliced histone H2A.Z variant that causes severe nucleosome destabilization

Nucleic Acids Research Advance Access published March 29, 2012

Nucleic Acids Research, 2012, 1–14
doi:10.1093/nar/gks267

H2A.Z.2.2 is an alternatively spliced histone H2A.Z variant that causes severe nucleosome destabilization

Clemens Bönisch[1], Katrin Schneider[2], Sebastian Pünzeler[1], Sonja M. Wiedemann[1], Christina Bielmeier[2], Marco Bocola[3], H. Christian Eberl[4], Wolfgang Kuegel[5], Jürgen Neumann[2], Elisabeth Kremmer[6], Heinrich Leonhardt[2,7], Matthias Mann[4,7], Jens Michaelis[4,7,8], Lothar Schermelleh[2,*] and Sandra B. Hake[1,7,*]

[1]Department of Molecular Biology, Adolf-Butenandt-Institute, Ludwig-Maximilians-University Munich, 80336 Munich, [2]Department of Biology, Biozentrum, Ludwig-Maximilians-University Munich, 82152 Planegg-Martinsried, [3]Department of Biochemistry II, University Regensburg, 93053 Regensburg, [4]Department of Proteomics and Signal Transduction, Max-Planck-Institute of Biochemistry, 82152 Martinsried, [5]Department of Chemistry, Ludwig-Maximilians-University Munich, [6]Institute of Molecular Immunology, Helmholtz Center Munich, German Research Center for Environmental Health, [7]Center for Integrated Protein Science Munich (CIPSM), 81377 Munich and [8]Department of Physics, Ulm University, 89081 Ulm, Germany

Received November 8, 2011; Revised and Accepted March 9, 2012

ABSTRACT

The histone variant H2A.Z has been implicated in many biological processes, such as gene regulation and genome stability. Here, we present the identification of H2A.Z.2.2 (Z.2.2), a novel alternatively spliced variant of histone H2A.Z and provide a comprehensive characterization of its expression and chromatin incorporation properties. Z.2.2 mRNA is found in all human cell lines and tissues with highest levels in brain. We show the proper splicing and *in vivo* existence of this variant protein in humans. Furthermore, we demonstrate the binding of Z.2.2 to H2A.Z-specific TIP60 and SRCAP chaperone complexes and its active replication-independent deposition into chromatin. Strikingly, various independent *in vivo* and *in vitro* analyses, such as biochemical fractionation, comparative FRAP studies of GFP-tagged H2A variants, size exclusion chromatography and single molecule FRET, in combination with *in silico* molecular dynamics simulations, consistently demonstrate that Z.2.2 causes major structural changes and significantly destabilizes nucleosomes. Analyses of deletion mutants and chimeric proteins pinpoint this property to its unique C-terminus. Our findings enrich the list of known human variants by an unusual protein belonging to the H2A.Z family that leads to the least stable nucleosome known to date.

INTRODUCTION

In the eukaryotic nucleus, DNA is packaged into chromatin. The fundamental unit of this structure is the nucleosome consisting of a histone octamer (two of each H2A, H2B, H3 and H4) that organizes ~147 bp of DNA (1). In order to allow or prevent nuclear regulatory proteins access to the DNA, the chromatin structure has to be flexible and dynamic. Several mechanisms ensure controlled chromatin changes, one being the incorporation of specialized histone variants (2,3).

Variants of the histone H2A family are the most diverse in sequence and exhibit distinct functions (4,5), comprising DNA damage repair, transcriptional regulation, cell cycle control and chromatin condensation, though the exact mechanisms of action are not fully understood yet. Interestingly, the highest sequence variation among H2A variants is found in the C-terminus, suggesting that differences in structure and biological function might be

*To whom correspondence should be addressed. Tel: +49 89 2180 75435; Fax: +49 89 2180 75425; Email: sandra.hake@med.uni-muenchen.de
Correspondence may also be addressed to Lothar Schermelleh. Tel: +44 1865 613264; Fax: +49 89 2180 74236;
Email: lothar.schermelleh@bioch.ox.ac.uk
Present address:
Lothar Schermelleh, Department of Biochemistry, University of Oxford, South Park Road, Oxford OX1 3QU, UK.

primarily attributed to this domain (6–9). One of the best investigated and highly conserved but also functionally enigmatic histone variant is H2A.Z. This variant is essential in most eukaryotes and possesses unique functions (10,11). H2A.Z is involved in transcriptional regulation, chromosome segregation and mitosis, acting in an organism- and differentiation-dependent manner (12,13). Furthermore, H2A.Z has been implicated in regulating epigenetic memory (14) and in inhibiting read-through antisense transcription (15). In higher eukaryotes, H2A.Z might play a role in heterochromatin organization (16), genome stability and chromosome segregation (17). Despite many efforts to elucidate the exact biological functions of H2A.Z, its roles have been and remain controversial (18). Furthermore, deregulation of H2A.Z expression or localization seems to be connected to the development of several neoplasias (19–23). Interestingly, in vertebrates two non-allelic genes coding for two highly similar H2A.Z proteins, H2A.Z.1 and H2A.Z.2, exist (24) (previously named H2A.Z-1 and H2A.Z-2, prefixes were changed due to a new histone variant nomenclature; Talbert P.B., manuscript in preparation). They have a common origin in early chordate evolution, are both acetylated on the same N-terminal lysines (25–27) and might be ubiquitinated on either one of the two C-terminal lysines (28).

Here, we report the identification and structural characterization of H2A.Z.2.2 (Z.2.2), an unusual alternative splice form of H2A.Z. We show that Z.2.2 mRNA is expressed to different degrees in all human cell lines and tissues examined, with highest levels found in brain. Cell biological and biochemical analyses consistently reveal the presence of two distinct Z.2.2 populations within the cell. The majority of Z.2.2 is freely dispersed in the nucleus, whereas only a minority is stably incorporated into chromatin, most likely through the H2A.Z-specific p400/NuA4/TIP60 (TIP60) and SRCAP chaperone complexes. *In vivo* and *in vitro* analyses, in agreement with molecular dynamic (MD) simulations, demonstrate that due to its unique docking domain Z.2.2 chromatin incorporation leads to severely unstable nucleosomes. Our data provide compelling evidence that a novel H2A.Z variant exists in humans that plays a distinct and novel role in chromatin structure regulation.

MATERIALS AND METHODS

See Supplementary Materials and Methods section for detailed protocols.

Cell culture, transfection, FACS and cloning

Cell lines were grown in DMEM medium (PAA) supplemented with 10% FCS (Sigma) and 1% penicillin/streptomycin at 37°C and 5% CO_2. Cells were transfected using FuGene HD (Roche Applied Science) according to the manufacturer's instructions. For details on cell selection, FACS and cloning of expression plasmids see Supplementary Materials and Methods section.

RNA expression analysis

RNA isolation and cDNA generation were performed as previously described (29). Data were analyzed with the advanced relative quantification tool of the Lightcycler 480 (Roche) software including normalization to HPRT1 and HMBS levels. Statistical evaluation was done using *t*-test (two-tailed distribution, heteroscedastic). Total RNA from different human tissues was commercially acquired from: Applied Biosystems: normal lung, breast and tumor breast, lung and ovary; Biochain: tumor lung, breast, thyroid and bone, normal testis, cerebellum, cerebral cortex, hippocampus, thalamus and total fetal brain; amsbio: frontal lobe.

Histone extraction, RP–HPLC purification, sucrose gradient, cellular fractionation and salt stability experiments

Acid extraction of histones was done as previously described (30). Histones were separated by RP–HPLC as previously described (29). Fractions were dried under vacuum and stored at −20°C.

Details on MNase digest and sucrose gradient fractionation can be found in Supplementary Materials and Methods section.

Fractionation and salt stability experiments were carried out as described previously (31–33) with minor changes. For details on these methods see Supplementary Materials and Methods section.

Antibodies

For the generation of a Z.2.2-specific antibody (αZ.2.2), a peptide spanning the last C-terminal amino acids GGEKRRCS of Z.2.2 was synthesized (Peptide Specialty Laboratories GmbH) and coupled to BSA and OVA, respectively. Development of Z.2.2-specific monoclonal antibodies in rats was done as previously described (29). The αZ.2.2 clone 1H11-11 of rat IgG1 subclass was applied in this study. Rabbit αZ.2.2 antibody (rabbit 2, bleed 3) was generated by the Pineda-Antikörper-Service company using the identical peptide epitope followed by affinity purification. Following other primary antibodies were used: αGAPDH (sc-25778, Santa Cruz), αGFP (Roche Applied Science), αH2A (ab 13923, abcam), αH3 (ab1791, abcam) and αH2A.Z (C-terminus: ab4174, abcam; N-terminus: ab18263, abcam). Following secondary antibodies and detection kits were used in immunoblots: GFP-Z.2.2 and GFP-Bbd histones (αGFP) and endogenous Z.2.2 (αZ.2.2) were detected using HRP-conjugated secondary antibodies (Amersham) with ECL advance (Amersham), all other proteins were detected using ECL (Amersham). Detection of recombinant proteins to evaluate histone stoichiometry of *in vitro* assembled nucleosomes was carried out using IRDye-labeled secondary antibodies (LI-COR).

Fluorescence microscopy of cells and chromosomes

Preparation of cells and chromosome spreads for fluorescence microscopy was done as previously reported (34). Wide-field fluorescence imaging was performed on

a PersonalDV microscope system (Applied Precision) equipped with a 60×/1.42 PlanApo oil objective (Olympus), CoolSNAP ES2 interline CCD camera (Photometrics), Xenon illumination and appropriate filtersets. Iterative 3D deconvolution of image *z*-stacks was performed with the SoftWoRx 3.7 imaging software package (Applied Precision).

FRAP and exponential fitting

For details see Supplementary Materials and Methods section.

Stable isotope labeling with amino acids in cell culture (SILAC) and mass spectrometric identification of H2A.Z-specific chaperone complexes

HeLa cells expressing GFP-Z.2.1 or GFP-Z.2.2 were SILAC labeled and nuclear extracts were prepared as described before (35,36). High-resolution LC MS/MS analysis was performed on an Orbitrap platform: details on the experimental procedure are found in Supplementary Materials and Methods section. Mass spectrometric (MS) operation and raw data analysis (37) are described in Supplementary Materials and Methods section. A complete list of all proteins identified is found in Supplementary Table S1.

Immunoflurescence microscopy of cell cycle-dependent GFP-Z.2.1 and GFP-Z.2.2 chromatin incorporation

Details on the experimental labeling (38) and microscopy procedures are found in Supplementary Materials and Methods section.

Expression of recombinant human histone proteins in *Escherichia coli*, *in vitro* octamer and nucleosome reconstitution

Histones were expressed, purified and assembled into octamers as described (39) and mononucleosomes were assembled on DNA containing the 601-positioning sequence (40) according to (39,41). For details on *in vitro* octamer and nucleosome reconstitution, see Supplementary Materials and Methods section.

Single molecule Förster resonance energy transfer

Single molecule Förster resonance energy transfer (smFRET) single molecule burst analysis followed by the removal of multi-molecular events (42–45) are described in detail in the Supplementary Materials and Methods section.

Molecular modeling and MD simulations

The molecular modeling suite YASARA-structure version 9.10.29 was employed, utilizing the AMBER03 force field (46) for the protein and the general amber force field (GAFF) (47) throughout this study. The partial charges were computed using the AM1/BCC procedure (48) as implemented in YASARA structure (49). The starting point for molecular modeling was the crystal structure of a nucleosome core particle containing the histone variant H2A.Z (PDB 1F66) (50). Missing side chain atoms were added (Glu E 634). The missing N-terminal and C-terminal residues were not modeled, although they might interact with the neighboring DNA, e.g. in the case of missing C-terminal residues in H2A.Z (119–128; GKKGQQKTV). All structures were solvated in a water box with 0.9% NaCl and neutralized (51). The structures were initially minimized using steepest descent and simulating annealing procedures. All deletions and mutations were introduced sequentially using YASARA structure. MD simulations were carried out at 300 K over 2.5 ns in an NPT ensemble using PME. All simulations were performed four times using various starting geometries. The 2.5 ns MD trajectories were sampled every 25 ps, resulting in 100 simulation frames per run, which were evaluated after an equilibration phase of 500 ps to derive statistical averages and properties of the corresponding variant. Finally, the interaction energy of H2A and H3 was calculated from a simulation of the solvated octamer and the isolated $(H3–H4)_2$ tetramer or the isolated respective H2A.Z–H2B dimer. The interaction energy is calculated as energy difference of the solvated octamer minus the solvated $(H3–H4)_2$ tetramer and H2A.Z–H2B dimer.

RESULTS

Alternative splicing of H2A.Z.2 occurs *in vivo*

Two non-allelic intron-containing genes with divergent promoter sequences that code for H2A.Z variants exist in vertebrates (24,27). In humans, the H2A.Z.2 (H2AFV) primary transcript is predicted to be alternatively spliced thereby generating five different gene products (Supplementary Figure S1A). Using PCR and confirmed by sequencing we detected not only H2A.Z.2.1 (Z.2.1) but also H2A.Z.2.2 (Z.2.2) mRNA, though none of the other splice variants in human cells (Supplementary Figure S1B) showing that the H2A.Z.2 primary transcript is indeed alternatively spliced *in vivo*. Interestingly, database searches found Z.2.2 mRNA to be predicted in chimpanzee (*Pan troglodytes*) and Northern white-cheeked gibbon (*Nomascus leucogenys*) as well. In addition, the coding sequence of the unique exon 6 was present downstream of the *H2AFV* locus of several other primate genomes, such as gorilla (*Gorilla gorilla gorilla*), macaque (*Macaca mulatta*), orangutan (*Pongo abelii*) and white-tufted-ear marmoset (*Callithrix jacchus*) (data not shown). In all of these primates, with the exception of marmoset, the resulting protein sequence, if translated, is 100% identical to the unique human Z.2.2 peptide. Further searches revealed that the genomes of horse, and to a certain extent also rabbit and panda bear, contain sequences downstream of their *H2AFV* loci that could, if translated, lead to proteins with some similarities to human Z.2.2, although they are much more divergent and even longer (rabbit, panda bear). Due to these differences, it is highly likely that those species do not express a Z.2.2 protein homolog. Surprisingly, we could not detect Z.2.2-specific sequences in mouse, rat or other eukaryotic genomes, suggesting that Z.2.2 might be primate specific.

Next, we wanted to determine to what degree all three H2A.Z mRNAs are expressed in different human cell lines and tissues and performed quantitative PCR (qPCR).

Z.2.2 mRNA was present to different degrees in all human cell lines and tissues tested, though less abundant than Z.1 and Z.2.1 mRNAs that are expressed in similar amounts (Supplementary Figure S1C and D). Z.2.2 constituted between 5% and 15% of total Z.2 transcripts in all cell lines and tissues, with the exception of brain, where it was statistically significant upregulated ($p = 1.7 \times 10^{-4}$; Figure 1A). In some regions of this particular organ Z.2.2 accounted for up to 50% of all Z.2 transcripts pointing toward an exciting brain-specific function of this novel variant.

Encouraged by our findings we next investigated whether the endogenous protein is present *in vivo*. The distinctive feature of Z.2.2 is its C-terminus that is 14 amino acids shorter and contains six amino acids differences compared to Z.2.1 (Figure 1B). Due to this shortened C-terminal sequence, ubiquitination sites at positions K120 and K121 (28) and part of the H3/H4 docking domain (50) are lost in Z.2.2. We generated antibodies against Z.2.2's unique C-terminal amino acids (αZ.2.2) in rats and rabbits and confirmed their specificity in immunoblots (IB) with recombinant Z.2.1 and Z.2.2 proteins (Supplementary Figure S1E and data not shown). We extracted histones from several human and mouse cell lines, purified them by reversed phase–high performance liquid chromatography (RP–HPLC) and analyzed obtained fractions by IB (Figure 1C). Using αZ.2.2 (polyclonal rabbit), we observed a signal of the calculated weight of Z.2.2 that elutes shortly before Z.1- and Z.2.1-containing fractions in all human samples. Similar results were obtained with a monoclonal αZ.2.2 rat antibody (data not shown). In agreement with the finding that Z.2.2-specific exon 6 sequences are mainly restricted to primate genomes, we could detect Z.2.2 protein in human but not in mouse cells (Figure 1C). In summary, our data show that Z.2.2 protein indeed exists *in vivo*, albeit at a low expression level.

GFP-Z.2.2 is partially incorporated into chromatin

Having demonstrated the existence of this novel variant *in vivo*, we next sought to clarify whether Z.2.2 constitutes a bona fide histone by being part of the chromatin structure. Due to high background of all our αZ.2.2 antibodies in IB with cell extracts (data not shown), we generated

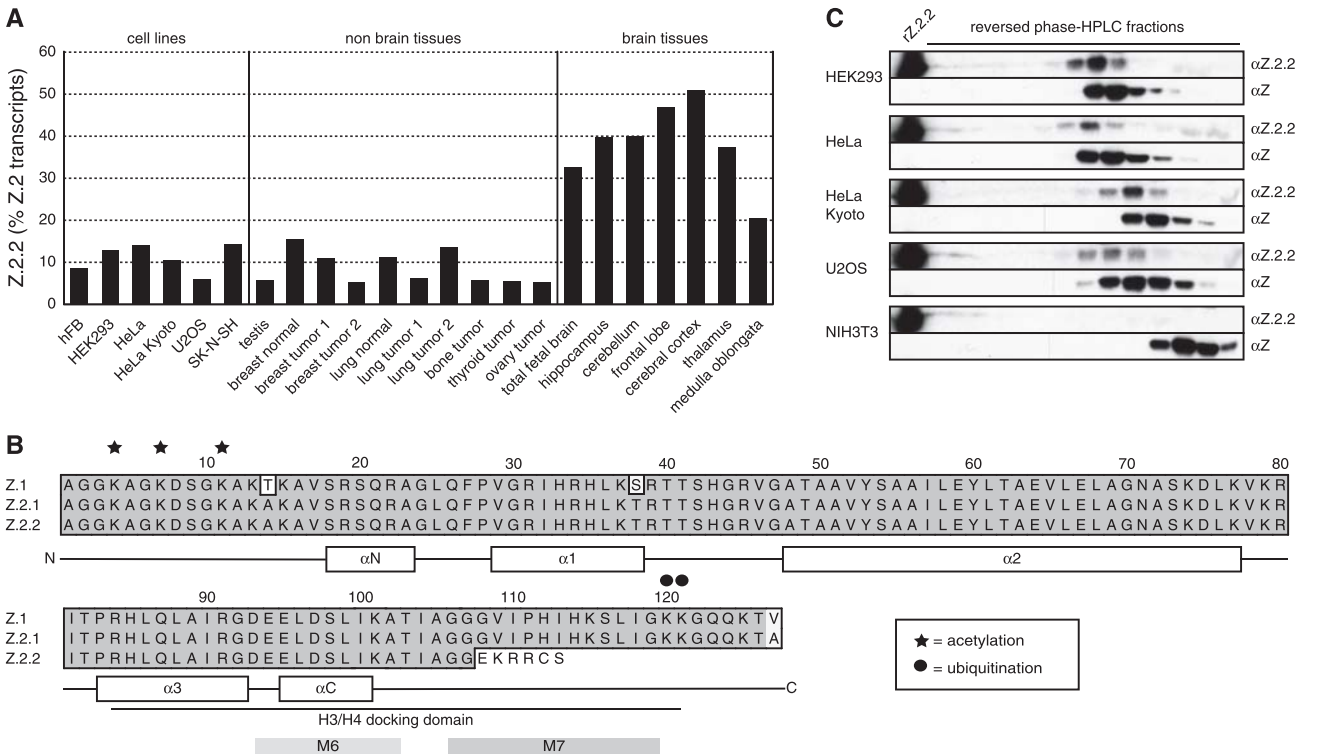

Figure 1. Identification of Z.2.2. (**A**) qPCR with cDNA from different human cell lines and tissues using primers specific for Z.2.1 and Z.2.2. Data were normalized to HPRT1 and HMBS expression levels. Controls generated without reverse transcriptase (no RT) were used to assess amplification threshold. Shown are the levels of Z.2.2 mRNA as percentages of total Z.2 transcripts (Z.2.1 + Z.2.2). For an evaluation of absolute expression levels see Supplementary Figure S1C and D. (**B**) Amino acid alignment of human Z.1, Z.2.1 and Z.2.2 proteins using ClustalW Alignment (MacVector 10.0.2). Identical amino acids are highlighted in dark gray, similar amino acids in light gray and changes are set apart on white background. Known acetylation sites are depicted with stars and ubiquitination sites with circles. A schematic representation of the secondary structure of Z.1 and Z.2.1 is shown below the alignment, including depiction of the H3/H4 docking domain (50). M6 and M7 boxes indicate regions important for H2A.Z-specific biological functions in *D. melanogaster* (60). (**C**) IB analyses of RP–HPLC purified fractions from different human (HEK293, HeLa, HeLa Kyoto and U2OS) and mouse (NIH3T3) cell lines using a polyclonal rabbit αZ.2.2 and αH2A.Z (αZ, C-terminal) antibodies. Recombinant Z.2.2 protein (rZ.2.2) was loaded in the first lane as positive control for αZ.2.2 antibody. Similar results were obtained when using a monoclonal rat αZ.2.2 antibody (data not shown).

HeLa Kyoto cell lines stably expressing GFP-tagged H2A variants (HK-GFP cells) for subsequent analyses. Expression levels of GFP-tagged histone variants were determined by FACS (Supplementary Figure S2A) and by comparing expression levels of GFP-tagged variants with endogenous H2A.Z proteins in IB (Supplementary Figure S2B). GFP-Z.1 and -Z.2.1 were expressed in similar amounts as the endogenous H2A.Z protein, and GFP-Z.2.2 expression levels were considerably lower than those of other GFP-tagged H2A variants, with the exception of GFP-H2A.Bbd (Barr body deficient; Bbd). These data show that all GFP-H2A variants were not expressed in abnormal amounts in cell clones used for further analyses.

In fluorescence microscopy, GFP-Z.2.2 exhibited a sole but rather diffuse nuclear distribution similar to GFP-Bbd, suggesting that both variants might have similar properties (Figure 2A). Additionally, GFP-Z.2.2 was detected in condensed mitotic chromosomes, with a faint residual staining in the surrounding area (Figure 2B), suggesting that it is incorporated into chromatin, although to a lesser extent than other GFP-H2A variants. To discriminate between a potential non-specific DNA binding and nucleosomal incorporation of Z.2.2 we purified mononucleosomes by sucrose gradient centrifugation. GFP-Z.2.2 was detected by IB in fractions containing mononucleosomes (Figure 2C), suggesting that Z.2.2 is indeed a nucleosomal constituent.

To analyze the extent of Z.2.2 chromatin incorporation in more detail, we isolated soluble (*sol*) and chromatin (*chr*) fractions from HK-GFP cells. IB analyses revealed, as expected, that similar to GFP-Bbd, GFP-Z.2.2 is predominantly nuclear soluble, with only minor amounts present in chromatin (Figure 3A). Based on fractionation and fluorescence imaging results, we hypothesized that this novel variant behaves in a different manner as compared to other H2A variants with regard to chromatin exchange mobility *in vivo*. To test this prediction, we performed fluorescence recovery after photobleaching (FRAP) experiments with HK-GFP cells. Using spinning disk confocal microscopy we monitored the kinetic behavior of H2A variants with variable intervals over 2 min (short-term) up to several hours (long-term) after bleaching a 5 μm × 5 μm square nuclear region (Figure 3B and Supplementary Figure S3). As expected, GFP alone showed the highest mobility. In contrast, GFP-H2A, -Z.1 and -Z.2.1 showed a slow recovery, which is in agreement with a previous report (52). GFP-Bbd has been described to exhibit low nucleosomal stability and a fast FRAP kinetic (53), which we also observed in our experiment. Interestingly, GFP-Z.2.2 showed an even faster recovery than GFP-Bbd, with ~80% of initial fluorescence reached after 1 min. Careful assessment and bi-exponential fitting of FRAP data allowed us to also calculate ratios of fractions with fast, intermediate and slow recovery and their respective half-time of recovery ($t_{1/2}$) as an indication of exchange rate thereby revealing quantitative differences between Z.2.2 and other H2A variants (Figure 3D, Supplementary Figure S3C and E). For Z.2.2 as well as for Bbd, we identified a fast fraction of unbound or very transiently

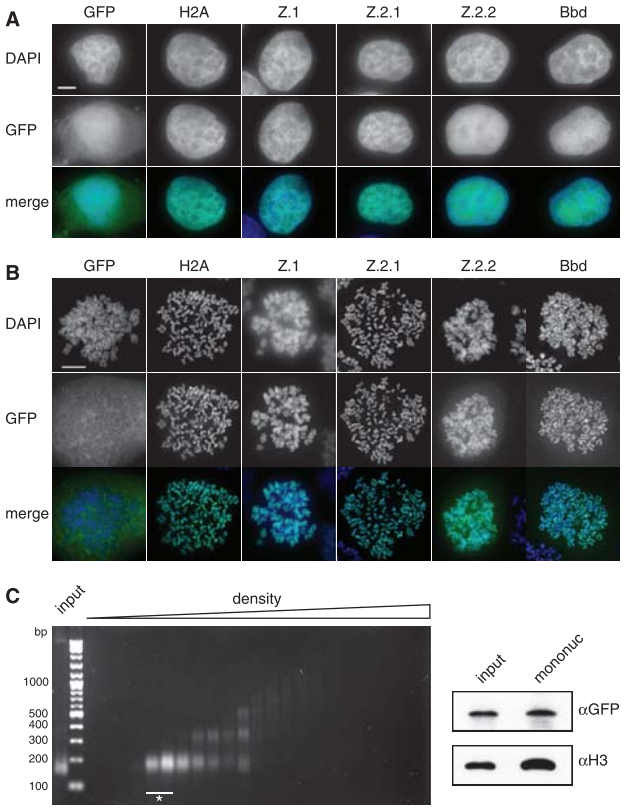

Figure 2. Z.2.2 localizes to the nucleus and is partially incorporated into chromatin. (**A**) Fluorescence imaging of stably transfected HeLa Kyoto cells shows nuclear localization of all GFP-H2A variants (middle). DNA was counterstained with DAPI (top). Overlay of both channels in color is shown at the bottom (Merge; GFP: green, DAPI: blue). Scale bar = 5 μm. (**B**) Deconvolved images of metaphase spreads of HeLa Kyoto cells stably expressing GFP-H2A variants (middle). Merged images in color are shown below (GFP: green; DAPI: blue). Scale bar = 10 μm. (**C**) Chromatin from HeLa Kyoto cells stably expressing GFP-Z.2.2 was digested with MNase followed by a purification of mononucleosomes using sucrose gradient centrifugation. Isolated DNA from subsequent sucrose gradient fractions was analyzed by agarose gel electrophoresis (left). Fractions containing pure mononucleosomes (marked with asterisk) were combined and analyzed by IB (right) using αGFP antibody for the presence of GFP-Z.2.2 (top), and αH3 (bottom).

interacting molecules (78%, $t_{1/2}$ ~ 1.1 s and 52%, $t_{1/2}$ ~ 2.5 s, respectively; for comparison GFP $t_{1/2}$ ~ 0.4 s) and a substantially slower fraction with a $t_{1/2}$ in the range of 7–9 min. In contrast, GFP-H2A, -Z.1 and -Z.2.1 showed no fast mobile fraction but intermediate slow fractions with $t_{1/2}$ in the range of 8–17 min and a second even slower class exchanging with a $t_{1/2}$ of a few hours. For comparison, we measured the linker histone H1.0 (54–57) and the histone binding protein HP1α (58,59), both DNA-associated proteins, and found that HP1α shows an overall much faster recovery than all H2A variants. In contrast to Z.2.2 and Bbd, no unbound fraction of H1.0 was detected. More importantly, with regards to the bound Z.2.2 and Bbd fractions overall H1.0 showed a faster recovery, arguing against an unspecific DNA-association of Z.2.2 and Bbd. In agreement with cell biological and biochemical analyses,

these data clearly demonstrate that a large fraction of the splice variant Z.2.2 is very rapidly exchanged or chromatin unbound, and a minor population is incorporated into chromatin.

Z.2.2's unique docking domain, but not its shortened length, weakens chromatin association

The functional importance of specific C-terminal domains of H2A.Z has previously been demonstrated by nucleosomal structure analyses (7,50) and in rescue experiments in flies (60). Since the C-terminus of Z.2.2 is shorter and has a distinct sequence when compared to Z.1 and Z.2.1, it is not clear which of these features determines Z.2.2's unusual chromatin-association.

Therefore, we generated deletion and domain-swap constructs (Supplementary Figure S3D) for FRAP experiments (short-term: Figure 3C and long-term: Supplementary Figure S3B). Surprisingly, C-terminal deletions of GFP-H2A ($H2A^{111}$) and GFP-Z.2.1 ($Z.2.1^{113}$) to mimic the shortened length of Z.2.2 did not affect their original mobility in short-term and only modestly in long-term FRAP. Hence, the mere shortening of the C-terminus is not sufficient to weaken stable chromatin association.

To investigate whether the unique six C-terminal amino acids of Z.2.2 are sufficient to generate highly mobile proteins, we created a further C-terminally truncated GFP-H2A construct ($H2A^{105}$) and added the Z.2.2 specific C-terminal six amino acids ($H2A^{105}$ + CZ.2.2). Although both mutant constructs are slightly more mobile than $H2A^{111}$, their indistinguishable recovery kinetics demonstrate that the unique six C-terminal amino acids of Z.2.2 alone are not sufficient to cause its extreme mobility *in vivo*.

To explore whether the complete Z.2.2 docking domain is able to induce high-protein mobility, we transferred the respective domain of either Z.2.1 (amino acids 91–127) or Z.2.2 (amino acids 91–113) onto a C-terminally truncated H2A ($H2A^{88}$ + CZ.2.1 and $H2A^{88}$ + CZ.2.2, respectively). Interestingly, only the docking domain of Z.2.2, but not the one of Z.2.1, confers high mobility. In conclusion, the six unique C-terminal amino acids of Z.2.2 prevent chromatin-association of a large proportion of this protein, but only when present in the context of the preceding H2A.Z-specific docking domain sequence.

Z.2.2 interacts with H2A.Z-specific TIP60 and SRCAP chaperone complexes and is deposited into chromatin outside of S-phase

Our so far obtained data strongly imply that at least a minor amount of the cellular Z.2.2 protein is incorporated into nucleosomes. Since previous studies have shown that evolutionary conserved Swr1-related ATP-dependent chromatin remodelers specifically exchange canonical H2A–H2B with H2A.Z–H2B dimers within nucleosomes (10,61), we wondered if such complexes are also able to actively deposit Z.2.2 into chromatin. HK cells and HK cells stably expressing GFP-Z.2.1 or -Z.2.2 were SILAC labeled, soluble nuclear proteins isolated, GFP-tagged

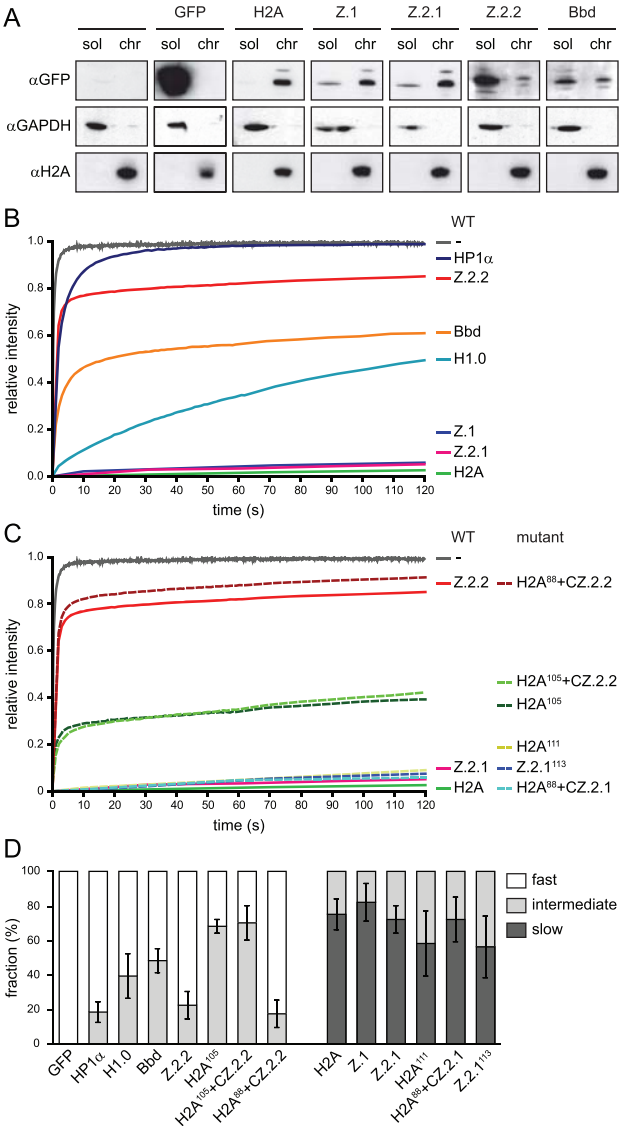

Figure 3. The majority of Z.2.2 protein is nuclear soluble and highly mobile in a sequence-dependent manner. (**A**) HK-GFP cells were subjected to biochemical fractionation. Fractions *sol* and *chr* of identical cell equivalents were probed in IB with αGFP (top), αH2A (middle) and αGAPDH (bottom). (**B**) FRAP quantification curves of average GFP signal relative to fluorescence intensity prior to bleaching are depicted for GFP, GFP-tagged wild-type H2A variants, linker histone H1.0 and heterochromatin protein 1α (HP1α). Mean curves of 10–29 cells are shown for each construct. Error bars are omitted for clarity. (**C**) FRAP quantification curves similar to (**B**) are depicted for GFP, GFP-tagged wild-type H2A, Z.2.1, Z.2.2 and mutant constructs. (**D**) Quantitative evaluation of FRAP curves. Plot shows calculated mobility fraction sizes of different wild-type and mutant H2A variant constructs, as well as H1.0 and HP1α, based on bi-exponential fitting of FRAP data. Error bars indicate SD (see Supplementary Figure S3 for long-term FRAP and for numerical values).

Z.2.1 and Z.2.2-associated proteins precipitated using GFP nanotrap beads and identified by quantitative mass spectrometry (Figure 4 and Supplementary Table S1 for a complete list of all identified proteins). Whereas the majority of proteins are background binders clustering

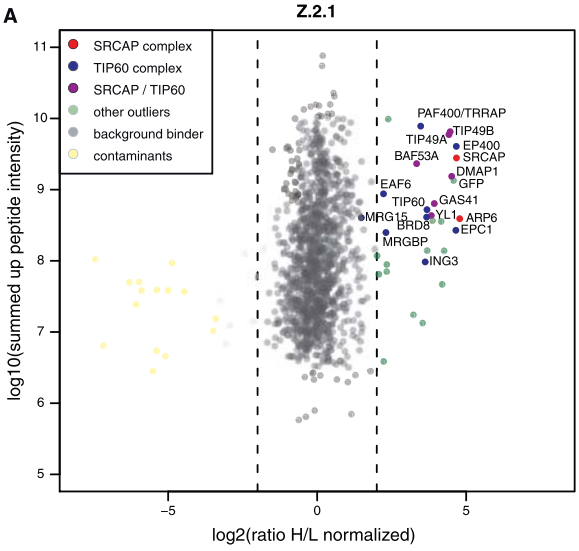

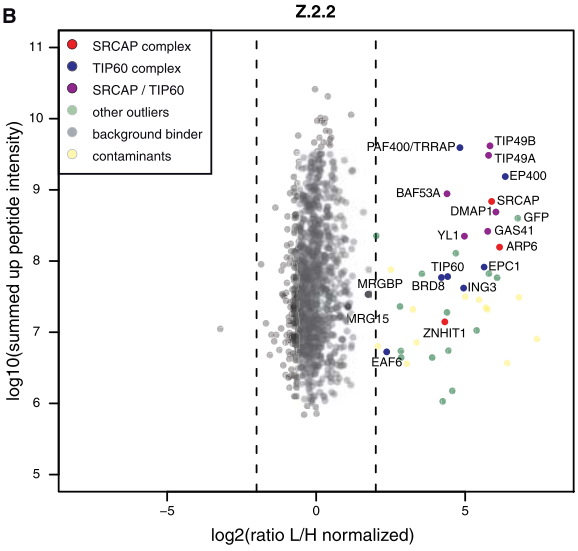

C

protein name	ratio H/L Z.2.1	ratio L/H Z.2.2 (ratio H/L)	complex
EP400	25,43	81,32 (0,012)	TIP60
EPC1	25,18	49,73 (0,020)	
TIP60	12,86	21,30 (0,047)	
BRD8	12,75	18,42 (0,054)	
ING3	12,34	30,86 (0,032)	
PAF400	11,10	28,32 (0,035)	
MRGBP	4,95	3,34 (0,299)	
MEAF6	4,68	5,16 (0,194)	
MRG15	*2,79*	*2,05 (0,488)*	
DMAP1	22,85	65,40 (0,015)	TIP60 / SRCAP
TIP49B	22,05	57,00 (0,018)	
TIP49A	21,42	55,18 (0,018)	
GAS41	15,24	54,06 (0,018)	
YL1	14,24	31,44 (0,032)	
BAF53A	10,10	20,98 (0,048)	
ARP6	27,52	71,25 (0,014)	SRCAP
SRCAP	25,51	59,24 (0,017)	
ZNHIT1	NA	19,93 (0,050)	
GFP	23,82	108,88 (0,009)	

Figure 4. Z.2.2 associates with H2A.Z-specific SRCAP and TIP60 chaperone complexes. GFP-pull-downs for H2A.Z-specific chaperone complexes are shown. HK cells stably expressing GFP-Z.2.1 (**A**) and GFP-Z.2.2 (**B**) were SILAC-labeled and subjected to single-step affinity purifications of soluble nuclear proteins in a 'forward' (GFP-Z.2.1) or 'reverse' (GFP-Z.2.2) pull-down using GFP nanotrap beads. In each panel the ratio of the identified proteins after MS is plotted. Proteins known to interact with H2A.Z are indicated in the following way: members of the SRCAP complex in red, members of the TIP60 complex in blue and shared subunits in purple. Potential novel H2A.Z-interacting proteins are shown as green dots ('other outliers') and are distinguished from background binders (gray dots) and contaminants (yellow dots). See also Supplementary Table S1 for a list of all identified proteins. (**C**) List of the SRCAP and TIP60 complex members and their normalized binding intensity to Z.2.1 or Z.2.2. Note that for comparison reasons the obtained H/L ratios of GFP-Z.2.2 binders (numbers in brackets) were calculated in the corresponding L/H ratios. See also Supplementary Table S1 for a list of all identified proteins and their normalized H/L ratios.

around 0, specific interactors can be found on the right side having a high ratio H/L or ratio L/H for Z.2.1 and Z.2.2, respectively. In accordance with previous studies (62–65), we found GFP-Z.2.1 to be part of two major complexes, the SRCAP and the p400/NuA4/TIP60 (TIP60) complexes (Figure 4A), as we were able to detect all of their thus far identified members, with the exception of actin, as significant outliers. Interestingly, GFP-Z.2.2 also associated with both SRCAP and TIP60 complexes (Figure 4B), showing an almost identical binding composition as GFP-Z.2.1 (Figure 4C). These results strongly imply that Z.2.2 is, similar to other H2A.Z variants, actively deposited into chromatin through specific chaperone complexes.

Based on these results, we predicted that Z.2.1 and Z.2.2 should be incorporated into chromatin in a highly similar spatial manner. Since both SRCAP and TIP60 chaperone complexes are evolutionary conserved between different species, we tested mouse C127 cells that do not express endogenous Z.2.2 for their ability to deposit GFP-Z.2.2. Hereby we should be able to distinguish whether SRCAP and TIP60 complexes are sufficient for deposition, or if other potential primate-specific factors are needed. GFP-Z.2.1 and -Z.2.2 were transiently expressed in C127 cells, S-phase stages highlighted by EdU-incorporation and co-localization patterns visualized by fluorescence microscopy (Figure 5). GFP-Z.2.1 and -Z.2.2 showed an almost identical chromatin localization and deposition pattern, suggesting that Z.2.2 is, like Z.2.1, deposited through SRCAP and TIP60 complexes. In accordance with a recent study, we observed an enrichment of both H2A.Z variants in facultative heterochromatin regions in interphase nuclei (66). Surprisingly, although H2A.Z is expressed in all cell cycle phases (67), and GFP-Z.2.1 and -Z.2.2 expression is driven by a constitutive active promoter, chromatin deposition of both proteins is underrepresented at replication foci. This result underlines our findings that Z.2.2 interacts with all members of both TIP60 and SRCAP complexes and is actively and not passively deposited, as would have been the case during S-phase when nucleosomes are highly exchanged.

Structural changes in Z.2.2's C-terminus prevent histone octamer folding and enhance DNA breathing on structurally destabilized nucleosomes

Our findings thus far imply that Z.2.2 is incorporated into nucleosomes and most likely targeted by TIP60 and

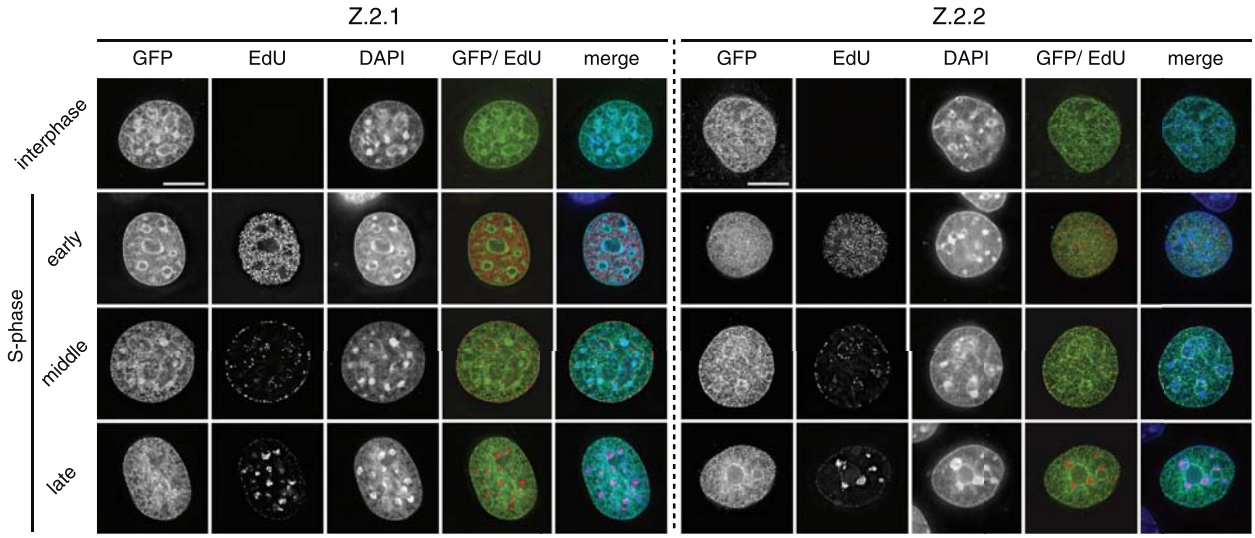

Figure 5. Z.2.1 and Z.2.2 are actively deposited into chromatin and are under-represented at replication foci. C127 cells transiently expressing GFP-Z.2.1 (left) and -Z.2.2 (right) were pulse labeled with EdU to visualize replication foci and to identify S-phase stages. DNA was counterstained with DAPI and analyzed by wide-field deconvolution microscopy. To remove the unbound fraction in GFP-Z.2.2 expressing cells, an *in situ* extraction was performed prior to fixation. Cells in early, middle and late S-phases were distinguished due to their characteristic differential EdU replication labeling patterns of eu- and heterochromatic regions. Merged images in color are shown alongside (GFP: green; EdU: red; DAPI: blue). Scale bar = 5 μm.

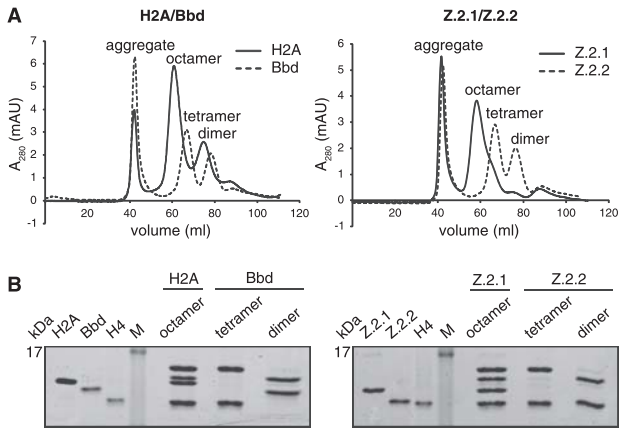

Figure 6. Z.2.2 does not constitute stable histone octamers with H2B, H3 and H4 *in vitro*. (**A**) Size exclusion chromatography of refolding reactions using recombinant human H3, H4 and H2B proteins together with either H2A (solid line) or Bbd (dashed line) (left overlay) or with either Z.2.1 (solid line) or Z.2.2 (dashed line) (right overlay). Peaks corresponding to aggregates, histone octamers, tetramers or dimers are labeled respectively. (**B**) Fractions corresponding to H2A-containing octamers, Bbd-containing tetramers and dimers (left) or Z.2.1-containing octamers and Z.2.2-containing tetramers and dimers (right) were analyzed by 18% SDS–PAGE and stained with Coomassie brilliant blue.

SRCAP complexes. Then why does a large fraction of the cellular Z.2.2 protein pool shows a high mobility and is freely dispersed in the nucleus? One plausible possibility is that Z.2.2 severely destabilizes nucleosomes due to its divergent C-terminal docking domain and is hence rapidly exchanged. To test this hypothesis, we used an *in vitro* reconstitution system. Recombinant human H2A variants together with H3, H2B and H4 (Supplementary Figure S4A) were refolded by dialysis, and formed complexes purified by size exclusion chromatography. As expected, both H2A and Z.2.1 containing samples readily formed histone octamers (Figure 6A, solid lines). Bbd served as a negative control, because it has been demonstrated to not form octamers under these conditions (41), a result we also observed (Figure 6A left, dotted line). Interestingly, in accordance with our FRAP data, Z.2.2 behaved like Bbd in that it only formed Z.2.2–H2B dimers, but did not complex together with $(H3–H4)_2$ tetramers to generate octamers (Figure 6A right, dotted line), which was further confirmed by SDS–PAGE analyses of the separate fractions (Figure 6B). Thus, like for Bbd the incorporation of Z.2.2 destabilizes the interface between Z.2.2–H2B dimers and $(H3–H4)_2$ tetramers in a C-terminal sequence dependent manner (Supplementary Figure S4B and C). In conclusion, the Z.2.2 docking domain is sufficient to prevent octamer formation.

Although no Z.2.2 containing histone octamers could be generated *in vitro*, our results using GFP-Z.2.2 strongly suggest that Z.2.2 can be part of nucleosomes. To test this *in vitro* and to evaluate the effect of Z.2.2 on nucleosome stability, we reconstituted mononucleosomes by mixing Z.2.2–H2B dimers, $(H3–H4)_2$ tetramers and DNA containing a 'Widom 601' DNA positioning sequence in a 2:1:1 ratio. As controls, we reconstituted H2A or Z.2.1 containing nucleosomes by mixing octamers and DNA in a 1:1 ratio. As expected, analysis of all nucleosomes by native PAGE showed a single band before and after heat shift (Figure 7A), indicating a unique position on the 'Widom 601' DNA template. Purification of nucleosomes from a native gel and analysis of the protein content by

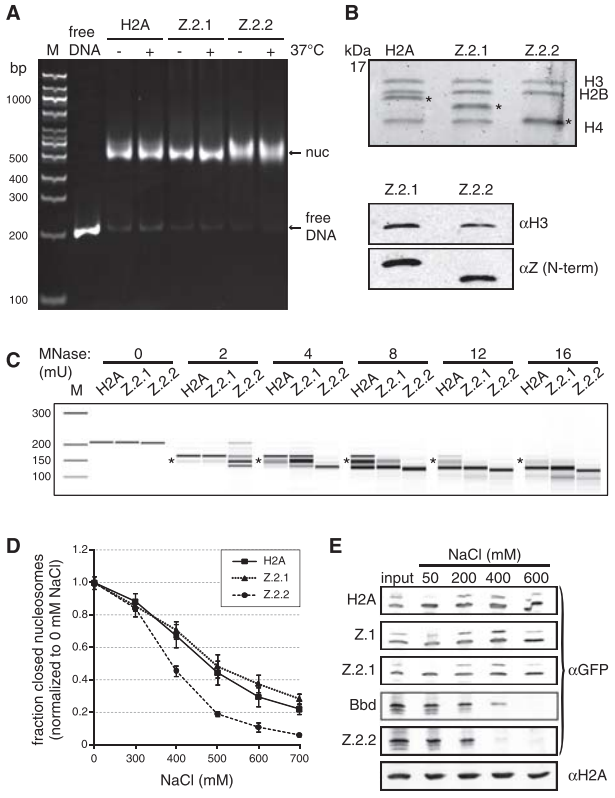

Figure 7. Z.2.2-containing nucleosomes are less resistant to MNase digestion and increased ionic strength. (**A**) H2A, Z.2.1 or Z.2.2 containing nucleosomes were assembled on DNA by salt gradient deposition, incubated at 4°C or 37°C to evaluate DNA positioning and separated by a native 5% PAGE gel. (**B**) Agarose-gel-electro-eluted material from (A) was analyzed by 18% SDS–PAGE and Coomassie stained to evaluate stoichiometry of histones after nucleosome assembly (top). Stars indicate H2A variants that were used for assembly. Further evaluation of histone stoichiometry after nucleosome assembly was done by IB using a LI-COR instrument (bottom). Assembled nucleosomes containing Z.2.1 or Z.2.2 were immunoblotted and the amount of histones was visualized using an αH3 antibody (top) and an N-terminal αZ antibody (recognizes all H2A.Z variants, bottom). (**C**) Mononucleosomes containing either H2A, Z.2.1 or Z.2.2 were digested with increasing concentrations of MNase and extracted DNA was separated using Bioanalyzer. Stars indicate DNA length of 146 bp. For detailed electropherogram analyses of fragment lengths in each sample see Supplementary Figure S5. (**D**) Mononucleosomes containing either H2A, Z.2.1 or Z.2.2 histones together with double dye labeled DNA were incubated with increasing amounts of salt. smFRET measurement values of each salt concentration were normalized to 0 mM NaCl. Error bars represent SEM of six measurements. (**E**) Chromatin from HK-GFP cells was isolated and incubated with increasing amounts of salt. Chromatin-bound histones were precipitated and detected by IB using αGFP antibody. Staining with αH2A was used as loading control.

SDS–PAGE (Coomassie staining and immunoblot) showed that Z.2.2 was indeed incorporated into nucleosomes (Figure 7B). All nucleosomes were further evaluated for their resistance to MNase cleavage as an indicator of stably organized nucleosomes and to determine nucleosomal DNA length (Figure 7C and Supplementary Figure S5). We observed fragments corresponding to protected nucleosomal DNA with the length of 146 bp for all variant nucleosomes tested. The appearance of smaller, subnucleosomal fragments indicates that DNA breathing occurred (68). Interestingly, DNA of Z.2.2 nucleosomes is less protected, since subnucleosomal fragments were obtained at lower MNase concentrations than with H2A or Z.2.1 nucleosomes. Additionally, at higher MNase concentrations a stable DNA fragment of about 120 bp was most abundant for Z.2.2 nucleosomes (Supplementary Figure S5), indicating that this might be the preferred DNA length wrapped around this octamer. These data suggest that increased DNA breathing occurs in Z.2.2 nucleosomes, which as a result might be less stable. To quantify nucleosome stability *in vitro* we measured salt-dependent changes in nucleosome structure using smFRET (69). In line with the results presented above, Z.2.2 containing recombinant nucleosomes lost their compact structure at lower salt concentrations than Z.2.1 or H2A-containing ones (Figure 7D). To investigate whether the observed Z.2.2-dependent nucleosome destabilization is true in the context of chromatin, we isolated chromatin from HK cells expressing GFP-H2A variants and incubated it with buffer containing increasing amounts of salt. Histones that remained stable chromatin components were precipitated and detected by IB (Figure 7E). As observed with FRET techniques, Z.2.2-containing nucleosomes disintegrated between 200 and 400 mM NaCl, and were therefore even less stable than Bbd-containing ones. In summary, incorporation of Z.2.2 leads to a severely reduced nucleosome stability due to C-terminal sequence dependent changes in its docking domain and subsequent loss of its interaction with histone H3.

Our FRAP data suggest that the Z.2.2 C-terminal amino acids might have a direct influence on the nucleosomal structure by affecting interactions with DNA and/or adjacent histones. Based on the existing structural data (50), we performed MD simulations of nucleosomes containing Z.1 (Supplementary Figure S7) or Z.2.2. In addition, we also included the deletion mutant Z.2.1^{113}, which did not show any change in short-term FRAP (Figure 3C), but some increase in mobility in long-term FRAP (Supplementary Figure S3B) in our assay. These *in silico* models revealed that changes in the C-terminus of H2A.Z strongly affect its protein structure (Figure 8A). Strikingly, different statistical descriptors over the MD-trajectory like distance and mobility (B-factor) show in contrast to Z.1 and Z.2.1^{113} unique properties for the Z.2.2 tail. Only Z.2.2 leads to a substantial structural change in the C-terminus resulting in an increased distance to histone H3, which in turn makes a hydrogen bond interaction between peptide backbone NH of Cys112 in Z.2.2 and the oxygen in the Gln55 side chain in H3 impossible (Figure 8B). Additionally, an increase in the B-factor for Z.2.2 indicates a substantially enhanced mobility of Z.2.2's C-terminus (Figure 8C). We also calculated the Z.2.2–H3 interaction energy and observed a switch from negative to positive values in the case of Z.2.2 suggesting that this histone variant destabilizes the nucleosome (Figure 8D). In summary, these data suggest that the C-terminal sequence of Z.2.2 leads to a more dynamic structure that in turn loses binding to histone

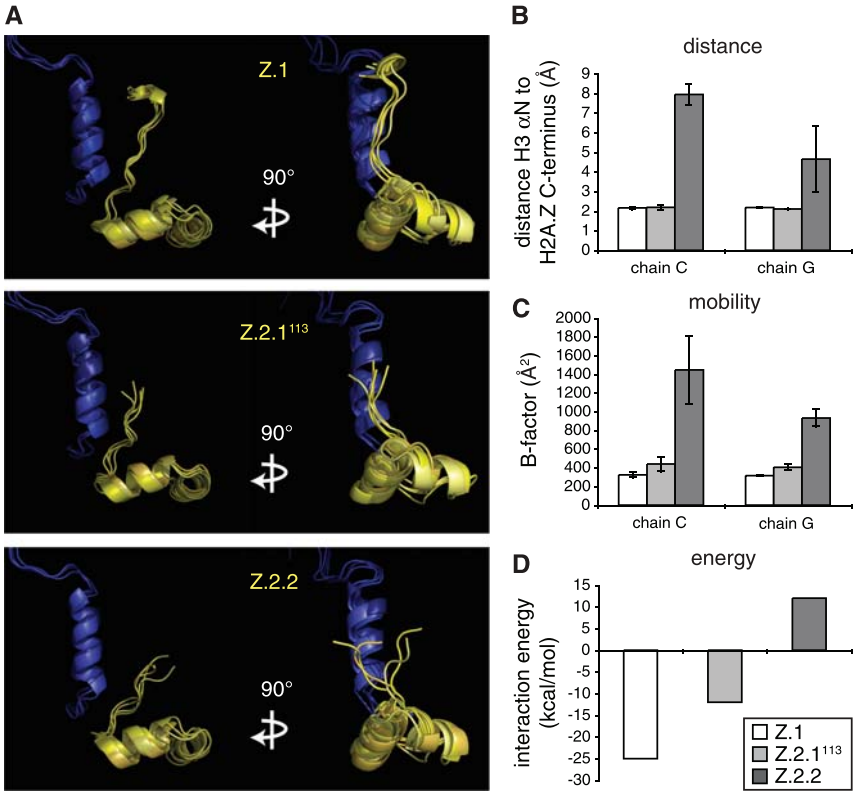

Figure 8. Unique Z.2.2 C-terminal amino acids cause significant changes in protein and nucleosome structure. (**A**) *In silico* models of Z.1, Z.2.1^{113} and Z.2.2 C-terminal C-chains (yellow; from amino acids 84 to C-terminus, including the complete docking domain) together with the E-chain of histone H3 (blue; amino acids 33–60, including αN-helix). Side (left) and frontal views (right) of four MD simulations are shown respectively. See Supplementary Figure S7 for complete *in silico* model of H2A.Z-containing nucleosome. (**B**) Simulated distances between peptide backbone NH of amino acids 112 in H2A.Z (His or Cys, respectively) variants and the oxygen in the Gln55 sidechain in H3 based on *in silico* nucleosome models containing either Z.1 (white), Z.2.1^{113} (light gray) or Z.2.2 (dark gray) proteins. Error bars represent SD of four independent simulations. (**C**) Simulated mobility measuring B-factor values between amino acids 108 and 113 in respective H2A.Z variant C-termini. Error bars represent SD of four independent simulations. (**D**) Simulated interaction energy between tetramer versus respective H2A.Z variant-containing dimers.

H3 and destabilizes the nucleosomal structure, providing a reasonable explanation for the observed *in vivo* and *in vitro* data.

DISCUSSION

In this work, we have identified a previously unknown histone H2A.Z variant and provide a comprehensive characterization of its nucleosomal properties. This alternatively spliced variant, Z.2.2, is present to different degrees in all human cell lines and tissues investigated, with a significant enrichment in brain. Z.2.2 contains a shortened and in six amino acids divergent C-terminus compared to Z.1 and Z.2.1 that is necessary, but not sufficient, to weaken chromatin association. Only in the context of the unique Z.2.2 docking domain does the C-terminal sequence negatively affect nucleosome stability *in vitro* and *in vivo*. To our knowledge, Z.2.2 has the strongest destabilizing effect on nucleosomal structure compared to other histone H2A variants reported to date.

Only one other histone variant, macroH2A, has been shown thus far to be alternatively spliced (70). Here, like our observation with H2A.Z, two independent genes *mH2A1* and *mH2A2* exist in mammals, with only mH2A1 being alternatively spliced resulting in functional different proteins (71). In our study, we demonstrate that the human H2A.Z.2 (H2AFV) primary transcript is alternatively spliced generating Z.2.1 and Z.2.2 mRNAs and proteins. These observations suggest that Z.2.2 is tightly regulated in a tissue-specific manner through alternative splicing and/or RNA stability. Our findings now raise the intriguing possibility that alternative splicing of histone variants might not be rare but more common than previously thought. If true, it will be of interest to reevaluate other intron-containing histone variant genes with regard to their possible alternative transcripts and protein products.

Bioinformatic genome analyses revealed the existence of Z.2.2-specific sequences only in humans, old and new world primates and to some extend in other mammals, with the exclusion of mouse, rat and even lower eukaryotes. It remains to be seen, whether Z.2.2's evolution is indeed limited to primates only. Primate-specific gene products have been often identified in human brain and reproductive tissues (72), supporting the notion that

their RNAs and proteins might be essential to adaptive changes leading to human development and further speculates that primate-specific genes might be important in reproductive function and disease. Since we have found Z.2.2 transcripts to be strongly enriched in brain samples of higher brain function in comparison to other tissues and cell types, it will be of great interest to determine in future studies, if this novel variant might play an important functional role in this particular organ. These observations also raise the interesting question of how alternative splicing and/or differential stability of H2AFV transcripts are tissue specifically regulated.

Another intriguing feature of Z.2.2 is its influence on nucleosome stability. Although Z.2.2 localizes exclusively to the nucleus, only a minor proportion is stably incorporated into chromatin. The only other exception in humans known thus far is Bbd, which has previously been demonstrated to destabilize the nucleosome structure (41,53,73). Bbd, similar to Z.2.2, is a shorter H2A variant with an unusual C-terminus and a considerable different primary histone fold sequence that might explain its ability to destabilize nucleosomes. In agreement, a recent study demonstrated that the incomplete C-terminal docking domain of Bbd results in structural alterations in nucleosomes and that those are in turn associated with an inability of the chromatin remodeler RSC to both remodel and mobilize nucleosomes (8). Z.2.2, on the other hand, is identical to Z.2.1, except that its C-terminus is 14 amino acids shorter and in six amino acids altered. How can this small change in Z.2.2's primary sequence lead to such drastic effects on chromatin association?

We show that Z.2.2 can be part of a bona fide nucleosome and that it interacts with the H2A.Z-specific TIP60 and SRCAP chaperone complexes. These complexes have been shown to catalyze the exchange of H2A–H2B dimers with H2A.Z–H2B dimers in nucleosomes and our finding therefore suggests that both complexes are also involved in an active chromatin incorporation of Z.2.2. Supporting this idea is the observation that both Z.2.1 and Z.2.2 are incorporated into chromatin in a replication-independent manner, even in mouse cells that do not express endogenous Z.2.2. Both H2A.Z variants are not primarily deposited at replication foci, not even in middle S-phase when facultative heterochromatin is replicated, where the majority of the H2A.Z protein pool is found in interphase cells (66). Our findings are in agreement with a model proposed by Hardy and Robert, in which H2A.Z variants are randomly deposited into chromatin by specific chaperone complexes in a replication-independent manner coupled to a subsequent targeted H2A.Z depletion (74). As a consequence, an enrichment of H2A.Z at non-transcribed genes and heterochromatin regions over several cell generations can be observed (74). It might be possible that INO80 facilitates this eviction function, as it has been shown to exchange nucleosomal H2A.Z–H2B dimers with free H2A–H2B dimers (75). It will be of interest in future studies to determine whether Z.2.2 exchange is subjected to a similar mechanism. Taken together, our findings strongly imply that Z.2.2 is actively deposited into chromatin through the interaction with evolutionary conserved chaperone complexes. Nevertheless, a large fraction of Z.2.2 protein is not chromatin bound and we have mapped the region crucial for high FRAP mobility to its docking domain. In addition to Z.2.2's unique C-terminal amino acids this region spans the highly conserved acidic patch responsible for deposition (76), the M6 region that is functionally essential in fly H2A.Z (60) and required for the interaction with the SWR1 complex in yeast (77). Strikingly, *in silico* simulation of Z.2.2 predicted dynamic structural changes that in turn weaken interaction with histone H3 and destabilize the nucleosome structure. Such a gross structural alteration explains why Z.2.2 is not able to form stable octamers *in vitro* and leads to enhanced DNA breathing in a nucleosomal context. Hence, Z.2.2 incorporation into chromatin disrupts nucleosomes more easily and supports a model in which Z.2.2 is more rapidly exchanged than Z.2.1.

What functional outcome might Z.2.2 cause when incorporated into chromatin? And how is the variant composition of Z.2.2 containing nucleosomes? It has been shown that a special class of nucleosomes containing both H2A.Z and H3.3 variants exists in humans (78). These nucleosomes are enriched at promoters, enhancers and insulator region and promote the accessibility of transcription factors to these DNA regions (78), most likely due to their extreme sensitivity to disruption (79). Since these studies nicely demonstrate that differential nucleosome stabilities due to the incorporation of different histone variants influence transcriptional regulation, it is tempting to speculate that Z.2.2 might also affect chromatin-related processes. Future experiments will shed light on Z.2.2 function(s), especially with regard to its increased expression in human brain areas, and explain why and where nucleosomal destabilization is needed. This is of particular interest, since Bbd that also leads to nucleosomal destabilization is almost exclusively present in testis (80–82) in contrast to the apparently ubiquitously expressed Z.2.2, possibly pointing toward distinct roles of both destabilizing H2A variants in different tissues. Our data suggest that additional interesting, yet unidentified, histone variants may exist and await their discovery.

SUPPLEMENTARY DATA

Supplementary Data are available at NAR Online: Supplementary Table S1, Supplementary Figures S1–S7 and Supplementary Materials and Methods.

ACKNOWLEDGEMENTS

The authors thank S. Dambacher, M. Kador, H. Klinker, C. Mehlhorn, M. Holzner and F. Müller-Planitz for advice and help. The authors also thank U. Rothbauer for providing various GFP-Trap beads to initially test GFP pull-down efficiency. The authors are grateful to D. Rhodes, E. Bernstein, R. Schneider, M. Hendzel, T. Misteli and S. Matsunaga for reagents. The authors are indebted to E. Bernstein for critical examination of the

manuscript. The authors thank especially the Hake lab and members of the Adolf-Butenandt Institute for constructive discussions.

FUNDING

German Research Foundation (DFG), SFB Transregio 5 (to S.B.H., E.K., H.L. and L.S.); the BioImaging Network Munich and the German Ministry for Education and Research (BMBF) (to H.L.); the Center for Integrated Protein Science Munich (CIPSM) (to H.L., J.M., M.M. and S.B.H.); the European Research Council (to J.M.); the International Max-Planck Research School for Molecular and Cellular Life Sciences (IMPRS-LS) (to S.P., S.M.W. and K.S.); the International Doctorate Program NanoBio Technology (IDK-NBT) (to K.S.). Funding for open access charge: DFG.

Conflict of interest statement. None declared.

REFERENCES

1. van Holde,K.E. (1988) *Chromatin*. Springer, New York.
2. Bonisch,C., Nieratschker,S.M., Orfanos,N.K. and Hake,S.B. (2008) Chromatin proteomics and epigenetic regulatory circuits. *Exp. Rev. Proteomics*, **5**, 105–119.
3. Bernstein,E. and Hake,S.B. (2006) The nucleosome: a little variation goes a long way. *Biochem. Cell Biol.*, **84**, 505–517.
4. Boulard,M., Bouvet,P., Kundu,T.K. and Dimitrov,S. (2007) Histone variant nucleosomes: structure, function and implication in disease. *Subcell. Biochem.*, **41**, 71–89.
5. Redon,C., Pilch,D., Rogakou,E., Sedelnikova,O., Newrock,K. and Bonner,W. (2002) Histone H2A variants H2AX and H2AZ. *Curr. Opin. Genet. Dev.*, **12**, 162–169.
6. Ausio,J. and Abbott,D.W. (2002) The many tales of a tail: carboxyl-terminal tail heterogeneity specializes histone H2A variants for defined chromatin function. *Biochemistry*, **41**, 5945–5949.
7. Wang,A.Y., Aristizabal,M.J., Ryan,C., Krogan,N.J. and Kobor,M.S. (2011) Key functional regions in the histone variant H2A.Z C-terminal docking domain. *Mol. Cell. Biol.*, **31**, 3871–3884.
8. Shukla,M.S., Syed,S.H., Goutte-Gattat,D., Richard,J.L., Montel,F., Hamiche,A., Travers,A., Faivre-Moskalenko,C., Bednar,J., Hayes,J.J. *et al.* (2011) The docking domain of histone H2A is required for H1 binding and RSC-mediated nucleosome remodeling. *Nucleic Acids Res.*, **39**, 2559–2570.
9. Vogler,C., Huber,C., Waldmann,T., Ettig,R., Braun,L., Izzo,A., Daujat,S., Chassignet,I., Lopez-Contreras,A.J., Fernandez-Capetillo,O. *et al.* (2010) Histone H2A C-terminus regulates chromatin dynamics, remodeling, and histone H1 binding. *PLoS Genet.*, **6**, e1001234.
10. Billon,P. and Cote,J. (2011) Precise deposition of histone H2A.Z in chromatin for genome expression and maintenance. *Biochim Biophys Acta*, **1819**, 290–302.
11. Marques,M., Laflamme,L., Gervais,A.L. and Gaudreau,L. (2010) Reconciling the positive and negative roles of histone H2A.Z in gene transcription. *Epigenetics*, **5**, 267–272.
12. Draker,R. and Cheung,P. (2009) Transcriptional and epigenetic functions of histone variant H2A.Z. *Biochem. Cell Biol.*, **87**, 19–25.
13. Svotelis,A., Gevry,N. and Gaudreau,L. (2009) Regulation of gene expression and cellular proliferation by histone H2A.Z. *Biochem. Cell Biol.*, **87**, 179–188.
14. Brickner,D.G., Cajigas,I., Fondufe-Mittendorf,Y., Ahmed,S., Lee,P.C., Widom,J. and Brickner,J.H. (2007) H2A.Z-mediated localization of genes at the nuclear periphery confers epigenetic memory of previous transcriptional state. *PLoS Biol.*, **5**, e81.
15. Zofall,M., Fischer,T., Zhang,K., Zhou,M., Cui,B., Veenstra,T.D. and Grewal,S.I. (2009) Histone H2A.Z cooperates with RNAi and heterochromatin factors to suppress antisense RNAs. *Nature*, **461**, 419–422.
16. Rangasamy,D., Berven,L., Ridgway,P. and Tremethick,D.J. (2003) Pericentric heterochromatin becomes enriched with H2A.Z during early mammalian development. *EMBO J.*, **22**, 1599–1607.
17. Rangasamy,D., Greaves,I. and Tremethick,D.J. (2004) RNA interference demonstrates a novel role for H2A.Z in chromosome segregation. *Nat. Struct. Mol. Biol.*, **11**, 650–655.
18. Zlatanova,J. and Thakar,A. (2008) H2A.Z: view from the top. *Structure*, **16**, 166–179.
19. Dryhurst,D., McMullen,B., Fazli,L., Rennie,P.S. and Ausio,J. (2012) Histone H2A.Z prepares the prostate specific antigen (PSA) gene for androgen receptor-mediated transcription and is upregulated in a model of prostate cancer progression. *Cancer Lett.*, **315**, 38–47.
20. Valdes-Mora,F., Song,J.Z., Statham,A.L., Strbenac,D., Robinson,M.D., Nair,S.S., Patterson,K.I., Tremethick,D.J., Stirzaker,C. and Clark,S.J. (2012) Acetylation of H2A.Z is a key epigenetic modification associated with gene deregulation and epigenetic remodeling in cancer. *Genome Res.*, **22**, 307–321.
21. Conerly,M.L., Teves,S.S., Diolaiti,D., Ulrich,M., Eisenman,R.N. and Henikoff,S. (2010) Changes in H2A.Z occupancy and DNA methylation during B-cell lymphomagenesis. *Genome Res.*, **20**, 1383–1390.
22. Svotelis,A., Gevry,N., Grondin,G. and Gaudreau,L. (2010) H2A.Z overexpression promotes cellular proliferation of breast cancer cells. *Cell Cycle*, **9**, 364–370.
23. Hua,S., Kallen,C.B., Dhar,R., Baquero,M.T., Mason,C.E., Russell,B.A., Shah,P.K., Liu,J., Khramtsov,A., Tretiakova,M.S. *et al.* (2008) Genomic analysis of estrogen cascade reveals histone variant H2A.Z associated with breast cancer progression. *Mol. Syst. Biol.*, **4**, 188.
24. Eirin-Lopez,J.M., Gonzalez-Romero,R., Dryhurst,D., Ishibashi,T. and Ausio,J. (2009) The evolutionary differentiation of two histone H2A.Z variants in chordates (H2A.Z-1 and H2A.Z-2) is mediated by a stepwise mutation process that affects three amino acid residues. *BMC Evol. Biol.*, **9**, 31.
25. Beck,H.C., Nielsen,E.C., Matthiesen,R., Jensen,L.H., Sehested,M., Finn,P., Grauslund,M., Hansen,A.M. and Jensen,O.N. (2006) Quantitative proteomic analysis of post-translational modifications of human histones. *Mol. Cell Proteomics*, **5**, 1314–1325.
26. Bonenfant,D., Coulot,M., Towbin,H., Schindler,P. and van Oostrum,J. (2006) Characterization of histone H2A and H2B variants and their post-translational modifications by mass spectrometry. *Mol. Cell Proteomics*, **5**, 541–552.
27. Dryhurst,D., Ishibashi,T., Rose,K.L., Eirin-Lopez,J.M., McDonald,D., Silva-Moreno,B., Veldhoen,N., Helbing,C.C., Hendzel,M.J., Shabanowitz,J. *et al.* (2009) Characterization of the histone H2A.Z-1 and H2A.Z-2 isoforms in vertebrates. *BMC Biol.*, **7**, 86.
28. Sarcinella,E., Zuzarte,P.C., Lau,P.N., Draker,R. and Cheung,P. (2007) Monoubiquitylation of H2A.Z distinguishes its association with euchromatin or facultative heterochromatin. *Mol. Cell. Biol.*, **27**, 6457–6468.
29. Wiedemann,S.M., Mildner,S.N., Bonisch,C., Israel,L., Maiser,A., Matheisl,S., Straub,T., Merkl,R., Leonhardt,H., Kremmer,E. *et al.* (2010) Identification and characterization of two novel primate-specific histone H3 variants, H3.X and H3.Y. *J. Cell. Biol.*, **190**, 777–791.
30. Shechter,D., Dormann,H.L., Allis,C.D. and Hake,S.B. (2007) Extraction, purification and analysis of histones. *Nat. Protoc.*, **2**, 1445–1457.
31. Wysocka,J., Reilly,P.T. and Herr,W. (2001) Loss of HCF-1-chromatin association precedes temperature-induced growth arrest of tsBN67 cells. *Mol. Cell. Biol.*, **21**, 3820–3829.
32. Wessel,D. and Flugge,U.I. (1984) A method for the quantitative recovery of protein in dilute solution in the presence of detergents and lipids. *Anal. Biochem.*, **138**, 141–143.
33. Zhang,H., Roberts,D.N. and Cairns,B.R. (2005) Genome-wide dynamics of Htz1, a histone H2A variant that poises repressed/basal promoters for activation through histone loss. *Cell*, **123**, 219–231.

34. Hake,S.B., Garcia,B.A., Kauer,M., Baker,S.P., Shabanowitz,J., Hunt,D.F. and Allis,C.D. (2005) Serine 31 phosphorylation of histone variant H3.3 is specific to regions bordering centromeres in metaphase chromosomes. *Proc. Natl Acad. Sci. USA*, **102**, 6344–6349.
35. Vermeulen,M., Eberl,H.C., Matarese,F., Marks,H., Denissov,S., Butter,F., Lee,K.K., Olsen,J.V., Hyman,A.A., Stunnenberg,H.G. *et al.* (2010) Quantitative interaction proteomics and genome-wide profiling of epigenetic histone marks and their readers. *Cell*, **142**, 967–980.
36. Vermeulen,M., Mulder,K.W., Denissov,S., Pijnappel,W.W., van Schaik,F.M., Varier,R.A., Baltissen,M.P., Stunnenberg,H.G., Mann,M. and Timmers,H.T. (2007) Selective anchoring of TFIID to nucleosomes by trimethylation of histone H3 lysine 4. *Cell*, **131**, 58–69.
37. Cox,J. and Mann,M. (2008) MaxQuant enables high peptide identification rates, individualized p.p.b.-range mass accuracies and proteome-wide protein quantification. *Nat. Biotechnol.*, **26**, 1367–1372.
38. Salic,A. and Mitchison,T.J. (2008) A chemical method for fast and sensitive detection of DNA synthesis in vivo. *Proc. Natl Acad. Sci. USA*, **105**, 2415–2420.
39. Dyer,P.N., Edayathumangalam,R.S., White,C.L., Bao,Y., Chakravarthy,S., Muthurajan,U.M. and Luger,K. (2004) Reconstitution of nucleosome core particles from recombinant histones and DNA. *Methods Enzymol.*, **375**, 23–44.
40. Thastrom,A., Lowary,P.T., Widlund,H.R., Cao,H., Kubista,M. and Widom,J. (1999) Sequence motifs and free energies of selected natural and non-natural nucleosome positioning DNA sequences. *J. Mol. Biol.*, **288**, 213–229.
41. Bao,Y., Konesky,K., Park,Y.J., Rosu,S., Dyer,P.N., Rangasamy,D., Tremethick,D.J., Laybourn,P.J. and Luger,K. (2004) Nucleosomes containing the histone variant H2A.Bbd organize only 118 base pairs of DNA. *EMBO J.*, **23**, 3314–3324.
42. Gansen,A., Valeri,A., Hauger,F., Felekyan,S., Kalinin,S., Toth,K., Langowski,J. and Seidel,C.A. (2009) Nucleosome disassembly intermediates characterized by single-molecule FRET. *Proc. Natl Acad. Sci. USA*, **106**, 15308–15313.
43. Muller,B.K., Zaychikov,E., Brauchle,C. and Lamb,D.C. (2005) Pulsed interleaved excitation. *Biophys. J.*, **89**, 3508–3522.
44. Nir,E., Michalet,X., Hamadani,K.M., Laurence,T.A., Neuhauser,D., Kovchegov,Y. and Weiss,S. (2006) Shot-noise limited single-molecule FRET histograms: comparison between theory and experiments. *J. Phys. Chem. B*, **110**, 22103–22124.
45. Lee,N.K., Kapanidis,A.N., Wang,Y., Michalet,X., Mukhopadhyay,J., Ebright,R.H. and Weiss,S. (2005) Accurate FRET measurements within single diffusing biomolecules using alternating-laser excitation. *Biophys. J.*, **88**, 2939–2953.
46. Duan,Y., Wu,C., Chowdhury,S., Lee,M.C., Xiong,G., Zhang,W., Yang,R., Cieplak,P., Luo,R., Lee,T. *et al.* (2003) A point-charge force field for molecular mechanics simulations of proteins based on condensed-phase quantum mechanical calculations. *J. Comput. Chem.*, **24**, 1999–2012.
47. Wang,J., Wolf,R.M., Caldwell,J.W., Kollman,P.A. and Case,D.A. (2004) Development and testing of a general amber force field. *J. Comput. Chem.*, **25**, 1157–1174.
48. Jakalian,A., Jack,D.B. and Bayly,C.I. (2002) Fast, efficient generation of high-quality atomic charges. AM1-BCC model: II. Parameterization and validation. *J. Comput. Chem.*, **23**, 1623–1641.
49. Krieger,E., Darden,T., Nabuurs,S.B., Finkelstein,A. and Vriend,G. (2004) Making optimal use of empirical energy functions: force-field parameterization in crystal space. *Proteins*, **57**, 678–683.
50. Suto,R.K., Clarkson,M.J., Tremethick,D.J. and Luger,K. (2000) Crystal structure of a nucleosome core particle containing the variant histone H2A.Z. *Nat. Struct. Biol.*, **7**, 1121–1124.
51. Krieger,E., Nielsen,J.E., Spronk,C.A. and Vriend,G. (2006) Fast empirical pKa prediction by Ewald summation. *J. Mol. Graph Model.*, **25**, 481–486.
52. Higashi,T., Matsunaga,S., Isobe,K., Morimoto,A., Shimada,T., Kataoka,S., Watanabe,W., Uchiyama,S., Itoh,K. and Fukui,K. (2007) Histone H2A mobility is regulated by its tails and acetylation of core histone tails. *Biochem. Biophys. Res. Commun.*, **357**, 627–632.
53. Gautier,T., Abbott,D.W., Molla,A., Verdel,A., Ausio,J. and Dimitrov,S. (2004) Histone variant H2ABbd confers lower stability to the nucleosome. *EMBO Rep.*, **5**, 715–720.
54. Lever,M.A., Th'ng,J.P., Sun,X. and Hendzel,M.J. (2000) Rapid exchange of histone H1.1 on chromatin in living human cells. *Nature*, **408**, 873–876.
55. Th'ng,J.P., Sung,R., Ye,M. and Hendzel,M.J. (2005) H1 family histones in the nucleus. Control of binding and localization by the C-terminal domain. *J. Biol. Chem.*, **280**, 27809–27814.
56. Misteli,T., Gunjan,A., Hock,R., Bustin,M. and Brown,D.T. (2000) Dynamic binding of histone H1 to chromatin in living cells. *Nature*, **408**, 877–881.
57. Stasevich,T.J., Mueller,F., Brown,D.T. and McNally,J.G. (2010) Dissecting the binding mechanism of the linker histone in live cells: an integrated FRAP analysis. *EMBO J.*, **29**, 1225–1234.
58. Schmiedeberg,L., Weisshart,K., Diekmann,S., Meyer Zu Hoerste,G. and Hemmerich,P. (2004) High- and low-mobility populations of HP1 in heterochromatin of mammalian cells. *Mol. Biol. Cell.*, **15**, 2819–2833.
59. Cheutin,T., McNairn,A.J., Jenuwein,T., Gilbert,D.M., Singh,P.B. and Misteli,T. (2003) Maintenance of stable heterochromatin domains by dynamic HP1 binding. *Science*, **299**, 721–725.
60. Clarkson,M.J., Wells,J.R., Gibson,F., Saint,R. and Tremethick,D.J. (1999) Regions of variant histone His2AvD required for Drosophila development. *Nature*, **399**, 694–697.
61. Lu,P.Y., Levesque,N. and Kobor,M.S. (2009) NuA4 and SWR1-C: two chromatin-modifying complexes with overlapping functions and components. *Biochem. Cell Biol.*, **87**, 799–815.
62. Cai,Y., Jin,J., Florens,L., Swanson,S.K., Kusch,T., Li,B., Workman,J.L., Washburn,M.P., Conaway,R.C. and Conaway,J.W. (2005) The mammalian YL1 protein is a shared subunit of the TRRAP/TIP60 histone acetyltransferase and SRCAP complexes. *J. Biol. Chem.*, **280**, 13665–13670.
63. Ruhl,D.D., Jin,J., Cai,Y., Swanson,S., Florens,L., Washburn,M.P., Conaway,R.C., Conaway,J.W. and Chrivia,J.C. (2006) Purification of a human SRCAP complex that remodels chromatin by incorporating the histone variant H2A.Z into nucleosomes. *Biochemistry*, **45**, 5671–5677.
64. Doyon,Y., Selleck,W., Lane,W.S., Tan,S. and Cote,J. (2004) Structural and functional conservation of the NuA4 histone acetyltransferase complex from yeast to humans. *Mol. Cell. Biol.*, **24**, 1884–1896.
65. Auger,A., Galarneau,L., Altaf,M., Nourani,A., Doyon,Y., Utley,R.T., Cronier,D., Allard,S. and Cote,J. (2008) Eaf1 is the platform for NuA4 molecular assembly that evolutionarily links chromatin acetylation to ATP-dependent exchange of histone H2A variants. *Mol. Cell. Biol.*, **28**, 2257–2270.
66. Hardy,S., Jacques,P.E., Gevry,N., Forest,A., Fortin,M.E., Laflamme,L., Gaudreau,L. and Robert,F. (2009) The euchromatic and heterochromatic landscapes are shaped by antagonizing effects of transcription on H2A.Z deposition. *PLoS Genet.*, **5**, e1000687.
67. Wu,R.S., Tsai,S. and Bonner,W.M. (1982) Patterns of histone variant synthesis can distinguish G0 from G1 cells. *Cell*, **31**, 367–374.
68. Ramaswamy,A., Bahar,I. and Ioshikhes,I. (2005) Structural dynamics of nucleosome core particle: comparison with nucleosomes containing histone variants. *Proteins*, **58**, 683–696.
69. Ha,T., Enderle,T., Ogletree,D.F., Chemla,D.S., Selvin,P.R. and Weiss,S. (1996) Probing the interaction between two single molecules: fluorescence resonance energy transfer between a single donor and a single acceptor. *Proc. Natl Acad. Sci. USA*, **93**, 6264–6268.
70. Rasmussen,T.P., Huang,T., Mastrangelo,M.A., Loring,J., Panning,B. and Jaenisch,R. (1999) Messenger RNAs encoding mouse histone macroH2A1 isoforms are expressed at similar levels in male and female cells and result from alternative splicing. *Nucleic Acids Res.*, **27**, 3685–3689.
71. Kustatscher,G., Hothorn,M., Pugieux,C., Scheffzek,K. and Ladurner,A.G. (2005) Splicing regulates NAD metabolite binding to histone macroH2A. *Nat. Struct. Mol. Biol.*, **12**, 624–625.

72. Tay,S.K., Blythe,J. and Lipovich,L. (2009) Global discovery of primate-specific genes in the human genome. *Proc. Natl Acad. Sci. USA*, **106**, 12019–12024.
73. Angelov,D., Verdel,A., An,W., Bondarenko,V., Hans,F., Doyen,C.M., Studitsky,V.M., Hamiche,A., Roeder,R.G., Bouvet,P. *et al.* (2004) SWI/SNF remodeling and p300-dependent transcription of histone variant H2ABbd nucleosomal arrays. *EMBO J.*, **23**, 3815–3824.
74. Hardy,S. and Robert,F. (2010) Random deposition of histone variants: a cellular mistake or a novel regulatory mechanism? *Epigenetics*, **5**, 368–372.
75. Papamichos-Chronakis,M., Watanabe,S., Rando,O.J. and Peterson,C.L. (2011) Global regulation of H2A.Z localization by the INO80 chromatin-remodeling enzyme is essential for genome integrity. *Cell*, **144**, 200–213.
76. Jensen,K., Santisteban,M.S., Urekar,C. and Smith,M.M. (2011) Histone H2A.Z acid patch residues required for deposition and function. *Mol. Genet. Genomics.*, **285**, 287–296.
77. Wu,W.H., Alami,S., Luk,E., Wu,C.H., Sen,S., Mizuguchi,G., Wei,D. and Wu,C. (2005) Swc2 is a widely conserved H2AZ-binding module essential for ATP-dependent histone exchange. *Nat. Struct. Mol. Biol.*, **12**, 1064–1071.
78. Jin,C., Zang,C., Wei,G., Cui,K., Peng,W., Zhao,K. and Felsenfeld,G. (2009) H3.3/H2A.Z double variant-containing nucleosomes mark 'nucleosome-free regions' of active promoters and other regulatory regions. *Nat. Genet.*, **41**, 941–945.
79. Jin,C. and Felsenfeld,G. (2007) Nucleosome stability mediated by histone variants H3.3 and H2A.Z. *Genes Dev.*, **21**, 1519–1529.
80. Chadwick,B.P. and Willard,H.F. (2001) A novel chromatin protein, distantly related to histone H2A, is largely excluded from the inactive X chromosome. *J. Cell. Biol.*, **152**, 375–384.
81. Ishibashi,T., Li,A., Eirin-Lopez,J.M., Zhao,M., Missiaen,K., Abbott,D.W., Meistrich,M., Hendzel,M.J. and Ausio,J. (2010) H2A.Bbd: an X-chromosome-encoded histone involved in mammalian spermiogenesis. *Nucleic Acids Res.*, **38**, 1780–1789.
82. Soboleva,T.A., Nekrasov,M., Pahwa,A., Williams,R., Huttley,G.A. and Tremethick,D.J. (2011) A unique H2A histone variant occupies the transcriptional start site of active genes. *Nat. Struct. Mol. Biol.*, **19**, 25–30.

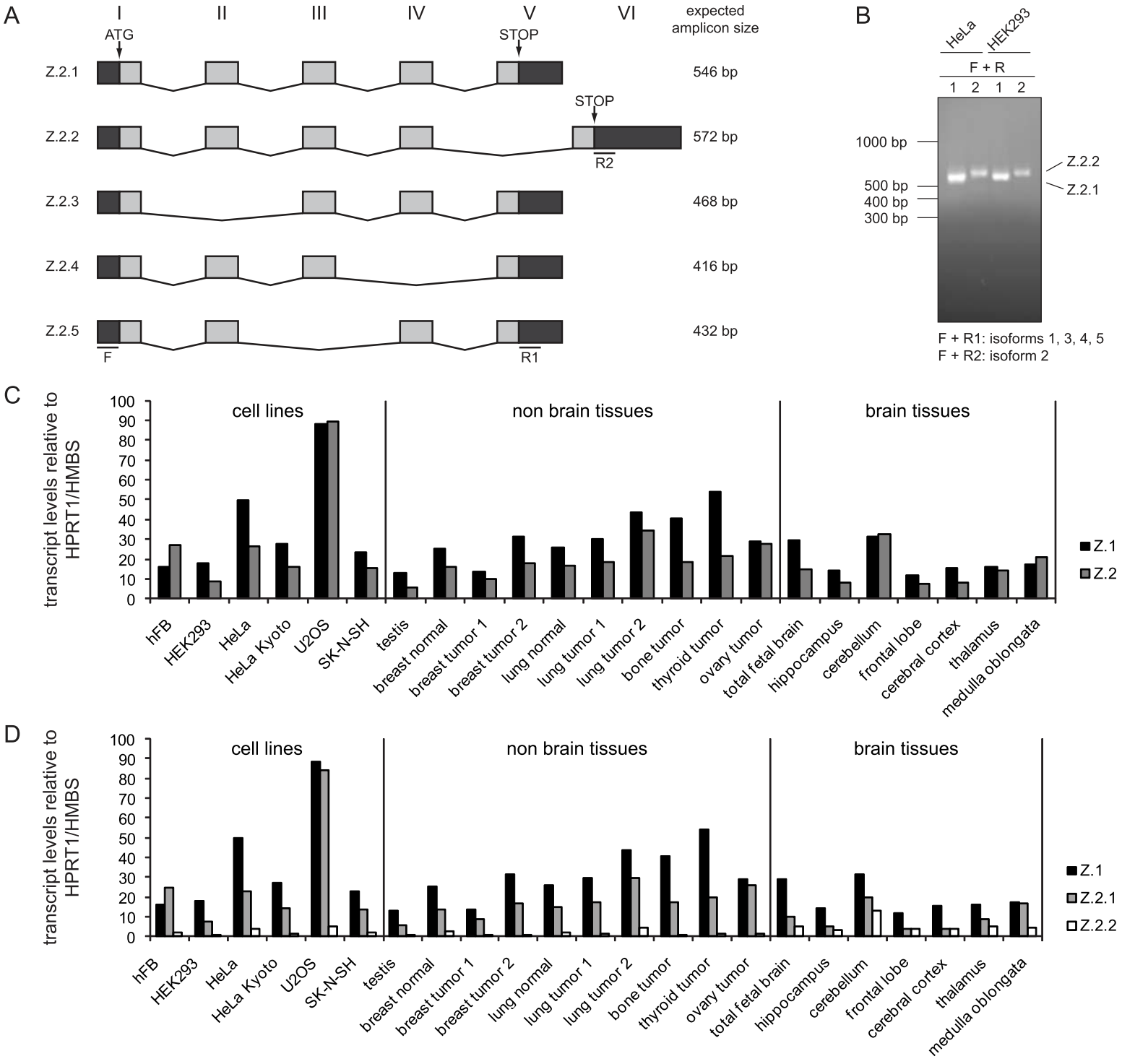

Supplementary Figure S1: Identification of Z.2.2.

(A) Schematic representation of exon/intron structure of the predicted five alternative human Z.2 (H2AFV) splice forms (http://www.ncbi.nlm.nih.gov/gene/94239). Untranslated sequences (UTR) are depicted in dark gray, coding regions in light gray and introns as kinked lines. Sizes of exons/introns are not drawn to scale. Primers used to amplify specific splice forms by PCR (see Supplementary Figure S1B) are shown as F (hybridizes to 5'UTR of all spliced mRNAs), R1 (specific for exon V of splice forms 1, 3, 4 and 5) and R2 (specific for exon VI of H2A.Z.2.2). Expected PCR amplicon sizes of each splice form are indicated on the right. **(B)** Agarose gel to visualize amplified DNA after PCR with cDNA generated from HeLa and HEK293 total RNA, respectively, using F+R1 (A, lanes 1 and 3) or F+R2 (B, lane 2 and 4) primer pairs. Expression levels of Z.1 and Z.2 (Z.2.1 + Z.2.2), and **(C)** of Z.1, Z.2.1 and Z.2.2 **(D)** mRNAs measured by qPCR and normalized to HPRT1 and HMBS. Controls generated without reverse transcriptase (no RT) were used to assess amplification threshold. **(E)** Immunoblot with recombinant Z.2.1, recombinant Z.2.2 and acid extracted HeLa histones to validate specificity of both, rat monoclonal and rabbit polyclonal antibodies (top). Equal loading was ensured by Ponceau staining of the membrane before antibody incubation (bottom).

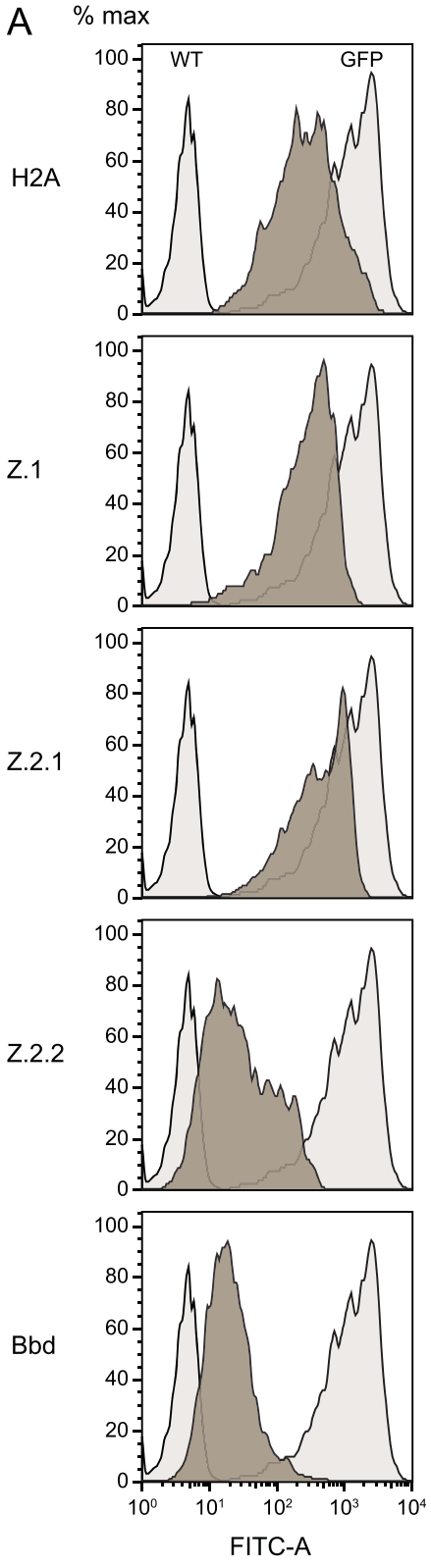

cell line	FITC-A (MFI)
WT	4,55
GFP	1583,25
H2A	431,85
Z.1	356,82
Z.2.1	546,64
Z.2.2	52,18
Bbd	30,86

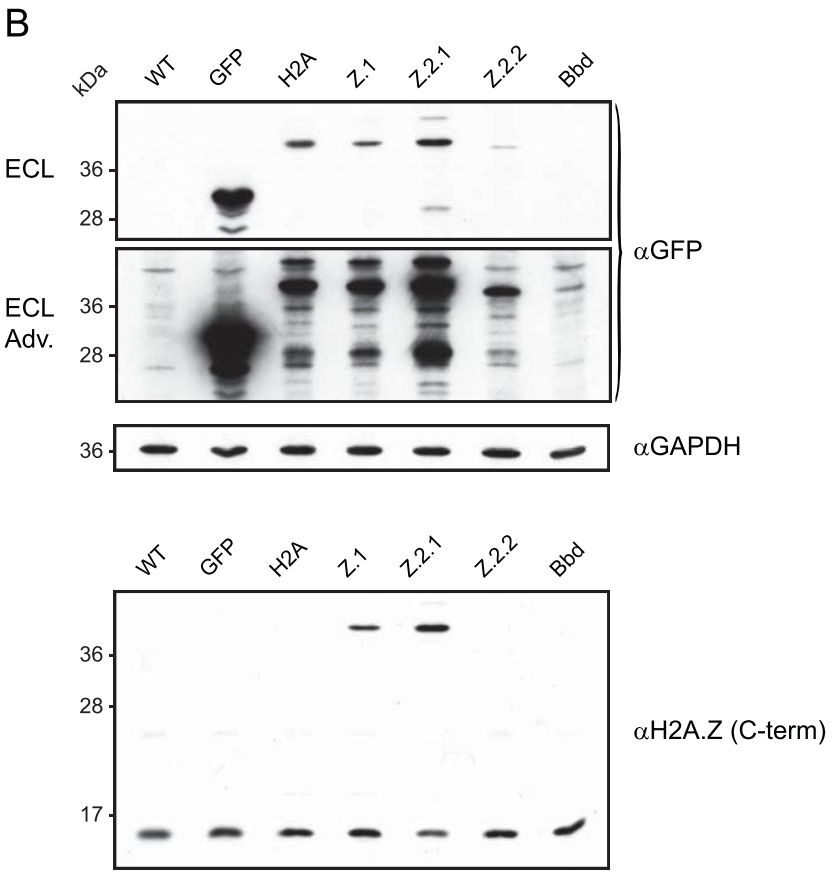

Supplementary Figure S2: Characterization of HeLa Kyoto cell lines stably expressing GFP-H2A variants.
(A) FACS profiles of representative HeLa Kyoto cell lines (single cell clones, dark gray) used in this study. WT and GFP controls (light gray) are shown for comparison. Table of mean fluorescence intensity (MFI) is shown on the right. **(B)** Immunoblot of whole cell extracts prepared from HeLa Kyoto cell lines stably expressing GFP-H2A variants. Immunoblot with αGFP antibody (top) to compare expression levels of different GFP-H2A variants. Expression of GFP-Z.2.2 and GFP-Bbd is much lower than for the other variants and GFP-Bbd is only detectable using ECL Advance. Equal loading was ensured by αGAPDH antibody. Immunoblot with antibody against H2A.Z C-terminus (bottom) shows similar expression of GFP tagged Z.1 and Z.2.1 compared with endogenous protein.

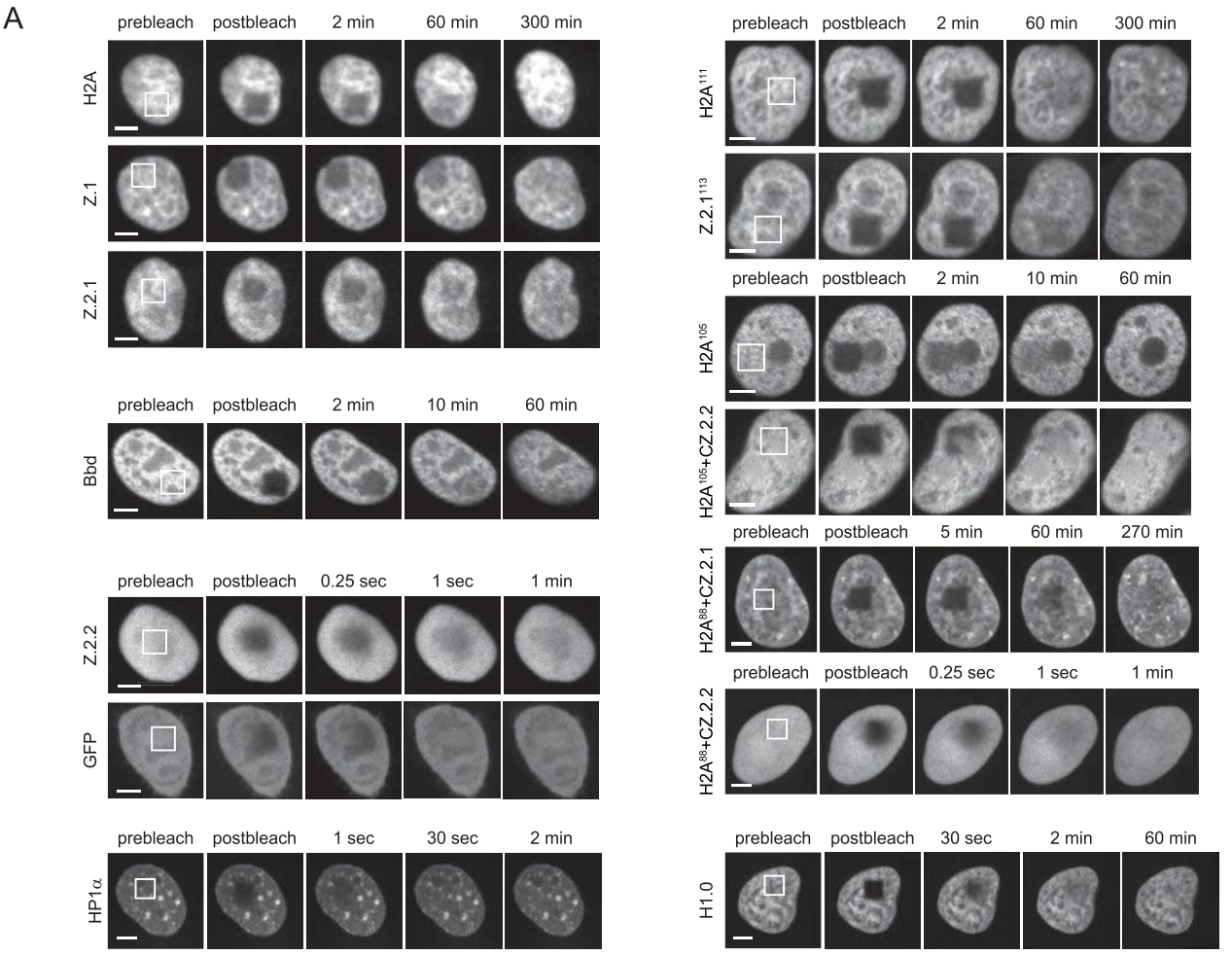
A
prebleach
postbleach
2 min
60 min
300 min
H2A
Z.1
Z.2.1
prebleach
postbleach
2 min
10 min
60 min
Bbd
prebleach
postbleach
0.25 sec
1 sec
1 min
Z.2.2
GFP
prebleach
postbleach
1 sec
30 sec
2 min
HP1α
prebleach
postbleach
2 min
60 min
300 min
H2A111
Z.2.1113
prebleach
postbleach
2 min
10 min
60 min
H2A105
H2A105+CZ.2.2
prebleach
postbleach
5 min
60 min
270 min
H2A88+CZ.2.1
prebleach
postbleach
0.25 sec
1 sec
1 min
H2A88+CZ.2.2
prebleach
postbleach
30 sec
2 min
60 min
H1.0

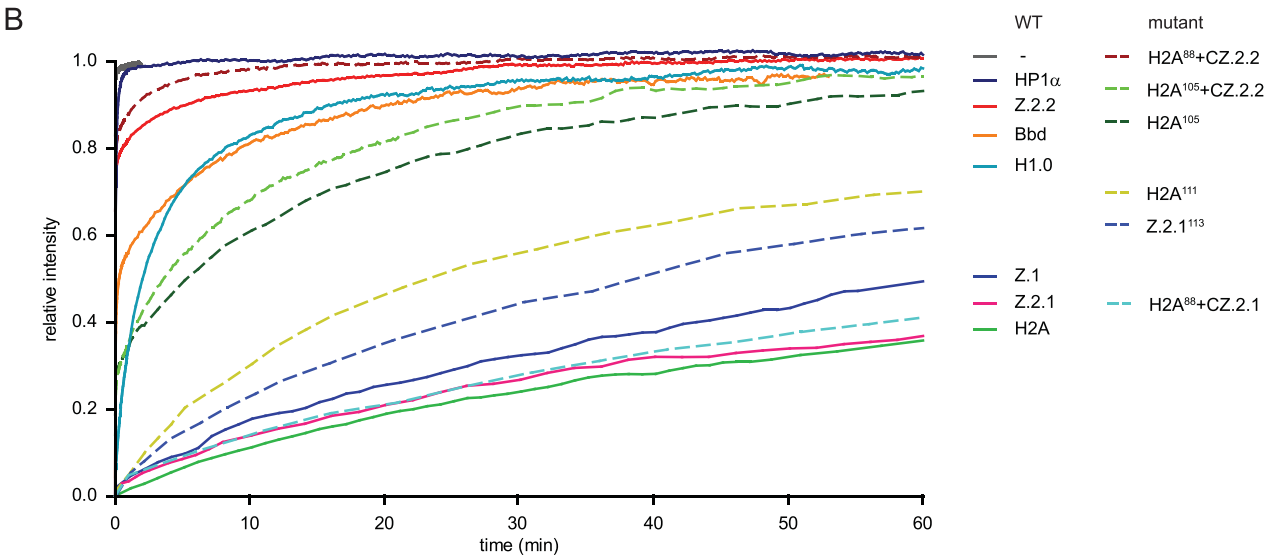
B
relative intensity
1.0
0.8
0.6
0.4
0.2
0.0
0
10
20
30
40
50
60
time (min)
WT
-
HP1α
Z.2.2
Bbd
H1.0
Z.1
Z.2.1
H2A
mutant
H2A88+CZ.2.2
H2A105+CZ.2.2
H2A105
H2A111
Z.2.1113
H2A88+CZ.2.1

C

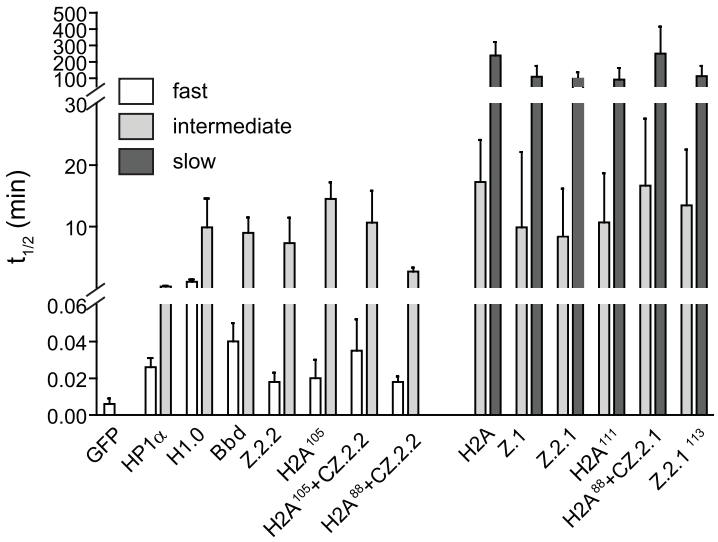

D

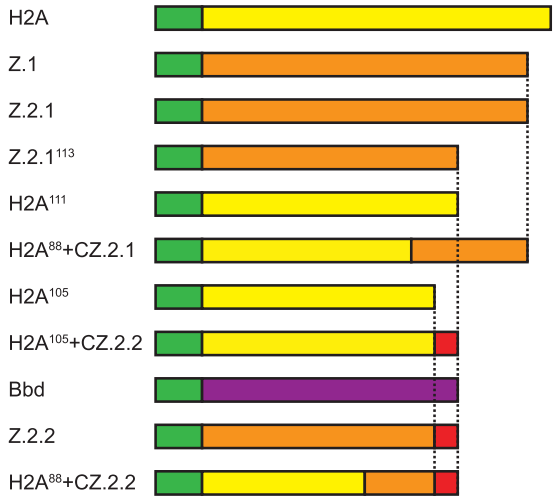

E

	N	$t_{1/2}$			fraction [%]		
		fast (s)	intermediate (min)	slow (h)	fast	intermediate	slow
GFP	17	0.4 ± 0.2	-	-	100	-	-
HP1α	14	1.6 ± 0.3	0.3 ± 0.1	-	82 ± 6	18 ± 6	-
H1.0	15	61.8 ± 23.5	9.9 ± 4.7	-	61 ± 13	39 ± 13	-
Bbd	14	2.5 ± 0.8	9.0 ± 2.5	-	52 ± 7	48 ± 7	-
Z.2.2	29	1.1 ± 0.3	7.3 ± 4.1	-	78 ± 8	22 ± 8	-
$H2A^{105}$	10	1.4 ± 0.3	14.5 ± 2.7	-	32 ± 4	68 ± 4	-
$H2A^{105}$+CZ.2.2	14	2.1 ± 1.0	10.6 ± 5.2	-	30 ± 10	70 ± 10	-
$H2A^{88}$+CZ.2.2	15	1.1 ± 0.2	2.7 ± 0.6	-	83 ± 8	17 ± 8	-
H2A	24	-	17.3 ± 6.8	4.0 ± 1.4	-	25 ± 9	75 ± 9
Z.1	13	-	8.4 ± 7.7	1.6 ± 0.7	-	18 ± 11	82 ± 11
Z.2.1	15	-	16.8 ± 9.5	4.9 ± 2.5	-	28 ± 8	72 ± 8
$H2A^{111}$	14	-	10.7 ± 8.0	1.5 ± 1.2	-	42 ± 19	58 ± 19
$H2A^{88}$+CZ.2.1	25	-	16.7 ± 10.9	4.2 ± 2.7	-	28 ± 13	72 ± 13
$Z.2.1^{113}$	13	-	13.5 ± 9.1	1.9 ± 1.1	-	44 ± 18	56 ± 18

Supplementary Figure S3: FRAP analysis of GFP-H2A variants.
(A) FRAP experiment to evaluate nucleosomal stability of wild type and mutant H2A variants using spinning disk confocal microscopy. A small nuclear area (box) of HeLa Kyoto cells expressing GFP-tagged H2A variants, H1.0, HP1α or GFP alone was photobleached and the recovery of the fluorescent signal was monitored for up to 5 hours. For each construct, selected time points of one exemplary time series are shown. Scale bar = 5 µm. **(B)** Long-term (60 min) FRAP quantification curves of average GFP signal recovery after photobleaching relative to flourescence intensity prior to bleaching are depicted for wild type (solid lines) and mutant (dashed lines) GFP-tagged H2A variant constructs, H1.0, HP1α and GFP. Mean curves of 10 to 29 individual cells are shown for each construct. For clarity error bars are omitted. (See also Figure 3B and 3C for short-term FRAP curves and Supplementary Figure S2E for numerical values and standard deviations). **(C)** Quantitative evaluation of FRAP curves. Plot shows calculated half-time of recovery ($t_{1/2}$) values of different control constructs, wild type and mutant H2A variant constructs based on bi-exponential fitting of FRAP data (± standard deviation (SD), see Fig. S2E for numerical values) **(D)** Schematic representation of GFP-tagged (green box) H2A variants deletion and domain swap constructs used in FRAP studies. H2A is depicted in yellow, Bbd in purple, Z.1/.2.1/.2.2 in orange with Z.2.2's unique C-terminal amino acids highlighted in red. **(E)** Table of mean half-time of recoveries ($t_{1/2}$) and respective mobility fraction sizes (± SD) as determined from exponential fitting. While a single exponential function was sufficient to fit GFP alone, all other GFP fusion proteins were fitted with a bi-exponential function identifying either a fast ($t_{1/2}$ < 62 s) and an intermediate fraction ($t_{1/2}$ 0.3-20 min), or an intermediate and a slow fraction ($t_{1/2}$ > 1.5 h).

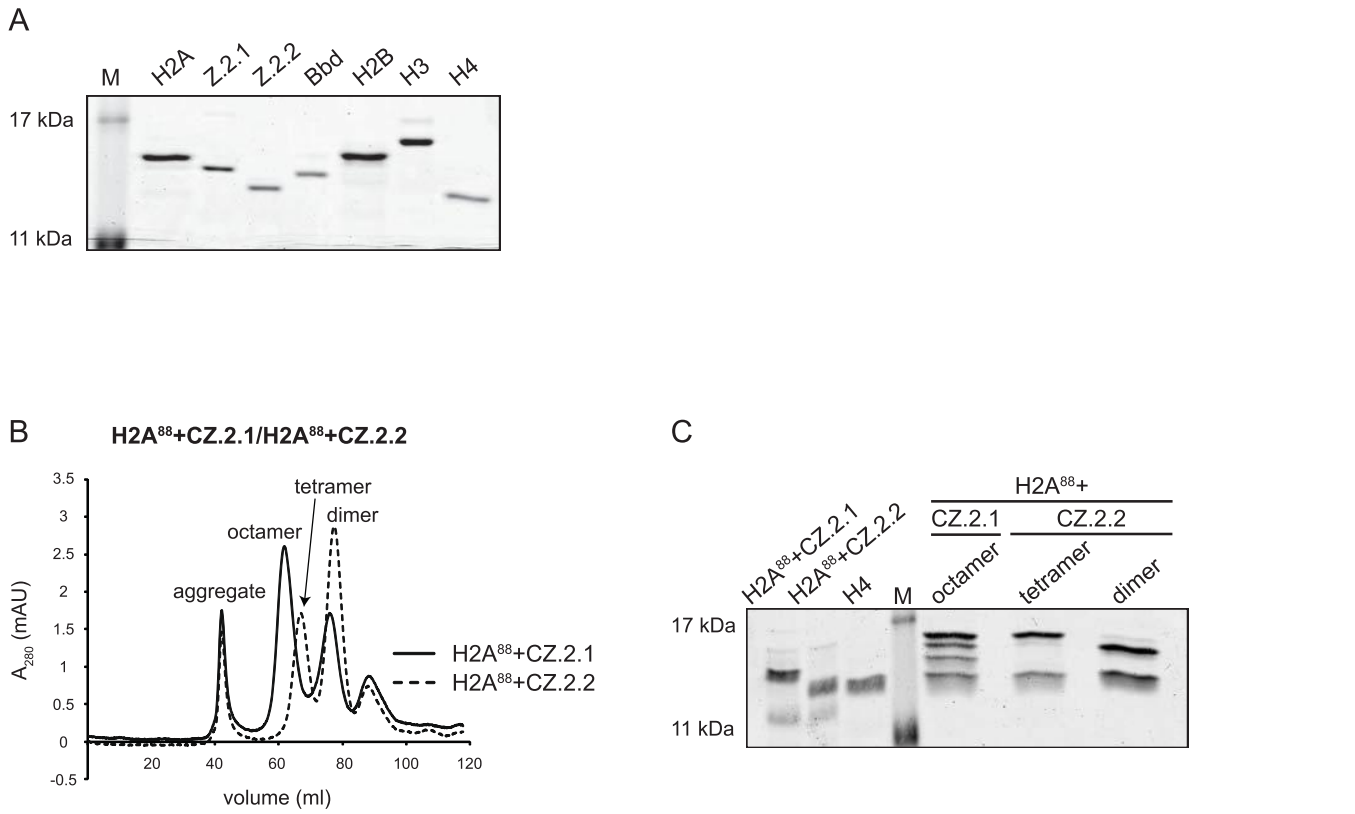

Supplementary Figure S4: Z.2.2 destabilizes histones octamers in a sequence-dependent manner.
(A) Evaluation of purity of recombinant human histone proteins. Human core histones (H3, H4, H2B, H2A) and H2A variants Bbd, Z.2.1 and Z.2.2 were expressed in E. coli. After purification, recombinant proteins were separated on 18% SDS-PAGE and stained with Coomassie brilliant blue. **(B)** Size exclusion chromatography of refolding reactions using recombinant histones, as described in Figure 6, but with the use of $H2A^{88}$+CZ.2.1 (solid line) and $H2A^{88}$+CZ.2.2 (dashed line) proteins instead of H2A. **(C)** Fractions corresponding to octamers, tetramers and dimers depicted in Supplementary Figure S4B were analyzed by 18% SDS-PAGE and stained with Coomassie brilliant blue.

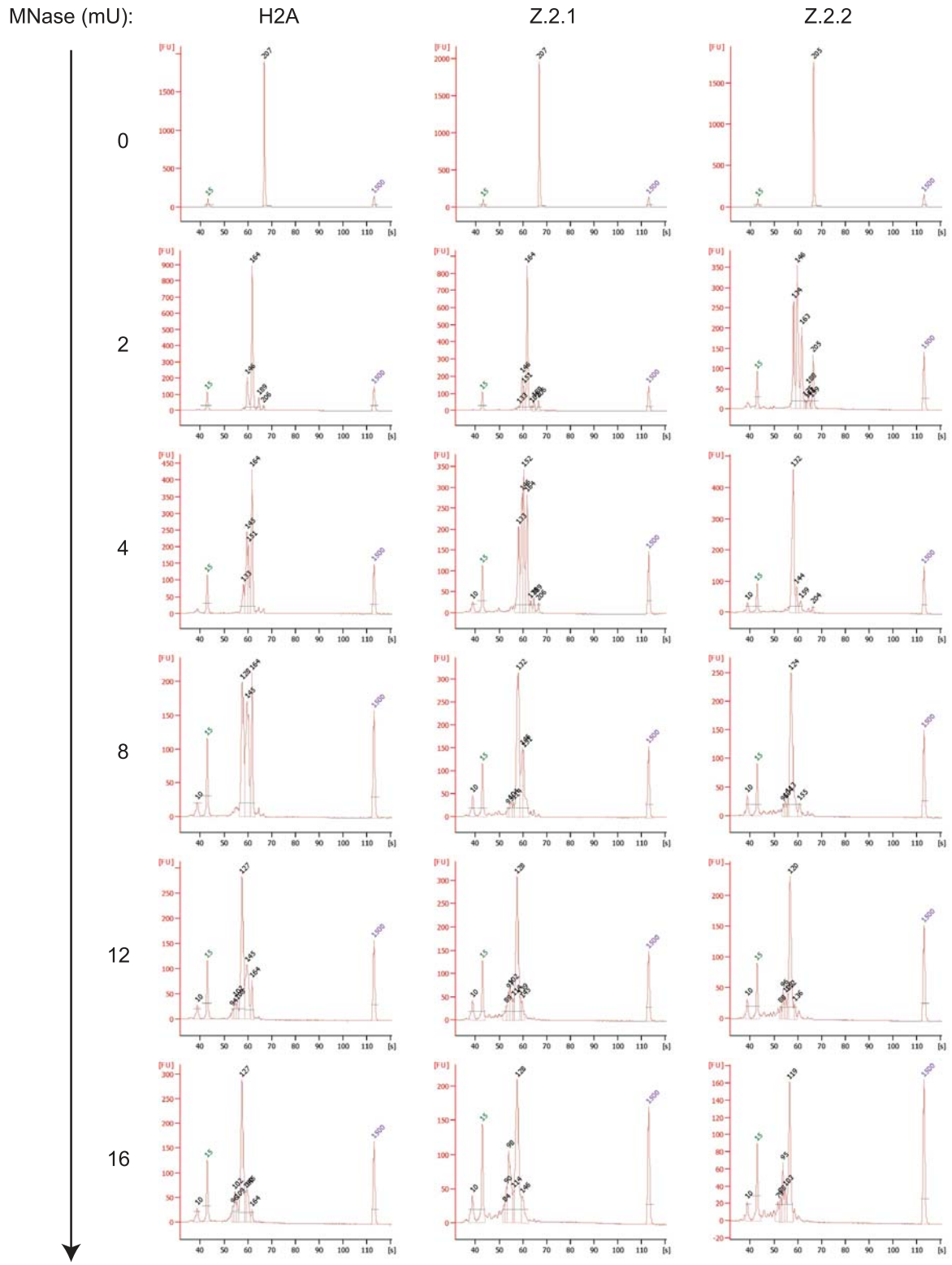

Supplementary Figure S5: MNase digest of mononucleosomes containing different H2A variants.
Electropherograms of deproteinized DNA fragments separated on a Bioanalyzer after digestion of mononucleosomes containing either H2A, Z.2.1 or Z.2.2 with increasing amounts of MNase (see also Figure 6C). Numbers indicate respective DNA fragment length in bp.

A

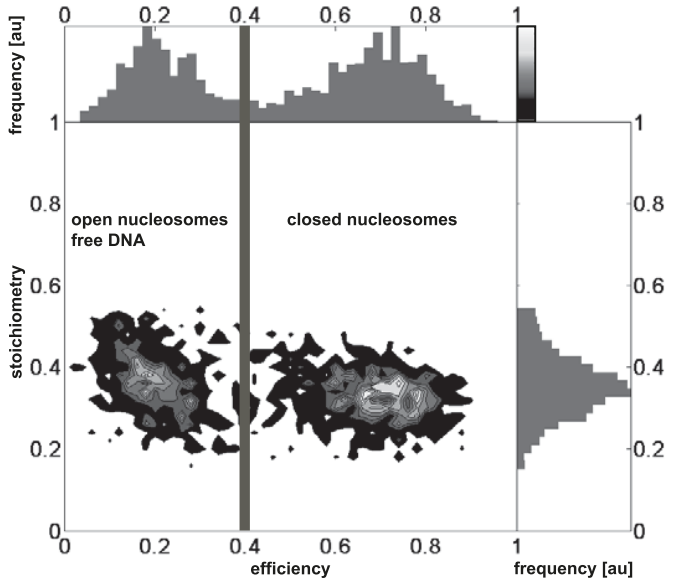

B

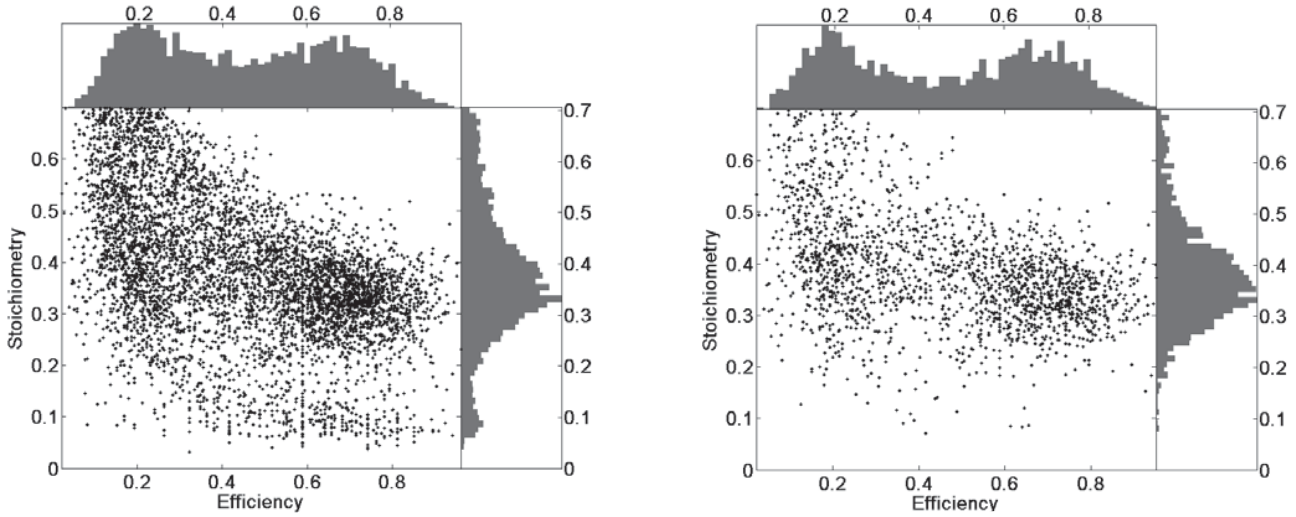

Supplementary Figure S6: smFRET analysis of mononucleosomes containing different H2A variants.
(A) Exemplary two-dimensional FRET efficiency versus stoichiometry histogram showing H2A Nucleosomes at 0 mM NaCl. Data is filtered using TDS < 1 and TDSred-PIE < 0.6 and a stoichiometry threshold (S = 0.15 – 0.55). The separation between low and high FRET at E = 0.4 (40% FRET efficiency) used to analyze the data presented here is marked by a dark grey line. **(B)** Composite of raw data, TDS and additional dynamic filter. The two dimensional plot of stoichiometry versus FRET efficiency recorded with a mononucleosome sample containing Z.2.1 (TE pH 7.6), together with the one-dimensional projections. Besides dual labeled nucleosomes, the sample contained also impurities of donor and acceptor only complexes. Only bursts within a stoichiometry range of S = 0 – 0.7 are shown. The high concentration of molecules in the sample combined with the significant amount of single labeled impurities cause strong multi-molecular trailing (left). A significant improvement of the data quality is reached by removing the multi-molecule events using TDS < 0.6 and TDSred-PIE < 0.6 (right).

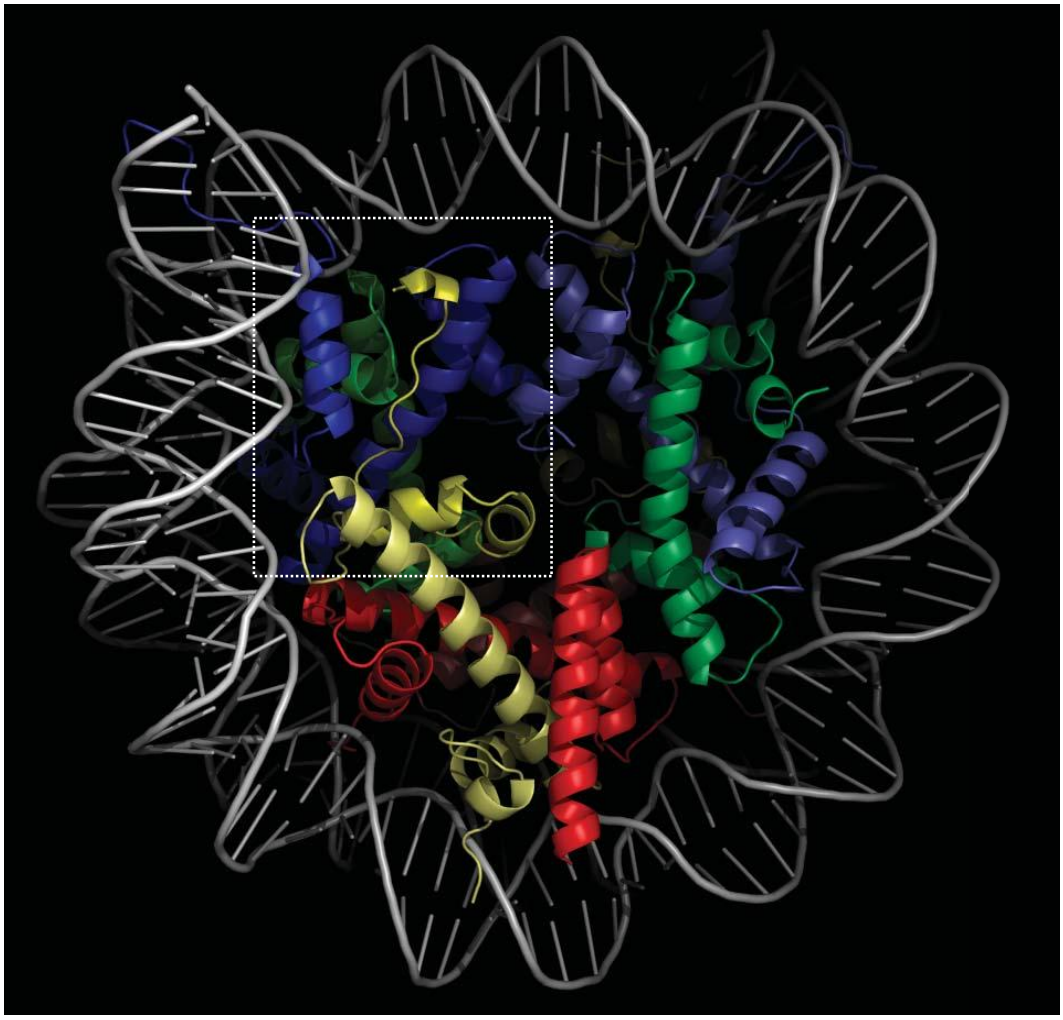

Supplementary Figure S7: Simulation of Z.1-containing nucleosome.
In silico model of nucleosome based on H2A.Z published crystal structure data (50) containing Z.1 (yellow), H2B (red), H3 (blue), H4 (green) and DNA (gray). Box highlights region depicted in Figure 8A.

"H2A.Z.2.2 is an alternatively spliced histone H2A.Z variant that causes severe nucleosome destabilization" by Bönisch et al.

SUPPLEMENTARY MATERIALS AND METHODS

Cell culture, transfection, FACS analysis and cloning

Cell lines were grown in DMEM medium (PAA) supplemented with 10% FCS (Sigma) and 1% penicillin/streptomycin or 50 µg/ml gentamicin (C127 cells) at 37°C and 5% CO_2. The following human cell lines were used in this study: HEK293 (embryonic kidney), HeLa (cervix carcinoma), HeLa Kyoto (cervix carcinoma), U2OS (osteosarcoma), hFB (fibroblasts), SK-N-SH (neuroblastoma), and the following mouse cell lines were used: NIH3T3 and C127. Human cell lines were transfected using FuGene HD (Roche Applied Science) and mouse C127 cells were transiently transfected using Lipofectamine 2000 (Invitrogen) according to the manufacturer's instructions. Z.2.1 and Z.2.2 were cloned from HeLa cDNA into pT7blue3 (Novagen). For expression in human cells, Z.2.1, Z.2.2, Bbd and deletion or domain swap mutants were cloned into the pEGFP-C1 vector (Clontech) to generate N-terminally tagged proteins. For simplicity eGFP-tagged constructs are referred to as GFP-tagged throughout the text. Plasmids coding for GFP-H2A (H2A type 1, NP_003501.1) and GFP-Bbd (H2A.Bbd type 2/3, NP_542451.1) were kindly provided by Emily Bernstein. The plasmid coding for GFP-Z.1 was a gift from Sachihiro Matsunaga, the H1.0-GFP construct was kindly given by M.J. Hendzel (1) and the GFP-HP1α construct was provided by T. Misteli (2). Stable cell lines were selected with 600 µg/ml G418 (PAA) and individual cell clones sorted by using a FACSAria machine (Becton Dickinson). Expression levels of GFP-proteins were quantified by using a FACSCanto machine (Becton Dickinson). For expression in *E. coli*, Z.2.1, Z.2.2, Bbd and domain swap mutants were cloned into the pET-21a(+) vector (Novagen). Plasmids for expression of recombinant human H2A, H2B, H3 and H4 were kindly provided by Robert Schneider. Cloning and PCR amplification accuracy was verified by sequencing (MWG).

Histone extraction, RP-HPLC purification, cellular fractionation, MNase digestion, sucrose gradient fractionation and salt stability experiments

Acid extraction of histones was done as previously described (3). Histones from HEK293 cells were separated by RP-HPLC as previously described (4). Fractions were dried under vacuum and stored at -20°C.

Fractionation experiments were carried out as described previously (5) with minor changes. Briefly, 2 x 10^7 cells were resuspended in 1 ml buffer A supplemented with 0.1% NP40, incubated for 10 min and collected by centrifugation. The pellet was washed once with buffer A and incubated in buffer B for 30 min. The resulting chromatin pellet was washed once with buffer B and resuspended in SDS loading buffer (chromatin fraction). After sonification (Diagenode Bioruptor) and denaturation, nucleic acids were degraded by benzonase (VWR) treatment. All centrifugations were performed at 6.500 *g* for 5 min at 4°C except the final one (20.000 *g* for 20 min at 4°C). The soluble fraction was obtained by combining the supernatants of all centrifugations (incl. washing steps). Proteins were pelleted as described (6) and resuspended in SDS loading buffer. Identical cell equivalents of soluble and chromatin fractions were analyzed by immunoblotting.

For MNase digestion, chromatin was prepared from 5 x 10^7 HK cells stably expressing GFP-Z.2.2 as described above, resuspended in 500 µl EX100 (10 mM HEPES pH 7.6, 100 mM NaCl, 1.5 mM $MgCl_2$, 0.5 mM EGTA, 10 % (v/v) glycerol, 1 mM DTT, 1 x Roche protease inhibitors) and digested with 1.5 U MNase (Sigma) for 20 min at 26°C. The reaction was stopped by addition of EGTA to a final concentration of 10 mM and centrifuged (3.200 *g* for 20 min at 4°C). A gradient of 5%-35% sucrose in EX100 was prepared using a Gradient Master (Biocomp), 400 µl of the supernatant after MNase digest were loaded on top and ultracentrifuged (30.000 rpm for 18 h at 4°C using a Beckmann SW41 rotor). Afterwards, 500 µl fractions were manually taken from top and analyzed for DNA content after RNase A and Proteinase K digest by agarose gel electrophoresis. Purity of mononucleosome containing fractions was verified using DNA 1000 reagents (Agilent Technologies) with the 2100 Bioanalyzer (Agilent Technologies). Pure mononucleosome fractions were combined, concentrated by TCA precipitation and analyzed by immunoblot.
For salt stability assays (7), chromatin was prepared in the same manner as in fractionation experiments. After washing with buffer B, chromatin was incubated with incubation buffer (10 mM TrisHCl pH 7.5, 1 mM DTT, 1 mM EDTA, 1x protease inhibitors (Roche Applied Science), 0.1% Triton X-100) containing different salt concentrations ranging from 50 mM to 600 mM NaCl for 1 h at room temperature. Chromatin was pelleted, solubilized in the same manner as in fractionation experiments and analyzed by immunoblotting.

FRAP and exponential fitting

FRAP experiments were performed using an UltraVIEW VoX spinning disk microscope system (PerkinElmer) equipped with a heated environmental chamber and CO_2 perfusion as previously described (4) with the following changes. To determine short-term recovery kinetics, 2D time series were recorded for 2 min to 1 h with time intervals between 0.1 s and 1 min depending on the recovery kinetics of the construct. For long-term recovery kinetics, image z-stacks were recorded with intervals between 1 min and 5 min. The central 3-5 image planes were average projected for quantitative evaluation. To correct for cell-to-cell differences in bleaching depth, the normalized mean intensity values of the first postbleach values were linearly interpolated to determine an estimated value for the time point t = 0. This value was subtracted from all mean fluorescence values after previous double normalization to correct for potential gain or loss of total fluorescence, e.g. by import and bleaching-by-acquisition.
The normalized FRAP curves were further evaluated and quantified by a commonly used fitting procedure (8): A sum of exponential time dependencies can be used to describe the intensity I(t) of the fluorescence recovery.

$$I(t) = I_0 * (1 - \sum_i A_i * e^{-\alpha_i t})$$

To discriminate at least two different species within our sample, we restricted our self to the bi-exponential case, where $A_1 + A_2 = 1$. Therefore the parameters α_1, α_2 and A had to be determined from the individual recovery curves by a least-square optimization algorithm. This was carried out automatically by a self-made python (www.python.org) script, which applied the *leastsq* function from the *scipy.optimize* package (www.scipy.org). Only curves with a reasonable set of resulting parameters were taken into account for the final summary, wherein the exponents α are transformed into their corresponding, more intuitive half-times of recovery.

$$T_1 = \frac{\ln 2}{\alpha_1}$$

Most of the recovery data were described adequately by this bi-exponential characteristic, manifested in a close approximation by the fitted curve. An evaluation of the goodness of the fits was therefore not necessary. However, in some experiments where GFP alone was expressed, a single exponential curve already allowed a sufficiently close approximation. Applying the bi-exponential model to these data sets leads to two almost identical exponentials, showing the invalidity of the more complex model. This categorization allowed us therefore to distinguish between two types of complexity: One type with only a single mobile species and on the other hand the case, where at least two mobile species are apparent. Extension to three mobile species did typically not result in significant improvement of the fits.

Stable isotope labeling with amino acids in cell culture (SILAC) and mass spectrometry (MS) identification of H2A.Z-specific chaperone complexes

HeLa cells expressing GFP-Z.2.1 or GFP-Z.2.2 were SILAC labeled and nuclear extracts were prepared as described before (9). Nuclear extracts were diluted in incubation buffer (150 mM NaCl, 50 mM Tris-HCl pH 8.0, 0.25% NP40) supplemented with complete protease inhibitors w/o EDTA (Roche) and 0.5 mM DTT to a concentration of 1.5 µg/µl. 400 µl solution were incubated with GFP trap (Chromotek) for 3 h at 4°C. Beads were washed 3 times with 1 ml incubation buffer, combined and eluted by boiling in loading buffer. Samples were loaded on 1D NuPAGE gels (Invitrogen), lanes cut into 8 slices, in gel digested with trypsin and desalted by stage tipping. Mass spectrometry (MS) was performed on an LTQ Orbitrap mass spectrometer as described before (10). Peptides were separated online to the mass spectrometer by using an easy nano-LC system (Proxeon Biosystems) with a 15-cm fused silica emitter with an inner diameter of 75 µm packed in house with RP ReproSil-Pur C18-AQ 3 µm resin (Dr. Maisch). Peptides were eluted with a segmented gradient from 5% to 60% B with a constant flow of 0.25 ml/min (solvent B: 80% acetonitrile, 0.5% acetic acid) over 110 min.

The MS was operated in data dependent mode. A full scan MS (m/z 300 - 1650) was acquired in the Orbitrap cell with a resolution of 60,000 at a theoretical m/z ratio of 400 after accumulation of 1,000,000 ions in the C-trap (maximum filling time of 1000 ms); the lock mass option was enabled to improve mass accuracy. The 5 most intense ions from the preview survey scan were isolated (target value of 5,000 ions at a maximum filling time of 150 ms) fragmented by collision-induced dissociation (collision energy 35 %) and measured in the ion trap concurrently to full scan acquisition in the Orbitrap. Precursor ion charge state screening was enabled, and all unassigned charge states as well as singly charged peptides were rejected. The dynamic exclusion list was set to a maximum of 500 entries with a maximum retention period of 90 s and a relative mass window of 5 ppm.

Raw data were analyzed using the MaxQuant software suite (11) (version 1.2.2.7) with the integrated Andromeda search engine (11) at default parameters using the IPI human database version 3.68 concatenated with a database containing common contaminants. For further analysis we removed contaminants and defined a ratio cutoff of 4 (Z.2.1 pull-down) and 0.25 (Z.2.2 pull-down). A complete list of all proteins identified is found in Supplementary Table S1.

EdU replication labeling, *in situ* extraction and fluorescence microscopy to assay cell cycle dependent GFP-Z.2.2 chromatin incorporation

C127 cells were pulse labeled for 25 min with 10 μM 5-ethynyl-2′-deoxyuridine (EdU, Baseclick) 48 h after transfection with GFP-Z.2.1 or -Z.2.2 plasmids, and immediately subjected to *in situ* extraction or fixation. For *in situ* extraction, GFP-Z.2.2 transfected cells were washed with PBS and incubated 15 sec in permeabilization buffer (0.1% Triton X-100, 150 mM NaCl in PBS). Thereafter, cells were fixed for 10 min at room temperature with 2% formaldehyde (Sigma) in PBS containing 0.1% Triton X-100. Cells expressing GFP-Z.2.1 were not *in situ* extracted and were fixed with 2% formaldehyde in PBS for 10 min at room temperature. All washing steps after fixation were performed with 0.02% Tween20 in PBS (PBST). After permeabilization with 0.2% Triton X-100 in PBS for 10 min, cells were blocked for at least 1 h in blocking buffer (2% BSA in PBST). Before EdU-detection, cells were incubated 1 h with GFP-booster (Chromotek) diluted in blocking buffer. Incorporated EdU was detected by incubating cells 30 min in 100 mM Tris-HCl pH 7, 4 mM $CuSO_4$, 20 μM azide dye Alexa Fluor 594 (Invitrogen) and 50 mM sodium ascorbate (adapted from (12)). Cells were counterstained with 200 ng/ml DAPI in PBST for 10 min and mounted on microscope slides in Vectashield mounting medium (Vector Laboratories).
Wide-field imaging was performed on a PersonalDV microscope system (Applied Precision) equipped with a 60x/1.42 PlanApo oil objective (Olympus), CoolSNAP ES2 interline CCD camera (Photometrics), Xenon illumination and appropriate filter sets. Image stacks were recorded with a z-distance of 200 nm and subjected to a constrained iterative deconvolution (enhanced ratio, 10 cycles, medium noise filtering, SoftWoRX, 3.7. imaging software package, Applied Precision).

Expression and purification of recombinant human histone proteins in *E.coli*, *in vitro* octamer and mononucleosome reconstitution and MNase digestion of recombinant mononucleosomes

Histones were expressed, purified and assembled into octamers as described (13). DNA for mononucleosome assembly was obtained from a pUC18 plasmid containing 25 repeats of the 601 nucleosome positioning sequence (14) kindly donated by Daniela Rhodes. After AvaI digestion, monomeric DNA was purified by gel electrophoresis and electroeluted using the Elutrap system (Whatman). Assembly of nucleosomes was performed by salt gradient deposition (13,15). For H2A and Z.2.1 nucleosomes, respective octamers and DNA were mixed in a 1:1 ratio; for Z.2.2 nucleosomes, Z.2.2-H2B dimers, $(H3\text{-}H4)_2$ tetramers and DNA were mixed in a 2:1:1 ratio. Assembly of histones on DNA was evaluated by EMSA using 5% native PAGE or native 1.5% agarose gels. Incubation of mononucleosomes for 1 h at 37°C (15) did not change position as evaluated by 5% native PAGE (data not shown). To analyze the histone content of nucleosomes after assembly, the corresponding band was excised from native 1.1% agarose gels, nucleosomes were electroeluted using the Elutrap system and protein content was analyzed by 18% SDS-PAGE after Benzonase treatment by Coomassie staining or immunoblot.
Equal amounts of nucleosomes (1 μg) were digested with different amounts of MNase (Sigma) for 10 min at 37 °C in MNase digest buffer (13.85 mM TrisHCl ph 7.5, 67 mM KCl, 10.75% Glycerol, 1 mM DTT, 5 mM $CaCl_2$). The reaction was stopped by addition of nine volumes of 5 mM EGTA. DNA was deproteinized by phenol/chloroform extraction, ethanol precipitated and analyzed using DNA 1000 reagents (Agilent Technologies) with the 2100 Bioanalyzer (Agilent Technologies).

Single molecule Förster resonance energy transfer (smFRET)

Single molecule burst analysis:

To gain information on salt dependent nucleosome stability single-molecule Förster resonance energy transfer (smFRET) measurements of dual labeled nucleosomes freely diffusing through the focal volume of a confocal microscope were performed. To this end a dual labeled 159 bp DNA was prepared using dye-labeled primers (IBA), a DNA template containing the 601 (14) sequence and six additional bases on each side together with dNTPs (Finnzymes) and the Phusion DNA-polymerase (Finnzymes) in a PCR reaction. Dye labels were at position 65 (donor dye, Tamra) and position 20 on the reverse strand (acceptor dye, Alexa647). A mixture of this labeled DNA and unlabeled DNA (molar ratio of 1:50) was used for mononucleosome assembly (see above).

It is well known, that ultra-low concentrations of nucleosomes are prone to become instable in typical experimental geometries (16). To minimize such effects measurements were performed using a 1:250 mixture of double labeled to unlabeled nucleosomes at a total concentration of 25 nM in commercially available TE buffer (Sigma-Aldrich, pH 7.6) containing 10 mM DTT and 0 mM, 300 mM, 400 mM, 500 mM, 600 mM and 700 mM NaCl, respectively. The samples were incubated at the respective salt concentration for 1 hour at 21°C before a drop of 20 µl was put onto cover slips (Marienfeld) for data collection. The cover slips were cleaned with 2% Hellmanex III (Hellma) and water prior to silanization for 15 min with 2% (3-aminopropyl)triethoxysilane (Sigma-Aldrich) in Acetone, and coating with 40 mg/100 µl polyethylene glycol (mPEG-SVA MW 5000, Laysan Bio Inc.) in ddH_2O for 1 h.

The confocal measurements were performed on a custom built experimental setup using pulsed interleaved excitation (PIE) (17) with lasers at 532 nm (Pico-TA-Picoquant, power before the objective 80µW) and 640 nm (LDH-D-C-640, Picoquant, power before the objective 80 µW) at a repetition rate of 26.66 MHz. The fluorescence was separated for polarization and color and detected on four avalanche-photo-diodes (green channel AQRH-14, red channel AQR-16, Perkin Elmer). Photon arrival times were recorded using four single-photon-counting-modules (Becker&Hickl SPC-150) and data was processed using custom software written in MATLAB (MathWorks). Since the anisotropy of the molecules was not of importance for this study, photons of identical wavelength but different polarization were merged into one detector channel. Data were collected for 10 min and the collected photons were sorted into three different channels, namely donor detection after direct excitation (green), acceptor detection after direct excitation (red) and acceptor detection after donor excitation (fret). Labeled complexes diffusing through the focal volume of the microscope resulted in bursts of detected photons. An all photons burst search (APBS) was applied with the criteria of detecting at least 3 photons within 500 µs with a total of at least 60 photons per burst (18). From the photon bursts, the Stoichiometry (S) and FRET Efficiency (E) were calculated (including the predetermined correction factor) according to:

$$E = \frac{GR}{GR + \gamma * GG} \text{ , and } S = \frac{GR + \gamma * GG}{GR + \gamma * GG + RR}$$

Where GR are the red photons after green excitation, RR are the red photons after red excitation, GG are the green photons after green excitation and y is a factor correcting for the different efficiencies of the red and green detection channels (19). Multi-molecular events were removed from the data as described below using $TDS < 1$ and $TDS_{red\text{-}PIE} < 0.6$ for all complexes not showing molecular dynamics. Remaining

donor-only and acceptor-only bursts were removed using a stoichiometry threshold (S = 0.15 – S = 0.55).
Due to the chosen labeling positions on the nucleosome, closed nucleosomes have the donor and acceptor dyes positioned adjacent to each other leading to a high FRET state with an efficiency of ~80% while open or incomplete nucleosomes show a very low FRET signal. The fraction of closed nucleosomes was quantified for each salt concentration by analyzing how many of the detected fluorescence bursts have $E >$ 40% (Supplementary Figure S6A). The data was normalized to the fraction of closed molecules at 0 mM NaCl to allow for a comparison of the salt dependence for the three investigated samples (H2A, Z.2.1, Z.2.2).

Removal of multi-molecular events
Nucleosomes are prone to become instable at low concentrations as well as when interacting with surfaces. Thus in order to avoid artifacts the duration of the experiment has to be minimized. To address this difficulty relatively high nucleosome concentrations were used in the experiments to ensure that the occurrence of multi-complex bursts is not negligible. For a homogeneous population with only a single FRET species this is not a problem, however if several FRET states exist, multi-molecule events of different species will alter the determined FRET values. Moreover, impurities such as complexes labeled with only donor or acceptor observed simultaneously with double-labeled complexes will also lead to changes in FRET efficiencies. However, as two independently diffusing complexes do not enter and exit the excitation volume exactly at the same time it is possible to differentiate these multi-molecular events from single molecule events and to exclude them from further analysis. Independently diffusing molecules involved in a multi-molecule event will yield different values for the mean-macro-time (i.e. the time where 50% of the respective photons have arrived) for all photons of a burst, as compared to that for the photons of one color. We therefore calculated the characteristic Time-Deviation-Signal (TDS) defined as

$$TDS = \left((D_{total} - D_{green}) + \left|T_{total} - T_{green}\right|\right) * (1 - P) + \left((D_{total} - D_{fret}) + \left|T_{total} - T_{fret}\right|\right) * P * \gamma \quad \textbf{(1)}$$

where D_x is the burst duration, T_x is the mean-macro-time, y is a factor correcting for the different efficiencies of the red and green detection channels and P is the proximity ratio given by the number of photons in the burst as $P = GR/(GR+GG)$.

In eq. 1 we compute the TDS of the green and red channels simultaneously and adjust the relative value to the percentage of photons detected. In addition, multi-molecule events containing low (0%) FRET and donor only complexes (which cannot be found using eq. 1) can also be determined using a PIE setup and defining:

$$TDS_{red-PIE} = (D_{total} - D_{red}) + \left|T_{total} - T_{red}\right| \quad \textbf{(2)}$$

To demonstrate the capabilities of this analysis scheme a sample containing Z.2.1 nucleosomes (TE pH 7.6, 0 mM NaCl) as well as impurities of donor only and acceptor only complexes was measured. In order to stress the discussed effects for this control experiment, the concentration of labeled complexes was increased to ~150 pM. By using thresholds of $TDS < 1$ and $TDS_{red\text{-}PIE} < 0.6$ in the TDS parameter space we are able to remove most of the observed trailing (i.e. events with high S and medium to low E) caused by multi-molecule events as well as photo-physics and receive a distribution showing populations of distinct FRET efficiencies and stoichiometries (Supplementary Figure S6B).

REFERENCES

1. Th'ng, J.P., Sung, R., Ye, M. and Hendzel, M.J. (2005) H1 family histones in the nucleus. Control of binding and localization by the C-terminal domain. *J Biol Chem*, **280**, 27809-27814.
2. Cheutin, T., McNairn, A.J., Jenuwein, T., Gilbert, D.M., Singh, P.B. and Misteli, T. (2003) Maintenance of stable heterochromatin domains by dynamic HP1 binding. *Science*, **299**, 721-725.
3. Shechter, D., Dormann, H.L., Allis, C.D. and Hake, S.B. (2007) Extraction, purification and analysis of histones. *Nat Protoc*, **2**, 1445-1457.
4. Wiedemann, S.M., Mildner, S.N., Bonisch, C., Israel, L., Maiser, A., Matheisl, S., Straub, T., Merkl, R., Leonhardt, H., Kremmer, E. *et al.* (2010) Identification and characterization of two novel primate-specific histone H3 variants, H3.X and H3.Y. *J Cell Biol*, **190**, 777-791.
5. Wysocka, J., Reilly, P.T. and Herr, W. (2001) Loss of HCF-1-chromatin association precedes temperature-induced growth arrest of tsBN67 cells. *Mol Cell Biol*, **21**, 3820-3829.
6. Wessel, D. and Flugge, U.I. (1984) A method for the quantitative recovery of protein in dilute solution in the presence of detergents and lipids. *Anal Biochem*, **138**, 141-143.
7. Zhang, H., Roberts, D.N. and Cairns, B.R. (2005) Genome-wide dynamics of Htz1, a histone H2A variant that poises repressed/basal promoters for activation through histone loss. *Cell*, **123**, 219-231.
8. Phair, R.D., Gorski, S.A. and Misteli, T. (2004) Measurement of dynamic protein binding to chromatin in vivo, using photobleaching microscopy. *Methods Enzymol*, **375**, 393-414.
9. Vermeulen, M., Eberl, H.C., Matarese, F., Marks, H., Denissov, S., Butter, F., Lee, K.K., Olsen, J.V., Hyman, A.A., Stunnenberg, H.G. *et al.* (2010) Quantitative interaction proteomics and genome-wide profiling of epigenetic histone marks and their readers. *Cell*, **142**, 967-980.
10. Vermeulen, M., Mulder, K.W., Denissov, S., Pijnappel, W.W., van Schaik, F.M., Varier, R.A., Baltissen, M.P., Stunnenberg, H.G., Mann, M. and Timmers, H.T. (2007) Selective anchoring of TFIID to nucleosomes by trimethylation of histone H3 lysine 4. *Cell*, **131**, 58-69.
11. Cox, J. and Mann, M. (2008) MaxQuant enables high peptide identification rates, individualized p.p.b.-range mass accuracies and proteome-wide protein quantification. *Nat Biotechnol*, **26**, 1367-1372.
12. Salic, A. and Mitchison, T.J. (2008) A chemical method for fast and sensitive detection of DNA synthesis in vivo. *Proc Natl Acad Sci U S A*, **105**, 2415-2420.
13. Dyer, P.N., Edayathumangalam, R.S., White, C.L., Bao, Y., Chakravarthy, S., Muthurajan, U.M. and Luger, K. (2004) Reconstitution of nucleosome core particles from recombinant histones and DNA. *Methods Enzymol*, **375**, 23-44.
14. Thastrom, A., Lowary, P.T., Widlund, H.R., Cao, H., Kubista, M. and Widom, J. (1999) Sequence motifs and free energies of selected natural and non-natural nucleosome positioning DNA sequences. *J Mol Biol*, **288**, 213-229.
15. Bao, Y., Konesky, K., Park, Y.J., Rosu, S., Dyer, P.N., Rangasamy, D., Tremethick, D.J., Laybourn, P.J. and Luger, K. (2004) Nucleosomes

containing the histone variant H2A.Bbd organize only 118 base pairs of DNA. *Embo J*, **23**, 3314-3324.
16. Gansen, A., Valeri, A., Hauger, F., Felekyan, S., Kalinin, S., Toth, K., Langowski, J. and Seidel, C.A. (2009) Nucleosome disassembly intermediates characterized by single-molecule FRET. *Proc Natl Acad Sci U S A*, **106**, 15308-15313.
17. Muller, B.K., Zaychikov, E., Brauchle, C. and Lamb, D.C. (2005) Pulsed interleaved excitation. *Biophys J*, **89**, 3508-3522.
18. Nir, E., Michalet, X., Hamadani, K.M., Laurence, T.A., Neuhauser, D., Kovchegov, Y. and Weiss, S. (2006) Shot-noise limited single-molecule FRET histograms: comparison between theory and experiments. *J Phys Chem B*, **110**, 22103-22124.
19. Lee, N.K., Kapanidis, A.N., Wang, Y., Michalet, X., Mukhopadhyay, J., Ebright, R.H. and Weiss, S. (2005) Accurate FRET measurements within single diffusing biomolecules using alternating-laser excitation. *Biophys J*, **88**, 2939-2953.

2.4 Structure, function and dynamics of nuclear subcompartments

Available online at www.sciencedirect.com

SciVerse ScienceDirect

Current Opinion in Cell Biology

Structure, function and dynamics of nuclear subcompartments

M Cristina Cardoso[1], Katrin Schneider[2], Robert M Martin[3] and Heinrich Leonhardt[2]

The nucleus contains a plethora of different dynamic structures involved in the regulation and catalysis of nucleic acid metabolism and function. Over the past decades countless factors, molecular structures, interactions and posttranslational modifications have been described in this context. On the one side of the size scale X-ray crystallography delivers static snapshots of biomolecules at atomic resolution and on the other side light microscopy allows insights into complex structures of living cells and tissues in real time but poor resolution. Recent advances in light and electron microscopy are starting to close the temporal and spatial resolution gap from the atomic up to the cellular level. Old challenges and new insights are illustrated with examples of DNA replication and nuclear protein dynamics.

Addresses
[1] Department of Biology, Technische Universität Darmstadt, Germany
[2] Department of Biology II, Center for Integrated Protein Science, Ludwig Maximilians University Munich, Planegg-Martinsried, Germany
[3] Institute of Molecular Medicine, Faculty of Medicine, University of Lisbon, Portugal

Corresponding authors: Cardoso, M Cristina (cardoso@bio.tu-darmstadt.de) and Leonhardt, Heinrich (H.Leonhardt@lmu.de)

Current Opinion in Cell Biology 2012, **24**:79–85

This review comes from a themed issue on
Cell structure and dynamics
Edited by Jason Swedlow and Gaudenz Danuser

Available online 5th January 2012

0955-0674/$ – see front matter
Published by Elsevier Ltd.

DOI 10.1016/j.ceb.2011.12.009

Nuclear structures and protein dynamics

The by far largest molecules in the nucleus are the chromosomes that occupy discrete territories and are anchored at the nuclear envelope [1••,2]. The fact that most nuclear processes occur or at least start at chromosomes makes them the chief organizing factor in the nucleus. Proteins involved in DNA replication, transcription and RNA processing were found enriched in focal structures [3]. The variety of nuclear structures illustrated in Figure 1 raises the question of how these distinct structures are assembled and maintained in the absence of subdividing membranes.

Fluorescence photobleaching experiments demonstrated a surprisingly high mobility of proteins in the nucleus [4••] suggesting that the occurrence of discrete nuclear structures is the net result of association, dissociation and diffusion events. These experiments also indicated that distinct structures could be generated by stable binding as well as rapid exchange of its components [5]. The combination of fluorescence photobleaching experiments with kinetic modeling can in principle provide quantitative data on intracellular binding properties [6]. The occurrence of multiple and variable interactions with unknown numbers of binding sites, however, make it difficult to mathematically dissect out individual mobility classes. Thus, despite the present sophistication of the kinetic modeling [7] the inherent limitations of these ensemble measurements call for complementation by single molecule tracings as discussed below.

Temporal and spatial dimensions of nuclear functions

One of the fundamental nuclear functions and the most prominent and critical event during the cell cycle is the precise duplication of the entire (epi)genetic information. The challenges of DNA replication are easily summarized. Roughly speaking, human cells need to replicate about 6 billion (6×10^9) base pairs in half a day, starting at thousands of sites on 46 chromosomes, precisely copying each and every base pair once and only once. The discovery and biochemical characterization of the DNA double helix and DNA polymerases outlined the basic mechanism but could not explain the efficiency, precision and coordination of cellular DNA replication [8]. Since then an amazing complexity unfolded as countless new factors were identified that contribute to the efficiency and precision of DNA replication.

It is clear that DNA replication *in vivo* is more than just the sum of all participating factors and especially the overall coordination and precision is far from being reproducible *in vitro*. Already early fractionation experiments indicated that newly synthesized DNA and most of the replication activity was associated with higher order structures [9,10]. At the cellular level DNA replication can be visualized by incorporation of modified nucleotides [11], immunofluorescence staining of replication factors [12], expression of fluorescent fusion proteins in living cells [13] and appears highly organized in focal structures (Figure 2). The subnuclear distribution of these foci changes throughout the S-phase [13] in a pattern that roughly corresponds to the underlying chromatin states [14–18] and changes during differentiation [19,20]. Recent studies have addressed how DNA replication is

Figure 1

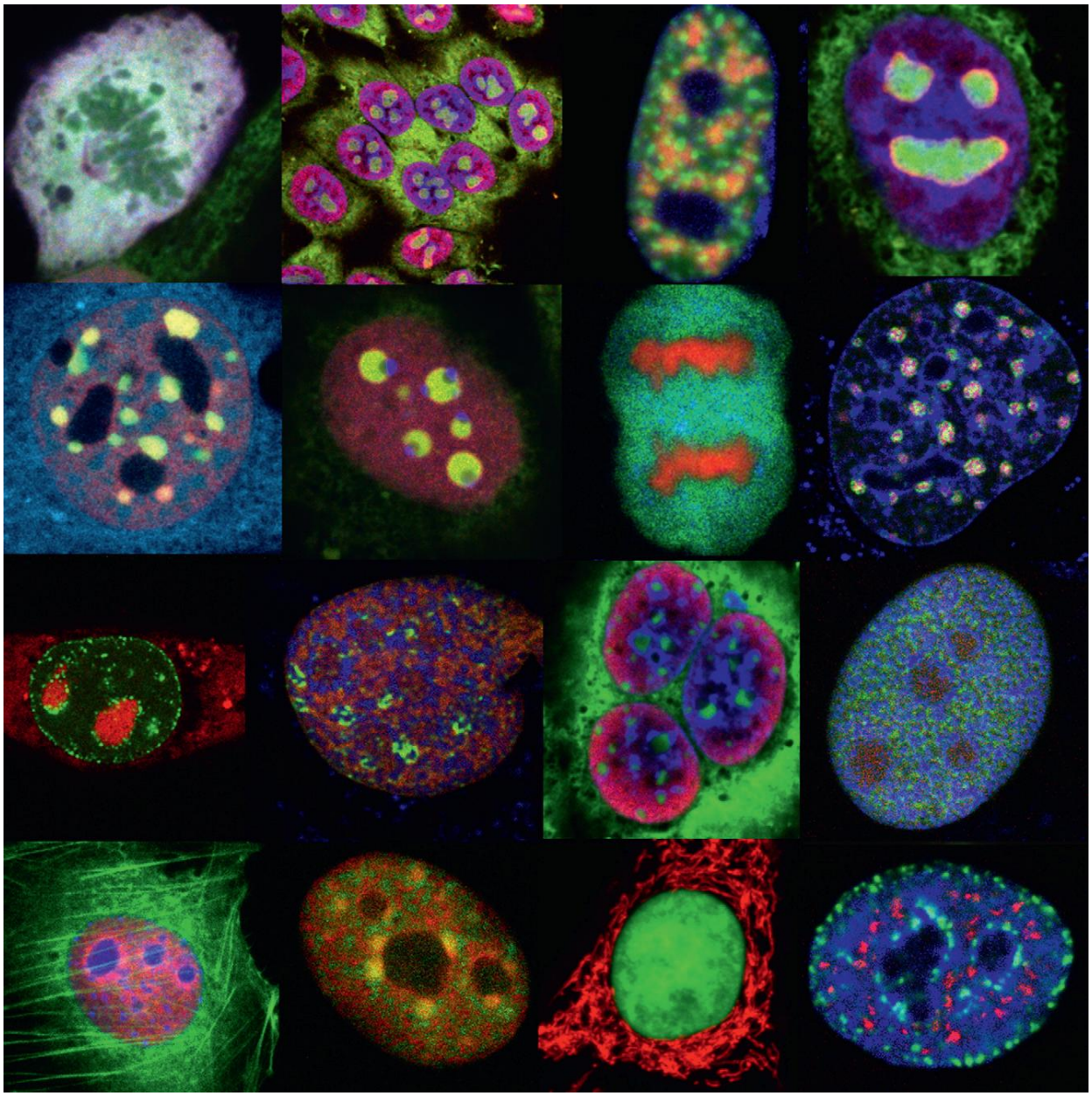

The variety of nuclear structures and subcompartments. This colorful assembly shows a random collection of nuclear structures observed and studied in our lab over the past years. All these distinct structures have in common that they are formed by dynamic assembly and disassembly processes in the absence of organizing membranes.

activated within these foci and how the cell can cope with replicative stress [21,22]. The sizes and numbers of these foci, as obtained from light microscopy analysis, could not be directly linked with numbers of replication units measured *in vitro* in stretched DNA fibers. This and other lines of evidence lead to the hypothesis that the replication foci detected by light microscopy correspond to spatially clustered DNA replication units [23•,24]. Recent studies employing super resolution light microscopy methods, namely STED [25], 3D-SIM and SMI microscopy [26], as well as electron microscopy [27] provided first evidence to the existence of 4000–5000

Figure 2

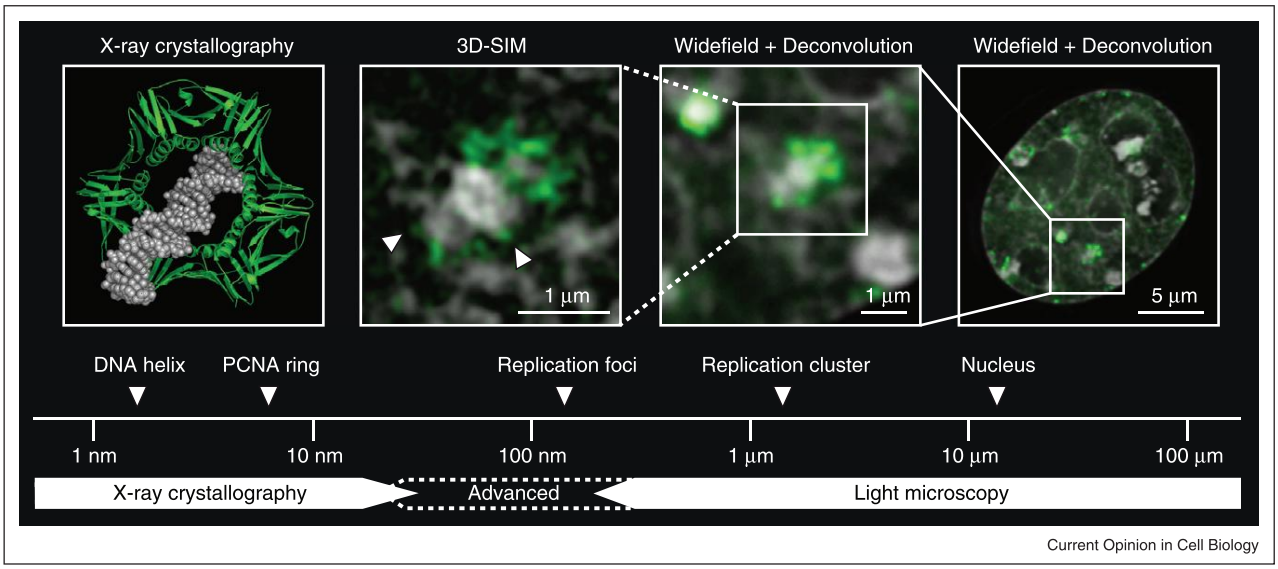

DNA replication from atomic to cellular scale. This scheme illustrates the orders of magnitude from the level of the well-known crystal structures of key components of DNA replication to the cellular level. The DNA double helix (gray) has a diameter of about two nanometers and the entire diploid genome a combined length of about 2 m, all condensed into a nucleus with a diameter of 5–20 μm. The homotrimeric PCNA ring (green, PDB ID: 1AXC), the central loading platform for DNA replication factors, has a diameter of about 8 nm while the microscopically discernable, cellular replication foci and clusters are in the range from 100 to 2000 nm.

replication units of 125 nm average size at any given time throughout S-phase (Figure 2). These types of studies provide the basis for building and testing qualitative and quantitative models of genome replication.

By way of explanation it is easy to implicate the higher order structures present in living cells but it is hard if not impossible to prove a functional role with the usual methods. In this sense, mutational analysis of nuclear proteins allowed mapping functional domains mediating interactions with other factors involved in particular nuclear functions. In the case of DNA replication, local enrichment of factors involved not only in the DNA synthesis process *per se* but also in cell cycle regulation [28], DNA methylation [29], chromatin assembly [30] and repair of DNA damage [31] was found. Several of these factors were shown to accumulate at replication sites during S-phase via a short peptide sequence mediating binding to the DNA polymerase clamp PCNA [32] and independent from the catalytic domain of the respective enzymes. As PCNA forms homotrimers wrapping around the DNA (Figure 2) with maximally three binding sites for interacting factors sharing the same binding interface, the question arises as to how all these interactions can take place. Furthermore, it was unclear whether such targeting sequences leading to local enrichment of enzymes are required *in vivo* for the function of the enzymes in the particular nuclear process.

These questions were addressed by fluorescence photobleaching/activation experiments in living cells. Several enzymes including DNA ligase I, the flap endonuclease Fen1 and Dnmt1 as well as mutants thereof were photobleached simultaneously with PCNA and their relative kinetics of recovery measured. Whereas PCNA did not exchange over periods of several minutes, the enzymes interacting with it were only transiently associated with replication sites and their entire pools exchanged over periods of a few seconds [33,34,35•]. This analysis suggests that the processivity of DNA replication and the coordination of the different enzymatic activities rely on a stable core component loaded on DNA and transiently interacting factors ensuring the temporal availability of the shared binding site in the stable PCNA ring. This type of kinetics involving the interplay of transient and stable components was also observed in other nuclear processes such as DNA repair [36]. Interestingly, mutating the PCNA interacting domain at least in the DNA methyltransferase Dnmt1 did not prevent DNA methylation but lowered its efficiency [33]. Thus, local enrichment of factors via protein–protein interactions increases the efficiency of enzymatic reactions *in vivo* but does not seem to be an absolute requirement for nuclear function.

Last but not least, also the time scale poses some challenges as the diffusion rate of the participating proteins, the kinetics of their interactions and the incorporation of

single nucleotides are much faster than the imaging rate of regular light microscopy. As discussed below, single molecule tracing offers exciting new insights into the millisecond range but still misses out on contextual information.

Dynamics and interactions of single molecules in the nucleus

The visualization of cellular components by immunofluorescence staining with antibodies, by *in situ* hybridization for detection of specific nuclei acids and with fluorescently tagged proteins have uncovered a variety of subnuclear compartments [3] as discussed above (Figure 1).

Throughout the last decade systematic analysis of protein dynamics mostly from fluorescence photobleaching/activation experiments [37] has changed our view of static nuclear compartments and revealed new principles of macromolecular complexes [38]. These types of analysis though do not reveal the behavior of individual molecules but rather describe the average behavior of molecular ensembles. In biology important and meaningful information is often lost in the averaging over large numbers of molecules. As an example, the apparent exclusion of multiple nuclear proteins from the nucleolus observed in numerous fixed and living cell studies could be interpreted as lack of accessibility of this major nuclear compartment [39] for these proteins. *In vitro* measurements with nucleoli isolated from Xenopus oocyte nuclei though revealed a low-density structure permeable to molecules such as dextrans [40•]. This apparent contradiction prompted studies of the dynamic behavior of single molecules in living cells.

The tracing of single molecules in cells [41] has been limited by the low signal-to-noise ratio and the small number of photons emitted by the available fluorophores. On the one hand, total internal reflection (TIRF) microscopy [42] gives the best signal-to-noise ratio but is only applicable to structures such as the plasma membrane within about 100 nm distance from the surface. On the other hand, methods based on fluorescence fluctuation such as fluorescence correlation microscopy [43] measure the mobility of single molecules with very high temporal resolution (in the microsecond range) but are restricted to mobile species and to a femtoliter volume within the cell. Direct tracing of single molecules inside cells albeit difficult has been made possible by the development of improved, highly sensitive cameras. This allowed probing to what extent nuclear structures limit the mobility and access of individual proteins by tracing the mobility of fluorescently labeled inert proteins (streptavidin and ovalbumin; [44•,45]). Whereas steady state average distribution (Figure 3, top panel) suggests exclusion of streptavidin protein from the nucleolus, high-speed single molecule tracing microscopy (Figure 3, bottom panel and Movie) clearly indicate that single average size proteins have unrestricted access to the nucleolus and all nuclear subcompartments. Nonetheless, in-depth analysis of the nuclear mobility of proteins uncovered transient trapping on the order of tens of milliseconds. This trapping was mostly pronounced at heterochromatin and least pronounced within the nucleolus. General trapping of factors in specific compartments modulates their local concentration and may thus directly impact on enzymatic reaction velocity and enhance their specificity [46].

Several recent studies use single particle tracking to study the intranuclear dynamics as well as nuclear-cytoplasm

Figure 3

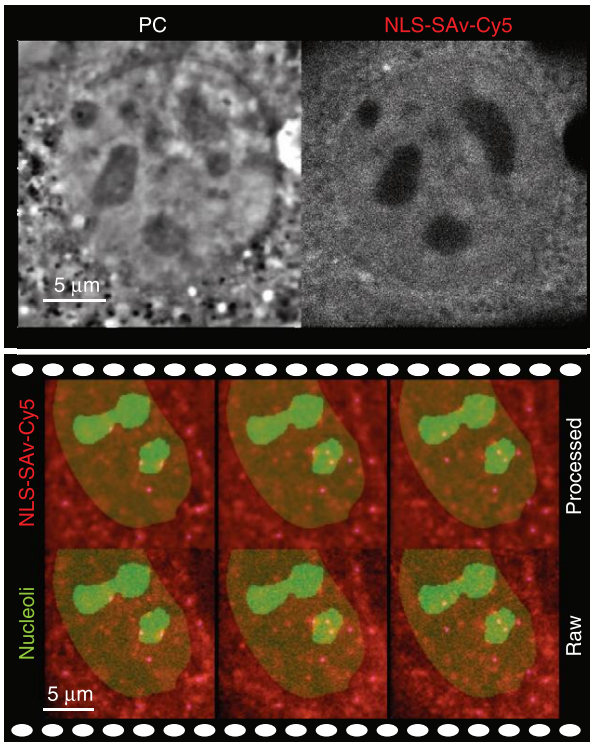

Distribution and dynamics of nuclear proteins. Confocal fluorescence microscopy analysis (top panel) suggests that the probe protein streptavidin (NLS-SAv-Cy5) is, like many other nuclear proteins, excluded from nucleoli which, due to their higher density, appear as dark structures in the phase contrast (PC) image. Single molecule tracing (bottom panel) provide an alternative explanation for this bulk steady-state distribution. Snapshots of a high speed (191 Hz) time lapse microscopy (full sequence in supplementary Movie) of single NLS-SAv-Cy5 protein (red) molecules in and out of nucle(ol)ar (green) subcompartments are shown. The corresponding movie shows streptavidin molecules (NLS-SAv-Cy5) after microinjection into the cytoplasm of C2C12 mouse myoblasts. Raw single molecule data are displayed at the bottom and the same data processed using a 2–20 pixel band pass filter. One pixel corresponds to 96 nm and the whole object field shown is 12.2 µm × 12.2 µm. Further details are described in [44].

transport of, for example, RNP particles [47–49]. The larger size and slower mobility of these particles combined with multiple labels per particle facilitate imaging with good signal-to-noise ratio. Recent improvements in sample illumination strategies [50], increase the signal-to-noise ratio and facilitate direct tracing of single molecules, their interactions and enzymatic reactions in living cells with high spatial and temporal resolution in the range of tens of nanometers and milliseconds.

Outlook

Currently cells are being studied at different size and time scales. The recent development of super resolution light microscopy methods [51] enables the study of cellular structures at ever-increasing resolution far below the classic Abbe diffraction limit approaching the range of electron microscopy and X-ray crystallography (Figure 2). The integration of structural information obtained with different methods at different size scales has been impressively demonstrated by fitting crystal structures into cryo-electron microscopy density maps to assemble a functional architecture of the complete multi-subunit RNA polymerase I [52]. The rapidly increasing capabilities of cryo-electron microscopy to resolve bigger complexes at higher resolution facilitate the combination with advanced light microscopy. Likewise, dramatic advances in electron microscopic tomography recently enabled the direct study of polyribosomes in human cells [53].

Correlative light and electron microscopy in combination with electron microscopic tomography and super resolution light microscopy have recently been used to elucidate intermediate steps of abscission in dividing human cells [54]. In addition to increased spatial resolution, the single molecule light microscopy techniques discussed above expand the time resolution down to the microsecond scale.

Besides the rapid development of advanced electron and light microscopy technologies new reagents like chromobodies that are ten times smaller than conventional antibodies and detectable in living cells [54,55] as well as new genetically encoded tags and contrasting approaches [56••] will further facilitate correlative microscopy and thus the acquisition and integration of structural data over several orders of magnitude.

Last but not least, as imaging data are produced at an ever-increasing rate and volume around the world, at different size and time scales, with different methods and instruments, standardization becomes an essential and urgent prerequisite to compare, integrate, model and thus utilize this accumulating wealth of data [57].

Acknowledgements

We thank all past and present members of our laboratory for their countless contributions over the past years. We are indebted to Volker Buschmann, David Grünwald and Andreas Maiser for image material. Our research has been supported by grants of the Deutsche Forschungsgemeinschaft (DFG), the Volkswagen foundation and the German Ministry for Education and Research (BMBF).

Appendix A. Supplementary data

Supplementary data associated with this article can be found, in the online version, at doi:10.1016/j.ceb.2011.12.009.

References and recommended reading

Papers of particular interest, published within the period of review, have been highlighted as:

- • of special interest
- •• of outstanding interest

1. •• Bolzer A, Kreth G, Solovei I, Koehler D, Saracoglu K, Fauth C, Muller S, Eils R, Cremer C, Speicher MR *et al.*: **Three-dimensional maps of all chromosomes in human male fibroblast nuclei and prometaphase rosettes**. *PLoS Biol* 2005, **3**:e157.
A major tour de force study visualizing all 46 chromosomes in a human fibroblast and in addition the authors measure and discuss their relative distribution in the nucleus.

2. Cremer T, Cremer C: **Chromosome territories, nuclear architecture and gene regulation in mammalian cells**. *Nat Rev Genet* 2001, **2**:292-301.

3. Spector DL: **Nuclear domains**. *J Cell Sci* 2001, **114**:2891-2893.

4. •• Phair RD, Misteli T: **High mobility of proteins in the mammalian cell nucleus**. *Nature* 2000, **404**:604-609.
The first fluorescence photobleaching recovery measurements demonstrating the surprisingly high mobility of proteins in the nucleus of living mammalian cells.

5. Lamond AI, Spector DL: **Nuclear speckles: a model for nuclear organelles**. *Nat Rev Mol Cell Biol* 2003, **4**:605-612.

6. Phair RD, Scaffidi P, Elbi C, Vecerova J, Dey A, Ozato K, Brown DT, Hager G, Bustin M, Misteli T: **Global nature of dynamic protein–chromatin interactions in vivo: three-dimensional genome scanning and dynamic interaction networks of chromatin proteins**. *Mol Cell Biol* 2004, **24**:6393-6402.

7. Mueller F, Mazza D, Stasevich TJ, McNally JG: **FRAP and kinetic modeling in the analysis of nuclear protein dynamics: what do we really know**. *Curr Opin Cell Biol* 2010, **22**:403-411.

8. Chagin VO, Stear JH, Cardoso MC: **Organization of DNA replication**. In *The Nucleus*. Edited by Misteli T, Spector DL. Cold Spring Harbor Laboratory; 2010:a000737. Cold Spring Harb Perspect Biol, vol 2.

9. Berezney R, Coffey DS: **Nuclear protein matrix: association with newly synthesized DNA**. *Science* 1975, **189**:291-293.

10. Leonhardt H, Cardoso MC: **Targeting and association of proteins with functional domains in the nucleus: the insoluble solution**. *Int Rev Cytol* 1995, **162B**:303-335.

11. Nakamura H, Morita T, Sato C: **Structural organizations of replicon domains during DNA synthetic phase in the mammalian nucleus**. *Exp Cell Res* 1986, **165**:291-297.

12. Bravo R, Macdonald-Bravo H: **Existence of two populations of cyclin/proliferating cell nuclear antigen during the cell cycle: association with DNA replication sites**. *J Cell Biol* 1987, **105**:1549-1554.

13. Leonhardt H, Rahn HP, Weinzierl P, Sporbert A, Cremer T, Zink D, Cardoso MC: **Dynamics of DNA replication factories in living cells**. *J Cell Biol* 2000, **149**:271-280.

14. Casas-Delucchi CS, Brero A, Rahn HP, Solovei I, Wutz A, Cremer T, Leonhardt H, Cardoso MC: **Histone acetylation controls the inactive X chromosome replication dynamics**. *Nat Commun* 2011, **2**:222.

15. Casas-Delucchi CS, van Bemmel JG, Haase S, Herce HD, Nowak D, Meilinger D, Stear JH, Leonhardt H, Cardoso MC:

Histone hypoacetylation is required to maintain late replication timing of constitutive heterochromatin. *Nucleic Acids Res* 2011. doi:10.1093/nar/gkr1723.

16. Lima-de-Faria A, Jaworska H: **Late DNA synthesis in heterochromatin**. *Nature* 1968, **217**:138-142.

17. O'Keefe RT, Henderson SC, Spector DL: **Dynamic organization of DNA replication in mammalian cell nuclei: spatially and temporally defined replication of chromosome-specific alpha-satellite DNA sequences**. *J Cell Biol* 1992, **116**:1095-1110.

18. Wu R, Terry AV, Singh PB, Gilbert DM: **Differential subnuclear localization and replication timing of histone H3 lysine 9 methylation states**. *Mol Biol Cell* 2005, **16**:2872-2881.

19. Hiratani I, Leskovar A, Gilbert DM: **Differentiation-induced replication-timing changes are restricted to AT-rich/long interspersed nuclear element (LINE)-rich isochores**. *Proc Natl Acad Sci USA* 2004, **101**:16861-16866.

20. Hatton KS, Dhar V, Brown EH, Iqbal MA, Stuart S, Didamo VT, Schildkraut CL: **Replication program of active and inactive multigene families in mammalian cells**. *Mol Cell Biol* 1988, **8**:2149-2158.

21. Ge XQ, Blow JJ: **The licensing checkpoint opens up**. *Cell Cycle* 2009, **8**:2320-2322.

22. Ge XQ, Blow JJ: **Chk1 inhibits replication factory activation but allows dormant origin firing in existing factories**. *J Cell Biol* 2010, **191**:1285-1297.

23. • Jackson DA, Pombo A: **Replicon clusters are stable units of chromosome structure: evidence that nuclear organization contributes to the efficient activation and propagation of S phase in human cells**. *J Cell Biol* 1998, **140**:1285-1295.
A thorough quantitative analysis of replication sites *in situ* in mammalian cells and the relationship to replication forks and their progression in stretched DNA fibers.

24. Sadoni N, Cardoso MC, Stelzer EH, Leonhardt H, Zink D: **Stable chromosomal units determine the spatial and temporal organization of DNA replication**. *J Cell Sci* 2004, **117**:5353-5365.

25. Cseresnyes Z, Schwarz U, Green CM: **Analysis of replication factories in human cells by super-resolution light microscopy**. *BMC Cell Biol* 2009, **10**:88.

26. Baddeley D, Chagin VO, Schermelleh L, Martin S, Pombo A, Carlton PM, Gahl A, Domaing P, Birk U, Leonhardt H *et al.*: **Measurement of replication structures at the nanometer scale using super-resolution light microscopy**. *Nucleic Acids Res* 2010, **38**:e8.

27. Koberna K, Ligasova A, Malinsky J, Pliss A, Siegel AJ, Cvackova Z, Fidlerova H, Masata M, Fialova M, Raska I *et al.*: **Electron microscopy of DNA replication in 3-D: evidence for similar-sized replication foci throughout S-phase**. *J Cell Biochem* 2005, **94**:126-138.

28. Cardoso MC, Leonhardt H, Nadal-Ginard B: **Reversal of terminal differentiation and control of DNA replication: cyclin A and Cdk2 specifically localize at subnuclear sites of DNA replication**. *Cell* 1993, **74**:979-992.

29. Leonhardt H, Page AW, Weier HU, Bestor TH: **A targeting sequence directs DNA methyltransferase to sites of DNA replication in mammalian nuclei**. *Cell* 1992, **71**:865-873.

30. Gerard A, Koundrioukoff S, Ramillon V, Sergere JC, Mailand N, Quivy JP, Almouzni G: **The replication kinase Cdc7-Dbf4 promotes the interaction of the p150 subunit of chromatin assembly factor 1 with proliferating cell nuclear antigen**. *EMBO Rep* 2006, **7**:817-823.

31. Otterlei M, Warbrick E, Nagelhus TA, Haug T, Slupphaug G, Akbari M, Aas PA, Steinsbekk K, Bakke O, Krokan HE: **Post-replicative base excision repair in replication foci**. *Embo J* 1999, **18**:3834-3844.

32. Warbrick E: **The puzzle of PCNA's many partners**. *Bioessays* 2000, **22**:997-1006.

33. Schermelleh L, Haemmer A, Spada F, Rosing N, Meilinger D, Rothbauer U, Cardoso MC, Leonhardt H: **Dynamics of Dnmt1 interaction with the replication machinery and its role in postreplicative maintenance of DNA methylation**. *Nucleic Acids Res* 2007, **35**:4301-4312.

34. Sporbert A, Domaing P, Leonhardt H, Cardoso MC: **PCNA acts as a stationary loading platform for transiently interacting Okazaki fragment maturation proteins**. *Nucleic Acids Res* 2005, **33**:3521-3528.

35. • Sporbert A, Gahl A, Ankerhold R, Leonhardt H, Cardoso MC: **DNA polymerase clamp shows little turnover at established replication sites but sequential de novo assembly at adjacent origin clusters**. *Mol Cell* 2002, **10**:1355-1365.
A combined fluorescence photobleaching and spatial recovery analysis of DNA replication demonstrating that replication foci do not move but rather disassemble and reassemble at the DNA to be replicated next.

36. Mortusewicz O, Leonhardt H, Cardoso MC: **Spatiotemporal dynamics of regulatory protein recruitment at DNA damage sites**. *J Cell Biochem* 2008, **104**:1562-1569.

37. Bancaud A, Huet S, Rabut G, Ellenberg J: **Fluorescence perturbation techniques to study mobility and molecular dynamics of proteins in live cells: FRAP, photoactivation, photoconversion, and FLIP**. *Cold Spring Harbor Protocols* 2010. 2010:pdb top90.

38. Misteli T: **Protein dynamics: implications for nuclear architecture and gene expression**. *Science* 2001, **291**:843-847.

39. Pederson T: **The nucleolus**. In *The Nucleus,* edn 2010/11/26. Edited by Misteli T, Spector DL.Cold Spring Harbor Laboratory; 2010:a000638. Cold Spring Harb Perspect Biol, vol 3..

40. • Handwerger KE, Cordero JA, Gall JG: **Cajal bodies, nucleoli, and speckles in the Xenopus oocyte nucleus have a low-density, sponge-like structure**. *Mol Biol Cell* 2005, **16**:202-211.
A detailed biophysical analysis of the structural characteristics of nuclear 'organelles', their protein concentration and their permeability to macromolecules.

41. Siebrasse JP, Kubitscheck U: **Single molecule tracking for studying nucleocytoplasmic transport and intranuclear dynamics**. *Methods Mol Biol* 2009, **464**:343-361.

42. Reck-Peterson SL, Derr ND, Stuurman N: **Imaging single molecules using total internal reflection fluorescence microscopy (TIRFM)**. *Cold Spring Harbor Protocols* 2010. 2010:pdb top73.

43. Medina MA, Schwille P: **Fluorescence correlation spectroscopy for the detection and study of single molecules in biology**. *BioEssays* 2002, **24**:758-764.

44. • Grünwald D, Martin RM, Buschmann V, Bazett-Jones DP, Leonhardt H, Kubitscheck U, Cardoso MC: **Probing intranuclear environments at the single-molecule level**. *Biophys J* 2008, **94**:2847-2858.
Using an inert protein the accessibility of subnuclear compartments was measured in living mammalian cells with a very high temporal and spatial resolution.

45. Speil J, Kubitscheck U: **Single ovalbumin molecules exploring nucleoplasm and nucleoli of living cell nuclei**. *Biochem Biophys Acta* 2010, **1803**:396-404.

46. Leonhardt H, Rahn HP, Cardoso MC: **Functional links between nuclear structure, gene expression, DNA replication, and methylation**. *Crit Rev Eukaryot Gene Expr* 1999, **9**:345-351.

47. Grünwald D, Singer RH, Rout M: **Nuclear export dynamics of RNA–protein complexes**. *Nature* 2011, **475**:333-341.

48. Mor A, Suliman S, Ben-Yishay R, Yunger S, Brody Y, Shav-Tal Y: **Dynamics of single mRNP nucleocytoplasmic transport and export through the nuclear pore in living cells**. *Nat Cell Biol* 2010, **12**:543-552.

49. Siebrasse JP, Veith R, Dobay A, Leonhardt H, Daneholt B, Kubitscheck U: **Discontinuous movement of mRNP particles in nucleoplasmic regions devoid of chromatin**. *Proc Natl Acad Sci USA* 2008, **105**:20291-20296.

50. Ritter JG, Veith R, Veenendaal A, Siebrasse JP, Kubitscheck U: **Light sheet microscopy for single molecule tracking in living tissue**. *PloS One* 2010, **5**:e11639.

51. Schermelleh L, Heintzmann R, Leonhardt H: **A guide to super-resolution fluorescence microscopy**. *J Cell Biol* 2010, **190**:165-175.

52. Kuhn CD, Geiger SR, Baumli S, Gartmann M, Gerber J, Jennebach S, Mielke T, Tschochner H, Beckmann R, Cramer P: **Functional architecture of RNA polymerase I**. *Cell* 2007, **131**:1260-1272.

53. Brandt F, Carlson LA, Hartl FU, Baumeister W, Grunewald K: **The three-dimensional organization of polyribosomes in intact human cells**. *Mol Cell* 2010, **39**:560-569.

54. Guizetti J, Schermelleh L, Mantler J, Maar S, Poser I, Leonhardt H, Muller-Reichert T, Gerlich DW: **Cortical constriction during abscission involves helices of ESCRT-III-dependent filaments**. *Science* 2011, **331**:1616-1620.

55. Rothbauer U, Zolghadr K, Tillib S, Nowak D, Schermelleh L, Gahl A, Backmann N, Conrath K, Muyldermans S, Cardoso MC *et al.*: **Targeting and tracing antigens in live cells with fluorescent nanobodies**. *Nat Methods* 2006, **3**:887-889.

56. •• Shu X, Lev-Ram V, Deerinck TJ, Qi Y, Ramko EB, Davidson MW, Jin Y, Ellisman MH, Tsien RY: **A genetically encoded tag for correlated light and electron microscopy of intact cells, tissues, and organisms**. *PLoS Biol* 2011, **9**:e1001041.
The authors report a new genetically encoded tag for *in situ* visualization of proteins in correlative light and electron microscopy.

57. Swedlow JR, Lewis SE, Goldberg IG: **Modelling data across labs, genomes, space and time**. *Nat Cell Biol* 2006, **8**:1190-1194.

2.5 Cyclin B1 degrading F-box protein NIPA is localized to the nuclear pore complex

Cyclin B1 degrading F-box protein NIPA is localized to the nuclear pore complex

Kulinski M[1]*, Schneider K[2]*, Illert AL[3], Lemeer S[4], Kuster B[4], Leonhardt H[2] and Duyster J[3]

[1]Department of Internal Medicine III, Technical University of Munich, 81675 Munich, Germany

[2]Department of Biology and Center for Integrated Protein Science, Ludwig Maximilians University Munich (LMU), 82152 Planegg-Martinsried, Germany

[3]Department of Hematology/Oncology, University Medical Center Freiburg, 79106 Freiburg, Germany

[4]Chair of Proteomics and Bioanalytics, Technische Universität München, 85354 Freising, Germany

* - Both authors equally contributed to this work

Abstract

NIPA (nuclear interaction partner of ALK) is an F-box-containing protein that defines a nuclear SCF-type ubiquitin ligase (SCF^{NIPA}), which targets nuclear cyclin B1 for ubiquitination and proteasomal degradation, thereby contributing to the timing of mitotic entry. Here we show that NIPA is localized to the nucleoplasmic site of the nuclear pore complex (NPC). Interestingly, we identified the nucleoporin TPR as a scaffold protein, which forms a very stable interaction with NIPA at the NPC. The C3HC zinc-finger motif located in the N-terminus of NIPA is responsible for the interaction with the nucleoporin TPR and disruption of this domain leads to mislocalization of NIPA from the NPC to the nuclear interior. Moreover, inactivation of TPR by RNAi results in destabilization and subsequent degradation of NIPA. Based on the localization of the F-box protein at the inner site of the nuclear pore, we propose an intriguing mechanism for cyclin B1 degradation, through formation of a "cyclin trap" directly at the gate, targeting the substrate for ubiquitination just upon entry to the nucleus.

Introduction

Subcellular compartmentalization of the cell by membrane systems allows for the separation of essential processes. As a result, the transport of material between those compartments is crucial to maintain proper cellular functions. The passive and active nucleocytoplasmic transport through the doublelipid bilayer of the nuclear envelope is regulated by the nuclear pore complexes (NPCs), large multiprotein gateways composed of several copies of ~ 30 different nucleoporins (NUPs)[1,2].

NPC architecture is based on the octagonal symmetry with distinct, structured subunits: cytoplasmic and nuclear coaxial rings placed on the periphery of outer and inner nuclear membrane, respectively; the main translocation channel is formed of eight elongated structures termed spokes and connects

both coaxial rings thereby also forming a spoke ring; peripheral NPC components, such as short, cytoplasmic filaments emanating towards the cytoplasm and filaments forming the nuclear basket converging into the distal ring [3-7]. The nuclear basket, also called a "fish trap", can facilitate interactions between transport complexes and serves as a docking site during cargo translocation[8-10]. The central architectural element of the nuclear basket is constituted by the translocated promoter region (TPR), which is anchored to the NPC by NUP153[11,12]. TPR is a 267-kDa protein of a bipartite structure: a large N-terminal domain forming a double coiled-coil and a nonhelical, highly acidic C-terminal domain, not dominated by a particular type of secondary structure[13,14]. Besides its structural role in the assembly of the nuclear basket, TPR has been shown to be involved in mRNA export control[15,16], activation of the *met* oncogene[17], nuclear protein export[18,19] as well as spindle checkpoint control[20,21] and ERK2 nucleo-cytoplasmic translocation[22], thus demonstrating multifunctional properties of the NPC. Additionally, recent studies point towards the involvement of NPC components in DNA damage repair[23,24], regulation of both transcription[25,26] and autophagy[27] as well as in posttranslational modification with small ubiquitin-related modifier (SUMO) proteins[28-30], suggesting a prominent role for the nuclear periphery in cellular physiology.

We previously identified NIPA (nuclear interaction partner of anaplastic lymphoma kinase) as an F-box-like protein, which together with SKP1/CUL1/ROC1 defines the SCF^{NIPA} complex as a family member of the SCF-type ubiquitin ligases[31-34]. NIPA is responsible for the subcellular regulation of its substrate, cyclin B1, in interphase, thereby contributing to the timing of mitotic entry[31]. Cell cycle dependent inactivation of the SCF^{NIPA} complex is governed by the inhibitory phosphorylation of NIPA in late G_2 phase by the action of cyclinB1-CDK1 and ERK2 kinases[33,35], leading to the disruption of E3-ligase activity. Although the molecular mechanism of protein degradation that controls cell proliferation is well known, many mechanistic questions still remain elusive[36].

Here we show that NIPA is associated with the NPC by a direct interaction with the nucleoporin TPR. We identify the zinc-finger motif within NIPA to be responsible for the binding to TPR and moreover that disruption of this domain leads to the dissociation of NIPA from the NPC. We therefore propose an intriguing mechanism for the regulation of cyclin B1 nuclear abundance by recruiting ubiquitin ligase mediated degradation to the gates of the inner nuclear envelope.

Materials and methods

Plasmids, antibodies and immunological procedures.

Details of the construction of various plasmids are available from the authors upon request. The plasmids for FLAG-NIPA-pcDNA3.1 wild type, zinc-finger mutant and nuclear localization signal (NLS) mutant were kindly provided by C. v Klitzing. GFP-NIPA wild type and GFP-NIPA zinc-finger mutant

were subcloned into pEGFP-C3 vector (Clontech). cDNA of NIPA was cloned into pcDNA-N-SF-TAP (vector was kindly provided by M. Ueffing[37]). pcDNA3.1-FbxO9, pcDNA3.1-Fbw2 and pcDNA3.1-Fbw11 plasmids were a generous gift provided by F. Bassermann. Vector encoding human pEGFP-TPR was obtained from Addgene (Addgene plasmid 35024, P. Frosst[18]). Plasmid transfections were performed using TurboFect (Thermo Fisher) or Lipofectamin 2000 (Invitrogen) according to the manufacturer's instructions. Antibodies used in this study included mouse monoclonal antibodies from Sigma-Aldrich (β-actin (AC-15); FLAG-M2), Santa Cruz (NIPA (B-10, sc-365058)), ActiveMotif (α-tubulin (5-B-1-2)) and Abcam (NUP153 (QE5)); rabbit polyclonal and monoclonal antibodies from Sigma-Aldrich (ZC3HC1 (HPA024023)), Abcam (p-NIPA (ab63557)) and Cell Signaling (NUP98 (C37G10)); and goat polyclonal antibodies from Santa Cruz (TPR (C-20); Lamin B (M-20)). All secondary antibodies used for immunofluorescence were from Invitrogen (Anti-Rabbit IgG, Alexa Fluor® 488; Anti-Rabbit IgG, Alexa Fluor® 594; Anti-Mouse IgG, Alexa Fluor® 594; Anti-Mouse IgG, Alexa Fluor® 488 and Anti-Goat IgG, Alexa Fluor® 594). Extract preparation, immunoprecipitation and immunoblotting were performed as previously described[31,34,35]. Nuclear fractionation was performed using Dounce homogenizer as previously described[38].

Immunofluorescence staining and structured illumination microscopy.

Cells were grown to 80% confluence on high precision microscope cover glasses (Roth), fixed with formaldehyde and permeablized with 0.5% Triton X-100 in PBS containing 0.02% Tween-20 (PBST). After blocking (2% BSA in PBST) for 1 h), staining was carried out by incubation with the primary antibodies (1 h at 1:200-1:500 dilutions in 2% BSA). Slides were then incubated with secondary antibodies (typically 1:400 in 2% BSA), postfixed with formaldehyde and nuclei were counterstained with DAPI (1 μg/ml in PBST). Finally, cover glasses were mounted onto microscope slides (SuperFrost® PLUS) in VECTASHIELD® (Vector Laboratories). Confocal images were taken with an Ultra*VIEW* VoX spinning disc microscope (PerkinElmer) assembled to an Axio Observer D1 inverted stand (Zeiss) and using a 63x/1.4 NA Plan-Apochromat oil immersion objective.

3D-SIM was performed on a DeltaVision OMX V3 (Applied Precision) system equipped with a 100x/1.40 NA PlanApo oil immersion objective (Olympus), Cascade II: 512 EMCCD cameras (Photometrics) and 405, 488 and 593 nm diode lasers as previously described[39,40].

Live cell microscopy, fluorescence loss in photobleaching and quantitative fluorescence recovery after photobleaching analysis

Live cell imaging, fluorescence loss in photobleaching (FLIP) and fluorescence recovery after photobleaching (FRAP) experiments were performed on an Ultra*VIEW* VoX spinning disc microscope (PerkinElmer) as described before[41]. For acquisition the 488 nm laser line was set to 8-20%

transmission and the exposure time was set to 200 ms. For bleaching the 488 nm laser line was set to 100% transmission.

In FLIP experiments a rectangular region in the nucleus of 5x5 µm was repeatedly bleached. 2-4 cells were bleached in parallel. After 2 initial prebleach frames with a time interval of 5 s, 21 bleach cycles were performed. Each bleach cycle consisted of a bleaching event of ~500 ms followed by 2 postbleach frames with a time interval of 5 s. To evaluate the data, the mean intensity of the peripheral region, was determined over time. The outer border was determined using the "Auto threshold" function and the inner border was determined by eroding the selected region 4 times. Afterwards, the background intensity was subtracted from these results and the intensities relative to the first postbleach frame were determined. The measurements were performed in Fiji[42] followed by calculations in Excel.

In FRAP experiments a rectangular bleach region, covering approximately half of the nucleus, was chosen. Like in the FLIP experiments 2-4 cells were bleached in parallel. In order to capture fast kinetics (Fig. 1D) 10 prebleach frames with a time interval of 1 s were recorded, followed by a bleach event of ~700-900 ms and 60 frames with a time interval of 1 s and further 4 frames with a time interval of 1 min. For the detection of slow dynamic processes (Fig. 4D) z-stacks of 3 µm with a step size of 1 µm were recorded every 2 min. After 2-12 prebleach frames, the points were subsequently bleached manually, with a 10-15 s delay between bleaching and the first postbleach frame.

In long term imaging experiments a z-stack of 10.5 µm with a step size of 1.5 µm was recorded every 10 min for about 30 h. To avoid photodamage of the cells the ATOF of the laser was set to low transmission values of 8%.

siRNA

siRNAs were purchased from Eurofins and were used to transfect subconfluent HeLa or U2OS cells using Lipofectamine 2000 (Invitrogen) according to the manufacturer's instructions. NIPA siRNA corresponded to sense CAGAUUGAAUCGUCCAUGA•d(TT)[31] and TPR siRNA to sense GUAAUGAGCAGCAAGCCAG•d(TT)[43]. A firefly luciferase siRNA served as a control.

Purification of NIPA interactors

HEK293T cells were transfected with an NIPA-tandem-Strep-single-FLAG-tagged (NIPA-SF-TAP) construct as described previously[44]. Purification was performed as described[45]. The final eluate was boiled in LDS buffer, and then separated on a NuPAGENovex 4-12% Bis-Tris Mini Gel. Gel lanes containing separated immunocomplexes were cut into slices and in-gel trypsin digestion was performed following standard protocols.

LC-MS/MS and data analysis

Dried samples were dissolved in 0.1% formic acid (FA) prior to LC-MS/MS analysis. Nanoflow LC-MS/MS was performed by coupling a nanoLC-Ultra (Eksigent, CA) to a LTQ Orbitrap XL mass spectrometer (Thermo Fisher Scientific, GER), using a 20mm x 75 um ReproSil-Pur C18 (Dr. Maisch, GER) precolumn followed by a 400 mm x 50 um ReproSil-Pur C18 (Dr. Maisch, GER) analytical column. Peptide mixtures were analyzed during a 110 min gradient from 0 to 40% B (0.1% FA in AcN). The eluent was sprayed via emitter tips (New Objective) butt-connected to the analytical column.

The mass spectrometer was operated in data dependent mode, automatically switching between MS and MS/MS. Full scan spectra (from m/z 350 – 1200) were acquired in the Orbitrap with a resolution of 60 000 (at m/z 400) after accumulation to target value of 1E6. The 15 most intense ions at a threshold above 5000 ion counts were selected for collision-induced fragmentation in the linear ion trap (LTQ) at a normalized collision energy of 35%. Peak lists were extracted from MS data files using Mascot Distiller v2.2.1 (Matrix Science, UK) and subsequently searched against the Human IPI database version v3.68 using Carbamidomethyl cysteine as a fixed modification and Oxidation (M), Phospho (ST) as variable modifications. Trypsin was specified as the proteolytic enzyme and up to two missed cleavages were allowed. The mass tolerance of the precursor ion was set to 5ppm and for fragmentations to 0.6 Da. Data interpretation was performed with Scaffold2, v3.3.0. Proteins were filtered using a minimal protein identification probability of 99% and minimal peptide identification probability of 95%.

Cell culture

HeLa, U2OS, primary NIPA-deficient MEFs[46] and HEK293T cells were cultivated in DMEM supplemented with 10% FCS and penicillin/streptomycin or gentamycin in a humidified atmosphere of 5% CO_2 at 37°C.

Results

We previously characterized NIPA as an F-box containing protein, which is localized exclusively in the nucleus, by using affinity-purified polyclonal murine NIPA antiserum[31]. This antibody yielded a bright immunofluorescent signal, staining the whole nuclear interior. Recently, more specific antibodies, raised against human NIPA protein, have become commercially available (Sigma-Aldrich HPA024023 and Santa Cruz sc-365058) showing explicit staining of the nuclear periphery. As shown in Figure 1A (and Supplementary Figure 1) these antibodies detect NIPA at the nuclear periphery. To gain more insights into the precise localization of NIPA at the nuclear periphery, we performed super-resolution imaging, with 3D-structured illumination microscopy (3D-SIM)[40]. With this imaging technique, we analyzed the localization in respect to the nucleoporin NUP153 and a structural component of the

nuclear lamina, LaminB[47,48]. NIPA was found at the nuclear periphery in a region still stained by DAPI, but rather below NUP153 and Lamin B, suggesting not the nuclear membrane localization but rather a nuclear basket association (Fig. 1B).

Although immunostaining can reveal protein location in the steady state, it is not sufficient to provide information about the dynamic localization[49]. To obtain a more detailed picture of the subcellular localization and dynamics of NIPA, we generated a GFP-NIPA^{WT} fusion protein and examined the localization by a combination of fluorescence loss in photobleaching (FLIP) and fluorescence recovery after photobleaching (FRAP) (Fig. 1 C, D).

In FLIP experiments, the molecules in a region within the cell are repeatedly photobleached by an intense laser pulse. A decrease in intensity outside the bleached region allows for assessing the mobility of a protein between intracellular compartments and for measuring the kinetics of recruitment to the bleached region from various cellular areas[50]. When massively overexpressed, GFP-NIPA^{WT} shows a diffuse nuclear localization in contrast to the endogenous protein, which is localized at the nuclear envelope (compare Fig. 1A and 1C middle panel). However, when GFP-NIPA^{WT} levels were low, a profound localization to the nuclear periphery was observed (Fig. 1C, lower panel). The repeated bleaching in the small nuclear region resulted in almost complete loss of fluorescence inside the nucleus, leaving a strong signal in the peripheral compartment. These results show that the NIPA molecules at the nuclear envelope do not diffuse through the bleached area in the observed time frame of two minutes, indicating that NIPA is bound stably at the nuclear envelope. In contrast to this, the diffuse nuclear fraction of the protein when artificially high overexpressed is very mobile, comparable to free diffusing GFP. Together these results indicate that NIPA is stably bound to the nuclear periphery. In a complementary approach we used FRAP to further analyze the dynamics of GFP-NIPA^{WT}. In FRAP experiments, the recovery of intensity in a bleached region is observed over time. The faster the recovery, the more mobile the protein is. Like in the FLIP experiment, we could observe a very fast recovery of the nuclear fraction of GFP-NIPA^{WT} in high expressing cells, comparable to free GFP in the nucleus (Fig. 1D). However, in low expressing cells, we did not see a recovery at the nuclear periphery even after five minutes. Full recovery takes up to one hour (Fig. 4D), confirming the strong association of GFP-NIPA with the nuclear envelope.

Next, we wanted to determine if NIPA localization at the nuclear envelope changes during cell cycle progression. Live imaging of cells expressing low GFP-NIPA^{WT} was performed while the cell entered and accomplished mitosis (Fig. 1E). The nuclear envelope is disassembled during mitosis in higher eukaryotes and integral membrane proteins, such as lamin receptors or nuclear pore proteins, are dispersed throughout the endoplasmic reticulum[51,52]. NIPA shows a strong membrane co-localization until the cell reaches mitosis, where the envelope localization disappeared, most probably around

nuclear envelope breakdown (NEB) (Fig. 1E). At that time the cell entered prometaphase and NIPA became soluble in the cytoplasm. Membrane localization reappeared around nuclear envelope assembly, analogous to other NPC proteins[53]. All these data suggest, that NIPA is strongly anchored to the nuclear envelope.

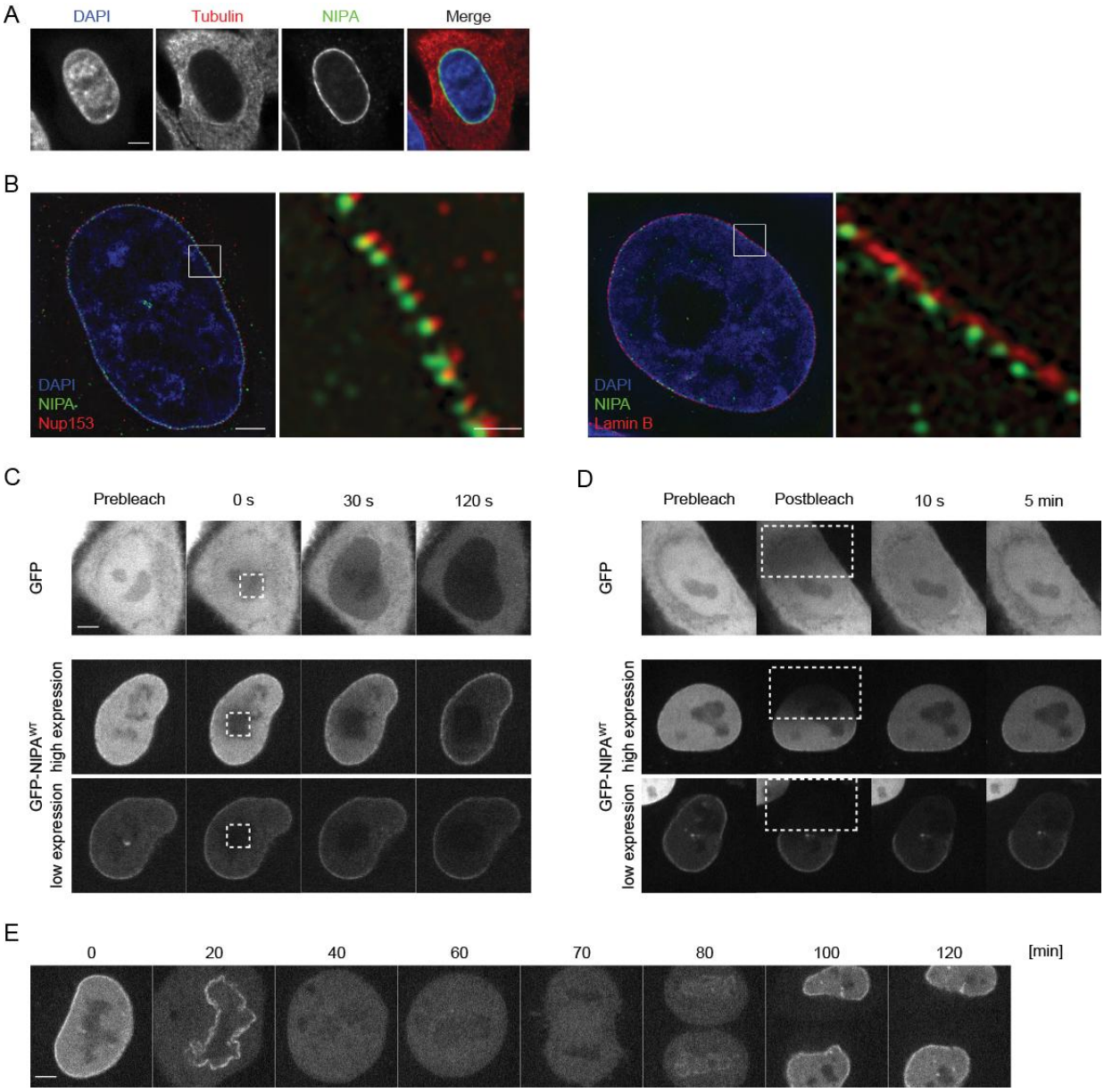

Figure 1. NIPA is localized and stably bound to the nuclear envelope. All experiments were performed in HeLa cells. (A) Representative confocal image of a cell stained with antibodies against endogenous NIPA (green) and Tubulin (red). Nuclei were counterstained with DAPI (blue). (B) 3D-SIM super-resolution images of cells stained with antibodies against endogenous NIPA (green) and NUP153 or Lamin B (red). Nuclei were counterstained with DAPI (blue). Eight-fold magnifications of the outlined regions are shown. (C) Representative FLIP experiment of GFP and GFP-NIPA^{WT} in high and low expressing cells. A rectangular region of 5x5 µm indicated by the dashed line was repeatedly bleached. (D) Representative FRAP experiment of GFP and GFP-NIPA in high and low expressing cells. A rectangular region covering half of the nucleus indicated by the dashed line was bleached once and the recovery in this area was observed over time. (E) Life cell imaging of a representative GFP-NIPA transfected HeLa cell undergoing mitotic division. Images in A, C-E were acquired at a confocal spinning disc microscope and optical mid sections are shown in all images. Scale bars: 5 µm and 1 µm (magnifications).

In order to determine biologically relevant interactions of NIPA, we combined tandem affinity purification (TAP) with mass spectrometric analyses. Table 1 shows a selected list of targets found in our screen.

Identified protein	Accesion Nr	MW	# of Assigned Spectra	Sequence coverage
Isoform 1 of Nuclear-interacting partner of ALK|C3HC zinc finger-like	IPI00301421	55 kDa	477	58%
Nucleoprotein TPR|TPR/MLP1/MLP2-like protein	IPI00742682	267 kDa	316	30%
Isoform 1 of S-phase kinase-associated protein 1	IPI00301364	19 kDa	15	15%
Isoform 1 of Cytoplasmic FMR1-interacting protein 1	IPI00644231	145 kDa	32	12%
Prohibitin-2	IPI00027252	33 kDa	23	24%
Ubiquitin and ribosomal protein S27a precursor	IPI00179330	18 kDa	21	30%

Table 1. Identification of NIPA interactors by mass spectrometry. HEK293T cells were transfected with a NIPA-tandem-Strep-single FLAG-tagged (NIPA-SF-TAP) construct and after purification with Streptactin and FLAG resin, samples were separated on an SDS-PAGE Gelelectrophoresis. Gel lanes were cut into slices and in-gel trypsin digestion was performed followed by LC-MS/MS analysis. Table 1 represents proteins with the highest sequence coverage.

As a third score we identified S-phase kinase-associated protein 1 (SKP1), which together with NIPA builds a functional SCF ligase. Interestingly, as a top scoring protein we also identified the nucleoporin TPR with the highest sequence coverage. TPR is a structural element of the NPC constituting the nuclear basket. Thus it´s high affinity to NIPA found in the proteomic analysis strongly suggests a co-localization in this nuclear compartment. To further investigate the interaction between NIPA and TPR, we performed immunoprecipitation assays (Fig. 2). As a control we overexpressed different F-box proteins (FBPs) to eliminate the possibility that TPR was a “sticky” protein that bound non-specifically to other proteins *in vitro*. We transfected FLAG-tagged NIPA, FBXO9, FBW2 and FBW11 into HEK293T cells and performed precipitations using anti-FLAG beads. NIPA was the only F-box protein (among four tested) that co-immunoprecipitated with endogenous TPR (Fig. 2A). Additionally, after nuclear fractionation, FLAG-tagged NIPA was efficiently immunoprecipitating TPR from the nuclear extracts showing that the NIPA-TPR interaction takes place in the nucleus (Fig. 2B). *Vice versa* overexpressed TPR was able to co-immunoprecipitate endogenous NIPA (Fig. 2C) confirming a specific interaction between TPR and NIPA. Altogether, in agreement with the results of mass spectrometry, immunoprecipitation experiments proof that NIPA specifically binds to the nucleoporin TPR.

NIPA was previously characterized as an F-box protein, containing an NLS domain for the nuclear localization as well as a zinc-finger-like domain in the N-terminus as a potential substrate interaction motif[33] (Fig. 3A). Following the identification of TPR as an interaction partner of NIPA, we were interested to identify the exact TPR-binding region within NIPA. Therefore we generated FLAG-tagged NIPA constructs by introducing point mutations into the characteristic motifs and performed co-

immunoprecipitations against endogenous TPR (Fig. 3B). HEK293T cells were transfected with FLAG-tagged NIPA: wild type (WT); zinc-finger mutant (ΔZnF) and nuclear localization signal mutant (ΔNLS) along with an empty vector as a control and immunoprecipitation was performed using FLAG beads. Consistent with previous results, FLAG-NIPA^{WT} binds efficiently to TPR (Fig. 3B). Interestingly, a mutation in the zinc-finger-like domain of NIPA resulted in complete abrogation of the binding to TPR, showing substrate interaction abilities of the zinc-finger domain [33] (Fig. 3B).

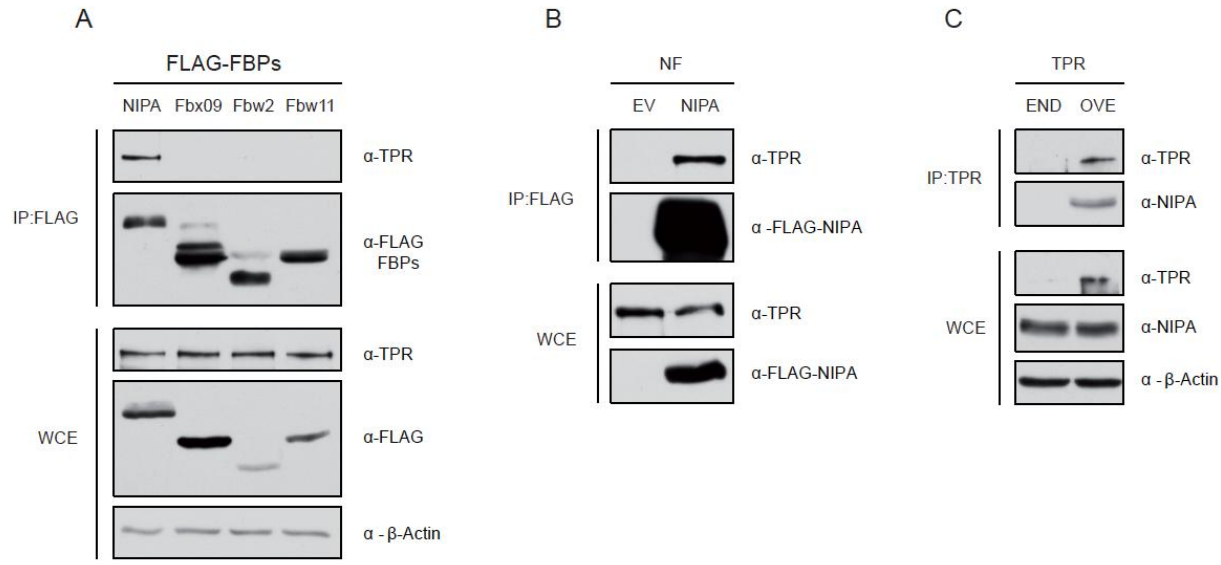

Figure 2. NIPA protein interacts with TPR. (A) HEK293T cells were transfected with the indicated FLAG-tagged F-box proteins (FBPs) and then immunoprecipitated (IP) with anti-FLAG beads. Immunocomplexes were probed with antibodies against indicated proteins. (B) FLAG-tagged NIPA was overexpressed in HEK293T cells and cell fractionation was performed to obtain nuclear fractions (NF). IP was performed using anti-FLAG beads, blotted and probed with anti-TPR antibody. Empty vector (EV) was transfected as a control. (C) TPR was overexpressed (OVE) in HEK293T cells and together with endogenous (END) protein immunoprecipitated with anti-TPR antibody. Co-immunoprecipitation with NIPA was detected in Western blot using anti-NIPA antibody. WCE – whole cell extracts.

In order to determine whether binding to TPR via the zinc-finger domain is required for NIPA to localize to the nuclear envelope we performed FLIP experiments using GFP-fusion proteins (Fig. 3C, Fig. S2). Cells expressing GFP-NIPA^{WT}, GFP-NIPA$^{\Delta ZnF}$ or GFP-NIPA$^{\Delta F\text{-box}}$ were repeatedly photobleached in a central nuclear region, and images were taken in between. GFP-NIPA^{WT} was localized at the nuclear membrane after photobleaching (Fig. 3C upper panel). In contrast, photobleaching of the GFP-NIPA$^{\Delta ZnF}$ protein resulted in the loss of fluorescence in the whole nucleus including the nuclear envelope (Fig. 3C middle panel). This indicates that the zinc-finger domain is necessary for anchoring NIPA to the NPC. Next we photobleached cells expressing the GFP-NIPA$^{\Delta F\text{-box}}$ mutant, to determine if a functional SCF-complex is required for anchoring NIPA to the NPC. Bleaching experiments demonstrated no requirement of a functional SCF complex, because the F-box mutant of NIPA, which is unable to bind to the SKP1 subunit of the SCF, was still present at the nuclear envelope after photobleaching (Fig. 3C, lower panel).

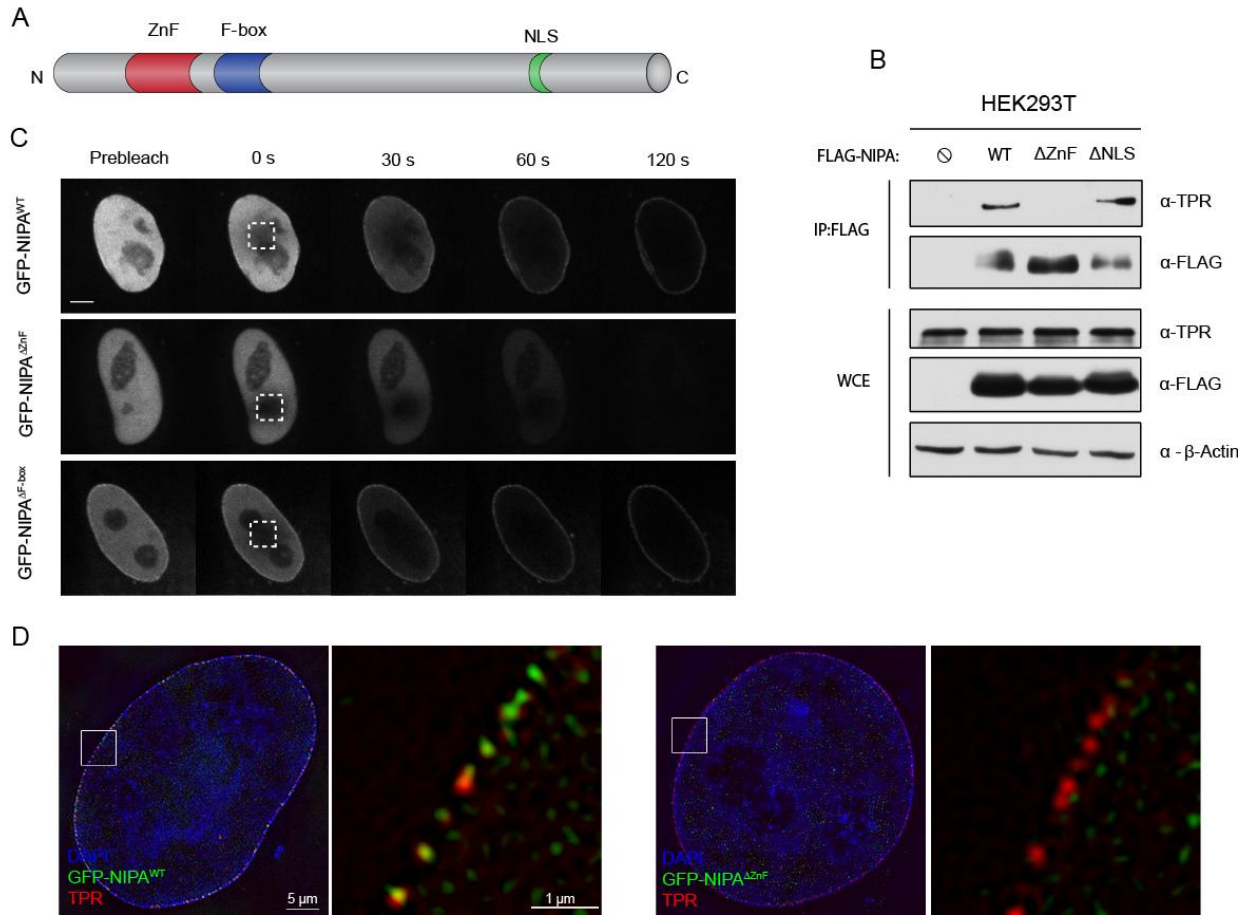

Figure 3. Zinc-finger motif in NIPA is responsible for the binding to TPR at the NPC. (A) Domain structure of NIPA depicting zinc-finger motif (ZnF), F-box motif and nuclear localization signal (NLS). (B) HEK293T cells were transfected with FLAG-tagged NIPA constructs: NIPA wild type (WT), NIPA zinc-finger mutant (ΔZnF) and NIPA nuclear localization signal mutant (ΔNLS) and empty vector (EV) as a control. Whole-cell extracts (WCE) were immunoprecipitated with anti-FLAG beads and the indicated proteins were detected by immunoblotting. (C) Representative FLIP experiment of GFP-NIPA^{WT}, GFP-NIPA$^{\Delta ZnF}$ mutant and GFPNIPA$^{\Delta F\text{-}box}$ mutant in HeLa cells performed at a spinning disc confocal microscope. A rectangular region indicated by the dashed line was repeatedly bleached. Scale bar: 5 µm. (D) Super-resolution 3D-SIM optical mid sections from HeLa cells transfected with GFP-NIPA^{WT} or GFP-NIPA$^{\Delta ZnF}$ mutant. The fixed cells were stained with antibodies against endogenous TPR (red) and the GFP signal was enhanced using the GFP-booster (ChromoTek, green). Nuclei were counterstained with DAPI (blue).

Finally we also applied super-resolution microscopy to study the importance of the zinc-finger domain for NIPA localization at the NPC (Fig. 3D). We investigated GFP-NIPA^{WT} and GFP-NIPA$^{\Delta ZnF}$ mutant protein in HeLa cells. In agreement with previous findings, the wild type protein was located at the NPC, co-localizing with TPR (Fig. 3D left panel), whereas the zinc-finger mutation resulted in subnuclear mislocalization of the protein from the NPC (Fig. 3D right panel). Taken together, these data strongly suggest that the zinc-finger domain encoded in the N-terminus of NIPA is responsible for the interaction with the nucleoporin TPR and that this interaction localizes NIPA to the nuclear pore complexes.

The role of TPR as an architectural element of the NPC was reported previously[11]. However, in another report the scaffolding abilities of TPR have been controversially discussed[12]. Therefore, we aimed to assess whether TPR is required for anchoring NIPA to the NPC. In order to determine the ability of TPR

to tether NIPA to the NPC, we suppressed TPR synthesis by synthetic siRNA in HeLa cells (Fig. 4A). As shown by western blot analysis, the level of TPR was specifically reduced after 72 h of treatment with siRNA with immunofluorescence. Interestingly, down-regulation of TPR at the same time leads to degradation of NIPA, whereas transient down-regulation of NIPA by siRNA treatment had no clear effect on TPR expression (Fig. 4A). These data indicate that TPR is required for the stability of NIPA.

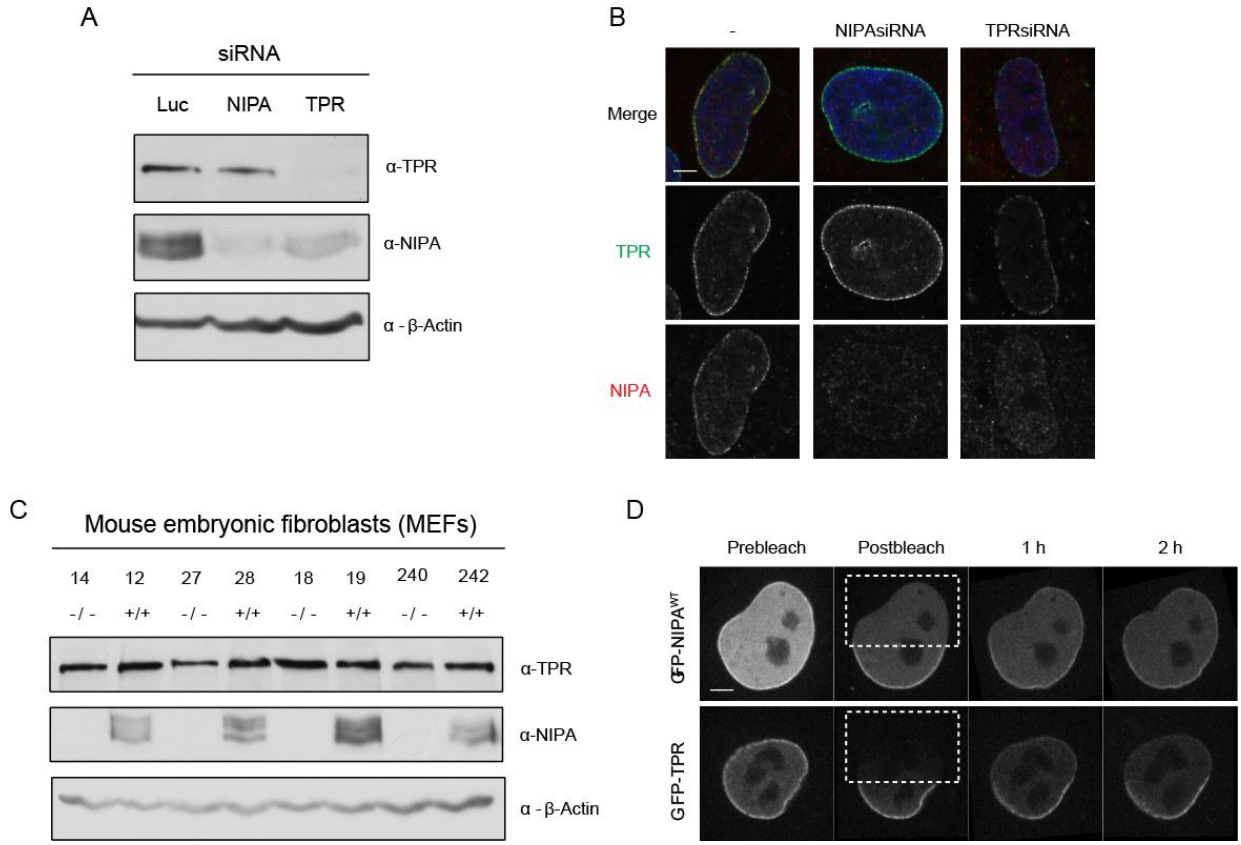

Figure 4. TPR constitutes the essential anchoring element for NIPA localization at the NPC. (A) HeLa cells were transfected with siRNA and subjected to immunoblotting with the indicated antibodies after 72 h. (B) U2OS cells were treated with siRNAs (NIPA and TPR) for 48 h and stained with antibodies against endogenous NIPA (red) or TPR (green). Nuclei were counterstained with DAPI (blue). Scale bar: 5 μm. (C) Different mouse embryonic fibroblasts (MEFs) cell lines derived from NIPA deficient (-/-) or NIPA wild type (+/+) mice were subjected to immunoblot analyses and probed with indicated antibodies. (D) Representative FRAP experiment in GFP-NIPA^{WT} or GFP-TPR expressing HeLa cells. A rectangular region covering half of the nucleus indicated by the dashed line was bleached once and the recovery in this area was observed over time with spinning disk confocal microscopy. Scale bar: 5 μm.

We next analyzed down-regulation of NIPA and TPR by siRNA for their nuclear envelope localization. As seen in Figure 4B, cells treated with TPR siRNA showed partial depletion of TPR which lead to severe down-regulation of NIPA from the whole nuclear compartment. In contrast, knockdown of NIPA with siRNA did not alter the localization of the TPR staining at the nuclear periphery (Fig. 4B). Furthermore, results from different immortalized MEF cell lines, obtained from NIPA wild type and knockout mice, showed similar TPR levels in cells lacking NIPA expression when compared to the wild type (Fig. 4C). Hence, TPR downregulation alters the distribution of NIPA in the nucleus and is

therefore crucial for its proper nuclear localization and stability, whereas NIPA depletion has no visible effect on TPR expression or localization.

To further investigate the anchoring abilities of TPR towards NIPA, we compared protein mobility using the method FRAP. We employed FRAP analysis to test the nuclear kinetics of the GFP-tagged NIPA and TPR by bleaching the fluorescence in half of the nucleus with a high-power laser and tracking the rate of nuclear membrane recovery over two hours. The recovery of GFP-TPR at the nuclear envelope was slower than that of GFP-NIPA, denoting slower TPR protein dynamics, thereby suggesting a stronger association with the nuclear envelope in comparison to NIPA (Fig. 4D). In summary, these results strongly indicate that TPR acts as a scaffold protein targeting NIPA to its stable binding site at the NPC.

Discussion

Post-translational modifications are fundamental controlling mechanisms responsible for intracellular signaling pathways. Ubiquitin-mediated proteasomal degradation of proteins plays an important role among them, since it was shown to be crucial for the control of cellular events like cell-cycle progression[54]. Due to their ability of substrate recognition, F-box proteins play the main role in ubiquitin-mediated proteolysis. We previously characterized a new SCF-E3 ligase SCF^{NIPA}, in which the nuclear F-box protein NIPA is responsible for targeting cyclin B1 for degradation in interphase, thereby contributing to the timing of mitotic entry[31].

In this study, we have analyzed the localization of NIPA in more detail and were able to show that NIPA is not only part of the nuclear envelope but is mainly localized to the nucleoplasmic face of the NPC. We found that the localization of NIPA to the NPC is mediated by its binding to the nucleoporin TPR at the nuclear basket. A previous study pointed out the controversial role of TPR as an architectural element of the NPC[12]. Although it was revealed that TPR is tethered to the NPC by the interaction with NUP153, the question whether TPR itself acts as a scaffold onto which other NPC components need to be assembled still remained elusive. Here we show that TPR is the anchoring protein for NIPA and that this strong interaction is essential for the proper localization of NIPA to the NPC. Silencing of TPR by synthetic siRNA resulted in destabilization of NIPA and it subsequent degradation, confirming the role of TPR as a scaffolding protein. We also identified the zinc-finger motif in NIPA as being responsible for the binding to TPR and showed that disruption of this domain leads to mislocalization of NIPA from the nuclear pore. In contrast, mutation of the F-box domain did not affect the localization, indicating that a functional SCF complex is not necessary for the association with the NPC. These findings implicate that NIPA is a nuclear pore associated protein and suggest a functional relevance for its localization.

Previous reports by others have shown that TPR is both a substrate and a scaffold for activated ERKs[22]. It was reported that phosphorylation of TPR by ERK stabilizes their interaction what in consequence positions ERK2 for the phosphorylation of further potential substrates at the NPC. In addition, ERK-TPR interaction regulates the translocation of activated ERK2[22]. Moreover, Kosako et al. demonstrated that ERK is a physiological nucleoporin kinase and suggested a role for TPR in ERK-mediated phosphorylation at the nuclear pore[55]. Interestingly, our recent study revealed NIPA as an exclusive substrate of ERK2 and that this phosphorylation leads to disruption of the SCF^{NIPA} activity[35]. Hence, we hypothesize the existence of a scaffold located at the NPC, constituted by the filaments of TPR, which allows for positioning of both, the kinase and the substrate, in close proximity. In this model, ERK2 may require a platform constituted by TPR to efficiently phosphorylate NIPA at the NPC. We observed lack of a phosphorylation in the SDS-PAGE when NIPA was overexpressed in cells with mutated zinc-finger motif, supporting our assumption (data not shown). Zinc-finger mutation abrogates the binding to TPR, leading to mislocalization of the protein to the nuclear interior (Fig. 3). As a result, it is conceivable that ERK2 cannot phosphorylate NIPA due to the loss of its anchoring site at the NPC.

Spatial control of the proteolysis is emerging as an important regulator of mitotic transitions[56]. Anaphase promoting complex/cyclosome (APC/C) could serve as an example of controlled protein degradation in space and time. It has been proposed that the Cdc20-APC/C complex, associated with the mitotic spindle, targets cyclin B for degradation in the early phase of mitotic exit therefore activating the Cdh1-APC/C complex further to target cyclin B for destruction throughout the cell, leading to mitotic exit[57]. Other regulatory mechanisms exist which rely on the compartmentalization of the protein turnover. For instance, ER-associated protein degradation (ERAD) is an ubiquitin-proteasome based system responsible for the degradation of membrane and luminal proteins of the endoplasmic reticulum, and E3 ligases participating in this process are localized to the ER/nuclear envelope[58,59]. Also SUMO proteases were recently connected with the filaments of the NPC[28,29,60]. All these evidence argue for the growing importance of the spatial control of protein degradation, restricting the recognition of substrates and functional proteolysis to specific cellular compartments.

Although at this moment, we can only speculate about the exact function that NIPA may have at the NPC, our findings, which revealed NIPA localization at the nuclear pore, are especially relevant with respect to the ubiquitin proteasome system. This study provides additional evidence on the specific localization of an E3 ligase, which could predestinate its function according to the substrate of NIPA – cyclin B1. Therefore we propose a model, complementing our previous observations[31], in which NIPA guards the genome integrity by controlling cyclin B1 abundance in space and time (outlined in Figure 5). Consistently, NIPA localizes to the nucleoplasmic site of the NPC by the interaction with TPR and is able to transfer ubiquitin directly on cyclin B1 when it crosses the nuclear barrier prematurely in interphase. Such a model suggests the formation of a “cyclin trap” directly at the gate, targeting cyclin

B1 for degradation just upon entry to the nucleus (Fig. 5A). At the G_2/M phase of the cell cycle, NIPA is phosphorylated, what leads to dissociation of the SCF^{NIPA}, allowing for accumulation of cyclin B1 and subsequent mitotic entry (Fig. 5B). Thus, according to our model, the NPC localization of NIPA could be essential for the spatial control of cyclin B1.

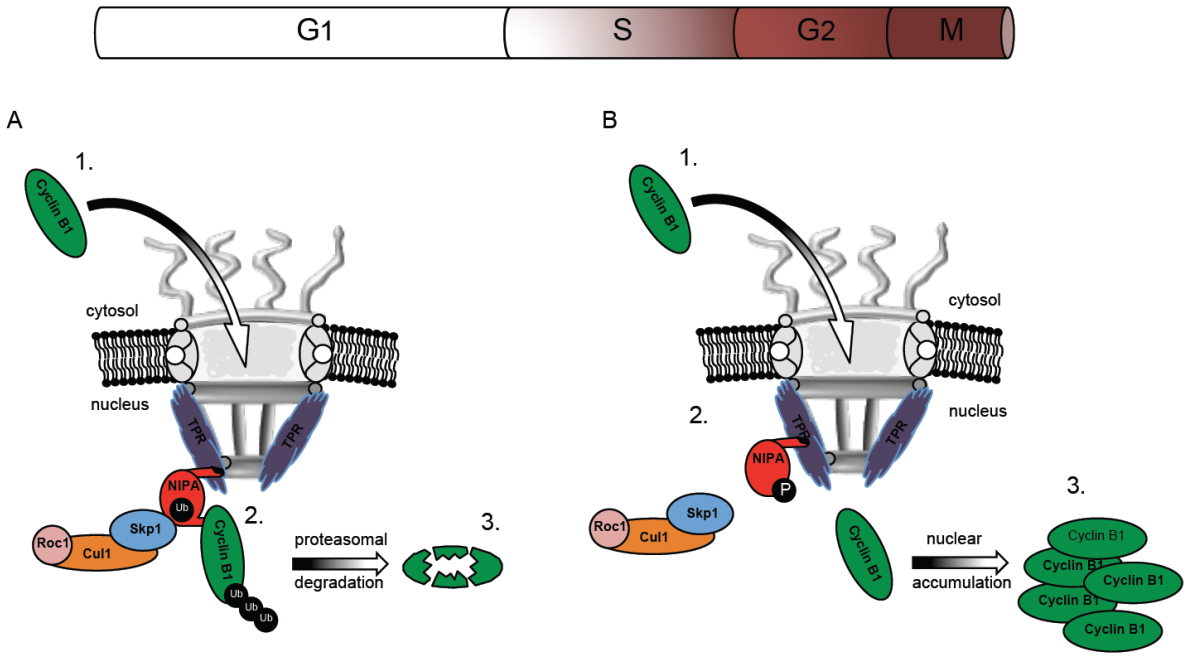

Figure 5. Theoretical model of SCF^{NIPA} activity in the regard to its nuclear localization. The model postulates that the SCF^{NIPA} complex is a gate guardian of the genome integrity by promoting degradation of cyclin B1 during interphase. (A) Cyclin B1 enters the nucleus through the NPC (1), is directly ubiquitinated (2) and headed for the proteasomal degradation (3). (B) In the G_2/M phase NIPA is phospohrylated (2), leading to the dissociation of the SCF^{NIPA} complex and its subsequent inactivation. Cyclin B1 can accumulate in the nucleus (3) triggering the G_2 – M transition.

Recently, Niepel et al. reported that Mlp1 and Mlp2, the yeast homologues of TPR, are major NPC basket components and showed that these proteins constitute a dynamic interactome, together with Esc1p and the proteasome[61]. This finding, which connects the proteasome to the vicinity of the nuclear pore, is a fascinating endorsement of our model suggesting that the whole protein degradation machinery might be organized at the same, specialized subcellular compartment – the nuclear pore complex. In this regard, TPR could function as a scaffold for NIPA, its regulatory kinase ERK2 as well as the proteasome within this model: upon translocation of cyclin B1 to the nucleus, NIPA directly transfers ubiquitin on the substrate, targeting it for immediate proteasomal degradation *in situ* and ERK2 directly controls NIPA during the cell cycle phases. Thus, our model provides an explanation for a tight and highly efficient guardian against the premature mitotic entry, maintaining genome integrity.

In summary, we have further characterized the previously identified F-box-containing protein NIPA as a novel nuclear pore associated protein and proposed that the specific localization of NIPA to the NPC may have a potential implication in the spatial control of cyclin B1 during mammalian cell cycle.

References

1. Cronshaw, J.M., Krutchinsky, A.N., Zhang, W., Chait, B.T. & Matunis, M.J. Proteomic analysis of the mammalian nuclear pore complex. *J Cell Biol* **158**, 915-927 (2002).
2. Raices, M. & D'Angelo, M.A. Nuclear pore complex composition: a new regulator of tissue-specific and developmental functions. *Nature reviews. Molecular cell biology* **13**, 687-699 (2012).
3. Unwin, P.N. & Milligan, R.A. A large particle associated with the perimeter of the nuclear pore complex. *J Cell Biol* **93**, 63-75 (1982).
4. Maimon, T., Elad, N., Dahan, I. & Medalia, O. The human nuclear pore complex as revealed by cryo-electron tomography. *Structure* **20**, 998-1006 (2012).
5. Lim, R.Y. & Fahrenkrog, B. The nuclear pore complex up close. *Current opinion in cell biology* **18**, 342-347 (2006).
6. Goldberg, M.W. & Allen, T.D. High resolution scanning electron microscopy of the nuclear envelope: demonstration of a new, regular, fibrous lattice attached to the baskets of the nucleoplasmic face of the nuclear pores. *J Cell Biol* **119**, 1429-1440 (1992).
7. Hoelz, A., Debler, E.W. & Blobel, G. The structure of the nuclear pore complex. *Annu Rev Biochem* **80**, 613-643 (2011).
8. Kiseleva, E.*, et al.* Yeast nuclear pore complexes have a cytoplasmic ring and internal filaments. *Journal of structural biology* **145**, 272-288 (2004).
9. Grossman, E., Medalia, O. & Zwerger, M. Functional architecture of the nuclear pore complex. *Annual review of biophysics* **41**, 557-584 (2012).
10. Shah, S., Tugendreich, S. & Forbes, D. Major binding sites for the nuclear import receptor are the internal nucleoporin Nup153 and the adjacent nuclear filament protein Tpr. *J Cell Biol* **141**, 31-49 (1998).
11. Krull, S., Thyberg, J., Bjorkroth, B., Rackwitz, H.R. & Cordes, V.C. Nucleoporins as components of the nuclear pore complex core structure and Tpr as the architectural element of the nuclear basket. *Mol Biol Cell* **15**, 4261-4277 (2004).
12. Hase, M.E. & Cordes, V.C. Direct interaction with nup153 mediates binding of Tpr to the periphery of the nuclear pore complex. *Mol Biol Cell* **14**, 1923-1940 (2003).
13. Zimowska, G., Aris, J.P. & Paddy, M.R. A Drosophila Tpr protein homolog is localized both in the extrachromosomal channel network and to nuclear pore complexes. *J Cell Sci* **110 (Pt 8)**, 927-944 (1997).
14. Hase, M.E., Kuznetsov, N.V. & Cordes, V.C. Amino acid substitutions of coiled-coil protein Tpr abrogate anchorage to the nuclear pore complex but not parallel, in-register homodimerization. *Mol Biol Cell* **12**, 2433-2452 (2001).
15. Skaggs, H.S.*, et al.* HSF1-TPR interaction facilitates export of stress-induced HSP70 mRNA. *J Biol Chem* **282**, 33902-33907 (2007).
16. Bangs, P.*, et al.* Functional analysis of Tpr: identification of nuclear pore complex association and nuclear localization domains and a role in mRNA export. *J Cell Biol* **143**, 1801-1812 (1998).
17. Park, M.*, et al.* Mechanism of met oncogene activation. *Cell* **45**, 895-904 (1986).

18. Frosst, P., Guan, T., Subauste, C., Hahn, K. & Gerace, L. Tpr is localized within the nuclear basket of the pore complex and has a role in nuclear protein export. *J Cell Biol* **156**, 617-630 (2002).
19. David-Watine, B. Silencing nuclear pore protein Tpr elicits a senescent-like phenotype in cancer cells. *PLoS One* **6**, e22423 (2011).
20. Lee, S.H., Sterling, H., Burlingame, A. & McCormick, F. Tpr directly binds to Mad1 and Mad2 and is important for the Mad1-Mad2-mediated mitotic spindle checkpoint. *Genes & development* **22**, 2926-2931 (2008).
21. De Souza, C.P., Hashmi, S.B., Nayak, T., Oakley, B. & Osmani, S.A. Mlp1 acts as a mitotic scaffold to spatially regulate spindle assembly checkpoint proteins in Aspergillus nidulans. *Mol Biol Cell* **20**, 2146-2159 (2009).
22. Vomastek, T.*, et al.* Extracellular signal-regulated kinase 2 (ERK2) phosphorylation sites and docking domain on the nuclear pore complex protein Tpr cooperatively regulate ERK2-Tpr interaction. *Mol Cell Biol* **28**, 6954-6966 (2008).
23. Lemaitre, C.*, et al.* The nucleoporin 153, a novel factor in double-strand break repair and DNA damage response. *Oncogene* **31**, 4803-4809 (2012).
24. Oza, P., Jaspersen, S.L., Miele, A., Dekker, J. & Peterson, C.L. Mechanisms that regulate localization of a DNA double-strand break to the nuclear periphery. *Genes & development* **23**, 912-927 (2009).
25. Franks, T.M. & Hetzer, M.W. The role of Nup98 in transcription regulation in healthy and diseased cells. *Trends Cell Biol* **23**, 112-117 (2013).
26. Sarma, N.J.*, et al.* The nuclear pore complex mediates binding of the Mig1 repressor to target promoters. *PLoS One* **6**, e27117 (2011).
27. Funasaka, T., Tsuka, E. & Wong, R.W. Regulation of autophagy by nucleoporin Tpr. *Scientific reports* **2**, 878 (2012).
28. Zhang, H., Saitoh, H. & Matunis, M.J. Enzymes of the SUMO modification pathway localize to filaments of the nuclear pore complex. *Mol Cell Biol* **22**, 6498-6508 (2002).
29. Lewis, A., Felberbaum, R. & Hochstrasser, M. A nuclear envelope protein linking nuclear pore basket assembly, SUMO protease regulation, and mRNA surveillance. *J Cell Biol* **178**, 813-827 (2007).
30. Werner, A., Flotho, A. & Melchior, F. The RanBP2/RanGAP1*SUMO1/Ubc9 complex is a multisubunit SUMO E3 ligase. *Molecular cell* **46**, 287-298 (2012).
31. Bassermann, F.*, et al.* NIPA defines an SCF-type mammalian E3 ligase that regulates mitotic entry. *Cell* **122**, 45-57 (2005).
32. Ouyang, T.*, et al.* Identification and characterization of a nuclear interacting partner of anaplastic lymphoma kinase (NIPA). *J Biol Chem* **278**, 30028-30036 (2003).
33. Bassermann, F.*, et al.* Multisite phosphorylation of nuclear interaction partner of ALK (NIPA) at G2/M involves cyclin B1/Cdk1. *J Biol Chem* **282**, 15965-15972 (2007).
34. Klitzing, C.*, et al.* APC/C(Cdh1)-mediated degradation of the F-box protein NIPA is regulated by its association with Skp1. *PLoS One* **6**, e28998 (2011).
35. Illert, A.L.*, et al.* Extracellular signal-regulated kinase 2 (ERK2) mediates phosphorylation and inactivation of nuclear interaction partner of anaplastic lymphoma kinase (NIPA) at G2/M. *J Biol Chem* **287**, 37997-38005 (2012).
36. Skaar, J.R. & Pagano, M. Control of cell growth by the SCF and APC/C ubiquitin ligases. *Current opinion in cell biology* **21**, 816-824 (2009).
37. Gloeckner, C.J., Boldt, K., Schumacher, A., Roepman, R. & Ueffing, M. A novel tandem affinity purification strategy for the efficient isolation and characterisation of native protein complexes. *Proteomics* **7**, 4228-4234 (2007).

38. Gu, H., Liang, Y., Mandel, G. & Roizman, B. Components of the REST/CoREST/histone deacetylase repressor complex are disrupted, modified, and translocated in HSV-1-infected cells. *Proc Natl Acad Sci U S A* **102**, 7571-7576 (2005).
39. Schneider, K.*, et al.* Dissection of cell cycle-dependent dynamics of Dnmt1 by FRAP and diffusion-coupled modeling. *Nucleic Acids Res* **41**, 4860-4876 (2013).
40. Schermelleh, L.*, et al.* Subdiffraction multicolor imaging of the nuclear periphery with 3D structured illumination microscopy. *Science* **320**, 1332-1336 (2008).
41. Thanisch, K.*, et al.* Targeting and tracing of specific DNA sequences with dTALEs in living cells. *Nucleic Acids Res* (2013).
42. Schindelin, J.*, et al.* Fiji: an open-source platform for biological-image analysis. *Nat Methods* **9**, 676-682 (2012).
43. Kuznetsov, N.V.*, et al.* The evolutionarily conserved single-copy gene for murine Tpr encodes one prevalent isoform in somatic cells and lacks paralogs in higher eukaryotes. *Chromosoma* **111**, 236-255 (2002).
44. Mendoza, M.C., Er, E.E. & Blenis, J. The Ras-ERK and PI3K-mTOR pathways: cross-talk and compensation. *Trends in biochemical sciences* **36**, 320-328 (2011).
45. Fernandez-Saiz, V.*, et al.* SCFFbxo9 and CK2 direct the cellular response to growth factor withdrawal via Tel2/Tti1 degradation and promote survival in multiple myeloma. *Nat Cell Biol* **15**, 72-81 (2013).
46. Illert, A.L.*, et al.* Targeted inactivation of nuclear interaction partner of ALK disrupts meiotic prophase. *Development* **139**, 2523-2534 (2012).
47. Moudry, P.*, et al.* Nucleoporin NUP153 guards genome integrity by promoting nuclear import of 53BP1. *Cell death and differentiation* **19**, 798-807 (2012).
48. Worman, H.J., Yuan, J., Blobel, G. & Georgatos, S.D. A lamin B receptor in the nuclear envelope. *Proc Natl Acad Sci U S A* **85**, 8531-8534 (1988).
49. Phair, R.D. & Misteli, T. High mobility of proteins in the mammalian cell nucleus. *Nature* **404**, 604-609 (2000).
50. Ishikawa-Ankerhold, H.C., Ankerhold, R. & Drummen, G.P. Advanced fluorescence microscopy techniques--FRAP, FLIP, FLAP, FRET and FLIM. *Molecules* **17**, 4047-4132 (2012).
51. Ellenberg, J.*, et al.* Nuclear membrane dynamics and reassembly in living cells: targeting of an inner nuclear membrane protein in interphase and mitosis. *J Cell Biol* **138**, 1193-1206 (1997).
52. Yang, L., Guan, T. & Gerace, L. Integral membrane proteins of the nuclear envelope are dispersed throughout the endoplasmic reticulum during mitosis. *J Cell Biol* **137**, 1199-1210 (1997).
53. Bodoor, K.*, et al.* Sequential recruitment of NPC proteins to the nuclear periphery at the end of mitosis. *J Cell Sci* **112 (Pt 13)**, 2253-2264 (1999).
54. Hershko, A. & Ciechanover, A. The ubiquitin system. *Annu Rev Biochem* **67**, 425-479 (1998).
55. Kosako, H.*, et al.* Phosphoproteomics reveals new ERK MAP kinase targets and links ERK to nucleoporin-mediated nuclear transport. *Nature structural & molecular biology* **16**, 1026-1035 (2009).
56. Pines, J. & Lindon, C. Proteolysis: anytime, any place, anywhere? *Nat Cell Biol* **7**, 731-735 (2005).
57. Raff, J.W., Jeffers, K. & Huang, J.Y. The roles of Fzy/Cdc20 and Fzr/Cdh1 in regulating the destruction of cyclin B in space and time. *J Cell Biol* **157**, 1139-1149 (2002).

58. Swanson, R., Locher, M. & Hochstrasser, M. A conserved ubiquitin ligase of the nuclear envelope/endoplasmic reticulum that functions in both ER-associated and Matalpha2 repressor degradation. *Genes & development* **15**, 2660-2674 (2001).
59. Bays, N.W., Gardner, R.G., Seelig, L.P., Joazeiro, C.A. & Hampton, R.Y. Hrd1p/Der3p is a membrane-anchored ubiquitin ligase required for ER-associated degradation. *Nat Cell Biol* **3**, 24-29 (2001).
60. Zhao, X., Wu, C.Y. & Blobel, G. Mlp-dependent anchorage and stabilization of a desumoylating enzyme is required to prevent clonal lethality. *J Cell Biol* **167**, 605-611 (2004).
61. Niepel, M*., et al.* The nuclear basket proteins Mlp1p and Mlp2p are part of a dynamic interactome including Esc1p and the proteasome. *Mol Biol Cell* (2013).

Supplementary figures

S1

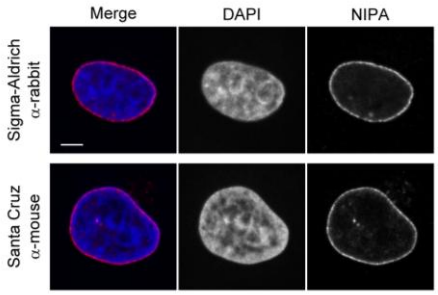

Supplementary Figure 1. Nuclear localization of NIPA detected with antibodies. The experiment was performed in HeLa cells. (A) Representative confocal image of cells stained with antibodies from Santa Cruz and Sigma-Aldrich against endogenous NIPA (red). Nuclei were counterstained with DAPI (blue). Images were acquired at a confocal spinning disc microscope and optical mid sections are shown. Scale bar: 5 µm.

S2

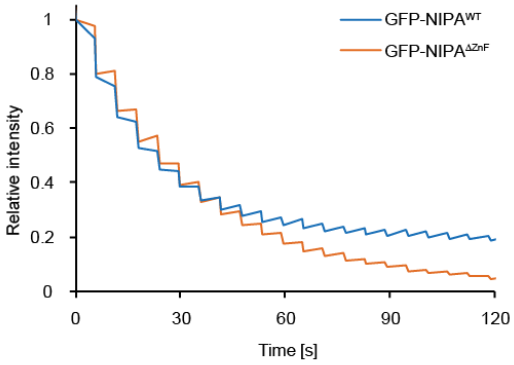

Supplementary Figure 2. Quantification of FLIP experiments shown in Figure 3C. Background corrected intensities of the peripheral region of the nucleus relative to the first postbleach image of GFP-NIPA^{WT} (blue) and GFP-NIPA$^{\Delta ZnF}$ (orange).

2.6 Targeting and tracing of specific DNA sequences with dTALEs in living cells

Nucleic Acids Research Advance Access published December 25, 2013

Nucleic Acids Research, 2013, 1–10
doi:10.1093/nar/gkt1348

Targeting and tracing of specific DNA sequences with dTALEs in living cells

Katharina Thanisch[1], Katrin Schneider[1], Robert Morbitzer[2], Irina Solovei[1], Thomas Lahaye[2], Sebastian Bultmann[1,*] and Heinrich Leonhardt[1,*]

[1]Department of Biology II, Humanbiology and Bioimaging, Center for Integrated Protein Science Munich (CIPSM), Ludwig Maximilians University Munich, 82152 Planegg-Martinsried, Germany and [2]Department of Biology I, Genetics, Ludwig Maximilians University Munich, 82152 Planegg-Martinsried, Germany

Received August 30, 2013; Revised November 5, 2013; Accepted December 4, 2013

ABSTRACT

Epigenetic regulation of gene expression involves, besides DNA and histone modifications, the relative positioning of DNA sequences within the nucleus. To trace specific DNA sequences in living cells, we used programmable sequence-specific DNA binding of designer transcription activator-like effectors (dTALEs). We designed a recombinant dTALE (msTALE) with variable repeat domains to specifically bind a 19-bp target sequence of major satellite DNA. The msTALE was fused with green fluorescent protein (GFP) and stably expressed in mouse embryonic stem cells. Hybridization with a major satellite probe (3D-fluorescent *in situ* hybridization) and co-staining for known cellular structures confirmed *in vivo* binding of the GFP-msTALE to major satellite DNA present at nuclear chromocenters. Dual tracing of major satellite DNA and the replication machinery throughout S-phase showed co-localization during mid to late S-phase, directly demonstrating the late replication timing of major satellite DNA. Fluorescence bleaching experiments indicated a relatively stable but still dynamic binding, with mean residence times in the range of minutes. Fluorescently labeled dTALEs open new perspectives to target and trace DNA sequences and to monitor dynamic changes in subnuclear positioning as well as interactions with functional nuclear structures during cell cycle progression and cellular differentiation.

INTRODUCTION

Covalent DNA and histone modifications play a key role in epigenetic gene regulation and have been intensively investigated over the past decades. While there is no doubt that higher order chromatin structures and nuclear genome organization also play important roles, they are far less amenable to systematic analysis due to their transient and fragile nature that can only be studied in the cellular context.

Multicolor fluorescent *in situ* hybridization (FISH) enabled the simultaneous visualization of multiple DNA sequences in fixed cells and indicated the territorial organization of all chromosomes in interphase nuclei (1). In general, the subnuclear distribution of chromosomal segments within the nucleus and with respect to chromosome territories seems to correlate with their gene density and transcriptional activity (2–4). Besides these general principles of genome organization, there is by now good evidence for spatial (re-)organization of the genome during differentiation (5). These changes in genome organization during cellular differentiation might be caused by changes in transcriptional activity, DNA and histone modifications as well as altered proteome composition. For example, the dramatic genome reorganization during myogenesis was linked to the expression of methylcytosine binding proteins (6). Likewise, developmental expression patterns of the nuclear envelope proteins Lamin A/C (LamA/C) and the Lamin B receptor (LBR) control peripheral tethering of facultative heterochromatin and gene expression patterns (7). To what extent and in which cases the relative nuclear position of genes is cause or consequence of transcriptional activity remains to be clarified.

*To whom correspondence should be addressed. Tel: +49 89 2180 74232; Fax: +49 89 2180 74236; Email: h.leonhardt@lmu.de
Correspondence may also be addressed to Sebastian Bultmann. Tel: +49 89 2180 74233; Fax: +49 89 2180 74236; Email: bultmann@bio.lmu.de
Present Address:
Thomas Lahaye, ZMBP-General Genetics, University of Tübingen, 72076 Tübingen, Germany.
Robert Morbitzer, ZMBP-General Genetics, University of Tübingen, 72076 Tübingen, Germany.

One challenge in addressing these basic questions is the temporal resolution, as changes in genome organization might be fast and transient. To study the dynamics of chromosomal loci, Lac operator repeats were inserted and traced with Lac repressor green fluorescent protein (GFP) fusion proteins (8). With this genetic tag, rapid movements of a DNA chromosome region were observed in response to gene activation (9,10). However, this method is limited to artificially inserted bacterial DNA sequences and thus not applicable to native endogenous DNA sequences. Alternatively, chromosome dynamics in general can be monitored with histone GFP fusions (11), but with this approach, specific DNA sequences cannot be distinguished.

A well-established technology to create recombinant specific DNA binding modules is based on the Cys_2His_2 zinc finger (ZF) domains and their 3-bp DNA recognition code (12–14). These domains can be combined to polydactyl zinc finger proteins (PZF) that bind user-defined DNA target sequences. PZF have been used for tracing and manipulating specific DNA sequences *in vivo* (15,16) as well as for gene activation and genome engineering (17–21). Nevertheless, PZF target choice is biased toward GC-rich sequences, and fusion of individual ZF modules can influence their individual binding specificity, making the generation of PZF for a desired sequence a laborious and cost-intensive process (22).

However, in the past years, a new technology has emerged that overcomes several of the limitations associated with the use of PZF as artificial DNA binding domains. Transcription activator-like effector proteins (TALEs) from the plant pathogen genus *Xanthomonas* contain a DNA binding domain that can be adjusted to bind any desired target sequence with high specificity (23–27). The central TALE DNA binding domain is composed of tandem arranged 33–35 amino acid repeats, with each repeat binding to one base. The base preference of the individual repeats is specified by amino acids 12 and 13, referred to as repeat variable diresidues (RVDs) (28,29). This straightforward correlation between RVD and bound nucleotide allows the fast and efficient generation of DNA binding modules for any user-defined target sequence leading to a broad application of designer TALEs (dTALEs) in genome engineering and as artificial transcription factors (23–27,30–32).

Here we describe the application of dTALEs as a tool for targeting and tracing of repetitive DNA sequences in living cells. We show that dTALEs can be used to visualize the dynamics of major satellite repeats in mouse embryonic stem cells (ESCs) throughout the cell cycle and to characterize their *in vivo* binding kinetics.

MATERIALS AND METHODS

Plasmid construction

H2B C-terminally fused to monomeric red fluorescent protein (H2B-mRFP) was described previously (33). The coding sequences of Cbx1 (NM_007622.3) and Cbx 5 (NM_007626.3) were amplified by polymerase chain reaction from pGST-Cbx1 (34) and wild-type E14 cDNA (35), respectively, placed under the control of the cytomegalovirus (CMV) promoter, and fused with mRFP by replacing the ligase I cDNA in the pCMV-mRFP-ligase I plasmid described previously (36). *TALE* genes were cloned in pEXPR IBA3 (IBA, Göttingen) by BsaI cut-ligation (enhanced GFP (eGFP), TALE N/C-terminal regions) and BpiI cut-ligation (TALE DNA binding domain), respectively. Therefore, the BpiI restriction site of pEXPR IBA3 was removed by site-directed mutagenesis using primers P1 and P2. Furthermore, the 3' BsaI overlap of the multiple cloning site was changed from GCGC to AAGG by site-directed mutagenesis using primers P3 and P4. eGFP (27), TALE N- and C-terminal regions were amplified with primers P5 and P6, P7 and P8, and P9 and P10, respectively. Thereby BsaI restriction sites and appropriate overlaps were added and the parts were subsequently assembled in pEXPR IBA3 by BsaI cut-ligation resulting in pEXPR IBA3 eGFP TALE N/C. The DNA binding domain was assembled as described in (24) and cloned via BpiI cut-ligation into the pre-assembled pEXPR IBA3 eGFP TALE N/C to generate the GFP-msTALE.

P1 pEXPR-IBA3 BpiI* F
GGATTGGGAAGATAATAGCAGGCATGC
P2 pEXPR-IBA3 BpiI* R
GCATGCCTGCTATTATCTTCCCAATCC
P3 pEXPR-IBA3 BsaI GCGC-AAGG F
CCATGGTCTCAAAGGTTGGAGCCACCCGC
P4 pEXPR-IBA3 BsaI GCGC-AAGG R
GCGGGTGGCTCCAACCTTTGAGACCATGG
P5 GFP F
TTTGGTCTCTAATGGTGAGCAAG
P6 GFP R
GTCTCAGGTGAAATCGCCCAT
P7 AvrBs3 N-term BsaI F
TTTGGTCTCTCACCATGGATCCCATTCGTTCGCG
CAC
P8 AvrBs3 N-term BsaI ATAA R
AAAGGTCTCATTATGGGAAGACCGCGTAAGGT
TCAGG
P9 AvrBs3 C-term BsaI ATAA F
TTTGGTCTCTATAAGGGAAGACGGCGCTGGAG
P10 AvrBs3 C-term (till BamHI) BsaI AAGG R
TTTGGTCTCCCTTAGGATCCGGGAGGCCGCCCC

Cell culture, transfection and fluorescence-activated cell sorting

HEK 293T cells were cultured and transfected as described before (27). J1 ESCs (37) were maintained on gelatin-coated dishes in Dulbecco's modified Eagle's medium supplemented with 16% fetal bovine serum (Biochrom), 0.1 mM ß-mercaptoethanol (Invitrogen), 2 mM L-glutamine, 1× MEM non-essential amino acids, 100 U/ml penicillin, 100 µg/ml streptomycin (PAA Laboratories GmbH), 1000 U/ml recombinant mouse LIF (Millipore), 1 µM PD032591 and 3 µM CHIR99021 [Axon Medchem, (38)]. Transfections in ESCs were performed using Lipofectamin 2000 (Invitrogen) according to the manufacturer's instructions. Fluorescence-activated cell sorting (FACS) was performed with an FACS Aria II (Becton Dickinson).

Generation of transgenic cell lines

ESCs stably carrying the GFP-msTALE construct were generated by transfecting wt J1 ESCs (37) followed by G418 antibiotic selection (750 μg/ml) and repeated sorting for eGFP expression. To obtain clonal transgenic cell lines, single cell sorting was performed. Single cell clones were analyzed by high content imaging using the Operetta system (PerkinElmer). 4′,6-diamidino-2-phenylindole (DAPI) and eGFP fusion proteins were excited, and the emission was recorded using standard filter sets and 200 ms exposure. For each well, nine different fields were imaged and analyzed with the Harmony analysis software. Double transgenic cell lines were generated by transfecting the stable GFP-msTALE cell line with mRFP-PCNA and H2B-mRFP followed by repeated sorting for eGFP and RFP expression.

Immunoprecipitation and western blot

Immunoprecipitation was performed as described before (39). One p100 of HEK293T cells transiently transfected with the GFP-msTALE fusion protein or stable GFP-msTALE ESCs, respectively, was harvested and lysed. GFP fusions were pulled down using the GFP-Trap (40) (Chromotek) and subjected to western blotting using a mouse monoclonal anti-GFP antibody (Roche, 11814460001). For comparison of protein levels, stable GFP-msTALE ESCs were lysed in Radio-Immunoprecipitation Assay (RIPA) buffer. Lysate from 750 000 cells was subjected to western blotting using a mouse monoclonal anti-GFP (Roche, 11814460001), rabbit polyclonal anti-CBX1 (Abcam, ab10478) and rabbit polyclonal anti-CENPB (Abcam, ab25743).

Immunofluorescence staining and microscopy

Immunostaining and 3D-FISH were performed as described previously (41). Briefly, cells cultured on coverslips were fixed with 4% paraformaldehyde for 10 min, washed with PBST (PBS, 0.01% Tween20) and permeabilized with 0.5% Triton X-100. Both primary and secondary antibodies were diluted in blocking solution (PBST, 4% bovine serum albumin). Coverslips with cells were incubated with primary and secondary antibody solutions in dark humid chambers for 1–2 h at room temperature; washings after primary and secondary antibodies were done with PBST. For immuno-FISH, both primary (anti-GFP) and secondary antibodies were applied first; subsequently, cells were postfixed with 4% paraformaldehyde and pre-treated for hybridization. Hybridization was carried out for 2 days at 37°C; posthybridization washings included 2 × Saline Sodium Citrate (SSC) at 37°C and 0.1 × SSC at 61°C (41). The probe for major satellite repeats was generated by polymerase chain reaction using mouse Cot1 DNA (primers: 5′-GCG AGA AAA CTG AAA ATC AC and 5’-TCA AGT CGT CAA GTG GAT G), labeled with Cy3-dUTP by nick-translation, and dissolved in hybridization mixture (50% formamide, 10% dextran sulfate, 1 × SSC) at a concentration of 10–20 ng/μl. For nuclear DNA counterstaining, DAPI was added to the secondary antibody solution to the final concentration 2 μg/ml. Coverslips were mounted in antifade medium (Vectashield, Vector Laboratories) and sealed with colorless nail polish.

Following primary antibodies were used: anti-GFP (Roche, 11814460001), anti-lamin B1 (Santa Cruz Biotechnology, sc-6217), anti-nucleophosmin (B23, Sigma-Aldrich, B0556), anti-kinetochores (Euroimmun AG, CA 1611-0101) and anti-H4K20me3 (Abcam, ab9053). The secondary antibodies were anti-rabbit conjugated to DyLight fluorophore 594 (Jackson ImmunoResearch, 711-505-152), anti-mouse conjugated to Alexa 488 and 555 (Invitrogen, A21202 and A31570), anti-goat conjugated to Cy3 (Jackson ImmunoResearch, 706-166-148) or Alexa 647 (Invitrogen, A21447) and anti-human conjugated to Cy3 (Jackson ImmunoResearch, 309-165-003). Single optical sections or stacks of optical sections were collected using a Leica TCS SP5 confocal microscope equipped with Plan Apo 63×/1.4 NA oil immersion objective and lasers with excitation lines 405, 488, 561 and 633 nm. Dedicated plug-ins in ImageJ program were used to compensate for axial chromatic shift between fluorochromes in confocal stacks, to create RGB images/stacks and to arrange them into galleries (42,43).

Live cell microscopy, fluorescence loss in photobleaching and quantitative fluorescence recovery after photobleaching analysis

Live cell imaging, fluorescence loss in photobleaching (FLIP) and fluorescence recovery after photobleaching (FRAP) experiments were performed on an Ultra*VIEW* VoX spinning disc microscope (PerkinElmer) as described before (44). Photobleaching was performed using two iterations with the acousto-optic tunable filter (AOTF) of the 488 nm laser line set to 100% transmission. For acquisition of FRAP or FLIP experiments, the 488 nm laser line was set to 20% transmission.

In FRAP experiments, a circular bleach region of 2.5 × 2.5 μm, covering one chromocenter (CC) per cell, was chosen. After 20 prebleach frames with a time interval of 200 ms, CCs in five cells were bleached (~650 ms). Then 150 postbleach frames were recorded with a time interval of 200 ms followed by 800 postbleach frames with a time interval of 500 ms. The mean intensity of this circular region was measured over time. Data correction, double normalization and calculation of the half time recovery ($t_{1/2}$) and the mobile fraction (*MF*) were performed as described before (45). The outline of the nucleus for the evaluation was determined using images obtained with bright field illumination. The results of 14 cells were averaged.

In FLIP experiments, approximately half of the cell was bleached in a rectangular region. Like in the FRAP experiments, multiple cells were bleached in parallel. After initial five prebleach frames with a time interval of 4 s, 40 bleach cycles were performed. Each bleach cycle consisted of a bleaching event of ~700 ms followed by 10 time frames with a time interval of 4 s. In each frame, a z-stack of 7 μm with a step size of 1 μm was recorded to check for axial drift. To evaluate the data, the mean intensity of a circular region of 20 × 20 pixel was determined over time.

The region covered either a CC in the unbleached half of a cell, in which the other half was repeatedly bleached [Figure 3B (1)], or in a neighboring unbleached cell [Figure 3B (2)]. Afterward, the background was subtracted from these results. The measurements were performed in Fiji (46) followed by calculations in Excel.

In long-term imaging experiments, a z-stack of 10.8–14.4 µm with a step size of 1.2 µm was recorded every 15 min for ~20 h. To avoid photodamage of the cells, the AOTF of the laser was set to low transmission values of 6–10%.

RESULTS AND DISCUSSION

Generation of a GFP-msTALE highlighting major satellite DNA in mouse cells

To test whether dTALEs are suitable to trace DNA sequences *in vivo*, we generated an N-terminal GFP fusion construct directed against the 19-bp sequence 5'-TGGCG AGAAAACTGAAAAT-3' of the murine major satellite repeat sequence using a golden-gate cloning-based approach (Supplementary Figure S1) (24). The 234-bp units of the major satellite repeat are present in 1000–10 000 copies per chromosome located in the centromeric periphery (47). Major satellite repeats constitute the major part of mouse CCs. These heterochromatin regions are clustered centromeres of acrocentric chromosomes located at the nuclear periphery and around the nucleoli (Figure 1A) (48). The distinct subnuclear localization and high copy number of major satellite repeats constitute an ideal model system to test the applicability of dTALEs for *in vivo* tracing of DNA sequences.

Using the dTALE directed against the major satellite repeat (GFP-msTALE), we generated a stable mouse ESC line by antibiotic selection followed by repeated FACS sorting. After single cell sorting, we established a clone that exhibited correct protein size of the GFP-msTALE compared with a transient transfection in HEK293T cells (Figure 1B). The cell line expressed relatively low levels of the GFP-msTALE compared with the endogenous heterochromatin-associated protein Cbx1 and the kinetochore binding protein CenpB (Supplementary Figure S2). To address the specificity of the TALE binding to the major satellite repeats, we performed fluorescence *in situ* hybridization on 3D-preserved cells (3D-FISH) (Figure 1C). Using a directly labeled probe directed against the major satellites combined with immunostaining, we observed strict co-localization of the GFP-msTALE with the major satellite foci. To further characterize the stable ESC line, the subnuclear localization of the GFP-msTALE in relation to several makers of nuclear structures was assessed. In interphase cells, the GFP signal exhibited a focal pattern co-localizing with DAPI-stained CCs as well as with trimethylated histone 4 lysine 20 (H4K20me3), a marker for constitutive heterochromatin highly enriched in major satellite repeats (46) (Figure 1D, upper panel). Furthermore, we found that kinetochores are localized in the periphery of the GFP foci consistent with the expected relative organization of CCs (Figure 1D, middle panel). Immunolabeling against nucleophosmin (B23), a marker enriched in nucleoli and lamin B1, revealed that the GFP foci localize around the nucleoli and in the nuclear periphery (Figure 1D, lower panel). For direct comparison, we transiently expressed two heterochromatin proteins (RFP-Cbx1 and RFP-Cbx5, also known as heterochromatin protein 1 beta and alpha), which co-localized with the GFP-msTALE at CCs (Supplementary Figure S3A and B) until G2 phase, when binding of both Cbx1 and Cbx5 is abolished (49). Taken together, these data demonstrate that the GFP-msTALE correctly highlights the localization of the major satellite DNA *in vivo*.

The GFP-msTALE enables DNA sequence tracing during the cell cycle *in vivo*

After establishing the correct localization of the GFP-msTALE, we analyzed its behavior during cell cycle progression. We generated double transgenic cell lines also expressing H2B-RFP (Supplementary Figure S3C) to visualize whole chromatin in combination with GFP-msTALE-bound CCs. To distinguish the different phases of DNA replication, we stably transfected the GFP-msTALE ESC line with the S-phase marker RFP-PCNA (50) and acquired time series over 20 h demonstrating the suitability of the approach for live cell imaging. We observed progression throughout S-phase with the GFP-msTALE exhibiting the typical focal pattern expected for major satellite DNA (Figure 2A, Supplementary Movie S1). Importantly, the GFP-msTALE was located at mid to late S-phase replication foci, correlating well with the replication of CCs (45,50) (Figure 2A and B).

Next, we analyzed the localization of the GFP-msTALE through mitosis. Although the dTALE still localized to chromosomes until mid prophase, it largely dissociated in mid to late prophase and reassociated in early telophase (Figure 2C). Residual binding in metaphase was visible on contrast enhancement and with higher expression levels (Supplementary Figure S3). It should be noted that while this work was under review, a smaller TALE construct targeting another major satellite repeat sequence was described that exhibited more stable DNA binding throughout mitosis (51). These results indicate that the chromatin condensation during mitosis might affect binding of the dTALE to its target sequences, an observation in line with the hypothesis that chromatin environment can influence dTALE binding and activity (27,52).

Analysis of *in vivo* protein dynamics reveals a strong but dynamic association of the GFP-msTALE with CCs

The observation that the dTALE is not associated with condensed chromosomes during mitosis prompted us to investigate the *in vivo* DNA binding kinetics of the GFP-msTALE in more detail. To quantify the binding dynamics of the GFP-dTALE in living cells, we performed FRAP and FLIP experiments. Both methods were used in a complementary approach (53,54), with intensity measurements focusing on single CCs, the prominent binding sites of the GFP-msTALE. For the FRAP experiment, we bleached a small circular region including one CC and quantified the recovery in this region over time (Figure 3A and C). The faster the recovery, the more transient is the binding dynamics. In contrast, for the FLIP

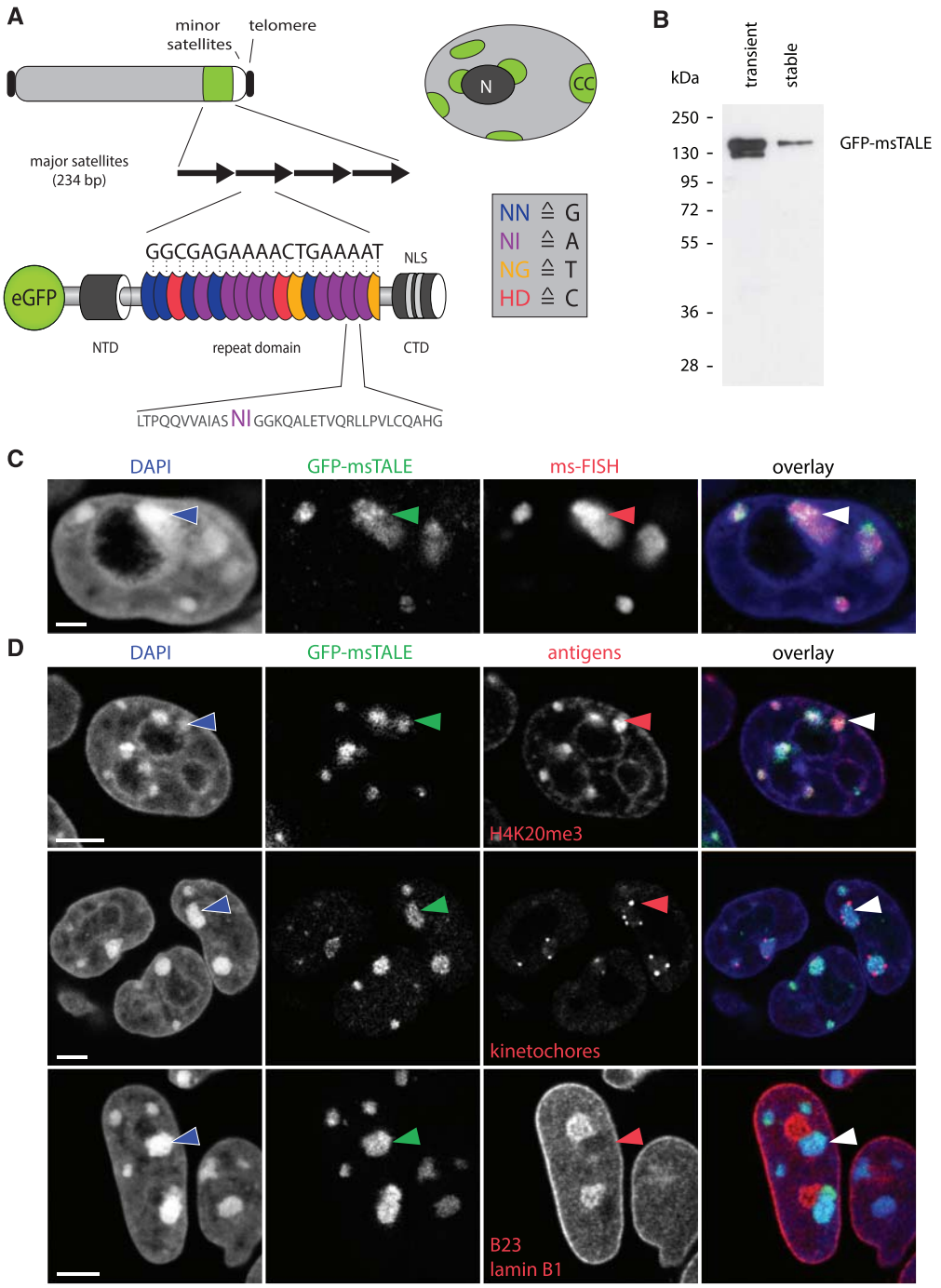

Figure 1. Localization of the GFP-msTALE to major satellite repeats in mouse pericentromeric heterochromatin. (**A**, top) Schematic representation of an acrocentric mouse chromosome with telomeres (black), major satellites (green), minor satellites (white) and the long arm of the chromosome (light gray). Overview of a nucleus showing multiple heterochromatin centers (CC, green), where the major satellite DNA is clustered. CCs localize next to the nuclear periphery and the nucleoli (dark gray, N) and are surrounded by less condensed chromatin (light gray). (A, bottom) Schematic representation of the GFP-msTALE aligned to its binding site within the major satellite repeats (black arrows). The dTALE is composed of an N-terminal domain (NTD), a C-terminal domain (CTD) bearing nuclear localization signals (NLS) and a central repeat domain. DNA target recognition is mediated by the RVDs within each TALE repeat (blue, purple, yellow and red ellipses for RVDs binding to the bases G, A, T and C, respectively, single letter code for amino acids and nucleotide bases). A representative repeat sequence with RVDs (purple) is shown below as close-up (single letter code for amino acids). The complete sequence is shown in Supplementary Figure S1. Note that the msTALE is lacking the C-terminal activation domain. For visualization and immunoprecipitation, the dTALE is N-terminally fused to GFP. (**B**) GFP-Trap pull-down from HEK293T cells transiently transfected with the GFP-msTALE construct (transient) and a J1 ESC clone stably expressing the GFP-msTALE (stable). Immunodetection by an anti-GFP antibody. (**C**) 3D-immuno-FISH on stable GFP-msTALE ESCs with probe directed against major satellite repeats (ms-FISH). Because the GFP signal is strongly reduced by 3D-FISH procedure, an anti-GFP antibody was used to visualize GFP-msTALE localization. Note strict co-localization of the GFP signal (green) and the FISH probe (red). Nuclei were counterstained with DAPI (blue).

(continued)

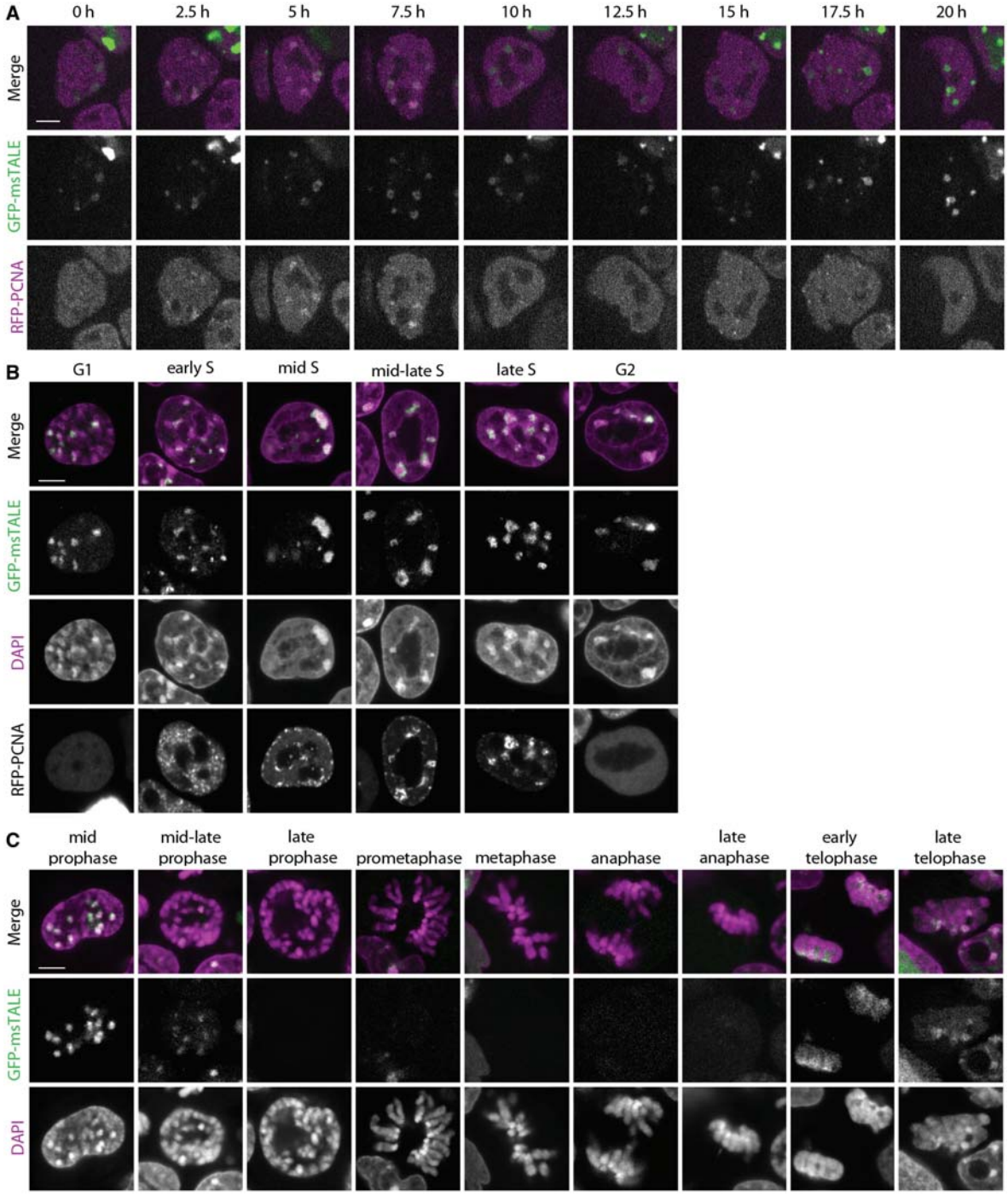

Figure 2. Cell cycle-dependent distribution of GFP-msTALE. (**A**) Live cell imaging of replicating stable GFP-msTALE cell line (green) stably transfected with RFP-PCNA (magenta). (**B**) Single confocal sections of fixed and RFP-PCNA co-transfected GFP-msTALE stable cell line (green) during DNA replication. DNA is visualized by DAPI (magenta). (**C**) Single confocal sections of fixed GFP-msTALE cell line (green) during mitosis. DNA is visualized by DAPI (magenta). Scale bars: 5 μm.

Figure 1. Continued
Arrowhead points at one of the CCs. (**D**) Immunostaining of ESCs stably expressing the GFP-msTALE (green). Upper panel, antibodies against heterochromatin (anti-H4K20me3, red) mark GFP-positive CCs. Middle panel, human antiserum binding to kinetochores reveals kinetochore clusters (red) at the surface of CCs. Lower panel, CCs marked with GFP-msTALE show a characteristic intranuclear localization abutting nuclear periphery or adjacent to the nucleoli (both shown in red). Nuclei were counterstained with DAPI (blue). Arrowheads mark one of the CCs in each exemplified nucleus. All images are single optical confocal sections. Scale bars: C, 5 μm; D, 2 μm.

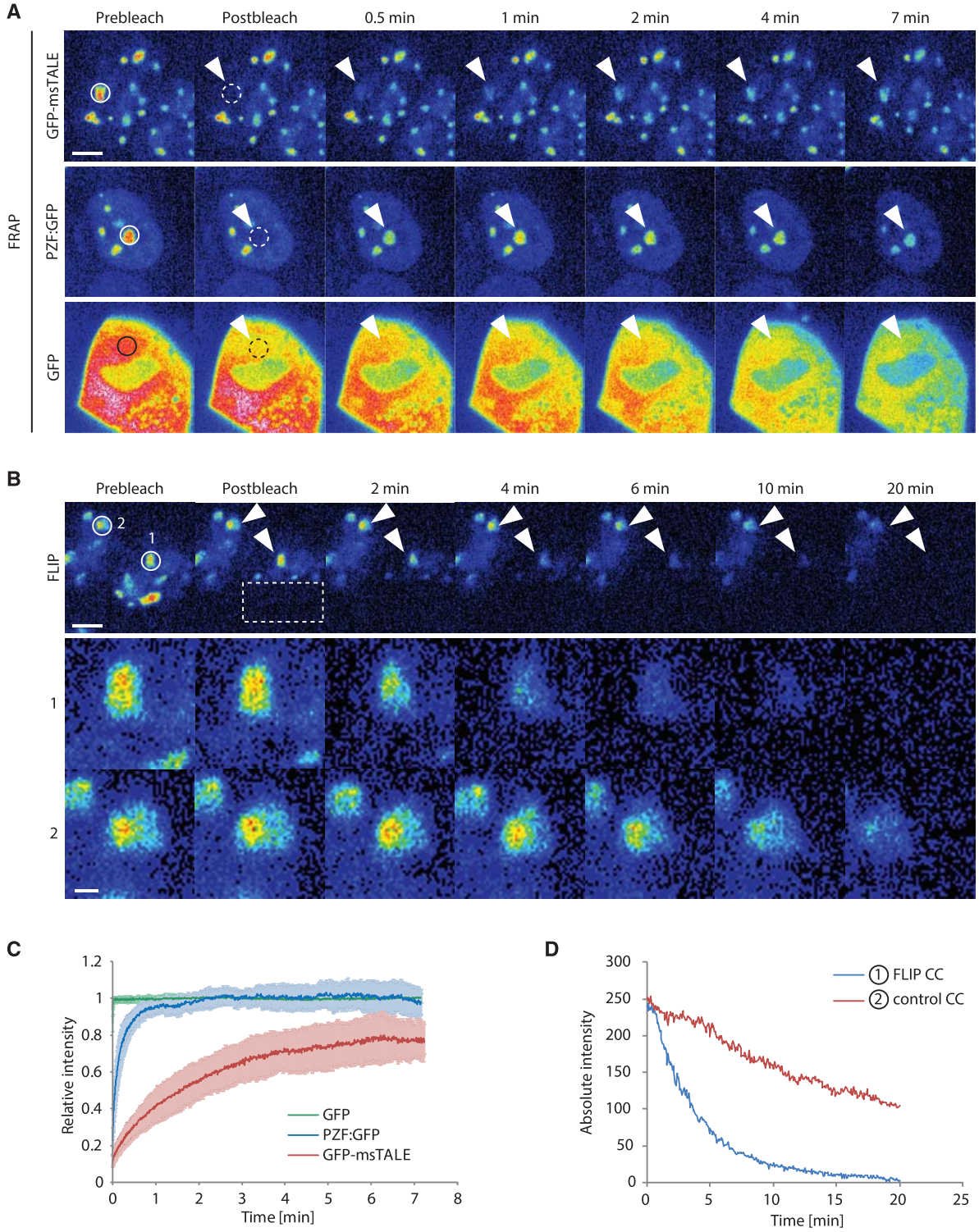

Figure 3. Comparative analysis of the dynamics of GFP, GFP-msTALE and PZF:GFP by FRAP and FLIP. Continuous lines indicate the intensity measurement areas, whereas dashed lines indicate the bleached regions. The arrowheads point to the intensity measurement areas in the postbleach time points. These regions are magnified by a factor of four in the lower panel of (B). Scale bars: 5 µm (upper panel) and 1 µm (lower panel, (B)). (**A**) Representative FRAP experiment for GFP, the stable GFP-msTALE cell line and PZF:GFP. A circular region (dashed line) with a diameter of 2.5 µm was bleached. (**B**) Representative FLIP experiment of the GFP-msTALE. A rectangular region indicated by the dashed line was repeatedly bleached. CCs in the unbleached half of the bleached cell (1) and in an unbleached reference cell (2) are highlighted. (**C**) Quantitative evaluation of FRAP experiments (average of 12–14 cells) comparing GFP-msTALE, PZF:GFP and GFP. Error bars represent standard deviation. (**D**) Representative background corrected, absolute intensities of two CCs in a bleached cell (1, blue line) and an unbleached reference cell (2, red line) illustrated in (B).

experiment we bleached half of the nucleus repeatedly and quantified the intensity of a CC in the unbleached half (Figure 3B and D). On protein dissociation from the binding site in the unbleached region and diffusion into the bleached region, a reduction of signal intensity in the unbleached half of the nucleus can be observed. The faster the signal decreases, the more transient is the binding dynamics. Thus, the binding dynamics of GFP-dTALEs can be analyzed without inducing damage at these sites by photobleaching. As the bleached regions and the measured region are separate from each other, this approach also takes into account the mobility between different compartments (55,56).

In our quantitative FRAP experiments with the GFP-msTALE, we observed a gradual slow increase in intensity over 7 min (Figure 3C). Even after this time, an immobile, not yet recovered fraction of ~20% was still detectable, indicating a strong binding of the dTALE to the major satellites. Unlike freely diffusing proteins such as GFP (44), no fast initial recovery of GFP-msTALE was detected in the bleached area (Figure 3A). Also the signal intensity outside CCs was rather low, indicating that most of the GFP-msTALE was bound to chromosomes. The stable interaction of GFP-msTALE with major satellites DNA seen in the FRAP experiments becomes directly evident from the complementary FLIP experiments. Even on repeated bleaching, GFP-msTALE fluorescence was detectable at the unbleached CCs within the same nucleus for up to 20 min (Figure 3D, line 1). Notably, reference measurement of CCs in the adjacent cell (Figure 3D, line 2) revealed a continuous loss of fluorescence (~50% over 20 min) because of image acquisition with these microscope settings, so that the actual dissociation of GFP-msTALE from CCs (Figure 3D, line 1) is even slightly slower. For comparison, we tested the ZF-based PZF:GFP binding to the major satellite repeats (15) and obtained a fast initial recovery together with a 10 times lower half time recovery value in FRAP experiments as well as a faster loss of fluorescence in FLIP experiments (Figure 3A and C and Supplementary Figure 4B) exhibiting less stable binding than the TALE construct.

In vitro studies revealed that dTALEs have K_d values in the low nanomolar to high picomolar range (27,57), indicating a strong binding affinity of dTALEs to DNA. Our *in vivo* binding studies demonstrate that dTALEs also strongly bind their target DNA sequence in a chromatin context, but not in a static mode, and reveal a rather dynamic interplay with chromatin. The depletion of GFP-msTALE from highly condensed chromatin during mitosis could be due to conformational changes of the DNA substrate weakening the binding or preventing rebinding that shifts the dynamic equilibrium toward the unbound state. This is consistent with the recent observation that condensation may affect binding and access of nuclear proteins to chromatin (33).

In summary, we could show that dTALEs can be engineered to bind and highlight repetitive DNA sequences *in vivo*. With the example of a dTALE designed to target the major satellite repeats in mouse cells, we showed that fluorescent dTALEs are suitable for live cell imaging of specific DNA sequences throughout the cell cycle. Moreover, we found that dTALEs can detect changes in chromatin condensation and that a dynamic interplay between dTALE and chromatin exists. In this study, we targeted repetitive DNA sequences; with more sensitive detection as used in single molecule tracing setups, eventually single copy genes might also become traceable.

Fluorescently labeled dTALEs open new perspectives to trace specific endogenous DNA sequences at high temporal and spatial resolution in living cells. Strict sequence dependent localization, higher affinity and easy assembly of dTALEs give this method an advantage over previous techniques based on overexpression of chromatin binding factors or ZF arrays in tracing and targeting of specific DNA sequences in living cells. This novel application of dTALEs will help to identify and elucidate cell cycle and development-specific changes in genome organization and chromatin dynamics.

SUPPLEMENTARY DATA

Supplementary Data are available at NAR Online.

ACKNOWLEDGEMENTS

The authors thank Dr Bert J. van der Zaal [Institute of Biology Leiden (IBL), Leiden University, Leiden] for providing the PZF:GFP construct. They thank Thomas Pyttel for generating the Cbx1 and Cbx5 expression constructs. Furthermore, they thank Dr Boris Joffe for comments and suggestions.

FUNDING

The Deutsche Forschungsgemeinschaft [SFB924 to T.L., SO1054 to I.S. and SFB646 to H.L.]; the Two Blades Foundation (to T.L.); the Nanosystems Initiative Munich [to H.L.]; the Bundesministerium für Bildung und Forschung [EpiSys to H.L.]; The International Max Planck Research School for Molecular and Cellular Life Sciences (IMPRS-LS) (to K.T. and K.S.); The Bundesministerium für Bildung und Forschung [3D-SR, in part to K.T.]. Funding for open access charge: Deutsche Forschungsgemeinschaft.

Conflict of interest statement. T.L. is a co-inventor of a patent application regarding the use of TALEs.

REFERENCES

1. Bolzer,A., Kreth,G., Solovei,I., Koehler,D., Saracoglu,K., Fauth,C., Muller,S., Eils,R., Cremer,C., Speicher,M.R. *et al.* (2005) Three-dimensional maps of all chromosomes in human male fibroblast nuclei and prometaphase rosettes. *PLoS Biol.*, **3**, e157.
2. Mahy,N.L., Perry,P.E. and Bickmore,W.A. (2002) Gene density and transcription influence the localization of chromatin outside of chromosome territories detectable by FISH. *J. Cell Biol.*, **159**, 753–763.
3. Branco,M.R. and Pombo,A. (2006) Intermingling of chromosome territories in interphase suggests role in translocations and transcription-dependent associations. *PLoS Biol.*, **4**, e138.
4. Osborne,C.S., Chakalova,L., Brown,K.E., Carter,D., Horton,A., Debrand,E., Goyenechea,B., Mitchell,J.A., Lopes,S., Reik,W.

et al. (2004) Active genes dynamically colocalize to shared sites of ongoing transcription. *Nat. Genet.*, **36**, 1065–1071.
5. Joffe,B., Leonhardt,H. and Solovei,I. (2010) Differentiation and large scale spatial organization of the genome. *Curr. Opin. Genet. Dev.*, **20**, 562–569.
6. Brero,A., Easwaran,H., Nowak,D., Grunewald,I., Cremer,T., Leonhardt,H. and Cardoso,M. (2005) Methyl CpG-binding proteins induce large-scale chromatin reorganization during terminal differentiation. *J. Cell Biol.*, **169**, 733–743.
7. Solovei,I., Wang,A.S., Thanisch,K., Schmidt,C.S., Krebs,S., Zwerger,M., Cohen,T.V., Devys,D., Foisner,R., Peichl,L. *et al.* (2013) LBR and lamin A/C sequentially tether peripheral heterochromatin and inversely regulate differentiation. *Cell*, **152**, 584–598.
8. Robinett,C.C., Straight,A., Li,G., Willhelm,C., Sudlow,G., Murray,A. and Belmont,A.S. (1996) In vivo localization of DNA sequences and visualization of large-scale chromatin organization using lac operator/repressor recognition. *J. Cell Biol.*, **135**, 1685–1700.
9. Tumbar,T. and Belmont,A.S. (2001) Interphase movements of a DNA chromosome region modulated by VP16 transcriptional activator. *Nat. Cell Biol.*, **3**, 134–139.
10. Gasser,S.M. (2002) Visualizing chromatin dynamics in interphase nuclei. *Science*, **296**, 1412–1416.
11. Kanda,T., Sullivan,K.F. and Wahl,G.M. (1998) Histone-GFP fusion protein enables sensitive analysis of chromosome dynamics in living mammalian cells. *Curr. Biol.*, **8**, 377–385.
12. Klug,A. (2010) The discovery of zinc fingers and their development for practical applications in gene regulation and genome manipulation. *Q. Rev. Biophys.*, **43**, 1–21.
13. Pabo,C.O., Peisach,E. and Grant,R.A. (2001) Design and selection of novel Cys2His2 zinc finger proteins. *Annu. Rev. Biochem.*, **70**, 313–340.
14. Segal,D.J. and Barbas,C.F. III (2000) Design of novel sequence-specific DNA-binding proteins. *Curr. Opin. Chem. Biol.*, **4**, 34–39.
15. Lindhout,B.I., Fransz,P., Tessadori,F., Meckel,T., Hooykaas,P.J. and van der Zaal,B.J. (2007) Live cell imaging of repetitive DNA sequences via GFP-tagged polydactyl zinc finger proteins. *Nucleic Acids Res.*, **35**, e107.
16. Casas-Delucchi,C.S., Becker,A., Bolius,J.J. and Cardoso,M.C. (2012) Targeted manipulation of heterochromatin rescues MeCP2 Rett mutants and re-establishes higher order chromatin organization. *Nucleic Acids Res.*, **40**, e176.
17. Cathomen,T. and Joung,J.K. (2008) Zinc-finger nucleases: the next generation emerges. *Mol. Ther.*, **16**, 1200–1207.
18. Urnov,F.D., Miller,J.C., Lee,Y.L., Beausejour,C.M., Rock,J.M., Augustus,S., Jamieson,A.C., Porteus,M.H., Gregory,P.D. and Holmes,M.C. (2005) Highly efficient endogenous human gene correction using designed zinc-finger nucleases. *Nature*, **435**, 646–651.
19. Porteus,M.H. and Carroll,D. (2005) Gene targeting using zinc finger nucleases. *Nat. Biotechnol.*, **23**, 967–973.
20. Segal,D.J., Dreier,B., Beerli,R.R. and Barbas,C.F.III. (1999) Toward controlling gene expression at will: selection and design of zinc finger domains recognizing each of the 5'-GNN-3' DNA target sequences. *Proc. Natl Acad. Sci. USA*, **96**, 2758–2763.
21. Joung,J.K. and Sander,J.D. (2012) TALENs: a widely applicable technology for targeted genome editing. *Nat. Rev. Mol. Cell Biol.*, **14**, 49–55.
22. DeFrancesco,L. (2011) Move over ZFNs. *Nat. Biotechnol.*, **29**, 681–684.
23. Zhang,F., Cong,L., Lodato,S., Kosuri,S., Church,G. and Arlotta,P. (2011) Efficient construction of sequence-specific TAL effectors for modulating mammalian transcription. *Nat. Biotechnol.*, **29**, 149–153.
24. Morbitzer,R., Elsaesser,J., Hausner,J. and Lahaye,T. (2011) Assembly of custom TALE-type DNA binding domains by modular cloning. *Nucleic Acids Res.*, **39**, 5790–5799.
25. Miller,J.C., Tan,S., Qiao,G., Barlow,K.A., Wang,J., Xia,D.F., Meng,X., Paschon,D.E., Leung,E., Hinkley,S.J. *et al.* (2011) A TALE nuclease architecture for efficient genome editing. *Nat. Biotechnol.*, **29**, 143–148.
26. Mahfouz,M.M., Li,L., Piatek,M., Fang,X., Mansour,H., Bangarusamy,D.K. and Zhu,J.K. (2012) Targeted transcriptional repression using a chimeric TALE-SRDX repressor protein. *Plant Mol. Biol.*, **78**, 311–321.
27. Bultmann,S., Morbitzer,R., Schmidt,C.S., Thanisch,K., Spada,F., Elsaesser,J., Lahaye,T. and Leonhardt,H. (2012) Targeted transcriptional activation of silent oct4 pluripotency gene by combining designer TALEs and inhibition of epigenetic modifiers. *Nucleic Acids Res.*, **40**, 5368–5377.
28. Boch,J., Scholze,H., Schornack,S., Landgraf,A., Hahn,S., Kay,S., Lahaye,T., Nickstadt,A. and Bonas,U. (2009) Breaking the code of DNA binding specificity of TAL-type III effectors. *Science*, **326**, 1509–1512.
29. Moscou,M. and Bogdanove,A. (2009) A simple cipher governs DNA recognition by TAL effectors. *Science*, **326**, 1501.
30. Cermak,T., Doyle,E., Christian,M., Wang,L., Zhang,Y., Schmidt,C., Baller,J., Somia,N., Bogdanove,A. and Voytas,D. (2011) Efficient design and assembly of custom TALEN and other TAL effector-based constructs for DNA targeting. *Nucleic Acids Res.*, **39**, 7879.
31. Mussolino,C., Morbitzer,R., Lutge,F., Dannemann,N., Lahaye,T. and Cathomen,T. (2011) A novel TALE nuclease scaffold enables high genome editing activity in combination with low toxicity. *Nucleic Acids Res.*, **39**, 9283–9293.
32. Bogdanove,A.J. and Voytas,D.F. (2011) TAL effectors: customizable proteins for DNA targeting. *Science*, **333**, 1843–1846.
33. Martin,R.M. and Cardoso,M.C. (2010) Chromatin condensation modulates access and binding of nuclear proteins. *FASEB J.*, **24**, 1066–1072.
34. Nielsen,A.L., Oulad-Abdelghani,M., Ortiz,J.A., Remboutsika,E., Chambon,P. and Losson,R. (2001) Heterochromatin formation in mammalian cells: interaction between histones and HP1 proteins. *Mol. Cell*, **7**, 729–739.
35. Sharif,J., Muto,M., Takebayashi,S., Suetake,I., Iwamatsu,A., Endo,T.A., Shinga,J., Mizutani-Koseki,Y., Toyoda,T., Okamura,K. *et al.* (2007) The SRA protein Np95 mediates epigenetic inheritance by recruiting Dnmt1 to methylated DNA. *Nature*, **450**, 908–912.
36. Mortusewicz,O., Rothbauer,U., Cardoso,M.C. and Leonhardt,H. (2006) Differential recruitment of DNA Ligase I and III to DNA repair sites. *Nucleic Acids Res.*, **34**, 3523–3532.
37. Li,E., Bestor,T. and Jaenisch,R. (1992) Targeted mutation of the DNA methyltransferase gene results in embryonic lethality. *Cell*, **69**, 915–926.
38. Ying,Q.L., Wray,J., Nichols,J., Batlle-Morera,L., Doble,B., Woodgett,J., Cohen,P. and Smith,A. (2008) The ground state of embryonic stem cell self-renewal. *Nature*, **453**, 519–523.
39. Meilinger,D., Fellinger,K., Bultmann,S., Rothbauer,U., Bonapace,I., Klinkert,W., Spada,F. and Leonhardt,H. (2009) Np95 interacts with de novo DNA methyltransferases, Dnmt3a and Dnmt3b, and mediates epigenetic silencing of the viral CMV promoter in embryonic stem cells. *EMBO Rep.*, **10**, 1259–1264.
40. Rothbauer,U., Zolghadr,K., Muyldermans,S., Schepers,A., Cardoso,M.C. and Leonhardt,H. (2008) A versatile nanotrap for biochemical and functional studies with fluorescent fusion proteins. *Mol. Cell Proteomics*, **7**, 282–289.
41. Solovei,I. and Cremer,M. (2010) 3D-FISH on cultured cells combined with immunostaining. *Methods Mol. Biol.*, **659**, 117–126.
42. Ronneberger,O., Baddeley,D., Scheipl,F., Verveer,P.J., Burkhardt,H., Cremer,C., Fahrmeir,L., Cremer,T. and Joffe,B. (2008) Spatial quantitative analysis of fluorescently labeled nuclear structures: problems, methods, pitfalls. *Chromosome Res.*, **16**, 523–562.
43. Walter,J., Joffe,B., Bolzer,A., Albiez,H., Benedetti,P.A., Muller,S., Speicher,M.R., Cremer,T., Cremer,M. and Solovei,I. (2006) Towards many colors in FISH on 3D-preserved interphase nuclei. *Cytogenet. Genome Res.*, **114**, 367–378.
44. Schneider,K., Fuchs,C., Dobay,A., Rottach,A., Qin,W., Wolf,P., Alvarez-Castro,J.M., Nalaskowski,M.M., Kremmer,E., Schmid,V. *et al.* (2013) Dissection of cell cycle-dependent dynamics of Dnmt1 by FRAP and diffusion-coupled modeling. *Nucleic Acids Res.*, **41**, 4860–4876.
45. Schermelleh,L., Haemmer,A., Spada,F., Rosing,N., Meilinger,D., Rothbauer,U., Cardoso,M.C. and Leonhardt,H. (2007) Dynamics

of Dnmt1 interaction with the replication machinery and its role in postreplicative maintenance of DNA methylation. *Nucleic Acids Res.*, **35**, 4301–4312.
46. Schindelin,J., Arganda-Carreras,I., Frise,E., Kaynig,V., Longair,M., Pietzsch,T., Preibisch,S., Rueden,C., Saalfeld,S., Schmid,B. *et al.* (2012) Fiji: an open-source platform for biological-image analysis. *Nat. Methods*, **9**, 676–682.
47. Vissel,B. and Choo,K.H. (1989) Mouse major (gamma) satellite DNA is highly conserved and organized into extremely long tandem arrays: implications for recombination between nonhomologous chromosomes. *Genomics*, **5**, 407–414.
48. Comings,D.E. (1980) Arrangement of chromatin in the nucleus. *Hum. Genet.*, **53**, 131–143.
49. Mateescu,B., England,P., Halgand,F., Yaniv,M. and Muchardt,C. (2004) Tethering of HP1 proteins to chromatin is relieved by phosphoacetylation of histone H3. *EMBO Rep.*, **5**, 490–496.
50. Leonhardt,H., Rahn,H.P., Weinzierl,P., Sporbert,A., Cremer,T., Zink,D. and Cardoso,M.C. (2000) Dynamics of DNA replication factories in living cells. *J. Cell Biol.*, **149**, 271–280.
51. Miyanari,Y., Ziegler-Birling,C. and Torres-Padilla,M.E. (2013) Live visualization of chromatin dynamics with fluorescent TALEs. *Nat. Struct. Mol. Biol.*, **20**, 1321–1324.
52. Deng,D., Yan,C., Pan,X., Mahfouz,M., Wang,J., Zhu,J.K., Shi,Y. and Yan,N. (2012) Structural basis for sequence-specific recognition of DNA by TAL effectors. *Science*, **335**, 720–723.
53. Ishikawa-Ankerhold,H.C., Ankerhold,R. and Drummen,G.P. (2012) Advanced fluorescence microscopy techniques–FRAP, FLIP, FLAP, FRET and FLIM. *Molecules*, **17**, 4047–4132.
54. Phair,R.D. and Misteli,T. (2001) Kinetic modelling approaches to in vivo imaging. *Nat. Rev. Mol. Cell Biol.*, **2**, 898–907.
55. Cole,N.B., Smith,C.L., Sciaky,N., Terasaki,M., Edidin,M. and Lippincott-Schwartz,J. (1996) Diffusional mobility of Golgi proteins in membranes of living cells. *Science*, **273**, 797–801.
56. Koster,M., Frahm,T. and Hauser,H. (2005) Nucleocytoplasmic shuttling revealed by FRAP and FLIP technologies. *Curr. Opin. Biotechnol.*, **16**, 28–34.
57. Meckler,J.F., Bhakta,M.S., Kim,M.S., Ovadia,R., Habrian,C.H., Zykovich,A., Yu,A., Lockwood,S.H., Morbitzer,R., Elsaesser,J. *et al.* (2013) Quantitative analysis of TALE-DNA interactions suggests polarity effects. *Nucleic Acids Res.*, **41**, 4118–4128.

Supplementary Figure 1: Nucleotide and amino acid sequence of the GFP-msTALE. The entire open reading frame of the fusion protein is shown: GFP is highlighted in green, repeat divariable residues (RVD) within each TALE repeat are highlighted in blue, purple, yellow and red for RVDs binding to the bases G, A, T and C, respectively. Single letter code is used for amino acids and nucleotide bases.

Supplementary Movie 1: Cell-cycle dependent distribution of GFP-msTALE. Live cell imaging of replicating stable GFP-msTALE cell line (green) cotransfected with RFP-PCNA (magenta).

Supplementary Figure 2: Expression of the stably integrated GFP-msTALE construct is relatively low compared to endogenous protein levels of major satellite associated proteins. Western blot showing protein levels of the GFP-msTALE, CenpB and Cbx1 in the stable GFP-msTALE ES cell line.

Supplementary Figure 3: Live cell imaging of GFP-msTALE together with chromatin associated proteins (A) Live cell imaging of replicating stable GFP-msTALE cell line (green) cotransfected with RFP-Cbx1 (magenta). (B) Live cell imaging of replicating stable GFP-msTALE cell line (green) cotransfected with RFP-Cbx5 (magenta). (C) Live cell imaging of replicating stable GFP-msTALE cell line (green) stably transfected with H2B-RFP (magenta). Arrowheads point towards one representative chromocenter. Scale bars: 5 µm.

Supplementary Figure 4: Comparative analysis of the dynamics of the GFP-msTALE , the PZF:GFP and GFP. (A) Representative FLIP experiments of the stable GFP-msTALE cell line and PZF:GFP (FLIP of the GFP-msTALE taken from Figure 3B for direct comparison). A rectangular region indicated by the dashed line was repeatedly bleached. Chromocenters in the unbleached half of the bleached cell (1) and in an unbleached reference cell (2) are highlighted. Continuous lines indicate the intensity measurement areas, whereas dashed lines indicate the bleached regions. Arrowheads point to the intensity measurement areas in the postbleach time points. These regions are magnified by a factor of four in the lower panels for both stable GFP-msTALE ESC line and the PZF:GFP. Scale bars: 5 µm (upper panels), 1 µm (lower panels). (B) Kinetic properties of GFP, GFP-msTALE and PZF:GFP analyzed by FRAP. N indicates the number of analyzed cells, *MF* the mobile fraction and $t_{1/2}$ the half time of recovery. Mean values ± standard deviation are listed.

Supplementary Figure 1

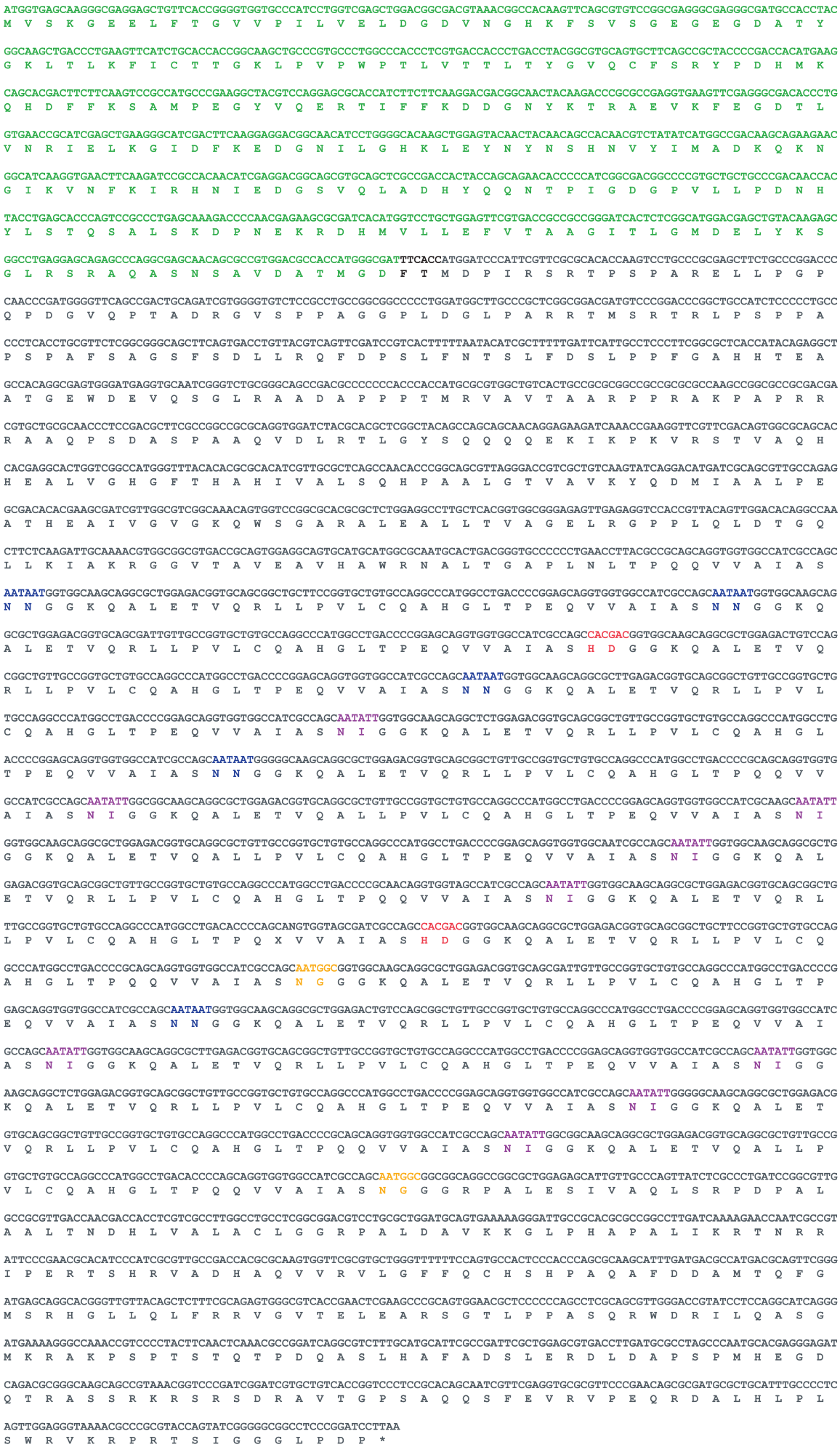

Supplementary Figure 2

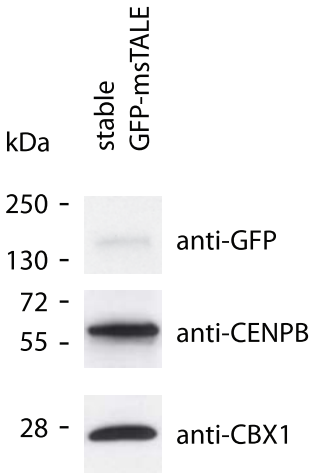

Supplementary Figure 3

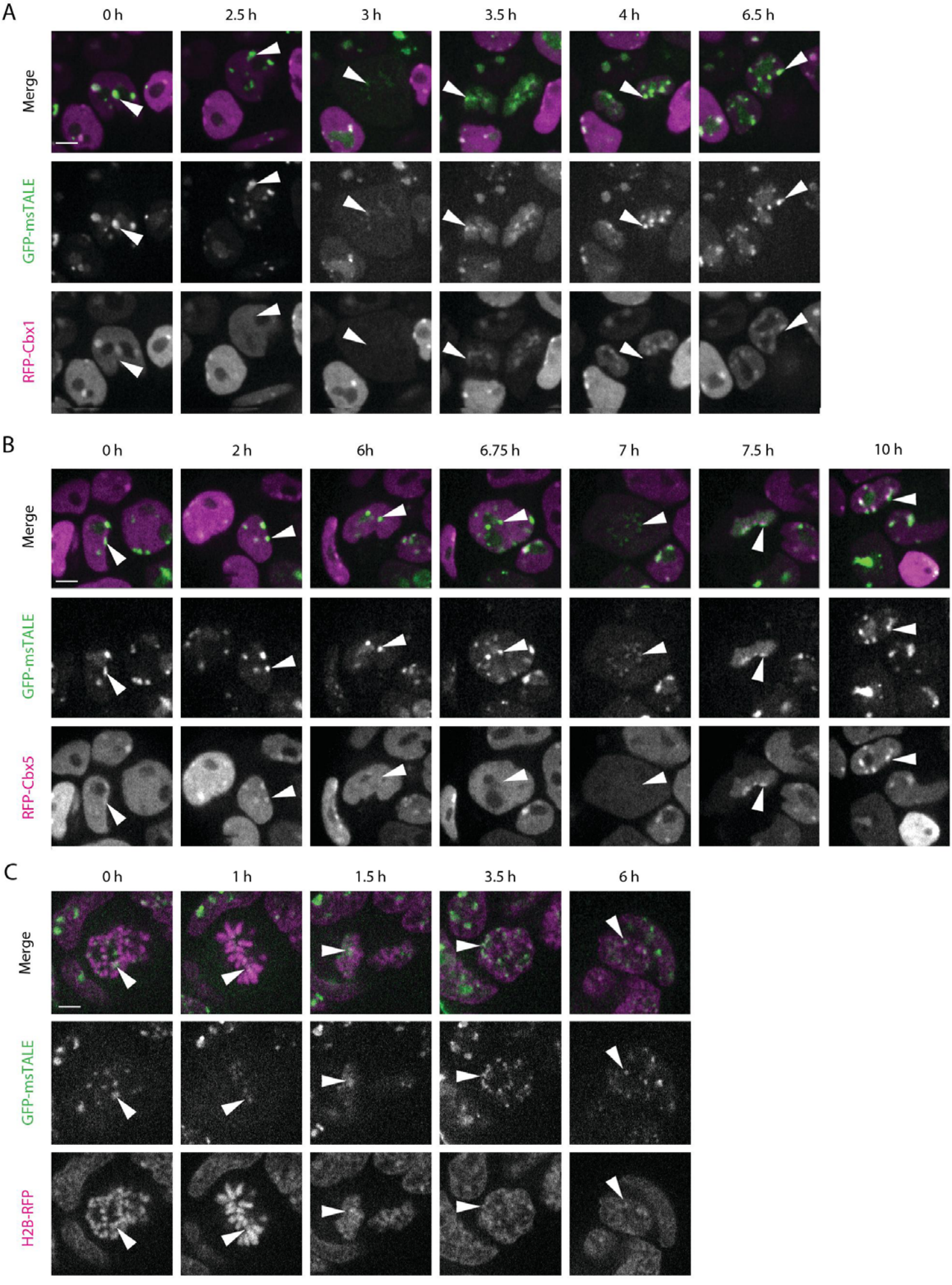

Supplementary Figure 4

A

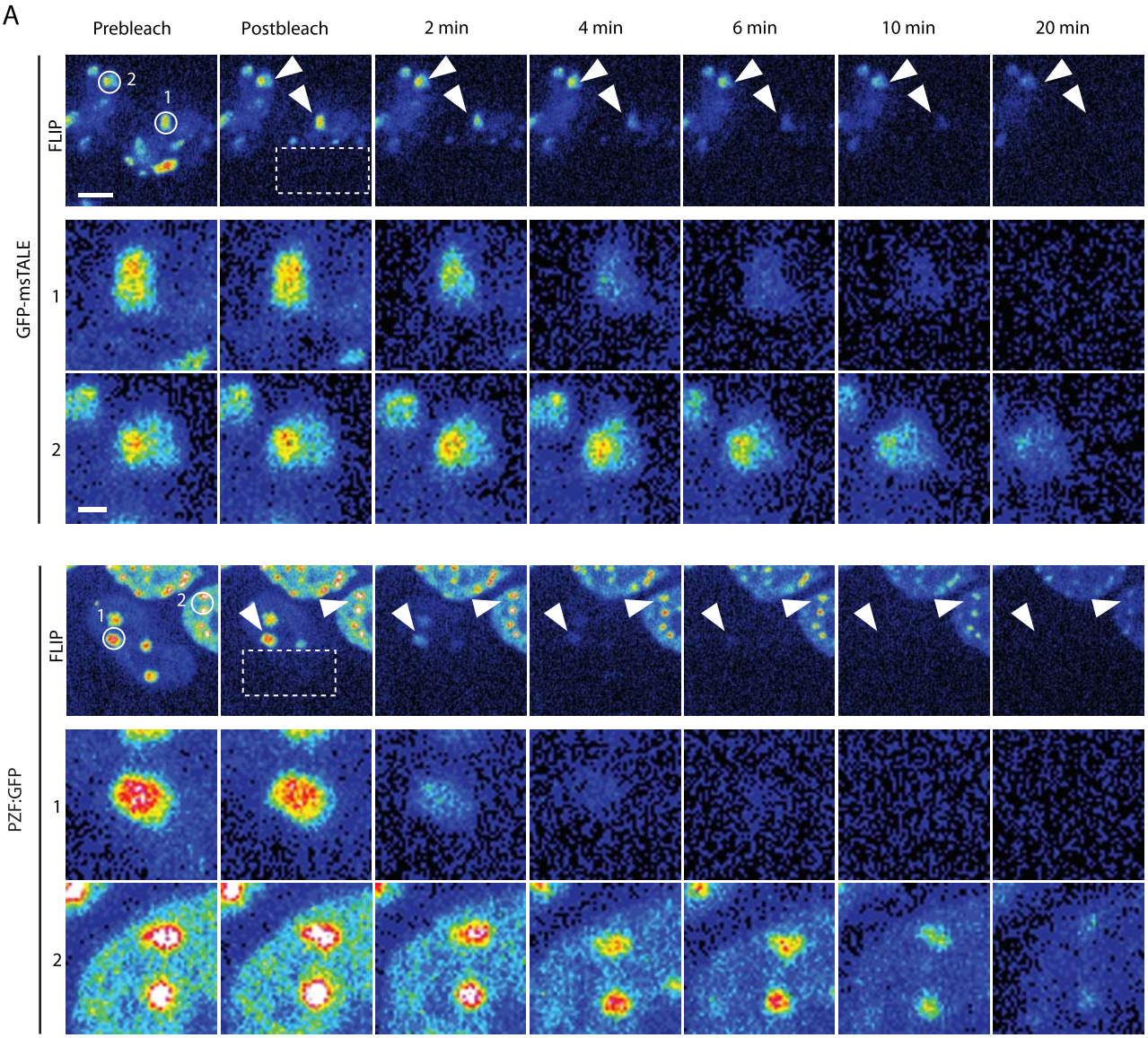

B

	N	*MF* [%] ± SD	$t_{1/2}$[s]
GFP	12	1.0±0.3	0.1±0.1
GFP-msTALE	14	0.7±0.1	77.8±21.2
PZF:GFP	12	1.0±0.1	6.9±3.5

2.7 Controlling the mobility of oligonucleotides in the nanochannels of mesoporous silica

Controlling The Mobility Of Oligonucleotides In The Nanochannels Of Mesoporous Silica

Timo Lebold, Axel Schlossbauer, Katrin Schneider, Lothar Schermelleh, Heinrich Leonhardt, Thomas Bein, and Christoph Bräuchle**

Oligonucleotides used in gene therapy and silencing are fragile compounds that degrade easily in biological environments. Porous biocompatible carrier particles may provide a useful strategy to deliver these therapeutics to their target sites. Development of appropriate delivery vehicles, however, requires a better understanding of the oligonucleotide-host interactions and the oligonucleotide dynamics inside carrier particles. We investigated template-free SBA-15 type mesoporous silica particles and report their loading characteristics with siRNA depending on the surface functionalization of their porous network. We show that the siRNA uptake capability of the particles can be controlled by the composition of the functional groups. Fluorescence recovery after photobleaching measurements revealed size-dependent mobility of siRNA and double-stranded DNA oligonucleotides within the functionalized silica particles and provided evidence for the stability of the oligonucleotides inside the pores. Hence, our study demonstrates the potential of mesoporous silica particles as a means for alternative gene delivery in nanomedicine.

1. Introduction

Within the last decade gene therapy, gene silencing and RNA interference (RNAi) methods have attracted increasing interest. However, the fragile oligonucleotides utilized in gene therapy and RNA interference are easily degraded and therefore require robust delivery strategies in order to reach their target site within the cell. In gene therapy, for example, the DNA needs to be transported into the cell nucleus, either actively or indirectly due to the disassembly of the nuclear envelope during mitosis, whereas siRNAs used in post-transcriptional gene-silencing only need to be delivered to the cytosol.[1–3] Consequently, very different target sites need to be addressed to achieve a safe and efficient delivery of the fragile oligonucleotides.[4–6]

Mesoporous silica, including the M41S materials introduced by the Mobil company[7,8] or Santa Barbara Amorphous (SBA) type materials,[9,10] represents a versatile class of porous nanomaterials. These materials break the long-standing pore size constraint of zeolites by offering pore sizes ranging from about 2–30 nm. Moreover, their specifications such as pore diameter, surface properties, and topologies can be tailor-made according to individual requirements. Various applications for mesoporous silica materials have been suggested, such as molecular sieves,[11] catalysis,[12] chromatography,[13] stabilization of conducting nanoscale wires[14–16] and novel drug-delivery systems.[17–25]

Recently, the potential of mesoporous silica nanoparticles with a diameter of about 100 nm for the delivery of siRNA into mammalian cells was highlighted.[26] In the present study we utilized SBA-15 type mesoporous silica particles with nanometer-sized template-free pores to carry potential gene therapeutics inside their porous network. By varying the chemical nature of the organic pore functionalizations, the loading behavior of the particles with siRNA can be tuned. We used fluorescence recovery after photobleaching (FRAP)[27–29] to investigate the dynamics of siRNA and short double-stranded DNA sequences inside the particles. Moreover, we show that the observed double-stranded oligonucleotides remain intact inside the carrier particles.

2. Results and Discussion

Four different modifications of SBA-15 materials were synthesized: (i) unfunctionalized (UN), functionalized with (ii) 10 mol% cyanopropyl (CP), (iii) 8 mol% aminopropyl + 2 mol% cyanopropyl (APCP), and (iv) 5 mol% aminopropyl + 5 mol% phenyl (APPh). Prior to the loading experiments, the

Dr. T. Lebold, Dr. A. Schlossbauer, Prof. T. Bein, Prof. C. Bräuchle
Center for Nanoscience (CeNS) and Center for Integrated Protein Science Munich (CIPSM)
Ludwig-Maximilians-Universität München
Department of Chemistry
Butenandtstraße 11, 81377 Munich, Germany
E-mail: christoph.braeuchle@cup.uni-muenchen.de; bein@lmu.de
K. Schneider, Dr. L. Schermelleh[+]
Ludwig-Maximilians-Universität München
Department of Biology
Großhaderner Straße 2, 82152 Planegg-Martinsried, Germany
Prof. H. Leonhardt
Center for Nanoscience (CeNS) and Center for Integrated Protein Science Munich (CIPSM)
Ludwig-Maximilians-Universität München
Department of Biology
Großhaderner Straße 2, 82152 Planegg-Martinsried, Germany
[+] Present Address: University of Oxford, Department of Biochemistry, Oxford OX1 3QU, United Kingdom

DOI: 10.1002/adfm.201101365

ADVANCED FUNCTIONAL MATERIALS
www.afm-journal.de

Materials Views
www.MaterialsViews.com

organic template was extracted from the SBA-15 materials (i–iv) and the template free materials resulted as white solid powders (for details see Materials and Methods).

Scanning electron microscopy (SEM) microscopy images of the SBA-15 materials revealed spherically shaped micrometer-sized particles that show a clear tendency to aggregate independent of their functionality. Moreover, in all samples fused aggregates can be observed that consist of two or more individual spherical particles (**Figure 1**a).

Figure 1b displays a schematic of an SBA-15 particle and cross-sections through a pore for the differently functionalized particles.

Nitrogen sorption isotherms of the different samples confirmed the porosity of the materials (Figure 1c). Accordingly, all synthesized SBA-15 materials contain a porous network that is accessible from the outside. Furthermore, the introduction of organic functionalizations leads to a reduction of the mean pore size by 0.7–1.7 nm compared to an unfunctionalized sample as seen by the resulting pore size distributions (Figure 1d, see also below).

One-dimensional X-ray diffractograms of the different synthesized SBA-15 materials indicate the mesoporous nature of the particles (Figure 1e). The XRD data further show that the introduction of functional groups leads to an increase in the 2θ value and thus to a reduction of the pore-to-pore distance compared to unfunctionalized SBA-15 (see Supporting Information (SI)).

The utilized oligonucleotides (siRNA and dsDNA) were labeled with a green (ATTO532) and a red excitable (ATTO647N) fluorescent dye at the 3′ and 5′ ends of the opposite strands, respectively (Figure 1f). With the dye pair being located on the same side of the double-strand, its stability can be tested through Förster Resonance Energy Transfer (FRET): upon excitation with green light, energy transfer will take place from the red emitting ATTO532 (donor) to the ATTO647N (acceptor) dye and its far-red fluorescence can be monitored. Since FRET is only effective within a distance of both dyes of about 2–10 nm, a denatured oligonucleotide does not yield a FRET signal (see SI).

Table 1 summarizes the data extracted from nitrogen sorption and XRD measurements. The term "pore-to-pore distance" used in combination with XRD data is not identical to the term "pore size" used for discussing nitrogen sorption data, since with X-ray diffractometry only the distance between the different layers (one center of a pore to the center of the adjacent pore) can be calculated and no direct conclusion about the wall thickness can be drawn (see SI). In contrast, nitrogen sorption methods directly yield the pore sizes. Both techniques clearly show that the introduction of functional groups leads to a reduction of the pore dimensions. With a reduction of the mean pore size from 8.9 nm (UN) to 7.8 nm (APPh), the pore-to-pore distance also shrinks from 13.5 nm (UN) to 10.7 nm (APPh). The differences in the BET surface areas result from the co-condensation of TEOS with the different functionalized organo-silanes, all having a specific influence on the condensation of the silica backbone and on the remaining pore volume. This behavior has already been reported in other articles, especially for aminopropyltriethoxysilane.[30–32]

Figure 2 shows images obtained with confocal laser scanning microscopy of the four differently functionalized SBA-15 materials suspended inside the buffered labeled-siRNA solution.

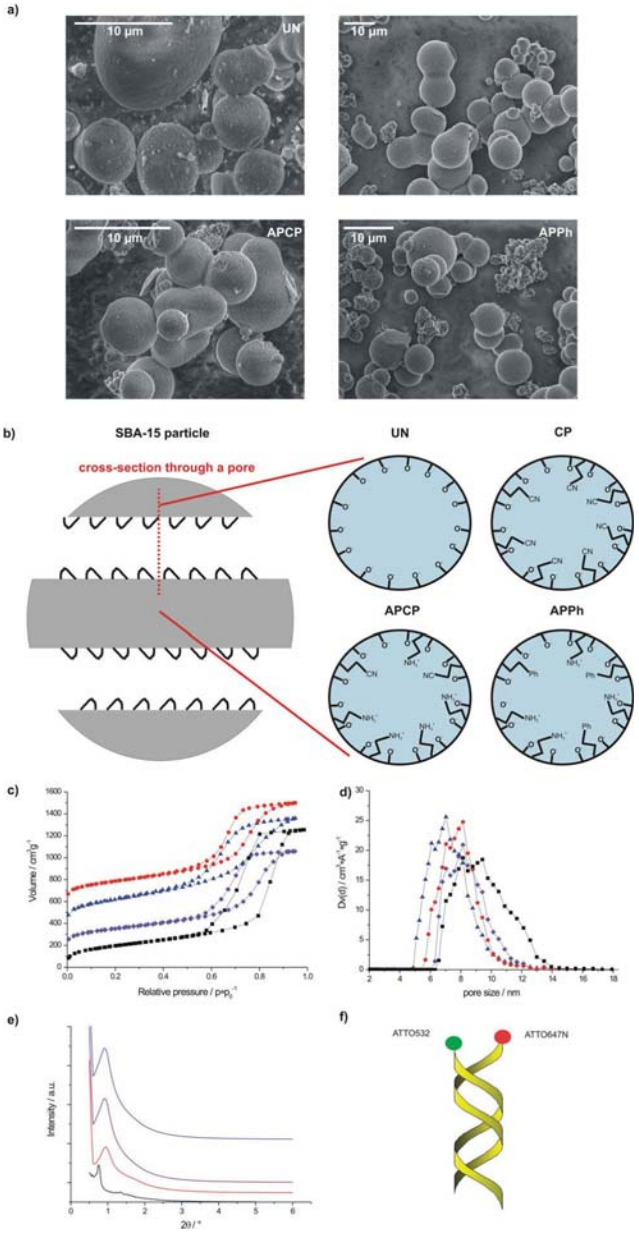

Figure 1. Characterization of the SBA-15 particles and utilized oligonucleotides. a) Scanning electron microscopy images of unfunctionalized (UN), cyanopropyl-functionalized (CP), aminopropyl/cyanopropyl-functionalized (APCP) and aminopropyl/phenyl-functionalized (APPh) SBA-15 particles. The synthesized particles are micrometer-sized, spherically shaped and tend to aggregate. b) Schematic of an SBA-15 particle and cross-sections through a pore for the differently functionalized particles. c) Nitrogen sorption isotherms of UN (black rectangles), CP (purple diamonds, 200 cm^3/g offset), APCP (blue triangles, 400 cm^3/g offset) and APPh (red dots, 600 cm^3/g offset). d) Pore size distribution for UN (black rectangles), CP (purple diamonds), APCP (blue triangles) and APPh (red dots). e) 1D XRD diffractograms for UN (black), APPh (red), CP (purple), and APCP (blue) SBA-15 particles. The introduction of functional groups results in a higher 2θ value and thus a smaller pore-to-pore distance. f) Schematic of an ATTO532 and ATTO647N labeled oligonucleotide double-strand. 20 bp siRNA as well as 20, 60, and 90 bp dsDNA sequences were loaded into the SBA-15 particles. The dye labels are situated on the same side of the opposite strands and thus allow for testing oligonucleotide stability by Förster resonance energy transfer (FRET).

Table 1. Nitrogen sorption and 1D-X-ray diffractometry (XRD) data. The mean pore size, the BET surface[47] and the mean pore volume were calculated from nitrogen sorption data. Additionally, the pore-to-pore distances obtained from X-ray diffractograms are listed (see SI).

	Nitrogen sorption			XRD
	Mean pore size [nm]	BET surface [m^2g^{-1}]	Mean pore volume [cm^3g^{-1}]	Pore-to-pore distance [nm]
UN	8.9	700	1.80	13.5
CP	8.2	580	1.27	11.0
APCP	7.2	815	1.33	11.1
APPh	7.8	680	1.33	10.7

The several micrometer-large mesoporous particles are seen as spherically shaped objects that occasionally aggregate. In confocal mid-sections of APPh particles the siRNA fluorescence can be clearly detected inside the particle indicating that the particles were successfully loaded with siRNA (Figure 2a). Since the confinement of the pore and the specific interaction with different functional groups can influence the extinction coefficient of the dye label significantly, only the relative amounts of siRNA incorporated inside the particles are evaluated here. For example, in APCP particles only about 75% of the amount of siRNA detected inside the APPh particles is observed indicated by a lower signal-to-noise ratio (Figure 2b). The observed variations in the fluorescence intensities cannot be simply due to a different quenching or enhancement of the fluorophore brightness through the different functional groups in the samples, since the free label dyes do not show significant fluorescence intensity fluctuations inside the four different samples (data not shown). Consequently, the observed variations must result from a different amount of incorporated siRNA. In contrast, CP and UN particles do not take up detectable amounts of siRNA (Figure 2c and d), even though the nitrogen sorption data of Table 1 clearly show that all four particle types are accessible and open to an exchange with the surrounding environment. With the utilized confocal microscopy setup concentrations of siRNA down to about 10^{-8} molL^{-1} in solution can be detected.

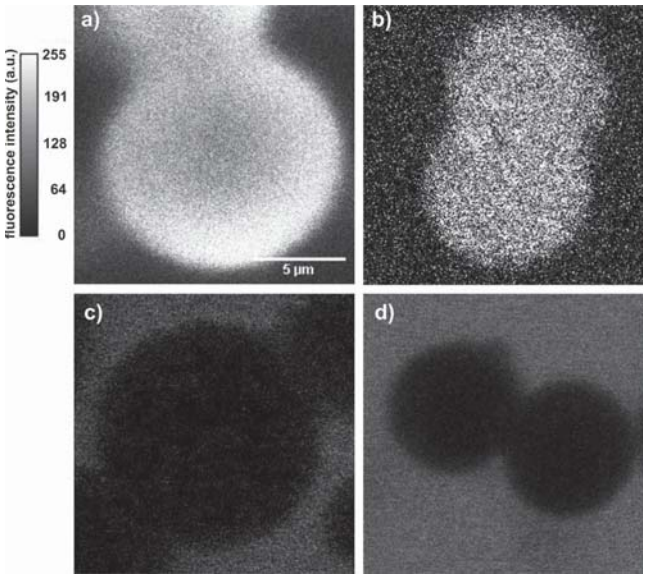

Figure 2. Loading characteristics of functionalized mesoporous SBA-15 particles. Confocal mid-sections of SBA-15 particles dissolved in a buffered solution containing fluorescently labeled siRNA and particles functionalized with a) aminopropyl and phenyl (APPh), b) aminopropyl and cyanopropyl (APCP), c) cyanopropyl (CP), or d) unfunctionalized particles (UN). The images were acquired by exciting the ATTO532 label and detecting the ATTO647N FRET fluorescence signal, thus only stable siRNA can be seen. While fluorescence of the labeled siRNA can be detected inside the APPh and APCP particles, CP and UN particles remain unloaded. Only weak fluorescence in the surrounding solution can be detected. The length and intensity scale bars apply to all panels (a–d).

The pore sizes calculated from nitrogen sorption of the different samples range from 7.2 nm (APCP), 7.8 nm (APPh), 8.2 nm (CP) to 8.9 nm (UN) (see Table 1). However, the overall loading behavior cannot be explained by a simple pore-size effect. The pore sizes of the CP and UN SBA-15 materials are even slightly larger than those with functionalizations that do allow siRNA incorporation. We thus attribute the observed behavior to an unfavorable interaction of the particle surfaces with the negatively charged siRNA. All investigated SBA-15 materials possess hydroxyl groups on their surface that may be partially deprotonated. These (deprotonated) hydroxyl groups and the cyanopropyl groups seem to repel the siRNA because of their negative charge density. In contrast, the aminopropyl-functionality attached to the pore walls of the APCP and APPh particles seems to favor siRNA uptake, which may result from hydrogen bonding between the negatively charged siRNA and the (protonated) amino groups. Taking these considerations into account, the increased loading capacity of APPh silica particles compared to the APCP particles could also result from the electrostatic repulsion between the negatively charged siRNA and the cyanopropyl-groups. Additionally, recent work from Mellaerts et al.[33] demonstrates that variations in the electrostatic interactions between a guest molecule, such as the drug itraconazole, and the pore walls, e.g., by adapting the water content inside the pores, lead to a different drug release rate and thus also different drug dynamics inside the SBA-15 network. A comparison with purely aminopropyl-functionalized SBA-15 particles was not possible, as the corresponding synthesis solution did not yield a mesoporous powder but an undefined gelated structure.

Notably, the successful loading of APPh and APCP particles was detected by the FRET signal of closely positioned ATTO532 and ATTO647N fluorophores. This clearly indicates that the siRNAs were present as double-stranded hybrid molecules, which is essential within the therapeutic context of gene silencing by RNA interference. Control measurements under denaturing conditions show a complete loss of FRET signal (see SI). No significant loss of siRNA fluorescence inside the APPh and APCP particles was observed within 48 h, demonstrating long-term stability of siRNAs inside the particles as well as inside the surrounding buffered solution.

The above results provide evidence that aminopropyl-containing functionalities favor siRNA uptake into the mesoporous materials. We next aimed to characterize the mobility of oligonucleotides inside functionalized SBA-15 particles. We therefore applied fluorescence recovery after photobleaching (FRAP) and kinetic modeling to determine the diffusion constants of

ADVANCED FUNCTIONAL MATERIALS
www.afm-journal.de

Materials Views
www.MaterialsViews.com

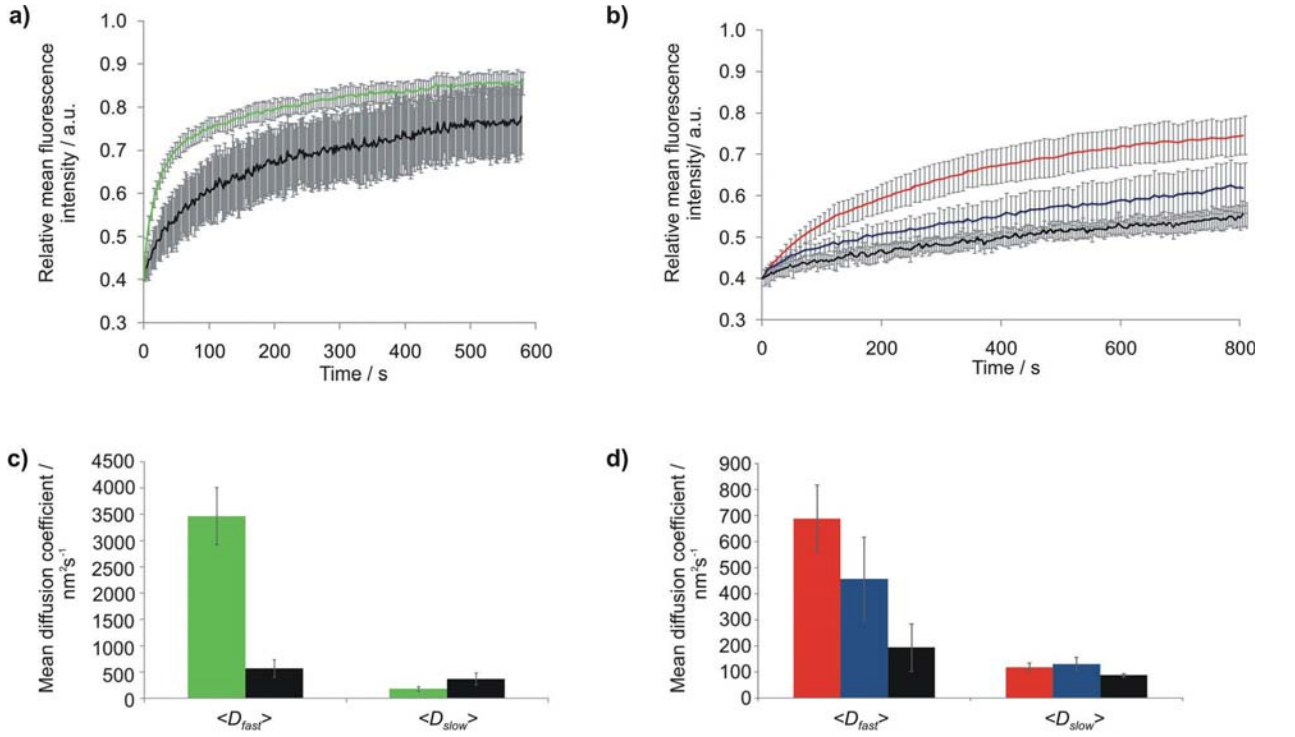

Figure 3. FRAP recovery curves and mean diffusion coefficients for the different oligonucleotides inside the functionalized SBA-15 particles. a) Recovery kinetics of the 20 bp siRNA molecules inside APCP functionalized particles (green) and inside APPh functionalized particles (black). b) APPh functionalized particles loaded with 20 bp DNA (red), 60 bp DNA (blue) and 90 bp DNA (black). c, d) Results of the kinetic modeling with diffusion coefficients $\langle D_{fast} \rangle$ and $\langle D_{slow} \rangle$ determined for the two mobile populations in each sample. c) siRNA inside APCP particles (green) and inside APPh particles (black). d) APPh particles loaded with 20 bp DNA (red), 60 bp DNA (blue) and 90 bp DNA (black). The error bars indicate standard deviation (a, b) and standard error (c, d).

(i) the 20 bp siRNA oligonucleotides inside APPh and APCP particles and (ii) DNA double-strands of different length (20, 60 and 90 bp) inside APPh particles. The utilized double-stranded labeled oligonucleotides have an estimated length of about 7 nm (20 bp), 21 nm (60 bp) and 31 nm (90 bp). All sequences were randomly chosen, however, it was ascertained that they do not form large hairpins or bubbles that might additionally affect diffusion. The measurements started 3 h after incubation of the particles with the oligonucleotide solution and DNA stability was again confirmed through FRET.

For FRAP experiments small circular regions of interest (ROIs) were bleached by a high intensity laser beam to result in a bleach spot with a diameter of about 2 µm. The bleaching sites were randomly chosen inside the particle, either centrally or closer to the edges. Fluorescence recovery was observed for 10 –15 min. Mean curves were calculated for the siRNA and the DNA sequences in the differently functionalized particles by averaging the recovery kinetics of at least 10 bleach spots each (**Figure 3**a, b).

We first measured the mobility of siRNA inside APCP and APPh particles (Figure 3a) and found significantly faster recovery kinetics of siRNAs inside the cyanopropyl-containing particles despite of their smaller pore size (see Table 1). As discussed for Figure 2 this may be due to an increased repulsive interaction between the siRNA and the cyanopropyl groups compared to the phenyl groups. A similar slowdown of the diffusing species upon insertion of phenyl groups was observed in a recent study.[34] It is important to note that the apparent standard deviations displayed in Figure 3a and b do not reflect the error in determining the mean fluorescence intensity, but originate from the inherent heterogeneity of the different mesoporous particles. Such heterogeneities are typical for these mesoporous silica materials due to the existence of adsorption sites, dead ends and structural defects.[35–39] The effective diameter of the circular bleaching ROI in the FRAP experiments was about 2 µm. Heterogeneities occurring within this length-scale might account for some of the variability of recovery kinetics observed for different bleaching sites. Detailed diffusion studies of molecules in mesoporous hosts have demonstrated that heterogeneities due to structural variations indeed occur on such a length-scale.[35]

Figure 3b displays mean recovery curves for the 20 bp (red), 60 bp (blue) and 90 bp (black) dsDNA sequences diffusing inside APPh SBA-15 particles. The results clearly demonstrate a size-dependent decrease of dsDNA mobility. In neither case full recovery was observed, indicating a distinct immobile fraction of molecules present inside the particles.[40] It is important to note that bleaching only implies that the fluorescent label attached to the DNA gets irreversibly inactivated and thus the DNA becomes invisible. However, the dsDNA is still present and, due to its immobility, may block the adsorption sites inside the particle, preventing new fluorescent oligonucleotides from diffusing to these sites. In contrast, bleached mobile DNA molecules should be able to diffuse out of the particle. The data

shown in Figure 3b clearly indicate that the fraction of immobile molecules increases significantly with increasing length of the DNA double-strand. This could be explained by stronger adsorption of longer dsDNA inside the porous network due to an increased negative charge.

Next, the mean fluorescence recovery curves were fitted to a diffusion model in order to extract diffusion coefficients and thereby quantify the mobility of the oligonucleotides inside the mesoporous particles. In order to describe the data adequately a model assuming two different diffusion coefficients was necessary (see exemplary data in the Supporting Information). The utilized model for the fluorescence recovery curve $f(t)$ is given in Equation 1.

$$f(t) = 1 - \phi + \phi \exp\left(\frac{-2t_{D_{fast}}}{t}\right)\left[I_0\left(\frac{2t_{D_{fast}}}{t}\right) + I_1\left(\frac{2t_{D_{fast}}}{t}\right)\right] + \theta\left(\phi \exp\left(\frac{-2t_{D_{slow}}}{t}\right)\left[I_0\left(\frac{-2t_{D_{slow}}}{t}\right) + I_1\left(\frac{-2t_{D_{slow}}}{t}\right)\right]\left(-\phi \exp\left(\frac{-2t_{D_{fast}}}{t}\right)\left[I_0\left(\frac{2t_{D_{fast}}}{t}\right) + I_1\left(\frac{2t_{D_{fast}}}{t}\right)\right]\right)\right) = f_{D_{fast}}(t) + \theta\left[f_{D_{slow}}(t) - f_{D_{fast}}(t)\right] \quad (1)$$

with $t_D = \omega^2/4D$ and thus the two diffusion coefficients $\langle D_{fast}\rangle$ and $\langle D_{slow}\rangle$. The superposition parameter θ indicates the relative contributions of the two populations. The values of ϕ (bleached fraction) and ω (full width at half maximum of the bleach spot) were extracted from the experimental data (for details of the modeling see Supporting Information). Modeling the mean fluorescence recovery curves of Figure 3a and b according to Eq. 1 yielded the two mean diffusion coefficients $\langle D_{fast}\rangle$ and $\langle D_{slow}\rangle$ for the mobile populations in each sample (see Figure 3c and d). The mean diffusion coefficients obtained from siRNA inside APCP particles (green) and inside APPh particles (black) are displayed in Figure 3c, whereas the data for 20 bp DNA (red), 60 bp DNA (blue) and 90 bp DNA (black) diffusing inside APPh particles are displayed in Figure 3d. The calculated values of $\langle D_{fast}\rangle$ and $\langle D_{slow}\rangle$ are listed in **Table 2**. The recovery kinetics of the 90 bp double-stranded DNA are too slow to be fitted accurately by the utilized model. Thus, only an upper limit for the mean diffusion coefficients could be determined. The mean diffusion coefficient of the faster diffusing population $\langle D_{fast}\rangle$ can be attributed to oligonucleotide molecules diffusing inside the mesoporous channels of the SBA-15 particles. The determined diffusion coefficients (see Table 2) lie within the range of those known for diffusion dynamics of organic molecules such as dyes or drugs inside mesoporous materials, which is in the range of hundreds to thousands nm^2/s,[34,36,41] and slightly above those found for intraparticle diffusion in zeolites.[42] The siRNA is significantly slower in the phenyl-containing particles and the DNA diffusion slows down with increasing double-strand length. A quantitative model for the relationship between the mean diffusion coefficients $\langle D_{fast}\rangle$ and the length of the dsDNA is beyond the scope of this publication. The real situation could only be approximated by the Stokes–Einstein equation[1] for an ellipsoid moving lengthwise inside the pore.[2] However, effects such as the interaction of the highly charged oligonucleotides with the channel walls that could influence the diffusion coefficients would not be included in this case.

Regarding the second slow diffusing population, it was previously shown that the presence of binding sites can be detected as an "effective diffusion coefficient".[44] This effective diffusion thus refers to a slowing down of the initially unhindered diffusion due to binding events. However, this would not necessarily explain a distinct second population, but a general decrease in the observed mean diffusion coefficient. Interestingly, $\langle D_{slow}\rangle$ does not show a clear trend for the different samples in contrast to $\langle D_{fast}\rangle$. If the oligonucleotides degraded, resulting in the presence of shorter labeled fragments, one would expect to find fragments with higher dynamics compared to the intact double-strands. We thus attribute the observation of a slow diffusion coefficient not to the existence of a distinct second slow diffusing population, but rather to a manifestation of the inherent heterogeneity of the samples resulting in a variation of the diffusion coefficients.[36]

3. Conclusion

In conclusion, this study shows that the loading behavior of oligonucleotides into SBA-15 particles critically depends on the surface functionalization. Unfunctionalized and cyanopropyl-functionalized SBA-15 could not be loaded with siRNA. We attribute this behavior to an unfavorable repulsive interaction of the negatively charged siRNA with the negative charge density of these functional groups. However, when adjusting the surface polarity of the particles by coating the channels with aminopropyl groups, the repulsive interactions get reduced, further hydrogen bonding sites and favorable Coulombic interactions are introduced and thus the particles become accessible for siRNA and can be loaded. Moreover, the SBA-15 particles could be loaded with DNA double-strands, ranging from 20 up to a double-strand sequence of 90 bp in length. The stretched-out 90 bp oligonucleotide double-strands have a length of about 31 nm including the labels. This is a striking observation, since the pore sizes of the mesoporous silica samples only range from about 7–9 nm. The fact that fairly long DNA sequences can be loaded into mesoporous silica

Table 2. Calculated mean diffusion coefficients for the fast and slow diffusing populations (±standard error of the mean).

	APPh [nm^2/s]	APCP [nm^2/s]
siRNA	$\langle D_{fast}\rangle = 5.7 * 10^2 + 1.7 * 10^2$	$\langle D_{fast}\rangle = 3.4 * 10^3 + 5.9 * 10^2$
	$\langle D_{slow}\rangle = 3.7 * 10^2 + 1.2 * 10^2$	$\langle D_{slow}\rangle = 1.8 * 10^2 + 4.9 * 10^1$
20 bp DNA	$\langle D_{fast}\rangle = 6.9 * 10^2 + 1.3 * 10^2$	—
	$\langle D_{slow}\rangle = 1.1 * 10^2 + 1.7 * 10^1$	—
60 bp DNA	$\langle D_{fast}\rangle = 4.6 * 10^2 + 1.6 * 10^2$	—
	$\langle D_{slow}\rangle = 1.3 * 10^2 + 2.6 * 10^1$	—
90 bp DNA	$\langle D_{fast}\rangle < 1.9 * 10^2 + 9.1 * 10^1$	—
	$\langle D_{slow}\rangle < 8.9 * 10^1 + 1.4 * 10^1$	—

opens up numerous potential applications in drug-delivery. Importantly, for all oligonucleotide sequences studied here, their stability inside the mesoporous materials could be proven by FRET. Our study also demonstrates that the diffusion dynamics of siRNA inside the template-extracted particles could be tuned through adding functional groups. The experiments show that the diffusion dynamics of the DNA critically depend on their length and that long DNA sequences show a higher tendency to get immobilized at adsorption sites inside the porous network.

Understanding the principles that govern oligonucleotide dynamics inside the channels of mesoporous silica is of great importance for the design of successful drug carriers with controlled retarded release of a drug over a prolonged period of time. Thus, our study shows that mesoporous silica materials are a versatile platform for siRNA delivery and that they enable alternative strategies for gene therapy.

4. Experimental Section

Preparation of Template-Free SBA-15 Particles: The large-pore SBA-15 spherical particles were synthesized following a procedure generally introduced by Katiyar et al.[45] and later used by Schlossbauer et al.[46] for producing mesoporous silica spheres as a matrix for biofunctionalization. The surfactant Pluronic P123 (3.0 g, poly(ethylene oxide)$_{20}$-poly(propylene oxide)$_{70}$-poly(ethylene oxide)$_{20}$) was dissolved in hydrochloric acid (60 mL, 1.5 molL^{-1}). Cetyltrimethyl ammonium bromide (CTAB, 0.6 g) was used as a co-surfactant in combination with 1,3,5-trimethylbenzene (TMB, 0.3 g) as a swelling agent to increase the pore diameter. CTAB and TMB were mixed with 25 mL of distilled water. After combining the aqueous solution with the acidic solution, ethanol (pure, 20 mL) was added under stirring. Subsequently, tetraethyl orthosilicate (TEOS, 10 mL) was added dropwise. The resulting mixture was stirred vigorously (500 rpm) at 35 °C for 45 min before being transferred into an autoclave (Parr Instrument Company) for hydrothermal treatment at 75 °C for 12 hours under static conditions. Subsequently, the mixture was treated at 125 °C for 12 h. The resulting white powder was filtered out, washed with distilled water (100 mL) and ethanol (pure, 100 mL) and dried at 60 °C for another 12 h. For the synthesis of functionalized silica particles, a certain molar fraction (up to 10 mol%) of the silica source (TEOS) was replaced with a functionalized silica source. The functionalized silica precursors were: $H_2NC_3H_6Si(OC_2H_5)_3$ for aminopropyl-, $C_6H_5Si(OC_2H_5)_3$ for phenyl- and $CNC_3H_6Si(OC_2H_5)_3$ for cyanopropyl-functionalization. Four different modifications of SBA-15 materials were synthesized: (i) unfunctionalized (UN), functionalized with (ii) 10 mol% cyanopropyl (CP), (iii) 8 mol% aminopropyl + 2 mol% cyanopropyl (APCP), and (iv) 5 mol% aminopropyl + 5 mol% phenyl (APPh).

Extraction of the organic template from the SBA-15 materials was performed by heating 1 g of the white powder twice under reflux at 90 °C for 30 min in 100 mL of a solution containing concentrated hydrochloric acid (10 mL) and ethanol (90 mL). The SBA-15 material was separated by filtration and washed with ethanol (100 mL) after each extraction step. The template-extracted samples were obtained as white solid powders.

Particle Characterization: The four different SBA-15 samples were characterized with scanning electron microscopy (SEM), nitrogen sorption and 1D X-ray diffractometry. SEM micrographs were recorded on a JEOL JSM-6500F scanning electron microscope. Nitrogen sorption measurements were performed on a Quantachrome Nova 4000e instrument. The structure of the SBA-15 powders was determined by using a Scintag XDS 2000 powder diffractometer in θ/θ Bragg-Brentano scattering geometry. From the obtained X-ray diffractograms the pore-to-pore distances were calculated (for details see Supporting Information).

Particle Loading with siRNA: First, the loading behavior of the particles with siRNA was examined. For this purpose, the differently functionalized SBA-15 powders obtained after surfactant removal were dissolved in PBS buffer (pH = 7.4) and labeled siRNA (20 bp) was added at a concentration of 10^{-5} molL^{-1} to each of the different SBA-15 samples. Then the samples were incubated for 3 h at room temperature in order to give the siRNA sufficient time to access the particles (control experiments showed that no increase of siRNA-dye-fluorescence could be observed inside the SBA-15 particles after that time). The particles were then microscopically investigated in a sample chamber immersed in the buffered siRNA solution. The following double-labelled siRNA double-strand was used: 5' GGA CUC CAG UGG UAA UCU AC ATTO647N 3'; 3' CCU GAG GUC ACC AUU AGA UG ATTO532 5' (IBA GmbH, Göttingen, Germany). The double-strand sequence was randomly chosen.

Microscopy Setup: The different oligonucleotide SBA-15 samples were measured on a LSM510 confocal laser scanning microscope (Carl Zeiss AG) as follows: only the green fluorescent dye label was excited with a He-Ne-laser emitting at 543 nm through a 40x/1.3 NA oil-immersion objective (Zeiss Plan Neofluar) The fluorescence was filtered by a beamsplitter (HFT, UV/488/543/633) in combination with a long-pass filter (LP 650) in order to detect the FRET fluorescence signal from the red fluorescent dye label. The FRET signal was detected with a photomultiplier.

Fluorescence Recovery after Photobleaching (FRAP) Measurements: The utilized confocal setup is identical to the setup introduced above with the following additional settings for the FRAP measurements: integration time per frame: 983 ms/frame; a new frame was recorded every 4 s; 10 scans before bleaching; circular bleaching region of 10 pixels in diameter. The bleaching sites were chosen randomly amongst different particles and also within the particle (either centrally or closer to the edges). For each sample at least 10 bleaching spots were analyzed. Individual recovery curves were extracted for each bleaching event and then averaged. The method of data evaluation in order to obtain fluorescence recovery curves is explained in detail in the Supporting Information.

DNA Sequences for FRAP Measurements: The following DNA double-strand sequences were used: 5' GGA CGC CAG GGG GAA GCG AC ATTO647N 3'; 3' CCT GCG GTC CCC CTT CGC TG ATTO532 5' for the 20bp DNA, 5' GGA CGC CAG GGG GAA GCG ACG GAC GCC AGG ATTO532 3'; 3' CCT GCG GTC CCC CTT CGC TGC CTG CGG TCC ATTO647N 5' for the 30 bp DNA, 5' GGA CGC CAG GGG GAA GCG ACG GAC GCC AGG CTG ATT TGA AGC TTA TGA CTT ATT GGA CCT ATTO532 3'; 3' CCT GCG GTC CCC CTT CGC CTC CTG CGG TCC GAC TAA ACT TCG AAT ACT GAA TAA CCT GGA ATTO647N 5' for the 60 bp DNA and 5' GGA CGC CAG GGG GAA GCG ACG GAC GCC AGG CTG ATT TGA AGC TTA TGA CTT ATT GGA CCT ATC TCT GAC ATA TTA TAC TAG GCT GTG TTT ATTO532 3'; 3' CCT GCG GTC CCC CTT CGC TGC CTG CGG TCC GAC TAA ACT TCG AAT ACT GAA TAA CCT GGA TAG AGA CTG TAT AAT ATG ATC CGA CAC AAA ATTO647N 5' for the 90 bp DNA (IBA GmbH, Göttingen, Germany). The procedures for loading the SBA-15 particles were identical to those for siRNA.

Supporting Information

Supporting Information is available from the Wiley Online Library or from the author.

Acknowledgements

We are grateful to A. Dobay for providing programs for FRAP data evaluation and to J. Michaelis for fruitful suggestions and discussions. K.S. and T.L. were supported by the International Doctorate Program NanoBioTechnology (IDK-NBT). Additionally, K.S. was also supported by the International Max Planck Research School for Molecular and Cellular Life Sciences (IMPRS-LS). Financial support from the Nanosystems

Initiative Munich (NIM), BioImaging Network (BIN) Munich, EpiSys (BMBF) and the SFB 749 (DFG) is gratefully acknowledged.

Received: June 17, 2011
Published online:

[1] A. R. Vanderkrol, L. A. Mur, M. Beld, J. N. M. Mol, A. R. Stuitje, *Plant. Cell.* **1990**, *2*, 291.
[2] J. M. Kooter, R. Vanblokland, P. Delange, M. Stam, J. N. M. Mol, *J. Cell. Biochem.* **1994**, 115.
[3] D. A. Dean, D. D. Strong, W. E. Zimmer, *Gene Ther.* **2005**, *12*, 881.
[4] H. Mok, S. H. Lee, J. W. Park, T. G. Park, *Nat. Mater.* **2010**, *9*, 272.
[5] K. A. Whitehead, R. Langer, D. G. Anderson, *Nat. Rev. Drug Discov.* **2010**, *9*, 412.
[6] S. C. Semple, A. Akinc, J. X. Chen, A. P. Sandhu, B. L. Mui, C. K. Cho, D. W. Y. Sah, D. Stebbing, E. J. Crosley, E. Yaworski, I. M. Hafez, J. R. Dorkin, J. Qin, K. Lam, K. G. Rajeev, K. F. Wong, L. B. Jeffs, L. Nechev, M. L. Eisenhardt, M. Jayaraman, M. Kazem, M. A. Maier, M. Srinivasulu, M. J. Weinstein, Q. M. Chen, R. Alvarez, S. A. Barros, S. De, S. K. Klimuk, T. Borland, V. Kosovrasti, W. L. Cantley, Y. K. Tam, M. Manoharan, M. A. Ciufolini, M. A. Tracy, A. de Fougerolles, I. MacLachlan, P. R. Cullis, T. D. Madden, M. J. Hope, *Nat. Biotechnol.* **2010**, *28*, 172.
[7] J. S. Beck, J. C. Vartuli, W. J. Roth, M. E. Leonowicz, C. T. Kresge, K. D. Schmitt, C. T. W. Chu, D. H. Olson, E. W. Sheppard, S. B. McCullen, J. B. Higgins, J. L. Schlenker, *J. Am. Chem. Soc.* **1992**, *114*, 10834.
[8] C. T. Kresge, M. E. Leonowicz, W. J. Roth, C. E. Vartuli, J. S. Beck, *Nature* **1992**, *359*, 710.
[9] D. Y. Zhao, J. L. Feng, Q. S. Huo, N. Melosh, G. H. Fredrickson, B. F. Chmelka, G. D. Stucky, *Science* **1998**, *279*, 548.
[10] D. Y. Zhao, Q. S. Huo, J. L. Feng, B. F. Chmelka, G. D. Stucky, *J. Am. Chem. Soc.* **1998**, *120*, 6024.
[11] S. J. L. Billinge, E. J. McKimmy, M. Shatnawi, H. Kim, V. Petkov, D. Wermeille, T. J. Pinnavaia, *J. Am. Chem. Soc.* **2005**, *127*, 8492.
[12] D. E. De Vos, M. Dams, B. F. Sels, P. A. Jacobs, *Chem. Rev.* **2002**, *102*, 3615.
[13] V. Rebbin, R. Schmidt, M. Fröba, *Angew. Chemie Int. Ed.* **2006**, *45*, 5210.
[14] N. Petkov, N. Stock, T. Bein, *J. Phys. Chem. B* **2005**, *109*, 10737.
[15] B. Ye, M. L. Trudeau, D. M. Antonelli, *Adv. Mat.* **2001**, *13*, 561.
[16] D. J. Cott, N. Petkov, M. A. Morris, B. Platschek, T. Bein, J. D. Holmes, *J. Am. Chem. Soc.* **2006**, *128*, 3920.
[17] H. A. Meng, M. Xue, T. A. Xia, Y. L. Zhao, F. Tamanoi, J. F. Stoddart, J. I. Zink, A. E. Nel, *J. Am. Chem. Soc.* **2010**, *132*, 12690.
[18] V. Cauda, H. Engelke, A. Sauer, D. Arcizet, C. Brauchle, J. Radler, T. Bein, *Nano Lett.* **2010**, *10*, 2484.
[19] A. Sauer, A. Schlossbauer, N. Ruthardt, V. Cauda, T. Bein, C. Bräuchle, *Nano Lett.* **2010**, *10*, 3684.
[20] T. Lebold, C. Jung, J. Michaelis, C. Brauchle, *Nano Lett.* **2009**, *9*, 2877.
[21] D. P. Ferris, Y. L. Zhao, N. M. Khashab, H. A. Khatib, J. F. Stoddart, J. I. Zink, *J. Am. Chem. Soc.* **2009**, *131*, 1686.
[22] I. Roy, T. Y. Ohulchanskyy, D. J. Bharali, H. E. Pudavar, R. A. Mistretta, N. Kaur, P. N. Prasad, *Proc. Natl. Acad. Sci. USA* **2005**, *102*, 279.
[23] S. Giri, B. G. Trewyn, V. S. Y. Lin, *Nanomed.* **2007**, *2*, 99.
[24] S. Giri, B. G. Trewyn, M. P. Stellmaker, V. S. Y. Lin, *Angew. Chemie Int. Ed.* **2005**, *44*, 5038.
[25] F. Torney, B. G. Trewyn, V. S. Y. Lin, K. Wang, *Nature Nanotech.* **2007**, *2*, 295.
[26] C. Hom, J. Lu, M. Liong, H. Luo, Z. Li, J. I. Zink, F. Tamanoi, *Small* **2010**, *6*, 1185.
[27] D. Axelrod, D. E. Koppel, J. Schlessinger, E. Elson, W. W. Webb, *Biophys. J.* **1976**, *16*, 1055.
[28] D. E. Koppel, D. Axelrod, J. Schlessinger, E. L. Elson, W. W. Webb, *Biophys. J.* **1976**, *16*, 1315.
[29] T. K. L. Meyvis, S. C. De Smedt, P. Van Oostveldt, J. Demeester, *Pharm. Res.* **1999**, *16*, 1153.
[30] A. Sayari, E. Da'na, *Chem. Eng. J.* **2011**, *166*, 445.
[31] J. H. Yim, J. A. Bae, S. H. Hwang, K. C. Song, J. K. Jeon, Y. S. Ko, *J. Nanosci. Nanotechnol.* **2010**, *10*, 290.
[32] S. R. Zheng, Q. Tao, Z. Y. Xu, J. H. Wang, F. L. Liu, H. Q. Wan, *Microp. Mesop. Mat.* **2010**, *131*, 177.
[33] R. Mellaerts, M. B. J. Roeffaers, K. Houthoofd, M. Van Speybroeck, G. De Cremer, J. A. G. Jammaer, G. Van den Mooter, P. Augustijns, J. Hofkens, J. A. Martens, *Phys. Chem. Chem. Phys.* **2011**, *13*, 2706.
[34] T. Lebold, L. A. Mühlstein, J. Blechinger, M. Riederer, H. Amenitsch, R. Köhn, K. Peneva, K. Müllen, J. Michaelis, C. Bräuchle, T. Bein, *Chem. Europ. J.* **2009**, *15*, 1661.
[35] A. Zürner, J. Kirstein, M. Doblinger, C. Bräuchle, T. Bein, *Nature* **2007**, *450*, 705.
[36] J. Kirstein, B. Platschek, C. Jung, R. Brown, T. Bein, C. Bräuchle, *Nat. Mater.* **2007**, *6*, 303.
[37] C. Jung, J. Kirstein, B. Platschek, T. Bein, M. Budde, I. Frank, K. Müllen, J. Michaelis, C. Bräuchle, *J. Am. Chem. Soc.* **2008**, *130*, 1638.
[38] M. B. J. Roeffaers, G. De Cremer, H. Uji-i, B. Muls, B. F. Sels, P. A. Jacobs, F. C. De Schryver, D. E. De Vos, J. Hofkens, *Proc. Natl. Acad. Sci. USA* **2007**, *104*, 12603.
[39] G. De Cremer, B. F. Sels, D. E. De Vos, J. Hofkens, M. B. J. Roeffaers, *Chem. Soc. Rev.* **2010**, *39*, 4703.
[40] E. A. J. Reits, J. J. Neefjes, *Nat. Cell. Biol.* **2001**, *3*, E145.
[41] G. De Cremer, M. B. J. Roeffaers, E. Bartholomeeusen, K. F. Lin, P. Dedecker, P. P. Pescarmona, P. A. Jacobs, D. E. De Vos, J. Hofkens, B. F. Sels, *Angew. Chemie Int. Ed.* **2010**, *49*, 908.
[42] M. Pfenniger, G. Calzaferri, *ChemPhysChem* **2000**, *1*, 211.
[43] A. Einstein, *Ann. Phys. Berlin* **1905**, *17*, 549.
[44] B. L. Sprague, R. L. Pego, D. A. Stavreva, J. G. McNally, *Biophys. J.* **2004**, *86*, 3473.
[45] A. Katiyar, S. Yadav, P. G. Smirniotis, N. G. Pinto, *J. Chromatogr. A* **2006**, *1122*, 13.
[46] A. Schlossbauer, D. Schaffert, J. Kecht, E. Wagner, T. Bein, *J. Am. Chem. Soc.* **2008**, *130*, 12558.
[47] S. Brunauer, P. H. Emmett, E. Teller, *J. Am. Chem. Soc.* **1938**, *60*, 309.

ADVANCED FUNCTIONAL MATERIALS

Supporting Information

for Adv. Funct. Mater., DOI: 10.1002/adfm.201101365

Controlling The Mobility Of Oligonucleotides In The Nanochannels Of Mesoporous Silica

Timo Lebold , Axel Schlossbauer , Katrin Schneider , Lothar Schermelleh , Heinrich Leonhardt , Thomas Bein , and Christoph Bräuchle **

SUPPORTING INFORMATION

Controlling the mobility of oligonucleotides in the nanochannels of mesoporous silica

By *Timo Lebold*, *Axel Schlossbauer*, *Katrin Schneider*, *Lothar Schermelleh*, *Heinrich Leonhardt*, *Thomas Bein** and *Christoph Bräuchle**

Dr. T. Lebold, Dr. A. Schlossbauer, Prof. T. Bein, Prof. C. Bräuchle
Center for Nanoscience (CeNS) and Center for Integrated Protein Science Munich (CIPSM)
Ludwig-Maximilians-Universität München
Department of Chemistry
Butenandtstraße 11
81377 Munich, Germany
E-mail: christoph.braeuchle@cup.uni-muenchen.de; bein@lmu.de

K. Schneider, Dr. L. Schermelleh
Ludwig-Maximilians-Universität München
Department of Biology
Großhaderner Straße 2
82152 Planegg-Martinsried, Germany

Prof. H. Leonhardt
Center for Nanoscience (CeNS) and Center for Integrated Protein Science Munich (CIPSM)
Ludwig-Maximilians-Universität München
Department of Biology
Großhaderner Straße 2
82152 Planegg-Martinsried, Germany

Calculation of pore-to-pore distances from X-ray diffractograms

From the obtained X-ray diffractograms first the 2θ-values of the signals were determined. The pore-to-pore distances, a_0-values, can then be calculated as follows:

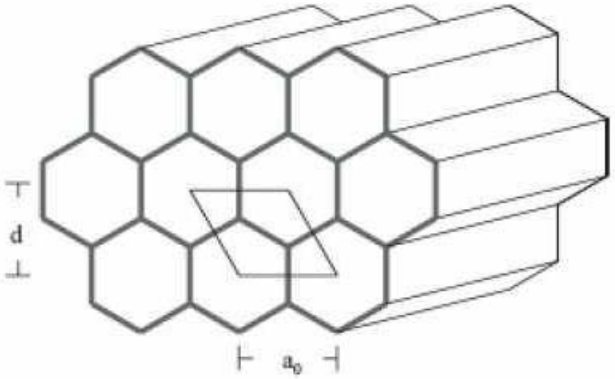

$$d = \frac{\lambda}{sin\theta}$$

$$\lambda = 1.54\,\text{Å}$$

$$a_0 = \frac{d}{sin60°}$$

Figure S1. Schematic of a hexagonal pore topology. The characteristic parameters d and the pore-to-pore distance a_0, which can be calculated from the 2θ-values obtained by X-ray diffractometry, are depicted.

Förster resonance energy transfer (FRET) as indicator for oligonucleotide stability

The suitability of the FRET signal as an indicator for siRNA stability is demonstrated in control measurement where siRNA was degraded through decreased pH (Figure S2). Only the ATTO 532 dye label was excited at 543 nm and both dye labels ATTO 532 and ATTO 647N were detected simultaneously. Dual-labeled siRNA excited by the green laser light shows emission in the far-red range due to FRET to the acceptor dye ATTO 647N but no emission of the donor ATTO 532 in the yellow range in a buffered solution at pH 7 (Figure S2a). In contrast, after induced denaturation by addition of hydrochloric acid, the FRET signal in the far-red detection range disappears while yellow emission of the ATTO 532 dye reappears (Figure S2b).

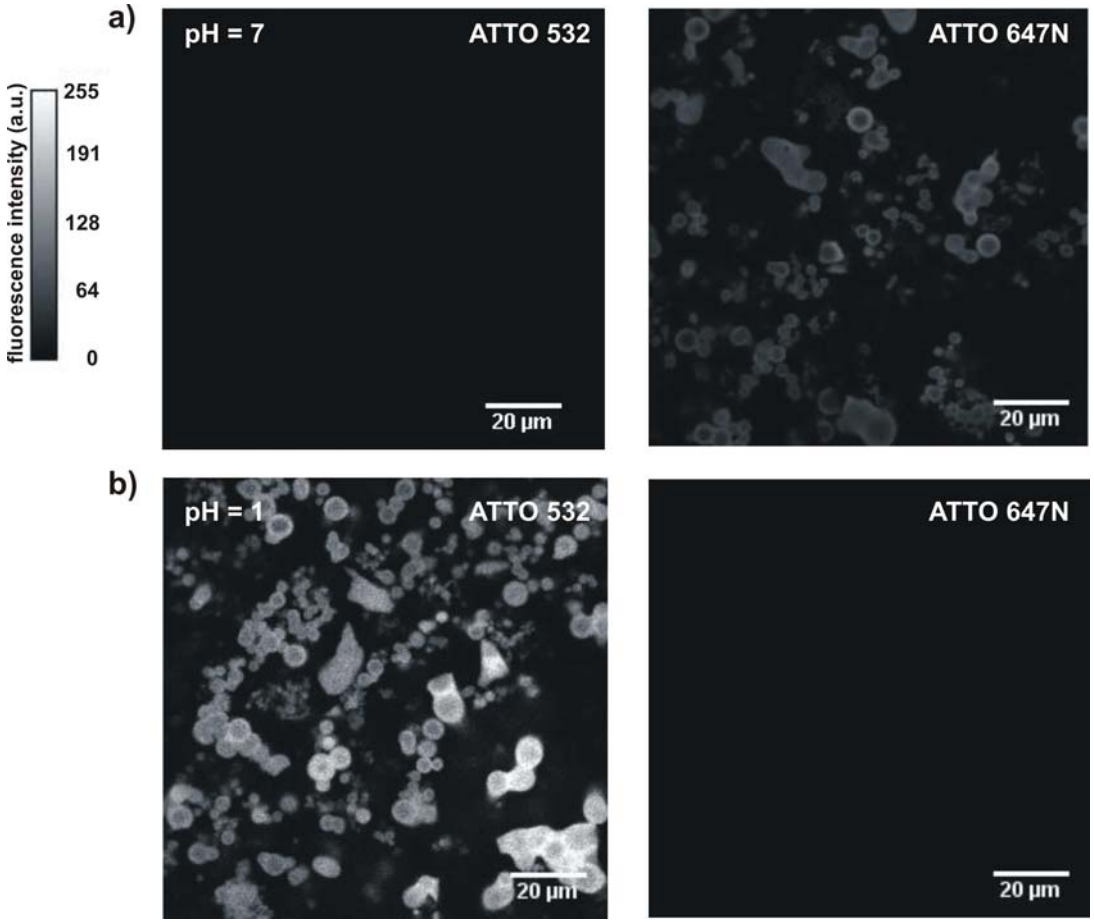

Figure S2. Förster resonance energy transfer (FRET) as an indicator for oligonucleotide stability. Dual-labeled siRNA inside aminopropyl- (5 mol %) and phenyl- (5 mol %) (APPh) functionalized SBA-15 particles. Fluorescence signal of ATTO 532 donor and ATTO 647N acceptor dye at pH 7 (a) and at pH 1 (b). After decreasing the pH the FRET signal of the acceptor dye disappears completely while the donor fluorescence is recovered indicating degradation of siRNA by denaturation. The intensity scale bar applies to all panels.

Quantitative evaluation of FRAP data

Evaluation of FRAP time series (see Movie 1) was performed with ImageJ[1] and automated processing by a set of self-developed macros. The imported image series was first converted to 8-bit and Gauss-filtered (2 pixel radius). Datasets with lateral drift of particles during recording were corrected by image registration using the *StackReg* plug-in of ImageJ. Next, for all images of the time series mean fluorescence intensities were extracted from three regions of interest (ROIs): the bleached region (B), the total particle area (T) and a background ROI outside the particles. The bleached region was defined as follows: the intensity of a cross-section through the spherical bleached

regions was measured in the first postbleach frame, yielding a roughly Gaussian shaped fluorescence intensity profile. Then, the full width at half maximum (FWHM, ω) was determined from that bleached profile after normalization to the prebleach frame. This parameter ω was used as the radius of the circular bleached region B and was implemented in the subsequent modeling of the data.

From the raw fluorescence intensity data of T and B the fluorescence background was subtracted. The resulting postbleach values were multiplied by $T_{postbleach}/T_t$ to correct for the possible superimposed gain or loss of total fluorescence during postbleach acquisition by import and bleaching-by-acquisition. To correct for particle-to-particle differences in bleaching depth, a value φ was subtracted from all mean fluorescence values such that the starting mean fluorescence intensity for all curves was equalized to an arbitrarily chosen value 0.4. Accordingly the bleached fraction ϕ for kinetic modeling (see below) was set to 0.6. The corrected values for T and B were normalized to the respective means of the last 5 prebleach values. In order to correct for a loss of fluorescence by the bleach pulse, the values for B were divided by values for T. The displayed mean fluorescence recovery curves can then be obtained by averaging at least 10 individual recovery curves.

Movie 1

FRAP series of dual-labeled siRNA loaded aminopropyl- and phenyl- (5 + 5 mol %) (APPh) functionalized SBA-15 particles.

Kinetic modeling of FRAP data

In order to extract diffusion coefficients from the recovery curve and thereby quantifying the molecular mobility, a certain diffusion model has to be assumed. The model used in this work has been introduced by Axelrod *et al.*[2] and further elaborated by Soumpasis[3] and McNally.[4] In the following paragraph the model will be described in brief.

We consider the photobleaching event as a simple irreversible first-order reaction with the rate $\alpha I(r)$, where α is the rate constant and $I(r)$ the bleaching intensity at a certain position r. The concentration of unbleached fluorophore $C(r,t)$ at a position r at time t is given by

$$\frac{dC(r,t)}{dt} = -\alpha I(r) C(r,t) \tag{S1}$$

due to the bleaching at this position.

So far, no diffusion is assumed. After bleaching with an intense light pulse for a time interval T, which needs to be short compared to the characteristic diffusion times, the concentration profile of the fluorophore at the beginning of the recovery phase ($t = 0$) is given by

$$C(r,o) = C_0 \exp\left[-\alpha T I(r)\right] \tag{S2}$$

with the initial homogeneous fluorophore concentration C_0. Eq. S2 is the solution to the differential Eq. S1. For simplicity, the "amount" of bleaching induced in time T is expressed by a parameter K

$$K \equiv \alpha T I(0) \tag{S3}$$

Assuming a Gaussian laser intensity profile, $I(r)$ can be written as

$$I(r) = \left(\frac{2P_0}{\pi\omega^2}\right) exp\left(\frac{-2r^2}{{\omega_G}^2}\right) \tag{S4}$$

with ω_G the half-width at e^{-2} height and P_0 the total laser power.

However, when a distinct small region of interest is bleached, the approximation of the laser intensity in the form of a circular disc profile describes the real situation better. For such a profile $I(r)$ is given by

$$I(r) = \begin{cases} \frac{P_0}{\pi\omega} & r \leq \omega \\ 0 & r > \omega \end{cases} \tag{S5}$$

where ω is the radius of the disc.
While Eq. S4 and Eq. S5 determine the geometry of the laser profile, Eq. S2 determines the bleaching behavior of the fluorophores with a certain bleaching rate $\alpha I(r)$.

The differential equation for a lateral transport of a single species of fluorophores through diffusion with a diffusion coefficient D is

$$\frac{\partial C(r,t)}{\partial t} = D\nabla^2 C(r,t) \tag{S6}$$

This description omits any active transport or flow. The fluorescence observed at time $t \geq 0$ is given by

$$F_K(t) = \left(\frac{q}{A}\right) \int I(r) C_K(r,t) d^2r \tag{S7}$$

where $C_K(r,t)$ is the solution of Eq. 6 for the K-dependent initial condition given in Eq. S2. The parameter q is the product of all quantum yields and A is the attenuation factor of the beam used for the observation of fluorescence recovery. Fluorescence recovery curves can be displayed conveniently in the following notation, called the fractional form $f_K(t)$

$$f_K(t) \equiv \frac{[F_K(t) - F_K(0)]}{[F_K(\infty) - F_K(0)]} \tag{S8}$$

According to Soumpasis[3] for uniform circular beams this fractional recovery curve can be modified to a simple closed form

$$f(t) = exp\left(\frac{-2\tau_D}{t}\right)\left[\mathrm{I}_0\left(\frac{2\tau_D}{t}\right) + \mathrm{I}_1\left(\frac{2\tau_D}{t}\right)\right] \quad \text{(S9)}$$

where I_0 and I_1 are modified Bessel functions and

$$\tau_D = \omega^2/4D \quad \text{(S10)}$$

for diffusion in two dimensions. In this form the fractional recovery curve is independent of the bleaching parameter K. This recovery model describes the data assuming one population and hence one diffusion coefficient D. McNally[4] adapted this fractional recovery curve, taking into account fractional bleaching, *i.e.* only part of the molecules are bleached, which is closer to the real situation.

$$f(t) = 1 - \phi + \phi exp\left(\frac{-2\tau_D}{t}\right)\left[\mathrm{I}_0\left(\frac{2\tau_D}{t}\right) + \mathrm{I}_1\left(\frac{2\tau_D}{t}\right)\right] \quad \text{(S11)}$$

where ϕ is the bleached fraction. This model can then be fitted to the data set, i.e., the fluorescence recovery curve $f(t)$. The model of Eq. S11 requires the parameters ϕ and the ω (see Eq. S10) that result from the evaluation of the experimental data.
For two diffusing populations Eq. S11 becomes

$$\begin{aligned} f(t) = 1 - \phi + \phi \exp\left(\frac{-2\tau_{D_1}}{t}\right)\left[\mathrm{I}_0\left(\frac{2\tau_{D_1}}{t}\right) + \mathrm{I}_1\left(\frac{2\tau_{D_1}}{t}\right)\right] \\ + \theta\left(\phi \exp\left(\frac{-2\tau_{D_2}}{t}\right)\left[\mathrm{I}_0\left(\frac{2\tau_{D_2}}{t}\right) + \mathrm{I}_1\left(\frac{2\tau_{D_2}}{t}\right)\right]\right. \\ \left. - \phi \exp\left(\frac{-2\tau_{D_1}}{t}\right)\left[\mathrm{I}_0\left(\frac{2\tau_{D_1}}{t}\right) + \mathrm{I}_1\left(\frac{2\tau_{D_1}}{t}\right)\right]\right) \\ = f_{D_1}(t) + \theta\left[f_{D_2}(t) - f_{D_1}(t)\right] \end{aligned} \quad \text{(S12)}$$

with the two diffusion coefficients D_1 and D_2. The superposition parameter θ controls the relative contributions of the two populations.

One *versus* two diffusing populations

In Figure S3 an exemplary recovery curve of siRNA diffusing inside an aminopropyl- and cyanopropyl-functionalized particle (black spots) is shown. Fitting the data using a model according to Eq. S11 assuming only one diffusing population (blue line) is not sufficient. In contrast, a model according to Eq. S12 assuming two mobile populations

(red line) can fit the data much better. A further increase of diffusion coefficients in the model does not significantly improve the quality of the fit. This data set shown in Figure S3 is typical and consequently all FRAP data sets were fitted using the model of Eq. S12 with two diffusion coefficients.

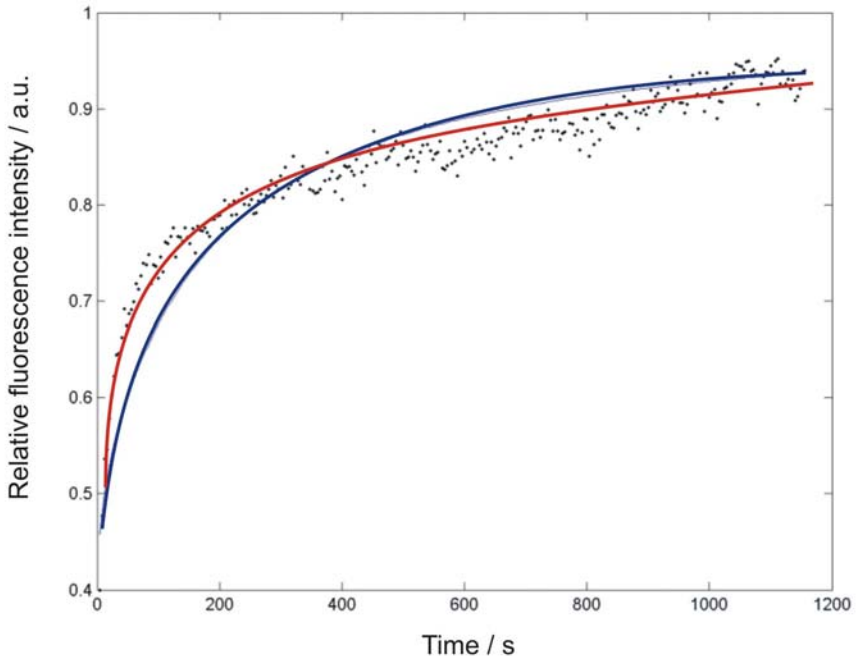

Figure S3. Data modeling with one and two diffusing populations. A typical fluorescence recovery curve (black spots) from siRNA inside an aminopropyl- (8 mol %) and cyanopropyl- (2 mol %) (APCP) functionalized SBA-15 particle. The data were fitted to a model according to Eq. S11 assuming only one diffusing population (blue line) and a model according to Eq. S12 assuming two diffusing populations (red line). The blue line does not fit the data adequately.

[1] http://rsb.info.nih.gov/ij/

[2] D. Axelrod, D. E. Koppel, J. Schlessinger, E. Elson, W. W. Webb, *Biophys J* **1976**, *16*, 1055.

[3] D. M. Soumpasis, *Biophys J* **1983**, *41*, 95.

[4] J. G. McNally, *Method Cell Biol* **2008**, *85*, 329.

2.8 Bayesian simultaneous analysis of multiple FRAP images with mixed-effect priors

Bayesian simultaneous analysis of multiple FRAP images with mixed-effect priors

Martina Feilke[1]and Katrin Schneider[2] and Volker J. Schmid*[1]

[1]Department of Statistics, Ludwig-Maximilians-University Munich, Ludwigstr. 33, 80539 Munich, Germany, [2] Department of Biology and Center for Integrated Protein Science, Ludwig Maximilians University Munich (LMU), 82152 Planegg-Martinsried, Germany

Email: Volker J. Schmid - volker.schmid@lmu.de;

*Corresponding author

Abstract

Background

The binding behaviour of molecules in the nuclei of living cells can be studied through the analysis of images from fluorescence recovery after photobleaching (FRAP) experiments. However, there is still a lack of methodology for the statistical evaluation of FRAP data, especially for the joint analysis of multiple dynamic images.

Results

We propose a mixed-effects model approach based on local compartment models. We use a hierarchical Bayesian nonlinear model with mixed-effect priors in order to obtain joint parameter estimates for all cell nuclei as well as to account for the heterogeneity of the nuclei population. We apply our method to a series of FRAP experiments of DNA methyltransferase 1 tagged to green fluorescent protein expressed in a somatic mouse cell line and compare the results to the application of three different fixed-effects models to the same series of FRAP experiments.

Conclusion

With the proposed mixed-effects model, the off-rates of the interactions the molecules of interest are involved in, and the variances of the random effects, which are associated with the particular cell nuclei, can be estimated with small variance. The proposed model is superior to and more robust than the tested models without random effects for all considered data situations. Therefore our model can be used for the joint analysis of data from FRAP experiments on various similar cell nuclei.

1 Introduction

Fluorescence recovery after photobleaching (FRAP) is an imaging technique to investigate the binding behaviour of molecules inside organisms, cells or cellular sub-compartments in vivo [1–3]. To analyse, for example, the dynamic properties of proteins of interest within the cell nucleus, the proteins are genetically tagged to a fluorescent protein (e.g. GFP) and expressed in cells of interest. A part of the molecules in the cell nucleus is bleached by a focused laser beam and the recovery in the bleached part of the nucleus is observed by capturing images of the nucleus in predefined time intervals [4]. Typically, such analyses are done on a couple of similar nuclei and the resulting rate estimators are summarized afterwards. However, the results often differ between nuclei, as the experiments are prone to random noise caused by cell-to-cell variation or the cellular status. To this end, we propose to analyse all nuclei together and account for the variance between nuclei by using mixed-effects models.

To date, for the analysis of data from FRAP experiments for the same molecule on multiple similar cell nuclei with a mathematical model, either the data of each recovery curve is analysed separately, and the results for all cell nuclei are regarded together (e. g. [5]), or the data of the different cell nuclei are pooled, averaged and then analysed (e. g. [4]). In the second case, the recovery curves of the cell nuclei are averaged to obtain a smooth curve that can then be analysed by the same mathematical model that is usually used for the analysis of one recovery curve. It is, however, vital, that only data of comparable fluorescent intensities are averaged [1].

Random effects are frequently used in linear models for longitudinal data. They account for the fact that subjects are sampled randomly from a heterogeneous population [6]. Typically random effects are combined with fixed effects, i. e. , the usual effects in a linear model, resulting into mixed-effects models. Mixed-effects models are used in many applications including agriculture, pharmacokinetics, and geophysics [6], as well as clinical trials [7]. In mixed-effects models, the relationships between a response variable and covariates, which are grouped by one or several factors, are described [6]. In our approach, fixed effects are parameters that are associated with the recovery curves of all cell nuclei, while random effects are parameters associated with the recovery curves of the individual cell nuclei.

The aim of a FRAP experiment is to infer the binding behaviour of the unbleached molecules in the cell nucleus from their speed of movement. Because the bleached and unbleached molecules are assumed to behave identically, we can infer from that the binding behaviour of all – bleached and unbleached – molecules of interest in the cell nucleus. See [8] for more information on FRAP experiments. In this paper we concentrate on half-nucleus FRAP (as opposed to circle FRAP or strip FRAP [1, 9]), which should cover representative fractions of heterogeneously distributed binding sites in all cell cycle stages [5]. An example for such data is given in Fig. 1. In the first post-bleach image (second image from left, after 0.15s) it is apparent that one half of the cell nucleus has been bleached. The recovery of fluorescence in this half can be tracked over time in the subsequent images.

We propose a Bayesian nonlinear regression with mixed-effect priors for the simultaneous analysis of

all recovery curves resulting from a series of FRAP experiments. In the methods section, we first present the compartment model and the differential equations associated with it. In order to demonstrate the potential of integrating mixed-effects into a nonlinear regression model in a Bayesian framework, we base our approach on a simplified kinetic model to get an analytical solution to the differential equations. Then, the regression model, which is based on the solution to the differential equations, is introduced together with the prior distributions for its parameters and the parameter estimation procedure. Thereafter, the data used in our analyses is described. In the subsequent section, we present the results from the application of the proposed model to a series of FRAP experiments of GFP-Dnmt1 expressed in a somatic mouse cell line. The paper ends with a discussion of the proposed approach.

2 Methods

2.1 FRAP experiments

In this paper, we use FRAP data sets of GFP-tagged DNA methyltransferase 1 (GFP-Dnmt1) expressed in mouse C2C12 myoblast cells [5], which were obtained from multiple cell nuclei and can therefore be utilized to illustrate how our nonlinear regression model can be used to fit all available data at once. DNA methylation at position 5 of cytosines within CpG dinocleotide sequences is an important biochemical process for the stable epigenetic gene silencing in vertebrates [10,11]. The maintenance methyltransferase Dnmt1 reestablishes methylation of hemi-methylated CpG sites generated during DNA replication in S phase and thus ensures propagation of genomic methylation pattern over many cell divisions.

In order to study the cell cycle dependent binding behaviour of wild type Dnmt1, we analysed data from cells in different cell cycle stages as identified by the nuclear distribution pattern of GFP-Dnmt1 [5]: 12 cells with diffuse nuclear distribution (mostly G1 phase and possibly also late G2 phase), 26 cells in early S phase with Dnmt1 association at early replication foci, and 11 cells in late S phase with Dnmt1 associating with late replicating heterochromatin clusters. For each cell, the concentration of unbleached GFP-Dnmt1 in the bleached half of the cell nucleus was documented every 0.15 seconds up to 779 times after the bleaching. For the cells with diffuse nuclear distribution, the concentration was measured 778 times for 10 cells. For the two remaining cells with diffuse nuclear distribution, 390 and 480 measurements, respectively, were available. 778 measurements were available for 24 cells in early S phase. For the other two cells in early S phase, 774 and 754 measurements, respectively, were available. For the cells in late S phase, 779 measurements were available for 11 cells, whereas 777 measurements were available for the twelfth cell. The original FRAP data has been normalized by a triple normalization procedure, see [5,12].

The major part of the FRAP data analysed in this paper has previously been published and analysed [5]. The goal of the experiment was to identify the contribution of two different kinds of interactions Dnmt1 is involved in in different cell cycle phases. The interactions can be attributed to two subdomains of Dnmt1, first, the proliferating cell nuclear antigen (PCNA)-binding domain (PBD) [5,13], and second, the targeting sequence (TS) domain, which targets Dnmt1 to the replication sites in S phase [5]. [5] use

the term "mobility classes" instead of the term "binding partners," because all interactions with similar on- and off-rates can not be distinguished [14], and, hence, build one mobility class (MC). Moreover, processes like anomalous diffusion, which are not related to binding, can also be represented by a MC.

2.2 Nonlinear recovery model

The movement of a molecule of interest in a cell nucleus is influenced by diffusion and by interactions, including binding reactions, the molecule is involved in [15–18]. It is possible to model this process by using the full reaction-diffusion equations [1,19,20]. As we strive for an analytical solution of the equations describing the movement of the molecule of interest, we use a simplification of the full reaction-diffusion equations. Usually, one of the following three simplifications is employed: the pure-diffusion scenario, the effective diffusion scenario or the reaction dominant scenario [1]. A pure-diffusion dominant scenario [1] is present, when most of the fluorescent molecules are free and interactions can be ignored. An effective diffusion scenario [1, 9, 20, 21] occurs "when the reaction process is much faster than diffusion" [1]. A reaction dominant scenario is present, when diffusion is very fast compared to the timescale of the image acquisition and to the reaction process [1].

The interactions Dnmt1 is involved in are described by on- and off-rates. In [5], where a correction value for diffusion was used, it was found, that in S phase, Dnmt1 is involved in interactions with relatively small off-rates, which means in the case of binding reactions, that the molecules of interest have a relatively long residence time (∼10-20s) at their binding sites. We have no sufficient information about the magnitude of the on-rate. For these reasons and because we aim to have an analytical solution to the ordinary differential equations describing the movement of Dnmt1 in order to be able to integrate mixed-effects into the regression model, we assume a reaction dominant scenario for our data.

In a reaction dominant FRAP scenario, diffusion is very fast in comparison to reaction processes and the time scale of the FRAP measurement [22–24] and the recovery curve in the bleached part of the cell nucleus can be modeled using a nonlinear regression model [1].

Here, we regard cases with two or three MCs [5]. In all considered cell cycle phases, a MC with a very long residence time compared to the time of image acquisition, is indicated [5]. For this MC we estimate only one parameter, and it is later also referred to as "immobile fraction". In cells with diffuse localization and in early S phase, one additional MC has been identified. For the late S phase, two additional MCs with different off-rates were found.

The binding sites to which the molecules of interest bind are assumed to be part of large complexes, which are relatively immobile on the time scale of the FRAP measurement and the molecular movement [1, 19]. A compartment model with two or three compartments (Fig. 2; the immobile fraction is ignored in this representation) is used to describe the change of the concentration of unbleached molecules in the bleached part of the cell nucleus. A similar procedure based on the reaction equation of a binding interaction was proposed by [1].

The on- and off-rates of the binding reaction are denoted by b_k^{on*} and b_k^{off}, $k = 0, ..., K$. As stated in [1], b_k^{on*} is actually a pseudo-on-rate. It is the product of the actual on-rate b_k^{on} and the concentration of vacant bindings sites belonging to MC k. It is constant during the entire recovery process, because we assume that the biological system is in equilibrium before the bleaching and because bleaching does not affect the number of vacant binding sites [1].

Let $f(t) = [Free](t)$ denote the concentration of the free molecules and $a_k(t) = [Bound_k](t)$ the concentration of the bound molecules in MC k at time t. We can describe the change of the concentration of the free and bound molecules based on the compartment model by the two differential equations

$$\frac{d}{dt}f(t) = \sum_{k=0}^{K}\left(-b_k^{on*}f(t) + b_k^{off}a_k(t)\right) + D_f\nabla^2 f(t), \tag{1}$$

with ∇^2 the Laplacian operator and D_f the diffusion coefficient for free proteins, and

$$\frac{d}{dt}a_k(t) = b_k^{on*}f(t) - b_k^{off}a_k(t). \tag{2}$$

The molecules in the cell nucleus are in equilibrium before the bleaching. In a diffusion-uncoupled FRAP scenario, the free molecules are moreover assumed to be in equilibrium again immediately after the bleaching. Therefore $f(t) = f_{eq}$, a constant, and equation (2) can be written as

$$\frac{d}{dt}a_k(t) \quad = \quad b_k^{on*}f_{eq} - b_k^{off}a_k(t). \tag{3}$$

Moreover, we do not have to model the change of the concentration of the free molecules, it suffices to model the change of concentration of the bound molecules, which means that equation (1) can be ignored.

With boundary condition $a_k(0) = 0$, which means that at time $t = 0$ (the time of the bleaching) the concentration of unbleached bound molecules in MC k in the bleached area equals zero, the solution of equation (3) is

$$a_k(t) \quad = \quad \frac{b_k^{on*}f_{eq}}{b_k^{off}} - \frac{b_k^{on*}f_{eq}}{b_k^{off}}\exp(-b_k^{off}t). \tag{4}$$

As the system is in equilibrium before bleaching we have $\frac{d}{dt}f(t) = 0$, $\frac{d}{dt}a_k(t) = 0$ and constant steady-state intensities f_{eq}, $a_{k,eq}$. Together with equation (3) we get

$$a_{k,eq} \quad = \quad \frac{b_k^{on*}f_{eq}}{b_k^{off}}, \tag{5}$$

and can therefore write equation (4) as

$$a_k(t) \quad = \quad a_{k,eq}(1 - \exp(-b_k^{off}t)). \tag{6}$$

The observed value during FRAP recovery is the total fluorescence intensity in the bleached area. It can be described by the sum of the bound and the free unbleached molecules plus an error. The sum of the bound and the free unbleached molecules is denoted by $total(t)$:

$$total(t) \quad = \quad f_{eq} + \sum_{k=0}^{K} a_k(t) \tag{7}$$

For our analysis, in each cell nucleus, the fluorescence intensity has been averaged over the bleached part of the cell nucleus. Therefore, in our analysis, f_{eq} is the average of the intensity of the free fluorescent molecules in the bleached half, and $a_k(t)$ is the average of the intensity of the bound fluorescent molecules in the bleached part of the nucleus. With equation (6) we can then write

$$total(t) \quad = \quad f_{eq} + \sum_{k=0}^{K} a_{k,eq}(1 - \exp(-b_k^{off} t)). \tag{8}$$

With $f_{eq} + \sum_{k=0}^{K} a_{k,eq} = 1$, which holds because the concentration of the unbleached molecules has been normalized to one, we arrive at

$$total(t) \quad = \quad 1 - \sum_{k=0}^{K} a_{k,eq} \exp(-b_k^{off} t). \tag{9}$$

2.3 Bayesian nonlinear mixed-effects model

In order to analyse all recovery curves from all nuclei simultaneously, we use a hierarchical Bayesian model (HBM). Such models consist of three levels:

1) Data model, here derived from the nonlinear model described above,

2) Prior model, here a mixed-effects model in order to account for the heterogeneity in the nuclei population,

3) Hyper prior model, prior assumptions on all unknown parameters in level 2).

2.3.1 Data model

The total observed concentration of unbleached molecules in the bleached part of the cell nucleus of cell j at time t_{ij} is denoted by $C(t_{ij})$. We assume Gaussian noise for the observations

$$C(t_{ij}) \sim N(total(t_{ij}), \sigma^2). \tag{10}$$

The true concentration of unbleached molecules is modeled by the nonlinear model

$$total(t_{ij}) = 1 - \sum_{k=0}^{K} a_{kj} \exp(-b_{kj}^{off} t), \tag{11}$$

similar to the recovery model in (9).

2.3.2 Prior model

In a Bayesian framework prior probability density functions (pdf) have to be defined for all unknown parameters. Here, for the parameters a_{kj} and b_{kj}^{off}, we use a mixed-effect decomposition of the form

$$a_{kj} = a_k + \alpha_{kj}, \; b_{kj}^{off} = \exp(f_k + \phi_{kj}) = \exp(f_k) \cdot \exp(\phi_{kj}), \tag{12}$$

with $b_k^{off} = \exp(f_k)$ and $\beta_{kj}^{off} = \exp(\phi_{kj})$. So each of these parameters is split into a fixed effect, which represents a joint parameter for all recovery curves of all cell nuclei, and a random effect representing

a curve-specific parameter. The prior for the parameter b_{kj}^{off} incorporates moreover the knowledge that transfer rates must be non-negative [25].

For the fixed effects, uniform priors of the form

$$p(a_k) = p(b_k^{off}) \propto \text{constant} \tag{13}$$

are used. These prior distributions are uninformative, what means that they do not contain any relevant information.

As prior distributions for the nuclei-specific random effects, we use multivariate Gaussian distributions and a multivariate log-normal distribution, respectively, which are given by

$$\alpha_{kj} \sim N(0, \tau_{\alpha_k}^2),\ \beta_{kj}^{off} \sim LN(0, \tau_{\beta_k^{off}}^2), \tag{14}$$

where $\tau_{\alpha_k}^2$ and $\tau_{\beta_k^{off}}^2$ are unknown variance parameters.

2.3.3 Hyper priors

Additional prior pdfs have to be defined for all other unknown parameters. As prior distributions for the unknown variance parameters, inverse Gamma distributions, which are given by

$$\tau_{\alpha_k}^2 \sim IG(c_k, d_k),\ \tau_{\beta_k^{off}}^2 \sim IG(e_k, g_k), \tag{15}$$

are used. The inverse Gamma distribution is known as a conjugate prior for the normal distribution.

By using uninformative priors for the parameters a_k and b_k^{off}, we ensure that as much variance as possible is covered by the fixed effects. Only the variability that is not covered by the fixed effects is captured by the random effects. The definition of the hyperpriors with prudently chosen parameters on the variances of the parameters α_{kj} and β_{kj}^{off} leads to a shrinkage of the random effects, so that they do not cover variance explained by the fixed effects [25].

If $K = 1$, which means that there is one MC in addition to the immobile fraction, we have to choose the parameters for the three inverse Gamma distributions

$$\tau_{\alpha_0}^2 \sim IG(c_0, d_0),\ \tau_{\alpha_1}^2 \sim IG(c_1, d_1),\ \tau_{\beta_1^{off}}^2 \sim IG(e_1, g_1). \tag{16}$$

For the diffuse and the early S phase, we choose the parameters $c_0 = c_1 = e_1 = 1$, $d_0 = d_1 = 10^{-3}$, and $g_1 = 10^{-4}$.

When $K = 2$, which means that there exist two MCs in addition to the immobile fraction, we have the inverse Gamma distributions

$$\tau_{\alpha_0}^2 \sim IG(c_0, d_0),\ \tau_{\alpha_1}^2 \sim IG(c_1, d_1),\ \tau_{\beta_1^{off}}^2 \sim IG(e_1, g_1), \tag{17}$$

$$\tau_{\alpha_2}^2 \sim IG(c_2, d_2),\ \tau_{\beta_2^{off}}^2 \sim IG(e_2, g_2). \tag{18}$$

Here, the chosen parameters are $c_0 = c_1 = e_1 = c_2 = e_2 = 1, d_0 = d_1 = d_2 = 10^{-3}, g_1 = 10^{-4}$, and $g_2 = 10^{-6}$. By choosing the first parameter of the inverse Gamma distribution to be 1 and the second

parameter to be considerably smaller than 1, we perform shrinkage of the variances of the random effects. The smaller the second parameter is with respect to 1, the stronger is the shrinkage of the variance of the corresponding random effect, and, hence, the more variance is covered by the corresponding fixed effect. We choose the parameters of the inverse Gamma distributions so that the mixing of the sampling paths of the fixed effects is adequate.

As prior for the variance σ^2 of the noise term ϵ_{ij}, we define an inverse Gamma distribution, which is a conjugate prior for the Normal distribution: $\sigma^2 \sim IG(a, b)$. We use the parameters $a = b = 1$.

2.3.4 Posterior distribution and MCMC inference

In the Bayesian framework, all conclusions are drawn form the posterior distribution. The posterior pdf can be computed via Bayes' theorem [26]:

$$p(\theta|y) = \frac{f(y|\theta)\pi(\theta)}{\int f(y|\tilde{\theta})\pi(\tilde{\theta})d\tilde{\theta}}, \tag{19}$$

with $f(y|\theta)$ the pdf of the data distribution defined in (10) and $\pi(\theta)$ the product of the prior distributions.

A Markov chain Monte Carlo (MCMC)-algorithm with Gibbs- and Metropolis-Hastings(MH)-update steps is applied to obtain samples from the full conditional distributions of the parameters of the nonlinear regression model, which can be derived from the posterior distribution. Therefore, in each iteration of the algorithm, a random sample from the conditional posterior distribution (given all other parameters and the data) is drawn for each parameter. The full conditional distributions of all parameters that are drawn in Gibbs steps can be found in the electronic appendix.

The parameters a_k and α_{kj} are drawn in Gaussian Gibbs steps, because their full conditional distributions are Gaussian distributions, from which one can sample directly. For the parameters σ^2, $\tau^2_{\alpha_k}$, and $\tau^2_{\beta_k^{off}}$, Gamma Gibbs steps are used, because the full conditional distributions of the parameters are Inverse Gamma distributions. The parameters b_k^{off} and β_{kj}^{off} are drawn in MH-steps with random walk proposals, because their full conditional distributions are not standard distributions. For the MC which is present in all considered cell cycle phases and has a very long residence time compared to the time of image acquisition ($k = 0$), the parameters b_0^{off} and β_{0j}^{off} are close to zero. Therefore, we set $b_0^{off} = \beta_{0j}^{off} = 0$ and estimate only the parameter a_0 for this immobile fraction [5, 8, 13].

The acceptance rate of the MH-algorithms was tuned to 30-60 %. For the diffuse phase ($K = 1$), we used 30,000 iterations after a burn-in phase of 20,000 iterations. 90,000 iterations were used for the early S phase ($K = 1$) and the late S phase ($K = 2$) after a burn-in phase of 10,000 iterations. The number of burn-in iterations was determined by visual inspection of the sampling paths. Point estimates for the parameters were obtained via the median of the sample for each parameter together with 95%-credible intervals.

To evaluate the model fit, we compared the mixed-effects model – which was fitted to the whole of the data resulting from the FRAP experiments – to

(I) a model without random effects fitted to the whole of the data,

(II) a model without random effects fitted to the individual recovery curves,

(III) a model without random effects fitted to the averaged recovery curves (all recovery curves of the same phase were averaged).

For each of these three scenarios, we fitted the following fixed-effects model to the data of each cell cycle phase:

$$C(t_i) = 1 - \sum_{k=0}^{K} a_k \exp(-b_k^{off} t_i) + \epsilon_i,\ \epsilon_i \sim N(0, \sigma^2). \tag{20}$$

In scenario I, we used 5,000 iterations for the diffuse and the early S phase. For the more complex model for the late S phase, 9,000 iterations after a burn-in of 7,000 iterations were used. In the second scenario, we used 1,000 iterations after a burn-in of 500 for the diffuse and late S phase, respectively. For the early S phase, 1,000 iterations after burn-in of 600 iterations were used. In scenario III, for the diffuse and the early S phase 1,000 iterations and for the late S phase, 1,300 iterations after a burn-in of 200 iterations were done. The Deviance Information Criterion (DIC) served as a measure of the model fit for the comparison of the mixed-effects model to the fixed-effects models I and II. We did not compare the mixed-effects model and fixed-effects model III on the basis of the DIC, because these two models were fit to different kinds of data. The fixed-effects model III in contrast to the mixed-effects model was not fitted to the whole of all recovery curves but to the averaged recovery curve per phase. The DIC can be calculated by the deviance of the medians $D(\theta_{med})$ plus two times the effective number of parameters p_D [27]:

$$DIC = D(\theta_{med}) + 2p_D.$$

The deviance is a measure of the fit of a model and is calculated by

$$D(\theta) = -2l(\theta),$$

where $l(\theta)$ is the log-likelihood. The effective number of parameters is a measure of the complexity of the model. It is the median deviance minus the deviance of the medians and is calculated by

$$p_D = \text{median}(D(\theta)) - D(\theta_{med}).$$

The effective number of parameters is high for models with a high effective model complexity. When comparing two models on the basis of their DIC, the model with the lower DIC is to be favoured.

All software was written in the programming languages `R` [28] and `C`.

3 Results

3.1 Mixed-effects model

By using the Bayesian regression model with mixed-effect priors we gain common parameter estimates for all cell nuclei through the estimation of the fixed effects, as well as curve specific parameter estimates through the estimation of the random effects, and estimates for the variances of the random effects.

In Fig. 3, for each phase (diffuse, early S and late S phase), the estimated joint recovery curve for all cell nuclei is shown together with the normalized data. The joint recovery curve is computed using the posterior medians of the MCMC-samples of the fixed effects.

The random effects take into account the variability resulting from the joint analysis of data of multiple cell nuclei, which is not covered by the fixed effects. In Fig. 4, the estimated joint recovery curve for all cell nuclei (black, solid line) is shown together with the cell nuclei-specific curves (coloured, dashed lines), which are computed using the posterior medians of the MCMC-samples of the curve-specific random effects.

The posterior median of the fixed parameters a_k and b_k^{off} together with 95%-credible intervals can be found in Table 1. All parameters could be estimated with small variance. For the diffuse phase, the posterior median of the fixed effect of the off-rate is denoted by b_1^{off} and equals 0.162 $(0.153, 0.176)$. For the early S phase, b_1^{off} equals 0.093 $(0.087, 0.098)$. In the presence of binding, the off-rate is the rate of the unbinding reaction where a protein is unsoldered from its binding site [8]. However, in the diffuse phase, the off-rate can not be interpreted in the same way. In both cases, we assumed that there is only one MC in addition to the immobile fraction ($K = 1$), based on [5]. The difference in the fixed-effect part of the off-rate (b_1^{off}) for the diffuse and the early S phase is in compliance with the finding of two different kinds of MCs in the diffuse and the early S phase [5]. For the late S phase, we assumed that there are two distinctive MCs in addition to the immobile fraction ($K = 2$) [5]. The posterior medians of the fixed effect of the off-rates are $b_1^{off} = 0.227$ $(0.193, 0.287)$ and $b_2^{off} = 0.044$ $(0.042, 0.047)$, which is in compliance with the finding that the protein Dnmt1 is involved in two distinctive interactions in the late S phase [5].

As it is of essential interest how much variance is captured by the random effects, point estimates for the random effects plus 95%-credible intervals were calculated and can be found in Table 2. For all three phases, the largest variability is contained in the random effects of the off-rate, followed by the variability in the random effects of the parameter a_{1j} and of the parameter a_{2j} (only late S phase). The least variability is contained in the random effects of the parameter a_{0j}, which can be interpreted as immobile fraction. Each of the credible intervals in Tables 1 and 2 embodies the true parameter with a probability of 95%. To quantify how much the fixed effects vary between the cells we additionally computed confidence intervals that are based on the estimated variances of the random effects. Hence, confidence intervals for the fixed effects a_k and f_k were calculated by employing the variances of the random effects $\tau_{\alpha_k}^2$ and $\tau_{\beta_k^{off}}^2$:

$$\left[\tilde{a}_k - z_{1-\alpha/2} \cdot \frac{\tau_{\alpha_k}^2}{n}; \tilde{a}_k + z_{1-\alpha/2} \cdot \frac{\tau_{\alpha_k}^2}{n}\right], \quad \left[\tilde{f}_k - z_{1-\alpha/2} \cdot \frac{\tau_{\beta_k^{off}}^2}{n}; \tilde{f}_k + z_{1-\alpha/2} \cdot \frac{\tau_{\beta_k^{off}}^2}{n}\right],$$

where $\tilde{a}_k$ is the median of a_k and $\tilde{f}_k$ is the median of f_k. In order to gain the confidence interval for the parameter $b_k^{off} = \exp(f_k)$, we applied the exponential function to the limits of the confidence interval for f_k. The confidence intervals for all three reviewed cell cycle phases are shown in Fig. 5.

3.2 Comparison between the mixed-effects model and the fixed-effects models

Table 3 provides the posterior medians of the fixed effects a_k and b_k^{off} together with 95%-credible intervals for fixed-effects model I, where regression model (20) was fitted to the whole of the data resulting from the FRAP experiments. In Table 4, the posterior medians of the fixed effects a_k and b_k^{off} together with 95%-credible intervals for fixed-effects model III, where regression model (20) was fitted to the averaged recovery curves, are shown. Table 5 provides the posterior medians of the fixed effects a_k and b_k^{off} together with 95%-credible intervals for fixed-effects model II, where regression model (20) was fitted to the individual recovery curves of all cell nuclei. All three tables provide the mentioned point estimates and credible intervals for each cell cycle phase under review. Table 6 contains the DIC, the effective number of parameters (p_D) and the deviance of the medians ($D(\theta_{med})$) for the proposed mixed-effects model and the fixed-effects models I and II introduced in section 2.3.4. In Fig. 6, the point estimates and the 95%-credible intervals for the mixed-effects model and fixed-effects models I and II are displayed.

Regarding the point estimates in Table 3, one sees that the point estimates for the fixed effects provided by fixed-effects model I are biased compared to the estimates provided by the mixed-effects model (Table 1). Fig. 6 and the comparison of Table 3 with Table 1 reveal that the 95%-credible intervals for the fixed parameters resulting from fitting fixed-effects model I to the whole of the data are considerably smaller than the credible intervals for the fixed parameters resulting from fitting the proposed mixed-effects model to the whole of the data. Therefore, it could be erroneously concluded that the estimation of the fixed parameters is more exact by using the fixed-effects model I than by using the proposed mixed-effects model. But for all three cell cycle phases (diffuse, early S and late S phase), when comparing the DIC of the mixed-effects model to the DIC of fixed-effects model I, it is obvious that the DIC is considerably lower for the mixed-effects model. The clearest result can be found for the late S phase, where the DIC of the mixed-effects model is almost two times lower than the DIC of fixed-effects model I. This means, that the proposed mixed-effects model provides a much better model fit than the fixed-effects model I and is thus superior to fixed-effects model I for all three cell cycle phases.

Regarding the point estimates resulting from fitting fixed-effects model II to the individual recovery curves (Table 5), we observe that most of them are biased with respect to the point estimates resulting from fitting the proposed mixed-effects model to the whole of the data (Table 1). When comparing the DIC of the mixed-effects model to the DIC of fixed-effects model II, it can be seen that the DIC of the mixed-effects model is lower than the DIC of fixed-effects model II for the diffuse and late S phase. For the early S phase, the DIC of fixed-effects model II is lower than the DIC of the mixed-effects model. But overall, the DIC is of the same magnitude for both models.

Fig. 6 reveals that most of the credible intervals for the fixed effects a_k and b_k^{off} resulting from fitting fixed-effects model III to the averaged recovery curves for the fixed effects a_k and b_k^{off} (Table 4) are broader or of approximately the same size as the corresponding credible intervals resulting from the proposed mixed-effects model (Table 1). Only for the fixed effect a_0, it is converse. This is due to the

difference in the number of data points between the two models. Therefore the estimation of the fixed effects is more exact when using the proposed mixed-effects model. Moreover, we are of the opinion that averaging the recovery curves induces a loss of information because not all available data is used and the variability contained in the data is not appropriately quantified, which is why we favour the proposed mixed-effects model over fixed-effects model III.

Overall, we conclude that the mixed-effects model is superior to the fixed-effects models I-III, because it adequately reflects the heterogeneity of the data caused by cell-to-cell variability through the estimation of the variances of the random effects. The heterogeneity of the data is also taken into account by fixed-effects model II, which gives point estimates of the fixed effects for each curve per cell cycle phase. However, estimating the variance through a mixed-effects model is the more appropriate and comfortable way to quantify the cell-to-cell variability. Moreover, the proposed mixed-effects model is more robust because it uses more information than the fixed-effects models I-III.

4 Discussion

Our objective was an approach with which data from FRAP experiments on various similar cell nuclei can be analysed simultaneously. Therefore the model has to take into account the variability contained in the data, which is due to the simultaneous consideration of several cell nuclei.

Using the proposed Bayesian nonlinear regression model with mixed-effect priors, we are able to do a joint analysis of the recovery curves of all available cell nuclei per cell cycle phase. So all available data resulting from different FRAP experiments can be used for the estimation of the parameters of interest and no data is ignored. Hence, a distinct benefit of the proposed model is that we fit only one model to the whole of the data arising from all available cell nuclei, which is more comfortable than fitting one model per cell nucleus and analysing the results afterwards and is also faster regarding the computation time. Curve-specific effects are taken into account by the use of random effects, which are, however, shrunk towards zero, so that most variability in the data is captured by the fixed effects. The variability of the parameters of interest can however be quantified through the estimation of the variance of the random effects. Consequently, by using the proposed model, we gain knowledge about the imprecision in the population of cell nuclei.

Algorithms for nonlinear model fitting have consistency problems by specifying starting values and have convergence issues. Therefore, the model is typically fitted several times using a grid of starting values or random starting values, and the best model is determined using an information criterion like Akaikes information criterion (AIC) or Bayesian information criterion (BIC). This results in a high computational burden. Using a Bayesian approach, the algorithm is guaranteed to converge. The resulting parameter estimates are not dependent on any starting values. Moreover, the regression model is very flexible. Mixed-effect priors on the nonlinear parameters could be incorporated easily into the nonlinear regression, which is a novel approach. In addition, the proposed technique allows to analyse all data at

once, hence reducing computation time. For our data, the whole analysis of all data took 13 minutes (diffuse phase), 56 minutes (early S phase), and 69 minutes (late S phase), respectively.

In our approach, the number of MCs for the molecule and the cell cycle phase is a fixed parameter that was adopted from a previous study using a refined compartmental approach [5].

We can conclude, that the mixed-effects model fits the data considerably better than all considered models without random effects for all three cell cycle phases. With the mixed-effects model, we get more accurate parameter estimates than with the fixed-effects models and additionally gain precious insight into the imprecision in the population of cell nuclei in the different cell cycle phases.

With the proposed mixed-effects model, estimates of the off-rates of the interactions the molecules of interest are involved in, and of the variances of the random effects are attained. Therefore the model is useful for the analysis of data from FRAP experiments on various similar cell nuclei. With that model, it is no longer necessary to analyse each recovery curve belonging to an experiment on one cell nucleus separately and summarize the results afterwards, or to pool and average the data of experiments on multiple similar cell nuclei to be able to analyse it. The data of FRAP experiments on different cell nuclei can rather be analysed simultaneously by one single model.

The main goal of this study is to show that the proposed technique can be used for the joint analysis of the data of many cells at once. This is a novel approach in the field of FRAP analysis. Although we use a simplified kinetic model here, the approach can easily be adapted to other FRAP experiments and any kinetic model for such FRAP experiments.

Competing interests

The authors declare that they have no competing interests.

Authors' contributions

KS performed the FRAP experiments. VS initiated this research. MF performed the statistical analysis of the data. MF and VS wrote the manuscript. KS proofread the manuscript. All authors read and approved the final manuscript.

Acknowledgements

We thank Prof. Dr. Heinrich Leonhardt (Biocenter Martinsried, LMU Munich) and Dr. Lothar Schermelleh (Department of Biochemistry, University of Oxford) for the provision of the data and helpful discussions. Thanks to Dr. Joseph W. Sakshaug for proofreading.

MF and VS were supported by Deutsche Forschungsgemeinschaft (DFG SCHM 2747/1-1). KS was supported by the International Max Planck Research School for Molecular and Cellular Life Sciences (IMPRS-LS).

References

1. Sprague BL, Pego RL, Stavreva DA, McNally JG: **Analysis of Binding Reactions by Fluorescence Recovery after Photobleaching**. *Biophysical Journal* 2004, **86**:3473–3495.
2. Meyvis TKL, De Smedt SC, van Oostveldt P, Demeester J: **Fluorescence Recovery After Photobleaching: A Versatile Tool for Mobility and Interaction Measurements in Pharmaceutical Research**. *Pharmaceutical Research* 1999, **16**(8):1153–1162.
3. Reits EA, Neefjes JJ: **From fixed to FRAP: measuring protein mobility and activity in living cells**. *Nature Cell Biology* 2001, **3**(6):E145–E147.
4. McNally JG: **Quantitative FRAP in Analysis of Molecular Binding Dynamics In Vivo**. *Methods in cell biology* 2008, **85**:329–351.
5. Schneider K, Fuchs C, Dobay A, Rottach A, Qin W, Wolf P, Álvarez Castro JM, Nalaskowski MM, Kremmer E, Schmid V, Leonhardt H, Schermelleh L: **Dissection of cell cycle-dependent dynamics of Dnmt1 by FRAP and diffusion-coupled modeling**. *Nucleid Acids Research* 2013, :1–17.
6. Pinheiro J, Bates D: *Mixed-Effects Models in S and S-PLUS*. New York: Springer Verlag 2000.
7. Brown H, Prescott R: *Applied Mixed Models in Medicine*. Chichester, UK: Wiley 1999.
8. Sprague BL, McNally JG: **FRAP analysis of binding: proper and fitting**. *TRENDS in Cell Biology* 2005, **15**(2):84–91.
9. Mueller F, Wach P, McNally JG: **Evidence for a Common Mode of Transcription Factor Interaction with Chromatin as Revealed by Improved Quantitative Fluorescence Recovery after Photobleaching**. *Biophysical Journal* 2008, **94**(8):3323–3339.
10. Bird A: **DNA methylation patterns and epigenetic memory**. *Genes & Development* 2002, **16**:6–21.
11. Spada F, Rothbauer U, Zolghadr K, Schermelleh L, Leonhardt H: **Regulation of DNA methyltransferase 1**. *Advances in Enzyme Regulation* 2006, **46**:224–234.
12. Dargatz C: *Bayesian Inference for Diffusion Processes with Applications in Life Sciences*. LMU Munich: Dissertation 2010.
13. Schermelleh L, Haemmer A, Spada F, Rösing N, Meilinger D, Rothbauer U, Cardoso MC, Leonhardt H: **Dynamics of Dnmt1 interaction with the replication machinery and its role in postreplicative maintenance of DNA methylation**. *Nucleid Acids Research* 2007, **35**(13):4301–4312.
14. Schneider K: *Analysis of cell cycle dependent kinetics of Dnmt1 by FRAP and kinetic modeling*. LMU Munich: Diploma Thesis 2009.
15. van Royen ME, Zotter A, Ibrahim SM, Geverts B, Houtsmuller AB: **Nuclear proteins: finding and binding target sites in chromatin**. *Chromosome Research* 2011, **19**:83–98.
16. Hemmerich P, Schmiedeberg L, Diekmann S: **Dynamic as well as stable protein interactions contribute to genome function and maintenance**. *Chromosome Research* 2011, **19**:131–151.
17. Mueller F, Mazza D, Stasevich TJ, McNally JG: **FRAP and kinetic modeling in the analysis of nuclear protein dynamics: what do we really know?** *Current Opinion in Cell Biology* 2010, **22**:403–411.
18. Mazza D, Abernathy A, Golob N, Morisaki T, McNally JG: **A benchmark for chromatin binding measurements in live cells**. *Nucleic Acids Research* 2012, **40**(15):e119.
19. Carrero G, Crawford E, Hendzel MJ, de Vries G: **Characterizing Fluorescence Recovery Curves for Nuclear Proteins Undergoing Binding Events**. *Bulletin of Mathematical Biology* 2004, **66**:1515–1545.
20. Beaudouin J, Mora-Bermúdez F, Klee T, Daigle N, Ellenberg J: **Dissecting the Contribution of Diffusion and Interactions to the Mobility of Nuclear Proteins**. *Biophysical Journal* 2006, **90**:1878–1894.
21. van Royen ME, Farla P, Mattern KA, Geverts B, Trapman J, Houtsmuller AB: **Fluorescence Recovery After Photobleaching (FRAP) to Study Nuclear Protein Dynamics in Living Cells**. *Methods in Molecular Biology* 2009, **464**:363–385.
22. Bulinski JC, Odde DJ, Howell BJ, Salmon TD, Waterman-Storer CM: **Rapid dynamics of the microtubule binding of ensconsin in vivo**. *Journal of Cell Science* 2001, **114**:3885–3897.
23. Coscoy S, Waharte F, Gautreau A, Martin M, Louvard D, Mangeat P, Arpin M, Amblard F: **Molecular analysis of microscopic ezrin dynamics by two-photon FRAP**. *Proceedings of the National Academy of Sciences of the United States of America* 2002, **99**(20):12813–12818.
24. Dundr M, Hoffmann-Rohrer U, Hu Q, Grummt I, Rothblum LI, Phair RD, Misteli T: **A kinetic framework for a mammalian RNA polymerase in vivo**. *Science* 2002, **298**:1623–1626.
25. Schmid VJ, Whitcher B, Padhani AR, Taylor NJ, Yang G: **A Bayesian Hierarchical Model for the Analysis of a Longitudinal Dynamic Contrast-Enhanced MRI Oncology Study**. *Magnetic Resonance in Medicine* 2009, **61**:163–174.
26. Carlin BP, Louis TA: *Bayes and Empirical Bayes Methods for Data Analysis*. London, U.K.: Chapman & Hall, 2nd edition 2000.

27. Spiegelhalter DJ, Best NG, Carlin BP, van der Linde A: **Bayesian Measures of Model Complexity and Fit**. *Journal of the Royal Statistical Society. Series B (Statistical Methodology)* 2002, **64**(4):583–639.

28. R Core Team: *R: A Language and Environment for Statistical Computing*. R Foundation for Statistical Computing, Vienna, Austria 2013, [http://www.R-project.org/]. [ISBN 3-900051-07-0].

Figures

Figure 1

Fluorescence recovery after photobleaching one half of the nucleus of a mouse C2C12 cell expressing GFP-Dnmt1 in late S phase. Images of a cell nucleus in a FRAP experiment: In the prebleach image, the complete cell nucleus is visible because all molecules are fluorescent. In the first postbleach image (acquired after 0.15 seconds), it is obvious that one half of the nucleus has been bleached. The subsequent images show the recovery of the fluorescence in the nucleus after 5, 10, 20 and 50 seconds.

Figure 2

(A) Compartment model with two compartments and (B) compartment model with three compartments. In a compartment model with two compartments, the molecules can be either free or bound. Exchange between the compartment of the free and the compartment of the bound molecules occurs with rates b_1^{on*} and b_1^{off}. In a compartment model with three compartments, the molecules can be either free or bound in one of two discriminable binding states. Exchange between the compartment of the free molecules and the compartments of the bound molecules occurs with rates b_1^{on*} and b_1^{off} and b_2^{on*} and b_2^{off}, respectively.

Figure 3

Normalized data together with estimated joint recovery curve. The estimated joint recovery curves for all cell nuclei using the posterior medians of the MCMC-samples of the fixed effects are shown together with the normalized data for all three reviewed cell cycle phases – (A) diffuse, (B) early S, (C) late S phase.

Figure 4

Estimated joint recovery curve together with cell nuclei-specific recovery curves. The cell nuclei-specific recovery curves using the posterior medians of the MCMC-samples of the random effects for all three reviewed cell cycle phases – (A) diffuse, (B) early S, (C) late S phase – are shown together with the estimated joint recovery curve.

Figure 5

Confidence intervals for the fixed effects of the mixed-effects model. The confidence intervals which are computed based on the estimated variances of the random effects for the fixed effects a_0, a_1, a_2, b_1^{off} and b_2^{off} resulting from fitting the mixed-effects model to the whole of the data are shown for all three reviewed cell cycle phases.

Figure 6

Point estimates and 95%-credible intervals for the fixed effects of the mixed-effects model and fixed-effects models I and II. The posterior medians of the fixed effects together with 95%-credible intervals are shown for the proposed mixed-effects model and fixed-effects models I and II for all three reviewed cell cycle phases.

Tables

Table 1

phase	number of recovery cuves	a_0	a_1	a_2	b_1^{off}	b_2^{off}
diffuse	12	0.005 (-0.001,0.011)	0.830 (0.813,0.848)		0.162 (0.153,0.176)	
early S	26	0.030 (0.022,0.037)	0.816 (0.796,0.834)		0.093 (0.087,0.098)	
late S	11	0.013 (0.004,0.027)	0.304 (0.264,0.349)	0.567 (0.515,0.603)	0.227 (0.193,0.287)	0.044 (0.042,0.047)

Table 1: Mixed-effects model: Fixed effects - median plus 95% credible interval

Table 2

phase	number of recovery cuves	$\tau^2_{\alpha_0}$	$\tau^2_{\alpha_1}$	$\tau^2_{\alpha_2}$	$\tau^2_{\beta_1}$	$\tau^2_{\beta_2}$
diffuse	12	0.0001 (0.0000,0.0002)	0.0009 (0.0004,0.0022)		0.0106 (0.0052,0.0273)	
early S	26	0.0004 (0.0002,0.0007)	0.0020 (0.0012,0.0036)		0.0484 (0.0291,0.0882)	
lateS	11	0.0003 (0.0001,0.0008)	0.0050 (0.0023,0.0133)	0.0053 (0.0024,0.0137)	0.0657 (0.0274,0.1967)	0.0423 (0.0205,0.1063)

Table 2: Mixed-effects model: Random effects - median plus 95% credible interval

Table 3

phase	number of recovery cuves	a_0	a_1	a_2	b_1^{off}	b_2^{off}
diffuse	12	0.005 (0.005,0.006)	0.829 (0.824,0.833)		0.159 (0.158,0.161)	
early S	26	0.032 (0.031,0.033)	0.809 (0.805,0.813)		0.086 (0.085,0.087)	
late S	11	0.015 (0.014,0.017)	0.317 (0.299,0.335)	0.544 (0.526,0.564)	0.201 (0.184,0.223)	0.042 (0.041,0.043)

Table 3: Fixed-effects model I (fitted to the whole of the data): Fixed effects - median plus 95% credible interval

Table 4

phase	number of recovery cuves	a_0	a_1	a_2	b_1^{off}	b_2^{off}
diffuse	1	0.005 (0.001,0.009)	0.826 (0.795,0.861)		0.158 (0.148,0.169)	
early S	1	0.032 (0.027,0.037)	0.808 (0.783,0.834)		0.086 (0.082,0.091)	
late S	1	0.016 (0.008,0.023)	0.318 (0.254,0.394)	0.542 (0.464,0.600)	0.195 (0.138,0.281)	0.042 (0.037,0.046)

Table 4: Fixed-effects model III (fitted to the averaged recovery curves): Fixed effects - median plus 95% credible interval

Table 5

phase	number of recovery cuves	a_0	a_1	a_2	b_1^{off}	b_2^{off}
diffuse	12	0.004 [-0.009,0.020]	0.823 [0.796,0.887]		0.154 [0.141,0.196]	
early S	26	0.034 [-0.003,0.063]	0.823 [0.726,0.893]		0.087 [0.056,0.144]	
late S	11	0.016 [-0.024,0.043]	0.283 [0.194,0.369]	0.582 [0.496,0.716]	0.245 [0.145,0.359]	0.044 [0.030,0.060]

Table 5: Fixed-effects model II (fitted to the individual recovery curves): Fixed effects - median [min,max]

Table 6

	Mixed-effects model			Fixed-effects model I			Fixed-effects model II		
	$D(\theta_{med})$	p_D	DIC	$D(\theta_{med})$	p_D	DIC	$D(\theta_{med})$	p_D	DIC
diffuse	-53392.85	99.79	-53193.28	-45393.74	4.35	-45385.03	-55236.87	1120.68	-52995.51
early S	-115018.90	115.19	-114788.50	-73488.93	2.64	-73483.65	-119244.20	1208.51	-116827.20
late S	-60660.14	250.06	-60160.02	-34218.34	4.69	-34208.96	-60946.83	2137.32	-56672.18

Table 6: Deviance of the medians ($D(\theta_{med})$), effective number of parameters (p_D) and DIC of the mixed-effects model and fixed-effects models I and II

Figures

Figure 1

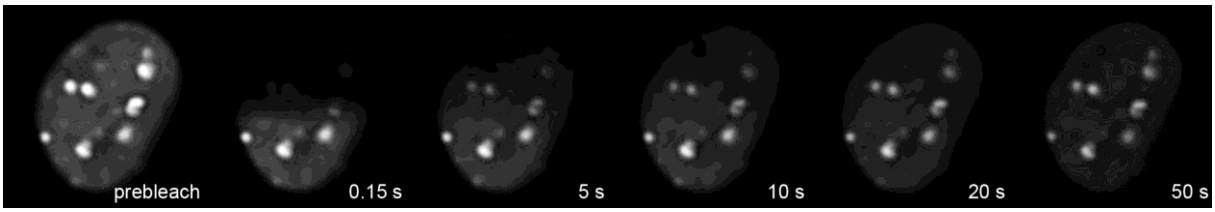

Figure 2

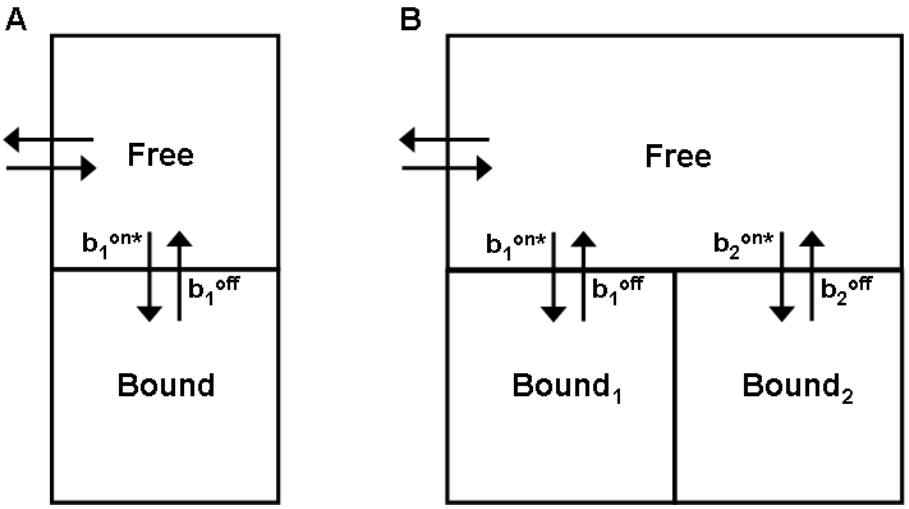

Figure 3

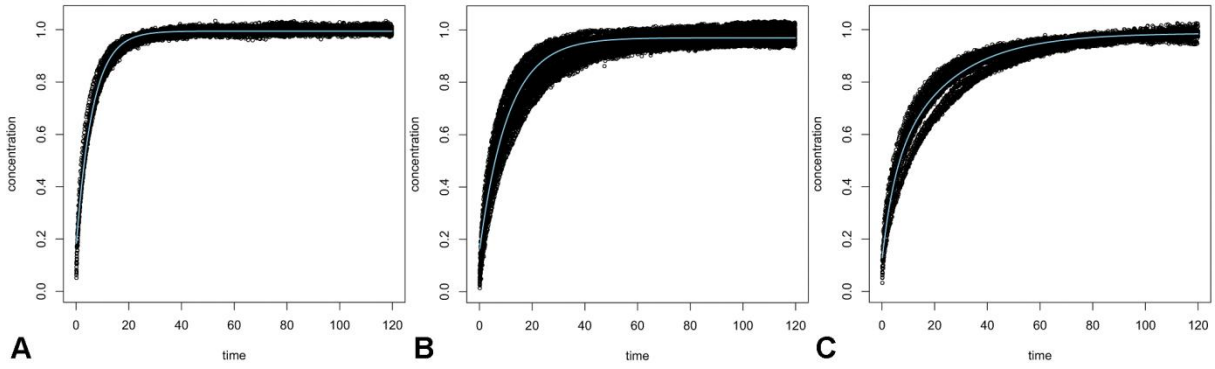

Figure 4

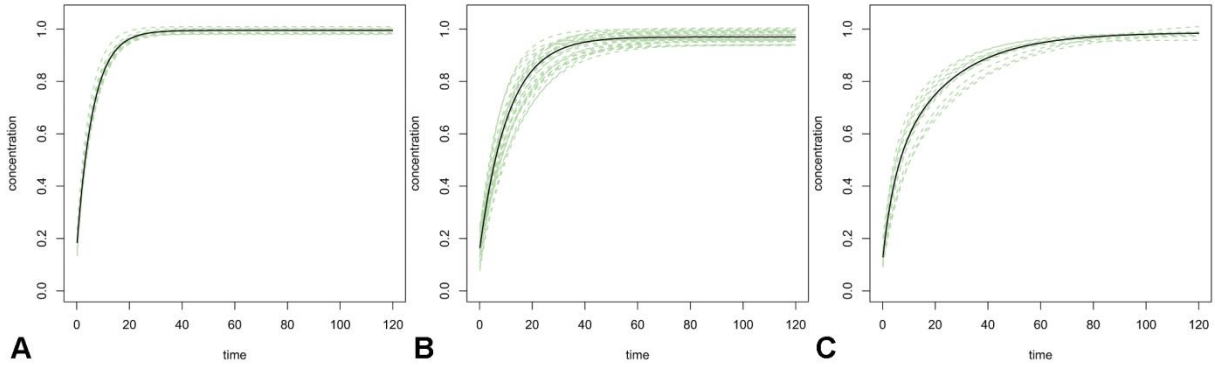

Figure 5

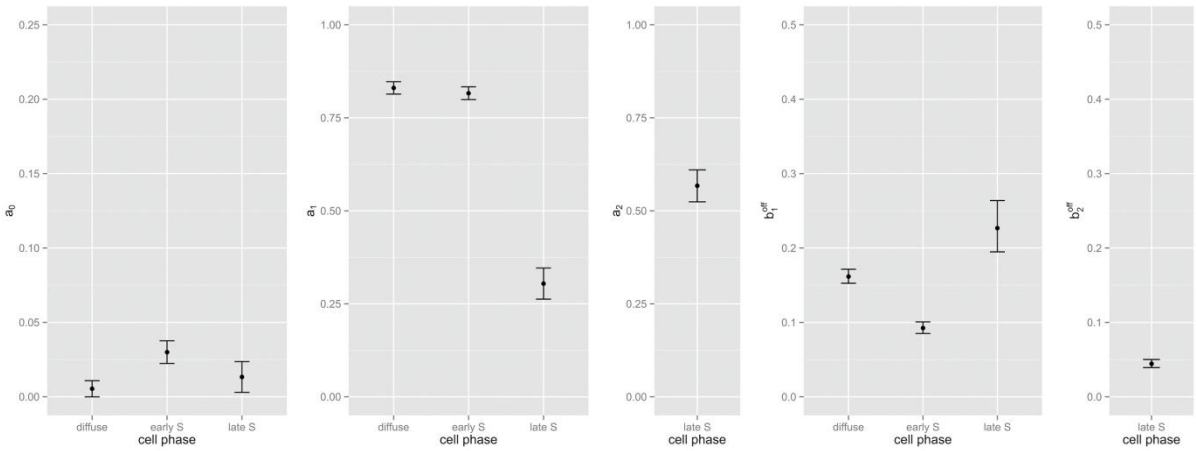

Figure 6

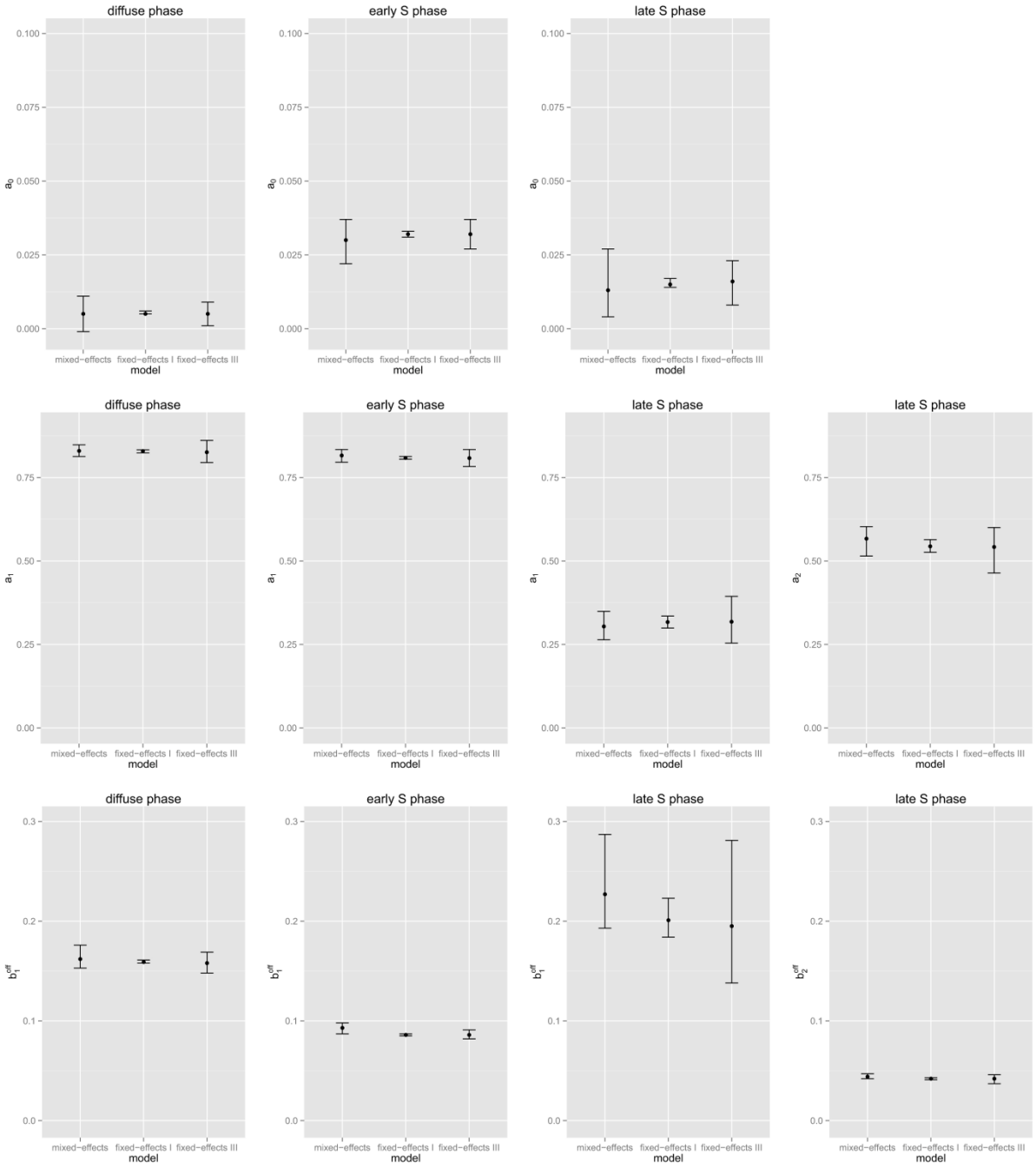
diffuse phase
early S phase
late S phase
late S phase
a_0
a_1
a_2
b_1^{off}
b_2^{off}
mixed−effects
fixed−effects I
fixed−effects III
model

Bayesian simultaneous analysis of multiple FRAP images with mixed-effect priors

Appendix - Full conditional distributions

For $K = 1, 2$, $k = 1, 2$:

$$a_0 \mid \cdot \sim N\left(\frac{m}{v}, \frac{1}{v}\right), \text{with } v = \frac{\sum_{j=1}^{J} T_j}{\sigma^2},$$

$$m = \sum_{j=1}^{J}\sum_{i=1}^{T_j} \frac{-C(t_{ij}) + 1 - \alpha_{0j} - \sum_{k=1}^{K} a_{kj}\exp(-b_{kj}^{off} t_{ij})}{\sigma^2}.$$

$$\alpha_{0j} \mid \cdot \sim N\left(\frac{m}{v + \frac{1}{\tau^2_{\alpha_0}}}, \frac{1}{v + \frac{1}{\tau^2_{\alpha_0}}}\right), \text{with } v = \frac{T_j}{\sigma^2},$$

$$m = \sum_{i=1}^{T_j} \frac{1 - C(t_{ij}) - a_0 - \sum_{k=1}^{K} a_{kj}\exp(-b_{kj}^{off} t_{ij})}{\sigma^2}.$$

$$\tau^2_{\alpha_0} \mid \cdot \sim IG(c_0 + \frac{J}{2}, \frac{1}{2}\sum_{j=1}^{J}\alpha_{0j}^2 + d_0)$$

$$p(b_k^{off} \mid \cdot) = p(\exp(f_k) \mid \cdot) \propto$$

$$\prod_{j=1}^{J}\prod_{i=1}^{T_j} \exp\left(-\frac{1}{2\sigma^2}(C(t_{ij}) - (1 - a_{0j} - \sum_{k=1}^{K} a_{kj}\exp(-\exp(f_k)\exp(\phi_{kj})t_{ij})))^2\right)$$

$$p(\beta_{kj}^{off} \mid \cdot) = p(\exp(\phi_{kj}) \mid \cdot) \propto$$

$$\prod_{i=1}^{T_j}\left(\exp\left(-\frac{1}{2\sigma^2}(C(t_{ij}) - (1 - a_{0j} - \sum_{k=1}^{K} a_{kj}\exp(-\exp(f_k)\exp(\phi_{kj})t_{ij})))^2\right)\right) \cdot \frac{1}{\tau_{\beta_k^{off}}\sqrt{2\pi}\exp(\phi_{kj})}\exp(-$$

$$\tau^2_{\alpha_k} \mid \cdot \sim IG(c_k + \frac{J}{2}, \frac{1}{2}\sum_{j=1}^{J}\alpha_{kj}^2 + d_k)$$

$$\tau^2_{\beta_k^{off}} \mid \cdot \sim IG(e_k + \frac{J}{2}, \frac{1}{2}\sum_{j=1}^{J}\phi_{kj}^2 + g_k)$$

$$\sigma^2 \mid \cdot \sim IG(a + \frac{1}{2}\sum_{j=1}^{J} T_j, b + \frac{1}{2}\sum_{j=1}^{J}\sum_{i=1}^{T_j}(C(t_{ij}) - (1 - a_{0j} - \sum_{k=1}^{K} a_{kj}\exp(-b_{kj}^{off} t_{ij})))^2)$$

If $K = 1$:

$$a_1 \mid \cdot \sim N\left(\frac{m}{v}, \frac{1}{v}\right), \text{ with } v = \sum_{j=1}^{J}\sum_{i=1}^{T_j} \frac{\exp(-2b_{1j}^{off} t_{ij})}{\sigma^2},$$

$$m = \sum_{j=1}^{J}\sum_{i=1}^{T_j} \frac{(-C(t_{ij}) - \alpha_{1j}\exp(-b_{1j}^{off} t_{ij}) + 1 - a_{0j})\exp(-b_{1j}^{off} t_{ij})}{\sigma^2}.$$

$$\alpha_{1j} \mid \cdot \sim N\left(\frac{m}{v + \frac{1}{\tau^2_{\alpha_1}}}, \frac{1}{v + \frac{1}{\tau^2_{\alpha_1}}}\right), \text{ with } v = \sum_{i=1}^{T_j} \frac{\exp(-2b_{1j}^{off} t_{ij})}{\sigma^2},$$

$$m = \sum_{i=1}^{T_j} \frac{(-C(t_{ij}) + 1 - a_{0j} - a_1\exp(-b_{1j}^{off} t_{ij}))\exp(-b_{1j}^{off} t_{ij})}{\sigma^2}.$$

If $K = 2$, for $k = 1, 2$:

$$a_k \mid \cdot \sim N\left(\frac{m}{v}, \frac{1}{v}\right), \text{ with } v = \sum_{j=1}^{J}\sum_{i=1}^{T_j} \frac{\exp(-2b_{kj}^{off} t_{ij})}{\sigma^2},$$

$$m = \sum_{j=1}^{J} \sum_{i=1}^{T_j} \frac{(-C(t_{ij}) - \alpha_{kj} \exp(-b_{kj}^{off} t_{ij}) - a_{-kj} \exp(-b_{-kj}^{off} t_{ij}) + 1 - a_{0j}) \exp(-b_{kj}^{off} t_{ij})}{\sigma^2},$$

$$\text{where} - k = 2, \text{if } k = 1, \text{ and} - k = 1, \text{ if } k = 2.$$

$$\alpha_{kj} \mid \cdot \sim N\left(\frac{m}{v + \frac{1}{\tau_{\alpha_k}^2}}, \frac{1}{v + \frac{1}{\tau_{\alpha_k}^2}}\right), \text{ with } v = \sum_{i=1}^{T_j} \frac{\exp(-2b_{kj}^{off} t_{ij})}{\sigma^2},$$

$$m = \sum_{i=1}^{T_j} \frac{(-C(t_{ij}) + 1 - a_{0j} - a_k \exp(-b_{kj}^{off} t_{ij}) - a_{-kj} \exp(-b_{-kj}^{off} t_{ij})) \exp(-b_{kj}^{off} t_{ij})}{\sigma^2},$$

$$\text{where} - k = 2, \text{if } k = 1, \text{ and} - k = 1, \text{ if } k = 2.$$

3. Discussion

Although Dnmt1 has been studied for over 25 years (Bestor et al., 1988), the detailed regulation of maintenance DNA methylation still remains to be elucidated. Especially the cell cycle dependency of the regulatory interactions increases the complexity considerably. In order to gain new insights into the regulation of DNA maintenance methylation, we set out to dissect the cell cycle-dependent dynamics of Dnmt1. Our approach of combining FRAP with kinetic modeling enabled us to get quantitative insights into the binding processes. Furthermore, FRAP and related methods enabled us to analyze the dynamics of the factors Uhrf1, Uhrf2 and the histone variant H2A.Z. Emphasizing the methodological aspect of this work, we also developed new strategies to label DNA sequences in living cells, characterized nanoparticles as vectors for nucleic acids and detected new interactions of the cell cycle regulator NIPA.

3.1 Spatio-temporal dynamics of epigenetic factors

3.1.1 Cell cycle-dependent localization and kinetics of Dnmt1

In order to dissect the cell cycle-dependent regulation of Dnmt1, we obtained detailed temporal and spatial information using FRAP in combination with kinetic modeling as well as 3D-SIM super-resolution microscopy (Schneider et al., 2013). By analyzing GFP-Dnmt1 mutants, we showed that both the PBD- and the TS domain-mediated interactions are necessary and sufficient for the localization and the dynamics of Dnmt1 in S phase. In early S phase, binding of the PBD to PCNA predominates. In late S phase, we observe a shift towards the TS domain-mediated binding to constitutive heterochromatin (Figure 10). Based on our customized kinetic model that will be discussed in 3.2.2, we estimated the mean residence time (T_{res}) describing the average binding time of the PBD and the TS domain to their targets. The T_{res} was about 10 s for the PBD and about 22 s for the TS domain. The short T_{res} indicate transient interactions, which are in the range of the binding behavior of many nuclear proteins (Phair and Misteli, 2000, Phair et al., 2004b). Transient interactions facilitate the fast reaction of nuclear processes to external and internal signals. Based on our measurements, we propose a two-loading-platform model, in which PCNA and constitutive heterochromatin function as relatively immobile platforms during S phase. Furthermore, the interaction of the TS domain with constitutive heterochromatin is stronger than the interaction of the PBD with PCNA. If the specific heterochromatic marks, the TS domain binds to, are in close proximity to replication sites, Dnmt1 binding is shifted towards heterochromatin, a situation mainly encountered in late S phase and presumably in G2. In early S phase, these heterochromatic sites are sparse, not accessible or distant to replications sites and therefore the interaction with PCNA is dominating. Besides specific binding partners, modifications changing the conformation of Dnmt1 might also be involved in the switch observed between early and late S phase. Several modifications of

Dnmt1 have been reported, such as acetylation, ubiquitination, phosphorylation, methylation and sumoylation (Du et al., 2010, Lee and Muller, 2009, Esteve et al., 2011), but their cell cycle-dependent appearance has to be further investigated. Furthermore, it is still uncertain, whether DNA methylation takes place on unpacked DNA or on DNA wrapped around nucleosomes. *In vitro* and *in vivo* studies give indications that Dnmts methylate mainly unpacked DNA, but to some extend Dnmt1 also seems to be capable of methylating specific sequences in nucleosomes (Felle et al., 2011a, Okuwaki and Verreault, 2004). The latter might function as a mechanism in G2 ensuring complete maintenance of methylation, if the process of maintenance methylation is much slower compared to replication and not enough Dnmt1 molecules can be recruited to unpacked DNA. Slow DNA methylation would result in hemimethylated sites in G2, which could explain the association of Dnmt1 with constitutive heterochromatin, which is CpG rich and replicates late, in this phase (Easwaran et al., 2004).

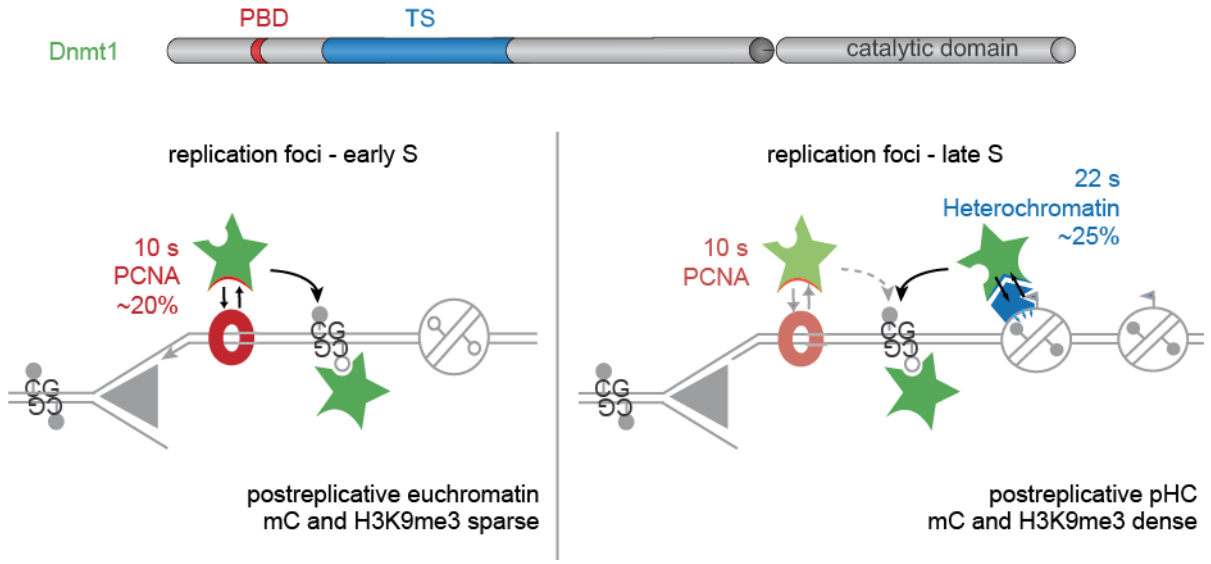

Figure 10: Two-loading-platform model for Dnmt1 in S phase. Dnmt1 binds via the PBD to PCNA and via the TS domain to constitutive heterochromatin. In early S phase, the interaction with PCNA is dominating. In late S phase, the specific heterochromatic marks, the TS domain binds to are present in close proximity to replications sites. This leads to a stronger TS domain-mediated interaction that dominates the Dnmt1 dynamics in late S phase.

Moreover, we identified another MC for Dnmt1 with a mean residence time of about 10 s present in all analyzed stages, including G1/late G2, when the Dnmt1 localization is diffusely distributed in the nucleus. This MC even persists in Dnmt1 mutants, where several regions are affected. In addition to mutations in the PBD and the TS domain, neither mutations in the ZnF (Frauer et al., 2011) nor N-terminal truncations (unpublished data; bachelor's thesis Anna Ulraum) resulted in faster kinetics in G1/late G2. Although we cannot exclude a specific, S phase independent interaction with for example chromatin, we attribute this fraction to anomalous diffusion in the nucleus. The common phenomenon of anomalous diffusion is further described and discussed in 3.2.3.

In addition to the temporal information, we analyzed the spatial distribution of Dnmt1 wild type (Dnmt1^{wt}), a TS domain mutant and a PBD mutant in late S phase. Using super-resolution microscopy, we found that the Dnmt1^{wt} localization is extended towards constitutive heterochromatin outside replication foci, if the PBD is mutated (GFP-Dnmt1^{Q162E}). Interestingly, only a part of the chromocenter is covered. Based on pulse-chase experiments with the replication marker EdU, we hypothesize that the regions GFP-Dnmt1^{Q162E} binds to consist of postreplicative heterochromatin containing the direct binding partner of the TS domain. The identity of this binding partner is still controversial and further discussed in 3.1.2. In addition, these results could point to a competition between the PBD mediated binding to PCNA and the TS domain mediated binding to postreplicative heterochromatin. This could explain the enrichment of Dnmt1 at constitutive heterochromatin in G2, when the replication of DNA is completed. PCNA would then be distributed diffusely in the nucleus and the TS domain could recruit a larger fraction of Dnmt1 molecules to constitutive heterochromatin.

An interesting question is how the interactions of the PBD and the TS domain influence the catalytic activity of Dnmt1. We obtained first insights into this question by performing a trapping assay, in which Dnmt1 is covalently bound to 5-aza-dC (see 1.4.2) (Schermelleh et al., 2005). The results confirmed that the PBD is not essential, but enhances the probability for the covalent complex formation by approximately a factor of two (Schermelleh et al., 2007). If a central part of the TS domain is removed (GFP-Dnmt1$^{\Delta TS}$), trapping is still possible *in vivo*, but the kinetics are considerably decreased. This finding is in accordance with the fact that a radioactive assay revealed that the methyl group is still transferred to DNA *in vitro* (PhD thesis, Qin, 2011). However, this mutant cannot rescue methylation in *Dnmt1* knockout ESCs indicating that the functional TS domain is essential for the maintenance of methylation *in vivo* (PhD thesis, Qin, 2011). Taken together, GFP-Dnmt1$^{\Delta TS}$ seems to be incapable of significantly restoring and maintaining methylation levels over several cell cycles *in vivo* due to its slow catalytic reaction kinetics.

3.1.2 Dynamic regulation of Dnmt1 by cofactors

Although we demonstrated that the TS domain is required for the correct localization and kinetics of Dnmt1 in S phase, the direct heterochromatic interaction partner of the TS domain remains unknown. Most likely the interaction partner is Uhrf1, however, it is still debated, whether it is the direct interaction partner of Dnmt1. It has been reported that *in vitro* Dnmt1 and Uhrf1 interact via the TS domain (Frauer and Leonhardt, 2011, Bashtrykov et al., 2013, Achour et al., 2008, Felle et al., 2011b), but controversial *in vivo* data about the localization of Uhrf1 during the cell cycle exist. If Uhrf1 mediates the targeting of Dnmt1 to hemimethylated DNA via its SRA domain, one would expect Uhrf1 at replication foci in early S phase. However, most publications describe only the association of Uhrf1 with heterochromatin, and they often do not mention, whether this association takes place throughout the cell cycle or only in a specific phase (Rothbart et al., 2013, Nishiyama et al., 2013). In

late S phase, Uhrf1 associates with PCNA or other replication markers, when constitutive heterochromatin is replicated, but it is unclear, if Uhrf1 associates with also PCNA in early S phase and if Uhrf1 is diffuse or associated with constitutive heterochromatin in G1 and G2. In some cases, Uhrf1 colocalization with PCNA in early S phase has been described using an anti-Uhrf1 antibody (Uemura et al., 2000) or a GFP fusion protein (Bostick et al., 2007). We observed that GFP-Uhrf1 and Uhrf1-GFP associate with chromocenters throughout the cell cycle (unpublished data; master's thesis Veronica Solis) and similar results have been published using antibodies (Citterio et al., 2004, Papait et al., 2007). In some publications that claim colocalization of Uhrf1 with PCNA, the early S phase stage is not shown (Sharif et al., 2007). Therefore, it is still not clear, whether Uhrf1 targets Dnmt1 to hemimethylated sites in early S phase. Trapping experiments that covalently bind Dnmt1 to 5-aza-dC revealed that Dnmt1 is covalently bound to DNA in early S phase, strongly indicating the presence of methylated sites in early replicating euchromatic DNA (Schermelleh et al., 2007, Schneider et al., 2013). If Dnmt1 binds via the TS domain to Uhrf1 at hemimethylated sites in early S phase, we would expect different kinetics and localization of GFP-Dnmt1$^{\Delta TS}$ compared to GFP-Dnmt1^{wt} in early S phase. Indeed, we observe a reduced association of GFP-Dnmt1$^{\Delta TS}$ with replications sites in early S phase and a change in the kinetics compared to GFP-Dnmt1^{wt}, but we cannot resolve a distinct TS domain mediated MC in early S phase with our model. Based on our results, we cannot definitely answer, whether the TS mediated interaction of Dnmt1 with constitutive heterochromatin is directly dependent on Uhrf1. *Uhrf1* knockout studies are only of limited informative value, because the low methylation levels in *Uhrf1* knockout cells (Sharif et al., 2007) could by itself already explain the almost diffuse localization of Dnmt1 in late S phase in these cells (Bostick et al., 2007).

Uhrf1 cannot only bind to hemimethylated DNA, but also to H3K9me3 (Bostick et al., 2007, Rottach et al., 2010, Rothbart et al., 2012). The function of H3K9me3 binding is still unclear, but it might act as a double safety mechanism to ensure methylation at heterochromatin and to protect euchromatic regions from inappropriate methylation. We were able to demonstrate that binding of H3K9me3 peptides further increases the specificity of Uhrf1 for hemimethylated DNA *in vitro* (Pichler et al., 2011). Vice versa, the affinity for H3K9me3 is enhanced by binding of hemimethylated DNA. In the literature, contradictory data about the question, whether the TTD or the PHD mediates the binding to H3K9me3 are present (Rottach et al., 2010, Karagianni et al., 2008). In recent publications, there is more and more evidence that the PHD has a general affinity for H3 or a specific affinity for unmodified H3R2 and that the TTD harbors the specificity for H3K9me3 (Rothbart et al., 2013, Xie et al., 2012, Cheng et al., 2013, Rajakumara et al., 2011, Wang et al., 2011, Pichler et al., 2011). In conclusion, coordinated action of both domains seems to be required for H3K9me3 binding. Due to contradictory data, it is still unclear, whether the interaction of Uhrf1 with H3K9me3 is essential for DNA methylation or not. Both scenarios have been reported (Rothbart et al., 2012, Liu et al., 2013a).

Differential analysis of methylated late replicating heterochromatic and early replicating euchromatic DNA might give new insights into the necessity of Uhrf1 histone binding for maintenance methylation.

Despite the similarity in the overall-domain structure between Uhrf1 and Uhrf2, Uhrf2 cannot restore the low methylation levels in *Uhrf1* knockout ESCs (Pichler et al., 2011). Furthermore, we found that Uhrf2 alone has no preference for hemimethylated DNA, but binding of Uhrf2 to H3K9me3 modified peptides induces a preference. Similar to Uhrf1 the affinity of Uhrf2 for H3K9me3 is enhanced by binding to hemimethylated DNA. Until now, no data from an *Uhrf2* knockout have been published that would give important information about its function. Nevertheless, we and other groups have demonstrated that Uhrf1 levels are high in ESCs and low in somatic cells (Hopfner et al., 2000, Fujimori et al., 1998), whereas Uhrf2 possesses an opposite expression pattern (Pichler et al., 2011). This opposite expression pattern has also been observed during embryoid body differentiation, hinting at different roles of Uhrf1 and Uhrf2 during differentiation and development. We hypothesized that Uhrf2 might have a tight control function in differentiated cells, whereas Uhrf1 is less stringent, allowing more plasticity in undifferentiated ESCs. Furthermore, it was shown that Uhrf2 binds strongly to 5hmC and that overexpression leads to increased 5hmC, 5fC and 5caC levels by Tet-mediated oxidation (Spruijt et al., 2013). These results could point to a role of Uhrf2 in DNA demethylation, supporting the hypothesis of Uhrf2 as a control protein in somatic cells possibly assisting in the removal of misplaced methylation marks. Further experiments have to be performed to analyze the distinct roles of Uhrf1 and Uhrf2 in DNA methylation and demethylation.

Recently, a new publication proposes a way, how Uhrf1 could indirectly target Dnmt1 to hemimethylated DNA sites. The authors have shown that the RING-finger type E3 ligase Uhrf1 ubiquitinates H3 on lysine 23 (H3K23ub) (Nishiyama et al., 2013). This new modification is bound by Dnmt1 via the TS domain (Nishiyama et al., 2013). The Uhrf1 RING mutant, which is defective in H3K23 ubiquitination, fails to mediate the rescue of DNA methylation levels in *Uhrf1* knockout cells and its overexpression leads to a diffuse Dnmt1 localization. As the H3K23ub modification seems to be replication-dependent, it is tempting to speculate that this modification occurs only on postreplicative chromatin and might be the link for S phase-dependent targeting of Dnmt1 to heterochromatin. These results are summarized in a stepwise loading model consisting of three steps (Figure 11). (1) Uhrf1 binds to hemimethylated DNA via the SRA domain in close proximity to H3K9me3 recognized by the TTD and the PHD and ubiquitinates H3K23 via the RING domain. (2) Dnmt1 is enriched at replication sites by binding to PCNA. (3) Dnmt1 binds to H3K23ub via the TS domain as a requirement for methylation of the hemimethylated site. In addition, there might be still undetected modifications or binding partners that mediate the binding of the TS domain to heterochromatin.

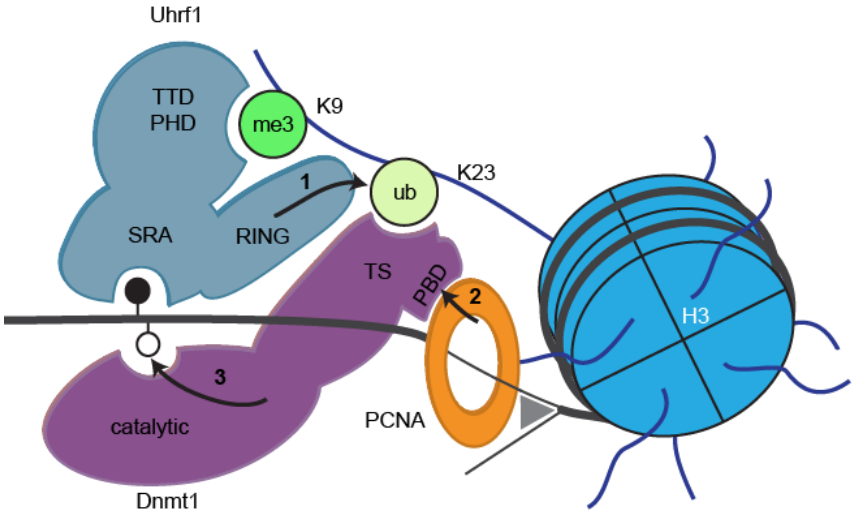

Figure 11: Stepwise loading model at hemimethylated DNA. (1) Uhrf1 binds to hemimethylated DNA via the SRA domain and to H3K9me3 via the TTD and PHD, leading to ubiquitination of H3K23 by the RING domain. (2) Interaction with PCNA enriches Dnmt1 at replication foci. (3) Dnmt1 binds to H3K23ub via the TS domain, followed by methylation of the hemimethylated CpG site. Only domains mediating the illustrated interactions are depicted. Closed and open lollipops indicate methylated and non-methylated CpG sites, respectively.

Another layer of complexity is added by the fact that the TS domain alone fused to GFP binds with very high affinity to constitutive heterochromatin throughout the cell cycle (Easwaran et al., 2004; diploma thesis Daniela Meilinger; master's thesis Veronica Solis). Only in early to mid S phase, the TS domain is less enriched at heterochromatin and a rather diffusely distributed fraction can be found in the nucleoplasm (data not shown, diploma thesis Daniela Meilinger). The potential of the TS domain to bind replication independent to constitutive heterochromatin has to be masked in the full length Dnmt1 protein, because we usually do not observe Dnmt1 association with heterochromatin in G1 or late G2 phase. This is in accordance with the structure of Dnmt1, in which the TS domain is inserted into the DNA-binding pocket of the catalytic domain (Takeshita et al., 2011). One hypothesis is that a conformation change upon binding to a specific signal like H3K23ub flips the TS domain out of the catalytic pocket, resulting in tight binding of Dnmt1 to its substrate, stabilizing the catalytic reaction of Dnmt1. The signal bound by the TS domain could be identical with the signal leading to the release of the TS domain from the catalytic pocket like H3K23ub or the TS domain could then bind another substrate, for instance, another histone modification like H3K9me3, methylated DNA or Uhrf1. Confocal imaging can be used to exclude potential interacting molecules, if they are not colocalizing with the TS domain. Therefore, it will be interesting to see the distribution of the new histone mark H3K23ub during the cell cycle.

A histone modification could be involved in the release of Dnmt1 from heterochromatin in late G2. Phosphorylation of H3S10 in late G2 by the Aurora B kinase leads to the dissociation of HP1 from H3K9me3 at constitutive heterochromatin (Mateescu et al., 2004, Hirota et al., 2005) and could serve

as a mechanism to remove Uhrf1 or Dnmt1 from heterochromatic sites. The association of Uhrf1 with H3K9me3 is independent of H3S10 phosphorylation (Rothbart et al., 2012). However, Dnmt1 might directly bind to H3K9me3 and could be released upon H3S10 phosphorylation (Patricia Wolf, data not shown). This would explain why Dnmt1 is lost from constitutive heterochromatin in late G2 (Easwaran et al., 2004). Furthermore, there is evidence that knockdown of Dnmt1 leads to reduced H3S10 phosphorylation (Monier et al., 2007), possibly caused by changes in the local chromatin environment due to local demethylation.

DNA methylation is not only orchestrated by targeting Dnmt1 to the correct sites, but also by regulating its abundance and activity. Besides the already mentioned ubiquitination by Uhrf1 and deubiquitination by Usp7 (1.2.1), inhibition of Dnmt1 by non-coding RNAs has been recently demonstrated (Di Ruscio et al., 2013). Accordingly, long non-coding RNAs, produced during transcription, inhibit Dnmt1 activity at these loci, thereby keeping actively transcribed regions unmethylated. Furthermore, the potential of active DNA demethylation by Tet proteins has added a new layer of regulatory potential to the field of DNA methylation (Pastor et al., 2013). Besides the pathways illustrated in the introduction (see 1.2), dehydroxymethylation of 5hmC to 5C directly by Dnmt3a and Dnmt3b has been reported *in vitro* (Chen et al., 2012). If the direct conversion of 5hmC to 5C by Dnmts occurred *in vivo*, this would open a large regulatory potential as Dnmt3a and Dnmt3b could immediately methylate the newly generated 5C sites back to 5mC. In cooperation with Tet proteins and Dnmt1 they would be able to regulate DNA methylation via numerous pathways in a very dynamic fashion.

3.1.3 Connection between DNA methylation and histone variants

DNA methylation might not only be connected to histone modifications, but also to histone variants. It has been reported that the incorporation of H2A.Z and DNA methylation are mutually exclusive in plants, indicating that H2A.Z protects DNA from methylation or vice versa (Zilberman et al., 2008). This mechanism seems to be conserved and has also been identified in mammals (Conerly et al., 2010). Moreover, inhibition of Dnmts by 5-aza-dC leads to incorporation of H2A.Z into chromatin and is essential for gene activation after 5-aza-dC treatment (Yang et al., 2012). The described results demonstrate the importance of histone variants as epigenetic regulators and hint at a connection with DNA methylation.

One way how histone variants may influence epigenetics is via changing nucleosome stability. It was very interesting to see that a splice variant of H2A.Z is present in human cells with highest levels in brain tissue (Bonisch et al., 2012). In contrast to H2A.Z, the splice variant of the isoform H2A.Z.2, termed H2A.Z.2.2, can affect nucleosome stability. In FRAP experiments we could attribute around 78% of the H2A.Z.2.2 molecules to a fast recovering fraction, whereas about 82% of the previously

characterized H2A.Z.2.1 molecules recovered slowly, pointing to an enhanced exchange of the splice variant in chromatin. Furthermore, we demonstrated that a specific sequence in the C-terminal part is necessary for the fast kinetic exchange of H2A.Z.2.2 by weakening the interaction with H3. Like H2A.Z, H2A.Z.2.2 interacts with the Tip60 and SRCAP chaperone complexes (Bonisch et al., 2012). This establishes an interesting link to Dnmt1, as Tip60 has been shown to regulate Dnmt1 levels by activating Uhrf1-dependent proteasomal degradation of Dnmt1 (Du et al., 2010). One could speculate that the incorporation of the active mark H2A.Z in chromatin constitutes a safety mechanism that degrades Dnmt1 at actively transcribed sites. Further experiments have to be performed in order to investigate this potential connection and the specific function of the splice variant H2A.Z.2.2. It will be interesting to analyze the functions of histone variants during development and disease, especially in connection to other epigenetic processes like DNA methylation.

3.2 Visualizing the invisible

For all complex nuclear processes, it is of fundamental importance to understand them not only *in vitro*, but also in an *in vivo* situation. Advanced microscopy in combination with fluorescent proteins like GFP offers a variety of techniques that enables us to gain deep insights into epigenetic regulation *in vivo*. New or improved ways of delivery, labeling or quantification of results can further help us to address biological questions about nuclear dynamics.

A great advantage of the photobleaching method FLIP (see 1.4.2) is the exposure of regions, where the proteins strongly binds to, if the binding sites have been masked by a large diffuse mobile fraction. For instance, by bleaching the mobile fraction, we revealed that the protein NIPA binds strongly to the nuclear periphery. Before, the localization of the protein has only been described as nuclear (Bassermann et al., 2005). NIPA is a mammalian ubiquitin E3 ligase that ubiquitinates cyclinB1 (Bassermann et al., 2005). At the G2/M transition, NIPA is inactivated by phosphorylation and cyclinB1 accumulates, allowing mitotic entry. Our data demonstrate that GFP-NIPA needs several hours to recover in a FRAP experiment at the nuclear periphery in contrast to the diffuse fraction in the nucleoplasm that recovers in the range of seconds. A functional role of the nuclear fraction cannot be excluded, however, antibody staining showed that this fraction is rather small for the endogenous protein and might be an overexpression artifact of the exogenous construct. Detection of hidden patterns of protein localization can reveal colocalization with other proteins that has been masked before and give therefore new functional insights. In this context, the localization of NIPA at the nuclear envelope has led the attention to *in vitro* data indicating the nucleoporin translated promoter region (TPR) as an interaction partner. Using *in vivo* FRAP and FLIP experiments in combination with *in vitro* coimmunoprecipitation experiments, we demonstrated that the ZnF domain of NIPA is mediating the interaction to TPR. The extracellular signal-regulated kinase (ERK2) phosphorylates NIPA at the G2/M transition (Illert et al., 2012) and interestingly it has been reported that ERK2 is also able to

phosphorylate the protein TPR, leading to a stabilization of their interaction (Vomastek et al., 2008). The same study hinted at a role of TPR in modulating the translocation of ERK2 into the nucleus. Furthermore, it has been shown that protein degradation can be linked to specific cellular compartments like the endoplasmic reticulum (ER) in a process called ER-associated degradation (ERAD) (Christianson and Ye, 2014). Based on our results, we hypothesize that NIPA could act as a "cyclin trap" at the nuclear pore complex by degrading its target cyclinB1 upon premature entry into the nucleus in interphase. Further studies will give important insights into the functional role of the cell cycle regulator NIPA at the nuclear envelope.

3.2.1 Limitations of photobleaching methods

The majority of today's imaging methods are based on fluorescent labels. This has the great advantage of multiplexing several molecules labeled with different colors combined with a very high contrast. For *in vivo* imaging approaches, usually fluorescent proteins are utilized. Besides GFP, a large variety of proteins with excitation and emission maxima in different wavelengths are available (Crivat and Taraska, 2012). The attachment of these large fluorescent proteins (about 30 kDa) can, however, change the properties of the tagged proteins. Therefore, immunofluorescent control experiments confirming the localization of the protein are required. If the location of the endogenous protein is different, methods based on fluorescent tags cannot be applied. For instance, the localization of Uhrf1 is still ambiguous as described in 3.1.2 and is probably influenced by the GFP-tag. Furthermore, experiments involving irreversible bleaching of labeled molecules might introducing phototoxic effects and thus damage the living cells. The influence of DNA damage on FRAP data has been only superficially investigated, because it has been assumed that no effects arise in the short period of acquisition. However, recruitment of Dnmt1 to damage sites has been already recorded in a time period as short as two minutes (Mortusewicz et al., 2005) and the period of image acquisition after bleaching can be extended to multiple hours (Bonisch et al., 2012). In addition, it has been reported that scattering of light could even induce photodamage in neighboring cells (Dobrucki et al., 2007). In our experiments we did not detect damaging effects in the desired observation times. However, it is very hard to exclude hidden effects that might influence the kinetics.

Besides the potential effects of cellular damage, cell movement is a known problem of photobleaching experiments (Goldman and Spector, 2005, Trembecka et al., 2010). The combination of image registration and a minimal total region of interest (ROI) have improved the evaluation, but only a perfect image registration gives absolutely reliable results. Especially half nucleus FRAP is challenging, because the loss of fluorescence is interpreted by the image registration algorithms as a strong movement of the cell and the registration of the last prebleach and the first postbleach images was not possible. Bleaching of a specific line or circle circumvents this problem, because the outline of the nucleus is always visible, but the averaged signal to noise ratio decreases due to the smaller area of

the bleached region. Moreover, the nuclear positioning of the small bleach regions influences the results, especially when placed at the boundary of the compartment (Mai et al., 2013). Furthermore, half nucleus FRAP is beneficial, if the localization is heterogeneous and the different compartments are too small to be selectively bleached. This is, for example, the case for the very small replication foci, Dnmt1 binds to in early S phase. Another effect that needs to be avoided is axial drift, which is often caused by temperature fluctuations. Therefore, a stable temperature outside and inside the incubator is recommended. In long-term FLIP or FRAP experiments, the imaging of z-stacks over time helps to detect and to compensate for axial drift (Bonisch et al., 2012).

The photoswitching properties of the fluorophore are often neglected in photobleaching experiments. Upon excitation some molecules are transformed to non-fluorescent dark states (Dickson et al., 1997). In this state, bleaching of the molecules is very likely. However, a small fraction of the GFP molecules can revert from this state in a process called photoswitching (Bourgeois et al., 2012). The size of this fraction is influenced by the excitation intensity, which is changing between acquisition and bleaching, whereupon the size of this fraction is changing. Hence, after bleaching, a part of the molecules switches back to the fluorescent state, which is noticeable as a small recovery of the average fluorescence in the whole nucleus after bleaching. Photoswitching was like bleaching by acquisition corrected to a large extent in the FRAP evaluation procedure. Recently, specialized corrections have been developed and should be implemented into the standard evaluation (Mueller et al., 2012). All in all, a lot of improvements have been made to increase the reproducibility of FRAP results by refining the evaluation for a more robust outcome of FRAP experiments.

3.2.2 Dependence of the model choice on the scientific question

The quantification of the results of a FRAP experiment is critical to provide objective parameters describing the curves. Usually, the FRAP curve is described by a mathematical equation with specific fixed and variable parameters. The process of finding the variable parameters of the equation that describe the curve optimally is referred to as fitting. Besides fitting the curve with simple exponential equations, several mathematical models are available consisting of sets of equations based on physical laws. The mathematical models include diffusion models, diffusion-reaction models and compartmental models (Figure 12). Choosing the appropriate fitting procedure out of the existing pool is not trivial and can lead to inaccurate results (Mueller et al., 2008). Kinetic models often depend on a specific geometry of the bleached region and the FRAP approach needs to be adjusted accordingly. Furthermore, the choice depends on the homogeneity of the dynamic populations. Often, the proteins do not only interact with one, but with multiple interaction partners. If the interactions are characterized by distinct association rates (k_{on}) and dissociation rates (k_{off}), they can be separated in the fit. However, if k_{on} and k_{off} values of interactions are too similar, they cannot be separated. Therefore, we are using the term mobility class (MC) to describe a dynamic subpopulation. Moreover,

a MC must not necessarily describe an interaction, but could also arise, for instance, from atypical diffusion like anomalous diffusion. The reciprocal of k_{off} is the T_{res} indicating the average binding time of the protein, if a single interaction is characterized.

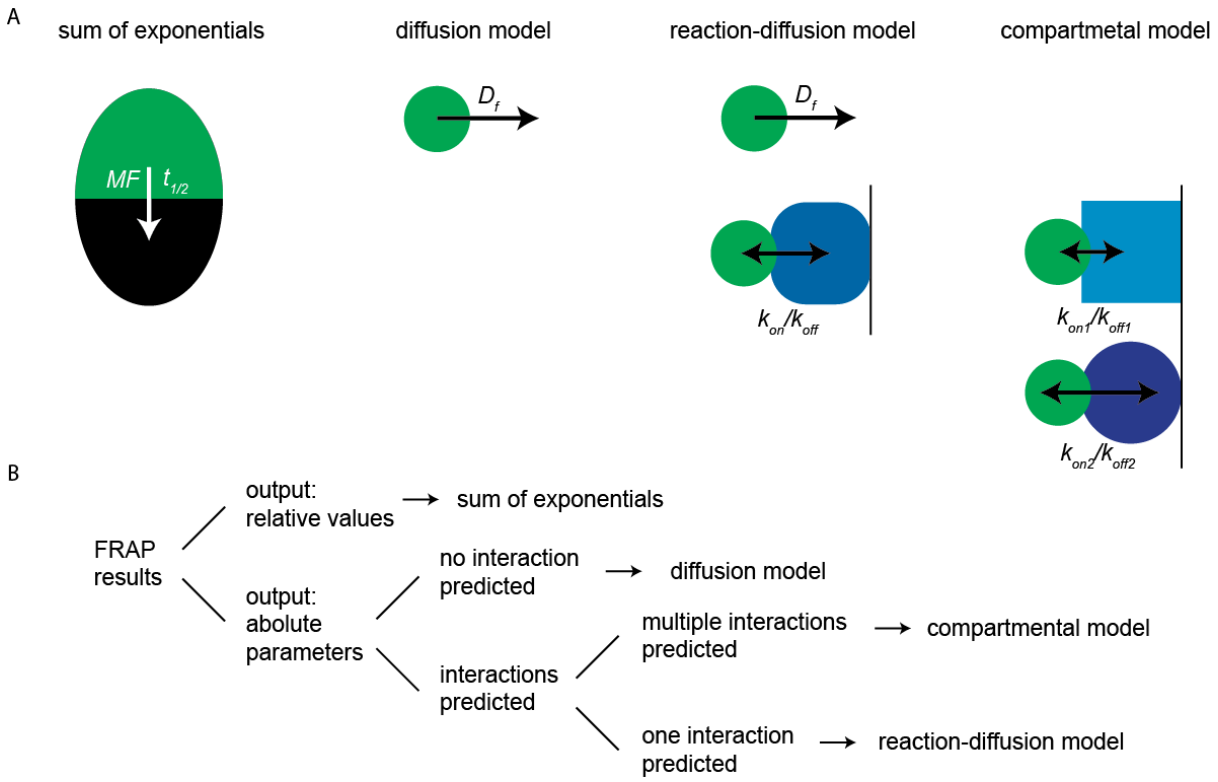

Figure 12: Choosing the appropriate model for the quantitative evaluation of FRAP experiments. (A) FRAP curves can be fitted with an exponential equation or a sum of exponential equations. The resulting $t_{1/2}$ and *MF* are dependent on the size and geometry of the bleached region and can only be compared to equivalent experiments. The other models are based on physical laws and allow the quantification of diffusion coefficients and/or association and dissociation coefficients (k_{on}/k_{off}), as depicted. **(B)** Flowchart representing the decision path leading to the choice of the appropriate model. If the number of interactions cannot be predicted, the results of different models need to be compared.

Sum of exponentials

The simplest equation to fit the corrected and normalized FRAP curve is an exponential equation (Phair et al., 2004a). From the exponent of the solution that yields the best fit, the half time recovery ($t_{1/2}$) can be calculated. If the curve does not approximate 1 during the recorded timeframe, the mobile fraction (*MF*) should be extracted as a second parameter. However, this value is dependent on the time the recovery has been recorded. Most FRAP curves extracted from nuclear proteins contain more than one MC and have therefore to be fitted with a sum of exponential equations (Phair et al., 2004b). This will result in multiple $t_{1/2}$ and a segmentation of the total populations into separate fractions. The decision of how many populations are present is not trivial and has to be carefully assessed (see 3.2.3). Using this method, proteins with different kinetic populations can be compared with each other. This has been applied before to study the number of kinetically distinct populations of the RNA polymerase II (Darzacq et al., 2007). We have fitted data with the sum of exponentials to analyze of kinetic populations of the canonical H2A.Z and a splice variant H2A.Z.2.2 (Bonisch et al.,

2012). H2A.Z and its splice variant contain different fractions of highly mobile and rather immobile proteins. The FRAP experiments revealed large differences between the relative amount of nucleosomal incorporation of the different constructs (see 3.1.3). However, the resulting parameters are not absolute values, but describe the protein in the chosen setup relative to other proteins and can only be used for a comparative analysis.

Diffusion model

Whenever absolute values like diffusion coefficients or association or dissociation rates (D_f, k_{on}, k_{off}) are required, special mathematical models have to be applied that are based on physical principles. The resulting parameters are protein specific and in principle independent of the setup. The models have to be tailored to the experimental approach or vice versa. One of the most frequently used models is the diffusion model. This requires data from a FRAP experiment with a specific geometry of the bleached region in order to determine the diffusion coefficient. Usually, the geometries include spot, spot array, rectangle or line bleaching (Hagen et al., 2009, Kang et al., 2012, van Royen et al., 2009, Xiong et al., 2014), but by subdividing the nucleus in squared regions, the diffusion coefficient can even be extracted from half nucleus FRAP (Beaudouin et al., 2006). In the last decades, sophisticated models have been developed, including a range of parameters like the bleach profile, nuclear 3D geometry or bleach duration (van Royen et al., 2009, Mazza et al., 2007, Braga et al., 2004). The more measurable parameters are taken into account the more realistic the results should be. We have applied spot FRAP in combination with a diffusion model for the analysis of the diffusion of oligonucleotides in nanoparticles (Lebold et al., 2012). Based on the assumption that the diffusion rate of the nucleotides inside the particles is correlated with the diffusion of nucleotides into the particles, we found interesting differences. The diffusion is dependent on the functionalizations of the particles as well as on the length of the oligonucleotides (see 3.2.4). Interestingly, we identified a second diffusion rate, which was rather independent of oligonucleotide length and particle functionalization. The nature of the second population is unclear, but one explanation would be that at least two types of diffusion are present. Studies using particle tracking give a much more detailed picture on the random walks of the molecules and allow the differentiation of a large number of diffusion types. Particle tracking has been applied to single dye molecules in nanoparticles (Kirstein et al., 2007). Analyzing the mean square displacement over time revealed indeed different types of structured and unstructured diffusion. A mixture of these different subclasses could lead to the second class, we observed.

Reaction-diffusion model

Even more complexity is generated in reaction-diffusion models that introduces one MC to the diffusion model (Sprague et al., 2004). The mobility class is described by k_{on} and k_{off} and the corresponding fractions of free and bound protein are determined, adding at least three more

parameters to the model. As most nuclear proteins diffuse and have at least one specific interaction partner, reaction-diffusion models are widely used in order to quantify FRAP-based molecular kinetics. Examples include RNA, transcription factors or HP1 (Braga et al., 2007, Sprague et al., 2004, Muller et al., 2009). However, extension of these models to two or more MCs is mathematically very complicated and in general not used for data obtained by FRAP experiments.

Compartmental model

If more than one interaction has to be quantified, a different type of model has to be applied. The only solution so far is a compartmental model that comes with the disadvantage of neglecting diffusion. This means that it is only applicable to proteins that diffuse so fast that all free proteins of the whole nucleus are bleached by the time of the first postbleach image is recorded. In contrast, binding has to be so strong that no proteins unbind during the short time between bleaching and recording the first postbleach image. Although compartmental models have been applied for a range of proteins (Phair et al., 2004b), most of them do not provide the necessary prerequisites. Hence, ignoring diffusion can lead to an incorrect estimation of binding time (Sprague et al., 2006). In order to address this problem, we have implemented a size-dependent correction factor for diffusion in the compartmental model used for half nucleus FRAP (Schneider et al., 2013). In our approach, GFP-multimers were analyzed in order to approximate the diffusion of proteins of different sizes in the nucleus. Besides the apparent advantage, the measurement of the correction factor is also error prone, because not only the molecular size, but also the shape of the control protein has to resemble the protein of interest in order to estimate diffusion correctly. Furthermore, the factor k_{diff} is only a correction factor and does not give information about the diffusion coefficient.

Often more than one model is applicable to the dataset, which generates the possibility to compare them with each other. For example, a protein with one MC should give the same k_{off} with a reaction diffusion model and with a compartmental model. First comparisons have revealed significant differences between the k_{on} and k_{off} values of the glucocorticoid receptor obtained with different bleach geometries in connection with different models (Mueller et al., 2008). By comparing the approaches, the errors were identified and the resulting improved model was applied to other transcription factors. So far no gold standard has been established for the quantification of FRAP experiments. This would be a major benefit as results obtained with different experimental parameters and different quantifications could be easily compared.

3.2.3 Limitations of the FRAP-based kinetic modeling

All the mathematical models try to reproduce reality, but have to be always a simplified version. Therefore, the user has to keep in mind the known limitations of these methods. All the described fitting options have the problem of potential overfitting (Mai et al., 2011). The more variable

parameters are included in a model, the closer the fit will be to the curve. Especially models with multiple MCs harbor a variety of parameters. Therefore, parameters have to be approximated and fixed in order to gain valuable results. In our approach, we have quantified the fraction of bleached molecules and fixed the k_{off} value of the MC with the slowest mobility (Schneider et al., 2013). Assuming that the slowest MC represents the catalytic reaction of Dnmt1, we based our estimations on *in vitro* data that have reported a dissociation rate of about 0.005 s^{-1}, which is equivalent to a mean residence time of 200 s (Song et al., 2011). After fixing the parameters, it has to be tested, whether a model with less MCs would give similar results compared to a model with more MCs. The model with the smallest numbers of parameters should always be preferred. The determination of the number of MCs is referred to as model choice, because different models for the various numbers of MCs exist. We have established specific model choice rules in order to choose the appropriate number of MCs for GFP-Dnmt1 in each cell cycle stage. The application of standard model choice criteria like the Akaike information criterion (Akaike, 1973) was not successful as the differences between the quality of the fits were too small. In order to obtain robust results, we wanted to find a way to model parameters that fit multiple cells instead of fitting individual cells and averaging the results. Therefore, we have included mixed-effects into a nonlinear regression model in a Bayesian framework (see 2.8). In order to assess this approach, the equations were based on a simplified compartmental model that neglects diffusion, but allows an analytical solution of the differential equations. The proposed mixed-effects model provides a much better fit than the fixed-effects model I and is thus more robust. This indicates that implementation of mixed-effects in more complex models can improve the robustness of the results.

Another limitation is the focus of FRAP models on the k_{off}. Changes in the k_{on} value influence the protein dynamics in the cell. For instance, a protein that binds with high affinity and specificity to its target, but stays associated only for a short time might give very similar kinetics as a protein that diffuses very slowly through the cell (Figure 13). In both cases, the FRAP curves can look very similar. The phenomenon that proteins that bind with high affinity to their targets and therefore diffuse only very short distances until the next binding site is present has been described as diffusion-coupled FRAP recovery (Sprague and McNally, 2005). As this diffusion-coupled recovery is often not corrected, the T_{res} values present an upper limit of the real value, because short times of diffusion might have interrupted this estimated binding time (Mueller et al., 2008). There are ways to detect diffusion-coupled recovery (Beaudouin et al., 2006), however, the ability to discriminate between those two cases is still limited.

A third limitation is that most models only account for normal Brownian diffusion. However, there is increasing evidence that diffusion in the nucleus is anomalous (Bancaud et al., 2009, Wachsmuth et al., 2000). This means that the root mean square displacement is not directly proportional to time. The

reasons are suspected in the crowded environment leading to hindrance of diffusion by obstacles or corralling in labyrinth-like environments (Sokolov, 2012, Saxton, 2001). A model for anomalous diffusion in point FRAP experiments have been developed recently (Daddysman and Fecko, 2013). The authors reported that diffusion in HeLa nuclei is anomalous and that GFP seems to diffuse according to normal diffusion in chromatin free regions in polytene *drosophila* nuclei.

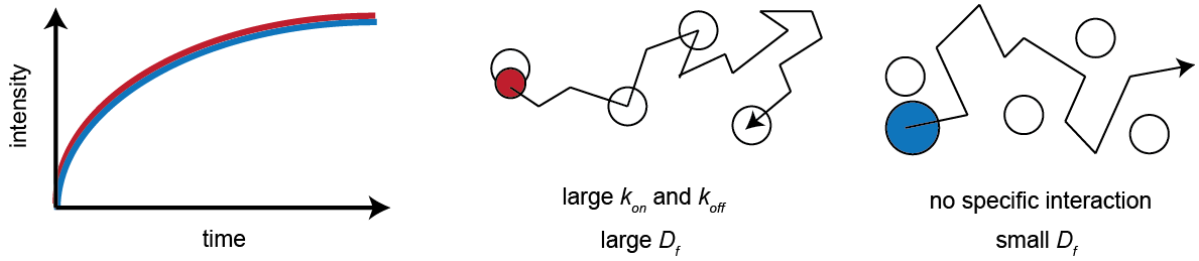

Figure 13: Intermixing of diffusion and binding in FRAP. Very similar FRAP curves can be explained by different kinetic properties of the molecules. Either, molecules that diffuse very fast and have large k_{on} and k_{off} values (red) or molecules that diffuse very slow and have no specific interaction (blue) could result in the illustrated kinetics.

In order to overcome these limitations in the future, cross validation of the results not only with other models, but also with other techniques using fluorescently labeled proteins in living cells should be conducted. The techniques include FCS and SPT. Both methods can be applied to extract diffusion coefficients and residence times. Recently, point FRAP and FCS have even been combined in one setup in order to gain comparable results with both methods (Im et al., 2013). In this way the cross validation is performed in one single experiment. Another approach has used data obtained with SPT in order to choose the correct model for FRAP and FCS analysis (Mazza et al., 2012). Here, all three methods were used to validate the results. With this approach they were able to detect and solve discrepancies in residence time and the fraction of bound protein. FCS is mainly used to determine diffusion rates of proteins, but with fluorescence cross correlation spectroscopy (FCCS) binding kinetics can be specifically determined between two differently labeled proteins and their diffusion coefficients can be directly compared (Schwille et al., 1997). This has the advantage that the binding partner is known, whereas in FRAP experiments this can only be indirectly determined by mutational analysis. Advantages of SPT and FCS are the drastic reduced phototoxic effect compared to FRAP as bleaching is not necessary. However, FRAP provides a much more global picture of dynamics inside a cell.

3.2.4 Application of complementary methods

Besides photobleaching methods, several other tools in fluorescence microscopy enable us to obtain detailed information about spatial and temporal regulation of molecules. Labeling proteins in *in vivo* experiments is commonly used, but DNA sequences have been so far mainly labeled in *in vitro* FISH experiments. We have applied dTALEs to visualize major satellite (ms) repetitive DNA sequences in the

nucleus in living cells (msTALE) (Thanisch et al., 2013). This enabled us to follow the movement of these repetitive sequences during the cell cycle or even differentiation. Instead, fluorescently tagged proteins like HP1 or MBDs have been used to visualize methylated sequences *in vivo*. Disadvantages are that heterochromatin-binding proteins might be specifically regulated in the cell. For instance, HP1 is displaced from chromatin by H3S10 phosphorylation in G2 (Hirota et al., 2005). We showed that our msTALE is still bound in G2, even when HP1 is diffusively localized in the nucleus. Recently, two more publications have also demonstrated the application of dTALEs to label repetitive DNA sequences (Miyanari et al., 2013, Ma et al., 2013). They demonstrated that also repetitive sequences like telomeres or minor satellites can be labeled. Furthermore, application of the bacterial CRISPR/Cas system, which is like the TAL effectors adaptable for site-specific genome engineering, even allowed the detection of single loci (Chen et al., 2013). Our analysis of the binding dynamics by FRAP revealed that the msTALE binds much stronger to DNA than a polydactyl Zn Finger (PZF:GFP) construct directed against a similar sequence (Lindhout et al., 2007). As it has been reported that the localization of DNA influences the transcriptional activity of the corresponding sequences (Reddy et al., 2008), the strong binding of the msTALE could be exploited to manipulate chromatic regions. It has been shown in zygotes that fusion of the nuclear envelope protein emerin to a polydactyl Zn Finger, binding to major satellite sequences, tethers pericentromeric heterochromatin to the nuclear periphery (Jachowicz et al., 2013). The authors found that their manipulation lead to defective silencing of pericentromeric heterochromatin and impaired development of the embryos.

The application of FRAP also gave valuable results for the characterization of other tools. We have used this method to learn about the diffusion of oligonucleotides in nanoparticles. The nanoparticles might be versatile vehicles to enable transport of proteins in single cells or whole tissues. We demonstrated that unfunctionalized and cyanopropyl-functionalized particles cannot be loaded with oligonucleotides (Lebold et al., 2012). Addition of aminopropyl or a combination of aminopropyl and phenyl groups enabled loading of the particles with siRNA. Furthermore it is possible to load fairly long oligonucleotides of 90 base pairs of DNA into the particles. Further fine-tuning of the functionalizations of the particles could result in vectors with different properties, like fast or slow release of nucleic acids, for different purposes. These findings are valuable when it comes to using the nanoparticles as carriers of therapeutics.

Besides labeling and delivery also high resolution spatial information is very valuable. Using super-resolution 3D-SIM microscopy, we analyzed not only in detail the association of Dnmt1 to chromocenters in late S phase, but also the detailed localization of NIPA at the nuclear envelope. We demonstrated that the latter is localized slightly inside the nuclear lamina and the nucleoporin Nup153, but on the same level as its interaction partner TPR. Increasing resolution is also gained with other methods like STED or localization microscopy (PALM, dSTORM). However, these methods lack

the increased z-resolution of 3D-SIM and only a maximum of two labels can be multiplexed (Schermelleh et al., 2010). However, they are being further developed and for localization microscopy first setups have reported an axial resolution of up to 20 nm (Xu et al., 2012).

3.3 Outlook

Besides our new findings and developments, many new ideas and questions are arising. We have shown that FRAP is a very powerful tool to study the nuclear dynamics *in vivo*. Therefore, further developments of this technique are still of great interest. Especially the combination with new technical innovations can extend the applicability of this method. Automation of not only the evaluation, but also the acquisition of imaging data has been further developed. Both, automated detection of cellular features and automated imaging at multiple positions have been demonstrated and the latter is already implicated in many commercial microscopy systems (Held et al., 2010, Conrad and Gerlich, 2010, Edelstein et al., 2010). Recently, these techniques have been combined, enabling automated FRAP on a confocal microscope (Conrad et al., 2011). A low resolution image is acquired in a defined region and immediately analyzed by the software Micropilot (Figure 14). If a cell in this image fulfills the preset requirements, a FRAP experiment with the selected cell is automatically started and recorded. Then, the scanning process is continued by acquisition of further low resolution images in the predefined area. The great advantage of performing experiments with a long recovery time without the need of intermediate user interactions allows the performance of FRAP experiments overnight. RNAi screens using automated confocal imaging have been successfully performed in the past (Neumann et al., 2010). Using Micropilot, FRAP-based screens can be run, gaining information about the localization and the kinetics of the proteins at the same time. Automatic FRAP experiments produce large datasets and generate the requirement for efficient data handling and processing. The macros for FRAP evaluation that have been developed in this thesis, could be further automatized and extended by adding quality criteria to automatically detect factors like z-drift.

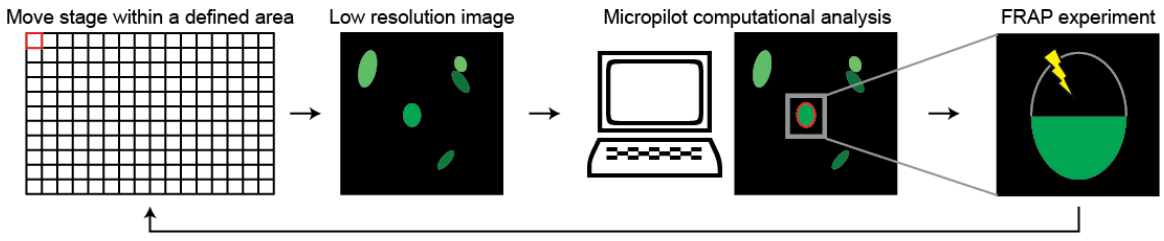

Figure 14: Automatic FRAP experiment. In order to detect cells fulfilling preset requirements, a low resolution image is acquired in a defined area. The image is analyzed by the software Micropilot. If a suitable cell is detected (red outline), a FRAP experiment is started. When the FRAP experiment is finished or If no suitable cell can be detected, the stage is moved and the next low resolution image in the defined area is acquired. The procedure will be repeated until the defined area has been scanned.

Furthermore, the evaluation at a single cell level could be enhanced by measuring the recovery in every pixel. Plotting the results in form of a heat map in the nucleus enhances the spatial resolution of

FRAP and diffusion-coupled kinetics in the nucleus could be illustrated. Usually the presence of diffusion-coupled kinetics is tested in an approach, in which the nucleus is segmented into stripes and differences in the kinetics are analyzed in respect to the distance to the bleach border (Beaudouin et al., 2006). In order to gain more resolution in FRAP experiments, one could also think of implementing a scanning system for bleaching in the widefield path of 3D-SIM microscopes that are fast enough for super-resolution live cell imaging (Shao et al., 2011). The fusion of both methods would allow maps of protein dynamics in relation to a marker protein with very high resolution.

Not only technical issues need to be addressed. Due to recent findings, new questions emerged regarding epigenetics and especially Dnmt1. Recently, mutations in Dnmt1 have been linked to the diseases hereditary sensory and autonomic neuropathy type 1 (HSAN1) and autosomal dominant cerebellar ataxia, deafness and narcolepsy (ADCA-DN) (Winkelmann et al., 2012, Klein et al., 2011). Interestingly, all mutations were located in the TS domain. It will be interesting to apply our knowledge about Dnmt1 in order to unravel how Dnmt1 is mechanistically linked to this disease. Furthermore, discoveries about the influence of factors like RNA on Dnmt1 regulation have been made. They revealed that non-coding RNAs block Dnmt1-mediated methylation at a large number of gene loci (Di Ruscio et al., 2013). Using deep sequencing of RNA, DNA methylation in combination with proteomics, global information about the regulation of DNA methylation will be unraveled that is not anymore limited to single loci. Most importantly, the discovery of Tet proteins and their DNA modifications hmC, fC and caC has opened a new field of questions concerning the role and regulation of epigenetic marks that need to be addressed.

In the future highly sophisticated techniques will be more and more important in order to understand biological questions. The interconnection of biological research and technology will help us to understand the dynamic regulation of epigenetic mechanisms in living cells, leading to further insights into the functional role of epigenetics during development and disease.

4. Annex

4.1 References

Achour, M., Jacq, X., Ronde, P., Alhosin, M., Charlot, C., Chataigneau, T., Jeanblanc, M., Macaluso, M., Giordano, A., Hughes, A. D., Schini-Kerth, V. B. & Bronner, C. 2008. The interaction of the SRA domain of ICBP90 with a novel domain of DNMT1 is involved in the regulation of VEGF gene expression. *Oncogene,* 27**,** 2187-97.

Akaike, H. 1973. Information theory and an extension of the maximum likelihood principle. *In:* PETROV, B. N. & CSAKI, F. (eds.) *2nd International Symposium on Information Theory.* Budapest: Akademiai Kiado.

Aran, D., Toperoff, G., Rosenberg, M. & Hellman, A. 2011. Replication timing-related and gene body-specific methylation of active human genes. *Hum Mol Genet,* 20**,** 670-80.

Arita, K., Ariyoshi, M., Tochio, H., Nakamura, Y. & Shirakawa, M. 2008. Recognition of hemi-methylated DNA by the SRA protein UHRF1 by a base-flipping mechanism. *Nature*.

Avvakumov, G. V., Walker, J. R., Xue, S., Li, Y., Duan, S., Bronner, C., Arrowsmith, C. H. & Dhe-Paganon, S. 2008. Structural basis for recognition of hemi-methylated DNA by the SRA domain of human UHRF1. *Nature,* 455**,** 822-5.

Axelrod, D., Koppel, D. E., Schlessinger, J., Elson, E. & Webb, W. W. 1976. Mobility measurement by analysis of fluorescence photobleaching recovery kinetics. *Biophysical Journal,* 16**,** 1055-1069.

Bancaud, A., Huet, S., Daigle, N., Mozziconacci, J., Beaudouin, J. & Ellenberg, J. 2009. Molecular crowding affects diffusion and binding of nuclear proteins in heterochromatin and reveals the fractal organization of chromatin. *EMBO J,* 28**,** 3785-98.

Bashtrykov, P., Jankevicius, G., Jurkowska, R. Z., Ragozin, S. & Jeltsch, A. 2013. The Uhrf1 protein stimulates the activity and specificity of the maintenance DNA methyltransferase Dnmt1 by an allosteric mechanism. *J Biol Chem*.

Bashtrykov, P., Jankevicius, G., Smarandache, A., Jurkowska, R. Z., Ragozin, S. & Jeltsch, A. 2012. Specificity of Dnmt1 for methylation of hemimethylated CpG sites resides in its catalytic domain. *Chem Biol,* 19**,** 572-8.

Bassermann, F., Von Klitzing, C., Munch, S., Bai, R. Y., Kawaguchi, H., Morris, S. W., Peschel, C. & Duyster, J. 2005. NIPA defines an SCF-type mammalian E3 ligase that regulates mitotic entry. *Cell,* 122**,** 45-57.

Bassett, A., Cooper, S., Wu, C. & Travers, A. 2009. The folding and unfolding of eukaryotic chromatin. *Curr Opin Genet Dev,* 19**,** 159-65.

Beaudouin, J., Mora-Bermudez, F., Klee, T., Daigle, N. & Ellenberg, J. 2006. Dissecting the contribution of diffusion and interactions to the mobility of nuclear proteins. *Biophys J,* 90**,** 1878-94.

Berman, B. P., Weisenberger, D. J., Aman, J. F., Hinoue, T., Ramjan, Z., Liu, Y., Noushmehr, H., Lange, C. P., Van Dijk, C. M., Tollenaar, R. A., Van Den Berg, D. & Laird, P. W. 2012. Regions of focal DNA hypermethylation and long-range hypomethylation in colorectal cancer coincide with nuclear lamina-associated domains. *Nat Genet,* 44**,** 40-6.

Bernstein, E. & Hake, S. B. 2006. The nucleosome: a little variation goes a long way. *Biochem Cell Biol,* 84**,** 505-17.

Bestor, T., Laudano, A., Mattaliano, R. & Ingram, V. 1988. Cloning and sequencing of a cDNA encoding DNA methyltransferase of mouse cells. The carboxyl-terminal domain of the mammalian enzymes is related to bacterial restriction methyltransferases. *J Mol Biol,* 203**,** 971-83.

Bestor, T. H. 1992. Activation of mammalian DNA methyltransferase by cleavage of a Zn binding regulatory domain. *EMBO J,* 11**,** 2611-7.

Bestor, T. H. 2000. The DNA methyltransferases of mammals. *Hum Mol Genet,* 9**,** 2395-402.

Billon, P. & Cote, J. 2012. Precise deposition of histone H2A.Z in chromatin for genome expression and maintenance. *Biochim Biophys Acta,* 1819**,** 290-302.

Bird, A. 2002. DNA methylation patterns and epigenetic memory. *Genes Dev,* 16**,** 6-21.

Bird, A. 2007. Perceptions of epigenetics. *Nature,* 447**,** 396-8.

Bird, A., Taggart, M., Frommer, M., Miller, O. J. & Macleod, D. 1985. A fraction of the mouse genome that is derived from islands of nonmethylated, CpG-rich DNA. *Cell,* 40**,** 91-9.

Boch, J., Scholze, H., Schornack, S., Landgraf, A., Hahn, S., Kay, S., Lahaye, T., Nickstadt, A. & Bonas, U. 2009. Breaking the code of DNA binding specificity of TAL-type III effectors. *Science,* 326**,** 1509-12.

Bonisch, C. & Hake, S. B. 2012. Histone H2A variants in nucleosomes and chromatin: more or less stable? *Nucleic Acids Res,* 40**,** 10719-41.

Bonisch, C., Schneider, K., Punzeler, S., Wiedemann, S. M., Bielmeier, C., Bocola, M., Eberl, H. C., Kuegel, W., Neumann, J., Kremmer, E., Leonhardt, H., Mann, M., Michaelis, J., Schermelleh, L. & Hake, S. B. 2012. H2A.Z.2.2 is an alternatively spliced histone H2A.Z variant that causes severe nucleosome destabilization. *Nucleic Acids Res,* 40**,** 5951-64.

Bostick, M., Kim, J. K., Esteve, P. O., Clark, A., Pradhan, S. & Jacobsen, S. E. 2007. UHRF1 plays a role in maintaining DNA methylation in mammalian cells. *Science,* 317**,** 1760-4.

Bourgeois, D., Regis-Faro, A. & Adam, V. 2012. Photoactivated structural dynamics of fluorescent proteins. *Biochem Soc Trans,* 40**,** 531-8.

Braga, J., Desterro, J. M. & Carmo-Fonseca, M. 2004. Intracellular macromolecular mobility measured by fluorescence recovery after photobleaching with confocal laser scanning microscopes. *Mol Biol Cell,* 15**,** 4749-60.

Braga, J., Mcnally, J. G. & Carmo-Fonseca, M. 2007. A reaction-diffusion model to study RNA motion by quantitative fluorescence recovery after photobleaching. *Biophys J,* 92**,** 2694-703.

Brenet, F., Moh, M., Funk, P., Feierstein, E., Viale, A. J., Socci, N. D. & Scandura, J. M. 2011. DNA methylation of the first exon is tightly linked to transcriptional silencing. *PLoS One,* 6**,** e14524.

Bronner, C., Achour, M., Arima, Y., Chataigneau, T., Saya, H. & Schini-Kerth, V. B. 2007. The UHRF family: oncogenes that are drugable targets for cancer therapy in the near future? *Pharmacol Ther,* 115**,** 419-34.

Bronner, C., Krifa, M. & Mousli, M. 2013. Increasing role of UHRF1 in the reading and inheritance of the epigenetic code as well as in tumorogenesis. *Biochem Pharmacol*.

Buck-Koehntop, B. A. & Defossez, P. A. 2013. On how mammalian transcription factors recognize methylated DNA. *Epigenetics,* 8**,** 131-7.

Cardoso, M. C. & Leonhardt, H. 1999. DNA methyltransferase is actively retained in the cytoplasm during early development. *J Cell Biol,* 147**,** 25-32.

Casas-Delucchi, C. S., Van Bemmel, J. G., Haase, S., Herce, H. D., Nowak, D., Meilinger, D., Stear, J. H., Leonhardt, H. & Cardoso, M. C. 2012. Histone hypoacetylation is required to maintain late replication timing of constitutive heterochromatin. *Nucleic Acids Res,* 40**,** 159-69.

Cauda, V., Schlossbauer, A., Kecht, J., Zurner, A. & Bein, T. 2009. Multiple core-shell functionalized colloidal mesoporous silica nanoparticles. *J Am Chem Soc,* 131**,** 11361-70.

Cedar, H. & Bergman, Y. 2009. Linking DNA methylation and histone modification: patterns and paradigms. *Nat Rev Genet,* 10**,** 295-304.

Cerda, M. C., Berrios, S., Fernandez-Donoso, R., Garagna, S. & Redi, C. 1999. Organisation of complex nuclear domains in somatic mouse cells. *Biol Cell,* 91**,** 55-65.

Chen, B., Gilbert, L. A., Cimini, B. A., Schnitzbauer, J., Zhang, W., Li, G. W., Park, J., Blackburn, E. H., Weissman, J. S., Qi, L. S. & Huang, B. 2013. Dynamic Imaging of Genomic Loci in Living Human Cells by an Optimized CRISPR/Cas System. *Cell,* 155**,** 1479-91.

Chen, C. C., Wang, K. Y. & Shen, C. K. 2012. The mammalian de novo DNA methyltransferases DNMT3A and DNMT3B are also DNA 5-hydroxymethylcytosine dehydroxymethylases. *J Biol Chem,* 287**,** 33116-21.

Cheng, J., Yang, Y., Fang, J., Xiao, J., Zhu, T., Chen, F., Wang, P., Li, Z., Yang, H. & Xu, Y. 2013. Structural insight into coordinated recognition of trimethylated histone H3 lysine 9 (H3K9me3) by the plant homeodomain (PHD) and tandem tudor domain (TTD) of UHRF1 (ubiquitin-like, containing PHD and RING finger domains, 1) protein. *J Biol Chem,* 288**,** 1329-39.

Cheng, X. 1995. Structure and function of DNA methyltransferases. *Annu Rev Biophys Biomol Struct,* 24**,** 293-318.

Cheutin, T., Mcnairn, A. J., Jenuwein, T., Gilbert, D. M., Singh, P. B. & Misteli, T. 2003. Maintenance of stable heterochromatin domains by dynamic HP1 binding. *Science,* 299**,** 721-5.

Choufani, S., Shuman, C. & Weksberg, R. 2013. Molecular findings in Beckwith-Wiedemann syndrome. *Am J Med Genet C Semin Med Genet,* 163C**,** 131-40.

Christianson, J. C. & Ye, Y. 2014. Cleaning up in the endoplasmic reticulum: ubiquitin in charge. *Nat Struct Mol Biol,* 21**,** 325-35.

Chuang, L. S.-H., Ian, H.-I., Koh, T.-W., Ng, H.-H., Xu, G. & Li, B. F. L. 1997. Human DNA-(Cytosine-5) Methyltransferase-PCNA Complex as a Target for p21WAF1. *Science,* 277**,** 1996-2000.

Citterio, E., Papait, R., Nicassio, F., Vecchi, M., Gomiero, P., Mantovani, R., Di Fiore, P. P. & Bonapace, I. M. 2004. Np95 Is a Histone-Binding Protein Endowed with Ubiquitin Ligase Activity. *Molecular and Cellular Biology,* 24**,** 2526-2535.

Collings, C. K., Waddell, P. J. & Anderson, J. N. 2013. Effects of DNA methylation on nucleosome stability. *Nucleic Acids Res,* 41**,** 2918-31.

Conerly, M. L., Teves, S. S., Diolaiti, D., Ulrich, M., Eisenman, R. N. & Henikoff, S. 2010. Changes in H2A.Z occupancy and DNA methylation during B-cell lymphomagenesis. *Genome Res,* 20**,** 1383-90.

Conrad, C. & Gerlich, D. W. 2010. Automated microscopy for high-content RNAi screening. *J Cell Biol,* 188**,** 453-61.

Conrad, C., Wunsche, A., Tan, T. H., Bulkescher, J., Sieckmann, F., Verissimo, F., Edelstein, A., Walter, T., Liebel, U., Pepperkok, R. & Ellenberg, J. 2011. Micropilot: automation of fluorescence microscopy-based imaging for systems biology. *Nat Methods,* 8**,** 246-9.

Cosgrove, M. S., Boeke, J. D. & Wolberger, C. 2004. Regulated nucleosome mobility and the histone code. *Nat Struct Mol Biol,* 11**,** 1037-43.

Crivat, G. & Taraska, J. W. 2012. Imaging proteins inside cells with fluorescent tags. *Trends Biotechnol,* 30**,** 8-16.

Daddysman, M. K. & Fecko, C. J. 2013. Revisiting point FRAP to quantitatively characterize anomalous diffusion in live cells. *J Phys Chem B,* 117**,** 1241-51.

Darzacq, X., Shav-Tal, Y., De Turris, V., Brody, Y., Shenoy, S. M., Phair, R. D. & Singer, R. H. 2007. In vivo dynamics of RNA polymerase II transcription. *Nat Struct Mol Biol,* 14**,** 796-806.

Dawson, M. A. & Kouzarides, T. 2012. Cancer epigenetics: from mechanism to therapy. *Cell,* 150**,** 12-27.

Di Ruscio, A., Ebralidze, A. K., Benoukraf, T., Amabile, G., Goff, L. A., Terragni, J., Figueroa, M. E., De Figueiredo Pontes, L. L., Alberich-Jorda, M., Zhang, P., Wu, M., D'alo, F., Melnick, A., Leone, G., Ebralidze, K. K., Pradhan, S., Rinn, J. L. & Tenen, D. G. 2013. DNMT1-interacting RNAs block gene-specific DNA methylation. *Nature*.

Dickson, R. M., Cubitt, A. B., Tsien, R. Y. & Moerner, W. E. 1997. On/off blinking and switching behaviour of single molecules of green fluorescent protein. *Nature,* 388**,** 355-8.

Digman, M. A. & Gratton, E. 2012. Scanning image correlation spectroscopy. *Bioessays,* 34**,** 377-85.

Dimitrova, D. S. & Berezney, R. 2002. The spatio-temporal organization of DNA replication sites is identical in primary, immortalized and transformed mammalian cells. *J Cell Sci,* 115**,** 4037-51.

Dobrucki, J. W., Feret, D. & Noatynska, A. 2007. Scattering of exciting light by live cells in fluorescence confocal imaging: phototoxic effects and relevance for FRAP studies. *Biophys J,* 93**,** 1778-86.

Dong, A., Yoder, J. A., Zhang, X., Zhou, L., Bestor, T. H. & Cheng, X. 2001. Structure of human DNMT2, an enigmatic DNA methyltransferase homolog that displays denaturant-resistant binding to DNA. *Nucleic Acids Res,* 29**,** 439-48.

Du, Z., Song, J., Wang, Y., Zhao, Y., Guda, K., Yang, S., Kao, H. Y., Xu, Y., Willis, J., Markowitz, S. D., Sedwick, D., Ewing, R. M. & Wang, Z. 2010. DNMT1 stability is regulated by proteins coordinating deubiquitination and acetylation-driven ubiquitination. *Sci Signal,* 3**,** ra80.

Easwaran, H. P., Schermelleh, L., Leonhardt, H. & Cardoso, M. C. 2004. Replication-independent chromatin loading of Dnmt1 during G2 and M phases. *EMBO Rep,* 5**,** 1181-6.

Edelstein, A., Amodaj, N., Hoover, K., Vale, R. & Stuurman, N. 2010. Computer control of microscopes using microManager. *Curr Protoc Mol Biol,* Chapter 14**,** Unit14 20.

Ellis, R. J. 2006. Molecular chaperones: assisting assembly in addition to folding. *Trends Biochem Sci,* 31**,** 395-401.

Esteller, M. 2011. Epigenetic changes in cancer. *F1000 Biol Rep,* 3**,** 9.

Esteve, P. O., Chang, Y., Samaranayake, M., Upadhyay, A. K., Horton, J. R., Feehery, G. R., Cheng, X. & Pradhan, S. 2011. A methylation and phosphorylation switch between an adjacent lysine and serine determines human DNMT1 stability. *Nat Struct Mol Biol,* 18**,** 42-8.

Feinberg, A. P. 2007. Phenotypic plasticity and the epigenetics of human disease. *Nature,* 447**,** 433-40.

Felle, M., Hoffmeister, H., Rothammer, J., Fuchs, A., Exler, J. H. & Langst, G. 2011a. Nucleosomes protect DNA from DNA methylation in vivo and in vitro. *Nucleic Acids Res,* 39**,** 6956-69.

Felle, M., Joppien, S., Nemeth, A., Diermeier, S., Thalhammer, V., Dobner, T., Kremmer, E., Kappler, R. & Langst, G. 2011b. The USP7/Dnmt1 complex stimulates the DNA methylation activity of Dnmt1 and regulates the stability of UHRF1. *Nucleic Acids Res,* 39**,** 8355-65.

Fellinger, K., Rothbauer, U., Felle, M., Langst, G. & Leonhardt, H. 2009. Dimerization of DNA methyltransferase 1 is mediated by its regulatory domain. *J Cell Biochem,* 106**,** 521-8.

Feng, S., Cokus, S. J., Zhang, X., Chen, P. Y., Bostick, M., Goll, M. G., Hetzel, J., Jain, J., Strauss, S. H., Halpern, M. E., Ukomadu, C., Sadler, K. C., Pradhan, S., Pellegrini, M. & Jacobsen, S. E. 2010. Conservation and divergence of methylation patterning in plants and animals. *Proc Natl Acad Sci U S A,* 107**,** 8689-94.

Fournier, A., Sasai, N., Nakao, M. & Defossez, P. A. 2012. The role of methyl-binding proteins in chromatin organization and epigenome maintenance. *Brief Funct Genomics,* 11**,** 251-64.

Frauer, C. & Leonhardt, H. 2009. A versatile non-radioactive assay for DNA methyltransferase activity and DNA binding. *Nucleic Acids Res,* 37**,** e22.

Frauer, C. & Leonhardt, H. 2011. Twists and turns of DNA methylation. *Proc Natl Acad Sci U S A,* 108**,** 8919-20.

Frauer, C., Rottach, A., Meilinger, D., Bultmann, S., Fellinger, K., Hasenoder, S., Wang, M., Qin, W., Soding, J., Spada, F. & Leonhardt, H. 2011. Different binding properties and function of CXXC zinc finger domains in Dnmt1 and Tet1. *PLoS One,* 6**,** e16627.

Fujimori, A., Matsuda, Y., Takemoto, Y., Hashimoto, Y., Kubo, E., Araki, R., Fukumura, R., Mita, K., Tatsumi, K. & Muto, M. 1998. Cloning and mapping of Np95 gene which encodes a novel nuclear protein associated with cell proliferation. *Mamm Genome,* 9**,** 1032-5.

Gamble, M. & Kraus, W. L. 2010. Multiple facets of the unique histone variant macroH2A: From genomics to cell biology. *Cell Cycle,* 9**,** 70-69.

Gautier, T., Abbott, D. W., Molla, A., Verdel, A., Ausio, J. & Dimitrov, S. 2004. Histone variant H2ABbd confers lower stability to the nucleosome. *EMBO Rep,* 5**,** 715-20.

Giri, S., Trewyn, B. G. & Lin, V. S. 2007. Mesoporous silica nanomaterial-based biotechnological and biomedical delivery systems. *Nanomedicine (Lond),* 2**,** 99-111.

Goldman, M. A., Holmquist, G. P., Gray, M. C., Caston, L. A. & Nag, A. 1984. Replication timing of genes and middle repetitive sequences. *Science,* 224**,** 686-92.

Goldman, R. D. & Spector, D. L. 2005. *Live cell imaging : a laboratory manual,* Cold Spring Harbor, N.Y., Cold Spring Harbor Laboratory Press.

Goll, M. G. & Bestor, T. H. 2005. Eukaryotic cytosine methyltransferases. *Annu Rev Biochem,* 74**,** 481-514.

Goll, M. G., Kirpekar, F., Maggert, K. A., Yoder, J. A., Hsieh, C. L., Zhang, X., Golic, K. G., Jacobsen, S. E. & Bestor, T. H. 2006. Methylation of tRNAAsp by the DNA methyltransferase homolog Dnmt2. *Science,* 311**,** 395-8.

Gorski, S. A., Dundr, M. & Misteli, T. 2006. The road much traveled: trafficking in the cell nucleus. *Curr Opin Cell Biol,* 18**,** 284-90.

Guo, J. U., Su, Y., Zhong, C., Ming, G. L. & Song, H. 2011. Hydroxylation of 5-methylcytosine by TET1 promotes active DNA demethylation in the adult brain. *Cell,* 145**,** 423-34.

Hagen, G. M., Caarls, W., Lidke, K. A., De Vries, A. H., Fritsch, C., Barisas, B. G., Arndt-Jovin, D. J. & Jovin, T. M. 2009. Fluorescence recovery after photobleaching and photoconversion in multiple arbitrary regions of interest using a programmable array microscope. *Microsc Res Tech,* 72**,** 431-40.

Halfmann, R. & Lindquist, S. 2010. Epigenetics in the extreme: prions and the inheritance of environmentally acquired traits. *Science,* 330**,** 629-32.

Hannum, G., Guinney, J., Zhao, L., Zhang, L., Hughes, G., Sadda, S., Klotzle, B., Bibikova, M., Fan, J. B., Gao, Y., Deconde, R., Chen, M., Rajapakse, I., Friend, S., Ideker, T. & Zhang, K. 2013. Genome-wide methylation profiles reveal quantitative views of human aging rates. *Mol Cell,* 49**,** 359-67.

Hashimoto, H., Horton, J. R., Zhang, X., Bostick, M., Jacobsen, S. E. & Cheng, X. 2008. The SRA domain of UHRF1 flips 5-methylcytosine out of the DNA helix. *Nature,* 455**,** 826-9.

Hashimoto, H., Liu, Y., Upadhyay, A. K., Chang, Y., Howerton, S. B., Vertino, P. M., Zhang, X. & Cheng, X. 2012. Recognition and potential mechanisms for replication and erasure of cytosine hydroxymethylation. *Nucleic Acids Res,* 40**,** 4841-9.

Held, M., Schmitz, M. H., Fischer, B., Walter, T., Neumann, B., Olma, M. H., Peter, M., Ellenberg, J. & Gerlich, D. W. 2010. CellCognition: time-resolved phenotype annotation in high-throughput live cell imaging. *Nat Methods,* 7**,** 747-54.

Hemmerich, P., Schmiedeberg, L. & Diekmann, S. 2011. Dynamic as well as stable protein interactions contribute to genome function and maintenance. *Chromosome Res,* 19**,** 131-51.

Henderson, I. R. & Jacobsen, S. E. 2007. Epigenetic inheritance in plants. *Nature,* 447**,** 418-24.

Hermann, A., Schmitt, S. & Jeltsch, A. 2003. The human Dnmt2 has residual DNA-(cytosine-C5) methyltransferase activity. *J Biol Chem,* 278**,** 31717-21.

Hiratani, I., Ryba, T., Itoh, M., Yokochi, T., Schwaiger, M., Chang, C. W., Lyou, Y., Townes, T. M., Schubeler, D. & Gilbert, D. M. 2008. Global reorganization of replication domains during embryonic stem cell differentiation. *PLoS Biol,* 6**,** e245.

Hirota, T., Lipp, J. J., Toh, B. H. & Peters, J. M. 2005. Histone H3 serine 10 phosphorylation by Aurora B causes HP1 dissociation from heterochromatin. *Nature,* 438**,** 1176-80.

Hopfner, R., Mousli, M., Jeltsch, J. M., Voulgaris, A., Lutz, Y., Marin, C., Bellocq, J. P., Oudet, P. & Bronner, C. 2000. ICBP90, a novel human CCAAT binding protein, involved in the regulation of topoisomerase IIalpha expression. *Cancer Res,* 60**,** 121-8.

Illert, A. L., Zech, M., Moll, C., Albers, C., Kreutmair, S., Peschel, C., Bassermann, F. & Duyster, J. 2012. Extracellular signal-regulated kinase 2 (ERK2) mediates phosphorylation and inactivation of nuclear interaction partner of anaplastic lymphoma kinase (NIPA) at G2/M. *J Biol Chem,* 287**,** 37997-8005.

Illingworth, R. S., Gruenewald-Schneider, U., Webb, S., Kerr, A. R., James, K. D., Turner, D. J., Smith, C., Harrison, D. J., Andrews, R. & Bird, A. P. 2010. Orphan CpG islands identify numerous conserved promoters in the mammalian genome. *PLoS Genet,* 6**,** e1001134.

Im, K. B., Schmidt, U., Kang, M. S., Lee, J. Y., Bestvater, F. & Wachsmuth, M. 2013. Diffusion and binding analyzed with combined point FRAP and FCS. *Cytometry A,* 83**,** 876-89.

Indiani, C. & O'donnell, M. 2006. The replication clamp-loading machine at work in the three domains of life. *Nat Rev Mol Cell Biol,* 7**,** 751-61.

Ishikawa-Ankerhold, H. C., Ankerhold, R. & Drummen, G. P. 2012. Advanced fluorescence microscopy techniques--FRAP, FLIP, FLAP, FRET and FLIM. *Molecules,* 17**,** 4047-132.

Ito, S., Shen, L., Dai, Q., Wu, S. C., Collins, L. B., Swenberg, J. A., He, C. & Zhang, Y. 2011. Tet proteins can convert 5-methylcytosine to 5-formylcytosine and 5-carboxylcytosine. *Science,* 333**,** 1300-3.

Iwata, A., Nagashima, Y., Matsumoto, L., Suzuki, T., Yamanaka, T., Date, H., Deoka, K., Nukina, N. & Tsuji, S. 2009. Intranuclear degradation of polyglutamine aggregates by the ubiquitin-proteasome system. *J Biol Chem,* 284**,** 9796-803.

Jachowicz, J. W., Santenard, A., Bender, A., Muller, J. & Torres-Padilla, M. E. 2013. Heterochromatin establishment at pericentromeres depends on nuclear position. *Genes Dev,* 27**,** 2427-32.

Jeltsch, A. 2006. On the enzymatic properties of Dnmt1: specificity, processivity, mechanism of linear diffusion and allosteric regulation of the enzyme. *Epigenetics,* 1**,** 63-6.

Joffe, B., Leonhardt, H. & Solovei, I. 2010. Differentiation and large scale spatial organization of the genome. *Curr Opin Genet Dev,* 20**,** 562-9.

Jurkowska, R. Z., Jurkowski, T. P. & Jeltsch, A. 2011. Structure and function of mammalian DNA methyltransferases. *Chembiochem,* 12**,** 206-22.

Kaminskas, E., Farrell, A. T., Wang, Y. C., Sridhara, R. & Pazdur, R. 2005. FDA drug approval summary: azacitidine (5-azacytidine, Vidaza) for injectable suspension. *Oncologist,* 10**,** 176-82.

Kang, M., Day, C. A., Kenworthy, A. K. & Dibenedetto, E. 2012. Simplified equation to extract diffusion coefficients from confocal FRAP data. *Traffic,* 13**,** 1589-600.

Karagianni, P., Amazit, L., Qin, J. & Wong, J. 2008. ICBP90, a novel methyl K9 H3 binding protein linking protein ubiquitination with heterochromatin formation. *Mol Cell Biol,* 28**,** 705-17.

Kemp, M. G., Ghosh, M., Liu, G. & Leffak, M. 2005. The histone deacetylase inhibitor trichostatin A alters the pattern of DNA replication origin activity in human cells. *Nucleic Acids Res,* 33**,** 325-36.

Kimura, H., Hayashi-Takanaka, Y. & Yamagata, K. 2010. Visualization of DNA methylation and histone modifications in living cells. *Curr Opin Cell Biol,* 22**,** 412-8.

Kirstein, J., Platschek, B., Jung, C., Brown, R., Bein, T. & Brauchle, C. 2007. Exploration of nanostructured channel systems with single-molecule probes. *Nat Mater,* 6**,** 303-10.

Klein, C. J., Botuyan, M. V., Wu, Y., Ward, C. J., Nicholson, G. A., Hammans, S., Hojo, K., Yamanishi, H., Karpf, A. R., Wallace, D. C., Simon, M., Lander, C., Boardman, L. A., Cunningham, J. M., Smith, G. E., Litchy, W. J., Boes, B., Atkinson, E. J., Middha, S., Pj, B. D., Parisi, J. E., Mer, G., Smith, D. I. & Dyck, P. J. 2011. Mutations in DNMT1 cause hereditary sensory neuropathy with dementia and hearing loss. *Nat Genet,* 43**,** 595-600.

Koster, M., Frahm, T. & Hauser, H. 2005. Nucleocytoplasmic shuttling revealed by FRAP and FLIP technologies. *Curr Opin Biotechnol,* 16**,** 28-34.

Kouzarides, T. 2007. Chromatin modifications and their function. *Cell,* 128**,** 693-705.

Lande-Diner, L., Zhang, J., Ben-Porath, I., Amariglio, N., Keshet, I., Hecht, M., Azuara, V., Fisher, A. G., Rechavi, G. & Cedar, H. 2007. Role of DNA methylation in stable gene repression. *J Biol Chem,* 282**,** 12194-200.

Lebold, T., Schlossbauer, A., Schneider, K., Schermelleh, L., Leonhardt, H., Bein, T. & Bräuchle, C. 2012. Controlling The Mobility Of Oligonucleotides In The Nanochannels Of Mesoporous Silica. *Advanced Functional Materials,* 22**,** 106-112.

Lee, B. & Muller, M. T. 2009. SUMOylation enhances DNA methyltransferase 1 activity. *Biochem J,* 421**,** 449-61.

Lee, J. Y. & Lee, T. H. 2012. Effects of DNA methylation on the structure of nucleosomes. *J Am Chem Soc,* 134**,** 173-5.

Leonhardt, H., Page, A. W., Weier, H. U. & Bestor, T. H. 1992. A targeting sequence directs DNA methyltransferase to sites of DNA replication in mammalian nuclei. *Cell,* 71**,** 865-73.

Leonhardt, H., Rahn, H. P., Weinzierl, P., Sporbert, A., Cremer, T., Zink, D. & Cardoso, M. C. 2000. Dynamics of DNA replication factories in living cells. *J Cell Biol,* 149**,** 271-80.

Li, E., Bestor, T. H. & Jaenisch, R. 1992. Targeted mutation of the DNA methyltransferase gene results in embryonic lethality. *Cell,* 69**,** 915-26.

Li, G. & Reinberg, D. 2011. Chromatin higher-order structures and gene regulation. *Curr Opin Genet Dev,* 21**,** 175-86.

Lindhout, B. I., Fransz, P., Tessadori, F., Meckel, T., Hooykaas, P. J. & Van Der Zaal, B. J. 2007. Live cell imaging of repetitive DNA sequences via GFP-tagged polydactyl zinc finger proteins. *Nucleic Acids Res,* 35**,** e107.

Lister, R., Pelizzola, M., Dowen, R. H., Hawkins, R. D., Hon, G., Tonti-Filippini, J., Nery, J. R., Lee, L., Ye, Z., Ngo, Q. M., Edsall, L., Antosiewicz-Bourget, J., Stewart, R., Ruotti, V., Millar, A. H., Thomson, J. A., Ren, B. & Ecker, J. R. 2009. Human DNA methylomes at base resolution show widespread epigenomic differences. *Nature,* 462**,** 315-22.

Liu, X., Gao, Q., Li, P., Zhao, Q., Zhang, J., Li, J., Koseki, H. & Wong, J. 2013a. UHRF1 targets DNMT1 for DNA methylation through cooperative binding of hemi-methylated DNA and methylated H3K9. *Nat Commun,* 4**,** 1563.

Liu, Y., Aryee, M. J., Padyukov, L., Fallin, M. D., Hesselberg, E., Runarsson, A., Reinius, L., Acevedo, N., Taub, M., Ronninger, M., Shchetynsky, K., Scheynius, A., Kere, J., Alfredsson, L., Klareskog, L., Ekstrom, T. J. & Feinberg, A. P. 2013b. Epigenome-wide association data implicate DNA

methylation as an intermediary of genetic risk in rheumatoid arthritis. *Nat Biotechnol,* 31**,** 142-7.

Liu, Y., Oakeley, E. J., Sun, L. & Jost, J. P. 1998. Multiple domains are involved in the targeting of the mouse DNA methyltransferase to the DNA replication foci. *Nucleic Acids Res,* 26**,** 1038-45.

Luger, K. 2006. Dynamic nucleosomes. *Chromosome Res,* 14**,** 5-16.

Luger, K., Mader, A. W., Richmond, R. K., Sargent, D. F. & Richmond, T. J. 1997. Crystal structure of the nucleosome core particle at 2.8 A resolution. *Nature,* 389**,** 251-60.

Ma, H., Reyes-Gutierrez, P. & Pederson, T. 2013. Visualization of repetitive DNA sequences in human chromosomes with transcription activator-like effectors. *Proc Natl Acad Sci U S A*.

Maeshima, K., Hihara, S. & Eltsov, M. 2010. Chromatin structure: does the 30-nm fibre exist in vivo? *Curr Opin Cell Biol,* 22**,** 291-7.

Mai, J., Trump, S., Ali, R., Schiltz, R. L., Hager, G., Hanke, T., Lehmann, I. & Attinger, S. 2011. Are assumptions about the model type necessary in reaction-diffusion modeling? A FRAP application. *Biophys J,* 100**,** 1178-88.

Mai, J., Trump, S., Lehmann, I. & Attinger, S. 2013. Parameter importance in FRAP acquisition and analysis: a simulation approach. *Biophys J,* 104**,** 2089-97.

Mai, W. X. & Meng, H. 2013. Mesoporous silica nanoparticles: A multifunctional nano therapeutic system. *Integr Biol (Camb),* 5**,** 19-28.

Mak, A. N., Bradley, P., Bogdanove, A. J. & Stoddard, B. L. 2013. TAL effectors: function, structure, engineering and applications. *Curr Opin Struct Biol,* 23**,** 93-9.

Margot, J. B., Aguirre-Arteta, A. M., Di Giacco, B. V., Pradhan, S., Roberts, R. J., Cardoso, M. C. & Leonhardt, H. 2000. Structure and function of the mouse DNA methyltransferase gene: Dnmt1 shows a tripartite structure. *J Mol Biol,* 297**,** 293-300.

Margot, J. B., Ehrenhofer-Murray, A. E. & Leonhardt, H. 2003. Interactions within the mammalian DNA methyltransferase family. *BMC Mol Biol,* 4**,** 7.

Marzluff, W. F., Wagner, E. J. & Duronio, R. J. 2008. Metabolism and regulation of canonical histone mRNAs: life without a poly(A) tail. *Nat Rev Genet,* 9**,** 843-54.

Mateescu, B., England, P., Halgand, F., Yaniv, M. & Muchardt, C. 2004. Tethering of HP1 proteins to chromatin is relieved by phosphoacetylation of histone H3. *EMBO Rep,* 5**,** 490-6.

Maunakea, A. K., Nagarajan, R. P., Bilenky, M., Ballinger, T. J., D'souza, C., Fouse, S. D., Johnson, B. E., Hong, C., Nielsen, C., Zhao, Y., Turecki, G., Delaney, A., Varhol, R., Thiessen, N., Shchors, K., Heine, V. M., Rowitch, D. H., Xing, X., Fiore, C., Schillebeeckx, M., Jones, S. J., Haussler, D., Marra, M. A., Hirst, M., Wang, T. & Costello, J. F. 2010. Conserved role of intragenic DNA methylation in regulating alternative promoters. *Nature,* 466**,** 253-7.

Mazza, D., Abernathy, A., Golob, N., Morisaki, T. & Mcnally, J. G. 2012. A benchmark for chromatin binding measurements in live cells. *Nucleic Acids Res,* 40**,** e119.

Mazza, D., Cella, F., Vicidomini, G., Krol, S. & Diaspro, A. 2007. Role of three-dimensional bleach distribution in confocal and two-photon fluorescence recovery after photobleaching experiments. *Appl Opt,* 46**,** 7401-11.

Mccabe, M. T., Davis, J. N. & Day, M. L. 2005. Regulation of DNA methyltransferase 1 by the pRb/E2F1 pathway. *Cancer Res,* 65**,** 3624-32.

Meissner, A., Mikkelsen, T. S., Gu, H., Wernig, M., Hanna, J., Sivachenko, A., Zhang, X., Bernstein, B. E., Nusbaum, C., Jaffe, D. B., Gnirke, A., Jaenisch, R. & Lander, E. S. 2008. Genome-scale DNA methylation maps of pluripotent and differentiated cells. *Nature,* 454**,** 766-70.

Mellert, K., Lamla, M., Scheffzek, K., Wittig, R. & Kaufmann, D. 2012. Enhancing endosomal escape of transduced proteins by photochemical internalisation. *PLoS One,* 7**,** e52473.

Misteli, T. 2001. Protein dynamics: implications for nuclear architecture and gene expression. *Science,* 291**,** 843-7.

Miyanari, Y., Ziegler-Birling, C. & Torres-Padilla, M. E. 2013. Live visualization of chromatin dynamics with fluorescent TALEs. *Nat Struct Mol Biol,* 20**,** 1321-4.

Moir, R. D., Yoon, M., Khuon, S. & Goldman, R. D. 2000. Nuclear lamins A and B1: different pathways of assembly during nuclear envelope formation in living cells. *J Cell Biol,* 151**,** 1155-68.

Moldovan, G. L., Pfander, B. & Jentsch, S. 2007. PCNA, the maestro of the replication fork. *Cell,* 129**,** 665-79.

Monier, K., Mouradian, S. & Sullivan, K. F. 2007. DNA methylation promotes Aurora-B-driven phosphorylation of histone H3 in chromosomal subdomains. *J Cell Sci,* 120**,** 101-14.

Moore, L. D., Le, T. & Fan, G. 2013. DNA methylation and its basic function. *Neuropsychopharmacology,* 38**,** 23-38.

Morison, I. M., Ramsay, J. P. & Spencer, H. G. 2005. A census of mammalian imprinting. *Trends Genet,* 21**,** 457-65.

Mortusewicz, O., Ame, J. C., Schreiber, V. & Leonhardt, H. 2007. Feedback-regulated poly(ADP-ribosyl)ation by PARP-1 is required for rapid response to DNA damage in living cells. *Nucleic Acids Res,* 35**,** 7665-75.

Mortusewicz, O., Schermelleh, L., Walter, J., Cardoso, M. C. & Leonhardt, H. 2005. Recruitment of DNA methyltransferase I to DNA repair sites. *Proc Natl Acad Sci U S A,* 102**,** 8905-9.

Moscou, M. J. & Bogdanove, A. J. 2009. A simple cipher governs DNA recognition by TAL effectors. *Science,* 326**,** 1501.

Mousli, M., Hopfner, R., Abbady, A. Q., Monte, D., Jeanblanc, M., Oudet, P., Louis, B. & Bronner, C. 2003. ICBP90 belongs to a new family of proteins with an expression that is deregulated in cancer cells. *Br J Cancer,* 89**,** 120-7.

Mueller, F., Morisaki, T., Mazza, D. & Mcnally, J. G. 2012. Minimizing the impact of photoswitching of fluorescent proteins on FRAP analysis. *Biophys J,* 102**,** 1656-65.

Mueller, F., Wach, P. & Mcnally, J. G. 2008. Evidence for a common mode of transcription factor interaction with chromatin as revealed by improved quantitative fluorescence recovery after photobleaching. *Biophys J,* 94**,** 3323-39.

Muller, K. P., Erdel, F., Caudron-Herger, M., Marth, C., Fodor, B. D., Richter, M., Scaranaro, M., Beaudouin, J., Wachsmuth, M. & Rippe, K. 2009. Multiscale analysis of dynamics and interactions of heterochromatin protein 1 by fluorescence fluctuation microscopy. *Biophys J,* 97**,** 2876-85.

Nan, X., Ng, H. H., Johnson, C. A., Laherty, C. D., Turner, B. M., Eisenman, R. N. & Bird, A. 1998. Transcriptional repression by the methyl-CpG-binding protein MeCP2 involves a histone deacetylase complex. *Nature,* 393**,** 386-9.

Neumann, B., Walter, T., Heriche, J. K., Bulkescher, J., Erfle, H., Conrad, C., Rogers, P., Poser, I., Held, M., Liebel, U., Cetin, C., Sieckmann, F., Pau, G., Kabbe, R., Wunsche, A., Satagopam, V., Schmitz, M. H., Chapuis, C., Gerlich, D. W., Schneider, R., Eils, R., Huber, W., Peters, J. M., Hyman, A. A., Durbin, R., Pepperkok, R. & Ellenberg, J. 2010. Phenotypic profiling of the human genome by time-lapse microscopy reveals cell division genes. *Nature,* 464**,** 721-7.

Nishiyama, A., Yamaguchi, L., Sharif, J., Johmura, Y., Kawamura, T., Nakanishi, K., Shimamura, S., Arita, K., Kodama, T., Ishikawa, F., Koseki, H. & Nakanishi, M. 2013. Uhrf1-dependent H3K23 ubiquitylation couples maintenance DNA methylation and replication. *Nature*.

Okano, M., Bell, D. W., Haber, D. A. & Li, E. 1999. DNA methyltransferases Dnmt3a and Dnmt3b are essential for de novo methylation and mammalian development. *Cell,* 99**,** 247-57.

Okuwaki, M. & Verreault, A. 2004. Maintenance DNA methylation of nucleosome core particles. *J Biol Chem,* 279**,** 2904-12.

Padeken, J. & Heun, P. 2013. Centromeres in nuclear architecture. *Cell Cycle,* 12.

Papait, R., Pistore, C., Negri, D., Pecoraro, D., Cantarini, L. & Bonapace, I. M. 2007. Np95 is implicated in pericentromeric heterochromatin replication and in major satellite silencing. *Mol Biol Cell,* 18**,** 1098-106.

Park, Y. J. & Luger, K. 2008. Histone chaperones in nucleosome eviction and histone exchange. *Curr Opin Struct Biol,* 18**,** 282-9.

Pastor, W. A., Aravind, L. & Rao, A. 2013. TETonic shift: biological roles of TET proteins in DNA demethylation and transcription. *Nat Rev Mol Cell Biol,* 14**,** 341-56.

Peng, D. F., Kanai, Y., Sawada, M., Ushijima, S., Hiraoka, N., Kosuge, T. & Hirohashi, S. 2005. Increased DNA methyltransferase 1 (DNMT1) protein expression in precancerous conditions and ductal carcinomas of the pancreas. *Cancer Sci,* 96**,** 403-8.

Peters, A. H., O'carroll, D., Scherthan, H., Mechtler, K., Sauer, S., Schofer, C., Weipoltshammer, K., Pagani, M., Lachner, M., Kohlmaier, A., Opravil, S., Doyle, M., Sibilia, M. & Jenuwein, T. 2001. Loss of the Suv39h histone methyltransferases impairs mammalian heterochromatin and genome stability. *Cell,* 107**,** 323-37.

Phair, R. D., Gorski, S. A. & Misteli, T. 2004a. Measurement of dynamic protein binding to chromatin in vivo, using photobleaching microscopy. *Methods Enzymol,* 375**,** 393-414.

Phair, R. D. & Misteli, T. 2000. High mobility of proteins in the mammalian cell nucleus. *Nature,* 404**,** 604-9.

Phair, R. D., Scaffidi, P., Elbi, C., Vecerova, J., Dey, A., Ozato, K., Brown, D. T., Hager, G., Bustin, M. & Misteli, T. 2004b. Global nature of dynamic protein-chromatin interactions in vivo: three-dimensional genome scanning and dynamic interaction networks of chromatin proteins. *Mol Cell Biol,* 24**,** 6393-402.

Pichler, G., Wolf, P., Schmidt, C. S., Meilinger, D., Schneider, K., Frauer, C., Fellinger, K., Rottach, A. & Leonhardt, H. 2011. Cooperative DNA and histone binding by Uhrf2 links the two major repressive epigenetic pathways. *J Cell Biochem,* 112**,** 2585-93.

Politz, J. C., Scalzo, D. & Groudine, M. 2013. Something silent this way forms: the functional organization of the repressive nuclear compartment. *Annu Rev Cell Dev Biol,* 29**,** 241-70.

Portela, A. & Esteller, M. 2010. Epigenetic modifications and human disease. *Nat Biotechnol,* 28**,** 1057-68.

Probst, A. V. & Almouzni, G. 2011. Heterochromatin establishment in the context of genome-wide epigenetic reprogramming. *Trends Genet,* 27**,** 177-85.

Qin, W. 2011. *Studies of interacting proteins controlling DNA methyltransferase 1.* PhD thesis, Ludwig-Maximilians-Universität.

Qureshi, I. A. & Mehler, M. F. 2010. Epigenetic mechanisms underlying human epileptic disorders and the process of epileptogenesis. *Neurobiol Dis,* 39**,** 53-60.

Rajakumara, E., Wang, Z., Ma, H., Hu, L., Chen, H., Lin, Y., Guo, R., Wu, F., Li, H., Lan, F., Shi, Y. G., Xu, Y., Patel, D. J. & Shi, Y. 2011. PHD finger recognition of unmodified histone H3R2 links UHRF1 to regulation of euchromatic gene expression. *Mol Cell,* 43**,** 275-84.

Ramsahoye, B. H., Biniszkiewicz, D., Lyko, F., Clark, V., Bird, A. P. & Jaenisch, R. 2000. Non-CpG methylation is prevalent in embryonic stem cells and may be mediated by DNA methyltransferase 3a. *Proc Natl Acad Sci U S A,* 97**,** 5237-42.

Rathousky, J., Zukalova, M., Kooyman, P. J. & Zukal, A. 2004. Synthesis and characterization of colloidal MCM-41. *Colloids and Surfaces A: Physicochemical and Engineering Aspects,* 241**,** 81-86.

Reddy, K. L., Zullo, J. M., Bertolino, E. & Singh, H. 2008. Transcriptional repression mediated by repositioning of genes to the nuclear lamina. *Nature,* 452**,** 243-7.

Rhind, N. 2006. DNA replication timing: random thoughts about origin firing. *Nat Cell Biol,* 8**,** 1313-6.

Richardson, B. 2003. Impact of aging on DNA methylation. *Ageing Research Reviews,* 2**,** 245-261.

Robertson, K. D., Uzvolgyi, E., Liang, G., Talmadge, C., Sumegi, J., Gonzales, F. A. & Jones, P. A. 1999. The human DNA methyltransferases (DNMTs) 1, 3a and 3b: coordinate mRNA expression in normal tissues and overexpression in tumors. *Nucleic Acids Res,* 27**,** 2291-8.

Romer, T., Leonhardt, H. & Rothbauer, U. 2011. Engineering antibodies and proteins for molecular in vivo imaging. *Curr Opin Biotechnol,* 22**,** 882-7.

Rothbart, S. B., Dickson, B. M., Ong, M. S., Krajewski, K., Houliston, S., Kireev, D. B., Arrowsmith, C. H. & Strahl, B. D. 2013. Multivalent histone engagement by the linked tandem Tudor and PHD domains of UHRF1 is required for the epigenetic inheritance of DNA methylation. *Genes Dev,* 27**,** 1288-98.

Rothbart, S. B., Krajewski, K., Nady, N., Tempel, W., Xue, S., Badeaux, A. I., Barsyte-Lovejoy, D., Martinez, J. Y., Bedford, M. T., Fuchs, S. M., Arrowsmith, C. H. & Strahl, B. D. 2012. Association of UHRF1 with methylated H3K9 directs the maintenance of DNA methylation. *Nat Struct Mol Biol,* 19**,** 1155-60.

Rottach, A., Frauer, C., Pichler, G., Bonapace, I. M., Spada, F. & Leonhardt, H. 2010. The multi-domain protein Np95 connects DNA methylation and histone modification. *Nucleic Acids Res,* 38**,** 1796-804.

Rouleau, J., Macleod, A. R. & Szyf, M. 1995. Regulation of the DNA methyltransferase by the Ras-AP-1 signaling pathway. *J Biol Chem,* 270**,** 1595-601.

Rountree, M. R., Bachman, K. E. & Baylin, S. B. 2000. DNMT1 binds HDAC2 and a new co-repressor, DMAP1, to form a complex at replication foci. *Nat Genet,* 25**,** 269-77.

Russo, V. E. A., Martienssen, R. A. & Riggs, A. D. 1996. *Epigenetic Mechanisms of Gene Regulation,* Woodbury, Cold Spring Harbor Laboratory Press.

Saito, Y., Kanai, Y., Nakagawa, T., Sakamoto, M., Saito, H., Ishii, H. & Hirohashi, S. 2003. Increased protein expression of DNA methyltransferase (DNMT) 1 is significantly correlated with the malignant potential and poor prognosis of human hepatocellular carcinomas. *Int J Cancer,* 105**,** 527-32.

Saxton, M. J. 2001. Anomalous subdiffusion in fluorescence photobleaching recovery: a Monte Carlo study. *Biophys J,* 81**,** 2226-40.

Schaefer, M. & Lyko, F. 2010. Solving the Dnmt2 enigma. *Chromosoma,* 119**,** 35-40.

Schermelleh, L., Haemmer, A., Spada, F., Rosing, N., Meilinger, D., Rothbauer, U., Cardoso, M. C. & Leonhardt, H. 2007. Dynamics of Dnmt1 interaction with the replication machinery and its role in postreplicative maintenance of DNA methylation. *Nucleic Acids Res,* 35**,** 4301-12.

Schermelleh, L., Heintzmann, R. & Leonhardt, H. 2010. A guide to super-resolution fluorescence microscopy. *J Cell Biol,* 190**,** 165-75.

Schermelleh, L., Spada, F., Easwaran, H. P., Zolghadr, K., Margot, J. B., Cardoso, M. C. & Leonhardt, H. 2005. Trapped in action: direct visualization of DNA methyltransferase activity in living cells. *Nat Methods,* 2**,** 751-6.

Schlossbauer, A., Sauer, A. M., Cauda, V., Schmidt, A., Engelke, H., Rothbauer, U., Zolghadr, K., Leonhardt, H., Brauchle, C. & Bein, T. 2012. Cascaded photoinduced drug delivery to cells from multifunctional core-shell mesoporous silica. *Adv Healthc Mater,* 1**,** 316-20.

Schmiedeberg, L., Weisshart, K., Diekmann, S., Meyer Zu Hoerste, G. & Hemmerich, P. 2004. High- and low-mobility populations of HP1 in heterochromatin of mammalian cells. *Mol Biol Cell,* 15**,** 2819-33.

Schneider, K., Fuchs, C., Dobay, A., Rottach, A., Qin, W., Wolf, P., Alvarez-Castro, J. M., Nalaskowski, M. M., Kremmer, E., Schmid, V., Leonhardt, H. & Schermelleh, L. 2013. Dissection of cell cycle-dependent dynamics of Dnmt1 by FRAP and diffusion-coupled modeling. *Nucleic Acids Res,* 41**,** 4860-76.

Schwille, P., Meyer-Almes, F. J. & Rigler, R. 1997. Dual-color fluorescence cross-correlation spectroscopy for multicomponent diffusional analysis in solution. *Biophys J,* 72**,** 1878-86.

Seisenberger, S., Peat, J. R., Hore, T. A., Santos, F., Dean, W. & Reik, W. 2013. Reprogramming DNA methylation in the mammalian life cycle: building and breaking epigenetic barriers. *Philos Trans R Soc Lond B Biol Sci,* 368**,** 20110330.

Shao, L., Kner, P., Rego, E. H. & Gustafsson, M. G. 2011. Super-resolution 3D microscopy of live whole cells using structured illumination. *Nat Methods,* 8**,** 1044-6.

Sharif, J., Muto, M., Takebayashi, S., Suetake, I., Iwamatsu, A., Endo, T. A., Shinga, J., Mizutani-Koseki, Y., Toyoda, T., Okamura, K., Tajima, S., Mitsuya, K., Okano, M. & Koseki, H. 2007. The SRA protein Np95 mediates epigenetic inheritance by recruiting Dnmt1 to methylated DNA. *Nature,* 450**,** 908-12.

Shen, L., Wu, H., Diep, D., Yamaguchi, S., D'alessio, A. C., Fung, H. L., Zhang, K. & Zhang, Y. 2013. Genome-wide analysis reveals TET- and TDG-dependent 5-methylcytosine oxidation dynamics. *Cell,* 153**,** 692-706.

Shogren-Knaak, M., Ishii, H., Sun, J. M., Pazin, M. J., Davie, J. R. & Peterson, C. L. 2006. Histone H4-K16 acetylation controls chromatin structure and protein interactions. *Science,* 311**,** 844-7.

Siebrasse, J. P., Grunwald, D. & Kubitscheck, U. 2007. Single-molecule tracking in eukaryotic cell nuclei. *Anal Bioanal Chem,* 387**,** 41-4.

Slowing, Ii, Vivero-Escoto, J. L., Wu, C. W. & Lin, V. S. 2008. Mesoporous silica nanoparticles as controlled release drug delivery and gene transfection carriers. *Adv Drug Deliv Rev,* 60**,** 1278-88.

Smith, Z. D. & Meissner, A. 2013. DNA methylation: roles in mammalian development. *Nat Rev Genet,* 14**,** 204-20.

Sokolov, I. M. 2012. Models of anomalous diffusion in crowded environments. *Soft Matter,* 8**,** 9043.

Somanathan, S., Suchyna, T. M., Siegel, A. J. & Berezney, R. 2001. Targeting of PCNA to sites of DNA replication in the mammalian cell nucleus. *J Cell Biochem,* 81**,** 56-67.

Song, J., Rechkoblit, O., Bestor, T. H. & Patel, D. J. 2011. Structure of DNMT1-DNA complex reveals a role for autoinhibition in maintenance DNA methylation. *Science,* 331**,** 1036-40.

Spector, D. L. 2001. Nuclear domains. *J Cell Sci,* 114**,** 2891-3.

Sporbert, A., Gahl, A., Ankerhold, R., Leonhardt, H. & Cardoso, M. C. 2002. DNA polymerase clamp shows little turnover at established replication sites but sequential de novo assembly at adjacent origin clusters. *Mol Cell,* 10**,** 1355-65.

Sprague, B. L. & Mcnally, J. G. 2005. FRAP analysis of binding: proper and fitting. *Trends Cell Biol,* 15**,** 84-91.

Sprague, B. L., Muller, F., Pego, R. L., Bungay, P. M., Stavreva, D. A. & Mcnally, J. G. 2006. Analysis of binding at a single spatially localized cluster of binding sites by fluorescence recovery after photobleaching. *Biophys J,* 91**,** 1169-91.

Sprague, B. L., Pego, R. L., Stavreva, D. A. & Mcnally, J. G. 2004. Analysis of binding reactions by fluorescence recovery after photobleaching. *Biophys J,* 86**,** 3473-95.

Spruijt, C. G., Gnerlich, F., Smits, A. H., Pfaffeneder, T., Jansen, P. W., Bauer, C., Munzel, M., Wagner, M., Muller, M., Khan, F., Eberl, H. C., Mensinga, A., Brinkman, A. B., Lephikov, K., Muller, U., Walter, J., Boelens, R., Van Ingen, H., Leonhardt, H., Carell, T. & Vermeulen, M. 2013. Dynamic readers for 5-(hydroxy)methylcytosine and its oxidized derivatives. *Cell,* 152**,** 1146-59.

Stasevich, T. J., Mueller, F., Brown, D. T. & Mcnally, J. G. 2010. Dissecting the binding mechanism of the linker histone in live cells: an integrated FRAP analysis. *EMBO J,* 29**,** 1225-34.

Tahiliani, M., Koh, K. P., Shen, Y., Pastor, W. A., Bandukwala, H., Brudno, Y., Agarwal, S., Iyer, L. M., Liu, D. R., Aravind, L. & Rao, A. 2009. Conversion of 5-methylcytosine to 5-hydroxymethylcytosine in mammalian DNA by MLL partner TET1. *Science,* 324**,** 930-5.

Takeshita, K., Suetake, I., Yamashita, E., Suga, M., Narita, H., Nakagawa, A. & Tajima, S. 2011. Structural insight into maintenance methylation by mouse DNA methyltransferase 1 (Dnmt1). *Proc Natl Acad Sci U S A,* 108**,** 9055-9.

Thanisch, K., Schneider, K., Morbitzer, R., Solovei, I., Lahaye, T., Bultmann, S. & Leonhardt, H. 2013. Targeting and tracing of specific DNA sequences with dTALEs in living cells. *Nucleic Acids Res*.

Trembecka, D. O., Kuzak, M. & Dobrucki, J. W. 2010. Conditions for using FRAP as a quantitative technique--influence of the bleaching protocol. *Cytometry A,* 77**,** 366-70.

Trojer, P. & Reinberg, D. 2007. Facultative heterochromatin: is there a distinctive molecular signature? *Mol Cell,* 28**,** 1-13.

Tuorto, F., Liebers, R., Musch, T., Schaefer, M., Hofmann, S., Kellner, S., Frye, M., Helm, M., Stoecklin, G. & Lyko, F. 2012. RNA cytosine methylation by Dnmt2 and NSun2 promotes tRNA stability and protein synthesis. *Nat Struct Mol Biol,* 19**,** 900-5.

Uemura, T., Kubo, E., Kanari, Y., Ikemura, T., Tatsumi, K. & Muto, M. 2000. Temporal and spatial localization of novel nuclear protein NP95 in mitotic and meiotic cells. *Cell Struct Funct,* 25**,** 149-59.

Unoki, M., Brunet, J. & Mousli, M. 2009. Drug discovery targeting epigenetic codes: the great potential of UHRF1, which links DNA methylation and histone modifications, as a drug target in cancers and toxoplasmosis. *Biochem Pharmacol,* 78**,** 1279-88.

Van Attikum, H. & Gasser, S. M. 2005. The histone code at DNA breaks: a guide to repair? *Nat Rev Mol Cell Biol,* 6**,** 757-65.

Van Royen, M. E., Farla, P., Mattern, K. A., Geverts, B., Trapman, J. & Houtsmuller, A. B. 2009. Fluorescence Recovery After Photobleaching (FRAP) to Study Nuclear Protein Dynamics in Living Cells. *Methods Mol Biol,* 464**,** 363-85.

Vickaryous, M. K. & Hall, B. K. 2006. Human cell type diversity, evolution, development, and classification with special reference to cells derived from the neural crest. *Biol Rev Camb Philos Soc,* 81**,** 425-55.

Vogel, M. C., Papadopoulos, T., Muller-Hermelink, H. K., Drahovsky, D. & Pfeifer, G. P. 1988. Intracellular distribution of DNA methyltransferase during the cell cycle. *FEBS Lett,* 236**,** 9-13.

Vomastek, T., Iwanicki, M. P., Burack, W. R., Tiwari, D., Kumar, D., Parsons, J. T., Weber, M. J. & Nandicoori, V. K. 2008. Extracellular signal-regulated kinase 2 (ERK2) phosphorylation sites and docking domain on the nuclear pore complex protein Tpr cooperatively regulate ERK2-Tpr interaction. *Mol Cell Biol,* 28**,** 6954-66.

Wachsmuth, M., Waldeck, W. & Langowski, J. 2000. Anomalous diffusion of fluorescent probes inside living cell nuclei investigated by spatially-resolved fluorescence correlation spectroscopy. *J Mol Biol,* 298**,** 677-89.

Wang, C., Shen, J., Yang, Z., Chen, P., Zhao, B., Hu, W., Lan, W., Tong, X., Wu, H., Li, G. & Cao, C. 2011. Structural basis for site-specific reading of unmodified R2 of histone H3 tail by UHRF1 PHD finger. *Cell Res,* 21**,** 1379-82.

Winkelmann, J., Lin, L., Schormair, B., Kornum, B. R., Faraco, J., Plazzi, G., Melberg, A., Cornelio, F., Urban, A. E., Pizza, F., Poli, F., Grubert, F., Wieland, T., Graf, E., Hallmayer, J., Strom, T. M. & Mignot, E. 2012. Mutations in DNMT1 cause autosomal dominant cerebellar ataxia, deafness and narcolepsy. *Hum Mol Genet,* 21**,** 2205-10.

Xie, S., Jakoncic, J. & Qian, C. 2012. UHRF1 double tudor domain and the adjacent PHD finger act together to recognize K9me3-containing histone H3 tail. *J Mol Biol,* 415**,** 318-28.

Xiong, R., Deschout, H., Demeester, J., De Smedt, S. C. & Braeckmans, K. 2014. Rectangle FRAP for Measuring Diffusion with a Laser Scanning Microscope. *Methods Mol Biol,* 1076**,** 433-41.

Xu, K., Babcock, H. P. & Zhuang, X. 2012. Dual-objective STORM reveals three-dimensional filament organization in the actin cytoskeleton. *Nat Methods,* 9**,** 185-8.

Xu, S. & Powers, M. A. 2013. In vivo analysis of human nucleoporin repeat domain interactions. *Mol Biol Cell,* 24**,** 1222-31.

Yang, X., Noushmehr, H., Han, H., Andreu-Vieyra, C., Liang, G. & Jones, P. A. 2012. Gene reactivation by 5-aza-2'-deoxycytidine-induced demethylation requires SRCAP-mediated H2A.Z insertion to establish nucleosome depleted regions. *PLoS Genet,* 8**,** e1002604.

Zemach, A., Mcdaniel, I. E., Silva, P. & Zilberman, D. 2010. Genome-wide evolutionary analysis of eukaryotic DNA methylation. *Science,* 328**,** 916-9.

Zentner, G. E. & Henikoff, S. 2013. Regulation of nucleosome dynamics by histone modifications. *Nat Struct Mol Biol,* 20**,** 259-66.

Zhang, Z., Wippo, C. J., Wal, M., Ward, E., Korber, P. & Pugh, B. F. 2011. A packing mechanism for nucleosome organization reconstituted across a eukaryotic genome. *Science,* 332**,** 977-80.

Zilberman, D., Coleman-Derr, D., Ballinger, T. & Henikoff, S. 2008. Histone H2A.Z and DNA methylation are mutually antagonistic chromatin marks. *Nature,* 456**,** 125-9.

Ziller, M. J., Muller, F., Liao, J., Zhang, Y., Gu, H., Bock, C., Boyle, P., Epstein, C. B., Bernstein, B. E., Lengauer, T., Gnirke, A. & Meissner, A. 2011. Genomic distribution and inter-sample variation of non-CpG methylation across human cell types. *PLoS Genet,* 7**,** e1002389.

4.2 Abbreviations

3D-SIM: three-dimensional space structured illumination microscopy

5caC: 5-carboxcytosin

5fC: 5-formylcytosin

5hmC: 5-hydroxymethylcytosin

5hmU: 5-hydroxyuracil

5mC: 5-methylcytosin

Ac: acetylation

ADCA-DN: autosomal dominant cerebellar ataxia, deafness and narcolepsy

AID: activation induced cytidine deaminase

APOBEC: apolipoprotein B mRNA editing enzyme, catalytic polypeptide-like

BAH: bromo adjacent homology

BBD: bar body deficient

BER: base excision repair

BrdU: bromodeoxyuridine

CpG: cytosine-phosphatidyl-guanine

Da: dalton

D_f : diffusion coefficient

DMAP1: Dnmt1-associated protein 1

Dnmt: DNA methyltransferase

dTALE: designer transcription activator-like effector

EdU: ethynyldeoxyuridine

ER: endoplasmic reticulum

ERAD: ER-associated degradation

ERK2: extracellular signal-regulated kinase

ESC: embryonic stem cell

Fab: fragment antigen-binding

FCCS: fluorescence cross correlation spectroscopy

FCS: fluorescence correlation spectroscopy

FLIM: fluorescence lifetime imaging microscopy

FLIP: fluorescence loss in photobleaching

FRAP: fluorescence recovery after photobleaching

FRET: Förster resonance energy transfer

GFP: green fluorescent protein

HDAC: histone deacetylase

HSAN1: hereditary sensory and autonomic neuropathy type 1

k_{off} : dissociation rate

k_{on}: association rate

MBD: methyl-CpG-binding domain

MBP: methyl-CpG-binding protein

MC: mobility class

Me: methylation

MF: mobile fraction

ms: major satellite

NIPA: nuclear interaction partner of anaplastic lymphoma kinase

NLS: nuclear localization signal

NuA4: nucleosomal acetyltransferase of H4

p400: E1A-binding protein p400

PALM: photoactivated localization microscopy

PBD: PCNA binding domain

PBHD: polybromo homology domain

PCNA: proliferating cell nuclear antigen

PHD: plant homeodomain

PZF: polydactyl zinc finger

RFC: replication factor C

RFP: red fluorescent protein

RICS: raster scan image correlation spectroscopy

RING: really interesting new gene

ROI: region of interest

RVD: repeat-variable-diresidue

s: second

SAM: S-adenosyl-L-methionine

SET: Suv39, Enhancer-of-zeste, Trithorax

SPR: surface plasmon resonance

SPT: single particle tracking

SRA: SET and RING associated

SRCAP: Snf2-Related CREBBP activator protein

STED: stimulated emission depletion

STORM: direct stochastic optical reconstruction microscopy

Suv: suppressor of Variegation

$t_{1/2}$: half time recovery

TDG: thymine-DNA glycosylase

Tet: ten-eleven- translocation

Tip60: Tat-interactive protein 60

TIRF: total internal reflection fluorescence

TPR: translated promoter region

T_{res}: mean residence time

TS: targeting sequence

TTD: tandem tudor domain

Ub: ubiquitination

Ubc9: ubiquitin carrier protein

Ubl: ubiquitin-like

Uhrf: ubiquitin-like, containing PHD and RING finger domains

wt: wild type

ZnF: zinc finger

4.3 List of publications

1. Pichler G, Wolf P, Schmidt CS, Meilinger D, **Schneider K**, Frauer C, Fellinger K , Rottach A and Leonhardt H (**2011**). Cooperative DNA and histone binding by Uhrf2 links the two major repressive epigenetic pathways. **J. Cell Biochem.**, 112, 2585-93.

2. Cardoso MC, **Schneider K**, Martin RM and Leonhardt H (**2012**). Structure, function and dynamics of nuclear subcompartments. **Curr Opin Cell Biol.**, 24, 79-85.

3. Lebold T, Schlossbauer A, **Schneider K**, Schermelleh L, Leonhardt H, Bein T and Bräuchle C (**2012**). Controlling the mobility of oligonucleotides in the nanochannels of Mesoporous Silica. **Adv Funct Mater**, 22, 106-112.

4. Bönisch C, **Schneider K**, Pünzeler S, Wiedemann SM, Bielmeier C, Bocola M, Eberl HC, Kuegel W, Neumann J, Kremmer E, Leonhardt H, Mann M, Michaelis J, Schermelleh L and Hake SB (**2012**). H2A.Z.2.2 is an alternatively spliced histone H2A.Z variant that causes severe nucleosome destabilization. **Nucleic Acids Res.**, 40, 5951-64.

5. **Schneider K***, Fuchs C*, Dobay A, Rottach A, Qin W, Wolf P, Álvarez-Castro J, Nalaskowski M, Kremmer E, Schmid V, Leonhardt H and Schermelleh L (**2013**). Dissection of cell cycle-dependent dynamics of Dnmt1 by FRAP and diffusion-coupled modeling. **Nucleic Acids Res.**, 41, 4860-4876. * Joint first authors

6. Thanisch K, **Schneider K**, Morbitzer R, Solovei I, Lahaye T, Bultmann S, and Leonhardt H (**2013**). Targeting and tracing of specific DNA sequences with dTALEs in living cells. **Nucleic Acids Res.**

7. Feilke M, **Schneider K** and Schmid V. Bayesian simultaneous analysis of a series of FRAP images. **Under review at Stat Appl Genet Mol Biol.**

8. Kulinski M*, **Schneider K***, Illert AL, Lemeer S, Kuster B, Leonhardt H and Duyster J. Cyclin B1 degrading F-box protein NIPA is localized to the nuclear pore complex. **Manuscript in preparation**. * Joint first authors

4.4 Contributions

Declaration of contributions to "Dissection of cell cycle-dependent dynamics of Dnmt1 by FRAP and diffusion-coupled modeling"

This project was conceived by Heinrich Leonhardt, Lothar Schermelleh and Akos Dobay. I performed all biological experiments, except the experiments resulting in the data presented in supplementary figure 1 and 10. Together with Christiane Fuchs, Lothar Schermelleh, Volker Schmid and Akos Dobay, I refined the FRAP evaluation and the mathematical model. Furthermore, I evaluated the FRAP data. Christiane Fuchs developed the mathematical model as well as the corresponding model choice criteria, wrote the software and estimated the model parameters. I wrote the first draft of the manuscript, except the method sections "Mathematical Model", "Model choice", "Parameter estimation" and "Numerics" (supplementary methods), which were written by Christiane Fuchs. In addition, I finalized the manuscript together with Lothar Schermelleh, Christiane Fuchs and Heinrich Leonhardt and prepared the figures together with Lothar Schermelleh.

Declaration of contributions to "Cooperative DNA and Histone Binding by Uhrf2 Links the Two Major Repressive Epigenetic Pathways"

For this project, I established the strategy to perform and evaluate the FRAP experiments and automatized the latter. Then, I carried out and evaluated the FRAP experiments together with Patricia Wolf. Furthermore, I helped assemble the Figure 3C and the corresponding results and method sections. Together with Patricia Wolf, I acquired and processed the images for the cover picture.

Declaration of contributions to "H2A.Z.2.2 is an alternatively spliced histone H2A.Z variant that causes severe nucleosome destabilization"

Together with Lothar Schermelleh, I established the strategy to perform and evaluate the FRAP experiments with a very long observation time. In addition, I created the tools for the automated FRAP evaluation. Christina Bielmeier and I performed and evaluated the FRAP experiments. The curve fitting strategy was established by Jürgen Neumann, assisted by Lothar Schermelleh and me. Fitting of the curves was carried out by Jürgen Neumann and I further organized the results. With the help of Lothar Schermelleh, I assembled the Figure 3B-D and supplementary figure S3A-C, E. In the end, I proofread the manuscript.

Declaration of contributions to "Structure, function and dynamics of nuclear subcompartments"

I prepared figure 2, assisted Heinrich Leonhardt with literature research and proofread the manuscript.

Declaration of contributions to "Cyclin B1 degrading F-box protein NIPA is localized to the nuclear pore complex"

I conceived and developed this project together with Michal Kulinski and performed and evaluated all microscopy related experiments (FRAP, FLIP, long-term imaging, immunofluorescence, confocal spinning disc microscopy and 3D-SIM). Moreover, I prepared and wrote the corresponding figures and method sections, respectively. The first draft of the manuscript was written by Michal Kulinski and complemented by me.

Declaration of contributions to "Targeting and tracing of specific DNA sequences with dTALEs in living cells"

I carried out the initial experiments and developed the strategy to perform and evaluate the FRAP and FLIP experiments. Further FRAP, FLIP and long-term imaging experiments were performed by Katharina Thanisch and me. Moreover, I evaluated the FRAP and FLIP experiments and created figure 3, supplementary figure 4 and the supplementary movie. I wrote the first draft of the results part "Analysis of *in vivo* protein dynamics reveals a strong but dynamic association of the GFP-msTALE with CCs", the method sections "Live cell microscopy, fluorescence loss in photobleaching and quantitative fluorescence recovery after photobleaching analysis" and proofread the manuscript.

Declaration of contributions to "Controlling The Mobility Of Oligonucleotides In The Nanochannels Of Mesoporous Silica"

I evaluated the FRAP data using a protocol that was developed together with Lothar Schermelleh, organized the data and assisted Akos Dobay in the application of the kinetic model. Furthermore, I proofread the manuscript.

Declaration of contributions to "Bayesian simultaneous analysis of multiple FRAP images with mixed-effect priors"

I provided the data that has been also used to a large extend in Schneider et al., 2013 "Dissection of cell cycle-dependent dynamics of Dnmt1 by FRAP and diffusion-coupled modeling". Furthermore, I commented on the manuscript and proofread it.

4.5 Declaration

Eidesstattliche Erklärung

Ich versichere hiermit an Eides statt, dass die vorgelegte Dissertation von mir selbständig und ohne unerlaubte Hilfe angefertigt ist.

München, den ....

(Unterschrift)

Erklärung

Hiermit erkläre ich, *

☐ dass die Dissertation nicht ganz oder in wesentlichen Teilen einer anderen Prüfungskommission vorgelegt worden ist.

☐ dass ich mich anderweitig einer Doktorprüfung ohne Erfolg **nicht** unterzogen habe.

☐ dass ich mich mit Erfolg der Doktorprüfung im Hauptfach .....

und in den Nebenfächern .....

bei der Fakultät für ..... der .....

(Hochschule/Universität)

unterzogen habe.

☐ dass ich ohne Erfolg versucht habe, eine Dissertation einzureichen oder mich der Doktorprüfung zu unterziehen.

München, den..... .....

(Unterschrift)

*) Nichtzutreffendes streichen

4.6 Acknowledgment

This work would not have been possible without the great support of many persons to whom I want to address my gratitude here:

First of all, I would like to thank my doctor father and supervisor **Prof. Dr. Heinrich Leonhardt**. I am very grateful for the unique opportunity to conduct my PhD thesis in your group. Thanks for many fruitful discussions about ongoing projects as well as future plans, for the appreciation of my work and for constant support throughout the entire period of my PhD. The time in your lab not only influenced my scientific, but also my personal development.

Many thanks also to **Dr. Lothar Schermelleh,** who supervised me in a large part of my PhD. Thank you for your support, for always motivating and encouraging me and for introducing me to the world of microscopy and image analysis. Special thanks for the numerous scientific discussions, always leading to new ideas and approaches.

I would like to thank **all collaboration partners**. I am very grateful for the opportunity to make a contribution to wonderful collaborations and to work with excellent scientists. Thank you for the great atmosphere and for everything I have learned from you. A special thank you goes to the people, I worked closely with: **Dr. Christiane Fuchs (great thanks for your hard work), Dr. Michal Kulinski, Dr. Clemens Bönisch, Antonia Jack, Dr. Sandra Hake, Dr. Timo Lebold, Dr. Robert Morbitzer, Martina Feilke and Prof. Volker Schmid**.

I am grateful to the external members of my thesis advisory committee, **Dr. Sandra Hake** and **Prof. Jens Michaelis**, for the interest in my work, the motivating discussions and valuable feedback during the meetings.

I thank **Dr. Hans-Jörg Schäffer, Dr. Ingrid Wolf** and **Maxi Reif** from the IMPRS coordination office for the financial support and the great time I had during all the IMPRS seminars, soft skill workshops and retreats. I am grateful to be part of such a wonderful PhD program. Thanks also to my IMPRS colleagues, who are a great support. I would like to thank the IDK-NBT for the financial support and the organization of the interesting lectures and workshops. Special thanks to **Marilena Pinto, Dr. Marie-Christine Blüm** and **Dr. Susanne Henning**.

A very big thank you goes to **all members of the Leonhardt group** for the very friendly and supportive atmosphere. A special thank you goes to **Katharina, Patricia, Andrea, Garwin, Sebastian, Irina, Weihua, Christine, Christina (Bielmeier), Danny** and **Karin** for the joint efforts on scientific projects. **Anja** and **Susanne**, thank you for helping me patiently with all the big, small and tiny problems and for organizing the lab and very enjoyable events. I would like to thank the “microscopy team” including **Andreas, Jürgen, Yolanda, Barbara, Daniel, Hartmann, Sebastian, Irina** for great discussions, great

support and for everything I have learned from you. Thanks to Anna, Julia, Anke and Veronica for your interest and your great commitment to the projects. I thank **Weihua, Daniel, Wen, Nan, Katharina, Patricia, Mengxi and Elisabeth** for the great atmosphere in both offices.

Ein besonderer Dank geht an meine **Familie**. Besonders an meine Eltern, die mich immer unterstützt und ermutigt haben. Ohne Euch wäre diese Arbeit nicht möglich gewesen wäre.

Am Ende möchte ich noch meinem Freund **Ulli** danken. Vielen Dank, dass du an meiner Seite bist. Danke für deine Unterstützung und Motivation, aber auch dafür, dass du mir immer wieder klar machst wie wichtig das Leben neben der Arbeit ist.